

# DEVELOPMENT AND APPLICATION OF BITUMINOUS MATERIALS FOR CIVIL INFRASTRUCTURES

EDITED BY: Hui Yao, Zhanping You, Dawei Wang, Feng Li, Yue Hou and  
Jie Ji

PUBLISHED IN: *Frontiers in Materials*



# frontiers

## Frontiers eBook Copyright Statement

The copyright in the text of individual articles in this eBook is the property of their respective authors or their respective institutions or funders. The copyright in graphics and images within each article may be subject to copyright of other parties. In both cases this is subject to a license granted to Frontiers.

The compilation of articles constituting this eBook is the property of Frontiers.

Each article within this eBook, and the eBook itself, are published under the most recent version of the Creative Commons CC-BY licence.

The version current at the date of publication of this eBook is CC-BY 4.0. If the CC-BY licence is updated, the licence granted by Frontiers is automatically updated to the new version.

When exercising any right under the CC-BY licence, Frontiers must be attributed as the original publisher of the article or eBook, as applicable.

Authors have the responsibility of ensuring that any graphics or other materials which are the property of others may be included in the CC-BY licence, but this should be checked before relying on the CC-BY licence to reproduce those materials. Any copyright notices relating to those materials must be complied with.

Copyright and source acknowledgement notices may not be removed and must be displayed in any copy, derivative work or partial copy which includes the elements in question.

All copyright, and all rights therein, are protected by national and international copyright laws. The above represents a summary only. For further information please read Frontiers' Conditions for Website Use and Copyright Statement, and the applicable CC-BY licence.

ISSN 1664-8714

ISBN 978-2-88971-541-1

DOI 10.3389/978-2-88971-541-1

## About Frontiers

Frontiers is more than just an open-access publisher of scholarly articles: it is a pioneering approach to the world of academia, radically improving the way scholarly research is managed. The grand vision of Frontiers is a world where all people have an equal opportunity to seek, share and generate knowledge. Frontiers provides immediate and permanent online open access to all its publications, but this alone is not enough to realize our grand goals.

## Frontiers Journal Series

The Frontiers Journal Series is a multi-tier and interdisciplinary set of open-access, online journals, promising a paradigm shift from the current review, selection and dissemination processes in academic publishing. All Frontiers journals are driven by researchers for researchers; therefore, they constitute a service to the scholarly community. At the same time, the Frontiers Journal Series operates on a revolutionary invention, the tiered publishing system, initially addressing specific communities of scholars, and gradually climbing up to broader public understanding, thus serving the interests of the lay society, too.

## Dedication to Quality

Each Frontiers article is a landmark of the highest quality, thanks to genuinely collaborative interactions between authors and review editors, who include some of the world's best academicians. Research must be certified by peers before entering a stream of knowledge that may eventually reach the public - and shape society; therefore, Frontiers only applies the most rigorous and unbiased reviews.

Frontiers revolutionizes research publishing by freely delivering the most outstanding research, evaluated with no bias from both the academic and social point of view. By applying the most advanced information technologies, Frontiers is catapulting scholarly publishing into a new generation.

## What are Frontiers Research Topics?

Frontiers Research Topics are very popular trademarks of the Frontiers Journals Series: they are collections of at least ten articles, all centered on a particular subject. With their unique mix of varied contributions from Original Research to Review Articles, Frontiers Research Topics unify the most influential researchers, the latest key findings and historical advances in a hot research area! Find out more on how to host your own Frontiers Research Topic or contribute to one as an author by contacting the Frontiers Editorial Office: [frontiersin.org/about/contact](http://frontiersin.org/about/contact)



# DEVELOPMENT AND APPLICATION OF BITUMINOUS MATERIALS FOR CIVIL INFRASTRUCTURES

Topic Editors:

**Hui Yao**, Beijing University of Technology, China

**Zhanping You**, Michigan Technological University, United States

**Dawei Wang**, RWTH Aachen University, Germany

**Feng Li**, Beihang University, China

**Yue Hou**, Beijing University of Technology, China

**Jie Ji**, Beijing University of Civil Engineering and Architecture, China

**Citation:** Yao, H., You, Z., Wang, D., Li, F., Hou, Y., Ji, J., eds. (2021). Development and Application of Bituminous Materials for Civil Infrastructures.

Lausanne: Frontiers Media SA. doi: 10.3389/978-2-88971-541-1

# Table of Contents

05	<b><i>Editorial: Development and Application of Bituminous Materials for Civil Infrastructures</i></b>
	Zhanping You, Jie Ji, Dawei Wang, Feng Li, Hui Yao and Yue Hou
07	<b><i>Analysis of Composite Skeleton Characteristics of Recycled Asphalt Mixture via Weight Analysis Method</i></b>
	Han Xiao, Yuzhuang Qiu, Kuanghuai Wu, Wenke Huang, Ruida Zhang, Li Chen, Xu Cai and Qiang Luo
16	<b><i>Comprehensive Laboratory Evaluations and a Proposed Mix Design Procedure for Cement-Stabilized Cohesive and Granular Soils</i></b>
	Yi Yang, Shengting Li, Cheng Li, Lijian Wu, Lvzhen Yang, Ping Zhang and Tuo Huang
27	<b><i>An Indoor Laboratory Simulation and Evaluation on the Aging Resistance of Polyether Polyurethane Concrete for Bridge Deck Pavement</i></b>
	Shifa Xu, Meng Xu, Yexing Zhang, Yutao Guo, Geng Peng and Ying Xu
37	<b><i>Study on Preparation Method of Terminal Blend Rubberized Asphalt Binder</i></b>
	Juan Xie, Yongning Zhang and Yueming Yang
49	<b><i>Composition Optimization and Field Application of Colored Emulsified Asphalt Seal Mixture</i></b>
	Zhilin Sun, Zhihang Zhu, Junhui Zhang and Chao Wu
58	<b><i>Effects of Tire Pressures and Test Temperatures on Permanent Deformation of Direct Coal Liquefaction Residue Mixture</i></b>
	Suo Zhi, Ji Jie, Zhang Ran, Wang Zhe, Yao Hui and Jin Dongzhao
67	<b><i>Experimental Investigation on Uniaxial Unconfined Compressive Properties of Ice on Asphalt Pavement Surface</i></b>
	Wei Luo, Hancheng Dan, Runzhong Zeng, Yao Rong and Dian Xie
77	<b><i>Analysis of the Influence of Temperature Field on the Dynamic Modulus of Rubber Asphalt Pavement</i></b>
	Guoqing Wang, Xinqiang Wang, Zhanyou Yan, Lusheng Qin and Zhanhua Gao
88	<b><i>Aging Properties and Mechanism of Microwave-Activated Crumb Rubber Modified Asphalt Binder</i></b>
	Tao Zhou, Jianing Zhou, Qidong Li and Bo Li
102	<b><i>Rutting Performance of Semi-Rigid Base Pavement in RIOHTrack and Laboratory Evaluation</i></b>
	Sheng Li, Mengmeng Fan, Lukai Xu, Wendi Tian, Huanan Yu and Ke Xu
112	<b><i>An Experimental Investigation on the Repairing Performance and Fatigue Life of Asphalt Pavement Potholes With an Inclined Interface Joint</i></b>
	Linyu Li, Yangquan Huang, Zhutao Shao and Dongya Ren
124	<b><i>Effect of Gradation Variability on Volume Parameter and Key Performances of HMA</i></b>
	Shutang Liu, Lin Zhu, Huiqin Zhang, Tao Liu, Ping Ji and Weidong Cao

- 135** *Shear Fatigue Performance of Epoxy Resin Waterproof Adhesive Layer on Steel Bridge Deck Pavement*  
Ying Xu, Xinpeng Lv, Chunfeng Ma, Fengming Liang, Jiafei Qi, Zhijing Chou and Shifa Xu
- 146** *Study on Quantitative Characterization of Morphological Characteristics and High Temperature Performance Evaluation of Coarse Aggregate Based on Computer Vision*  
Zhanliang Liu, Chen Zhang, Linlong Shao and Jiangfeng Wang
- 158** *The Self-Healing Performance of Carbon-Based Nanomaterials Modified Asphalt Binders Based on Molecular Dynamics Simulations*  
Yan Gong, Jian Xu, Er-hu Yan and Jun-hua Cai
- 170** *BIC-Based Data-Driven Rail Track Deterioration Adaptive Piecewise Modeling Framework*  
Yaqin Yang, Peng Xu, Guotao Yang, Long Chen and Junbo Li
- 181** *Relation Between Adhesion Properties and Microscopic Characterization of Polyphosphoric Acid Composite SBS Modified Asphalt Binder*  
Liangying Li, Zhiwei Li, Yongning Wang, Xiaolan Li and Bo Li
- 192** *Compaction Characteristics of Cold Recycled Mixtures with Asphalt Emulsion and Their Influencing Factors*  
Decai Wang, Hui Yao, Jinchao Yue, Shengneng Hu, Junfu Liu, Mei Xu and Siyu Chen
- 203** *Study on the Properties and Mechanisms of a Cement-Stabilized Aggregate Mixture With Vibration Mixing*  
Ping Li, Di Wei, Dongmei Zhang, Jianping Xiong and Sheng Xu



# Editorial: Development and Application of Bituminous Materials for Civil Infrastructures

Zhanping You<sup>1</sup>, Jie Ji<sup>2</sup>, Dawei Wang<sup>3</sup>, Feng Li<sup>4</sup>, Hui Yao<sup>5\*</sup> and Yue Hou<sup>5</sup>

<sup>1</sup>Department of Civil and Environmental Engineering, Michigan Technological University, Houghton, MI, United States, <sup>2</sup>School of Civil and Transportation Engineering, Beijing University of Civil Engineering and Architecture, Beijing, China, <sup>3</sup>Institute of Highway Engineering, RWTH Aachen University, Aachen, Germany, <sup>4</sup>School of Transportation Science and Engineering, Beihang University, Beijing, China, <sup>5</sup>Faculty of Architecture, Civil and Transportation Engineering, Beijing University of Technology, Beijing, China

**Keywords:** civil engineering, pavement materials, test method, characterization method, numerical simulation

## Editorial on the Research Topic

### Development and Application of Bituminous Materials for Civil Infrastructures

Pavement maintenance has become increasingly important with recent developments in the auto industry. Pavement distress affects pavement quality and service life, which in turn affects people's daily lives. Innovative pavement materials and technologies need to be developed to enable pavement to serve its purposes, especially looking to bituminous materials. A series of engineering problems can be solved by developing advanced characterization methods and new materials through the existing and innovative test and simulation methods.

The international journal "Frontiers in Materials" is a high-visibility journal publishing rigorously peer-reviewed research across the entire breadth of materials science and engineering. This special issue "Development and Application of Bituminous Materials for Civil Infrastructures" focuses on the recent development or emerging technologies of bituminous materials. The research areas of this special issue cover three sections: advanced pavement materials, advanced test methods and simulation models.

## OPEN ACCESS

### Edited and reviewed by:

John L. Provis,  
The University of Sheffield,  
United Kingdom

### \*Correspondence:

Hui Yao  
huiyao@mtu.edu

**Received:** 22 July 2021

**Accepted:** 25 August 2021

**Published:** 08 September 2021

### Citation:

You Z, Ji J, Wang D, Li F, Yao H and Hou Y (2021) Editorial: Development and Application of Bituminous Materials for Civil Infrastructures. *Front. Mater.* 8:745392. doi: 10.3389/fmats.2021.745392

- 1) Advanced Pavement Materials: Polyether polyurethane concrete (PPC) is proposed as a new pavement material for bridge decks. Test results show that the anti-aging and overall pavement performance were improved compared to traditional and Styrene-Butadiene-Styrene (SBS) modified asphalt mixtures (Xu et al.). Direct Coal Liquefaction Residue (DCLR) was used to improve the performance of asphalt mixtures and the permanent deformation was investigated with different tire pressures and temperatures (Zhi et al.). The uniform test design method of a colored emulsified asphalt seal mixture (CEASM) was proposed and different tests were used to study the various performance indicators, including storage stability, wear resistance, anti-slide, and color durability (Sun et al.). Different types of rubbers were used in the asphalt mixtures to form different structural layers in asphalt pavement. The dynamic moduli of asphalt mixtures under different temperatures were studied (Wang et al.). An effective mixing method was proposed to improve the high-temperature performance of Terminal Blend (TB) asphalt rubber. A series of tests was employed to evaluate and verify the performance of TB asphalt rubbers (Xie et al.). The shear fatigue life and performance of the epoxy resin waterproof adhesive layer were investigated with different temperatures, stress levels, and quantities of coating layer on bridge deck pavement. More coating on the pavement can improve the resistance to interlaminar shear fatigue failure (Xu et al.). Different modifiers were used to modify the asphalt binder, including SBS, Polyphosphoric Acids (PPA), furfural extraction oil, and dibutyl phthalate (DBP). The

adhesive properties of different asphalt binders were examined (Li et al.). Many types of granular soil materials from construction fields were mixed with different cement contents. The unconfined compressive strength was strongly related to soil properties and cement contents (Yang et al.). The effect of vibration mixing on the performance of cement-based mixtures was researched. Vibration mixing improved the dispersion uniformity of cement in aggregates and significantly enhanced the bonding strength between the cement and aggregates (Li et al.).

- 2) **Advanced Test Methods:** The aggregate skeleton of asphalt mixtures definitely affects the pavement performance, and the skeleton system can be more complex with reclaimed asphalt pavement (RAP). Three types of the contact points between aggregates were classified: new-new, new-old, and old-old. The distribution characteristics of asphalt mixtures with three contact points were analyzed through image processing (Xiao et al.). Deicing in the winter is always an issue of great interest for pavement engineers. The compression strength of ice under asphalt mixture was investigated to improve deicing equipment in the process of melting and crushing ice on pavement surfaces. Two failure modes, shear, and ductile failures can be observed from test results (Luo et al.). The compaction characteristics of cold recycle mixtures were studied, and five characteristic parameters were used to quantify the compaction of asphalt mixtures (Wang et al.). The rutting resistance of asphalt pavement in the RIOHTrack and laboratory was estimated and analyzed through different performance tests, including the dynamic modulus test, Hamburg rutting test, French rutting test, and asphalt pavement analyzer rutting test (Li et al.). The effect of the interface joint shape on the pavement life after pothole repairing was studied through the fatigue life test (Li et al.). Microwave-activated crumb rubber was used to modify asphalt binder. The properties and aging mechanism were studied through different tests, including penetration, softening point, ductility, viscosity, Dynamic Shear Rheometer (DSR), Gel Permeation Chromatography (GPC), and Fourier Transform Infrared Spectroscopy (FTIR) (Zhou et al.). The Coarse Aggregate Morphological Identification System (CAMIS) was employed and developed, allowing the shape features of aggregates above 2.36 mm to be identified based on computer images (Liu et al.). The gradation variability of the aggregates strongly relates to the volume parameters and performance of asphalt mixtures. The volume parameters include Air Voids (AV), Voids in Mineral Aggregate (VMA), Voids Filled with Asphalt (VFA), etc. The design method was analyzed and studied for the dense skeleton gradation (Liu et al.).
- 3) **Simulation Models:** The Molecular Dynamics (MD) method is a promising simulation tool to analyze materials at the nanoscale. Two carbon-based nanomaterials were used to modify asphalt binder, and the MD models were generated. The self-healing capability and properties of asphalt binders were investigated under different temperatures. The optimum contents of modifiers can be determined, and it was found that the modifier enhances the self-healing capability of asphalt binders (Gong et al.). An adaptive and piecewise model framework was proposed to analyze the deterioration process of rail track based on historical measurement data, and the progress of irregular deteriorations in the corresponding rail track sections can be monitored and displayed (Yang et al.).

Thirty manuscripts were received for possible publication in this special issue. Each manuscript was rigorously, fairly, and anonymously reviewed. Both the quality and originality of each paper were thoroughly checked. Finally, nineteen technical research articles were accepted and approved for publication.

Our editorial team members all appreciate the professional and dedicated support from the reviewers, and also thank all the authors for their efforts and investment in this special issue. In addition, we all are grateful to the editorial and support teams from the Journal of Frontiers in Materials, especially to Prof. John L. Provis, Prof. Nicola Maria Pugno, Dr. Pietro Benettoni, Dr. Michelle Cook, and Audra Taylor.

## AUTHOR CONTRIBUTIONS

All authors listed have made a substantial, direct, and intellectual contribution to the work and approved it for publication.

**Conflict of Interest:** The authors declare that the research was conducted in the absence of any commercial or financial relationships that could be construed as a potential conflict of interest.

**Publisher's Note:** All claims expressed in this article are solely those of the authors and do not necessarily represent those of their affiliated organizations, or those of the publisher, the editors and the reviewers. Any product that may be evaluated in this article, or claim that may be made by its manufacturer, is not guaranteed or endorsed by the publisher.

*Copyright © 2021 You, Ji, Wang, Li, Yao and Hou. This is an open-access article distributed under the terms of the Creative Commons Attribution License (CC BY). The use, distribution or reproduction in other forums is permitted, provided the original author(s) and the copyright owner(s) are credited and that the original publication in this journal is cited, in accordance with accepted academic practice. No use, distribution or reproduction is permitted which does not comply with these terms.*



# Analysis of Composite Skeleton Characteristics of Recycled Asphalt Mixture via Weight Analysis Method

Han Xiao, Yuzhuang Qiu, Kuanghuai Wu, Wenke Huang, Ruida Zhang, Li Chen, Xu Cai\* and Qiang Luo\*

School of Civil Engineering, Guangzhou University, Guangzhou, China

## OPEN ACCESS

### Edited by:

Hui Yao,  
Beijing University of Technology,  
China

### Reviewed by:

Tao Ma,  
Southeast University, China  
Yunchao Tang,  
Zhongkai University of Agriculture  
and Engineering, China

### \*Correspondence:

Xu Cai  
cx\_caixu@163.com  
Qiang Luo  
luoq\_yan@gzhu.edu.cn

### Specialty section:

This article was submitted to  
Structural Materials,  
a section of the journal  
Frontiers in Materials

**Received:** 02 May 2020

**Accepted:** 03 June 2020

**Published:** 09 July 2020

### Citation:

Xiao H, Qiu Y, Wu K, Huang W,  
Zhang R, Chen L, Cai X and Luo Q  
(2020) Analysis of Composite  
Skeleton Characteristics of Recycled  
Asphalt Mixture via Weight Analysis  
Method. *Front. Mater.* 7:203.  
doi: 10.3389/fmats.2020.00203

The aggregate skeleton of hot-mix recycled asphalt mixture comprises reclaimed asphalt pavement (RAP) and new aggregate and is a complex skeleton system containing old and new aggregates. The RAP content in the mixture directly determines the mechanical response characteristics of the composite skeleton, thus affecting the road performance. In order to explore the effect of RAP content on the characteristics of composite skeleton, in this study, the contact points in the composite skeleton were classified into three types: “new–new,” “new–old,” and “old–old.” On the basis of digital image technology and weight analysis methods, the distribution characteristics of the contact type of AC-13 mixture skeletons with different RAP contents were investigated; the correlation between the weight parameters of the contact type and the macroscopic mechanical properties of the mixture was studied. The results indicate that grading is the main factor that affects the total number of contact points; with increasing RAP content, the overall trend of “new–new” contact points is decreasing; the “old–old” contact points increase monotonously and then rapidly after the RAP content reached 40%; and the “new–old” contact points increase first and then decrease, with a peak corresponding to 30% RAP. With the increasing number of “new–old” contact points, the mechanical indexes of the recycled asphalt mixture were enhanced. The weight analysis method can more simply and clearly reflect the correlation between the contact type of coarse aggregate and the mechanical parameters of the mixture. In the mixing ratio design of the recycled asphalt mixtures, choosing a mixture with more “new–old” contact points achieved better road performance; therefore, effectively increasing RAP content may be one of the potential ways to enhance road performance.

**Keywords:** RAP, RAP content, contact points, composite skeleton, shear modulus

## INTRODUCTION

At present, the waste and old asphalt mixture produced by China’s highway maintenance and repair reaches hundreds of millions of tons every year (Chen, 2011; Zhang et al., 2020). The “Twelfth Five-Year Plan” clearly proposed that the recycling rate of highway old pavement material should reach over 95% in 2030, indicating that the strategic



focus of China's highway development gradually shifts from large-scale construction to equal emphasis on construction and maintenance. With more and more environmental considerations and the rising cost of construction materials, the addition of reclaimed asphalt pavement (RAP) to asphalt pavement mixture has become a necessary and economic method (Cong et al., 2016). Although many countries set 50% as the maximum RAP content, in practice, the content is mostly 15–30%, and RAP is even not allowed to be used in the surface layer of the road in some countries (Plati, 2019). Studies have shown that the RAP content of hot-mix recycled asphalt mixture is mostly controlled within the range 20–30%. High RAP content significantly reduces the durability of hot-mix recycled asphalt mixture (Valdés et al., 2011; Arshad and Qiu, 2013). Han et al. (2019) considered that the RAP content of the recycled mixture significantly affects its performance. With increasing RAP content, the tensile strength of the mixture usually increased, but the tensile strain decreased. Ai-Qadi et al. (2007, 2009) found that, although the use of RAP can enhance rutting performance, it may not necessarily improve its fatigue performance. The reason is that the higher stiffness of the old asphalt increases the strength of the mixture, which is more prone to fatigue cracking and low-temperature embrittlement. Zhang et al. (2019) pointed out that the use of RAP, instead of natural aggregates, significantly enhanced the dynamic stability of the recycled asphalt mixture. According to the result of the three-point bending test, RAP weakens the cracking resistance of the recycled asphalt mixture at low temperature. Mannan et al. (2015) pointed out that the incorporation of RAP would reduce the fatigue life of the mixture. The comparison between the fatigue performance of the asphalt mixture with 35% RAP and ordinary asphalt mixture indicated that the fatigue performance of the recycled asphalt mixture deteriorates, as evidenced by the four-point bending test, but that of the recycled asphalt mixture with aged asphalt is enhanced, as observed by the dynamic shear rheometer test. Wang D. et al. (2019) studied the performance of recycled asphalt mixtures using the repeated recycled RAP and experimentally evaluated the durability of the recycled asphalt mixtures. The results indicated that during the primary and the secondary aging processes, the creep performance of the recycled asphalt mixture both reduces and the mixture exhibits a brittle failure. Ma et al. (2015) reported that RAP was beneficial to enhancing the water stability of warm mix asphalt and hot-mix Asphalt mixtures. Furthermore, the water stability of the mixture increased with increasing RAP content. Based on the in-lab test on mixtures, Pradyumna et al. (2013) concluded that the addition of RAP can improve the performance of all the asphalt mixtures with 20% RAP.

The existing researches mainly focus on asphalt aging, regeneration mechanism, grading, *etc.*, but did not fully consider the characteristics of RAP itself and the contact/fusion with new materials. From the perspective of material composition, asphalt mixture is a typical multi-phase granular material. Several researchers investigated and determined the morphology of the coarse aggregate skeleton of asphalt mixture *via* digital image technology (Tan et al., 2009; Lopes et al., 2016; Li et al., 2019). Wang et al. (2016) concluded that, at the

same aggregate particle size, the thickness of the asphalt film increased with increasing amount of asphalt. At the same asphalt content, the thickness of the asphalt film increased with decreasing size of aggregate. Moaveni et al. (2016) pointed out that the asphalt film has a certain effect on the size and shape properties of RAP particles. Li et al. (2018) studied the effect of aggregate contact situations on the stability of asphalt mixture skeletons and concluded that, with increasing temperature, the aggregate skeleton significantly affected the stability of the asphalt mixture skeletons. The contact situations had a greater effect on the stability of the mixture at high temperatures. However, with increasing temperature, the effect of asphalt changed from viscous action to a lubricating effect; therefore, it became unfavorable for the stability of the mixture.

The recycled asphalt mixture containing RAP has interfaces with different strengths (Chen et al., 2020a). These contact interfaces restrain each other and affect the deformation consistency of the mixture together, which in turn affects the rheological properties of the material. Therefore, considering the characteristics of the composite skeleton system of the recycled asphalt mixture consisting of RAP and new aggregates is valuable (Ma et al., 2018; Ding et al., 2019; Chen et al., 2020b; Zhu et al., 2020). On this basis, the effect of RAP content on the characteristics of the composite skeleton is explored. In this study, the contact points in the composite skeleton were classified into three types: “new–new,” “new–old,” and “old–old.” Based on digital image technology and weight analysis method, the AC-13-type composite skeleton with different RAP contents was analyzed, and the distribution characteristics of the contact type were studied to find the correlation between the weight parameters of the contact type and the macroscopic mechanical properties of the mixtures.

Digital image processing technology was born in the 1960s. After continuous development, digital image processing technology has been widely used in various research fields (Chen et al., 2019; Tang et al., 2020). Digital image technology can be used to evaluate the internal structure of asphalt mixtures. Based on digital image processing technology, this paper analyzes the contact characteristics of coarse aggregates of recycled asphalt mixture and defines the three types of contact of coarse aggregates in the mixture.

## RAW MATERIALS

The aggregates used in the test include granite, agate, and old aggregate, as shown in **Figure 1**.

Among them, granite and old aggregate were taken from the Guangzhou Municipal Maintenance Office. Asphalt is No. 70 matrix asphalt with asphalt–aggregate ratio of 4.6%. The composition of gradation with RAP and target gradation is listed in **Table 1**. The relevant indexes of raw materials all meet the requirements in the “Technical Specifications for Construction of Highway Asphalt Pavement” (JTG F40-2017), and the technical indexes of the materials are listed in **Tables 2, 3**.



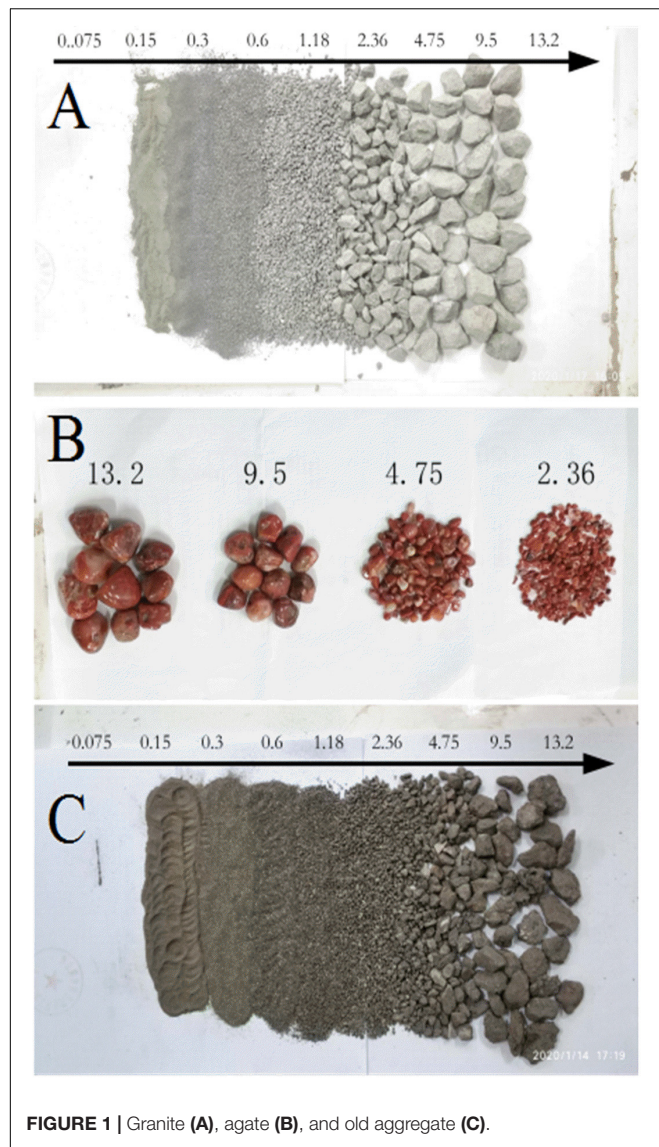


FIGURE 1 | Granite (A), agate (B), and old aggregate (C).

## EXPERIMENTAL DESIGN

### Mixture Design

The aggregate used in this test consists of granite and RAP. The asphalt used is No. 70 matrix asphalt. The composition of

TABLE 1 | AC-13 asphalt mixture gradation.

	Percent passing the following sieve (mm)/%									
Gradation	16	13.2	9.5	4.75	2.36	1.18	0.6	0.3	0.15	0.075
Target gradation	100	91.9	75.6	51.3	35	24.5	17.3	11.9	8.2	5.5
RAP	100	97.1	83.6	50.4	30.5	23.5	18.7	16.5	12.6	2

the target gradation is listed in **Table 1**. The RAP and granite were mixed proportionally, with RAP contents of 10, 20, 30, 40, and 50%. A cylindrical test piece was formed using a Marshall compactor after compacting 75 times on both sides. According to the aforementioned five contents, five sets of test pieces were formed. Ten test pieces were shaped from each set with diameter and height of  $101.6 \pm 0.2$  and  $63.5 \pm 1.3$  mm, respectively. The stability and flow value tests indicated the final asphalt-aggregate ratio to be 4.6%, which is the same as that of the old aggregate.

### Uniaxial Penetration and Uniaxial Compression Test

The uniaxial penetration test is a test method proposed by Bi and Sun (2005) for evaluating the shear resistance of asphalt mixtures. Peng et al. (2007) investigated that rotation compaction has less effect on uniformity than Marshall compaction and wheel shaping. Therefore, a Superpave Gyratory Compactor (SGC) was used to form cylindrical test pieces for the test after gyratory compaction of 50 times. The test piece for the uniaxial penetration test has a diameter of 100 mm and a height of 100 mm. For each RAP content, the set to be tested had six test pieces, of which three are used for uniaxial penetration test and the remaining three are used for uniaxial compression test. The test temperatures of the uniaxial compression test and the uniaxial penetration test are both  $60^{\circ}\text{C}$ , and the loading speed is  $1 \text{ mm}\cdot\text{s}^{-1}$ . The uniaxial penetration test uses a circular penetration surface with a diameter of 28.5 mm, as shown in **Figure 2**.

### Classification of the Contact Between Old and New Aggregates

#### Digital Image Processing Technology

The analysis of contact characteristics of aggregate in asphalt mixture is based on digital image technology. At present, there are two commonly used processing techniques for the image analysis of asphalt mixture: the two-dimensional image processing technology is based on charge-coupled device (CCD)

TABLE 2 | Technical indexes of granite.

Name of material	Tested items	Quality requirement	Test result	Test method
Coarse aggregate	Crushed percent of aggregate (%)	$\leq 26$	18.25	T0316
	Los Angeles abrasion (%)	$\leq 28$	17.3	T0317
	Water absorption (%)	$\leq 2.0$	0.6	T0304
	Relative density based on gross volume		2.57	T0304
	Apparent relative density	$\geq 2.6$	2.66	T0304
Fine aggregate	Apparent relative density	$\geq 2.5$	2.64	T0328
	Sand equivalent (%)	$\geq 60$	65	T0334

TABLE 3 | Main technical indexes of No. 70 matrix asphalt.

	Softening point/°C	Ductility/mm	Needle penetration/(0.1 mm)
No. 70 matrix asphalt	48.0	≥100	65
RAP asphalt	71.9	≥100	15.1

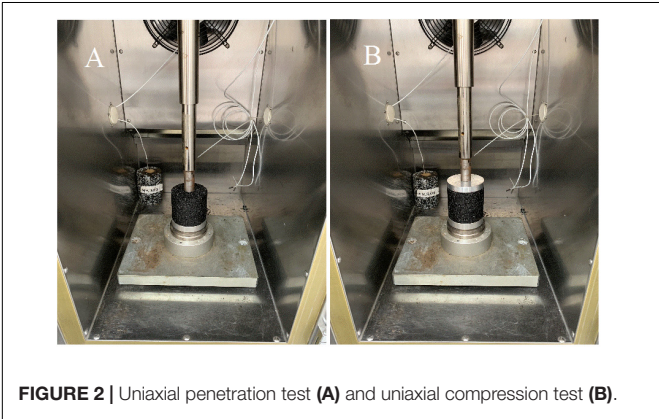


FIGURE 2 | Uniaxial penetration test (A) and uniaxial compression test (B).

TABLE 4 | Comparison between image processing technology.

Methods	Two-dimensional image processing technology based on charge-coupled device (CCD) digital camera	Two- or three-dimensional image processing technology based on X-ray CT
Advantages	Using different colors to distinguish various materials can obtain high-precision cross-sectional photographs; low cost, rapid imaging, and simple equipment	Non-destructive testing method to collect the attenuation signals when X-ray penetrates materials with different densities  Imaging and restructuring can be accomplished via a computer
Disadvantages	The acquisition of two-dimensional images requires cutting mixture, which is a destructive detection method and affected by illumination, imaging angle, and equipment	Under the current technical conditions, the image obtained by X-ray CT is relatively blurry. The most prominent problem is the identification of different substances in asphalt mixture  High technical cost
Reasons	Since CCD digital photography and X-ray CT non-destructive scanning have different precision and scope of application, considering the image quality requirements in the study, CCD digital camera-based photography technology was adopted to obtain the cross-section information of asphalt mixture	

digital camera and the 2D or 3D image processing technology is based on X-ray CT (Cai, 2013). In these two methods, a more suitable CCD digital camera-based technology was chosen according to the requirements and their advantages and disadvantages. The comparison is shown in Table 4.

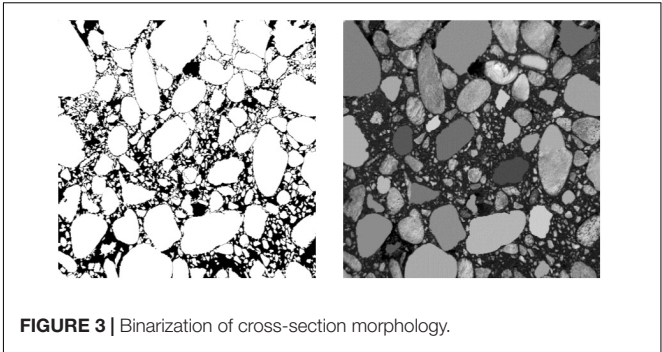


FIGURE 3 | Binarization of cross-section morphology.

Analysis of Contact Points in Coarse Aggregate

Wei Hong proposed the concept of “contacting pair” in the analysis of the spatial proximity relationship between aggregate particles and deemed that, when the boundary pixel distance of any two adjacent aggregates is less than a certain threshold, the aggregates contact with each other (Cai, 2013). However, because the asphalt mixture is a typical three-phase matter, the noise in the spatial domain limits the image effect not meeting the requirements of fine analysis during the process of taking digital images by digital camera. The resulting large errors especially affect the sharpness of the material edge of the image. In order to get more accurate data, the following processing was performed:

First, apply CCD digital camera to the cut test piece for collecting the cross-section information of the asphalt mixture. Use iPas to perform preliminary processing on the image, such as filter denoising, image enhancement, and determining the threshold.

Second, use the multi-resolution adaptive window segmentation algorithm to initially extract the aggregate boundary and binarize the image, as shown in Figure 3.

Subsequently, perform virtual screening on the binarized image slices, extract coarse and fine aggregates, and number them.

Finally, calculate the spatial proximity relationship between the aggregates, count the number of contact points, and mark the positions of the contact points.

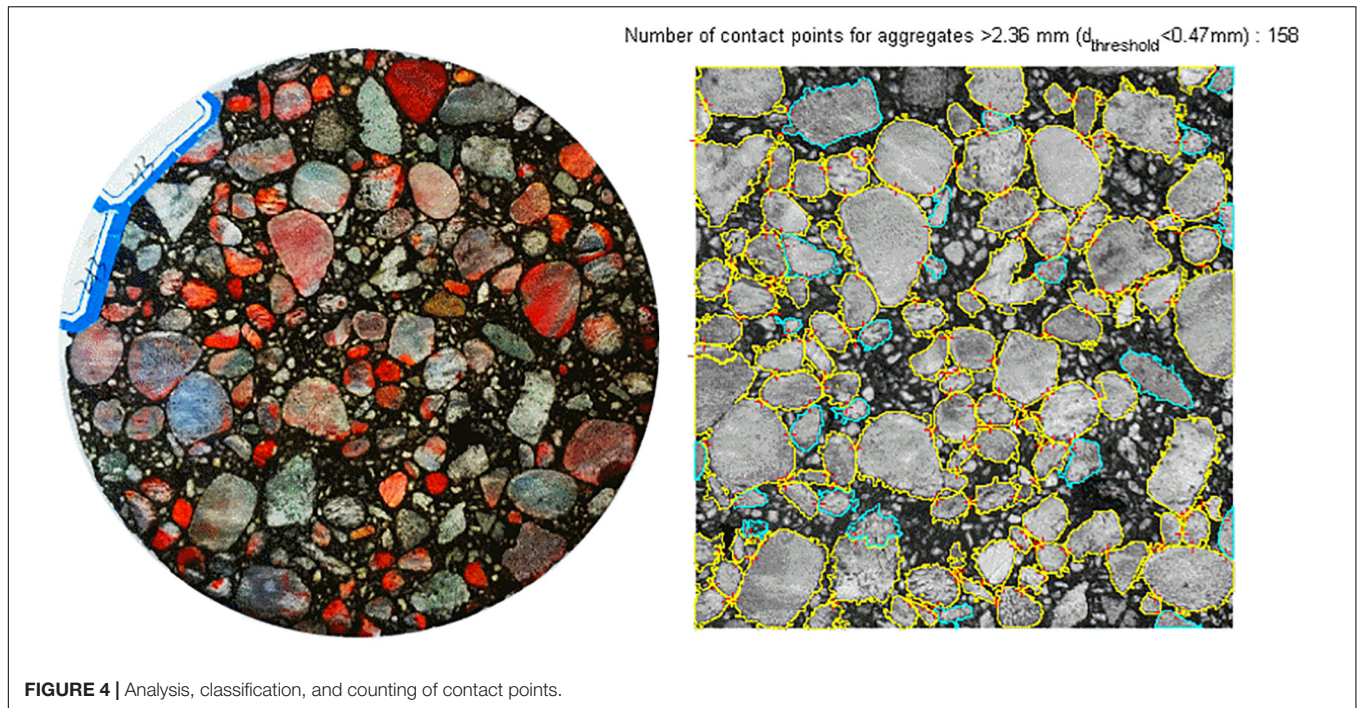
Determination of Contact Threshold

Based on the literature data, the selection of contact threshold has a crucial effect on the number of contact points. By analyzing the contact probability and referring to the reported results, it is reasonable to select 20–25% of the minimum calculated particle size of aggregate as the contact threshold (Elseifi et al., 2008; Duan, 2011; Coenen et al., 2012). Therefore, in this study, the contact threshold is directly taken as 20% of the minimum calculated particle size of the aggregate and will not be discussed in detail.

Dividing and Extraction of Contact Types

In order to observe the contact between new and old aggregates more clearly, the coarse aggregates in the new aggregates were replaced with agate to form additional gyratory-compacted





specimens. Among the contact points exceeding the contact threshold, the contact points composed of old materials and agate stone are defined as “new-old” type, the old materials and old materials are composed of “old-old” type, and the agate stone and agate stone are “new-new” type. According to the density of the material, the added amount of agate stone is determined by equal volume conversion and the gradation curve adopted was the same as the target gradation. In order to study the distribution of the three contact types at different RAP contents, the RAP content was set to 20, 30, 40, 60, and 80%. In the test, the cylindrical test pieces were formed after 50 times of gyratory compaction by the SGC. For every RAP content, two test pieces, with a diameter of 100 mm and a height of 100 mm, were shaped. Each test piece was cut using a cutting machine to get five circular slices. A CCD digital camera was used to capture the pictures of each section under the same lighting conditions, and the photographs were numbered. A total of eight cross-sectional photographs were obtained for each specimen.

Using iPas software, the two-dimensional cross-section image of asphalt mixture was processed and then associated with the method of manual observation and counting to combine the processed map and the physical distribution (Sefidmazgi, 2011; Sefidmazgi and Bahia, 2014; Cai et al., 2018). Finally, the number of the three types of contact points was counted, as shown in Figure 4.

### Weight Analysis of Contact Type

Weight analysis is a decision method that combines qualitative analysis and quantitative analysis. This method can be applied to the decision-making process of various issues

with multiple objectives and multiple criteria. In general, the contribution of each factor to target is different. For some issues, the contributions are significant enough to be measured by a number. The weight analysis method quantitatively provides contribution of various factors to the target through the analysis and the comparison of various factors.

Due to the difference in the amount of RAP used in the mechanical test and the dividing contact types, using cubic spline interpolation, quadratic fitting, and cubic fitting methods is necessary to first obtain the distribution of contact types corresponding to 10 and 50% RAP. On this basis, weight analysis was used to establish the correlation between the contact type and the mechanical parameters such as Marshall stability, uniaxial compressive strength, and uniaxial penetration. The specific method is as follows:

Set the weighting factor to be  $X$ , then the weight vector is  $(X_1, X_2, X_3)^T$ . The data obtained from the test results in the target matrix  $B = [b_1, b_2, \dots, b_5]^T$ , and  $c$  is a constant. Considering the relationship between the contact point type and RAP content, there are three types of contact point and five RAP contents, which can be combined to form a matrix (1):

$$A = \begin{pmatrix} a_{11} & \dots & a_{13} \\ \vdots & \ddots & \vdots \\ a_{51} & \dots & a_{53} \end{pmatrix} \quad (1)$$

Therefore, the equation,  $AX = cB$  was obtained, with  $c$  being constant. Apply MATLAB to solve the equation and obtain the weights of the three types of contact point.

**TABLE 5** | Results of the stability test.

RAP content	Number of test piece								Mean	Variance
	1	2	3	4	5	6	7	8		
10%	7.96	8.27	7.71	6.73	8.54	8.66	8.60	8.39	8.11	0.42
20%	10.3	11.71	9.06	11.22	11.4	10.43	10.39	10.66	10.65	0.68
30%	11.51	12.21	12.79	11.01	9.64	11.88	10.49	11.8	11.42	1.01
40%	12.8	12.51	12.1	11.17	16.1	11.89	10.68	13.24	12.56	2.74
50%	11.75	14.18	13.3	14.87	15.87	15.12	12.16	13.05	13.79	2.15

## EXPERIMENTAL RESULTS AND DATA ANALYSIS

### Results of Marshall Stability Test

The Marshall stability test is used to determine the breaking load and deformation resistance of the asphalt mixture test piece. The stabilities obtained by the Marshall test are listed in **Table 5**, where the mean value is the arithmetic average value after removing the maximum value and the minimum value.

**Table 5** shows that the Marshall stability of the asphalt mixture increases with increasing RAP content, mainly because with increasing amount of old asphalt, the strength and the rigidity of the asphalt binder gradually increase, making the recycled asphalt mixture exhibit higher Marshall stability macroscopically.

### Results of Uniaxial Compression and Uniaxial Penetration Tests

According to the T0713-2011 method in the specification JTG E20-2011, the results of uniaxial compression and uniaxial penetration tests are shown in **Tables 6, 7**, respectively.

**TABLE 6** | Result of the uniaxial compression test.

RAP content	Sample				
	1	2	3	Mean/KN	Variance
10%	12.73	12.32	12.04	12.36	0.12
20%	15.21	12.72	15.01	15.11	0.01
30%	17.22	17.32	16.51	17.02	0.19
40%	12.20	11.29	12.59	12.03	0.44
50%	12.80	11.90	11.33	12.01	0.55

*The second sample (20% RAP) exceeds the allowable range of error; therefore, the data set and the mean value of the remaining two sets were taken.*

**TABLE 7** | Result of the uniaxial penetration test.

RAP content	Sample					
	1	2	3	Mean/kN	Variance	$\tau_D/KN$
10%	3.55	3.86	3.01	3.47	0.19	1.84
20%	3.89	4.68	4.88	4.48	0.27	2.38
30%	5.02	4.92	4.11	4.69	0.25	2.49
40%	4.58	4.35	3.86	4.27	0.13	2.27
50%	5.43	4.95	4.16	4.85	0.41	2.58

**Table 6** shows that, with increasing RAP content, the compressive strength of the recycled asphalt mixture increases first, then decreases, and reaches the maximum at 30% RAP. **Table 7** shows that, with increasing RAP content, the penetration strength of the recycled asphalt mixture also increases. Unlike the result of the uniaxial compression test, there was no significant peak value in the penetration strength.

### Statistics of Contact Types in Composite Skeleton

The statistical data obtained as a result of combining digital technology and manual statistics to process and classify the contact points are shown in **Figure 5**.

**Figure 4** shows that, for consistent gradation, the total number of contact points is basically close. In this study, the total number of contact points at the same gradation is assumed to be the same to obtain the number of contact points corresponding to 0% RAP. With increasing RAP content, the number of new–new contact points decreases, while that of old–old contact points increases; the number of new–old contact points increases monotonously at first and then decreases monotonously after reaching the peak at 30% RAP. The statistical data of the three contact types were used to calculate the number of contact points at 10, 20, 30, 40, and 50% RAP by cubic spline interpolation, quadratic fitting, and cubic fitting, as listed in **Table 8**.

**Table 8** shows that the results obtained by the different fitting methods are different as well. From the perspective of distribution of contact types, the numbers of “new–old” contact points obtained by quadratic fitting and cubic fitting are more than that obtained by interpolation fitting, while the numbers of “new–new” contact points exhibit an opposite trend.

### Weight Analysis of Contact Type

According to the method introduced in “Dividing and Extraction of Contact Types”, the data in **Table 8** were used to obtain the data of weight, as shown in **Table 9**.

As listed in **Table 9**, the weight data obtained by quadratic fitting and cubic fitting are very close, especially on the weight of the old–old contact points, but they obviously differ from the interpolation data. For the old–old contact point of the uniaxial compression test, the negative sign of weight represents its weakening effect on the strength. An extreme situation is assumed: when the test piece is fully composed of RAP, the compression strength of the test piece should be weakened to its extreme value and even expands. However, the test piece

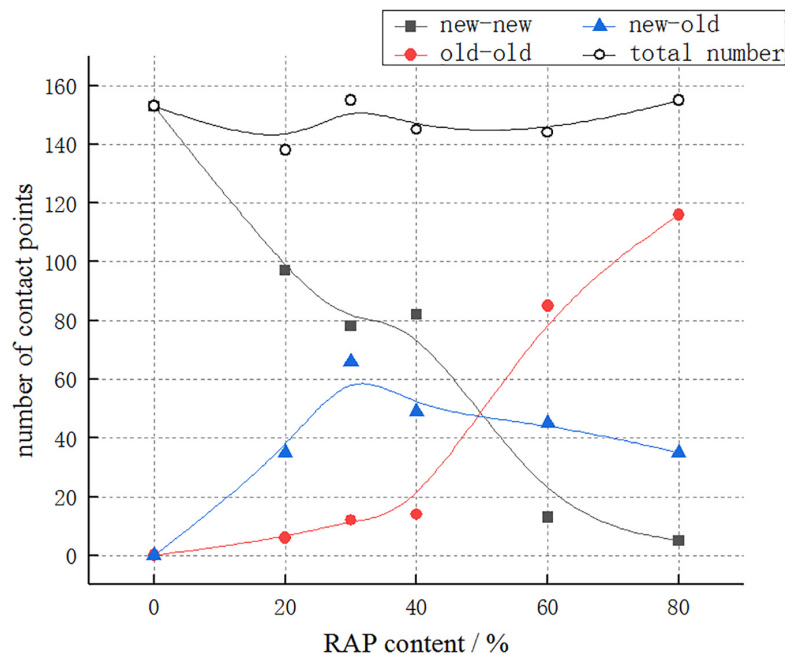


FIGURE 5 | Statistics of the number of contact points.

TABLE 8 | Data processing.

Processing method	Interpolation			Quadratic fitting			Cubic fitting		
	New-new	Old-old	New-old	New-new	Old-old	New-old	New-new	Old-old	New-old
10%	125	2	12	127	-1	23	129	-6	27
20%	97	6	35	103	4	39	106	-2	44
30%	78	12	66	82	14	50	83	10	53
40%	82	14	49	61	27	56	62	29	54
50%	54	40	47	44	45	57	42	52	51

TABLE 9 | Data of weight.

Test	Uniaxial penetration test			Uniaxial compression test			Marshall stability		
	New-new	Old-old	New-old	New-new	Old-old	New-old	New-new	Old-old	New-old
Interpolation	0.24	0.43	0.33	0.37	0.01	0.62	0.19	0.53	0.28
Quadratic fitting	0.20	0.12	0.68	0.12	-0.29	0.59	0.14	0.29	0.57
Cubic fitting	0.16	0.20	0.64	0.15	-0.15	0.70	0.12	0.31	0.57

still has a relatively good compressive strength for the full RAP. Therefore, the interpolation method having less effect of old-old contact point on the compressive strength is more reasonable. In addition, the numbers of old-old contact points in quadratic and cubic fittings show negative values at 10% RAP, which is not in line with the practical situation. In summary, the data obtained by interpolation fitting are selected for the next analysis.

### Relevant Weight of Marshall Stability

Table 9 shows that the new-old contact point accounts for the largest weight in affecting the stability. The old-old contact point type has the second largest weight but also very close to the

new-old contact point. Because the total number of contact points remains unchanged, less new-new contact points mean an increase in other contact points, also explaining the continuous increase in stability. The new-old and the old-old contact points contribute more to stability and are in agreement with the results of the weight analysis.

### Relevant Weight of Uniaxial Compression Strength

Combined with the statistics of contact points in Figure 5 and the weight analysis in Table 6, the rapid growth before 30% RAP results from the contribution of new-old contact points exceeding that of new-new contact points and increasing the



compressive strength. The weight reaches a peak value at 30% RAP and then decreases, and the downward trend of new–new contact points tends to be smooth at 40% RAP, exhibiting an overall compressive strength without a significant change.

### Relevant Weight of Uniaxial Penetration Strength

The literature data indicate that the high temperature stability of asphalt mixture is proportional to the RAP content, and it can be further concluded that the shear modulus of the three types of contact point is in the following order: old–old (RAP is 100%) > new–old (RAP is between 0 and 100%) > new–new (RAP is 0%), which is consistent with the results obtained by the weight analysis (Cheng et al., 2018; Wang Z. Y. et al., 2019). Combining with the trend of the contact points shown in **Figure 4**, the shear strength increases with increasing RAP content because the number of new–old and old–old contact points gradually increases. The significant drop after 30% is because the number of new–old contact points reaches its peak at 30%. The increase again at 40% results from the number of old–old contact points that continue to increase, and the proportion of the three types of contact point reaches a balance at 40%, exhibiting an extreme value. After the RAP content exceeds 40%, the number of old–old contact points increases sharply, and its contribution to the overall shear modulus becomes greater, exhibiting a continuous increase in strength.

## CONCLUSION

In conclusion, digital image processing technology and weight analysis methods were used in combination to study the types of contact points and mechanical properties of the recycled asphalt mixtures with different RAP contents and explore their correlations. The following conclusions were obtained:

1. The statistical data show that, at a constant gradation condition, the total number of the three types of contact point does not change with increasing RAP content.
2. With the increase of RAP content, the variations in the three types of contact point have their own characteristics. The overall trend of new–new contact points is decreasing, but there are small fluctuations at 30 and 40%. The overall trend of old–old contact points is increasing, but the increase at 40% becomes larger. The new–old contact point presents a parabolic trend, with a peak at 30%.
3. In the uniaxial penetration test, the shear modulus of the three contact points jointly determines the strength of the mixture, and the strength changes with the number of three contact points. In the uniaxial compression test, the force situation is more complicated than that in the uniaxial penetration test; the strength is mainly determined by the new–new and the new–old contact points. In the stability

test, the old–old contact point and the new–old contact point account for larger weights; therefore, the stability increases with increasing RAP content. The above analysis indicates that the new–old contact point always plays an important role. The optimal performance of a material can be enhanced by increasing the number of new–old contact points, as one of the possible means.

4. Weight analysis is an auxiliary analysis method, providing the correlation between the changing factor and the test results based on actual data, therefore explaining the data analysis results in a better way. The weight analysis results of the contact type indicate that this method can effectively obtain the main factors that affect the performance of the asphalt mixture.
5. Limitations of this study: Only the AC-13 asphalt mixture was analyzed. The results cannot characterize the dense-framework and void-type mixtures. The use of agate stone changes the friction between the particles, which results in the uniformity of the material under the same mixing process being different from the mixture using the new aggregate. The author's future research direction would be to carry out more types of mixture test research and explore the feasibility of improving the road performance of recycled asphalt mixture from the perspective of uniformity.

## DATA AVAILABILITY STATEMENT

The raw data supporting the conclusions of this article will be made available by the authors, without undue reservation.

## AUTHOR CONTRIBUTIONS

All authors listed have made a substantial, direct, and intellectual contribution to the work and approved it for publication.

## FUNDING

This work was financially supported by the National Natural Science Foundation of China (Grant Nos. 51708144 and 51878193).

## SUPPLEMENTARY MATERIAL

The Supplementary Material for this article can be found online at: <https://www.frontiersin.org/articles/10.3389/fmats.2020.00203/full#supplementary-material>

## REFERENCES

- Ai-Qadi, I. L., Carpenter, S. H., Roberts, G. L., Ozer, H., and Aurangzeb, Q. (2009). "Investigation of working binder in hot-mix asphalt containing recycled asphalt pavements," in *Proceedings of the 88th Annual Meeting of the Transportation Research Board*, Washington, DC.
- Ai-Qadi, I. L., Elseifi, M., and Carpenter, S. H. (2007). *Reclaimed Asphalt Pavement—A Literature Review*. Research Report FHWA- ICT- 07-001. Rantoul, IL: IDEALS.
- Arshad, H., and Qiu, Y. J. (2013). Effect of reclaimed asphalt pavement on the properties of asphalt binders. *Proc. Eng.* 54, 840–850. doi: 10.1016/j.proeng.2013.03.077

- Bi, Y. F., and Sun, L. J. (2005). Study on shear test method of asphalt mixture. *J. Tongji Univ. Nat. Sci. Ed.* 33, 1036–1040.
- Cai, X. (2013). *Rutting Resistance Evaluation and Structure Optimization of Asphalt Pavement*. PhD thesis, South China University Technology, Guangzhou.
- Cai, X., Wu, K. H., Huang, W. K., and Wan, C. (2018). Study on the correlation between aggregate skeleton characteristics and rutting performance of asphalt mixture. *Constr. Build. Mater.* 179, 294–301. doi: 10.1016/j.conbuildmat.2018.05.153
- Chen, J. Y. (2011). *Experimental Research on Recycling Method of Asphalt Pavement*. PhD thesis, Dalian University of Technology, Dalian.
- Chen, M., Tang, Y., Zou, X., Huang, K., Li, L., and He, Y. (2019). High-accuracy multi-camera reconstruction enhanced by adaptive point cloud correction algorithm. *Opt. Lasers Eng.* 122, 170–183. doi: 10.1016/j.optlaseng.2019.06.011
- Chen, T., Luan, Y., Ma, T., Zhu, J., Huang, X., and Ma, S. (2020a). Mechanical and microstructural characteristics of different interfaces in cold recycled mixture containing cement and asphalt emulsion. *J. Clean. Product.* 258:120674. doi: 10.1016/j.jclepro.2020.120674
- Chen, T., Ma, T., Huang, X., Ma, S., Tang, F., and Wu, S. (2020b). Microstructure of synthetic composite interfaces and verification of mixing order in cold-recycled asphalt emulsion mixture. *J. Clean. Product.* 263:121467. doi: 10.1016/j.jclepro.2020.121467
- Cheng, P. F., Kou, H. Y., and Li, J. H. (2018). Influence of the amount of used materials on the temperature and performance of mixing and compaction of hot recycled asphalt mixture. *China Foreign Highway* 38, 193–198. doi: 10.14048/j.issn.1671-2579.2018.05.042
- Coenen, A. R., Kutay, M. E., Sefidmazgi, N. R., and Bahia, H. U. (2012). Aggregate structure characterisation of asphalt mixtures using two-dimensional image analysis. *Road Mater. Pavement* 13, 433–454. doi: 10.1080/14680629.2012.711923
- Cong, P., Zhang, Y., and Liu, N. (2016). Investigation of the properties of asphalt mixtures incorporating reclaimed SBS modified asphalt pavement. *Constr. Build. Mater.* 113, 334–340. doi: 10.1016/j.conbuildmat.2016.03.059
- Ding, X., Chen, L., Ma, T., Ma, H., Gu, L., Chen, T., et al. (2019). Laboratory investigation of the recycled asphalt concrete with stable crumb rubber asphalt binder. *Constr. Build. Mater.* 203, 552–557. doi: 10.1016/j.conbuildmat.2019.01.114
- Duan, Y. H. (2011). *Basic Properties of Asphalt Mixture Based on X-ray CT*. Ph.D. thesis, South China University of Technology, Guangzhou.
- Elseifi, M. A., Ai-Qadi, I. L., Yang, S.-H., and Carpenter, S. H. (2008). Validity of asphalt binder film thickness concept in hot-mix asphalt. *Transp. Res. Rec.* 2057, 37–45. doi: 10.3141/2057-05
- Han, S., Cheng, X. P., Liu, Y. M., and Zhang, Y. C. (2019). Laboratory performance of hot mix asphalt with high reclaimed asphalt pavement (RAP) and fine reclaimed asphalt pavement (FRAP) content. *Materials* 12:2536. doi: 10.3390/ma12162536
- Li, J., Li, P., Su, J., Yang, L., and Wu, X. (2019). Coarse aggregate movements during compaction and their relation with the densification properties of asphalt mixture. *Int. J. Pavement Eng.* 1–12. doi: 10.1080/10298436.2019.1659263
- Li, P., Su, J., Ma, S., and Dong, H. (2018). Effect of aggregate contact condition on skeleton stability in asphalt mixture. *Int. J. Pavement Eng.* 21, 196–202. doi: 10.1080/10298436.2018.1450503
- Lopes, M., Mouillet, V., Bernucci, L., and Gabet, T. (2016). The potential of Attenuated Total Reflection Imaging in the mid-infrared for the study of recycled asphalt mixtures. *Constr. Build. Mater.* 124, 1120–1131. doi: 10.1016/j.conbuildmat.2016.08.108
- Ma, T., Wang, H., Huang, X., Wang, Z., and Xiao, F. (2015). Laboratory performance characteristics of high modulus asphalt mixture with high-content RAP. *Constr. Build. Mater.* 101, 975–982. doi: 10.1016/j.conbuildmat.2015.10.160
- Ma, T., Zhang, D., Zhang, Y., Wang, S., and Huang, X. (2018). Simulation of wheel tracking test for asphalt mixture using discrete element modelling. *Road Mater. Pavement* 19, 367–384. doi: 10.1080/14680629.2016.1261725
- Mannan, U. A., Islam, M. R., and Tarefder, R. A. (2015). Effects of recycled asphalt pavements on the fatigue life of asphalt under different strain levels and loading frequencies. *Int. J. Fatigue* 78, 72–80. doi: 10.1016/j.ijfatigue.2015.04.004
- Moaveni, M., Cetin, S., Brand, A. S., Dahal, S., Roesler, J. R., and Tutumluer, E. (2016). Machine vision based characterization of particle shape and asphalt coating in reclaimed asphalt pavement. *Transp. Geotech.* 6, 26–37. doi: 10.1016/j.trgeo.2016.01.001
- Peng, Y., Sun, L. J., Shi, Y. J., and Wang, Y. Q. (2007). Influencing factors of shear strength of asphalt mixtures. *J. Southeast Univ. Nat. Sci. Ed.* 37, 330–333.
- Plati, C. (2019). Sustainability factors in pavement materials, design, and preservation strategies: a literature review. *Constr. Build. Mater.* 211, 539–555. doi: 10.1016/j.conbuildmat.2019.03.242
- Pradyumna, T. A., Mittal, A., and Jain, P. K. (2013). Characterization of reclaimed asphalt pavement (RAP) for use in bituminous road construction. *Proc. Soc. Behav. Sci.* 104, 1149–1157. doi: 10.1016/j.sbspro.2013.11.211
- Sefidmazgi, N. R. (2011). *Defining Effective Aggregate Skeleton in Asphalt Mixture using Digital Imaging*. master's thesis, University of Wisconsin, Madison, WI.
- Sefidmazgi, N. R., and Bahia, H. U. (2014). Effect of compaction conditions on aggregate packing using 2-dimensional image analysis and the relation to performance of HMA. *Mater. Struct.* 47, 1313–1324. doi: 10.1617/s11527-014-0275-x
- Tan, Y. Q., Song, X. H., Ji, L., Chen, G. M., and Wu, X. T. (2009). Influence of coarse aggregate performance on high temperature performance of asphalt mixture. *China J. Highway Transp.* 22, 29–33. doi: 10.19721/j.cnki.1001-7372.2009.01.005
- Tang, Y., Chen, M., Wang, C., Luo, L., Li, J., and Zou, X. (2020). Recognition and localization methods for vision-based fruit picking robots: a review. *Front. Plant Sci.* 11:510. doi: 10.3389/fpls.2020.00510
- Valdés, G., Pérez-Jiménez, F., Miró, R., Martínez, A., and Botella, R. (2011). Experimental study of recycled asphalt mixtures with high percentages of reclaimed asphalt pavement (RAP). *Constr. Build. Mater.* 25, 1289–1297. doi: 10.1016/j.conbuildmat.2010.09.016
- Wang, D., Cannone Falchetto, A., Moon, K. H., Riccardi, C., Pei, J., and Wen, Y. (2019). Artificially prepared Reclaimed Asphalt Pavement (RAP)—an experimental investigation on re-recycling. *Environ. Sci. Pollut. Res.* 26, 35620–35628. doi: 10.1007/s11356-019-05970-w
- Wang, Z. Y., Li, J. U., Lou, M. L., Fang, K. J., Shi, Y., and Wang, P. (2019). Effect of RAP contents on performance of reactive cold mix recycled asphalt mixture. *J. Changsha Univ. Sci. Technol. Nat. Sci. Ed.* 16, 35–41.
- Wang, H., Zhang, R., Chen, Y., You, Z., and Fang, J. (2016). Study on microstructure of rubberized recycled hot mix asphalt based X-ray CT technology. *Constr. Build. Mater.* 121, 177–184. doi: 10.1016/j.conbuildmat.2016.05.166
- Zhang, J., Zhang, X., Liang, M., Jiang, H., Wei, J., and Yao, Z. (2020). Influence of different rejuvenating agents on rheological behavior and dynamic response of recycled asphalt mixtures incorporating 60% RAP dosage. *Constr. Build. Mater.* 238:117778. doi: 10.1016/j.conbuildmat.2019.117778
- Zhang, J. Z., Sun, H., Jiang, H. G., Xu, X. B., Liang, M., Hou, Y., et al. (2019). Experimental assessment of reclaimed bitumen and RAP asphalt mixtures incorporating a developed rejuvenator. *Constr. Build. Mater.* 215, 660–669. doi: 10.1016/j.conbuildmat.2019.04.202
- Zhu, J., Ma, T., Fan, J., Fang, Z., Chen, T., and Zhou, Y. (2020). Experimental study of high modulus asphalt mixture containing reclaimed asphalt pavement. *J. Clean. Prod.* 263:121447. doi: 10.1016/j.jclepro.2020.121447

**Conflict of Interest:** The authors declare that the research was conducted in the absence of any commercial or financial relationships that could be construed as a potential conflict of interest.

Copyright © 2020 Xiao, Qiu, Wu, Huang, Zhang, Chen, Cai and Luo. This is an open-access article distributed under the terms of the Creative Commons Attribution License (CC BY). The use, distribution or reproduction in other forums is permitted, provided the original author(s) and the copyright owner(s) are credited and that the original publication in this journal is cited, in accordance with accepted academic practice. No use, distribution or reproduction is permitted which does not comply with these terms.





# Comprehensive Laboratory Evaluations and a Proposed Mix Design Procedure for Cement-Stabilized Cohesive and Granular Soils

Yi Yang<sup>1</sup>, Shengting Li<sup>2\*</sup>, Cheng Li<sup>3</sup>, Lijian Wu<sup>2</sup>, Lvzhen Yang<sup>4</sup>, Ping Zhang<sup>5</sup> and Tuo Huang<sup>6</sup>

<sup>1</sup> Xiandai Investment Co., Ltd., Changsha University of Science and Technology, Changsha, China, <sup>2</sup> Key Laboratory of Transport Industry of Road Structure and Material, Research Institute of Highway, Ministry of Transport, Beijing, China, <sup>3</sup> School of Highway, Chang'an University, Xi'an, China, <sup>4</sup> Hunan Communication Polytechnic, Changsha, China, <sup>5</sup> School of Traffic and Transportation Engineering, Changsha University of Science and Technology, Changsha, China, <sup>6</sup> School of Traffic and Transportation Engineering, Changsha University of Science and Technology, Changsha, China

## OPEN ACCESS

### Edited by:

Hui Yao,  
Beijing University of Technology,  
China

### Reviewed by:

Yang (Alex) Zhang,  
Australian Road Research Board  
(ARRB), Australia  
Shifan Wu,  
Nanyang Technological University,  
Singapore

### \*Correspondence:

Shengting Li  
st.li@ioh.cn

### Specialty section:

This article was submitted to  
Structural Materials,  
a section of the journal  
Frontiers in Materials

**Received:** 29 May 2020

**Accepted:** 29 June 2020

**Published:** 30 July 2020

### Citation:

Yang Y, Li S, Li C, Wu L, Yang L,  
Zhang P and Huang T (2020)  
Comprehensive Laboratory  
Evaluations and a Proposed Mix  
Design Procedure  
for Cement-Stabilized Cohesive  
and Granular Soils.  
Front. Mater. 7:239.  
doi: 10.3389/fmats.2020.00239

Embankment subgrade soils classifying as A-4 to A-7-6 according to the AASHTO Soil Classification System can exhibit low bearing strength, high volumetric instability, and freeze-thaw susceptibility. These characteristics of soil are frequently identified as main factors leading to accelerated damage of pavement systems. Cement stabilization has been widely used to improve these soils conditions. The present study aims to help designers and practitioners better understand how cement stabilizations can influence soil index properties and mechanical properties before and after saturation. In this study, a total of 28 cohesive and granular soil materials obtained from nine construction sites were tested using 4–12% type I/II Portland cement contents. Specimens were prepared using a 2 inch by 2 inch compaction apparatus and tested for 28-day unconfined compressive strength (UCS) with and without vacuum saturation. Results indicated that statistically significant relationships exist between soil index properties, UCS, and cement content. Based on the laboratory test results, a laboratory evaluation procedure for cement stabilization mix design for both granular and cohesive soils is proposed.

**Keywords:** soil stabilization, cement stabilization, unconfined compressive strength, fines content, Atterberg limits, AASHTO group index

## INTRODUCTION

Embankment subgrade soils classifying as A-4 to A-7-6 according to the AASHTO Soil Classification System can exhibit low bearing strength, high volumetric instability, and freeze-thaw susceptibility, which are frequently identified as main factors leading to accelerated damage of pavement systems (White and Bergeson, 2001; White et al., 2004, 2008, 2018; Zhang et al., 2016, 2019; Li et al., 2020). Soil stabilization with cement has been studied during the past six decades over a variety of soil types (Balmer, 1958; Mitchell, 1976; Uddin et al., 1997; Lo and Wardani, 2002; Lorenzo and Bergado, 2004; Sariosseiri, 2008; Sariosseiri et al., 2011; Sarkar et al., 2012;

Rashid et al., 2014; Riaz et al., 2014; Yang et al., 2018; Li et al., 2020). Previous research indicated that Portland cement stabilized materials generally show superior performance than any other chemical stabilizer (Parsons and Milburn, 2003; Henry et al., 2005; Zhang et al., 2016, 2019; Li et al., 2017, 2018, Li C. et al., 2019). Multiple regression analysis is a valuable tool applied in geotechnical engineering (Li S. et al., 2019). Horpibulsuk (2012) reported the effectiveness of various percentages cement mixture on the specimen's strength development. Three strength development zones were presented: active, inert, and deterioration zone. In the active zone, the pores smaller than 0.1 micron significantly decreased due to cement hydration process, so the strength increased significantly. However, as content of cement additives increased, the desired water was not adequate for hydration, so the strength and quantity of cementitious materials decreased. Various studies have previously developed similar relationships between cement dosage and modified soil strength and other engineering properties, such as liquid limit, plasticity index, etc (Qubain et al., 2006; Sariosseiri et al., 2011; Du et al., 2013; Rashid et al., 2014). Spangler and Patel (1950) showed that the plastic limit was increased as cement content increased, and plasticity index was decreased as cement admixture content increased because the liquid limit was decreased.

To understand how the cement content can influence the strength and soil index properties of both cohesive and granular materials, the present study conducted a comprehensive laboratory evaluation. A total of 28 granular and cohesive materials were tested using 4–12% type I/II Portland cement contents. The laboratory results were analyzed using multivariate statistical analysis to assess influence of the cement content and soil index properties on post-stabilization material properties. Based on the laboratory test and statistical analysis results, a laboratory testing and evaluation procedure for cement stabilization mix design for both granular and cohesive soils is proposed.

## MATERIALS AND METHODS

In this study, a total of 28 granular and cohesive materials obtained from nine construction sites were tested using 4–12% type I/II Portland cement contents. **Table 1** summarizes the parent materials, particle size analyses, Atterberg limits, and soil classifications test results of the materials. The cohesive soils were collected from 25 test beds of eight project sites, and the parent materials of the cohesive soils were either glacial till or loess. The cohesionless granular soils were collected from three test beds of one project site, and their parent material was alluvium material.

## TESTING AND ANALYSIS METHODS

To classify the materials tested in this study, particle size analysis was conducted in accordance with ASTM D422-63 (2007) (ASTM, 2007). The distribution of particle sizes larger than 75  $\mu\text{m}$  (opening size of the No. 200 sieve) was determined

by sieving, and the distribution of particle sizes smaller than 75  $\mu\text{m}$  was determined by the hydrometer method. Atterberg limit testing was conducted in accordance with ASTM D4318-10 (2000) (ASTM, 2000) using the wet preparation method. Liquid limit tests were performed using the multipoint method. Based on these results, each sample was classified according to the AASHTO Soil Classification System and Unified Soil Classification System (USCS).

## Soil Compaction Test

The relationship between the moisture and dry unit weight of embankment materials was determined in accordance with ASTM D698 (2013) (ASTM, 2013) and ASTM D1557 (2009) (ASTM, 2009). Appropriate methods were chosen based on the grain size distributions for each sample. The tests were performed at five moisture contents, and the optimum moisture-density characteristics were obtained by fitting the data to the Li and Sego Fit model as described in Eq. 1

$$\gamma_d(w) = \frac{G_s \gamma_w}{\left(1 + \frac{w G_s}{S_m - S_m \left(\frac{w_m - w}{w_m}\right)^{n+1} \left(\frac{w_m^n + p^n}{(w_m - w) + p^n}\right)}\right)} \quad (1)$$

where  $\gamma_d$  = dry density of the soil,  $G_s$  = specific gravity of the soil,  $\gamma_w$  = density of water,  $w$  = moisture content of the soil,  $S_m$  = maximum degree of saturation,  $w_m$  = moisture content at  $S_m$ , and  $n$  and  $p$  are shape factors.

## ISU 2 Inch by 2 Inch Test

ISU 2 inch by 2 inch compaction apparatus is described in O'Flaherty et al. (1963). The test procedure was used to prepare 50.8 mm (2 inch) diameter by 50.8 mm (2 inch) height samples for unconfined compressive strength (UCS) testing. Standard Proctor optimum moisture content for each sample was determined based on the Li and Sego Fit model, and each sample was compacted at that moisture content. For cement treated materials, the optimum moisture content was determined using Eq. 2 with a water to cement (w/c) ratio of 0.25:

$$w_{\text{opt soil+cement}} = [(\% \text{ cement added by weight}) \times (w/c \text{ ratio})] + w_{\text{opt soil}} \quad (2)$$

The test procedure involved placing loose material in the compaction apparatus and dropping a 2.27 kg hammer from a drop height of about 0.31 m in a 50.8 mm diameter steel mold. O'Flaherty et al. (1963) provided guidance on the number of blows required to obtain standard Proctor densities for different soil types, 6, 7, 14 drop-hammer blows for AASHTO soil types A-7/A-6, A-4, and A-3/A-2/A-1, respectively. The number of blows were selected based on the soil type and equal number of blows were applied on both sides of the sample, to compact the sample uniformly.

After compaction, the 2 inch by 2 inch specimens were sealed using plastic wrap and aluminum foil, and were placed in sealed plastic bag. According to Winterkorn and Pamukcu (1990), cement stabilized specimens cured for 7 days at 43°C can be used to simulate 28 day curing strength. Unstabilized specimens were

**TABLE 1** | Soil index properties of the granular and cohesive subgrade materials tested in this study.

Construction site	Parent material	Gravel content (> 4.75 mm) (%)	Sand content (4.75 mm – 75 $\mu$ m) (%)	Silt content (75 $\mu$ m – 2 $\mu$ m) (%)	Clay content (< 2 $\mu$ m) (%)	Liquid limit, LL (%)	Plastic limit, PL (%)	Plastic Index, PI (%)	AASHTO classification	USCS classification
1# TB1	Glacial till	0.4	11.6	66.4	21.6	49	28	21	A-7-6 (21)	CL
1# TB2	Glacial till	3.9	25.8	34.7	35.6	45	34	11	A-7-5 (8)	CL
1# TB3	Glacial till	2.6	28.7	45.8	22.9	36	20	16	A-6 (9)	CL
1# TB4	Glacial till	1.8	24.6	50.9	22.7	34	17	17	A-6 (11)	CL
2# TB1	Glacial till	2.0	27.5	37.3	33.2	44	31	13	A-7-5 (9)	CL
2# TB2	Glacial till	5.0	31.6	31.9	31.5	40	19	21	A-6 (11)	CL
2# TB3 (Gray)	Glacial till	0.7	18.7	39.1	41.5	54	20	34	A-7-6 (28)	CH
2# TB3 (Brown)	Glacial till	0.6	29.2	33.7	36.5	40	20	20	A-6 (13)	CL
3# TB1	Weathered loess	0.7	46.0	26.4	26.9	31	25	6	A-4 (1)	CL-ML
4# TB1	Glacial till	1.8	37.6	32.9	27.7	31	12	19	A-6 (8)	CL
4# TB2	Glacial till	1.3	42.6	30.9	25.2	34	16	18	A-6 (7)	CL
4# TB3	Glacial till	11.3	36.1	31.2	21.4	33	11	22	A-6 (7)	CL
4# TB4	Glacial till	1.1	39.9	35.6	23.4	32	16	16	A-6 (6)	CL
4# TB5	Glacial till	2.0	40.3	34.8	22.9	30	16	14	A-6 (5)	CL
5# TB1	Manufactured materials	7.3	10.1	56.2	26.4	43	18	25	A-7-6 (20)	CL
5# TB2	Manufactured materials	5.3	25.5	48.0	21.2	42	19	23	A-7-6 (14)	CL
6# TB1	Alluvium	0.2	78.4	15.5	5.9	NP	NP	NP	A-2-4	SM
6# TB2	Alluvium	0.0	83.2	12.6	4.2	NP	NP	NP	A-2-4	SM
6# TB3	Alluvium	1.7	81.1	11.6	5.6	NP	NP	NP	A-2-4	SM
7# TB1	Loess	0.1	1.0	72.9	26.0	39	32	7	A-4 (10)	CL-ML
7# TB2	Loess	1.0	24.3	45.5	29.2	35	24	11	A-6 (8)	CL
7# TB3	Loess	2.0	29.2	45.9	22.9	28	17	11	A-6 (5)	CL
8# TB1	Loess	0.1	3.1	70.6	26.2	38	34	4	A-4 (7)	CL-ML
8# TB2	Loess	3.9	6.4	34.9	54.8	36	31	5	A-4 (6)	CL-ML
9# TB1	very deep loess	0.0	8.8	68.8	22.4	32	25	7	A-4 (7)	CL-ML
9# TB2	Very deep loess	0.0	1.3	73.3	25.4	35	27	8	A-4 (9)	CL
9# TB3	Very deep loess	0.1	4.2	69.6	26.1	35	23	12	A-6 (12)	CL
9# TB4	Very deep loess	0.0	6.4	72.0	21.6	31	24	7	A-4 (7)	CL-ML



**FIGURE 1** | Vacuum saturation of cement stabilized specimens.

tested shortly after compaction (no curing). Three samples were prepared at each cement content.

### UCS Test

The cured specimens were tested for UCS accordance with ASTM D 1633 (2014) (ASTM, 2014b). The standard requires use of either 101.6 mm diameter by 116.4 mm height Proctor samples with a height to diameter ratio ( $h/d$ ) of 1.15 or 71.1 mm diameter by 142.2 mm height samples with a  $h/d$  ratio of 2.0. Instead, 2 inch by 2 inch. specimens were used in this study which have a  $h/d$  ratio of 1.0. Based on laboratory evaluations, White et al. (2005) concluded that the UCS determined from 2 inch by 2 inch specimens can be multiplied by 0.86 to correlate with UCS of Proctor sized samples ( $h/d = 1.15$ ) or 0.90 to correlate with samples that have  $h/d = 2$ . The ASTM D1633 (2014) (ASTM, 2014b) also provides a similar guidance in relating UCS on samples with  $h/d = 2$  multiplying a factor of 1.10 to samples with  $h/d = 1.15$  for conversion.

The cured specimens were tested in unsaturated and saturated condition. The specimens were saturated using the vacuum saturated method as described in ASTM C593 (2014) (ASTM, 2014a). The specimens were placed on a perforated Plexiglas plate in a vacuum vessel as shown in **Figure 1**, and the chamber was evacuated to 609 MmHg for 30 minutes. Then the vacuum vessel was flooded to a depth sufficient to cover the soil specimens. After 1 h of soaking, the specimens were removed from the vessel to conduct UCS testing. For samples that become fragile and cannot be removed from water for UCS testing, the UCS is reported as 0 kPa.

### Multiple Regression Analysis

The multiple regression analysis was performed to evaluate that how the cement content and pre-treatment soil index properties can influence the soil index properties and UCS of the soils. Regression analyses were performed by incorporating the parameters as independent variables into a general multiple linear regression model as shown in Eq. 3.

$$\text{Predicted parameter} = b_0 + b_1X_1 + b_2X_2 \cdots b_nX_n \quad (3)$$

where

Predicted parameters = UCS, PI, GI, and  $F_{200}$ ,

$b_0$  = intercept,

$b_n$  = regression coefficients, and  $X_n$  = various parameters (cement content, LL,  $F_{200}$ , clay content, PI, and sand content).

Statistical significance of each variable was assessed based on  $p$  and  $t$  values. A statistical analysis software, JMP 10 was used to generate the statistical models based on testing data. The criteria for identifying the significance of a parameter was:  $p$  value  $< 0.05$  = significant,  $< 0.10$  = possibly significant,  $> 0.10$  = not significant, and  $t$ -value  $< -2$  or  $> +2$  = significant. The  $p$ -value indicated the significance of a parameter and the  $t$ -ratio value indicates the relative importance. The best fit model was determined based on the strength of the regression relationships assessed by the coefficient of determination ( $R^2$ ) values.

## LABORATORY TEST RESULTS

In the following sections, the results and analysis are separately for  $F_{200}$ , Atterberg limits, GI, and UCS, to present the influence of cement stabilization on these properties.

### Fines Content ( $F_{200}$ )

Results of  $F_{200}$  versus cement content are presented in **Figure 2**. The results indicated that  $F_{200}$  of both the cohesive and granular soils greatly decreased with increasing cement content due to the fine soil particles of the materials were bonded by the cement hydration and pozzolanic reactions.

Statistical analysis was conducted to predict  $F_{200}$  after treatment as a function of cement content,  $F_{200}$  before treatment, and Atterberg limits. Cement content,  $F_{200}$  before treatment, and LL were found to be statistically significant as shown in **Table 2**. PI and PL parameters were not statistically significant. The measured versus predicted  $F_{200}$  of soils after cement treatment from the multi-variate model are presented in **Figure 3**. The model showed an  $R^2$  of about 0.9 and RMSE of about 7%.

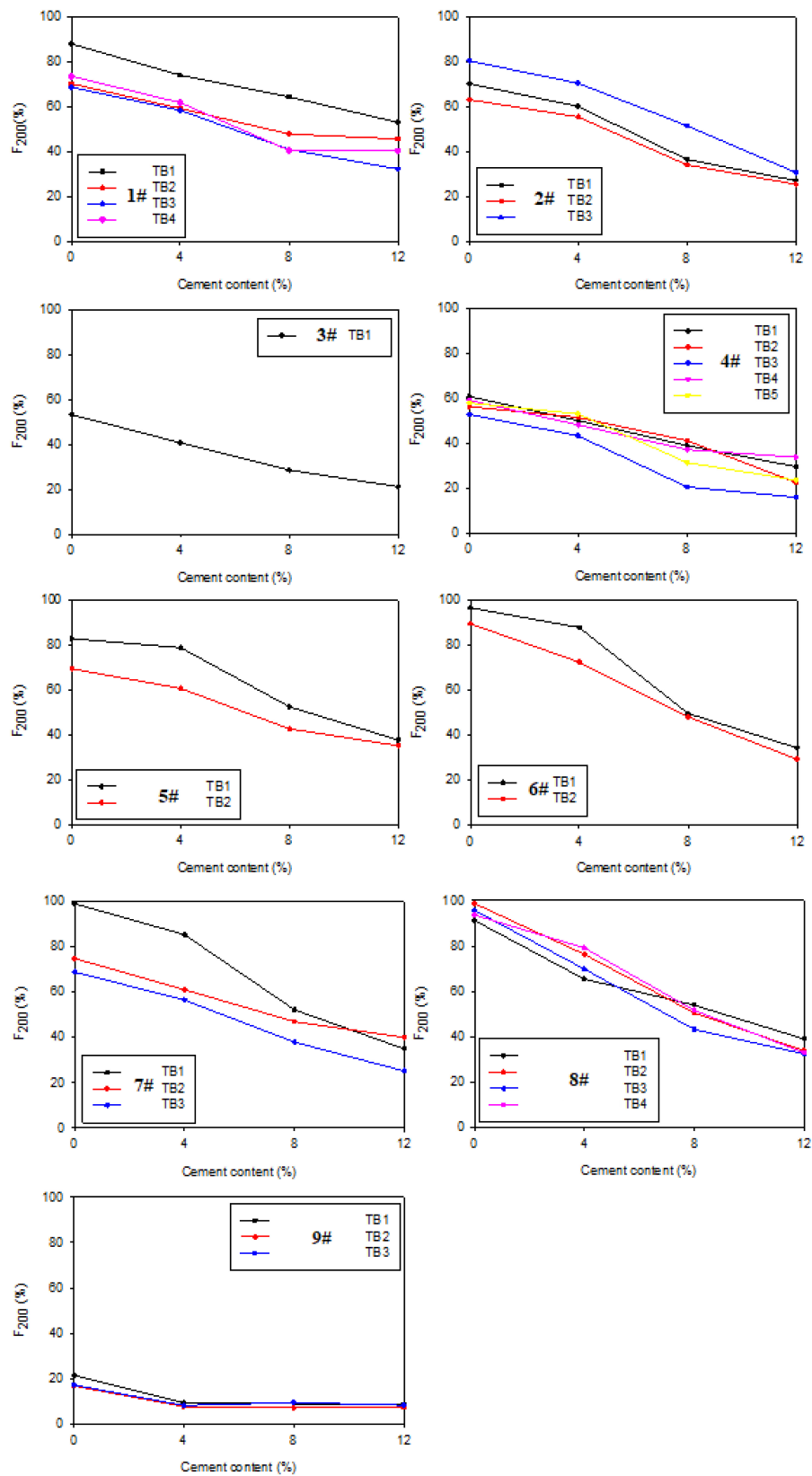
### Atterberg Limits

The  $F_{200}$  versus PI results of the untreated and cement treated soils with 4, 8, and 12% cement content are shown in **Figure 4**. The test results show that both of the PI and  $F_{200}$  decreased as the cement content increased. For soils treated with 12% cement, the PI values are zero, which indicates that the treated soils become to non-plastic.

Statistical analysis was conducted to predict PI after treatment as a function of cement content, clay content, silt content, and LL. Results are summarized in **Table 3**. Cement content and clay content were found to be statistically significant, while the remaining parameters were not statistically significant. Measured versus predicted PI (after treatment) results from the multi-variate model are presented in **Figure 5**. The model showed an  $R^2$  of about 0.5 and RMSE of about 5%.

### AASHTO Group Index (GI)

For a majority of the soils, the GI values decreased with increasing cement content. Statistical analysis was conducted



**FIGURE 2** |  $F_{200}$  versus cement content.

**TABLE 2** | Multi-variate analysis results to predict  $F_{200}$  after cement stabilization.

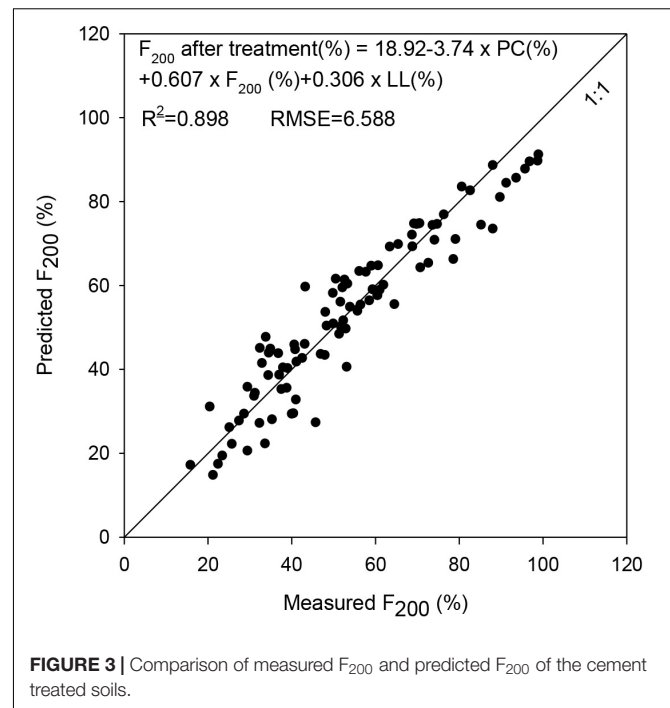
Parameter	Value	t Ratio	Probability >  t	$R^2$	RMSE
Intercept	18.92	3.96	<0.0001	0.90	6.588
Cement content (%)	-3.74	-24.88	<0.0001		
$F_{200}$ before treatment (%)	0.607	13.23	<0.0001		
LL (%)	0.306	2.79	0.0064		
Prediction expression	$F_{200}$ after treatment (%) = $18.92 - 3.74 \times \text{cement content (\%)} + 0.607 \times F_{200} (\%) + 0.306 \times \text{LL (\%)}$				

on the laboratory test results to predict GI after treatment as a function of cement content, clay content, silt content,  $F_{200}$ , LL, and PI. Results are summarized in **Table 4**. Cement content,  $F_{200}$ , LL, and PI were found to be statistically significant, while the remaining parameters were not statistically significant. Measured versus predicted GI (after treatment) results from the multi-variate model are presented in **Figure 6**. The model showed an  $R^2$  of about 0.7 and RMSE of about 3.

## Unconfined Compressive Strength

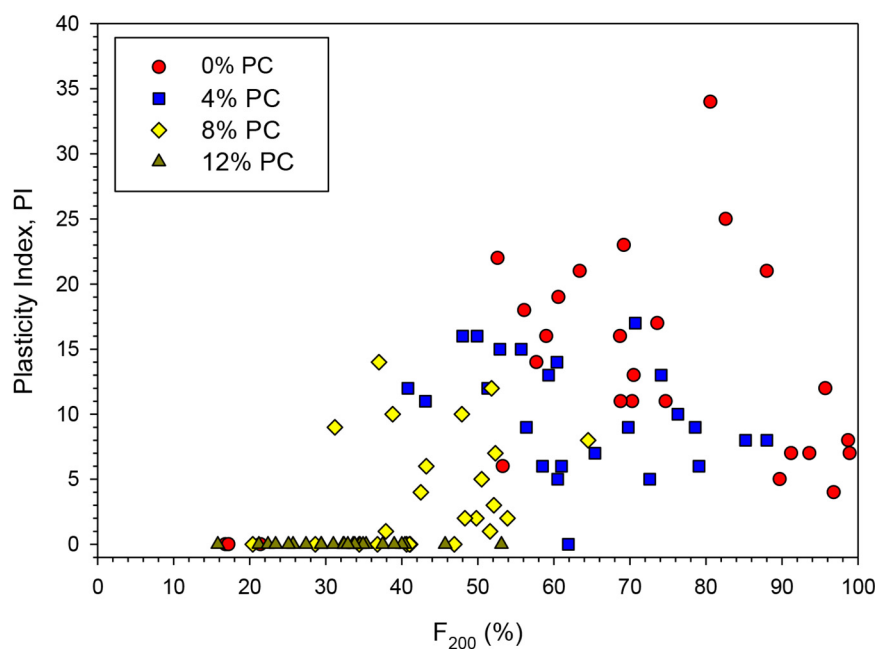
The results of unsaturated and vacuum saturated UCS of the materials at different cement contents are used for determining relationships between the cement content and pre- and post-saturation strength of the materials.

Results indicated that increasing UCS with increasing cement content, as expected. For a majority of the unstabilized materials, the soil specimens became fragile after vacuum saturation and could not be retrieved from the vessel. For those soils, UCS of 0 kPa is reported herein. Vacuum saturated stabilized specimens resulted in UCS



measurements that were on average about 1.5 times lower than the unsaturated specimens. The ratio of unsaturated and vacuum saturated UCS of stabilized specimens ranged from about 1.1 to 2.5.

Statistical analysis was also conducted to predict unsaturated and vacuum saturated UCS as a function of cement content, sand

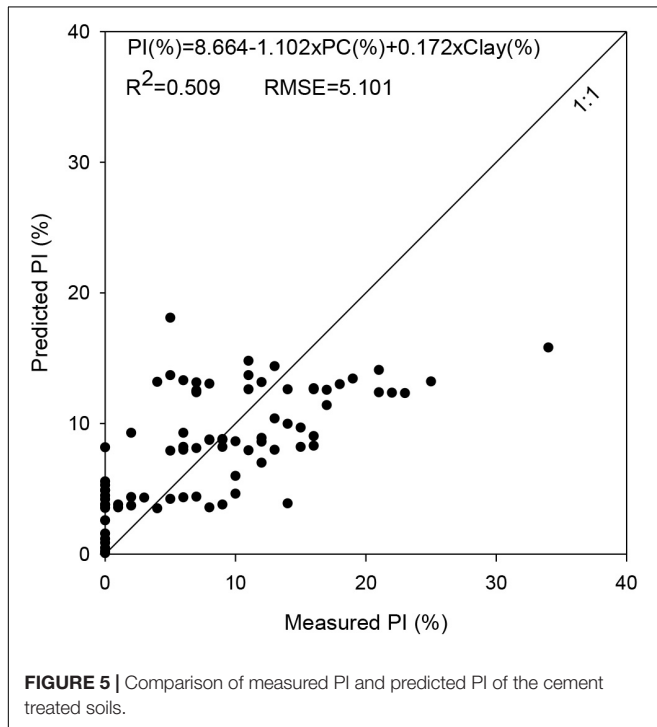




**TABLE 3 |** Multi-variate analysis results to predict PI after cement stabilization.

Parameter	Value	t Ratio	Probability >  t	R <sup>2</sup>	RMSE
Intercept	8.664	5.85	<0.0001	0.509	5.101
Cement Content (%)	-1.102	-10.04	<0.0001		
Clay content (%)	0.172	3.49	0.0007		
Prediction expression	PI after treatment (%) = 8.664 - 1.102 × cement content (%) + 0.172 × Clay content (%)				

Silt content, sand content, and LL were not statistically significant.

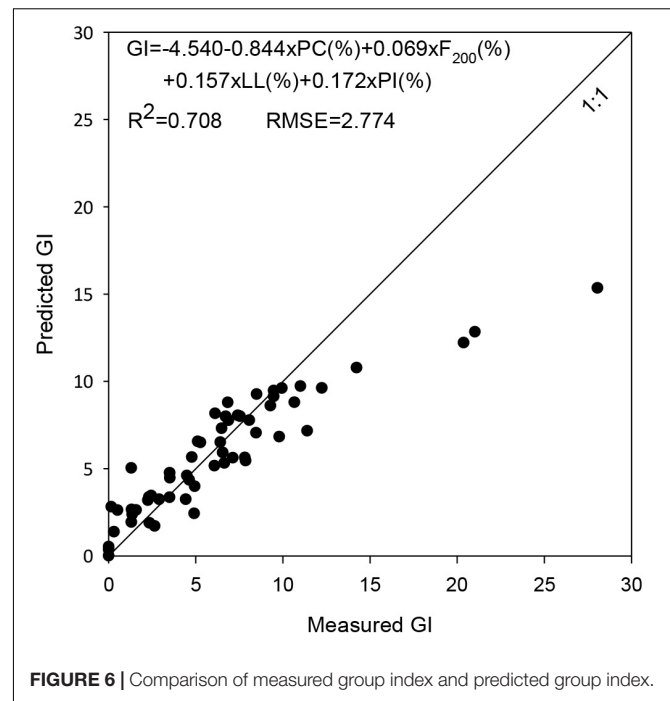
**FIGURE 5 |** Comparison of measured PI and predicted PI of the cement treated soils.

content, clay content, silt content,  $F_{200}$ , LL, and PI. Results are summarized in **Tables 5, 6**. The cement content, sand content,  $F_{200}$ , and LL were found to be statistically significant, while the remaining parameters were not statistically significant. Measured versus predicted UCS results from the multi-variate model are presented in **Figure 7**. The models showed an  $R^2$  of about 0.855 and RMSE of about 515 kPa for vacuum saturated UCS and 672 kPa for unsaturated UCS.

**TABLE 4 |** Multi-variate analysis results to predict GI after cement stabilization.

Parameter	Value	t Ratio	Probability >  t	R <sup>2</sup>	RMSE
Intercept	-4.540	-2.23	0.0281	0.708	2.774
Cement Content (%)	-0.844	-13.33	<0.0001		
$F_{200}$ (%)	0.069	2.85	0.0055		
LL (%)	0.157	2.98	0.0164		
PI (%)	0.172	2.45	0.0037		
Prediction expression	GI = -4.540 - 0.844 cement content (%) + 0.069 × $F_{200}$ (%) + 0.157 × LL (%) + 0.172 × PI (%)				

Silt content and clay content were not statistically significant.

**FIGURE 6 |** Comparison of measured group index and predicted group index.

## PROPOSED TESTING AND EVALUATION PROCEDURE

Based on the test results and experience obtain from this laboratory evaluation, a mix design procedure is proposed for sampling and testing, and requirements of cement stabilized soils.

**TABLE 5 |** Multi-variate analysis results to predict unsaturated UCS.

Parameter	Value	t Ratio	Probability >  t	R <sup>2</sup>	RMSE
Intercept	1465.38	3.61	0.0005	0.855	671.675
Cement content (%)	48.69	21.90	<0.0001		
Sand (%)	-13.26	-3.13	0.0023		
$F_{200}$ (%)	-9.24	-2.35	0.0209		
LL (%)	-11.28	-6.77	<0.0001		
Prediction expression	UCS (kPa) = 10103.4 + 335.7 × cement content (%) - 91.4 × Sand (%) - 77.8 × LL (%) - 63.7 × $F_{200}$ (%)				

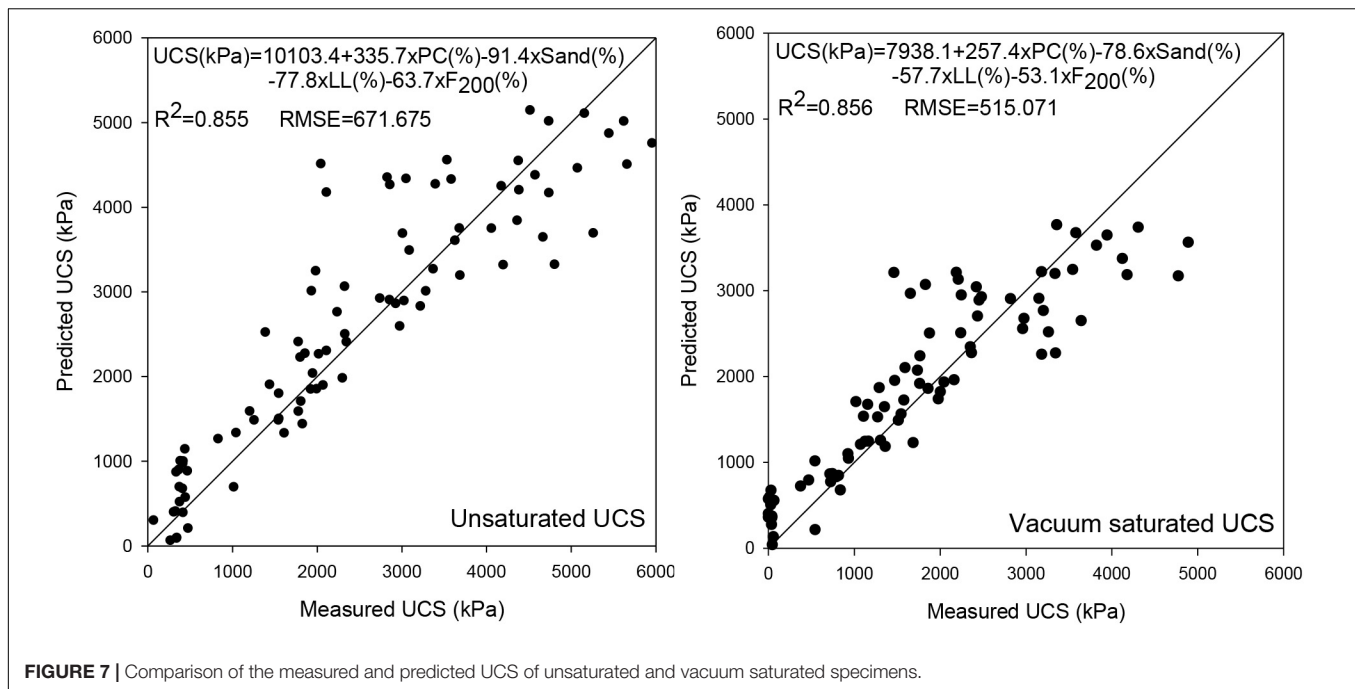
Note: Silt content and clay content were not statistically significant.

**TABLE 6 |** Multi-variate analysis results to predict vacuum saturated UCS.

Parameter	Value	t Ratio	Probability >  t	R <sup>2</sup>	RMSE
Intercept	1151.32	3.7	0.0004	0.856	515.071
Cement content (%)	37.33	21.89	<0.0001		
Sand (%)	-11.40	-3.51	0.0007		
$F_{200}$ (%)	-7.70	-2.56	0.0123		
LL (%)	-8.37	-6.55	<0.0001		
Prediction expression	UCS (kPa) = 7938.1 + 257.4 × cement content (%) - 78.6 × Sand (%) - 57.7 × LL (%) - 53.1 × $F_{200}$ (%)				

Silt content and clay content were not statistically significant.





## Sampling and Materials

Each soil sample to be used in chemical stabilization shall be 35 kg. The cement used for stabilization shall meet the requirements of Type I or I/II.

## Sample Preparation and Testing

The sulfate content of the soil shall be determined. If the soil consists of soluble sulfate content > 3,000 ppm or the material classifies as unsuitable, chemical stabilization shall not be performed unless consulted with the engineers.

For each soil type, prepare three samples each for the following five mixes:

1. Mix 1: Untreated soil.
2. Mix 2: 2% cement.
3. Mix 3: 4% cement.
4. Mix 4: 6% cement.
5. Mix 5: 8% cement.

To determine the quantity of cement to be added to the soil, multiply the cement percentage by the dry weight of the soil. Use cement that is from the same source(s) that will be used during construction.

## Moisture–Density Relationship

First, the moisture–density relationship of the different mixtures shall be determined. Then, UCS testing shall be performed at target moisture contents, as described below.

The moisture versus dry density relationship of untreated and cement-treated samples shall be determined using one of the following alternatives:

Alternative 1:

**Untreated Samples:** The maximum dry density and optimum moisture content of the untreated samples shall be determined using standard Proctor test in accordance with ASTM D698 (2013) (ASTM, 2013). A minimum 3-point Proctor is recommended.

**Treated Samples:** The maximum dry density and optimum moisture content shall be determined in accordance with ASTM D558 (2019) (ASTM, 2019). All treated samples must be compacted within 1 h of mixing. A minimum 3-point Proctor is recommended.

Alternative 2:

The maximum dry density and optimum moisture content of untreated and treated samples shall be determined using the ISU 2 inch by 2 inch. Moisture–Density Test Method, per Chu et al. (1995). In preparing samples using the 2 inch by 2 inch method, use the method of O’Flaherty et al. (1963) for guidance on the total number of drop-hammer blows depending on the soil type to obtain results similar to the standard Proctor test.

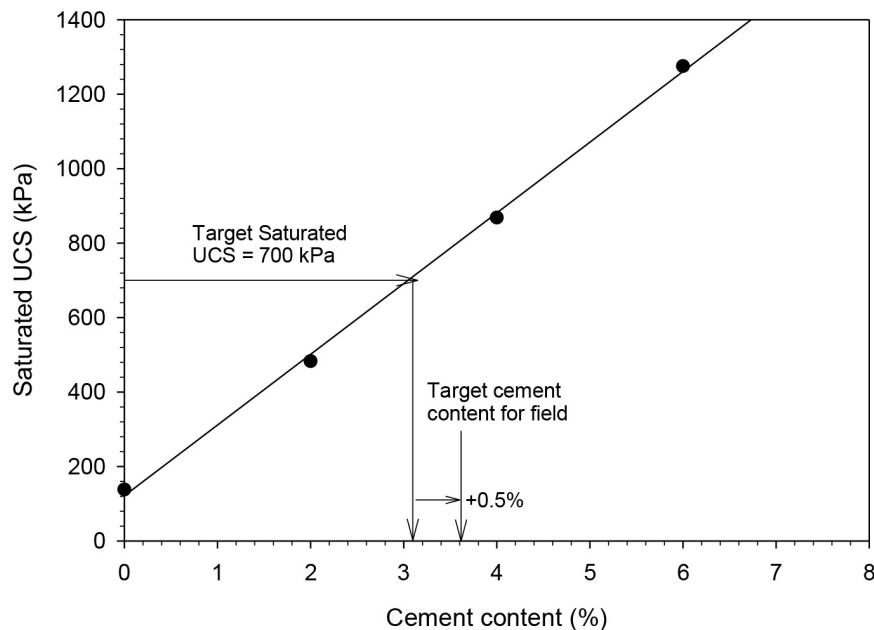
Alternative 3:

First, determine the optimum moisture content of the untreated soil using standard Proctor test in accordance with ASTM D698 (2013) (ASTM, 2013). Then use the following equation to determine the optimum moisture content of treated samples, by using a water to cement (w/c) ratio of 0.25:

$$w_{opt\ soil+cement} = [(\% \text{ cement added by weight}) \times (w/c \text{ ratio})] + w_{opt\ soil} \quad (4)$$

## Unconfined Compressive Strength

The UCS tests shall be performed on compacted samples at respective optimum moisture contents for untreated and treated soils, in accordance with ASTM D1633-00 (2014) (ASTM,



**FIGURE 8 |** Determination of target cement content for field application.

2014b). As an alternative, tests can be performed on 2 inch by 2 inch samples prepared per Alternative 2 above.

For each mix, prepare three samples for UCS testing for a total of 12 samples. Wrap each sample immediately after compaction with a plastic wrap and aluminum foil and store in a moisture-proof and airtight bag. All treated samples shall be cured at 38°C for 7 days. Untreated samples shall be cured for no more than 24 h.

After curing, all samples shall be vacuum saturated in accordance with ASTM C593 (2014) (ASTM, 2014a). For samples that become fragile and cannot be retrieved from water for UCS testing, report the UCS as 0 kPa.

### Target Cement Content Determination

The data obtained from UCS testing shall be plotted on a graph with cement content on *x*-axis and saturated UCS on *y*-axis. The average UCS of three samples shall be reported on the *y*-axis. The cement content corresponding to a saturated UCS of 700 kPa shall be determined. A 0.5% cement shall be added to determine the target cement content for the field application, as illustrated in **Figure 8**.

## SUMMARY AND CONCLUSION

Results of a laboratory study focused on cement stabilization of 28 soils obtained from 9 active construction sites are presented in this paper. The materials consisted of glacial till, loess, and alluvium sand. Type I/II Portland cement was used for stabilization of these materials. 2 inch by 2 inch specimens of treated and untreated specimens were prepared, cured, and tested for UCS with and without vacuum saturation. The  $F_{200}$ ,

Atterberg limits, and AASHTO GI were determined before and after treatment. The results were analyzed using multi-variate regression analysis to assess influence of the various soil index properties on post-stabilization material properties. Key findings from the test results and analysis are as follows:

1.  $F_{200}$  of the material decreased with increasing cement content for a majority of the soils. The percent cement content,  $F_{200}$  before treatment, and liquid limit were found to be statistically significant in predicting the  $F_{200}$  after treatment. The multi-variate model showed an  $R^2$  of about 0.9 and RMSE of about 7% in predicting the  $F_{200}$  after treatment.
2. With the exception of a few materials, the liquid limit and plasticity index of all materials decreased with increasing cement content. The percent cement content and clay content parameters were found to be statistically significant in predicting the plasticity index of materials after stabilization. The multi-variate model showed an  $R^2$  of about 0.5 and RMSE of about 5%.
3. The GI values decreased with increasing cement content for a majority of the soils. The percent cement content,  $F_{200}$ , liquid limit, and plasticity index parameters were found to be statistically significant in predicting the group index values after treatment. The multi-variate model showed an  $R^2$  of about 0.7 and RMSE of about 3.
4. The UCS of specimens increased with increasing cement content, as expected. The average saturated UCS of the unstabilized materials varied between 0 and 400 kPa. The average saturated UCS of stabilized materials varied between 0.3 and 2,000 kPa at 4% cement content, 0.8 and 3700 kPa at 8% cement content, and 1.1 and 4,900 kPa at

12% cement content. The laboratory testing and evaluation procedure for cement stabilization mix design targets a 700 kPa saturated UCS. The UCS of the saturated specimens was on average 1.5 times lower than that of the unsaturated specimens.

5. The percent cement content, sand content, fines content, and liquid limit were found to be statistically significant in predicting unsaturated and vacuum saturated UCS. The models showed an  $R^2$  of about 0.85 and RMSE of about 500 kPa for vacuum saturated specimens and 700 kPa for unsaturated specimens.

## DATA AVAILABILITY STATEMENT

All datasets presented in this study are included in the article/supplementary material.

## AUTHOR CONTRIBUTIONS

SL conducted the laboratory works and data analysis, and prepared the project report and manuscript. YY prepared part of the manuscript. CL, LY, PZ, LW, and TH reviewed the article and gave some valuable feedbacks. All authors contributed to the article and approved the submitted version.

## REFERENCES

- ASTM (2000). *Standard Test Methods for Liquid Limit, Plastic Limit, and Plasticity Index of Soils. Annual BOOK of ASTM Standards, ASTM D4318 - 00*. West Conshohocken, PA: ASTM.
- ASTM (2007). *ASTM D422 - 63(2007)e1 Standard Test Method for Particle Size Analysis of Soils*. West Conshohocken, PA: American Standards for Testing Methods.
- ASTM (2009). *Standard Test Methods for Laboratory Compaction Characteristics of Soil Using Modified Effort (56,000 ft-lbf/ft<sup>3</sup>(2,700 kN-m/m<sup>3</sup>))*. West Conshohocken, PA: ASTM International.
- ASTM (2013). *Standard Test Methods for Laboratory Compaction Characteristics of Soil Using Standard Effort (12,400 ft-lbf/ft<sup>3</sup>(600 kN-m/m<sup>3</sup>))*. West Conshohocken, PA: ASTM International.
- ASTM (2014a). *Standard Specification for Fly Ash and Other Pozzolans for Use With Lime for Soil Stabilization. Annual Book of ASTM Standards, ASTM C593-05*. West Conshohocken, PA: ASTM.
- ASTM (2014b). *Standard Test Methods for Compressive Strength of Molded Soil-Cement Cylinders. Annual Book of ASTM Standards, ASTM D1633-17*. West Conshohocken, PA: ASTM.
- ASTM (2019). *Standard Test Methods for Moisture-Density (Unit Weight) Relations of Soil-Cement Mixtures ASTM D558 / D558M - 19*. West Conshohocken, PA: American Standards for Testing Methods.
- Balmer, G. G. (1958). *Shear Strength And Elastic Properties Of Soil-Cement Mixture Under Triaxial Loading*. Skokie, IL: Portland Cement Association Research and Development Laboratories.
- Chu, T. Y., Davidson, D. T., Goecker, W. L., and Moh, Z. C. (1955). Soil Stabilization with lime fly ash mixtures: preliminary studies with silty and clayey soils. *Highway Res. Board Bull.* 108, 102–112.
- Du, Y.-J., Jiang, N.-J., Liu, S.-Y., Jin, F., Singh, D. N., and Puppala, A. J. (2013). Engineering properties and microstructural characteristics of cement-stabilized zinc-contaminated kaolin. *Can. Geotechn. J.* 51, 289–302. doi: 10.1139/cgj-2013-0177
- Henry, K. S., Olson, J. P., Farrington, S. P., and Lens, J. (2005). *Improved Performance of Unpaved Roads During Spring Thaw*. Hanover: Engineer Research and Development Center Cold Regions Research.
- Horpiulsuk, S. (2012). *Strength and Microstructure of Cement Stabilized Clay*. London: INTECH Open Access Publisher.
- Li, C., Ashlock, J. C., Lin, S., and Vennapusa, P. K. R. (2018). In situ modulus reduction characteristics of stabilized pavement foundations by multichannel analysis of surface waves and falling weight deflectometer tests. *Construct. Build. Mater.* 188, 809–819. doi: 10.1016/j.conbuildmat.2018.08.163
- Li, C., Ashlock, J. C., White, D. J., and Vennapusa, P. K. R. (2019). Mechanistic-based comparisons of stabilised base and granular surface layers of low-volume roads. *Intern. J. Pavem. Eng.* 20, 112–124. doi: 10.1080/10298436.2017.1321417
- Li, S., Wu, L., Bian, X., Song, C., Li, P., and Han, Z. (2019). “Statistically analysis for stability of various protection modes of expansive soil cutting slope,” in *Proceedings of the 2019 International Conference on Virtual Reality and Intelligent Systems (ICVRIS)*, Jishou.
- Li, C., Vennapusa, P. K. R., Ashlock, J., and White, D. J. (2017). Mechanistic-based comparisons for freeze-thaw performance of stabilized unpaved roads. *Cold Reg. Sci. Technol.* 141, 97–108. doi: 10.1016/j.coldregions.2017.06.004
- Li, C., Zheng, J., Zhang, Z., Sha, A., and Li, J. (2020). Morphology-based indices and recommended sampling sizes for using image-based methods to quantify degradations of compacted aggregate materials. *Construct. Build. Mater.* 230:116970. doi: 10.1016/j.conbuildmat.2019.116970
- Lo, S. R., and Wardani, S. P. R. (2002). Strength and dilatancy of a stabilized by a cement and fly ash mixture. *Can. Geotechn. J.* 39, 77–89.
- Lorenzo, A., and Bergado, D. T. (2004). Fundamental parameters of cement-admixed clay-New approach. *J. Geotechn. Geoenviron. Eng.* 130, 1042–1050. doi: 10.1061/(asce)1090-0241(2004)130:10(1042)
- Mitchell, J. K. (1976). “The properties of cement-stabilized soils,” in *Proceeding of the Residential Workshop On Materials And Methods For Low Cost Road, Rail, And Reclamation Works*, Leura.
- O’Flaherty, C. A., Edgar, C. E., and Davidson, D. T. (1963). “The iowa state compaction apparatus: a small sample apparatus for use in obtaining density

## FUNDING

The authors would like to thank the Science and Technology Innovation Special Fund Project of Central Government Public Welfare Research Institutes (Grant No. 2019-C504) and Guizhou Province Department of Transport Research Project Fund (Grant No. 2020-122-013) for sponsoring this study. The financial supports provided by Natural Science Foundation of Shaanxi Province in China (Grant No. 2019JQ-498), the key scientific and technological projects of transportation industry (Project No. 2019-MS2-039), and the Science and Technology Progress and Innovation Project of Hunan Provincial Department of Transportation (Grant No. 201904) are greatly appreciated.

## ACKNOWLEDGMENTS

A project report “Cement stabilization of embankment materials” that the corresponding author SL submitted to Iowa DOT in 2015, which has been documented in the National Transportation Library. The manuscript summarizes the key findings of the technical report, so the manuscript is more concise and can help more readers to learn this work.

- and strength measurements of soils and soil-additives,” in *Proceedings of the Special Report Prepared for Presentation at the 42nd Annual Meeting of the Highway Research Board*, Ames.
- Parsons, R. L., and Milburn, J. P. (2003). Engineering behavior of stabilized soils. *Transport. Res. Record J. Transport. Res. Board* 1837, 20–29.
- Qubain, B. S., Heirendt, K. M., and Li, J. (2006). “Quality assurance and quality control requirements for lime and cement subgrade stabilization,” in *Proceedings of the Pavement Mechanics and Performance-GeoShanghai International Conference*, Wayne, PA.
- Rashid, A. S. A., Kalatehjari, R., Noor, N. M., Yaacob, H., Moayedi, H., and Sing, L. K. (2014). Relationship between liquidity index and stabilized strength of local subgrade materials in a tropical area. *Measurement* 55, 231–237. doi: 10.1016/j.measurement.2014.05.018
- Riaz, S., Aadil, N., and Waseem, U. (2014). Stabilization of subgrade soils using cement and lime: a case study of Kala Shah Kaku, Lahore, Pakistan. *Pak. J. Sci.* 66, 39–44.
- Sariosseiri, F. (2008). *Critical State Framework For Interpretation Of Geotechnical Properties Of Cement Treated Soils*. Ph. D thesis, Washington State University, Pullman, WA.
- Sariosseiri, F., Razavi, M., Carlson, K., and Bahareh, G. (2011). Stabilization of soils with portland cement and CKD and application of CKD on slope erosion control. *Geo Front.* 2011, 778–787.
- Sarkar, G., Islam, M. R., Alamgir, M., and Rokonzaman, M. (2012). Study on the geotechnical properties of cement based composite fine-grained soil. *Intern. J. Adv. Struct. Geotechn. Eng.* 1, 42–49.
- Spangler, M., and Patel, O. (1950). “Modification of a Gumbotil soil by lime and Portland cement admixtures,” in *Proceedings of the Twenty-Ninth Annual Meeting of the Highway Research Board Held*, Washington, DC.
- Uddin, K., Balasubramaniam, A. S., and Bergado, D. T. (1997). Engineering behaviors of cement-treated bangkok soft clay. *Geotechn. Eng. J.* 28, 89–119.
- White, D. J., and Bergeson, K. L. (2001). Long-term strength and durability of hydrated fly-ash road bases. *Transport. Res. Record* 1755, 151–159. doi: 10.3141/1755-16
- White, D. J., Ceylan, H., Jahren, C. T., Phan, T. H., Kim, S. H., Gopalakrishnan, K., et al. (2008). *Performance Evaluation Of Concrete Pavement Granular Subbase-Pavement Surface Condition Evaluation*. Moines, IA: State Library of Iowa.
- White, D. J., Harrington, D., and Thomas, Z. (2005). *Fly Ash Soil Stabilization For Non-Uniform Subgrade Soils, Volume I: Engineering Properties And Construction Guidelines*. Ames, IA: Center for Portland Cement Concrete Pavement Technology (PCC Center).
- White, D. J., Vennapusa, P., and Jahren, C. T. (2004). *Determination of the Optimum Base Characteristics for Pavements*. Ames, IA: Iowa Department of Transportation.
- White, D. J., Vennapusa, P., Tutumluer, E., Vavrik, W., Moaveni, M., and Gillen, S. (2018). Spatial verification of modulus for pavement foundation system. *Transport. Res. Record* 2672, 333–346. doi: 10.1177/0361198118782266
- Winterkorn, H. F., and Pamukcu, S. (1990). “Soil stabilization and grouting,” in *Foundation Engineering Handbook*, ed. H.-Y. Fang (New York, NY: Van Nostrand Reinhold).
- Yang, B., Zhang, Y., Ceylan, H., Kim, S., and Gopalakrishnan, K. (2018). Assessment of soils stabilized with lignin-based byproducts. *Transport. Geotech.* 17, 122–132. doi: 10.1016/j.trgeo.2018.10.005
- Zhang, Y., Johnson, A. E., and White, D. J. (2016). Laboratory freeze-thaw assessment of cement, fly ash, and fiber stabilized pavement foundation materials. *Cold Reg. Sci. Technol.* 122, 50–57. doi: 10.1016/j.coldregions.2015.11.005
- Zhang, Y., Johnson, A. E., and White, D. J. (2019). Freeze-thaw performance of cement and fly ash stabilized loess. *Transport. Geotechn.* 21:100279. doi: 10.1016/j.trgeo.2019.100279

**Conflict of Interest:** YY was employed by the Xiandai Investment Co., Ltd.

The remaining authors declare that the research was conducted in the absence of any commercial or financial relationships that could be construed as a potential conflict of interest.

Copyright © 2020 Yang, Li, Li, Wu, Yang, Zhang and Huang. This is an open-access article distributed under the terms of the Creative Commons Attribution License (CC BY). The use, distribution or reproduction in other forums is permitted, provided the original author(s) and the copyright owner(s) are credited and that the original publication in this journal is cited, in accordance with accepted academic practice. No use, distribution or reproduction is permitted which does not comply with these terms.



# An Indoor Laboratory Simulation and Evaluation on the Aging Resistance of Polyether Polyurethane Concrete for Bridge Deck Pavement

Shifa Xu<sup>1,2\*</sup>, Meng Xu<sup>1,2,3</sup>, Yexing Zhang<sup>1</sup>, Yutao Guo<sup>1</sup>, Geng Peng<sup>1</sup> and Ying Xu<sup>4</sup>

<sup>1</sup> School of Civil and Transportation Engineering, Beijing University of Civil Engineering and Architecture, Beijing, China,

<sup>2</sup> Beijing Advanced Innovation Center for Future Urban Design, Beijing University of Civil Engineering and Architecture,

Beijing, China, <sup>3</sup> Shandong Provincial Engineering Laboratory of Transportation Safety and Emergency Support Technology, Shandong Jiaotong University, Jinan, China, <sup>4</sup> Beijing Urban Traffic Infrastructure Engineering Research Center, Beijing

University of Civil Engineering and Architecture, Beijing, China

## OPEN ACCESS

### Edited by:

Zhanping You,  
Michigan Technological University,  
United States

### Reviewed by:

Haifang Wen,  
Washington State University,  
United States  
Pedro Romero,  
The University of Utah, United States

### \*Correspondence:

Shifa Xu  
xu-sf@126.com

### Specialty section:

This article was submitted to  
Structural Materials,  
a section of the journal  
Frontiers in Materials

**Received:** 30 March 2020

**Accepted:** 29 June 2020

**Published:** 30 July 2020

### Citation:

Xu S, Xu M, Zhang Y, Guo Y,  
Peng G and Xu Y (2020) An Indoor  
Laboratory Simulation and Evaluation  
on the Aging Resistance of Polyether  
Polyurethane Concrete for Bridge  
Deck Pavement. *Front. Mater.* 7:237.  
doi: 10.3389/fmats.2020.00237

Polyether polyurethane concrete (PPC) is a new engineering material used for bridge deck pavement. In this article, the aging resistance performance of PPC for long-term service is evaluated. Based on the actual climate and environment conditions of bridge deck pavement, the indoor laboratory simulation considering various environmental factors was first proposed, and then the indoor accelerated aging tests of PPC were carried out. Finally, the Cantabro test, the low-temperature bending beam test, the rutting test, the splitting test under freeze-thaw cycle, and four-point bending fatigue test were conducted on the aged PPC specimens. The performances of anti-loose, resistance to permanent deformation, low temperature, water stability, and fatigue resistance were evaluated and compared with styreneic block copolymers (SBS) modified asphalt mixture (SBSM). Test results showed that PPC had good anti-aging performance, and the road performance of PPC after aging was still better than that of non-aging SBSM, which can be used for the long-term service as a bridge deck pavement material.

**Keywords:** polyether polyurethane concrete, bridge deck pavement, road performance, anti-aging performance, simulation and evaluation

## INTRODUCTION

As an important part of bridge, the durability of bridge deck pavement is always a hot topic in the field of transportation infrastructure engineering (Wang and Liu, 2013; Sun and Chen, 2014; Geng et al., 2016; Qian et al., 2016; Hee et al., 2017; Zhang et al., 2018). At present, most of the bridge deck pavement materials are hot-mixed asphalt concretes. In many regions, there exists long-time high temperature in summer and fast cooling in winter. Asphalt materials are easy to deform at high temperature and crack at low temperature due to the strong temperature sensitivity. In addition, the phenomenon of vehicles that are overlimited and with overload has become more and more serious, leading to the shear failure of the pavement. If water continues to invade, it may further result in the loose failure of the structure (Guan et al., 2005; Yang, 2013). For these reasons, considering the remarkable progress in the traditional asphalt-based materials (Hou et al., 2017; Xu et al., 2018; Yang et al., 2020a,b), they still cannot achieve the long life of bridge deck pavement requirements.

Polyurethane polymer has good flexibility and elasticity suitable for service with long-term dynamic deflection. In addition, it has good mechanical properties, wide adhesion applicability,



and low temperature sensitivity and can thus replace the asphalt materials to achieve the long-term service life of bridge deck pavement. Moreover, the polyether polyurethane concrete (PPC) can be mixed and constructed at room temperature, which significantly saves energy and reduces emission. Therefore, PPC has good engineering applicability as bridge deck pavement material.

In recent years, there have been many researches carrying out on the performance evaluation and application of polymer concrete all through the world. Li et al. (2019) carried out the experimental research on the key performances of polyurethane permeable mixture and analyzed the differences in mechanical properties and functional characteristics between polyurethane permeable mixture and porous asphalt mixture. Lu et al. (2019a,b) developed a sustainable permeable pavement material with recycled ceramic aggregate and biobased polyurethane adhesives. The mechanical properties, functional characteristics, and environmental performance of the material were evaluated and compared with the porous asphalt mixture. Lu et al. (2020) also analyzed the influences of saturation on the permeable pavement using the new polyurethane binder through finite element simulation. Lu et al. (2020) found that different graded PUPMs (polyurethane-bound pervious mixtures) have different failure characteristics, where the ductility can be increased by adjusting the aggregate gradation. Wang et al. (2014) carried out the experimental research on the strength and road performance of porous polyurethane macadam mixture and tested the influences of binder consumption and Macadam shape on its strength and road performance. Chen et al. (2018a) conducted studies on the anti-icing and de-icing performances of polymer concrete. They found that the icing time of polymer concrete was significantly longer than that of traditional asphalt concrete, and the work required to destroy the ice layer on its surface was only 50% of that of asphalt concrete. Chen et al. (2018b) discussed the durability and functional performance of porous polyurethane mixture (PPM) instead of open-graded friction course (OGFC) in porous pavement. Wang et al. (2017b) conducted studies on the effects of various composition factors on the easy loosening of poroelastic road surface (PERS). Wang et al. (2017a) explored the possibility of using PERS on urban roads in cold areas. Gao et al. (2019) evaluate the comprehensive properties of polyurethane rubber particle mixture (PRPM) at high temperature, anti-aging, and skid resistance and showed PRPM had superior comprehensive performance, but slightly lower skid resistance. Biligiri et al. (2013) conducted studies on the basic material (stiffness) characteristics of PERS related to pavement design. Cong et al. (2018) conducted studies on the PPMs and asphalt-bonded porous mixtures (APMs), which showed that the PPM obtained three times' higher stability and over one order of magnitude greater fatigue life than APM. Polyurethane mixtures are mainly used in the following fields: OGFC, PPM, PERS, and self-stressing deicing mixture (Cong et al., 2019).

Wang et al. (2018) developed the PPC as the bridge deck pavement material, evaluated its road performance, and proposed that the residual splitting strength under freeze-thaw cycles should be used as the water stability index of PPC. They found that the dynamic stability and low-temperature bending

tensile strain of PPC were nearly 10 times higher than asphalt mixture, and the fatigue life was more than 1 million times. The splitting strength under freeze-thaw cycle is similar to that of SMA asphalt mixture without freeze-thaw cycle. Based on the above findings, PPC has excellent road performance, but as a polymer material, its molecular chain may have degradation reaction affected by many environmental factors including air, temperature, light, water, and so on. Besides, polyurethane binder is a thermosetting material and does not have the self-healing performance as asphalt material. Therefore, in engineering practice, the properties of polyurethane binder will be irreversibly affected by aging under the severe environmental conditions, resulting in the decrease of the cohesive force between the aggregate and polyether polyurethane binder, and finally affect the physical and mechanical properties of PPC. Although some scholars have conducted some research on polyurethane mixtures, the anti-aging property of polyurethane concrete used as a bridge deck pavement material is still one of the most significant problems for the pavement industry.

In this study, the indoor laboratory accelerated aging tests were used to simulate the severe environmental conditions of PPC during the regular service life. The aging resistances of PPC were evaluated and compared with the non-aging styreneic block copolymers (SBS) modified asphalt mixture (SBSM), based on a number of road performance tests, which will provide the theoretical and experimental basis for future application of PPC as a bridge deck pavement material.

## RAW MATERIALS AND TEST METHODS

### Raw Materials

#### Polyurethane Binder

The self-developed single-component polyether polyurethane, which is a black thermosetting material, can be mixed at room temperature. It has good adhesion performance with aggregate after curing, and the test results are shown in **Table 1**. Polyurethane binder for pavement is mainly formed by polymerization addition of polyether polyol and polyisocyanate. In the material design, the multifunctional oxazolidine curing agent is used, which can preferentially react with water to generate amino ( $-NH_2$ ), hydroxy ( $-OH$ ), and then cross-link with isocyanate ( $-NCO$ ) to form elastomer with network structure that can effectively reduce the generation of bubbles and improve the strength of elastomer.

#### Asphalt

In this study, SBSM is also tested for comparison, where SBS-modified asphalt with penetration ( $25^\circ C$ , 0.1 mm) of 66, ductility of 37 cm at  $5^\circ C$ , softening point of  $73^\circ C$ , and elastic recovery rate of 95% at  $25^\circ C$  is used.

#### Mineral Aggregate

The aggregate was basalt, and the filler was limestone mineral powder. All the technical indexes met the requirements of Technical Specifications for Construction of Highway Asphalt Pavement in China (JTG F40-2004, 2004), as shown in **Table 2**.

**TABLE 1** | Technical properties of polyurethane.

Test	Unit	Technical quality requirements	Result	Test method
Density	g/cm <sup>3</sup>	—	1.1	GB/T. 4472-2011, 2011
Tensile strength (25°C)	MPa	≥2.0	2.5	GB/T. 16777-2008, 2008
Elongation at break (25°C)	%	≥150	155	
Surface dry time (25°C)	h	0.5–4	1.5	
Inside dry time (25°C)	h	8–25	14	
Water impermeability (0.3 MPa, 24 h)	—	Impermeable	Impermeable	
Water absorption rate	%	≤4	2	GB/T. 1034-2008, 2008
Kinematic viscosity (25°C)	mPa.s	≤3,000	2,550	JTG E20/T 0619

**TABLE 2** | Technical properties of aggregate.

Type	Technical properties	Aggregate A	Aggregate B
Coarse aggregate	Apparent density (g/cm <sup>3</sup> )	2.913	2.921
	Bulk density (g/cm <sup>3</sup> )	2.876	2.882
	Water absorption (%)	0.44	0.46
	Crushing value (%)	9.5	10.4
	Los Angeles abrasion value (%)	10.5	11.9
	Content of needle and flake (%)	4.6	3.3
	<0.075-mm content (%)	0.5	0.6
Fine aggregate	Apparent density (g/cm <sup>3</sup> )	2.725	
Mineral powder	Apparent density (g/cm <sup>3</sup> )	2.718	

### Preparation of Mixture and Mix Ratio

Polyether polyurethane concrete (hereinafter referred to as PPC-13) and SBSM (hereinafter referred to as SBSM-13) with the maximum nominal particle size of 13 mm were selected for the comparative tests, and the gradation of mineral aggregate is shown in **Table 3**.

The Marshall design method was used for the mixture design. The material properties of PPC and asphalt mixture are different, and the requirements of stability and voidage are also different. Previous research (Shi, 2018) shows that the voidage of PPC can meet the requirements within the range of 2.0–3.5%. According to the test results, the binder–aggregate ratio of PPC-13 and SBSM-13 is 7 and 5.4%, respectively.

The preparation of PPC specimen was as follows: after the aggregate was evenly mixed according to the designed gradation, it was added into the mixing pot for dry mixing at room temperature for 90 s. Then the polyurethane binder was evenly mixed with the aggregate for 90 s. Finally, the mineral powder was added and mixed for 90 s, where the PPC specimen was formed after curing at room temperature for a certain time.

## TEST DESIGN

### Indoor Laboratory Simulation Aging Test

At present, there are very few studies on the aging resistance of PPC as a bridge deck pavement material in the actual service environment, and there is no official specification for reference. In this study, to reflect the effects of the actual

service environmental conditions on bridge deck pavement, the indoor laboratory simulation test was designed. The methods of photothermal coupling aging and thermo-oxidative aging were applied on the PPC specimens; based on a number of road performance tests after aging, the effects of temperature and ultraviolet (UV) light on the road performance of PPC were studied. The non-aging SBSM was used for comparison; since the performance of aged PPC is better than the non-aging SBSM, the performance of aged PPC is better than that of aged SBSM. Moreover, sometimes the aged SBSM specimens are fragile and too easy to fail; in this case, the non-aging SBSM specimen was used for testing.

### Thermo-Oxidative Aging Simulation

At high temperature in summer, polyurethane binder will have oxidation reaction, that is, thermo-oxidative aging. Polyether polyurethane concrete is mixed at room temperature, so its thermo-oxidative aging generally occurs after paving. In China, the temperature of bridge deck in summer can reach approximately 60°C. In order to simulate the thermo-oxidative aging of PPC under high temperature in summer, PPC specimens were placed in the ventilation oven at 60°C for 1, 2, 3, 4, 5, and 6 weeks, respectively, to simulate the thermo-oxidative aging in actual environment conditions.

Relevant research (Luo et al., 1999; Shen et al., 2014; Ionita et al., 2020) shows that the thermo-oxidative aging of polyurethane will increase with the increase of temperature. In order to improve the aging rate and to realize the thermo-oxidative aging effect for long-term service of bridge deck pavement in a short time, 90°C was selected as the accelerated aging condition, where the effect of temperature difference on the aging resistance of PPC was also compared.

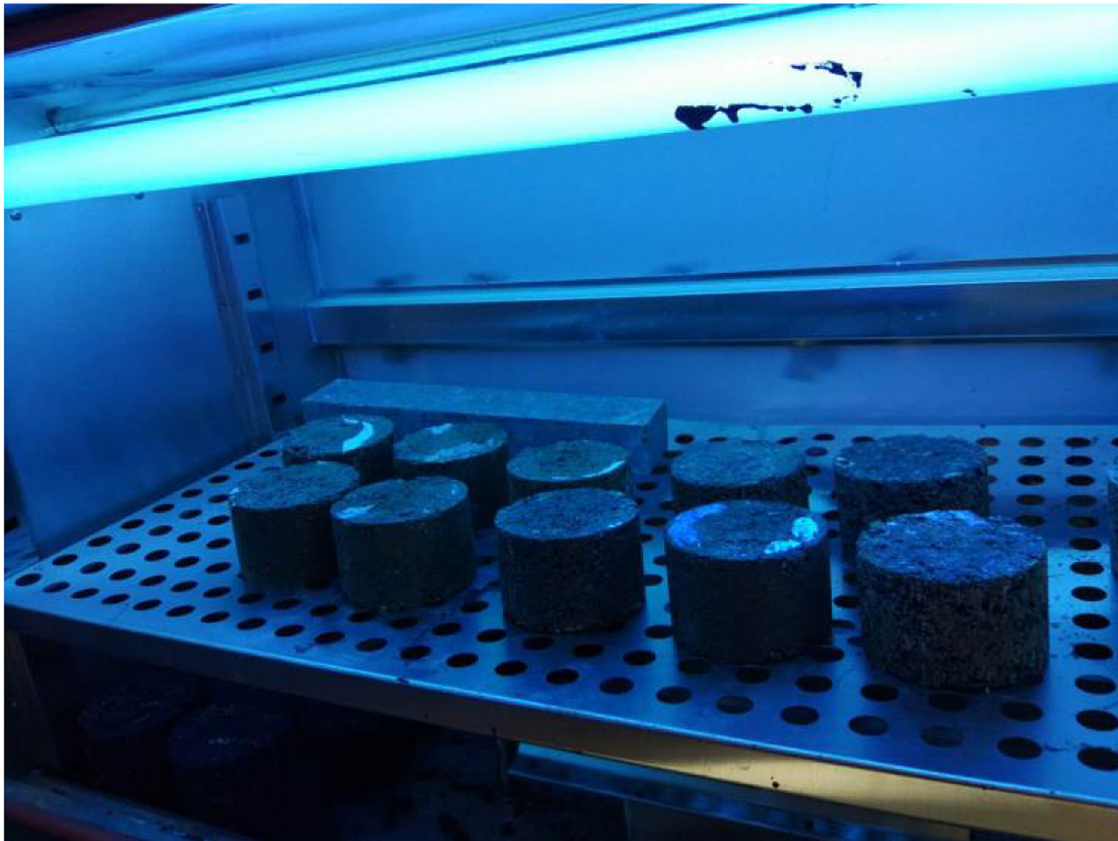
### Photothermal Coupling Aging Simulation

The photochemical reaction of polyurethane binder, such as molecular chain breaking or group falling off, will occur under sunlight irradiation, known as photoaging. The UV radiation ability is the strongest in sunlight, which may result in significant damage to polyurethane binder. Therefore, to simulate the most critical state, the self-developed UV aging weatherometer with irradiance of 160 W·m<sup>-2</sup> and test temperature of 60°C was used to irradiate the PPC specimens for 1, 2, 3, 4, 5, and 6 weeks, respectively, as shown in **Figure 1**.



**TABLE 3** | Gradation of aggregate.

Gradation type	Mass percentage passing the following sieve (mm) (%)									
	0.075	0.15	0.3	0.6	1.18	2.36	4.75	9.5	13.2	16
PPC-13	5.6	11.7	13.9	16.6	22.4	31.8	50.4	76.7	95.9	100
SBSM-13	5.6	11.7	13.9	16.6	22.4	31.8	50.4	76.7	95.9	100



**FIGURE 1** | Polyether polyurethane concrete specimens in ultraviolet aging weatherometer.

Based on the meteorological data, the annual UV radiation amount in Beijing is  $294.8 \text{ (MJ} \cdot \text{m}^{-2})$ . According to the equivalent conversion between the indoor and outdoor radiation energy, the UV irradiation using weatherometer for 1 week is equivalent to that of the bridge deck in the natural environment for 120 days.

### Road Performance Test After Aging

In this study, three test conditions of  $60^\circ\text{C}$  aging,  $90^\circ\text{C}$  aging, and photothermal coupling aging were applied on the PPC specimens and the non-aging SBSM specimens, and then a number of road performance tests were carried out for comparison.

#### Anti-loose performance

Cantabro durability test can be used to evaluate the phenomenon of aggregate falling off under traffic load due to insufficient cohesion. According to the Standard Test Methods of Bitumen

and Bituminous Mixtures for Highway Engineering in China (JTG E20-2011, 2011), Cantabro test was carried out. After aging, PPC specimens were immersed in  $20^\circ\text{C}$  water bath for 20 h. The comparison group was non-aging SBSM.

It is found that the mass loss of PPC is kept within 3% under various environmental conditions in the initial test, indicating that PPC has good anti-loose performance, but at the same time, the mass loss cannot effectively quantify the relationship between anti-loose performance and aging conditions of PPC. In this study, the splitting strength loss before and after the test is used as the evaluation index of anti-loose performance. The splitting strength loss is calculated according to the following Eq. (1)

$$\nabla P = \frac{P_0 - P_1}{P_0} \times 100\% \quad (1)$$



**FIGURE 2 |** Low-temperature cracking test on the UTM-25 servo hydraulic multifunctional material test system.

where  $\nabla P$  is the splitting strength loss (%),  $P_0$  is the splitting strength before test (MPa), and  $P_1$  is the splitting strength after test (MPa).

#### **Low-temperature crack resistance**

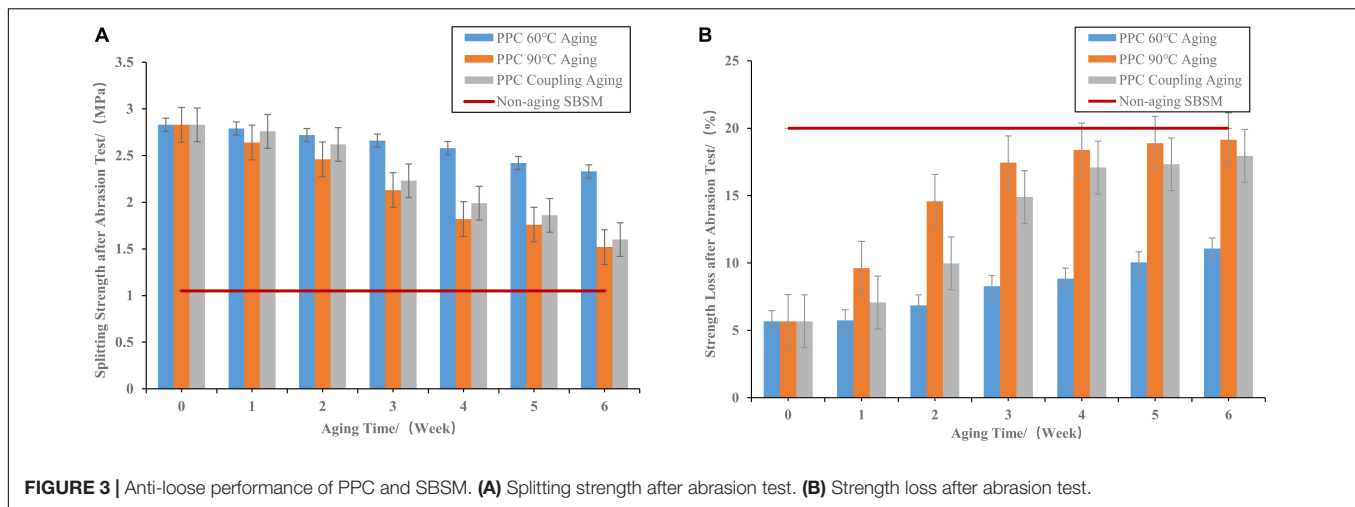
Low-temperature cracking is a common pavement distress in cold regions. Polyether polyurethane concrete, as a bridge deck pavement material, is required to maintain good low-temperature crack resistance for long-term service. In this study, referring to the Standard Test Methods of Bitumen and Bituminous Mixtures for Highway Engineering in China (JTG E20-2011, 2011), the low-temperature bending beam test was conducted. The test specimens were formed by wheel milling and cut into the small beam with the size of 250 mm × 30 mm × 35 mm. The low-temperature performance of the small beam at different aging stages was tested at  $-10^{\circ}\text{C}$  using the UTM-25 servo hydraulic multifunctional material test system, as shown in **Figure 2**.

#### **Resistance to permanent deformation**

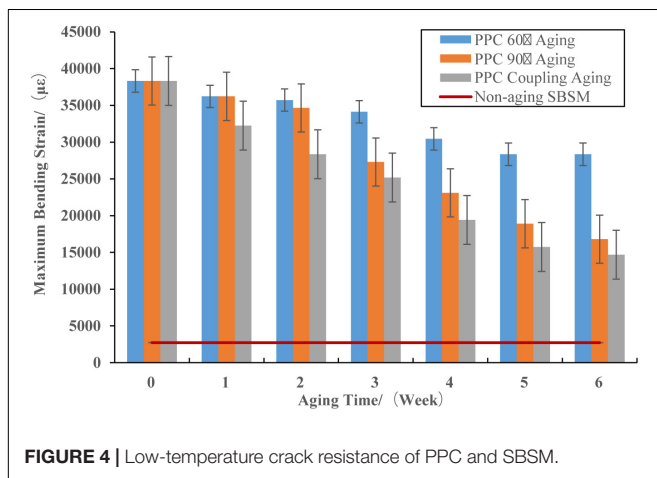
In this study, according to the Standard Test Methods of Bitumen and Bituminous Mixtures for Highway Engineering in China (JTG E20-2011, 2011), the rutting test of mixture was carried out to evaluate the PPC resistance to permanent deformation by measuring the dynamic stability of PPC after aging. In the test, the wheel-rolling method was used to form a 300-mm × 300-mm × 50-mm rutting test specimen. During the test, the tire pressure was 0.7 MPa, the test temperature was  $60^{\circ}\text{C}$ , and the rolling speed was 42 times/min.

#### **Water stability test**

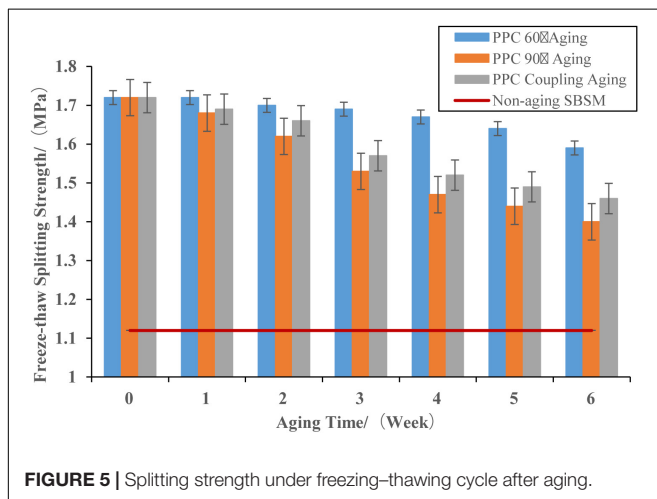
When the bridge deck pavement is in regular service, water vapor in the environment will lead to the degradation and swelling of polyurethane binder, and the dynamic water pressure and scouring force under the load will lead to the decrease of the binding force between the binder and aggregate, which will



**FIGURE 3 |** Anti-loose performance of PPC and SBSM. **(A)** Splitting strength after abrasion test. **(B)** Strength loss after abrasion test.



**FIGURE 4 |** Low-temperature crack resistance of PPC and SBSM.



**FIGURE 5 |** Splitting strength under freezing–thawing cycle after aging.

eventually cause the pavement damage. Especially in summer and winter, the temperature change is significant, and the precipitation is large, and the water temperature in the deck pavement changes frequently. In order to simulate the water

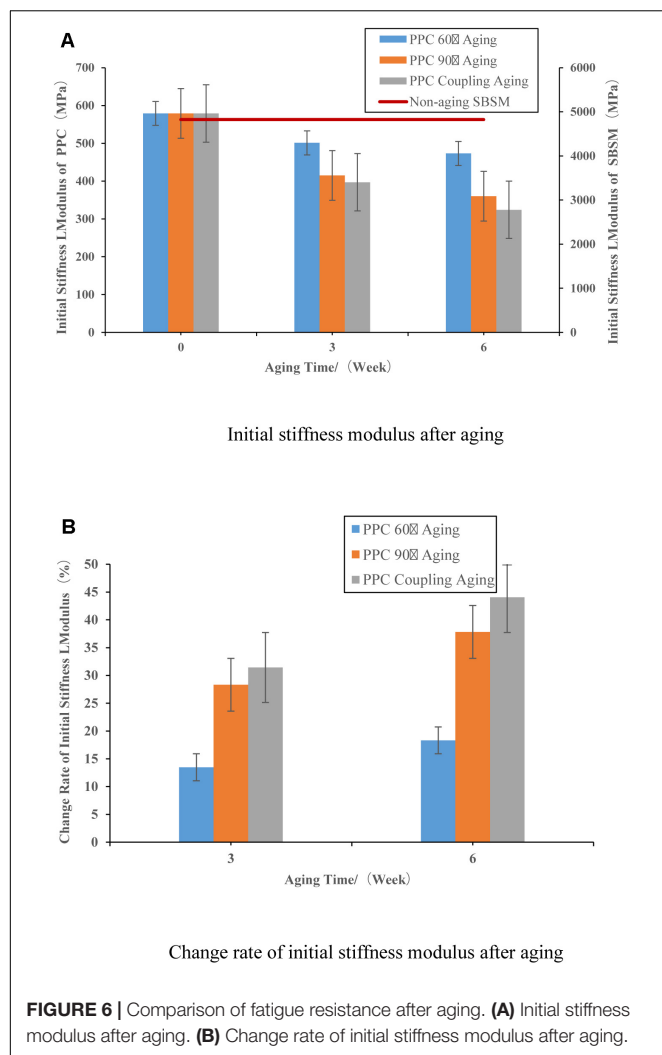
temperature change of PPC in the actual service environment, the aged PPC specimens were tested under freeze–thaw cycle. According to the Standard Test Methods of Bitumen and Bituminous Mixtures for Highway Engineering in China (JTG E20-2011, 2011), the freeze–thaw split test method was adopted. After the test sample was saturated with water in vacuum for 15 min, it was placed in the environment of  $-18^{\circ}\text{C}$  for 16 h, and then the test sample was treated in constant temperature water bath of  $60^{\circ}\text{C}$  for 24 h and finally in constant-temperature water bath of  $25^{\circ}\text{C}$  for 2 h.

#### Fatigue resistance test

In order to evaluate the fatigue resistance of PPC after aging, the four-point bending fatigue test was carried out on the UTM-25 hydraulic servo control system, where loading strain  $1,200\ \mu\epsilon$  was selected to reflect the impact of heavy load traffic. The loading mode was sine wave, the loading frequency was 10 Hz, the test temperature was  $15^{\circ}\text{C}$ , and the test specimen was  $380\text{-mm} \times 63.5\text{-mm} \times 50\text{-mm}$  beam.

It was found that the fatigue life of PPC was more than 1 million times under various environmental conditions, indicating that PPC had good fatigue resistance performance. Meanwhile, the fatigue life cannot effectively quantify the relationship between PPC fatigue resistance and the aging conditions. Some studies (Ni and Yin, 2005) have shown that the initial stiffness modulus of the material can be used to characterize its ability to bear the repeated loads. Under the same strain conditions, the smaller the initial stiffness modulus of the concrete is, the stronger its ability to bear the repeated loads. In this study, the stiffness modulus of the test specimens after the 50th cycle of loading at the strain level of  $1,200\ \mu\epsilon$  was set as the initial stiffness modulus. The initial stiffness modulus of PPC and SBSM under different environmental conditions was tested, and the change rate of the initial stiffness modulus was used as the evaluation index of fatigue resistance. The change rate of the initial stiffness modulus is calculated according to the following Eq. (2):

$$\nabla S = \frac{S_0 - S_1}{S_0} \times 100\% \quad (2)$$



where  $\nabla S$  is the loss rate of initial stiffness modulus (%),  $S_0$  is the initial stiffness modulus before aging (MPa), and  $S_1$  is the initial stiffness modulus after aging (MPa).

## TEST RESULTS AND ANALYSIS

### Anti-loose Performance

**Figure 3** compared the anti-loose performance of aged PPC and non-aging SBSM, and error bars were applied to illustrate the deviation of testing results of PPC under different aging conditions. The following can be found:

- After 6 weeks of aging, the splitting strength loss of PPC at 90°C was about 1.7 times of that at 60°C, indicating that the thermo-oxidative aging effect at 90°C was more significant.
- After 6 weeks of aging, the splitting strength loss of PPC under the condition of photothermal coupling aging (17.95%) was significantly greater than that of 60°C (11.07%), indicating that UV light and heat exhibit

significant coupling effect, which was more significant than the effect of single thermo-oxidative aging on the anti-loose performance of PPC, and thermo-oxidative aging at 60°C had a greater impact on anti-loose performance of PPC than that of UV aging.

- For all the three aging conditions, the splitting strength of PPC decreased. After 6 weeks of aging, the splitting strength of PPC under three aging conditions was 2.33, 1.52, and 1.60 MPa, which were still significantly higher than that of the non-aging SBSM (1.05 MPa). The loss rate of strength under three conditions was 11.07, 19.15, and 17.95%, respectively, and was also lower than that of the non-aging SBSM (20%), which showed that PPC had better anti-loose performance than the SBSM for long-term service.

### Low-Temperature Cracking Resistance

**Figure 4** compares the maximum bending tensile strain of aged PPC and non-aging SBSM, and error bars were applied to illustrate the deviation of maximum bending tensile strain of PPC under different aging conditions. The following can be found:

- After 6 weeks of aging, the maximum bending strain decreasing rate of 90°C thermo-oxidative aging (56%) was about 2.2 times of 60°C (26%), indicating that the thermo-oxidative aging effect at 90°C was more significant, which was basically consistent with the previous analysis.
- The decreasing rate of the maximum bending strain under photothermal coupling aging (61%) was significantly higher than that under 60°C (26%). Therefore, it was concluded that UV light and heat exhibit significant coupling effect, which was more significant than the effect of single thermo-oxidative aging on the low-temperature performance of PPC, and UV light had a greater impact on low-temperature performance of PPC than the high temperature of the road surface during the service life. The main reasons are as follows: first, some of the molecular chains in polyurethane undergo oxidation reaction at high temperature, and some chemical bonds break, resulting in the decrease of material performance. And the higher the temperature is, the more violent the reaction will be. Second, UV light can irradiate into the internal microstructure of the material, and long-term irradiation causes large amounts of the chemical bonds break in polyurethane, and the free radicals gradually solidify, resulting in the increasing in the material rigidity and decreasing in flexibility at low temperature. The bending and tensile properties thus decrease.
- For all the three aging conditions, the maximum bending tensile strain of PPC decreased. However, after 6 weeks of aging, the maximum bending tensile strain of PPC was 28,350, 16,835, and 14,721  $\mu\epsilon$ , which were still better than that of non-aging SBSM (2,723  $\mu\epsilon$ ), which showed that PPC had better low-temperature crack resistance performance than SBSM for long-term service.



## Resistance to Permanent Deformation

The dynamic stability of non-aging PPC was 46,835 (s/mm); after 6 weeks of aging, the dynamic stability values of PPC under three aging conditions were 47,598, 48,125, and 49,661 s/mm. For the non-aging SBSM, it was 6,640 (s/mm). It can be found that, after aging, the dynamic stability of PPC did not change significantly and was significantly higher than that of SBSM. Therefore, PPC has better resistance to permanent deformation than SBSM. The reason is that the deformation of PPC under high temperature and traffic load will gradually recover after unloading.

## Water Stability

**Figure 5** compares the freeze–thaw splitting strength of PPC under three aging conditions, and error bars were applied to illustrate the deviation of freeze–thaw splitting strength of PPC under different aging conditions. The following can be found:

1. After 6 weeks of aging, the decreasing rate of freeze–thaw splitting strength at 90°C thermo-oxidative aging (18.6%) was about 2.4 times of that at 60°C (7.6%), which was similar to the previous conclusion.
2. By comparing the freeze–thaw splitting strength of PPC under 60°C and photothermal coupling aging conditions, it can be found that the freeze–thaw splitting strength decreasing rate of PPC under photothermal coupling aging (15.1%) was about 2 times of that under 60°C (7.6%). It showed that in the actual service environment of bridge deck pavement, UV light and heat exhibit significant coupling effect, which was more significant than the effect of single thermo-oxidative aging on the water stability of PPC.
3. The freeze–thaw splitting strength of PPC decreased under three aging conditions. However, after 6 weeks of aging, the freeze–thaw splitting strength of PPC under three aging conditions was 1.59, 1.40, and 1.46 MPa, respectively, which were significantly higher than that of non-aging SBSM (1.12 MPa). Results show that the water stability of PPC is better than that of SBSM.

## Fatigue Resistance Performance

**Figures 6A,B** compare the fatigue resistance of aged PPC and non-aging SBSM, and error bars were applied to illustrate the deviation of testing results of PPC under different aging conditions. The following are found:

1. After 6 weeks of aging, the change rate of initial stiffness modulus of PPC at 90°C (37.8%) was about 2.1 times of that at 60°C (18.3%), indicating that the aging effect at 90°C was more significant.
2. Under the condition of photothermal coupling aging, the change rate of initial stiffness modulus of PPC (44.0%) was 2.4 times of that at 60°C, which indicated that UV light had a greater impact on the fatigue resistance of PPC in the actual service environment of bridge deck pavement.
3. The initial stiffness modulus of PPC decreased under three aging conditions. After 6 weeks of aging, the initial

stiffness moduli of PPC under three aging conditions were 473, 360, and 324 MPa, which were significantly lower than the non-aging SBSM (4,823 MPa). It showed that the ability of PPC to bear repeated load under constant loading was better than that of SBSM, and PPC had good fatigue resistance. The reason is that, when polyurethane binder reacts with thermo-oxidative aging and photothermal coupling aging, the chemical bond with small bond energy breaks, the molecular weight decreases, and cracks gradually appear, which leads to the decrease of stiffness modulus.

## SUMMARIES AND CONCLUSION

As a new pavement material, the performance and material composition of PPC are significantly different from the traditional asphalt mixture. In this article, indoor laboratory tests were used to simulate the aging of PPC in the long-term service by photothermal coupling aging and thermo-oxidative aging. Compared with the non-aging SBSM, the properties of PPC after aging are systematically analyzed and evaluated. The main conclusions are as follows:

1. The indoor simulation method of the outdoor environment effects on PPC was proposed. The ventilation oven was used to simulate the thermo-oxidative aging under the high temperature of the road surface at 60; 90°C was used as the indoor thermo-oxidative accelerated aging condition. The self-developed UV weatherometer was used to simulate the photothermal coupling aging of PPC during service with irradiation of  $160 \text{ W} \cdot \text{m}^{-2}$  and test temperature of 60°C.
2. According to the results of Cantabro test, after 6 weeks of aging, the splitting strength loss of PPC at 90°C was about 1.7 times of that at 60°C. Ultraviolet light and heat exhibit significant coupling effect that had a greater impact on the anti-loose performance of PPC than the single thermo-oxidative aging at 60°C. The splitting strength of PPC under three aging conditions was significantly higher than that of the non-aging SBSM, and the loss rate of strength was also lower than that of the non-aging SBSM, which indicated that PPC had better anti-loose performance than SBSM for long-term service.
3. According to the results of low-temperature bending beam test, aging rate of 90°C was approximately 2.2 times of 60°C. The UV light had a greater impact on the low-temperature performance of PPC than that of 60°C. After 6 weeks of aging, the maximum bending tensile strain of PPC was still better than that of the non-aging SBSM, which showed that PPC had better low-temperature crack resistance than SBSM for the long-term service.
4. According to the rutting test results, after aging, the dynamic stability of PPC did not change significantly and was significantly higher than that of the non-aging SBSM, which indicated that PPC had stronger ability of permanent deformation resistance than that of SBSM.

5. According to the results of freeze–thaw splitting test, the aging rate at 90°C was approximately 2.4 times of that at 60°C. Ultraviolet light and heat exhibit significant coupling effect that had a greater impact on the water stability of PPC than the single thermo-oxidative aging at 60°C. After 6 weeks of aging, the freeze–thaw splitting strength of PPC under three aging conditions was significantly higher than that of non-aging SBSM, indicating that the water stability of PPC was better than that of SBSM.
6. According to the results of four-point bending fatigue test, the fatigue life of PPC under various test environments was more than 1 million times under 1,200- $\mu\epsilon$  strain level. The change rate of initial stiffness modulus of PPC at 90°C was about 2.1 times of that at 60°C. The UV light had a greater impact on the fatigue resistance of PPC than that of 60°C. After 6 weeks of aging, the initial stiffness modulus of PPC under three aging conditions was significantly lower than the non-aging SBSM, which indicated that PPC had better fatigue resistance.
7. The research results of this study provide a reference for the future engineering application of polyether polyurethane as a bridge deck pavement material. However, because of the lack of field engineering project application, the reliability of indoor simulation method still needs to be verified and optimized in future studies, and more studies on the interaction mechanism between

polyurethane and ore interface will be conducted to relate the chemophysical changes to the observed mechanical changes.

## DATA AVAILABILITY STATEMENT

The raw data supporting the conclusions of this article will be made available by the authors, without undue reservation.

## AUTHOR CONTRIBUTIONS

SX and MX: conceptualization and writing-original draft preparation. SX, MX, and YZ: methodology. MX, YG, GP, and YX: investigation. YZ, YG, and GP: the data curation. SX, MX, and YX: writing-review and editing. YX, YG, and GP: visualization. SX: supervision, project administration and funding acquisition. All authors contributed to the article and approved the submitted version.

## FUNDING

This article was supported by the National Natural Science Foundation of China (Nos. 51978034 and 51678028) and the Beijing University of Civil Engineering and Architecture's Beijing Advanced Innovation Center for Future Urban Design's major scientific and technological project "Technology and Application of Disaster Reduction and Emission Reduction for Major Road Projects in the Capital" (No. X18159).

## REFERENCES

- Biligiri, K. P., Kalman, B., and Samuelsson, A. (2013). Understanding the fundamental material properties of low-noise poroelastic road surfaces. *Intern. J. Pavement Eng.* 14, 12–23. doi: 10.1080/10298436.2011.608798
- Chen, J., Ma, X., Wang, H., Xie, P. Y., and Huang, W. (2018a). Experimental study on anti-icing and deicing performance of polyurethane concrete as road surface layer. *Construct. Build. Mater.* 161, 598–605. doi: 10.1016/j.conbuildmat.2017.11.170
- Chen, J., Yin, X., Wang, H., and Ding, Y. (2018b). Evaluation of durability and functional performance of porous polyurethane mixture in porous pavement. *J. Clean. Product.* 188, 12–19. doi: 10.1016/j.jclepro.2018.03.297
- Cong, L., Wang, T., Tan, L., Yuan, J., and Shi, J. (2018). Laboratory evaluation on performance of porous polyurethane mixtures and OGFC. *Construct. Build. Mater.* 169, 436–442. doi: 10.1016/j.conbuildmat.2018.02.145
- Cong, L., Yang, F., Guo, G. H., Ren, M., and Tan, L. (2019). The use of polyurethane for asphalt pavement engineering applications: a state-of-the-art review. *Construct. Build. Mater.* 225, 1012–1025. doi: 10.1016/j.conbuildmat.2019.07.213
- Gao, J. F., Wang, H. N., Chen, J. K., Meng, X. W., and You, Z. (2019). Laboratory evaluation on comprehensive performance of polyurethane rubber particle mixture. *Construct. Build. Mater.* 224, 29–39. doi: 10.1016/j.conbuildmat.2019.07.044
- GB/T. 1034-2008 (2008). *Plastic-Determination of Water Absorption*. Beijing: General Administration of Quality Supervision, Inspection and Quarantine.
- GB/T. 16777-2008 (2008). *The Methods for Building Waterproofing Coating*. Beijing: General Administration of Quality Supervision, Inspection and Quarantine.
- GB/T. 4472-2011 (2011). *Determination of Density and Relative Density for Chemical Products*. Beijing: General Administration of Quality Supervision, Inspection and Quarantine.
- Geng, L. T., Xu, Q., Ren, R. B., Wang, L. Z., Yang, X. L., and Wang, X. Y. (2016). Performance research of high-viscosity asphalt mixture as deck-paving materials for steel bridges. *Road Mater. Pavement Design* 18, 1–13.
- Guan, Y. S., Chi, Z. H., and Zong, H. (2005). Analysis and Countermeasure for early disease of long-span steel bridge deck pavement. *J. China Foreign Highways* 25, 99–101.
- Hee, M. P., Ji, Y. C., and Hyun, J. L. (2017). Performance evaluation of a high durability asphalt binder and a high durability asphalt mixture for bridge deck pavements. *Construct. Build. Mater.* 23, 219–225. doi: 10.1016/j.conbuildmat.2008.01.001
- Hou, Y., Wang, L., Wang, D., Qu, X., and Wu, J. (2017). Using a molecular dynamics simulation to investigate the asphalt nano-cracking under external loading conditions. *Appl. Sci.* 7:770. doi: 10.3390/app7080770
- Ionita, D., Cristea, M., and Gaina, C. (2020). Prediction of polyurethane behaviour via time-temperature superposition: meanings and limitations. *Polymer Test.* 83:106340. doi: 10.1016/j.polymertesting.2020.106340
- JTG E20-2011 (2011). *Standard Test Methods of Bitumen and Bituminous Mixtures for Highway Engineering*. Beijing: Ministry of Transport of the People's Republic of China.
- JTG F40-2004 (2004). *Technical Specifications for Construction of Highway Asphalt Pavements*. Beijing: Ministry of Transport of the People's Republic of China.
- Li, T. S., Lu, G. Y., Wang, D. W., Hong, B., Tan, Y. Q., and Oeser, M. (2019). Key properties of high performance polyurethane bounded pervious mixture. *China J. Highway Transp.* 32, 162–173.
- Lu, G. Y., Liu, P. F., Törzs, T., Wang, D. W., Oeser, M., and Grabe, J. (2020). Numerical analysis for the influence of saturation on the base course of



- permeable pavement with a novel polyurethane binder. *Construct. Build. Mater.* 240, 1–10.
- Lu, G. Y., Liu, P. F., Wang, Y. H., Sabine, F., Wang, D. W., and Oeser, M. (2019a). Development of a sustainable pervious pavement material using recycled ceramic aggregate and bio-based polyurethane binder. *J. Clean. Product.* 220, 1052–1060. doi: 10.1016/j.jclepro.2019.02.184
- Lu, G. Y., Renken, L., Li, T. S., Wang, D. W., and Oeser, M. (2019b). Experimental study on the polyurethane-bound pervious mixtures in the application of permeable pavements. *Construct. Build. Mater.* 202, 838–850. doi: 10.1016/j.conbuildmat.2019.01.051
- Luo, S. G., Zhang, J. G., Tan, H. M., Jing, F. Y., and Chen, F. T. (1999). Thermooxidative degradation of copolyether-urethane. *Chin. J. Appl. Chem.* 04, 14–17.
- Ni, F. J., and Yin, Y. M. (2005). Fatigue properties of asphalt mixture with fiberglass polyester mat. *J. Traff. Transp. Eng.* 03, 31–35.
- Qian, Z. D., Liu, Y., Liu, C. B., and Zheng, D. (2016). Design and skid resistance evaluation of skeleton-dense epoxy asphalt mixture for steel bridge deck pavement. *Construct. Build. Mater.* 114, 851–863. doi: 10.1016/j.conbuildmat.2016.03.210
- Shen, G. L., Sun, S. Y., and Chen, Z. L. (2014). Study on aging mechanism and research methods of polyurethane. *Aging Appl. Synth. Mater.* 43, 57–64.
- Shi, Z. X. (2018). *Development and Evaluation of High Performance Materials for Steel Bridge Deck Pavement*. Master thesis, Beijing University of Civil Engineering and Architecture, Beijing.
- Sun, H. J., and Chen, S. (2014). Study on the influence of materials and structural factors on the durability of asphalt pavement of concrete bridge. *J. China Foreign Highway* 6, 260–263.
- Wang, D., Liu, P., Leng, Z., Leng, C., Lu, G., Buch, M., et al. (2017a). Suitability of PoroElastic road surface (PERS) for urban roads in cold regions: mechanical and functional performance assessment. *J. Clean. Product.* 165, 1340–1350. doi: 10.1016/j.jclepro.2017.07.228
- Wang, D., Schacht, A., Leng, Z., Leng, C., Kollmann, J., and Oeser, M. (2017b). Effects of material composition on mechanical and acoustic performance of poroelastic road surface (PERS). *Construct. Build. Mater.* 135, 352–360. doi: 10.1016/j.conbuildmat.2016.12.207
- Wang, H. M., Li, R. K., Wang, X., Ling, T. Q., and Zhou, G. (2014). Strength and road performance for porous polyurethane mixture. *China J. Highway Transp.* 27, 24–31.
- Wang, R. W., Hu, Z. H., Shi, J. L., Li, S. F., Xu, S. F., and Duan, W. Z. (2018). Development and pavement performance evaluation of paving materials with high molecular polymer. *Road Construct. Mach. Construct. Mechan.* 35, 39–42.
- Wang, Z. Y., and Liu, L. J. (2013). Study on the durability of highway bridge under heavy traffic. *Appl. Mechan. Mater.* 340, 100–103. doi: 10.4028/www.scientific.net/amm.340.100
- Xu, H., Li, H., Tan, Y., Wang, L., and Hou, Y. (2018). A Micro-scale investigation on the behaviors of asphalt mixtures under freeze-thaw cycles using entropy theory and a computerized tomography scanning technique. *Entropy* 20:68. doi: 10.3390/e20020068
- Yang, Q., Hong, B., Lin, J., Wang, D., Zhong, J., and Oeser, M. (2020a). Study on the reinforcement effect and the underlying mechanisms of a bitumen reinforced with recycled glass fiber chips. *J. Clean. Product.* 251:119768. doi: 10.1016/j.jclepro.2019.119768
- Yang, Q., Li, X., Zhang, L., Qian, Y., Qi, Y., Kouhestani, H. S., et al. (2020b). Performance evaluation of bitumen with a homogeneous dispersion of carbon nanotubes. *Carbon* 158, 465–471. doi: 10.1016/j.carbon.2019.11.013
- Yang, W. M. (2013). *Study on Diseases for Asphalt Concrete Paved on Bridge*. Master thesis, Chang'an University, Xi'an.
- Zhang, H. L., Zhang, G. W., Han, F. F., Zhang, Z. P., and Lv, W. J. (2018). A lab study to develop a bridge deck pavement using bisphenol A unsaturated polyester resin modified asphalt mixture. *Construct. Build. Mater.* 159, 83–98. doi: 10.1016/j.conbuildmat.2017.10.126

**Conflict of Interest:** The authors declare that the research was conducted in the absence of any commercial or financial relationships that could be construed as a potential conflict of interest.

Copyright © 2020 Xu, Xu, Zhang, Guo, Peng and Xu. This is an open-access article distributed under the terms of the Creative Commons Attribution License (CC BY). The use, distribution or reproduction in other forums is permitted, provided the original author(s) and the copyright owner(s) are credited and that the original publication in this journal is cited, in accordance with accepted academic practice. No use, distribution or reproduction is permitted which does not comply with these terms.



# Study on Preparation Method of Terminal Blend Rubberized Asphalt Binder

Juan Xie<sup>1,2\*</sup>, Yongning Zhang<sup>1</sup> and Yueming Yang<sup>1</sup>

<sup>1</sup> School of Traffic and Transportation Engineering, Changsha University of Science and Technology, Changsha, China,

<sup>2</sup> National Engineering Laboratory of Highway Maintenance Technology, Changsha University of Science and Technology, Changsha, China

## OPEN ACCESS

### Edited by:

Hui Yao,  
Beijing University of Technology,  
China

### Reviewed by:

Lingyun You,  
Michigan Technological University,  
United States  
Jiaqi Chen,  
Central South University, China

### \*Correspondence:

Juan Xie  
xiejuan08@126.com

### Specialty section:

This article was submitted to  
Structural Materials,  
a section of the journal  
Frontiers in Materials

**Received:** 30 May 2020

**Accepted:** 24 July 2020

**Published:** 11 August 2020

### Citation:

Xie J, Zhang Y and Yang Y (2020)  
Study on Preparation Method  
of Terminal Blend Rubberized Asphalt  
Binder. *Front. Mater.* 7:279.  
doi: 10.3389/fmats.2020.00279

Terminal Blend (TB) asphalt rubber is prepared by being sheared with high speed for a long time at a high temperature and has good low temperature performance and anti-fatigue performance. But due to the aging of asphalt and desulfurization and degradation of crumb rubber, the high temperature performance of TB is not ideal. In order to propose an effective way to solve this problem and improve the high temperature performance, a series of TB-B and TB-C asphalt were prepared with crumb rubber by changing dosage and preparation temperature in nitrogen environment and soluble crumb rubber in atmospheric environment, respectively. As a comparison group, TB-A asphalt was prepared using crumb rubber under atmospheric environment. Dynamic shear rheometer (DSR) and binding beam rheometer (BBR) were used to investigate the rheological characteristics, polymer segregation experiment was performed to evaluate the storage stability, and Fourier Transform Infrared (FTIR) spectroscopy and thermogravimetric analysis were carried out to explore the aging degree of asphalt. TB-A had good storage stability but was brittle due to serious asphalt aging during preparation, and its high and low temperature performance were not good. The introduction of nitrogen could effectively decline aging degree and guaranteed TB-B best comprehensive performance among these three kinds of modified asphalt. Soluble crumb rubber was obtained by pretreating crumb rubber and making it desulfurize and degrade, which reduced the preparation and consequently inhibit the occurrence of aging. The high and low temperature properties of TB-C met specification, but storage stability was not insufficient when crumb rubber content was more than 15%. Overall, both preparation in nitrogen environment with conventional crumb rubber and preparation in atmospheric environment with soluble crumb rubber can effectively alleviate the aging degree of TB asphalt.

**Keywords:** crumb rubber modified asphalt, terminal blend, preparation process, asphalt aging, rubber powder degradation, rheology

## INTRODUCTION

With the rapid development of automobile possession, the amount of waste tires has proliferated. The traditional disposal methods of waste tires, such as incineration, landfill and piling up not only occupy a lot of land resources but also easily breed mosquitoes and cause fires (Xie et al., 2019; Yan et al., 2020). Waste tires can be ground at normal temperature or in liquid nitrogen to obtain rubber powder, which has been proved to be an effective modifier

to asphalt. The emergence of asphalt rubber provides an environmentally friendly way to waste tires (Yang et al., 2017; Nanjegowda and Biligiri, 2020; Wang et al., 2020). So far, asphalt rubber has been developed for many years and widely used in the United States, South Africa and some other countries. However, asphalt rubber prepared with typical wet process has poor storage stability and high viscosity. It requires special stirring equipment to avoid segregation and can only be used in short time, which hinders its promotion and application (Zhou et al., 2014; Hosseinneshad et al., 2019; Pouranian et al., 2020). Based on this, an alternative rubber modified asphalt known as Terminal Blend rubberized asphalt binder (TB asphalt) has attracted increasing concerns since the 1980s. Unlike rubber modified asphalt produced through traditional wet process, TB asphalt is generally prepared with less crumb rubber content under higher shear temperature and has the characteristics of low viscosity, good storage stability, and thus has good application prospects (Lo Presti et al., 2012; Lo Presti, 2013; Zeinali et al., 2014; Han et al., 2016).

Similar to polymer modified asphalt, TB asphalt can be produced directly in asphalt plants. The characteristics of processing technology includes high temperature (200~300°C), high pressure (>1 atm) and high shear speed (3000~8000 r/min) (Han et al., 2016; Wen et al., 2021). Under such strict preparation conditions, the swelling of rubber powder in typical wet is replaced by the desulfurization and depolymerization of rubber, and smooth and uniform binder is obtained (Ghavibazoo and Abdelrahman, 2014). Compared with asphalt rubber, TB asphalt has better low temperature performance, fatigue performance, storage stability, anti-aging performance and workable performance (Han et al., 2017; Lin et al., 2017). The University of California, Berkeley and the Federal Highway Administration took accelerated pavement test via heavy vehicle simulators (HVS) and found that TB asphalt had better fatigue performance than asphalt rubber and was suitable for dense graded mixture (Qi et al., 2006; Santucci, 2009; Tang et al., 2017). Lin found that during the preparation of TB asphalt, light components such as aliphatic generated because of the desulfurization and degradation of rubber powder, which increased the low temperature properties of TB asphalt (Lin et al., 2018). Abdelrahman found that with the rise of interaction temperature and the extension of interaction time, the diffusion rate and degradation rate of rubber powder in the asphalt was promoted, thereby the storage stability was improved (Ghavibazoo and Abdelrahman, 2013). Tang used rolling thin film oven test (RTFO) and pressure aging vessel test (PAV) to investigate the aging performance of TB asphalt, and found that TB asphalt had better anti-aging performance than base asphalt (Tang et al., 2019). However, the desulfurization and degradation of TB rubber powder under high temperature conditions break the cross link bonds and damage the network structure of the system, which leads to the greatly loss of viscosity and elasticity and the deterioration of high temperature performance (Tang et al., 2016). In previous studies, the ways to improve high-temperature performance of TB asphalt can be divided into two categories. One is to optimize the preparation process (Ragab and Abdelrahman, 2014). Ragab et al. (2013) pointed out that

the degradation degree of rubber powder could be decreased by strictly controlling the preparation temperature. The crumb rubber can form three-dimensional network structure with the asphalt through adjusting the preparation process, which endue TB asphalt with both storage stability and high temperature performance (Ragab and Abdelrahman, 2014). However, it is not universal to improve the high temperature performance of TB asphalt via preparation process because the types of crumb rubber and asphalt may also be different (Ragab et al., 2015; Ghavibazoo et al., 2016). Wu increased the amount of crumb rubber in the asphalt and added a cross-linking agent to prepare TB asphalt with high viscosity and high storage stability. Compared with SBS modified asphalt, it was found that TB asphalt had better high temperature performance and lower temperature performance (Wu et al., 2013). The other is compound modification of TB asphalt. SBS (styrene-butadiene-styrene block copolymers), PPA (polyphosphoric acid), rock asphalt and nano-materials are commonly used compound modifier. Jin, Greene and Lin used SBS to modify TB asphalt, and they found that the addition of SBS was beneficial to the remodeling of the cross-linked network in TB asphalt, and then improved the high temperature performance without degrading the low temperature performance (Jan et al., 2014; Greene et al., 2015; Lin et al., 2018). Lin's research found that although the addition of PPA helped to improve the high temperature performance of TB asphalt, but it had negative impact on the cross-linking network in the asphalt, which in turn adversely affected the low temperature performance (Lin et al., 2017, 2018). Huang used rock asphalt to modify TB asphalt and carried out a series of experiments. The results showed that rock asphalt increased the high temperature performance of TB asphalt, but slightly decreased the low temperature performance (Huang et al., 2016). Han used modified TB asphalt with nano-silica and found that the rutting resistance of TB asphalt at high temperature was improved, but the crack resistance at low temperature was slightly reduced (Han et al., 2017). You added amorphous-poly-alpha-olefin (APAO) additives into TB asphalt and found that APAO enhanced the elastic components of asphalt, which increased both high and low temperature performance of TB asphalt (You et al., 2019).

At present, the performance of TB asphalt prepared by different asphalt plants varies enormously and there is no uniform specification (Xiao et al., 2015). Meanwhile, the existing studies generally focus on the properties of TB asphalt, and the specific research about the preparation method is relatively few. Normally, TB asphalt is prepared at high temperature (more than 200°C), which results in the rapid volatilization of light components in asphalt and the thermal-oxidative aging of asphalt (Zanzotto and Kennepohl, 1996). In asphalt plants, sealed oxygen-barrier asphalt tanks can ensure that TB asphalt is not aging under high temperature and pressure production conditions, but it is not easy to create such conditions in the laboratory. Huang proposed two different preparation methods to alleviate the aging phenomenon in the preparation of TB asphalt (Lv et al., 2019).

- (1) The temperature was reduced to 220°C, and the reaction time was extended to more than 10 h.
- (2) The crumb rubber was pretreated through desulfurization and depolymerization before being added to asphalt which reduced the interaction temperature and time of preparation.

However, the longer reaction time in Method 1 seriously affected the production efficiency, and did not play a positive role in preventing aging. The pretreatment of the crumb rubber in Method 2 required various auxiliary materials and the procedures were more complicated. Billiter et al. (1997) explored the preparation of asphalt rubber at high temperature and found that when the interaction temperature was 232~260°C, nitrogen could be used to create an oxygen-barrier environment. To prevent the asphalt from aging at high temperature, Zanzotto prepared the asphalt rubber in two steps. First, the asphalt rubber was thermally depolymerized in an autoclave, and then the rubber and asphalt were mixed at 170~180°C. But the two steps needed to be carried out continuously, which increased difficulty of operation (Zanzotto and Kennepohl, 1996).

To explore a simple and feasible method to reduce asphalt aging during the preparation process, this paper proposes two preparation methods and compares them with TB asphalt prepared in atmospheric environment. As shown below:

- (1) As a comparison group, TB-A asphalt was prepared using crumb rubber in atmospheric environment.
- (2) Crumb rubber was added to base asphalt under the protection of nitrogen to prepare TB-B asphalt through a self-developed nitrogen protection device.
- (3) TB-C asphalt was prepared using soluble crumb rubber at low temperature (<200°C).

The effect of processing technological parameters (such as rubber powder content and shearing temperature) on the physical properties of TB asphalt was investigated. To compare the rheological performance of TB asphalt prepared with different methods, dynamic shear rheology experiment was carried out. Meanwhile, bending beam rheometer was used to study the low temperature property of TB asphalt. Specially, the storage stability of TB asphalt was analyzed via polymer isolation experiment. Last but not least, the aging degree of asphalt during the preparation process was characterized with Fourier Transform Infrared spectrometer (FTIR), and its microscopic mechanism on TB asphalt was explored by thermogravimetric analyzer (TG).

## MATERIALS AND METHODS

### Materials

Base asphalt binder of grade 70 was supplied by Hunan Poly Company (Hunan, China). 80 mesh crumb rubber was purchased from Sichuan Lubaotong Company (Chengdu, China). The low Mooney soluble crumb rubber (Mooney viscosity 30, sol content 62.6%) was provided by Professor Shifeng Wang from

Shanghai Jiao Tong University. The technical parameters are shown in Tables 1, 2.

### Preparation of TB Asphalt

In this study, 5, 10, 15, 20, and 25% of crumb rubber were added to base asphalt under atmospheric and nitrogen environments, respectively. The mixture was then swelled in an oven at 180°C for 30 min. At last, the binder was mixed by high-speed shear instrument at a rate of 4000 r/min for 3 h at 220, 240, and 260°C. The modified asphalt prepared under atmospheric environment was recorded as TB-A, and the modified asphalt prepared under nitrogen environment was recorded as TB-B. It should be noted that after mixing the binder in nitrogen environment, it is necessary to continuously pass nitrogen until the temperature decrease to about 160°C. The nitrogen protection device was made by our laboratory, and the schematic diagram is shown in Figure 1. The device is hermetically sealed and nitrogen was introduced through nozzle. Similarly, to prepare TB-C, the soluble crumb rubber with the same content was added to base asphalt and then swelled in an oven at 180°C for 30 min, followed by being mixed with a high-speed shear instrument at 160, 180, and 200°C at a rate of 4000 r/min for 1 h.

### Test Methods

The penetration (25°C) and softening point of the TB asphalt were tested using the PNR 12 penetration meter and RKA 5 softening point meter (Antongpa, Austria). The digital ductility tester (Infra Test, Germany) was used to measure the ductility of the binder at 15°C and the tensile speed was 50 mm/min.

According to the JTG-T0628-2011 test method, the dynamic shear rheometer (DSR, MCR 302, Antongpa, Graz, Austria) was used to test the complex shear modulus and phase angle of the

TABLE 1 | Properties of base asphalt binder.

Item	Units	Test Results	Standard
Penetration (25°C, 5 s, 100 g)	0.1 mm	69	JTG E20-2011 T0604-2011
Softening temperature	°C	46.5	JTG E20-2011 T0606-2011
Ductility (15°C)	cm	>150	JTG E20-2011 T0605-2011
Solubility	%	99.87	JTG E20-2011 T0607-2011
Density (15°C)	g/cm <sup>3</sup>	1.039	JTG E20-2011 T0603-2011
RTFO treated at 163°C for 85 min			
Quality change	%	−0.024	JTG E20-2011 T0609-2011
Residual penetration ratio	%	61.7	JTG E20-2011 T0604-2011
Residual ductility (10°C)	cm	6.3	JTG E20-2011 T0605-2011

TABLE 2 | Properties of crumb rubber.

Item	Result	Standard
Water content (%)	0.96	HG/TXXX-2001 7.2.2
Ash content (%)	9.0	GB4498
Acetone extract content (%)	13.6	GB/T3516
Density (g/cm <sup>3</sup> )	0.96	GB/T533
Tensile strength (MPa)	6.2	GB/T528
Elongation at break (%)	850	GB/T52

binder. The rheological tests were carried out by parallel plates with a diameter of 25 mm and a spacing of 1 mm under strain controlling mode ( $\omega = 10$  rad/s).

According to the JTG-T0627-2011 test method, the bending creep stiffness and creep rate ( $m$ -value) of asphalt were measured using a bending beam rheometer (BBR, TE-BBR, Cannon, Tokyo, Japan). A contact load of 35 mN was applied to the rectangular asphalt samples (125 mm  $\times$  12.7 mm  $\times$  6.35 mm) prepared in advance at  $-12^{\circ}\text{C}$  and  $-18^{\circ}\text{C}$ .

The storage stability of TB asphalt was tested according to the polymer isolation experiment of JTG-T 0661-2011. The standard sample tube (about 25 mm in diameter and about 140 mm in length) filled with the asphalt sample was left in an oven at  $163^{\circ}\text{C}$  for 48 h, then was placed in the freezer for more than 4 h and cut into three sections. Finally, the softening points of the top and bottom samples were measured to determine the softening point difference.

According to the JTG-T0625-2011 test method, the viscosity of TB-A, TB-B, TB-C at  $177^{\circ}\text{C}$  was measured using a Brookfield rotary viscometer.

Fourier Transform Infrared (FTIR) spectroscopy (Thermo Fisher, Waltham, MA, United States) was used to characterize

the chemical structure of TB-A, TB-B, and TB-C. The spectrum ranged from  $4000$  to  $500\text{ cm}^{-1}$ , and scanning was repeated 32 times.

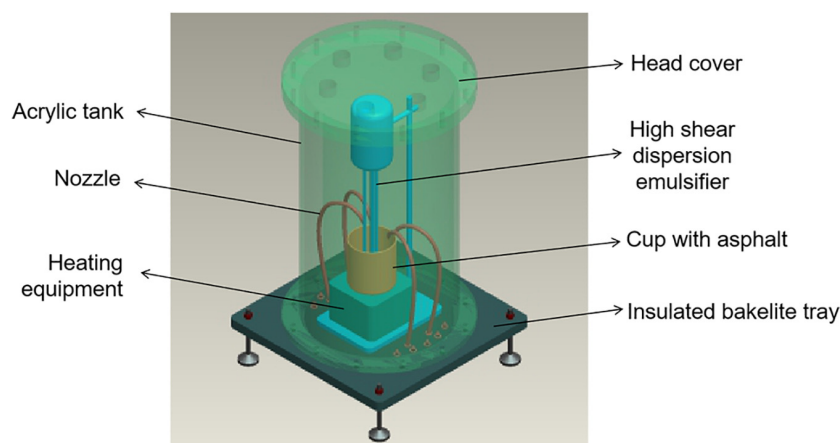
Thermal analysis of TB asphalt was performed by Thermogravimetry analyzer (TGA STA449F5, Netzsch, Germany) in a nitrogen atmosphere. About  $10 \pm 0.1$  mg sample was heated from  $50$  to  $700^{\circ}\text{C}$  in the furnace with a constant heating rate of  $10^{\circ}\text{C}/\text{min}$ .

## RESULTS AND DISCUSSION

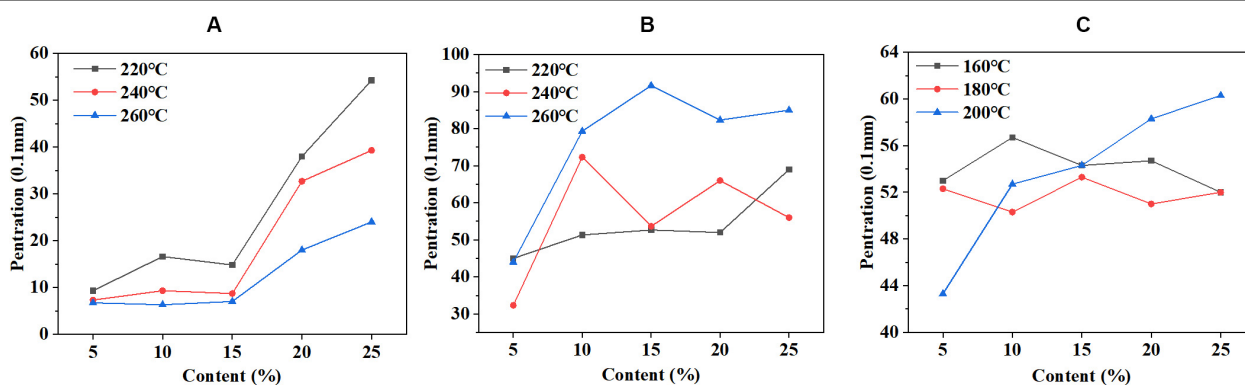
### Physical Properties

Penetration, softening point, and ductility are common indicators of the high and low temperature performance of asphalt. Studies show that the physical properties of TB asphalt are close to those of base asphalt (Huang et al., 2016). Therefore, the authors tested the physical properties of TB-A, TB-B, and TB-C, and compared and analyzed them with base asphalt.

It can be seen from **Figure 2** and **Table 3** that compared to base asphalt, TB-A asphalt has lower penetration and much



**FIGURE 1** | Schematic diagram of nitrogen environment box.



**FIGURE 2** | Penetration test results of TB asphalt. (A) TB-A. (B) TB-B. (C) TB-C.



**TABLE 3** | Softening point and Ductility test results of TB asphalt.

CR content Sample ID	TB-A			TB-B			TB-C		
	220°C	240°C	260°C	220°C	240°C	260°C	160°C	180°C	200°C
Softening point (°C)									
5%	—	—	—	38.0	55.3	47.1	50.5	51.1	53.7
10%	70.2	—	—	49.8	47.8	47.7	50.5	52.3	51.9
15%	74.8	—	—	52.8	51.4	46.1	52.2	52.6	54.0
20%	55.5	67.5	72.4	56.1	51.6	47.6	53.3	56.5	53.8
25%	56.0	56.3	58.8	51.6	52.8	45.4	56.9	57.0	55.0
Ductility (cm)									
5%	0.3	0.29	0.3	22.3	12.9	17.6	21.8	16.1	10
10%	0.61	0.31	0.28	28.4	34.3	84	20.2	17.5	10.7
15%	0.63	0.31	0.73	23.7	21	>100	12.1	9.9	9.8
20%	13.7	11.6	0.91	20.1	29	81.3	10.2	10.3	11.3
25%	56.6	12.3	1.2	20.5	20.4	78.2	10.4	8.6	11.1

“—” means that the softening point test temperature is greater than 80°C, and it is necessary to switch to glycerin for heating. Considering that the softening point of TB asphalt is not so high, it means that the requirements of TB asphalt are not met, so the test was not performed.

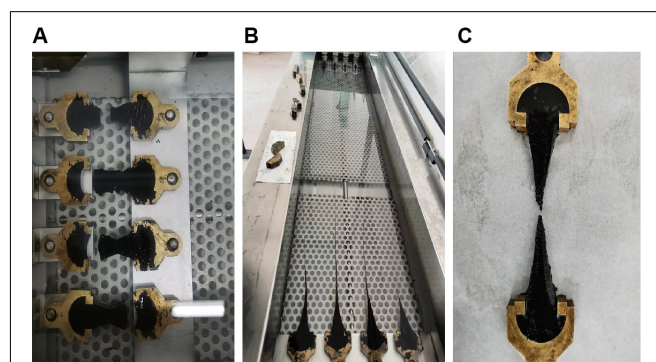
higher softening point. This is because at high temperatures, the light components in asphalt is excessively volatilized and the thermal oxygen aging of the binder occurs, which increases the asphaltene content and makes the asphalt become hard and brittle, and the higher the preparation temperature, the more obvious this phenomenon. In addition, with the increase of crumb rubber content, the penetration improves and the softening point declines as a whole, which may be related to the anti-aging agent contained in the crumb rubber.

There are two important reactions during the preparation process of TB asphalt, one is the aging of base asphalt, the other is the desulfurization and degradation of the crumb rubber. When the former dominates, TB asphalt obtained is hard and brittle, and vice versa. Compared with TB-A asphalt, the penetration and softening point of TB-B asphalt is closer to base asphalt, which means the protection of nitrogen during the preparation process has a positive effect on preventing TB asphalt from aging and the later reaction dominates. Meanwhile, the penetration of TB-B increases and the softening point decreases with preparation temperature. When the preparation temperature reaches 260°C and the crumb rubber content exceeds 10%, the penetration and softening point of TB-B tend to be stable. But the regularity of penetration changes with the amount of rubber powder is not obvious, which is consistent with some studies in the literature. With the increment of crumb rubber content, the penetration of TB asphalt decreased according to Wei and Song's research (Wei, 2016; Song, 2017), but increase in the studies of Huang et al. (2016), which indicates that the influence of crumb rubber on the penetration of TB asphalt is very complicated.

The softening point of TB-C asphalt increases with the soluble crumb rubber content and the preparation temperature. But the penetration of TB-C has different variation trend with soluble crumb rubber content at different preparation temperature. It is not significantly affected by crumb rubber content at 160 and 180°C. However, when the temperature increases to 200°C,

the penetration increases with the amount of soluble crumb rubber remarkably, which indicates that at 200°C the aging of base asphalt dominates. In addition, over the entire temperature range, the penetration of TB-C asphalt is lower than base asphalt, which may be due to that the crumb rubber swells and dissolves in asphalt and increases the viscosity of the asphalt.

Ductility is an indicator of the low-temperature plasticity of asphalt and closely related to the low-temperature performance. It was found in the test that the TB-A asphalt was very brittle, and easily broke at 15°C, as shown in **Figure 3A**. So the serious aging of TB-A asphalt prepared under atmospheric environment is confirmed again. As can be seen from **Table 3**, TB-B has the best low temperature ductility followed by TB-B, and TB-A has the worst. Besides, the ductility of TB-B asphalt is influenced greatly by preparation and reaches to the maximum at 260°C, much higher than the TB-B asphalt prepared at other temperature (**Figure 3B**). Its However, as shown in **Figure 3C**, the ductility of TB-C asphalt is smaller than TB-B asphalt. The reason could be that the crumb rubber in TB-C asphalt does not completely dissolve, so the system is not heterogeneous.

**FIGURE 3** | Ductility experiment. (A) TB-A. (B) TB-B. (C) TB-C.

## High Temperature Rheological Properties

In this section, the effects of crumb rubber content and preparation conditions on complex modulus ( $G^*$ ), phase angle ( $\delta$ ) and rutting coefficient ( $G^*/\sin\delta$ ) are analyzed. Complex modulus  $G^*$  is the ratio of maximum shear stress to maximum shear strain and characterizes the ability of the asphalt to resist deformation under repeated shear stress. Phase angle  $\delta$  is the time lag of the applied stress and the resulting strain, which reflects the viscoelasticity of the asphalt (Jin et al., 2019; Wang and Ye, 2020).

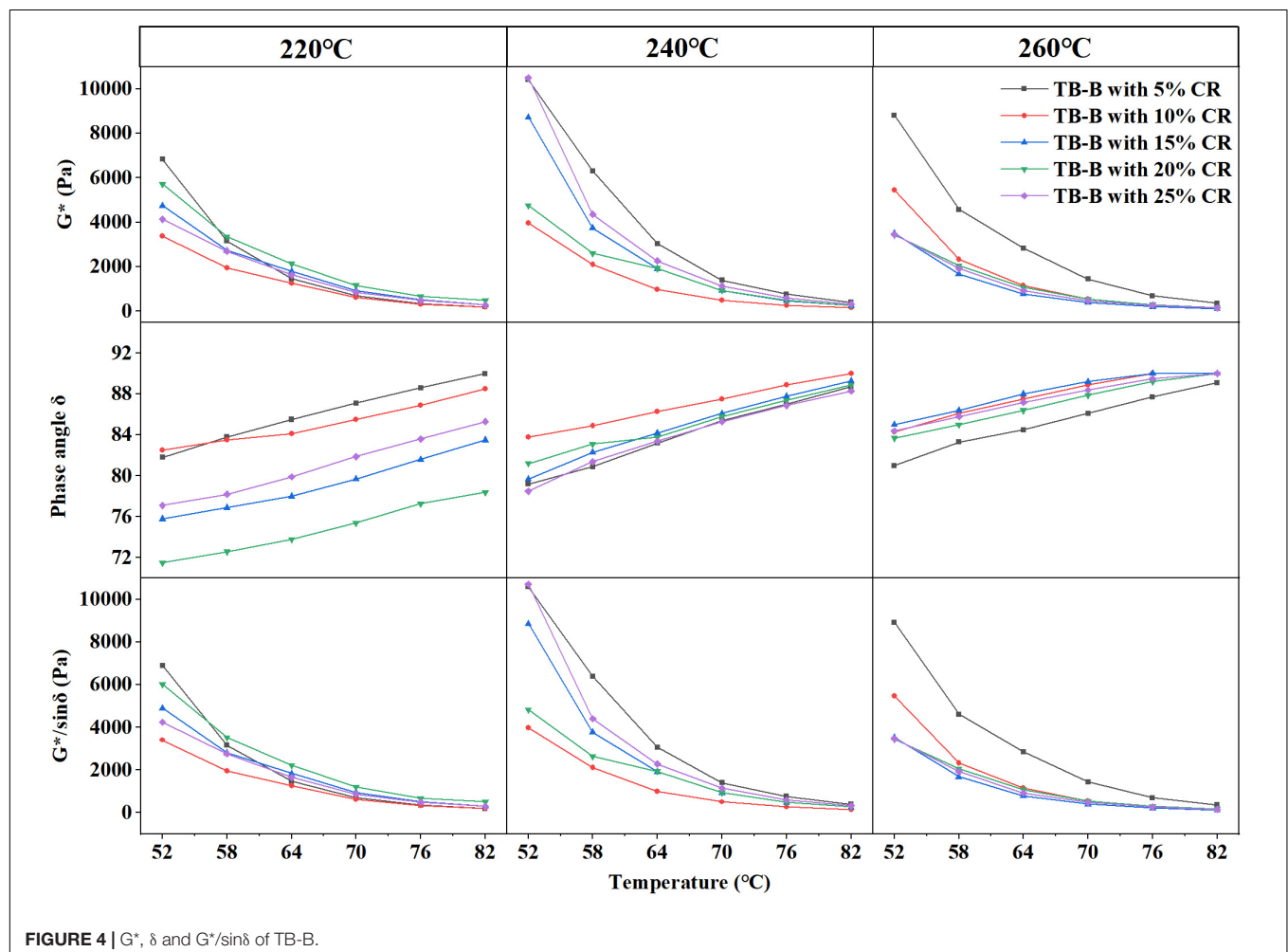
As shown in **Figures 4, 5**, TB-B has smaller  $G^*$  and  $G^*/\sin\delta$  but greater  $\delta$  than TB-C, which indicates that the elastic ratio of TB-B is lower than TB-C and the anti-deformability at high temperature of TB-B is worse. This phenomenon is resulted from the desulfurization and degradation of crumb rubber at high temperature and high-speed shear rate, which causes elastic losses results in the reduction of the deformation resistance and viscoelastic properties of the binder.

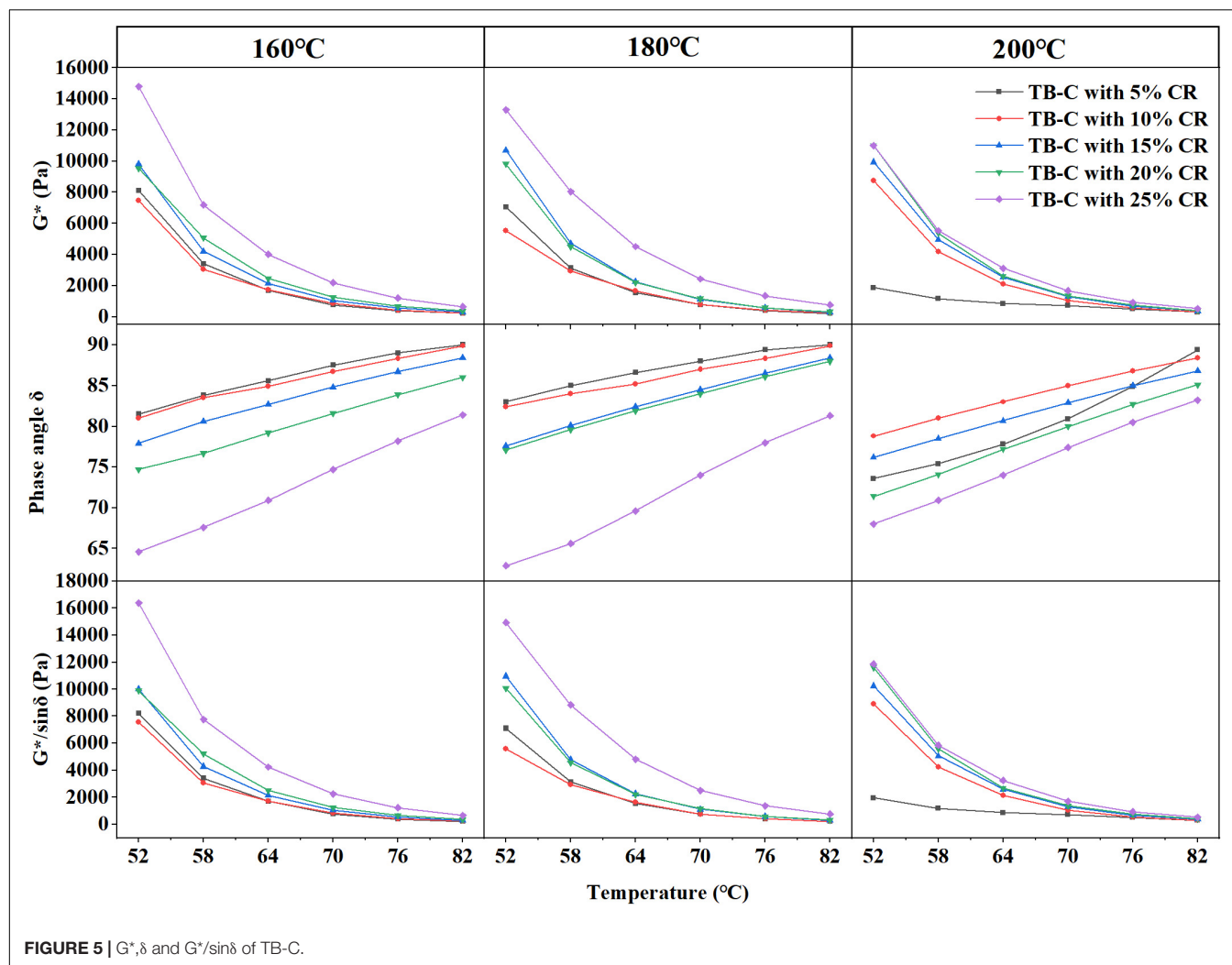
From **Figure 5** one can see that the  $G^*$  of TB-C asphalt increases and the phase angle  $\delta$  decreases with increment of

crumb rubber, which means that the increment of soluble crumb rubber helps improve the anti-deformability and elasticity of the modified asphalt. This is similar to rubber modified asphalt prepared by traditional wet process, which shows that the interaction mechanism between soluble crumb rubber and base asphalt is mainly swelling. In addition,  $G^*$ ,  $\delta$ , and  $G^*/\sin\delta$  of TB-C asphalt decreases when improve preparation temperature, which can be attributed to the aging of asphalt.

## Low Temperature Creep Properties

The bending beam rheometer (BBR) test is often used to evaluate low temperature creep properties of asphalt, and two parameters—creep stiffness  $S$  and creep rate  $m$  can be obtained from this test.  $S$  represents the toughness of asphalt under low temperature conditions, the larger the  $S$  value, the more brittle the asphalt material and the easier the road surface to crack. Creep rate  $m$  reflects the stress relaxation ability of asphalt at low temperature, the larger the  $m$  value, the better the stress relaxation ability of the asphalt material, and the lower the possibility of low temperature cracking. The BBR tests of TB asphalt prepared in this study were





performed under a stress of 100 g (980 mN) for 240 s (Li et al., 2017).

According to Superpave binder grade specifications, at the lowest design temperature the creep stiffness of asphalt loaded for 60 s should be less than 300 MPa, and  $m$ -value should be greater than 0.3. As shown in **Figure 6**, when the crumb rubber content is less than 15%, the creep stiffness and creep rate of TB-A asphalt at  $-12^\circ\text{C}$  and  $-18^\circ\text{C}$  do not meet the requirements of the specification, indicating that the low temperature grade of TB-A asphalt is higher than  $-12^\circ\text{C}$ . Besides, the creep stiffness of TB-A asphalt gradually increases and  $m$ -value gradually decreases when preparation temperature goes up. This means that when temperature is higher than  $220^\circ\text{C}$ , TB-A asphalt ages seriously. Further increase of temperature will exacerbate this phenomenon.

From **Figure 7** it can be found that at the same temperature, increasing content of crumb rubber decreases the creep stiffness and increases the  $m$ -value of TB-B asphalt. This is ascribed to that aliphatic small molecules generated from the desulfurization and

depolymerization of crumb rubber improves low temperature toughness and stress relaxation ability of the binder.

**Figure 8** shows the creep stiffness and  $m$ -value of TB-C asphalt. At the same temperature the creep stiffness of TB-C asphalt decreases and creep rate does not change much as the soluble crumb rubber content increases. As temperature increases, the influence of the rubber powder content on  $S$  and  $m$  declines.

From the above analysis we can draw such a conclusion that at the same test temperature, TB-A has the largest  $S$ , followed by TB-C and finally TB-B, but the order of  $m$  values is just the opposite. Thus TB-B has the best low temperature rheological performance, followed by TB-C, finally TB-A.

## Storage Stability

Due to the big difference of molecular weight, density and solubility parameters between rubber powder and asphalt, the storage stability of asphalt rubber prepared through traditional wet process is usually poor, which is a key issue restricting the development of rubber asphalt (Lin et al., 2018). According to the specification, to avoid segregation the softening

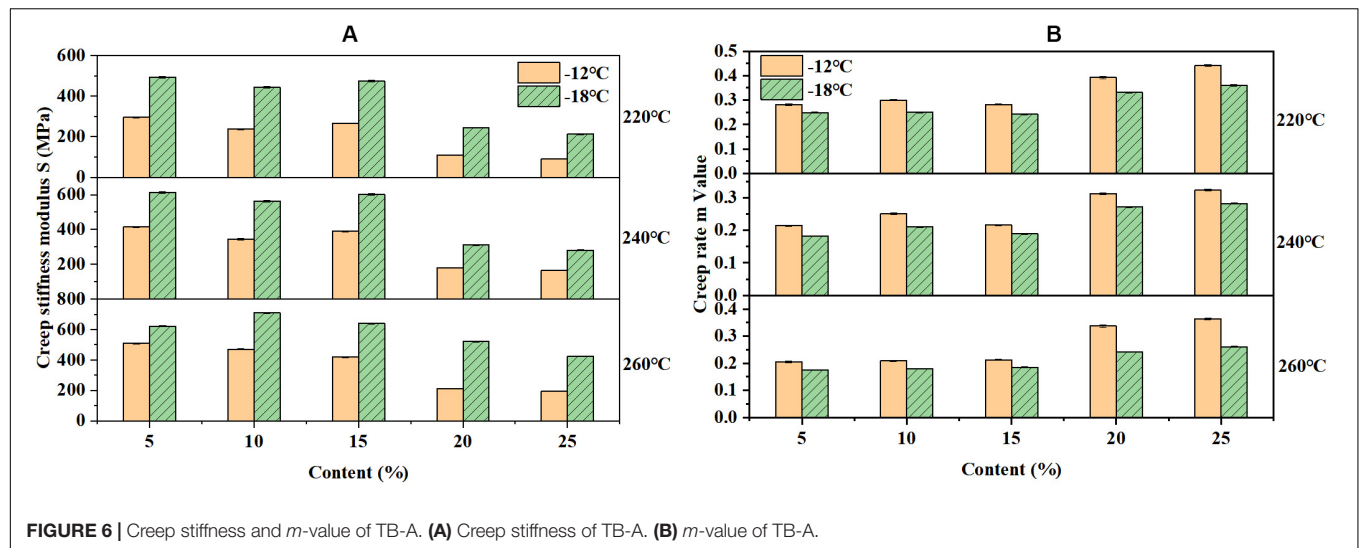


FIGURE 6 | Creep stiffness and  $m$ -value of TB-A. (A) Creep stiffness of TB-A. (B)  $m$ -value of TB-A.

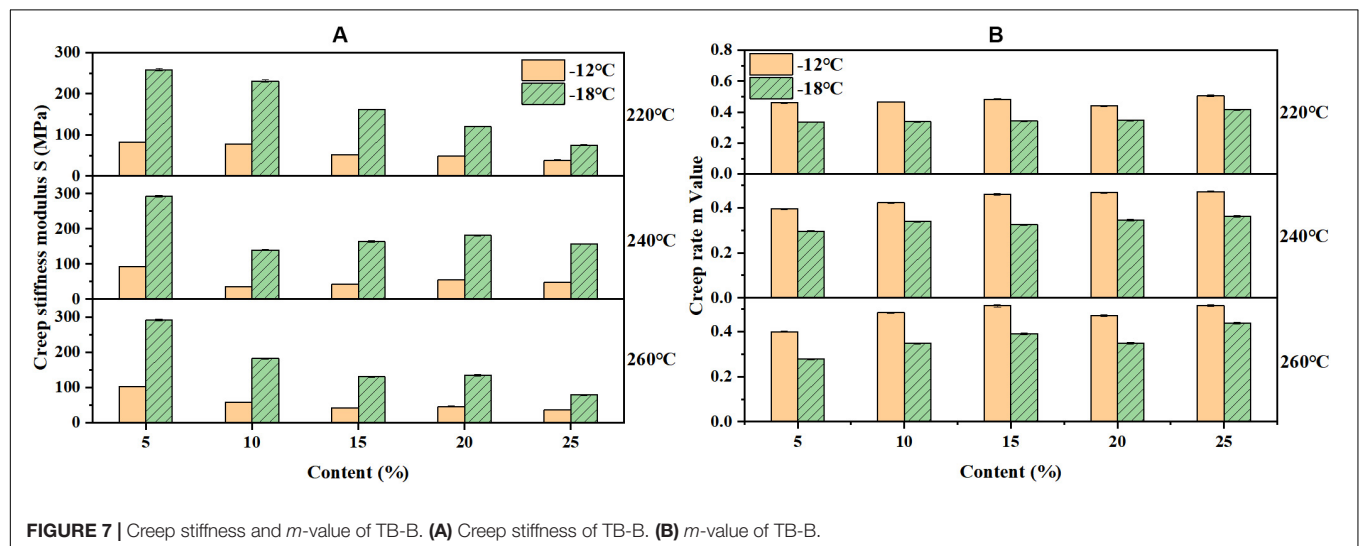


FIGURE 7 | Creep stiffness and  $m$ -value of TB-B. (A) Creep stiffness of TB-B. (B)  $m$ -value of TB-B.

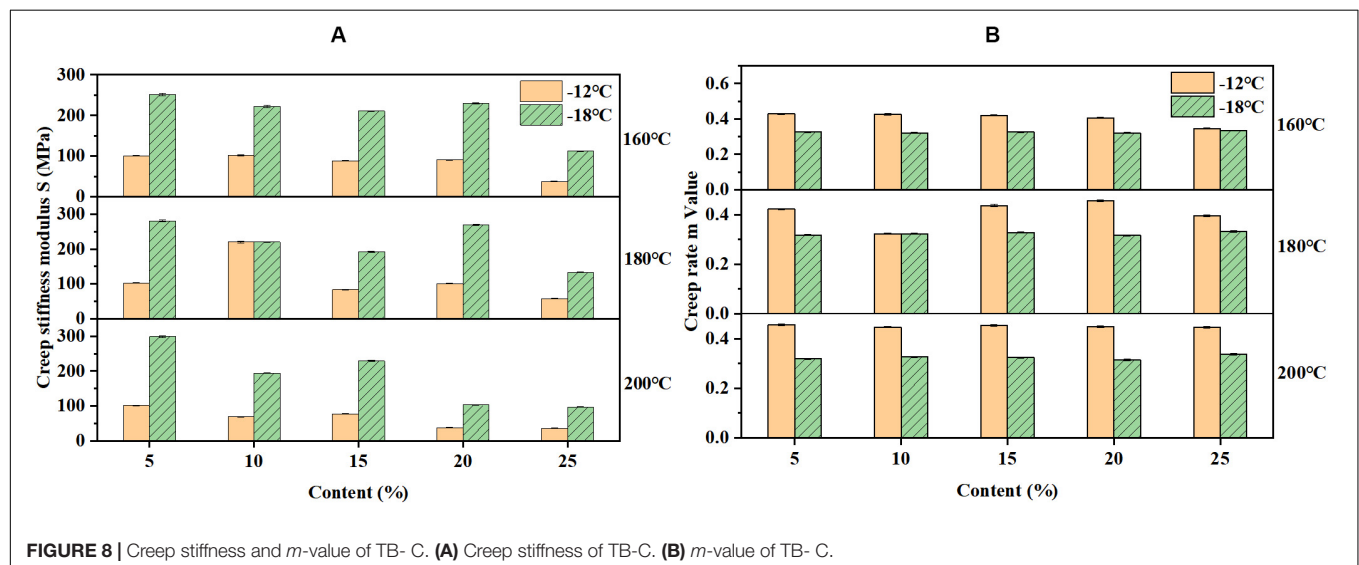


FIGURE 8 | Creep stiffness and  $m$ -value of TB-C. (A) Creep stiffness of TB-C. (B)  $m$ -value of TB-C.



**TABLE 4** | Softening point difference of TB asphalt (°C).

CR content Sample ID	TB-A			TB-B			TB-C		
	220°C	240°C	260°C	220°C	240°C	260°C	160°C	180°C	200°C
5%	—	—	—	0.7	0.05	0.15	0.5	0.95	0.85
10%	0.05	—	—	1.05	0.75	0	1.65	0.4	1.7
15%	0.3	—	—	0.8	2.2	0.1	0.1	0	4.6
20%	0.4	1	0.75	2.75	0	0.85	6.95	4.85	10.35
25%	0.2	0.8	0.55	0.15	1.25	0.55	9.75	11.15	11.8

“—” means that the softening point test temperature is greater than 80°C, and it is necessary to switch to glycerin for heating. Considering that the softening point of TB asphalt is not so high, it means that the requirements of TB asphalt are not met, so the test was not performed.

point difference of polymer modified asphalt after being stored for 48 h at high temperature should be less than 2.5°C. As an important performance evaluation index of modified asphalt, the storage stability of three types of TB asphalt prepared in this study was measured with polymer isolation experiment.

It can be seen from **Table 4** that the softening point difference of TB-A and TB-B are less than 2.5°C, but most samples of TB-C asphalt do not meet the specification. Also, an increase in the content of crumb rubber in the asphalt leads to an increase in the softening point difference. The lowering of the interaction temperature will aggravate the segregation of modified asphalt. This is because the increase of crumb rubber content in the asphalt increases the possibility of agglomeration between crumb rubber. When the interaction temperature is less than 220°C, the swelling of the crumb rubber in the asphalt is a key factor affecting the performance of the binder. When the interaction temperature is greater than 220°C, the desulfurization and depolymerization of the crumb rubber in the asphalt gradually replaces the swelling and gains the upper hand. When the interaction temperature reaches 260°C, the softening point difference of the modified asphalt is almost close to zero, indicating that the degree of desulfurization and depolymerization of the crumb rubber in the asphalt is already high. It can be seen from **Table 4** that if soluble crumb rubber is used to prepare TB asphalt, in order to avoid serious segregation, the soluble crumb rubber content in the asphalt should not be greater than 15%.

## Rotational Viscosity

Viscosity is often used to characterize the friction of molecules inside asphalt during flow. Construction compaction temperature can be determined by viscosity-temperature curves, the larger the viscosity, the higher the compaction temperature (Lo Presti et al., 2014; Xiao et al., 2015). Asphalt aging increases the proportion of asphaltene, thereby increase the polarity. In general, the increment of polarity decline the fluidity of asphalt, and consequently increase the viscosity (Zhang et al., 2020). So, viscosity is also used to characterize the degree of aging of asphalt. TB asphalt is prepared at high temperature and crumb rubber is decomposes into small molecular substances, which reduces the viscosity of the binder and is beneficial to construction application. Asphalt Rubber Usage Guide stipulates that the 177°C viscosity of TB asphalt should be less than 1.5 KPa

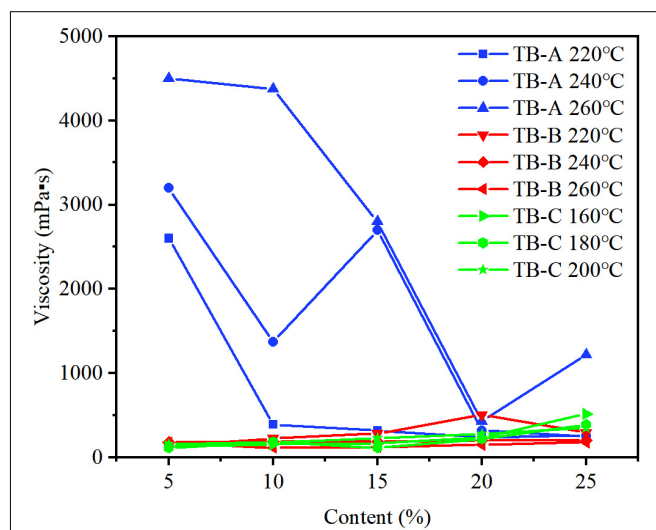
(State of California Department of Transportation, 2003). The 177°C viscosity of TB asphalt prepared by different methods was measured with rotary viscometer.

As shown in **Figure 9**, the 177°C viscosity of TB-B asphalt and TB-C asphalt meets the requirements of the specification. But, the viscosity of TB-A asphalt is much greater than that of TB-B asphalt and TB-C asphalt. This is because the excessive aging of TB-Asphalt increases the asphaltene content. Moreover, 20% is the optimal dosage to control viscosity for TB-A. In addition, the preparation temperature is a key factor affecting the viscosity of TB-B asphalt. As can be seen from **Figure 9**, the higher the temperature, more adequate the desulfurization and depolymerization of crumb rubber, and the lower the viscosity.

## FTIR Test Results and Analysis

Samples of TB-A, TB-B prepared with 15% crumb rubber content at 260°C and TB-C prepared with 15% at 180°C were used to carried out FTIR and TG analysis.

Fourier Transform Infrared spectrometer has been widely used in qualitative and quantitative analysis of organic compounds. The modification mechanism and aging degree

**FIGURE 9** | 177°C viscosity of TB asphalt.

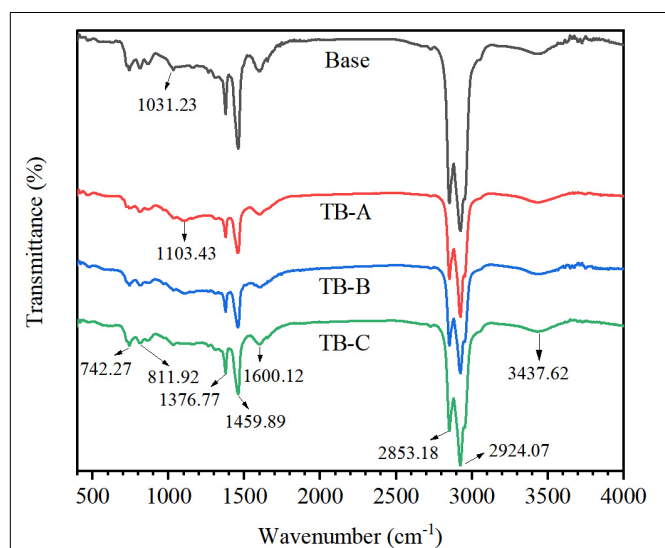


of asphalt can be explored by identifying the differences in the absorption spectrum functional groups in the asphalt at the molecular level (Zhang et al., 2020).

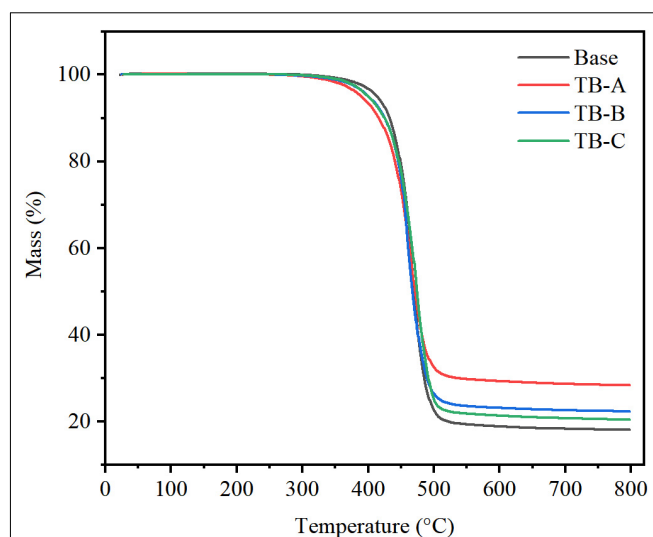
**Figure 10** is the FTIR spectrum of TB asphalt and base asphalt, the peak at  $3437.62\text{ cm}^{-1}$  is attributed to the stretching vibration of the intermolecular hydrogen bond, and the peaks at  $2853.18$  and  $2924.07\text{ cm}^{-1}$  are caused by the  $-\text{CH}_2-$  functional group. In the range of ( $4000\sim1300\text{ cm}^{-1}$ ), the absorption rate of TB asphalt is significantly smaller than base asphalt, indicating that the light component content of TB asphalt are lower compared to base asphalt. The peak at  $1600.12\text{ cm}^{-1}$  is generated by the vibration of the  $\text{C}=\text{C}$  conjugated double bond in benzene ring. Peaks at  $1459.89$  and  $1376.77\text{ cm}^{-1}$  represent the asymmetric vibration and umbrella vibration of the methyl group ( $\text{CH}_3$ ), respectively. In the fingerprint region ( $1300\sim400\text{ cm}^{-1}$ ), the peaks at  $742.27$  and  $811.92\text{ cm}^{-1}$  represent the  $\text{C}=\text{C}$  of the benzene ring. The peak at  $1031.23\text{ cm}^{-1}$  corresponds to the aromatic compounds in asphalt. However, the absorption rate of TB asphalt in this range is also lower than base asphalt, which indicates that the crumb rubber in TB asphalt has absorbed the aromatic compounds of asphalt. The peak at  $1103.43\text{ cm}^{-1}$  appearing in both TB-A and TB-B spectrum is due to the contraction vibration of the sulfoxide group ( $\text{S}=\text{O}$ ). But compared to TB-A, TB-B has a smaller absorption peak area, which means the asphalt aging occurs in the preparation process of both of them, but the aging degree of TB-B is less. Furthermore, the absorption rate of peak at  $1600\text{ cm}^{-1}$  in TB-C is slightly lower than TB-A and TB-B, which illustrates that the aging degree of TB-C is less due to its low preparation temperature (Huang et al., 2017).

## Thermogravimetric Analysis

Thermogravimetric analyzer is a technique that uses a thermal balance to measure the relationship between the mass of materials and temperature under a program-controlled temperature. It is



**FIGURE 10** | FTIR spectrum of TB asphalt and base asphalt.



**FIGURE 11** | TG curves for TB-A asphalt.

used to study the thermal stability and composition of materials (Chen et al., 2019).

**Figure 11** displays the mass change of TB asphalt with temperature. There are three main stages, the first is from room temperature to  $250^{\circ}\text{C}$ , there is almost no mass loss. The second is from  $250$  to  $390^{\circ}\text{C}$ , and mass-loss in this stage mainly comes from the decomposition of light components such as saturated and aromatic components and small molecular polymers. The third is from  $390$  to  $530^{\circ}\text{C}$  and the largest mass-loss occurs. That is because a large number of small molecular substances is generated from complex and **vigorously** chemical reaction.

During thermal weightlessness, the higher the aging degree, the larger the mass residual rate (Chen et al., 2019). The reason is that the component easily decomposing converts into relatively stable macromolecular structure, which increases the intermolecular force and thermal stability (Venudharan et al., 2018). From **Figure 11** one can see that the residual rate of TB-A is the highest compared to the base asphalt and is increased by 10.4% compared to base asphalt. Meanwhile, the residual rate of TB-B and TB-C asphalt are only 4.3 and 2.4% higher than those of base asphalt. This once again shows that the aging of the binder during the preparation of TB-A asphalt is more serious.

## CONCLUSION

In this study, to avoid excessive aging of TB asphalt during the preparation process, TB-B and TB-C asphalt were prepared using crumb rubber under nitrogen environment and soluble crumb rubber under atmospheric environment. The performance of TB-B and TB-C was compared with TB-A asphalt prepared using crumb rubber in the atmospheric environment. The physical properties, rheological properties, storage stability, and viscosity of the three TB asphalt were tested. Besides, in order to further analyze the aging degree and microscopic modification mechanism of TB-B and TB-C asphalt, the chemical analysis and

thermal analysis of TB asphalt and base asphalt were conducted. The main summary is as follows:

- (1) Chemical analysis and thermal analysis show that the aging degree of TB-B and TB-C asphalt is greatly reduced compared to TB-A, and the aging degree of TB-B is slightly greater than TB-C.
- (2) Through research on the physical and rheological properties of the three TB asphalts, it is found that TB-B asphalt has a lower resistance to deformation at high temperatures than TB-C asphalt, but has the best low temperature performance.
- (3) For the 177°C rotational viscosity of the three TB asphalts, the largest is TB-A and the smallest is TB-B. The viscosity of TB-B and TB-C are less than 1.5 MPa, indicating that the workable performance of TB-B and TB-C meets the requirements.
- (4) Based on comprehensive properties, the optimal preparation process of TB-B is: the content of crumb rubber in asphalt is 15%, the shearing temperature is 260°C, the shearing time is 3 h, and the shearing speed is 4000 r/min. The recommended preparation process of TB-C is: the content of crumb rubber in the asphalt is 15%, the interaction temperature is 180°C, the shearing time is 1h, and the shearing speed is 4000 r/min.
- (5) Using soluble crumb rubber under atmospheric environment and crumb rubber under nitrogen environment are both effective methods to inhibit asphalt aging during preparation process, but both have certain

shortcomings. Such as TB-B asphalt has insufficient resistance to rutting at high temperatures and the storage stability of TB-C is not ideal, and we will conduct in-depth research and propose solutions in our follow-up work.

## DATA AVAILABILITY STATEMENT

All datasets presented in this study are included in the article/supplementary material.

## AUTHOR CONTRIBUTIONS

JX is the supervisor of this research work and responsible for the editing and writing of manuscript. YZ conducted the experiments and performed the characterization and data analysis. YY helped in samples testing and data analysis. All authors involved the analysis of experimental data and manuscript preparation.

## FUNDING

This work was supported by the National Natural Science Foundation of China (51608056), the Education Department of Hunan Province (19B034), and Open Fund of National Engineering Laboratory for Highway Maintenance Technology (Changsha University of Science & Technology, kfj140105).

## REFERENCES

- Billiter, T. C., Davison, R. R., Glover, C. J., and Bullin, J. A. (1997). Production of asphalt-rubber binders by high-cure conditions. *Trans. Res. Rec.* 1586, 50–56. doi: 10.3141/1586-07
- Chen, Z., Wang, T., Pei, J., Amirhanian, S., Xiao, F., Ye, Q., et al. (2019). Low temperature and fatigue characteristics of treated crumb rubber modified asphalt after a long term aging procedure. *J. Clean. Product.* 234, 1262–1274. doi: 10.1016/j.jclepro.2019.06.147
- Ghavibazoo, A., and Abdelrahman, M. (2013). Composition analysis of crumb rubber during interaction with asphalt and effect on properties of binder. *Int. J. Pavement Eng.* 14, 517–530. doi: 10.1080/10298436.2012.721548
- Ghavibazoo, A., and Abdelrahman, M. (2014). Effect of Crumb Rubber Dissolution on Low-Temperature Performance and Aging of Asphalt–Rubber Binder. *Trans. Res. Rec.* 2445, 47–55. doi: 10.3141/2445-2446
- Ghavibazoo, A., Abdelrahman, M., and Ragab, M. (2016). Changes in composition and molecular structure of asphalt in mixing with crumb rubber modifier. *Road Mater. Pavement Design* 17, 906–919. doi: 10.1080/14680629.2016.1138878
- Greene, J., Chun, S., Nash, T., and Choubane, B. (2015). “Evaluation and Implementation of PG 76-22 Asphalt Rubber Binder in Florida,” in *Proceedings of the Transportation Research Board Meeting*, Washington, DC.
- Han, L., Zheng, M., Li, J., Li, Y., Zhu, Y., and Ma, Q. (2017). Effect of nano silica and pretreated rubber on the properties of terminal blend crumb rubber modified asphalt. *Construct. Build. Mater.* 157, 277–291. doi: 10.1016/j.conbuildmat.2017.08.187
- Han, L., Zheng, M., and Wang, C. (2016). Current status and development of terminal blend tyre rubber modified asphalt. *Construct. Build. Mater.* 128, 399–409. doi: 10.1016/j.conbuildmat.2016.10.080
- Hosseinnezhad, S., Kabir, S. F., Oldham, D., Mousavi, M., and Fini, E. H. (2019). Surface functionalization of rubber particles to reduce phase separation in rubberized asphalt for sustainable construction. *J. Clean. Product.* 225, 82–89. doi: 10.1016/j.jclepro.2019.03.219
- Huang, W., Lin, P., Tang, N., Hu, J., and Xiao, F. (2017). Effect of crumb rubber degradation on components distribution and rheological properties of Terminal Blend rubberized asphalt binder. *Construct. Build. Mater.* 151, 897–906. doi: 10.1016/j.conbuildmat.2017.03.229
- Huang, W., Lv, Q., and Cai, C. (2016). Research on Composite Modification by Terminal Blend Asphalt. *J. Build. Mater.* 19, 111–118.
- Jan, B. K., Piotr, R., Karol, J. K., Michał, S., and Paweł, C. (2014). Laboratory and field investigations of polymer and crumb rubber modified bitumen. *J. Civil Eng. Architect.* 8, 1327–1334. doi: 10.17265/1934-7359/2014.10.014
- Jin, J., Tan, Y., Liu, R., Zheng, J., and Zhang, J. (2019). Synergy Effect of Attapulgit, Rubber, and Diatomite on Organic Montmorillonite-Modified Asphalt. *J. Mater. Civil Eng.* 31, 04018388.04018381–04018388.04018388.
- Li, B., Huang, W., Tang, N., Hu, J., Lin, P., Guan, W., et al. (2017). Evolution of components distribution and its effect on low temperature properties of terminal blend rubberized asphalt binder. *Construct. Build. Mater.* 136, 598–608. doi: 10.1016/j.conbuildmat.2017.01.118
- Lin, P., Huang, W., Tang, N., and Xiao, F. (2017). Performance characteristics of Terminal Blend rubberized asphalt with SBS and polyphosphoric acid. *Construct. Build. Mater.* 141, 171–182. doi: 10.1016/j.conbuildmat.2017.02.138
- Lin, P., Huang, W., Tang, N., Xiao, F., and Li, Y. (2018). Understanding the low temperature properties of Terminal Blend hybrid asphalt through chemical and thermal analysis methods. *Construct. Build. Mater.* 169, 543–552. doi: 10.1016/j.conbuildmat.2018.02.060
- Lo Presti, D. (2013). Recycled Tyre Rubber Modified Bitumens for road asphalt mixtures: a literature review. *Construct. Build. Mater.* 49, 863–881. doi: 10.1016/j.conbuildmat.2013.09.007
- Lo Presti, D., Airey, G., and Partal, P. (2012). Manufacturing Terminal and Field Bitumen-Tyre Rubber Blends: the Importance of Processing Conditions. *Proc. Soc. Behav. Sci.* 53, 485–494. doi: 10.1016/j.sbspro.2012.09.899

- Lo Presti, D., Fecarotti, C., Clare, A. T., and Airey, G. (2014). Toward more realistic viscosity measurements of tyre rubber–bitumen blends. *Construct. Build. Mater.* 67, 270–278. doi: 10.1016/j.conbuildmat.2014.03.038
- Lv, Q., Zhou, L., and Huang, W. (2019). Yizhong Gaochucun Wendingxing De Rongjiexing Jiaofen Gaixing Liqing, C.N. Patent No. CN110079106A. C.N Patent.
- Nanjegowda, V. H., and Biligiri, K. P. (2020). Recyclability of rubber in asphalt roadway systems: a review of applied research and advancement in technology. *Resour. Conserv. Recycl.* 155:104655. doi: 10.1016/j.resconrec.2019.104655
- Pouranian, M. R., Notani, M. A., Tabesh, M. T., Nazeri, B., and Shishehbor, M. (2020). Rheological and environmental characteristics of crumb rubber asphalt binders containing non-foaming warm mix asphalt additives. *Construct. Build. Mater.* 238:117707. doi: 10.1016/j.conbuildmat.2019.117707
- Qi, X., Shenoy, A., Al-Khateeb, G., Arnold, T., Gibson, N., Youtcheff, J., et al. (2006). “Laboratory characterization and full-scale accelerated performance testing of crumb rubber asphalts and other modified asphalt systems,” in *Proceedings of the Asphalt Rubber Conference*, Palm Springs.
- Ragab, M., and Abdelrahman, M. (2014). Effects of Interaction Conditions on Internal Network Structure of Crumb Rubber–Modified Asphalts. *Trans. Res. Rec.* 2444, 130–141. doi: 10.3141/2444-15
- Ragab, M., Abdelrahman, M., and Ghavibazoo, A. (2013). Performance enhancement of crumb rubber–modified asphalts through control of the developed internal network structure. *Trans. Res. Rec.* 2371, 96–104. doi: 10.3141/2371-11
- Ragab, M., Abdelrahman, M., and Ghavibazoo, A. (2015). Effect of Dissolved Species from Crumb-Rubber Modifier on Micromechanical Properties of Asphalt Binder. *Adv. Civil Eng. Mater.* 4, 275–291.
- Santucci, B. L. (2009). Rubber roads: waste tires find a home. *Technol. Transfer Program* 1, 1–12.
- Song, C. (2017). Study on Road Performance of Durability Hot Recycled Mixture with High RAP Content Based on High Modulus Agent and Terminal Blend Rubber Modified Asphalt Composite Technology. *Highway Eng.* 42, 159–167.
- Tang, N., Huang, W., Hu, J., and Xiao, F. (2017). Rheological characterisation of terminal blend rubberised asphalt binder containing polymeric additive and sulphur. *Road Mater. Pavement Design* 19, 1288–1300. doi: 10.1080/14680629.2017.1305436
- Tang, N., Huang, W., and Xiao, F. (2016). Chemical and rheological investigation of high-cured crumb rubber-modified asphalt. *Construct. Build. Mater.* 123, 847–854. doi: 10.1016/j.conbuildmat.2016.07.131
- Tang, N., Lv, Q., Huang, W., Lin, P., and Yan, C. (2019). Chemical and rheological evaluation of aging characteristics of terminal blend rubberized asphalt binder. *Construct. Build. Mater.* 205, 87–96. doi: 10.1016/j.conbuildmat.2019.02.008
- State of California Department of Transportation (2003). *Asphalt Rubber Usage Guide*. Sacramento, CA: State of California Department of Transportation.
- Venudharan, V., Biligiri, K. P., and Das, N. C. (2018). Investigations on behavioral characteristics of asphalt binder with crumb rubber modification: rheological and thermo-chemical approach. *Construct. Build. Mater.* 181, 455–464. doi: 10.1016/j.conbuildmat.2018.06.087
- Wang, Q.-Z., Wang, N.-N., Tseng, M.-L., Huang, Y.-M., and Li, N.-L. (2020). Waste tire recycling assessment: road application potential and carbon emissions reduction analysis of crumb rubber modified asphalt in China. *J. Clean. Product.* 249:119411. doi: 10.1016/j.jclepro.2019.119411
- Wang, Z., and Ye, F. (2020). Experimental investigation on aging characteristics of asphalt based on rheological properties. *Construct. Build. Mater.* 231:117158. doi: 10.1016/j.conbuildmat.2019.117158
- Wei, X. (2016). Asphalt and Mixture Performance TB and SBS Compound Modified. *Highway Eng.* 41, 249–255.
- Wen, S., Liu, J., and Deng, J. (2021). Methods for the detection and composition study of fluid inclusions. *Fluid Inclusion Effect in Flotation of Sulfide Minerals* 27–68. doi: 10.1016/b978-0-12-819845-2.00003-x
- Wu, C., Liu, K., Li, A., and Liu, A. (2013). “Application Research and Engineering Practice on the Terminal Blend Rubberized Asphalt in Pavement,” in *2013 International Highway Technology Summit*.
- Xiao, F., Hou, X., Xu, O., Amirkhanian, S. N., and Wen, Y. (2015). Rheological Comparisons of Terminally Blended and Laboratory Blended Ground Tire Rubbers. *New Front. Road Airport Eng.*
- Xie, J., Yang, Y., Lv, S., Zhang, Y., Zhu, X., and Zheng, C. (2019). Investigation on Rheological Properties and Storage Stability of Modified Asphalt Based on the Grafting Activation of Crumb Rubber. *Polymers* 11:1563. doi: 10.3390/polym11101563
- Yan, K., Chen, J., You, L., and Tian, S. (2020). Characteristics of compound asphalt modified by waste tire rubber (WTR) and ethylene vinyl acetate (EVA): conventional, rheological, and microstructural properties. *J. Clean. Product.* 258:120732. doi: 10.1016/j.jclepro.2020.120732
- Yang, X., You, Z., Hasan, M. R. M., Diab, A., Shao, H., Chen, S., et al. (2017). Environmental and mechanical performance of crumb rubber modified warm mix asphalt using Evotherm. *J. Clean. Product.* 159, 346–358. doi: 10.1016/j.jclepro.2017.04.168
- You, L., Yan, K., Wang, D., Ge, D., and Song, X. (2019). Use of amorphous-poly-alpha-olefin as an additive to improve terminal blend rubberized asphalt. *Construct. Build. Mater.* 228:116774. doi: 10.1016/j.conbuildmat.2019.116774
- Zanzotto, L., and Kennepohl, G. J. (1996). Development of Rubber and Asphalt Binders by Depolymerization and Devulcanization of Scrap Tires in Asphalt. *Trans. Res. Rec.* 1530, 51–58. doi: 10.1177/0361198196153000107
- Zeinali, A., Blankenship, P. B., and Mahboub, K. C. (2014). “Comparison of performance properties of terminal blend tire rubber and polymer modified asphalt mixtures,” in *Second Transportation & Development Congress 2014*, American Society of Civil Engineers, 239–248.
- Zhang, M., Hao, P., Dong, S., Li, Y., and Yuan, G. (2020). Asphalt binder micro-characterization and testing approaches: a review. *Measurement* 151:107255. doi: 10.1016/j.measurement.2019.107255
- Zhou, H., Holikatti, S., and Vacura, P. (2014). Caltrans use of scrap tires in asphalt rubber products: a comprehensive review. *J. Traffic Trans. Eng.* 1, 39–48. doi: 10.1016/s2095-7564(15)30087-30088

**Conflict of Interest:** The authors declare that the research was conducted in the absence of any commercial or financial relationships that could be construed as a potential conflict of interest.

Copyright © 2020 Xie, Zhang and Yang. This is an open-access article distributed under the terms of the Creative Commons Attribution License (CC BY). The use, distribution or reproduction in other forums is permitted, provided the original author(s) and the copyright owner(s) are credited and that the original publication in this journal is cited, in accordance with accepted academic practice. No use, distribution or reproduction is permitted which does not comply with these terms.



# Composition Optimization and Field Application of Colored Emulsified Asphalt Seal Mixture

Zhilin Sun<sup>1\*</sup>, Zhihang Zhu<sup>1</sup>, Junhui Zhang<sup>2</sup> and Chao Wu<sup>1</sup>

<sup>1</sup> Key Laboratory of Special Environment Road Engineering of Hunan Province, Changsha University of Science and Technology, Changsha, China, <sup>2</sup> National Engineering Laboratory of Highway Maintenance Technology, Changsha University of Science and Technology, Changsha, China

## OPEN ACCESS

### Edited by:

Dawei Wang,  
RWTH Aachen University, Aachen,  
Germany

### Reviewed by:

Qiang Li,  
Nanjing Forestry University, China  
Yang Zhou,  
Southeast University, China

### \*Correspondence:

Zhilin Sun  
sunzhilin1979@csust.edu.cn

### Specialty section:

This article was submitted to  
Structural Materials,  
a section of the journal  
Frontiers in Materials

**Received:** 12 June 2020

**Accepted:** 14 July 2020

**Published:** 11 August 2020

### Citation:

Sun Z, Zhu Z, Zhang J and Wu C  
(2020) Composition Optimization  
and Field Application of Colored  
Emulsified Asphalt Seal Mixture.  
*Front. Mater.* 7:258.  
doi: 10.3389/fmats.2020.00258

A uniform test design method was used to investigate the storage stability, wear resistance performance, anti-slide performance, and color durability of a colored emulsified asphalt seal mixture (CEASM). The optimal mix proportions of the seal mixture were determined, and the engineering test application and effect evaluation analysis were performed. The results show that the clay, silica fume, pigment, mineral aggregate, and emulsified asphalt contents in the prepared mixture ranged from 15–17, 12–16, 10–14, 28–32, and 25–32%, respectively. In practical engineering applications, CEASM with a molding thickness of 2–3 mm stored in liquid form has a good storage stability and wear resistance, which is suitable for manual scraping pavement or mechanical spraying construction. In addition, it has been shown that colored pavement has the advantages of low cost, safety, environmental protection, convenient construction, good durability, and rapid molding. The CEASM also has great application prospects in color repaving for non-color roads, the early maintenance of colored pavement, and road disease maintenance. The results guide colored pavement designs to improve the storage stability of CEASM and enhance the color durability and crack resistance of colored pavements.

**Keywords:** colored pavement, preparation, optimal mix proportions, uniform design method, engineering application

## INTRODUCTION

Colored pavement has broad application prospects, such as inducing traffic and improving driving safety and transport smoothness (Ando et al., 2011; Xu et al., 2012). Such pavement can provide road divisions, beautify the environment, and contribute to mitigating heat islands (Synnefa et al., 2011). In addition, colored pavement prepared with emulsified asphalt as a binder has several advantages, such as low cost, convenient construction, and a wide raw material availability and application range. However, the effects of the natural environment and driving loads cause color decay and cracks to appear in the initial or recent colored pavement projects (Zhang et al., 2019a,b,c). The disadvantages of colored pavement, such as poor color durability, difficulty



of controlling the pavement color, and severe color contamination, limit its promotion and application. In addition, the initial problems of colored pavement have not been effectively solved, such as its poor anti-slide performance and insufficient high-temperature stability. Finally, few materials can be used for colored pavement maintenance. Therefore, the maintenance and repair of colored pavements have gradually become urgent issues that need to be solved.

Several researchers have conducted relevant research on colored pavement due to its increasing application in road construction. Bocci et al. (2012) studied the mechanical and photometric properties of colored pavements and indicated that it has a good wear resistance but poor permanent deformation resistance at high temperatures. Its remarkable photometric properties can improve the lighting design of tunnels, which reduces the costs from lighting equipment and energy use. The shoving, rutting, loose flaking, and poor color durability of colored pavement are still major distress types in long-term use (Lee and Kim, 2007). Tang et al. (2015) mixed aromatic oil with petroleum resin and functional polymers to prepare a colored binder. The colored binder was then mixed with pigment, aggregates, and additives to prepare colored asphalt mixtures. Light-colored synthetic asphalt (LCSA) binders were prepared using aromatic oil, petroleum resin, and various polymer modifiers. The bending beam test (BBR) results show that the binder prepared with SBS, EVA, and SBS + EVA had a better performance under low temperatures with better aging resistance in the seal pavement (Sengoz and Isikyakar, 2008; Tang et al., 2018; Zhou et al., 2020). He (2013) and Jin (2015) indicated that a network structure can be formed by the polymer modifiers in the LCSA binder, which significantly influences the performance at both high and low temperatures. Lin and Luo (2004) found that colored asphalt fading depends on the type and dosage of the dye, as well as the aging spans. The results also demonstrated that red dyes always had better fading resistances than green under ultraviolet light exposure. Gao et al. (2005) found that aged colored asphalt with an increased asphaltene content decreased the colloid contents, aromatic

phenol, and saturated phenol, and the original balanced system of asphalt colloids was destroyed, which resulted in deteriorated asphalt performances.

As mentioned, the diseases of colored asphalt pavement and the preparation of a colored asphalt binder have been widely studied. However, the complicated components and various raw materials of colored asphalt have left several problems to be solved for prepared colored asphalts and its mixture, especially regarding its poor color durability and storage stability. Therefore, a uniform design method was adopted here. The emulsified asphalt was modified by adding inorganic materials, such as clay and silica fume. Its mixture proportions and pavement performances were studied in combination with relevant tests to prepare CEASM with a good color durability and high storage stability.

## MATERIALS AND TESTS

### Raw Materials

Self-made light-colored emulsified asphalt was used in this study, and its specific technical indexes are shown in **Table 1**. As suggested by Ouyang et al. (2006) and Sasanipour et al. (2019), 325-mesh clay and D920 semi-encrypted silica fume were selected as the functional fillers. The technical indexes of silica fume are given in **Table 2**. The composite inorganic pigment of titanium red was selected, and its technical indexes are shown in **Table 3**. The utilized mineral components and mix proportions are summarized in **Table 4**.

### Preparation Process

The preparation process of CEASM is as follows:

- (1) Weigh 1000 g of clay, 1000 g of silica fume, 100 g of pigment, 2000 g of mineral aggregate, and 1500 g of emulsified asphalt for use.
- (2) Add tap water to the agitated tank at 11% of the total mass of clay, silica fume, pigments, and mineral aggregate.

**TABLE 1** | Conventional technical indexes of light-colored emulsified asphalt.

Items	Unit	Requirements of modified emulsified asphalt (PCR)	Requirements of modified emulsified asphalt (BCR)	Light-colored emulsified asphalt	Test methods
Demulsification speed	—	Measured	Measured	Low breaking	T0658
Charge	—	Measured	Measured	Cation	T0653
Screen residue (1.18 mm)	%	<0.1	<0.1	0	T0652
Asphalt standard viscosity $C_{25,3}$	s	8–25	12–60	27	T0621
<b>Evaporation residue</b>					
Solid content	%	>50	>60	61.9	T0651
Penetration (100 g, 25°C, 5 s)	0.1 mm	40–120	40–100	47.2	T0604
Softening point	°C	>50	>53	60.8	T0606
5°C ductility	cm	>20	>20	20.4	T0605
<b>Storage stability</b>					
1 d	%	<1	<1	0.95	T0655
5 d	%	<5	<5	1.7	



**TABLE 2 |** Technical indexes of the silica fume.

Items	GB/T 18736-2002 indexes	Typical value of 920 silica fume
SiO <sub>2</sub> content (%)	≥85	90–92.5
Cl content (%)	≤0.02	≤0.02
Loss on ignition (%)	≤6.0	≤4.0
Water content (%)	≤3.0	≤2.0
Water requirement ratio (%)	≤125	≤110
Specific surface area (m <sup>2</sup> /kg)	≥15000	18000

- (3) Place the agitated tank with water added under the spreader and gradually increase the speed of the debugged spreader to 500–800 rpm.
- (4) Weigh the clay, silica fume, and pigment and add them to the agitated tank and stir evenly at 500–800 rpm for 3–4 min.
- (5) Weigh the pigment, add it to the agitated tank, and stir evenly at 500–800 rpm for 3–4 min.
- (6) Weigh the emulsified asphalt and add it to the agitated tank. Adjust the speed to 1500–1600 rpm (the specific speed is related to the machine power and the size of spreader) and stir for 10–15 min.
- (7) Weigh the mineral aggregates and add them to the agitated tank in batches. Adjust the speed to 1500–2500 rpm and stir for 5 min.
- (8) Place the produced materials in a marked container for storage.

## Test Methods

Considering that CEASM has many components with various content ranges, it is time-consuming and costly to study its pavement performance. Therefore, a uniform test design method proposed by Kaitai and Yuan was used to investigate the effects of dosage for each component, including the clay, silica fume,

pigment, mineral aggregate, and emulsified asphalt. This method considers uniformly spaced values over the entire test range, and it is an application of the quasi Monte Carlo method from several theoretical approaches (Fang, 1994; Fang and Wang, 1994). Compared with the “comprehensive trials” and “orthogonal design”, the number of uniform design trials is significantly reduced.

The U\*<sub>10</sub>(10<sup>8</sup>) table was used for the uniform design (shown in **Table 5**). According to the rules of the table, the factors were placed in columns 1, 2, 4, 5, and 7. After performing several experiments, it was found that when the clay content was 65 g, the silica fume, pigment, mineral aggregate, and emulsified asphalt contents were 50 g, 50 g, 110 g, and 110 g, respectively. The prepared seal mixture had the advantages of easy storage and stability. Therefore, based on engineering experience, 10 levels for each factor were taken at the upper and lower intervals of these five values. The specific plan is given in **Table 6**. The amount of each component is expressed as a percent of the total mass. Replicable tests were performed for every test number included in **Table 6**. If the error for each replicated test result did not exceed ±5%, the test results were adopted as they were deemed reliable.

The storage stability, wear resistance performance, anti-slide performance, and color durability are key indicators that can be used to evaluate the performance of CEASM (Fu et al., 2007; Liang et al., 2015; Yu et al., 2018). Here, laboratory, storage stability, and wear resistance performance tests were performed to study the properties of CEASM. The anti-slide performance and color durability were investigated on a trial road section paved in Guangdong Province.

## 5-Day Storage Stability Tests

About 300 mL uniform CEASM sample is filtered by a 1.18-mm filter screen into the test tube of stability of asphalt emulsion. It is stored for 5 days at room temperature. Three parallel tests are carried out on each sample to test 5-day storage stability of CEASM.

**TABLE 3 |** Technical indexes of the composite titanium red pigment technique.

Product name	Types	Physical properties			Fastness properties			
		Average grain size (um) ≤	Asphalt absorption amount g/100 g	PH	Heat resistance (°C)	Light resistance (1–8)	Weathering resistance (1–5)	Acid and alkaline resistance (1–5)
Composite titanium red	R3001	2.5	14–22	6–9	250	8	5	5
	R3002	2.5	14–22	6–9	250	8	5	5
	R3053	2.5	14–22	6–9	250	8	5	5

**TABLE 4 |** Percent of each component of the mineral aggregate passing through screen aperture and the proportion of each blending.

Material type	Aperture size (mm)						Proportion (%)
	2.36	1.18	0.6	0.3	0.15	0.075	
Passing percentage of fine mineral aggregate (%)	100	100	99–100	58–60	20–21	4–6	38
Passing percentage of crude mineral aggregate (%)	100	100	3–5	0	0	0	52
Mesh of mineral powder			325				10

**TABLE 5** |  $U^*_{10}$  ( $10^8$ ) uniform test design.

Test no.	Factor A	Factor B	Factor C	Factor D	Factor E	Factor F	Factor G	Factor H
1	1	2	3	4	5	7	9	10
2	2	4	6	8	10	3	7	9
3	3	6	9	1	4	10	5	8
4	4	8	1	5	9	6	3	7
5	5	10	4	9	3	2	1	6
6	6	1	7	2	8	9	10	5
7	7	3	10	6	2	5	8	4
8	8	5	2	10	7	1	6	3
9	9	7	5	3	1	8	4	2
10	10	9	8	7	6	4	2	1

### Screen Residue Tests

The CEASM sample is stored for 10 days, and then 500 g uniform CEASM sample is filtered with a 1.18-mm filter screen at the room temperature. The test is used to determine the residue of CEASM on the screen.

### Wear Resistance Tests

The wear resistance performance of mixture can be determined by wet track abrasion test (WTAT). The evaluation indexes are 1-h and 6-day WTAT values. The instrument used in this test is wet track abrasion tester.

### Anti-slide Tests

The pendulum tester to determine the friction coefficient of pavement is used as the test method of anti-slide performance. It is a field test. The evaluation index is the pendulum friction coefficient value BPN. Each test position needs to be measured in parallel at 3 points, and the average value of measurement results of 3 test points is taken as the test result.

### Color Durability Tests

Many factors affect the color attenuation of colored pavement. It is difficult to accurately simulate the color attenuation speed and service condition change of colored pavement in the laboratory.

Therefore, through paving the trial section on the Huandao Road in Zhongshan City, Guangdong Province, the color durability is evaluated by observing the color change of pavement after opening to traffic for 6 months.

## RESULTS AND DISCUSSION

### Storage Stability

#### 5-Day Storage Stability

According to the requirements from the *Technical Specifications for Construction Highway Asphalt Pavements* (JTG F40-2004) in China, the 5-day storage stability index should be no more than 5%. The higher the 5-day storage stability value, the worse the 5-day storage stability. **Figure 1** shows the effects of different test factors on the 5-day storage stability of the mixture. It is seen from **Figure 1A** that with the increased clay content, the 5-day storage stability gradually increased to a stable value, but it had a decreasing tendency when the clay content reached approximately 21%. Therefore, the preferred mixing amount of clay was within 15–20%. As shown in **Figure 1B**, the silica fume content had little effect on the 5-day storage stability, so a content of 12–20% is suggested. As shown in **Figure 1C**, additional emulsified asphalt led to a better 5-day storage stability with a preferred mixing amount of over 20%. **Figures 1D,E** show that with the increasing amount of pigment and mineral aggregate, the 5-day storage stability had a decreasing trend. The pigment content should meet the color requirements after molding with a preferred mixing range from 10–14%. In addition, according to the requirements of the anti-slide performance of pavement after molding, the preferred amount of mixed mineral aggregate ranged from 28 to 38%.

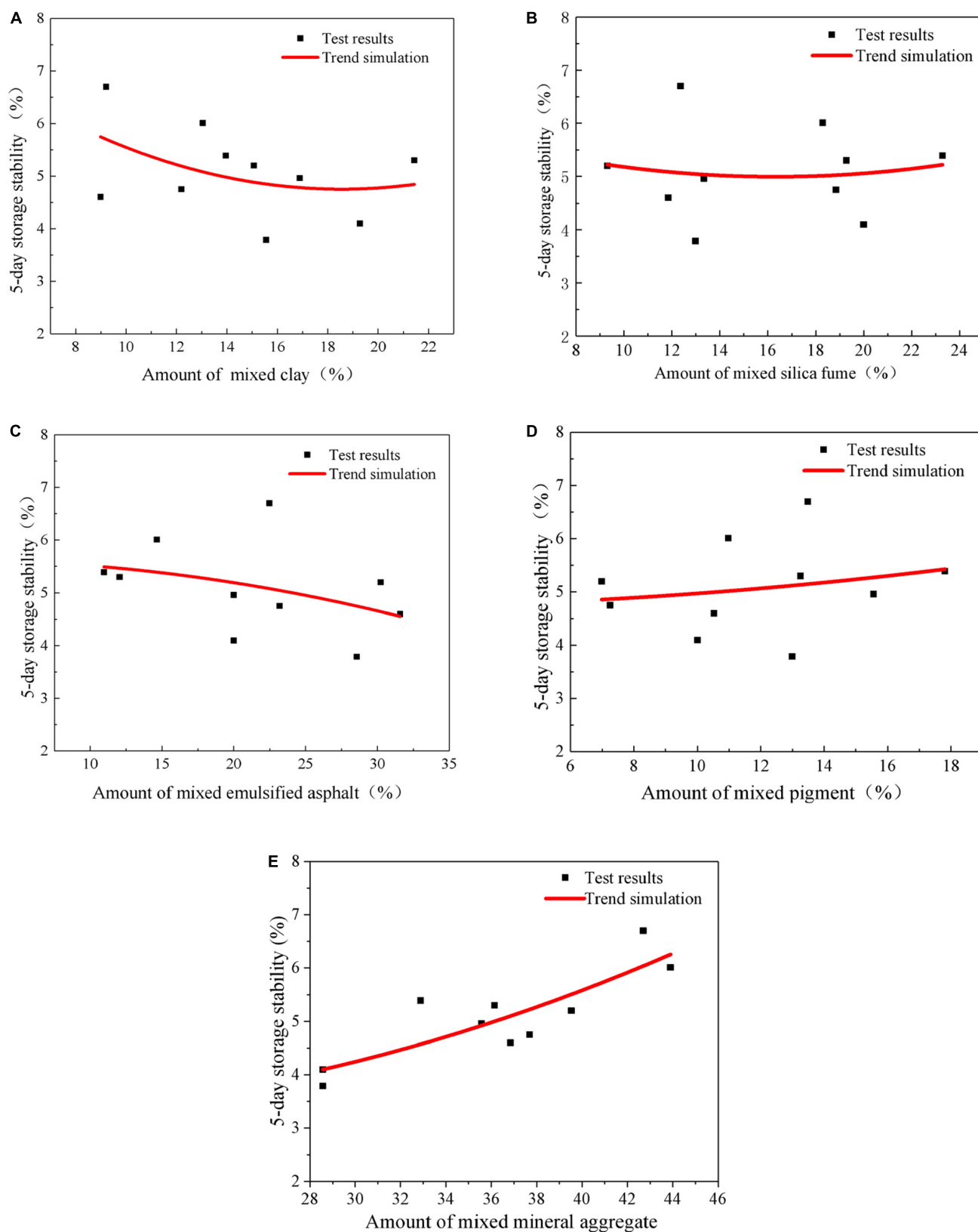
### Screen Residue

For CEASM, it is important to ensure that the emulsified asphalt particles are not severely condensated with the functional fillers after long-term storage. Screen residue is a key factor that can evaluate the storage stability of asphalt mixtures.

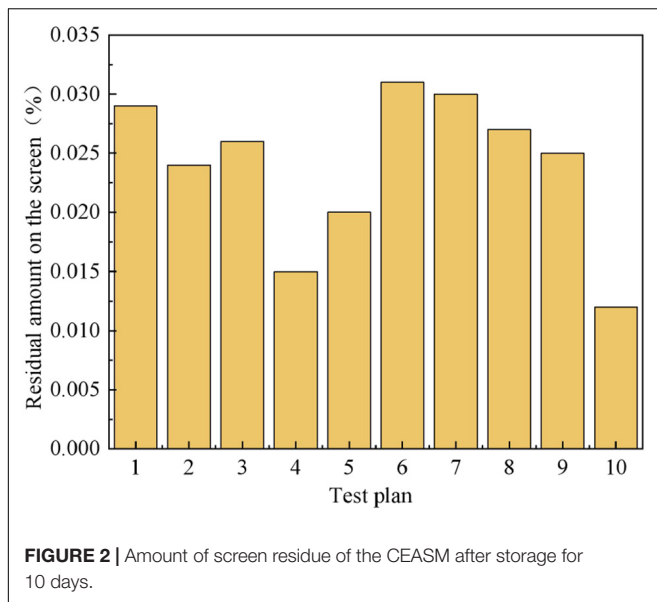
According to the requirements in the *Technical Specifications for Construction Highway Asphalt Pavements* (JTG F40-2004),

**TABLE 6** | Uniform design test plan.

Test no.	Total mass (g)	Clay		Silica fume		Pigment		Mineral aggregate		Emulsified asphalt	
		M(g)	P(%)	M(g)	P(%)	M(g)	P(%)	M(g)	P(%)	M(g)	P(%)
1	380	35	9.21	45	11.84	40	10.53	140	36.84	120	31.58
2	445	40	8.99	55	12.36	60	13.48	190	42.70	100	22.47
3	345	45	13.04	65	18.84	25	7.25	130	37.68	80	23.19
4	410	50	12.20	75	18.29	45	10.98	180	43.90	60	14.63
5	365	55	15.07	85	23.29	65	17.81	120	32.88	40	10.96
6	430	60	13.95	40	9.30	30	6.98	170	39.53	130	30.23
7	385	65	16.88	50	12.99	50	12.99	110	28.57	110	28.57
8	450	70	15.56	60	13.33	70	15.56	160	35.56	90	20.00
9	350	75	21.43	70	20.00	35	10.00	100	28.57	70	20.00
10	415	80	19.28	80	19.28	55	13.25	150	36.14	50	12.05



**FIGURE 1 |** Effect of different test factors on the 5-day storage stability of the mixtures. **(A)** Amount of mixed clay. **(B)** Amount of mixed silica fume. **(C)** Amount of mixed emulsified asphalt. **(D)** Amount of mixed pigment. **(E)** Amount of mixed mineral aggregate.



the residual modified emulsified asphalt on the sieve should be no more than 0.1%. As shown in **Figure 2**, the screen residue in the mixture for each test plan was less than 0.1%, and no agglomerated emulsified asphalt particles were produced. Therefore, the prepared emulsified asphalt mixture has a good storage stability.

## Wear Resistance Performance

Paved CEASM is subjected directly to various loads, so it should have a good wear resistance. **Figure 3** shows the effects of different test factors on the WTAT value of the mixtures. As shown in **Figure 3A**, as the clay increased, the 1-h and 6-day WTAT values did not vary regularly and the test results had a large dispersion. The influence of the clay content on the WTAT values was inconspicuous, indicating that an emulsion with a high viscosity coefficient formed from clay, and the emulsified asphalt had a limited influence on the formed structure of the mixture. Considering the wear resistance performance, the preferred mixing content of clay ranged from 9 to 17%.

It is seen from **Figure 3B** that there was a good correlation between the amount of mixed silica fume and the WTAT values. With greater silica fume contents, the 1-h and 6-day WTAT values increased, while the wear resistance performance of the mixture decreased significantly. Combined with the requirements of the test indexes, the preferred mixing content for silica fume ranged from 10 to 16%.

**Figure 3C** indicates that as the pigment increased, the 1-h and 6-day WTAT values increased first and then gradually stabilized. When the amount of mixed pigment was more than 15%, these values rapidly increased. This indicates that the pigment is not only the color source but also increases the compactness of the mixture after molding. In addition, when the pigment content was less than 8%, the color slightly lightened after molding.

Combined with the above analysis, the preferred amount of mixed pigment ranged from 8 to 15%.

**Figure 3D** shows that as the mineral aggregate content increased, the 1-h and 6-day WTAT values varied greatly. The large changes in the WTAT values resulted from the mixed proportions of mineral aggregate and the emulsified asphalt, which reflect the effects of the emulsified asphalt on the moisture damage resistance of the mixture. This also indicates that the quality of the structural system for mineral aggregate could be strongly related to the amount of mixed emulsified asphalt. According to the comprehensive analysis, the preferred amount of mixed mineral aggregate ranged from 28 to 32%.

As shown in **Figure 3E**, there was a strong effect of emulsified asphalt on the 1-h and 6-day WTAT values. With the increased emulsified asphalt content, the WTAT values were obviously reduced, indicating that emulsified asphalt influenced the moisture damage resistance and wear resistance performance of CEASM. Therefore, the preferred amount of mixed light-colored emulsified asphalt was within 25–32%.

## Anti-slide Performance

The CEASM paved on an original road reduces the depth of the pavement structure. To explore the effects of different pavement treatment methods and amounts of mixed aggregate on the frictional pendulum, the No. 7 test plan in the uniform design table was selected, where the contents of all components were within the suggested ranges, and anti-slide performance tests were performed. Basalt rock with a single grain size of 1.18 mm was selected as the aggregate for the asphalt mixture.

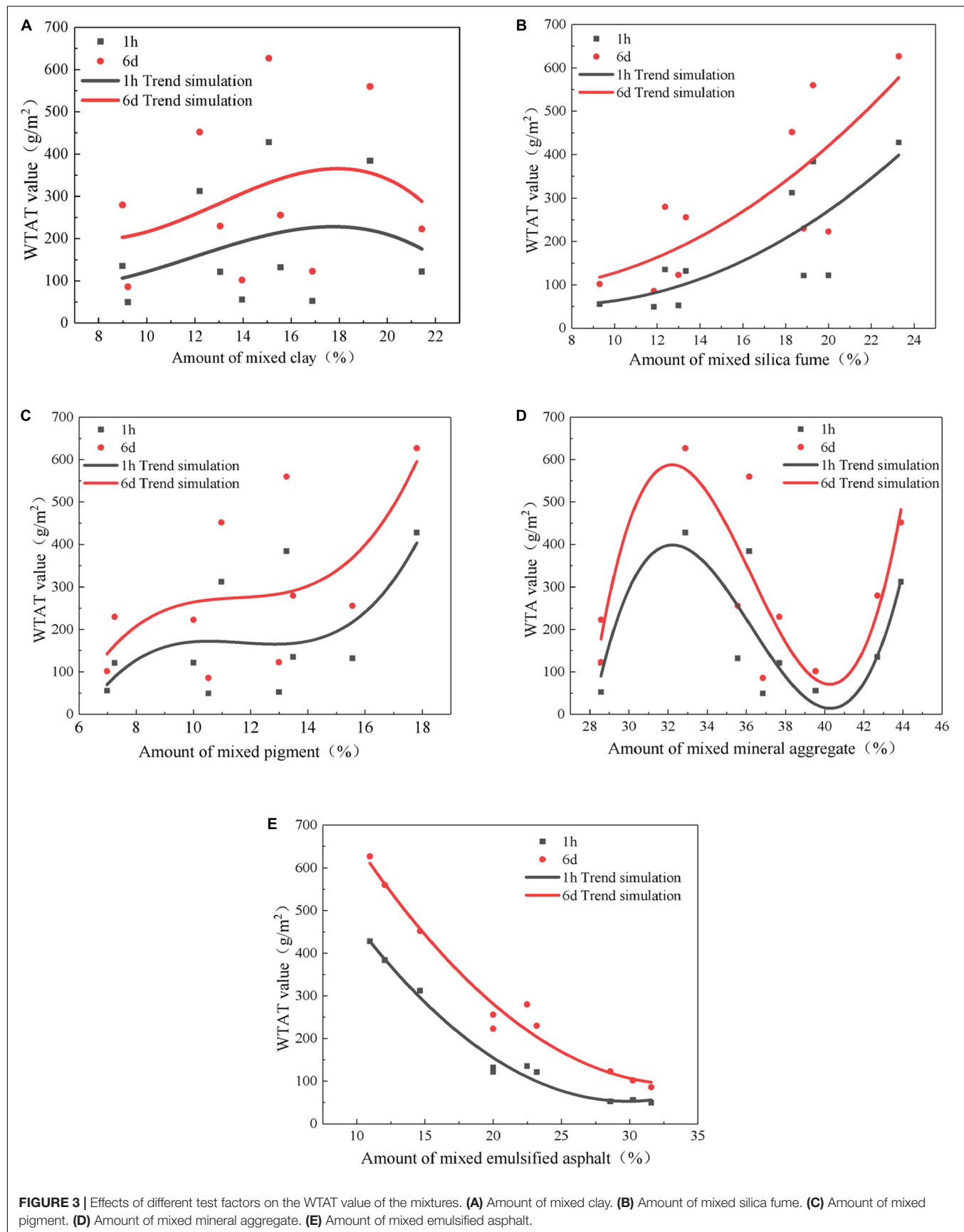
As seen in **Figure 4**, the friction pendulum value of the CEASM was larger than the specification requirement ( $BPN \geq 32$ ). It is therefore deduced that the anti-slide performance of the original road can be restored, which is improved by increasing the aggregate content. With the increased aggregate content, the BPN began to increase quickly but slowed when the amount of mixed aggregate was more than 10%. It is therefore proposed that if the trial road section has a strict anti-slide index, the amount of mixed aggregate should be 10%.

## Color Durability

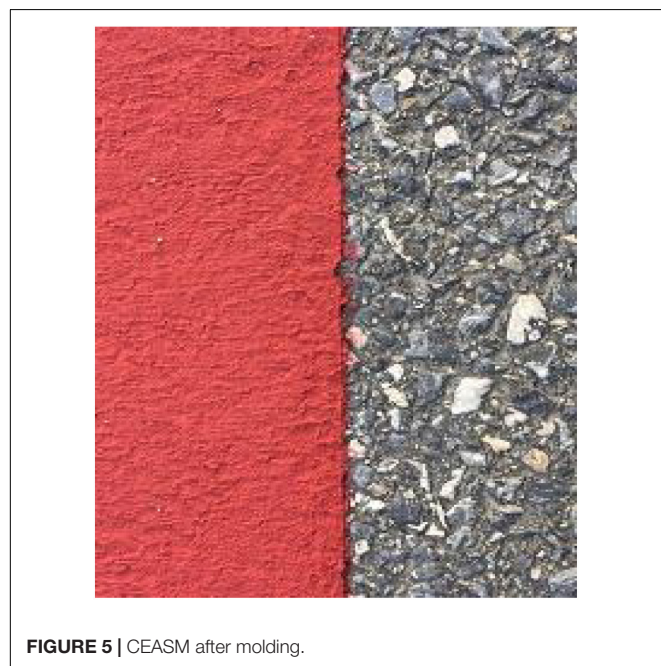
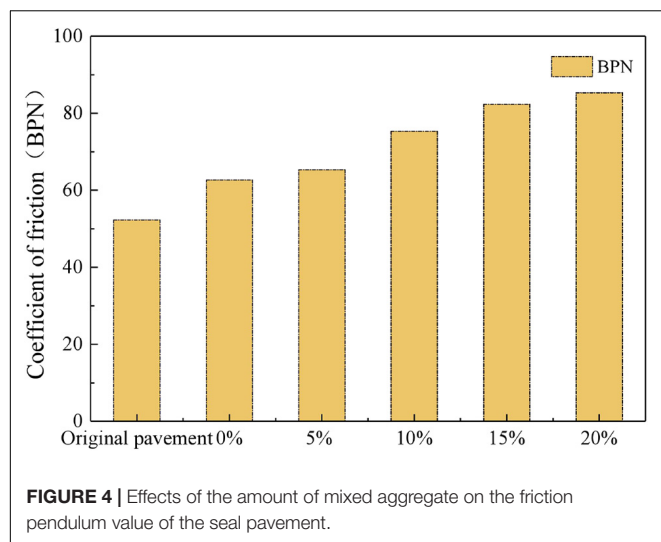
The color of pavement decays rapidly after some time. As several complex factors influence color attenuation, such as interactions with sunlight, rain washing, driving, and ground dust, it is difficult to accurately simulate the speed of color attenuation and changes in colored pavement through laboratory tests (Autelitano and Giuliani, 2019).

The pavement study from the trial section of the uniform design plan seven was performed to further explore the color durability of CEASM. Pavement color fading is significant due to the hot weather and abundant rain in Guangdong Province. Therefore, the trial road section in Huandao Road, Zhongshan, China, was selected, as shown in **Figure 5**. After the trial section was affected by the environment and driving for more than 6 months, there was nearly no color fading on the pavement and the aggregate maintained a good structure and shape, as shown in **Figure 6**.





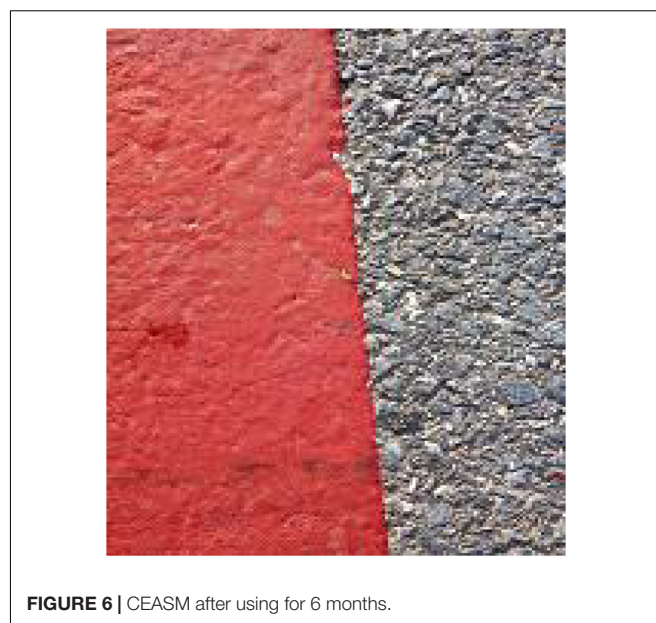
**FIGURE 3 |** Effects of different test factors on the WTAT value of the mixtures. **(A)** Amount of mixed clay. **(B)** Amount of mixed silica fume. **(C)** Amount of mixed pigment. **(D)** Amount of mixed mineral aggregate. **(E)** Amount of mixed emulsified asphalt.



Thus, the CEASM prepared in this study exhibited a good color durability.

## APPLICATION PLAN

In engineering applications, good construction workability and storage stability are required for CEASM (Zani et al., 2017). Combined with results for the storage stability and wear resistance, the mixture design that satisfies the requirements of engineering applications is shown in Table 7. When the road surface has a strict anti-slide requirement, basalt rock materials with a single grain size from 0.6 to 1.18 mm can be added. A general addition rule is 10%, which was recorded from the mass percentage of CEASM.



**TABLE 7 |** Application plan of CEASM.

Indexes	Clay (%)	Silica fume (%)	Pigment (%)	Mineral aggregate (%)	Emulsified asphalt (%)
5-day storage stability	15–20	12–20	10–14	28–38	> 20
1-h and 6-day WTAT value	9–17	10–16	8–15	28–32	25–32
Construction application	15–17	12–16	10–14	28–32	25–32

## CONCLUSION

The CEASM was prepared by mixing clay, silica fume, pigment, and mineral aggregate. The effects of each component content on the storage stability, wear resistance performance, anti-slide performance, and color durability were studied. The anti-slide performance and color durability for CEASM were tested by applying it to a trial road section in Zhongshan. These results found that there is an optimal mixture design. The main conclusions are summarized as follows.

- (1) Considering the storage stability, wear resistance performance, anti-slide performance, and color durability, the clay, silica fume, pigment, mineral aggregate, and emulsified asphalt contents in the prepared mixture are recommended to be in the ranges of 15–17, 12–16, 10–14, 28–32, and 25–32%, respectively.
- (2) Considering that CEASM may reduce the structural depth of pavement, the anti-slide performance of the pavement was tested after paving with CEASM. It was found that the friction pendulum value of pavement with CEASM was greater than 32 (above the specification requirements). Therefore, adding aggregates can improve the friction

pendulum value of colored seal pavements. In addition, the test of the road performance with CEASM showed that it had a good anti-slide performance and color durability.

- (3) When a strict anti-slide requirement was applied to the road surface, basalt rock materials with a single grain size from 0.6 to 1.18 mm are recommended. A general addition of 10% was recorded based on the mass percent of CEASM.

## DATA AVAILABILITY STATEMENT

The raw data supporting the conclusions of this article will be made available by the authors, without undue reservation.

## REFERENCES

- Ando, R., Inagaki, T., and Mimura, Y. (2011). Does colored pavement make non-signalized intersections safer? A case study in Japan. *Procedia Soc. Behav. Sci.* 20, 741–751. doi: 10.1016/j.sbspro.2011.08.082
- Autelitano, F., and Giuliani, F. (2019). Daytime and nighttime color appearance of pigmented asphalt surface treatments. *Constr. Build. Mater.* 207, 98–107. doi: 10.1016/j.conbuildmat.2019.02.100
- Bocci, M., Grilli, A., Cardone, F., and Virgili, A. (2012). Clear asphalt mixture for wearing course in tunnels: experimental application in the province of Bolzano. *Procedia Soc. Behav. Sci.* 53, 115–124. doi: 10.1016/j.sbspro.2012.09.865
- Fang, K. T. (1994). *Uniform Design and Uniform Design Table*. Beijing: Science Press. (in Chinese).
- Fang, K. T., and Wang, Y. (1994). *Number-theoretic Methods in Statistic*. London: Chapman and Hall.
- Fu, H. Y., Xie, L. D., Dou, D. Y., Li, L. F., Yu, M., and Yao, S. D. (2007). Storage stability and compatibility of asphalt binder modified by SBS graft copolymer. *Constr. Build. Mater.* 21, 1528–1533. doi: 10.1016/j.conbuildmat.2006.03.008
- Gao, M., Xiao, B., Liao, K., and Dai, Y. (2005). Study on the aging behavior of colored paving asphalt. *Sci. Tech. Engng.* 5, 401–405. (in Chinese) doi: 10.3969/j.issn.1671-1815.2005.07.005
- He, X. (2013). *Research on the Economical Colored Asphalt Binder and Mixture's Pavement Performance*. Master's thesis, Chang'an University, Shaanxi. doi: 10.7666/d.D407999
- Jin, N. S. (2015). Study on the pavement performance of colored asphalt and its mixture. *Petro. Asphalt.* 29, 48–51. (in Chinese).
- Lee, H., and Kim, Y. (2007). Laboratory evaluation of color polymer concrete pavement with synthetic resin binder for exclusive bus lanes. *Transport. Res. Rec.* 1991, 124–132. doi: 10.3141/1991-15
- Liang, M., Xin, X., Fan, W., Luo, H., Wang, X., and Xing, B. (2015). Investigation of the rheological properties and storage stability of CR/SBS modified asphalt. *Constr. Build. Mater.* 74, 235–240. doi: 10.1016/j.conbuildmat.2014.10.022
- Lin, D. F., and Luo, H. L. (2004). Fading and color changes in colored asphalt quantified by the image analysis method. *Constr. Build. Mater.* 18, 255–261. doi: 10.1016/j.conbuildmat.2004.01.004
- Ouyang, C. F., Wang, S. F., Zhang, Y., and Zhang, Y. X. (2006). Thermo-rheological properties and storage stability of SEBS/kaolin clay compound modified asphalts. *Eur. Polym. J.* 42, 446–457. doi: 10.1016/j.eurpolymj.2005.07.004
- Sasanipour, H., Aslani, F., and Taherinezhad, J. (2019). Effect of silica fume on durability of self-compacting concrete made with waste recycled concrete aggregates. *Constr. Build. Mater.* 227, 116598. doi: 10.1016/j.conbuildmat.2019.07.324
- Sengoz, B., and Isikyakar, G. (2008). Evaluation of the properties and microstructure of SBS and EVA polymer modified asphalt. *Constr. Build. Mater.* 22, 1897–1905. doi: 10.1016/j.conbuildmat.2007.07.013
- Synnefa, A., Karlessi, T., Gaitani, N., Santamouris, M., Assimakopoulos, D. N., and Papakatsikas, C. (2011). Experimental testing of cool colored thin layer

## AUTHOR CONTRIBUTIONS

ZS organized the research. ZZ and CW performed all tests. ZS and ZZ wrote the manuscript. ZS, ZZ, and JZ verified the manuscript. All authors contributed to the article and approved the submitted version.

## FUNDING

The authors gratefully acknowledge the financial support offered by the National Natural Science Foundation of China (Nos. 51878078 and 51911530215), the General Project of Education Department of Hunan Province (17C0049), and the Key Project of Open Research Fund of Key Laboratory of Special Environment Road Engineering of Hunan Province (kfj150501).

- asphalt and estimation of its potential to improve the urban microclimate. *Build. Environ.* 46, 38–44. doi: 10.1016/j.buildenv.2010.06.014
- Tang, P., Mo, L. T., Pan, C. L., Fang, H., Javilla, B., and Riara, M. (2018). Investigation of rheological properties of light colored synthetic asphalt binders containing different polymer modifiers. *Constr. Build. Mater.* 161, 175–185. doi: 10.1016/j.conbuildmat.2017.11.098
- Tang, X. D., Kong, C., Tian, J., Li, Y., Jin, Z. T., and Bai, H. Y. (2015). Preparation and pavement performance of colored asphalt. *Appl. Mech. Mater.* 727–728, 362–365. doi: 10.4028/727-728.362
- Xu, M., Pan, X., and Deng, Q. (2012). “Setting method of thin-layer antiskid colored pavement in tunnel based on increasing luminance of pavement”. in *Proceedings of the The 25th COTA International Conference of Transportation Professionals*, Columbus, OH: COTA, 3073–3083. doi: 10.1061/978078441244.2.313
- Yu, R. E., Zhu, X. J., Zhou, X., Kou, Y. F., Zhang, M. R., and Fang, C. Q. (2018). Rheological properties and storage stability of asphalt modified with nanoscale polyurethane emulsion. *Petrol. Sci. Technol.* 36, 85–90. doi: 10.1080/10916466.2017.1405028
- Zani, L., Giustozzi, F., and Harvey, J. (2017). Effect of storage stability on chemical and rheological properties of polymer-modified asphalt binders for road pavement construction. *Constr. Build. Mater.* 145, 326–335. doi: 10.1016/j.conbuildmat.2017.04.014
- Zhang, J. H., Peng, J. H., Liu, W. Z., and Lu, W. H. (2019a). Predicting resilient modulus of fine-grained subgrade soils considering relative compaction and matric suction. *Road Mater. Pavement Des.* 1–13. doi: 10.1080/14680629.2019.1651756
- Zhang, J. H., Peng, J. H., Zeng, L., Li, J., and Li, F. (2019b). Rapid estimation of resilient modulus of subgrade soils using performance-related soil properties. *Int. J. Pavement Eng.* 1–8. doi: 10.1080/10298436.2019.1643022
- Zhang, J. P., Tan, H. Q., Pei, J. Z., Qu, T., and Liu, W. L. (2019c). Evaluating crack resistance of asphalt mixture based on essential fracture energy and fracture toughness. *Int. J. Geomech.* 19:06019005. doi: 10.1061/(ASCE)GM.1943-5622.0001390
- Zhou, Y., Cai, J. S., Chen, R. X., Hou, D. S., Xu, J., Lv, K., et al. (2020). The design and evaluation of a smart polymer-based fluids transport inhibitor. *J. Clean. Prod.* 257:120528. doi: 10.1016/j.jclepro.2020.120528

**Conflict of Interest:** The authors declare that the research was conducted in the absence of any commercial or financial relationships that could be construed as a potential conflict of interest.

Copyright © 2020 Sun, Zhu, Zhang and Wu. This is an open-access article distributed under the terms of the Creative Commons Attribution License (CC BY). The use, distribution or reproduction in other forums is permitted, provided the original author(s) and the copyright owner(s) are credited and that the original publication in this journal is cited, in accordance with accepted academic practice. No use, distribution or reproduction is permitted which does not comply with these terms.



# Effects of Tire Pressures and Test Temperatures on Permanent Deformation of Direct Coal Liquefaction Residue Mixture

Suo Zhi<sup>1,2</sup>, Ji Jie<sup>1,2\*</sup>, Zhang Ran<sup>1,2</sup>, Wang Zhe<sup>1</sup>, Yao Hui<sup>3</sup> and Jin Dongzhao<sup>4</sup>

<sup>1</sup> School of Civil Engineering and Transportation, Beijing University of Civil Engineering and Architecture, Beijing, China,

<sup>2</sup> Beijing Advanced Innovation Center for Future Urban Design, Beijing University of Civil Engineering and Architecture, Beijing, China, <sup>3</sup> Beijing Key Laboratory of Traffic Engineering, College of Metropolitan Transportation, Beijing University of Technology, Beijing, China, <sup>4</sup> Department of Civil and Environmental Engineering, Michigan Technological University, Houghton, MI, United States

## OPEN ACCESS

### Edited by:

Antonio Caggiano,  
Darmstadt University of Technology,  
Germany

### Reviewed by:

Xiaoming Huang,  
Southeast University, China  
Tao Ma,  
Southeast University, China

### \*Correspondence:

Ji Jie  
jjjie@bucea.edu.cn

### Specialty section:

This article was submitted to  
Structural Materials,  
a section of the journal  
Frontiers in Materials

Received: 05 May 2020

Accepted: 07 July 2020

Published: 04 September 2020

### Citation:

Zhi S, Jie J, Ran Z, Zhe W, Hui Y  
and Dongzhao J (2020) Effects of Tire  
Pressures and Test Temperatures on  
Permanent Deformation of Direct Coal  
Liquefaction Residue Mixture.  
Front. Mater. 7:246.  
doi: 10.3389/fmats.2020.00246

The main objective of this research is to investigate the permanent deformation of asphalt mixtures containing direct coal liquefaction residue (DCLR) under various tire pressures and temperatures. Three types of asphalt mixtures, including control/DCLR/composite-DCLR modified asphalt mixture, were prepared by the Marshall design method. The rutting test was conducted under a tire pressure range of 0.7–1.0 MPa with a 0.1-MPa interval and at a temperature range of 55–70°C with a 5°C interval. Moreover, the dynamic stability and rutting depth of three asphalt mixtures were obtained to evaluate their resistance of permanent deformation. It was found that the rutting resistance of three asphalt mixtures declines with the increased tire pressures and temperatures. The asphalt mixture containing DCLR has a higher dynamic stability and lower rutting depth compared to the control asphalt mixture under the same conditions. Furthermore, the rutting resistance of composite-DCLR modified asphalt mixture is better than that of DCLR modified asphalt mixture. It indicates that the composite-DCLR is favorable for the improvement of rutting resistance of asphalt mixture. Moreover, the analysis of variance was applied, which analysis results showed that the rutting resistance of asphalt mixture is more sensitive to temperature than tire pressure. Based on the least-squares procedure, the relationship between dynamic stability and rutting depth was obtained, and the accuracy of the prediction is acceptable.

**Keywords:** direct coal liquefaction residue, tire pressure and temperature, permanent deformation, analysis of variance, regression model

## INTRODUCTION

Direct coal liquefaction residue (DCLR), the main by-product from the direct liquefaction process of coal, contains 30% by weight raw coal. It has been found that the DCLR accounts for 30–50% asphaltene materials and heavy oil, which has been considered as a construction material. Based on its performance characteristics, such as high softening point and asphaltene percentage, DCLR has been utilized to modify virgin asphalt binder to improve its high-temperature performance and has the potential to apply as an asphalt modifier (Shu, 2003; Gu, 2012). Because the properties and



component of DCLR are similar to Trinidad Lake Asphalt (TLA), it can potentially be a substitution of TLA (He, 2013; Zhao, 2015). Ji et al. (2014), Ji J. et al. (2015) studied the properties of asphalt binders containing DCLR and found that the DCLR additives improve the high-temperature properties but lower the low-temperature properties of asphalt binders. Meanwhile, the performance of DCLR modified asphalt mixture was studied. The results illustrated that the addition of DCLR into virgin asphalt binder could be a powerful approach to enhance the rutting resistance of asphalt mixture. The rutting resistance and moisture susceptibility of DCLR and composite-DCLR modified asphalt mixture are even better than those of asphalt mixture modified by styrene-butadiene-styrene (SBS) (Moghaddam et al., 2011; Zhao and Ji, 2014).

As one of main pavement distresses, the rutting often leads to the large-scale maintenance, as a result of bringing high economic consumption (Ma et al., 2017; Zhang et al., 2019). Therefore, the research on rutting of asphalt mixture is necessary and imminent. The performance of pavement is affected by many factors, such as tire pressure, materials, layer thickness, and environmental conditions (Saevardottir and Erlingsson, 2015; Ding and Zhao, 2019). High temperature and slow-speed vehicle are more likely to cause the rutting of pavement (Moghaddam et al., 2011, 2014; Al-Humeidawi, 2016). In most areas of China, the air temperature can reach 40°C in summer, and the actual road surface temperature can even reach up to 70°C, which dramatically increases the probability of rutting. Khan et al. (2013) predicted the rutting of the pavement by the accelerated test and found that the rutting potential is sensitive to repeated loads and high temperatures. The correlation equation relating to the progression of rutting depth versus number of passes was established (Chen et al., 2020).

The relationship on pavement strains between tire pressure and speed of loading was investigated by Chatti et al. (1996). They pointed out that at the bottom of the layer the horizontal strains increased with the tire pressure increases. The parameters of the temperature and loading were used as the major factors to predict the asphalt mixture permanent deformation (Ji X. P. et al., 2015). Alkhateeb et al. (2011) found that the rutting depth increased with the increase in temperature and tire pressure and with the decrease in subgrade strength by the finite element models. Park (2006) used a triaxial repetitive load test to obtain temperature conversion factor (TCF) parameters and revealed the variation in pavement temperature during full-scale trafficking. The test results showed that TCF could convert the traffic loading at multiple temperatures to its equivalent traffic at a specification temperature. Abed and Al-Azzawi (2012) noted that because of the change of material properties, the rutting depth increased in the leveling and base courses, but the stress level decreased in those layers. Salama and Chatti (2008) investigated the relative rutting damage of different axle types and truck configurations to the hot asphalt mixture. The trucks with wide single-wheel axles increase causing the pavement sensitive to the surface layers' creep, and wide single axles are more combative than dual wheels. Corte et al. (1994) and Attia and Ahmed (2014) studied the impact of tire pressure on overlay performance by the mechanistic-empirical pavement design method. It was noted

that the tire pressure plays a serious role on the longitudinal cracks, fatigue cracks, and asphalt pavement rutting and has no significant effect on rutting in base and subgrade layers.

From previous studies, it was summarized that the different axle loading and test temperature have various influences on the rutting resistance of HMA, but few studies were engaged in the permanent deformation of DCLR modified asphalt mixtures. As the DCLR is a relatively new and intricate material, the influence of tire pressures and temperatures on the permanent deformation of DCLR asphalt mixtures is worth being studied. The motivation of this study is to validate the possibility of using DCLR in the highway constructions and to evaluate the high-temperature performance of DCLR modified asphalt mixtures. It is of great scientific significance for the development and application of new environmental-friendly materials in pavement engineering.

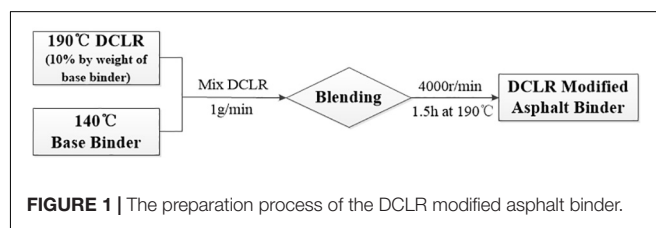
## OBJECTIVES AND SCOPES

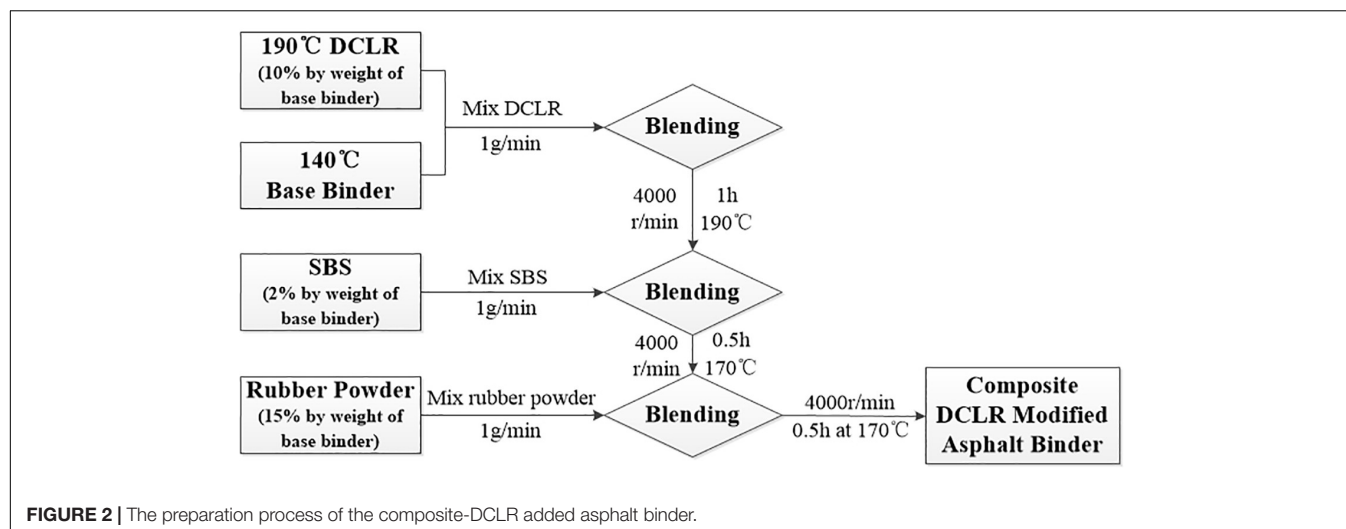
The main purpose of this research is to evaluate the permanent deformation of DCLR and composite-DCLR modified asphalt mixtures under various tire pressures and temperatures. The following tasks were listed for analysis:

- The three kinds of asphalt mixtures are the control asphalt mixtures, DCLR modified asphalt mixture, and composite-DCLR modified asphalt mixture. It is noted that three asphalt mixtures have the equal gradation and optimum asphalt content (OAC).
- Permanent deformation of three kinds of asphalt mixtures was evaluated using the rutting test under multiple tire pressures varying from 0.7 to 1.0 MPa with a 0.1-MPa interval and at temperatures ranging from 55 to 70°C with a 5°C interval.
- The permanent deformations of three kinds of asphalt mixtures related to different tire pressures and test temperatures were explored through the statistical analysis.

## Materials Asphalt Binders

Virgin asphalt binder was produced in South Korea with 80/100 penetration. Two types of modified asphalt binders were prepared through adding DCLR and composite-DCLR into the base asphalt binder. The specific preparation processes of DCLR modified asphalt and composite-DCLR modified asphalt were determined based on experimental experience and previous studies in the research group (Ji et al., 2019, 2020), shown in Figures 1, 2, respectively.



**TABLE 1 |**  $G^*/\sin\delta$  of three asphalt binders.

Temperature (°C)	Unaged stage					RTFO stage					PG grade
	58	64	70	76	82	58	64	70	76	82	
Base asphalt binder	2.18	0.96	0.45	0.23	–	4.62	1.97	0.91	0.45	–	58
DCLR modified asphalt binder	6.56	2.75	1.24	0.61	–	21.67	8.86	3.82	1.73	–	70
Composite-DCLR modified asphalt binder	37.31	20.24	11.09	6.39	3.86	49.44	27.13	15.82	7.54	4.54	82
Specification	$\geq 1.0$					$\geq 2.2$					

RTFO, Rolling Thin-Film Oven.

**TABLE 2 |** Stiffness and  $m$ -value of three asphalt binders.

Temperature (°C)	Stiffness (MPa)			$m$ -Value			PG
	–6	–12	–18	–6	–12	–18	
Base asphalt binder	49.631	134.026	226.225	0.442	0.361	0.282	–22
DCLR modified asphalt binder	86.083	220.909	–	0.337	0.275	–	–16
Composite-DCLR modified asphalt binder	–S(MPa)	81.518	164.386	–	0.337	0.312	–28
Specification		$<300.0$			$\geq 0.3$		

According to the Superpave performance grade (PG) specifications, the physical properties of the three kinds of asphalt binders were measured and are shown in **Tables 1, 2**.

## Aggregates

Limestone was chosen as an aggregate material, and it includes coarse aggregates with the size of 9.5–19.0 mm, 4.75–9.5 mm, 2.36–4.75 mm, and fine aggregates with the size of 0–2.36 mm. The powder left from the limestone was recycled as the mineral powder. The physical properties of the aggregates were measured according to the “Test Methods of Aggregate for Highway Engineering” (JTG E42-2005, 2005), and the results meet the specification requirement in China.

## Mixture Design

The type of the mixture was a recommended AC-20, which is popularly used in China. Its gradation is shown in **Figure 3**

and met the technical requirements specified in China. The target air void of all specimens was  $4 \pm 1.0\%$ . The OAC of the mixture was determined in accordance with the ASTM D1559, and the OAC was 4.2%.

The performances of the mixture also meet the technical requirements specified in China. In order to indicate the effect of three asphalts on the permanent deformation of three mixtures, the same gradation and OAC were used. The other testing conditions are the same as that of the control mixture. The performances of the three asphalt mixtures are shown in **Figure 4**.

## Test Methods

### Test Conditions

Three types of asphalt mixtures, the control asphalt mixture, DCLR modified asphalt mixture, and composite-DCLR modified asphalt mixture, were prepared for the rutting test. During the test, the test temperatures were selected to be from 55 to 70°C

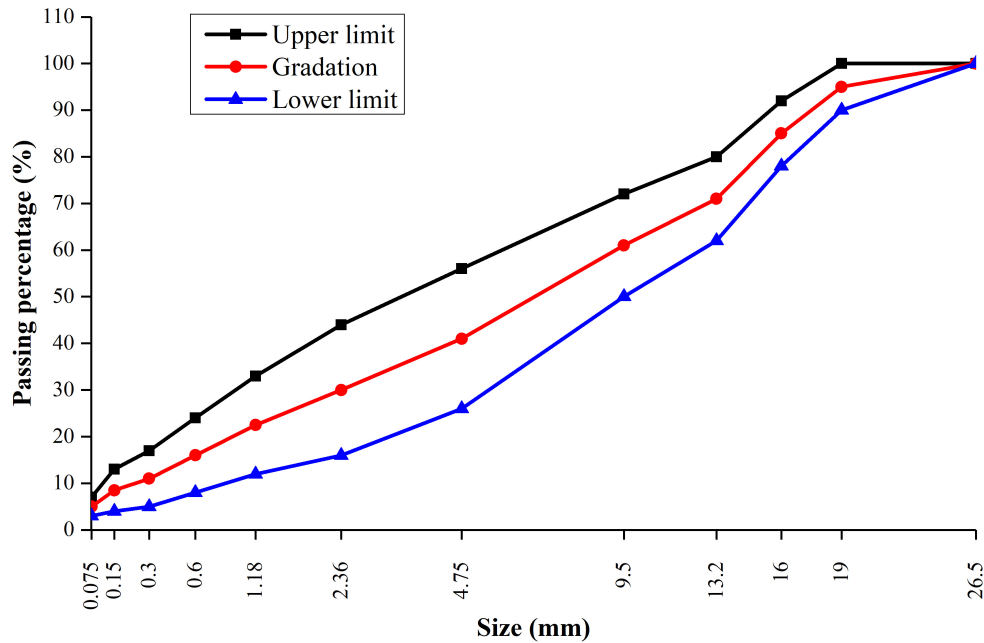


FIGURE 3 | Gradation of the mixture.

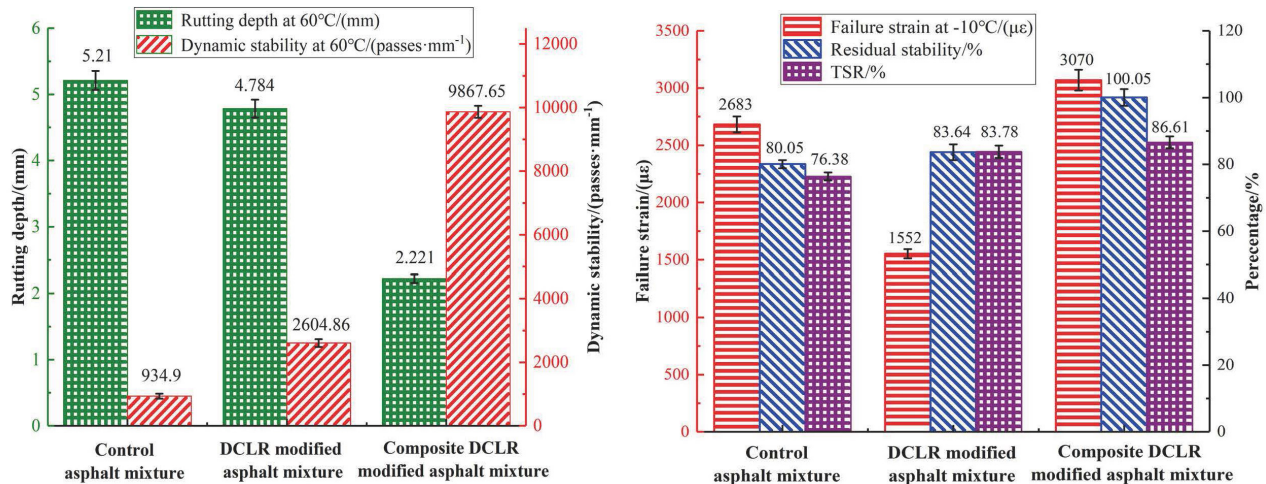
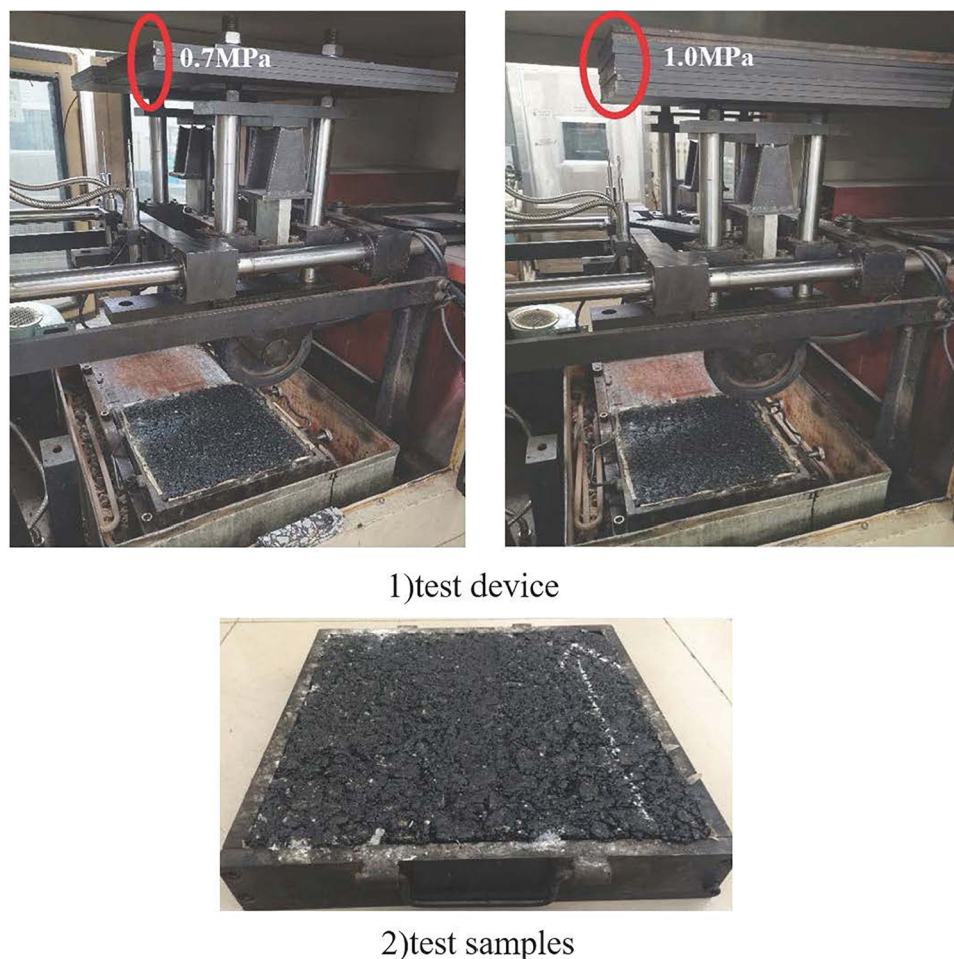


FIGURE 4 | Performances of three asphalt mixtures.

with a 5°C interval. And the tire pressures were determined to be from 0.7 to 1.0 MPa with a 0.1-MPa interval. The increase in tire pressure would be caused by the increased axle loading of vehicles. With the tire pressure increases, the contact area of the tire pavement is induced to a reduction. It may prompt an increase in tire-pavement contact stress, which deteriorates the pavement service conditions (Jamy and Najeeb, 1991; ASTM D1559, 2006; Wang and Machemehl, 2006; Abdel-Motaleb, 2007; Homsy et al., 2011). In China, the standard axle loading is specified as a single axle with the dual tires at 100 kN, and the standard tire pressure is 0.7 MPa. However, several surveys conducted in China revealed

the traffic volumes of trucks and their tire pressures had increased steadily in the last several decades. The truck axle loading was always larger than 100 kN, and tire pressure was higher than 0.7 MPa. Therefore, in this study, a tire pressure range of 0.7–1.0 MPa with a 0.1-MPa interval was selected in order to simulate the impact of high tire pressure on the pavement response. Additionally, the standard test temperature is 60°C during the process of the rutting test in China. However, the actual pavement temperature in summer months is also far higher than 60°C. Sometimes, the actual pavement temperature can achieve a peak at 70°C. In this study, to simulate the impact of temperature on pavement response, the



**FIGURE 5 |** Test device and samples.

test temperature range was selected to be from 55 to 70°C with a 5°C interval.

### Specimen Preparation

At least three specimens, with each sample the length is 300 mm, the width is 300 mm, and the depth is 50 mm, were tested to measure their resistance to rutting. Before testing, the specimens of the control mixture were cured at the room temperature for 12 h, and the specimens of the DCLR and composite-DCLR modified asphalt mixtures were cooled at room temperature for 48 h, as required by the China Specification “Test Methods of Asphalt and Asphalt Mixtures for Highway Engineering” (JTGE20-2011).

### Rutting Test

As reported by Test Methods of Asphalt and Asphalt Mixtures for Highway Engineering (JTGE20-2011), the standard experiment was supervised to apply a smooth rubber wheel load of 0.7 MPa on each wheel traveling at a speed of  $42 \pm 1$  passes/min on specimens at 60°C. The test device and samples are shown in Figure 5.

The two indexes of dynamic stability and rutting depth were obtained for three asphalt mixtures. The dynamic stability refers to the passes of each 1-mm deformation between 45 and 60 min, and the rutting depth reflects the total deformation during the 60 min in the test. High dynamic stability and low rutting depth indicates a stiff mixture, which is likely to be less sensitive to the temperature and loads.

## RESULTS AND DISCUSSION

### Properties of Three Asphalt Binders and Mixtures

The high-temperature PG (AASHTO T 315, 2012) and low-temperature PG (AASHTO T 313, 2012) of the asphalt binders were measured. The physical properties of three kinds of asphalt binders are presented in Tables 1, 2. The performances of the three asphalt mixtures are shown in Figure 5.

The test outcomes in Tables 1, 2 demonstrated that the composite-DCLR added asphalt binder has the highest high-temperature PG value and lowest low-temperature PG value.

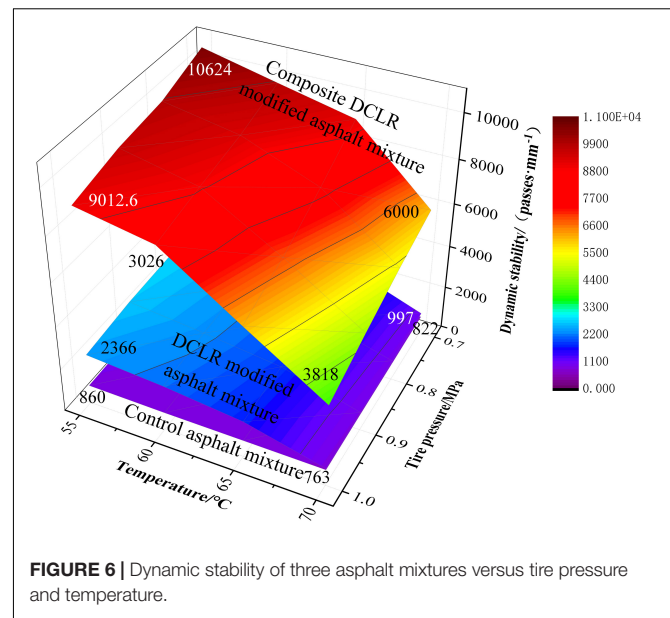


It indicated that the composite-DCLR significantly improved the high-temperature and low-temperature properties. From **Figure 5**, it is seen that the DCLR increased the dynamic stability, residual stability, and TSR of asphalt mixture while decreasing its rutting depth. This demonstrated that the addition of DCLR contributes to the improvement of high-temperature performance and moisture susceptibility of asphalt mixture. However, the DCLR decreased the low-temperature performance of asphalt mixture to some extent, which can be reflected by the test results of failure strain at  $-10^{\circ}\text{C}$ . This is the main reason why the composite-DCLR was used and investigated in this study. The composite-DCLR significantly improved the high-temperature performance and low-temperature performance of asphalt mixture. The reason may be that the composite-DCLR, which includes SBS and rubber powder, increases the bonding strength with the matrix of the asphalt binders and reinforces the network of modified asphalt binders. This possible effect causes the asphalt binder stiffer and leads to an improvement of properties of asphalt binder and mixture, especially for the high-temperature performance (Ji et al., 2017).

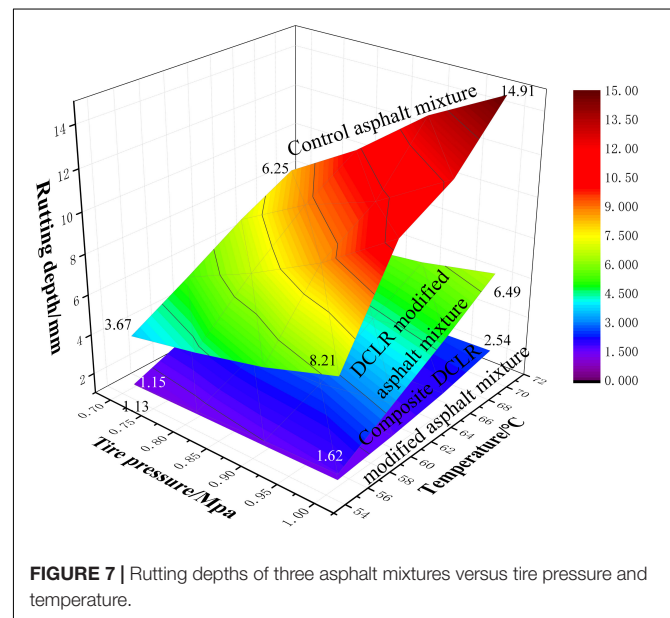
### Rutting Resistance of Three Mixtures

The permanent deformation of three asphalt mixtures was conducted using the rutting test under a test temperature range from 55 to  $70^{\circ}\text{C}$  with a  $5^{\circ}\text{C}$  interval and at a tire pressure range from 0.7 to 1.0 MPa with a 0.1-MPa interval. The rutting resistance of three asphalt mixtures was characterized in terms of the rutting depths and dynamic stabilities. The results are shown in **Figures 6, 7**.

In **Figure 6**, the dynamic stabilities of asphalt mixtures decrease with the increase in tire pressures and test temperatures, but the change amplitudes are different. The rise in tire pressure and test temperature led to a degeneration in dynamic stability and a deterioration in rutting potential. Moreover, when the tire pressure increased from 0.7 to 1.0 MPa under  $55\text{--}70^{\circ}\text{C}$ , the dynamic stabilities of asphalt mixtures decreased by 12.3, 25.0, and 20.6%, respectively. Furthermore, when test temperature increased from 55 to  $70^{\circ}\text{C}$  under the condition of 0.7- to 1.0-MPa tire pressures, the dynamic stabilities of asphalt mixtures decreased by 16.2, 66.4, and 49.6%, respectively. It can be deduced that the temperature has a more positive effect than the tire pressure on the permanent deformation. Although the dynamic stabilities of the DCLR modified asphalt mixture and composite-DCLR modified asphalt mixture decreased at a high rate, which were still higher compared with the control asphalt mixture. The DCLR and composite-DCLR had significant effects on the advancement of the rutting resistance. The composite-DCLR



**FIGURE 6** | Dynamic stability of three asphalt mixtures versus tire pressure and temperature.



**FIGURE 7** | Rutting depths of three asphalt mixtures versus tire pressure and temperature.

mixture had the highest dynamic stability compared to the other two asphalt mixtures under identical tire pressures and test temperatures, which indicated that the composite-DCLR mixture has the least sensitivity to the temperature and tire pressure. The

**TABLE 3** | Value range analysis of three asphalt mixtures.

Mix types	Dynamic stability/(passes $\text{mm}^{-1}$ )		Rutting depth/mm	
	Tire pressure	Temperature	Tire pressure	Temperature
Control mixture	115.68	155.66	5.01	6.78
DCLR mixture	471.96	1785.08	1.12	4.38
Composite-DCLR mixture	2077.54	4811.96	0.25	1.11

composite-DCLR modified asphalt mixture has higher elasticity, stiffness (Ji et al., 2016), and viscosity compared to the control asphalt mixture and DCLR modified asphalt mixture.

**Figure 7** displays that the increases in test temperature and tire pressure introduce an increase in rutting depth of asphalt mixtures. An increase in tire pressures or test temperatures yielded an increase in rutting potential. When tire pressure increased from 0.7 to 1.0 MPa, the rutting depths of asphalt mixtures increased by 95.8, 34.4, and 17.9%, respectively. When the test temperature increased from 55 to 70°C, the rut depths of asphalt mixtures increased by 307, 139, and 93.1%, respectively. The influence of the test temperature on the rutting resistance of asphalt mixtures is more noticeable than that of tire pressures, and the rutting depths of control asphalt mixture decreased at the highest rate. The base asphalt binder has the lowest high-temperature properties. The composite-DCLR modified asphalt mixture had the lowest rutting depth compared to

the other two asphalt mixtures under the same tire pressures and test temperatures. The composite-DCLR modified asphalt mixture had a good resistance to rutting. As a result, it can be concluded that the composite-DCLR modified asphalt mixture is identified as a good mixture for application in pavement construction.

## Analysis of Variance

Analysis of variance (ANOVA) is used for isolating the relevant factors and estimating the effects of these factors on the total deviation. In ANOVA, the *F*-value is defined as the ratio of the variance between treatments and variance in treatments. An enormous *F*-value represents more significant effects of the factor on the sample. In this article, the ANOVA was applied to detect the effects of multiple tire pressures and test temperatures on the permanent deformation of asphalt mixtures by using the ORIGIN software, and the confidence level was set as 0.95. The significant

**TABLE 4 |** Variance of ANOVA of three asphalt mixtures.

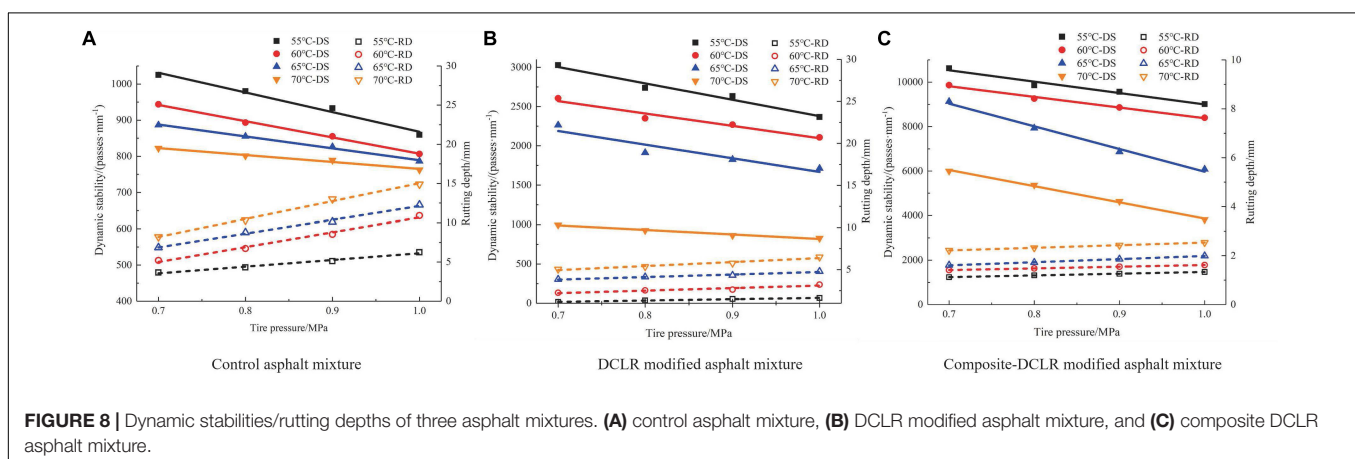
Mix types	Dynamic stability			Rutting depth		
	Variances	<i>F</i> -value	<i>P</i> -value	Variances	<i>F</i> -value	<i>P</i> -value
Control mixture	Tire pressure	14.5	0	Tire pressure	29.78	0
	Temperature	61.4	0	Temperature	50.81	0
DCLR mixture	Tire pressure	18.7	0	Tire pressure	17.12	0
	Temperature	288.6	0	Temperature	254.12	0
Composite-DCLR mixture	Tire pressure	28.3	0	Tire pressure	31.89	0
	Temperature	164.6	0	Temperature	355.19	0

As stated in the China Specification JTG E20-2011 (2011), during the rutting test, two sets of samples for each mixture are needed under each temperature and tire pressure test condition, respectively. Then, the total number of samples for each mixture is 32 for predicting the rutting model and analyzing the value range and variance of ANOVA.

**TABLE 5 |** Regression coefficients for three asphalt mixtures.

Mix types	$a_1$	$a_2$	$a_3$	$R^2$
Control mixture	−378.73/16.94	−10.06/30.4	1815.08/−33.43	0.92/0.95
DCLR mixture	−1493.05/3.09	−115.33/0.29	10441.10/−17.15	0.91/0.99
Composite-DCLR mixture	−6856.40/0.93	−320.64/0.07	33698.70/−3.72	0.92/0.96

The left and the right number of the slant are regression coefficients used to predict dynamic stability and rut depths for the mixes, respectively.



degree of variances can be detected using the range value in the value range analysis approach. The  $F$ -value is used to detect the significant degree of variances.

**Tables 3, 4** list the range value and ANOVA of permanent deformation affected by different tire pressures and test temperatures.

According to the results of ORIGIN software, there was no interaction between temperatures and tire pressures. The test results in **Tables 3, 4** illustrated that the temperature was a significant factor in the rutting resistance of asphalt mixtures. The rutting resistance of asphalt mixtures is more sensitive to temperature than tire pressure. The conclusion is coincident with the above outcomes of the rutting test.

## Development of the Prediction Model for Dynamic Stability and Rutting Depths

The prediction model of rutting resistance was developed to verify the correlation between the predicted value and the measured value of dynamic stability and rutting depth under different tire pressures and temperatures. In the model, the temperatures and tire pressures were independent variables. The constitution of the model was regressed based on the least-square procedure, shown in Eq. 1.

$$R_{DS, RD}(T, P) = a_1 \cdot T + a_2 \cdot P + a_3 \quad (1)$$

where,  $R_{DS, RD}(T, P)$  is the prediction results (dynamic stability and rutting depths) of mixtures;  $T$  is the temperature, °C;  $P$  is the tire pressure, MPa;  $a_1$ ,  $a_2$ , and  $a_3$  are regression coefficients.

The regression coefficients  $a_1$ ,  $a_2$ , and  $a_3$  and coefficient  $R^2$  value for three mixtures are listed in **Table 5** and **Figure 8**.

The coefficient  $R^2$  value of the prediction model ranges from 0.91 to 0.99. The test results in **Table 5** and **Figure 8** show that the dynamic stabilities and rutting depths of three asphalt mixtures have good linear correlations with the tire pressure or test temperature. Two parameters with three coefficients were used to predict the high-temperature performance of asphalt mixtures according to the dynamic stabilities and rutting depths, and the prediction is acceptable according to the accuracy. Furthermore, the model of dynamic stability and rutting depth is fitted by the laboratory test data, and the linear model better reflects the dynamic stability and rutting change under the laboratory conditions. The future study will be extended to the real road fields. The rutting reaction of the pavement under real load and temperature will show significant non-linear characteristics, and the non-linear model for correlation analysis will be applied in the future study.

## CONCLUSION

The DCLR and composite-DCLR were applied as additives to modify the virgin asphalt binder, and the corresponding preparation procedures of modified asphalt binders were illustrated. Meanwhile, the properties of modified asphalt binders were evaluated and estimated. Moreover, three asphalt mixtures,

including the control mixture, DCLR modified asphalt mixture, and composite-DCLR modified asphalt mixture, were designed. The permanent deformation of asphalt mixtures under different tire pressures and test temperatures were explored. Based on the above results and analysis, the conclusions are drawn below:

- The addition of DCLR or composite-DCLR improves the resistance to permanent deformation of asphalt mixtures. The composite-DCLR modified asphalt mixture has a better resistance to rutting compared to the control asphalt mixture and DCLR modified asphalt mixture. As a result, it is recommended that the composite-DCLR modified asphalt mixture is a better mixture for roads in tropical regions, where the rutting is one of the main distresses of pavement.
- The ANOVA was adopted to evaluate the development of tire pressures and test temperatures on the permanent deformation of three asphalt mixtures. The analysis results demonstrated that the rutting resistance of asphalt mixtures is more sensitive to the temperature than the tire pressure.
- The test temperatures and tire pressures have influence on the rutting resistance of asphalt mixtures. The prediction model was established to predict the dynamic stabilities and rutting depths of the asphalt mixtures based on the least-squares procedure, and the accuracy of the prediction is acceptable. However, the further improvement of accuracy of the model and the application of more parameters in the model are worth to be studied in the future.

## DATA AVAILABILITY STATEMENT

All datasets presented in this study are included in the article/supplementary material.

## AUTHOR CONTRIBUTIONS

All authors contributed to the article and approved the submitted version.

## FUNDING

This study was sponsored by the National Natural Science Foundation of China (51778038), Beijing Natural Science Foundation and Beijing Municipal Education Commission (grant number: KZ201910016017), the Fundamental Research Funds for Beijing Universities (ZC05), and Program for Changjiang Scholars and Innovative Research Team in University (IRT-17R06).

## ACKNOWLEDGMENTS

The authors appreciate Mr. Gao Jinqi for his help in the experiments.

## REFERENCES

- AASHTO T 313 (2012). *Standard Test Method for Determining Flexural Creep Stiffness of Asphalt Binder Using the Bending Beam Rheometer*. Washington, DC: American Association of State Highway and Transportation Officials.
- AASHTO T 315 (2012). *Standard Test Method for Determining The Rheological Properties of Asphalt Binder Using a Dynamic Shear Rheometer*. Washington, DC: American Association of State Highway and Transportation Officials.
- Abdel-Motaleb, M. E. (2007). Impact of high-pressure truck tires on pavement design in Egypt. *Emirates J. Eng. Res.* 12, 65–73.
- Abed, A. H., and Al-Azzawi, A. A. (2012). Evaluation of rutting depth in flexible pavements using finite element analysis and local empirical model. *Am. J. Eng. Appl. Sci.* 5, 163–169. doi: 10.3844/ajeassp.2012.163.169
- Al-Humeidawi, B. H. (2016). Experimental characterization of rutting performance of HMA designed with aggregate gradations according to Superpave and Marshall methods. *World J. Eng. Technol.* 4, 477–487. doi: 10.4236/wjet.2016.43048
- Alkhateeb, L. A., Saoud, A., and Al-Msouti, M. F. (2011). Rutting prediction of flexible pavements using finite element modeling. *Jordan J. Civil Eng.* 5, 173–190.
- ASTM D1559 (2006). *Standard Method of Test for Resistance to Plastic Flow of Bituminous Mixtures Using Marshall Apparatus*. West Conshohocken, PA: American Society of Testing and Materials.
- Attia, M. I. E., and Ahmed, M. A. (2014). Impact of vehicle class and tire pressure on pavement performance in MEPDG. *J. Eng. Res. Appl.* 4, 45–57. doi: 10.1055/s-0037-1604350
- Chatti, K., Kim, H. B., Yun, K. K., Mahoney, J. P., and Monismith, C. L. (1996). Field investigation into effects of vehicle speed and tire pressure on asphalt concrete pavement strains. *J. Trans. Res. Rec.* 1539, 66–71. doi: 10.1177/0361198196153900109
- Chen, T., Luan, Y., Ma, T., Zhu, J., Huang, X., and Ma, S. (2020). Mechanical and microstructural characteristics of different interfaces in cold recycled mixture containing cement and asphalt emulsion. *J. Clean. Prod.* 258:120674. doi: 10.1016/j.jclepro.2020.120674
- Corte, J. F., Brosseau, Y., Simoncelli, J. P., and Caroff, G. (1994). Investigation of rutting of asphalt surface layers: influence of binder and axle loading configuration. *Trans. Res. Rec.* 1436, 28–37.
- Ding, Y., and Zhao, X. P. (2019). Research on the influence of anti-rutting agent on the performance of AC-20C SBS composite modified asphalt mixture. *Highways Transp. Inner Mongolia* 3, 34–38.
- Gu, X. H. (2012). Properties and utilization of coal direct liquefaction residue. *Clean Coal Technol.* 18, 24–31.
- He, L. (2013). *Study on the Preparation and Performance of Asphalt Modified by Coal Liquefaction Residue*. M.Sc. Thesis, Chang'an University, Beilin.
- Homs, F., Bodin, D., Yotte, S., Breyse, D., and Balay, J. M. (2011). Multiple-axle loadings: shape parameters and their effect on the fatigue life. *Eur. J. Environ. Civil Eng.* 15, 743–758. doi: 10.3166/ejece.15.743-758
- Jamy, D., and Najeeb, A. (1991). *Evaluation of Tire Pressure, Tire Construction, Axle Configuration, and Axle Load on Flexible Pavement Performance*. M.Sc. Thesis, Texas A & M University, College Station, TX.
- Ji, J., Shi, Y. F., Li, P. F., Yang, S., Suo, Z., and Xu, S. F. (2015). Analysis of high-and-low temperature properties of asphalt mortar affected by DCLR and filler-asphalt ratio. *J. Xian Univ. Arch. Tech.* 8, 511–516.
- Ji, J., Shi, Y. F., Suo, Z., Xu, S. F., Yang, S., and Li, P. F. (2016). Comparison on properties of modified asphalt blended with DCLR and TLA. *J. Fuel Chem. Technol.* 43, 1061–1067.
- Ji, J., Wang, D., Suo, Z., Xu, Y., and Xu, S. F. (2017). Study on direct coal liquefaction residue influence on mechanical properties of flexible pavement. *Int. J. Pavement Res. Technol.* 11, 355–362. doi: 10.1016/j.ijprt.2017.09.006
- Ji, J., Wang, Z., Yao, H., Wang, D., Zhang, R., Diab, A., et al. (2019). A numerical study on rutting behaviour of direct coal liquefaction residue modified asphalt mixture. *Road Mater. Pavement Des.* 16, 1–15. doi: 10.1080/14680629.2019.1690029
- Ji, J., Wang, Z., Zhang, R., Wei, J. M., Suo, Z., You, Z. P., et al. (2020). Rutting resistance of direct coal liquefaction residue (DCLR) modified asphalt mixture under variable loads over a wide temperature range. *Constr. Building Mater.* 257:119489. doi: 10.1016/j.conbuildmat.2020.119489
- Ji, J., Zhao, Y. S., and Xu, S. F. (2014). Study on properties of the blends with Direct Coal Liquefaction Residue and asphalt. *Appl. Mech. Mater.* 488–489, 316–321. doi: 10.4028/www.scientific.net/amm.488-489.316
- Ji, X. P., Zheng, N. X., Niu, S. S., Meng, S., and Xu, Q. L. (2015). Development of a rutting prediction model for asphalt pavements with the use of an accelerated loading facility. *Road Mater. Pavement Des.* 17, 15–31. doi: 10.1080/14680629.2015.1055337
- JTG E20-2011 (2011). *Standard Test Material of Bitumen and Bituminous Mixtures for Highway Engineering*. Beijing: China Ministry of Transport.
- JTG E42-2005 (2005). *Test Methods of Aggregate for Highway Engineering*. Beijing: China Ministry of Transport.
- Khan, S., Nagabhuashana, M. N., Tiwari, D., and Jain, P. K. (2013). Rutting in flexible pavement: an approach of evaluation with accelerate pavement. *Proc. Soc. Behav. Sci.* 104, 149–157. doi: 10.1016/j.sbspro.2013.11.107
- Ma, J., Zhao, X. M., He, S. H., Song, H. X., Zhao, Y., Song, H. S., et al. (2017). Review of pavement detection technology. *J. Traffic Transp. Eng.* 17, 121–137.
- Moghaddam, T. B., Karim, M. R., and Abdelaziz, M. (2011). A Review on fatigue and rutting performance of asphalt mixes. *Sci. Res. Essays* 6, 670–682. doi: 10.5897/SRE10.946
- Moghaddam, T. B., Soltani, M., and Karim, M. R. (2014). Evaluation of permanent deformation characteristics of unmodified and polyethylene terephthalate modified asphalt mixtures using dynamic creep test. *Mater. Des.* 53, 317–324. doi: 10.1016/j.matdes.2013.07.015
- Park, D. W. (2006). Traffic loadings considering temperature for pavement rutting life. *KSCE J. Civil Eng.* 10, 259–263. doi: 10.1007/bf02830780
- Saevarsdottir, T., and Erlingsson, S. (2015). Modeling of responses and rutting profile of a flexible pavement structure in a heavy vehicle simulator test. *Road Mater. Pavement Des.* 16, 1–18. doi: 10.1080/14680629.2014.939698
- Salama, H. S., and Chatti, K. (2008). A laboratory investigation of the effect of multiple axle and truck configurations on HMA mixture rutting. *Road Mater. Pavement Des.* 29, 589–613. doi: 10.1080/14680629.2008.9690140
- Shu, G. P. (2003). *Coal Liquefaction Technology*. Beijing: China Coal Industry Publishing House, 115–117.
- Wang, F., and Machemehl, R. (2006). *Predicting Truck Tire Pressure Effects Upon Pavement Performance*. Texas: Center for Transportation Research, University of Texas at Austin.
- Zhang, R., You, Z. P., Wang, H. N., Ye, M. X., Yap, Y. K., and Si, C. (2019). The impact of bio-oil as rejuvenator for aged asphalt binder. *Constr. Build. Mater.* 196, 134–143. doi: 10.1016/j.conbuildmat.2018.10.168
- Zhao, Y. S. (2015). *Study on the Performances of DCLR Modified Asphalt and Asphalt Mortar*. M.Sc. Thesis, Beijing University of Civil Engineering and Architecture, Xicheng.
- Zhao, Y. S., and Ji, J. (2014). Study on the performances of direct coal liquefaction residue modified asphalt mixture. *Challenges Adv. Sustain. Trans. Syst.* 31, 319–324. doi: 10.1061/9780784413364.039

**Conflict of Interest:** The authors declare that the research was conducted in the absence of any commercial or financial relationships that could be construed as a potential conflict of interest.

Copyright © 2020 Zhi, Jie, Ran, Zhe, Hui and Dongzhao. This is an open-access article distributed under the terms of the Creative Commons Attribution License (CC BY). The use, distribution or reproduction in other forums is permitted, provided the original author(s) and the copyright owner(s) are credited and that the original publication in this journal is cited, in accordance with accepted academic practice. No use, distribution or reproduction is permitted which does not comply with these terms.





# Experimental Investigation on Uniaxial Unconfined Compressive Properties of Ice on Asphalt Pavement Surface

Wei Luo<sup>1,2</sup>, Hancheng Dan<sup>3\*</sup>, Runzhong Zeng<sup>1</sup>, Yao Rong<sup>2</sup> and Dian Xie<sup>1</sup>

<sup>1</sup> School of Civil Engineering and Architecture, East China Jiaotong University, Nanchang, China, <sup>2</sup> Jiangxi Transportation Institute, Nanchang, China, <sup>3</sup> School of Civil Engineering, Central South University, Changsha, China

## OPEN ACCESS

### Edited by:

Hui Yao,  
Beijing University of Technology,  
China

### Reviewed by:

Dongya Ren,  
Southwest Jiaotong University, China  
Elsa Garavaglia,  
Politecnico di Milano, Italy

### \*Correspondence:

Hancheng Dan  
danhancheng@csu.edu.cn

### Specialty section:

This article was submitted to  
Structural Materials,  
a section of the journal  
Frontiers in Materials

Received: 29 May 2020

Accepted: 04 August 2020

Published: 08 September 2020

### Citation:

Luo W, Dan H, Zeng R, Rong Y  
and Xie D (2020) Experimental  
Investigation on Uniaxial Unconfined  
Compressive Properties of Ice on  
Asphalt Pavement Surface.  
Front. Mater. 7:294.  
doi: 10.3389/fmats.2020.00294

Mechanical deicing is a method to remove the ice on the pavement surface, and the ice strength directly affects the difficulty and effectiveness of the mechanical deicing. This paper aims to investigate the compression strength of ice to facilitate the deicing equipment to crush ice. In this paper, a large-scale freezing laboratory is employed to simulate low-temperature environment, and the uniaxial unconfined compressive tests of artificial freshwater ice under different temperature conditions are carried out through the uniaxial loading system. The compressive strength and modulus of ice are obtained when the substrate is asphalt pavement. The test result shows that the ice compressive strength and modulus respectively distribute from 0.36 to 3.67 MPa and 11.7 to 359.1 MPa when ice temperature varies from  $-0.7$  to  $-7.5^{\circ}\text{C}$ . The relations between ice temperature and compressive strength are approximately in a linear manner, while the relation of compressive modulus and ice temperature shows good power function and exponential relationships, respectively, when ice temperature ranges from  $-8$  to  $-5^{\circ}\text{C}$  and from  $-5$  to  $0^{\circ}\text{C}$ . Furthermore, the failure mechanism of ice under relatively lower temperature is due to the development of cut-through cracks inside the ice. The failure mode divides into shear failure and ductile failure and the failure ice is mainly composed of large ice strips and bulks. For the ice with relatively higher temperature especially the ice close to melting point temperature, the ice failure mode is compressive and ductile, and the failure ice is mainly composed of granular ice crystals.

**Keywords:** ice, compressive strength, compressive modulus, asphalt pavement, failure mode

## INTRODUCTION

The ice formed on the surface of civil structures exerts adverse impacts on the engineering construction and its normal use (Hanbali, 1994; Dan et al., 2019a,b). It is well known that the wet asphalt pavement is more likely to be frozen in the low-temperature environment especially in moist mountain area (Dan et al., 2014, 2020a). The area in western China often suffers from freezing rain during the winter, and ice on the asphalt pavement reduces the pavement skid resistance and subsequently endangers the traffic safety (Gustafson, 1982; Zhu et al., 2012; Dan et al., 2020c).

For instance, a massive ice disaster occurred in western China. Thereinto, the Guizhou province suffers from the most severe ice disaster during the winter in 2008 (Chen et al., 2008). The ice thickness reaches 20 cm and caused many serious traffic accidents. Accordingly, the ice pavement problems with respect to ice warning and deicing should be taken seriously (Dan et al., 2014). Currently, many technologies were developed to deice (Croutch and Harttey, 1992; Petrenko, 1999; Sarkar and Farzaneh, 2009), including the mechanical deicing technology (SHRP, 1994; Taggart et al., 2002; Dan et al., 2020b). In general, the ice strength directly affects the difficulty and effectiveness of the mechanical deicing (Oksanen, 1983; SHRP, 1994; Tan, 2008). So far, there are few studies on the ice strength when the substrate is asphalt pavement. Nonetheless, relatively more researches have presented to measure the ice strength under certain conditions in the other research fields (Gow and Williamson, 1972; Haynes and Mellor, 1977; Sodhi, 2001; Marion and Jakubowski, 2004; Kärnä et al., 2010).

Gow and Williamson (1972) used a novel technique to measure the linear compressibility of ice at relatively low pressures. A mean linear compressibility of  $3.7 \text{ Mb}^{-1}$  was obtained at  $-10^\circ\text{C}$ . Haynes and Mellor (1977) developed a simple but accurate method for making lateral restraint compressive strength tests on right circular cylinders. Sodhi (2001) conducted small-scale indentation tests with compliant structures and freshwater ice sheets. The results of the present study with compliant structures show that there is ductile deformation of ice at low indentation speeds and continuous brittle crushing at high indentation speeds. Kärnä and Jochmarm (2003) discussed some of failure modes observed while different ice formations were acting on the lighthouse, and the details of the bending failure mode and ice crushing were described. Marion and Jakubowski (2004) presented a new model for estimating the compressibility of ice based on chemical thermodynamic principles and compared these model results with previous work. Their estimate of ice compressibility demonstrated significant temperature dependence. Yurtseven and Kilit (2009) calculated the isothermal compressibility using the experimental data for the heat expansion of ice I in the pre-melting region. By analyzing the data at various pressures, compressibility is predicted as functions of temperature and pressure near the melting point in ice I. Kärnä et al. (2010) conducted a study of dynamic interaction processes between a drifting ice sheet and a conical offshore structure. They used the conventional test techniques to study the ice failure process due to upward and downward breaking cones.

These researchers have made essential contributions to understanding ice strength and modulus under various conditions, however, most of them focus on the case that ice temperature is below  $-10^\circ\text{C}$ , and few researches were conducted when the ice temperature is above  $-10^\circ\text{C}$ . The Guizhou province locates in the south of mid-latitude region of the northern hemisphere, and the minimum air temperature during winter is above  $-10^\circ\text{C}$ . Thus, the temperature of ice formed on the pavement is basically not below  $-10^\circ\text{C}$  (Chen et al., 2008). Therefore, this paper aims to investigate the compression strength of ice to facilitate the deicing equipment to crush ice, and the laboratory study is carried out to understand

the compressive properties of ice on asphalt pavement above  $-10^\circ\text{C}$ . After removing the covered ice layer, the performance of anti-skid resistance is improved and the traffic accidents is reduced accordingly.

## EXPERIMENTAL PROGRAM

The factors that influence mechanical property of ice are various (e.g., the ice temperature, load speed, specimen size, and the substrate type). In this paper, we mainly focus on the study on the ice compressive strength and modulus for various ice temperatures when the substrate is asphalt pavement. The current researchers carried out some studies on the compressive failure mode of ice under different loading speeds (Sinha, 1981; Timco and Frederking, 1982; Weertman, 1983; Schulson, 2001; Petrovic, 2003; Montagnat et al., 2014). It can be found that the ice failure process under fast loading is complex with uncertainty, and the ice strength and the compressive modulus are not exact to determine (Schulson, 2001). Therefore, the research emphasizes the case of slow loading speed (the quasi static loading) in this paper.

### Specimen Production

The schematic diagram of test specimen is shown in **Figure 1**. The Marshall specimen (compacted and molded asphalt mixture) is a substrate with rough surface on which the ice is formed under a low-temperature environment in order to ensure the ice specimen cannot move during the compression process. The asphalt mixture is AC-13, of which the mean texture depth is 0.75 mm. The impermeable adhesive tape twines around on the top of the Marshall Specimen and the height of protruding over the top is about 40 mm (**Figure 1**). Therefore, it forms a cup shape and is watertight. Then, the “cup shape specimen” is filled with fresh water and put into freezing laboratory under a low-temperature environment for enough time and the fresh water will be frozen. The ice specimen is columnar and Ice-1h, which is of the hexagonal crystal structure. The crystal growth direction is perpendicular to the substrate surface. The following steps are to peel off the adhesive tape and smooth ice surface with special polisher (because the surface of ice is generally concave-convex, it affects contact performance between ice surface and loading platen) (**Figure 1**). Then, the height of the ice cylinder is measured with a Vernier caliper and the ice temperature is tested with a platinum temperature sensor.

It should be pointed out that according to the field investigation and research results, the road surface can form the thickest of about 20 cm ice in the road section of severe icing in Guizhou Province, and the greatest thickness of ice is about 4 cm. Generally, the method of mechanical deicing will be adopted, and the strength of ice has a great influence on the selection of mechanical deicing equipment. Therefore, the 40 mm depth ice is chosen for testing.

### Equipment and Scheme

Ice is essentially formed in a wet and low-temperature environment. The large-scale freezing laboratory is constructed

for simulating this kind of environment. The air temperature, rainfall, wind speed, and pavement temperature can be controlled. The experimental model of pavement is filled with building materials (asphalt mixture), and it is constructed in the freezing laboratory and subjected to low temperature and wet conditions.

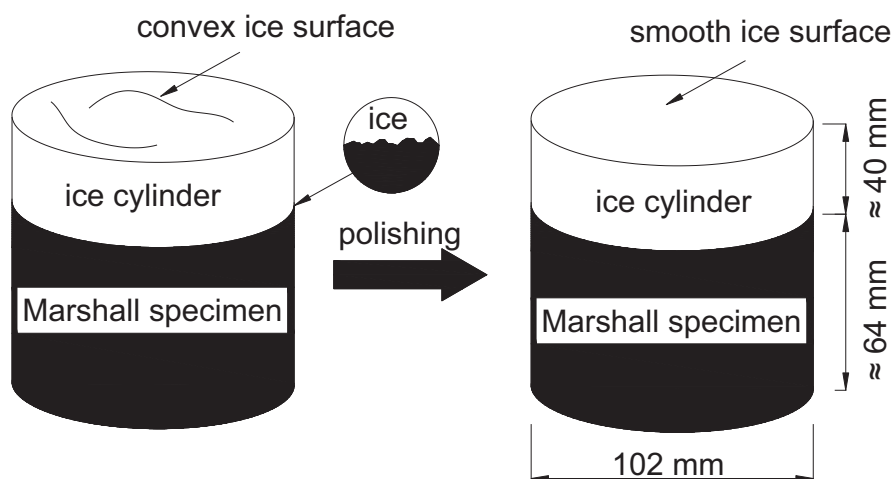
The schematic diagram of test platform is shown in **Figure 2**. The specimen used to be compressed is placed on a metal cushion, which is put on an asphalt pavement surface. The thickness of the metal cushion depends on the distance between the ice specimen and the loading platen. In order to ensure the uniformity of force applied on the ice top, the centers of loading platen and ice top should be in a line. Then, the uniaxial loading system will work and the loading platen will increasingly move toward the ice specimen until it makes contact with the ice top surface. The movement speed of the loading platen can be controlled and changed through a computer system. As load

increases, the ice on the Marshall specimen will be broken down and lose strength.

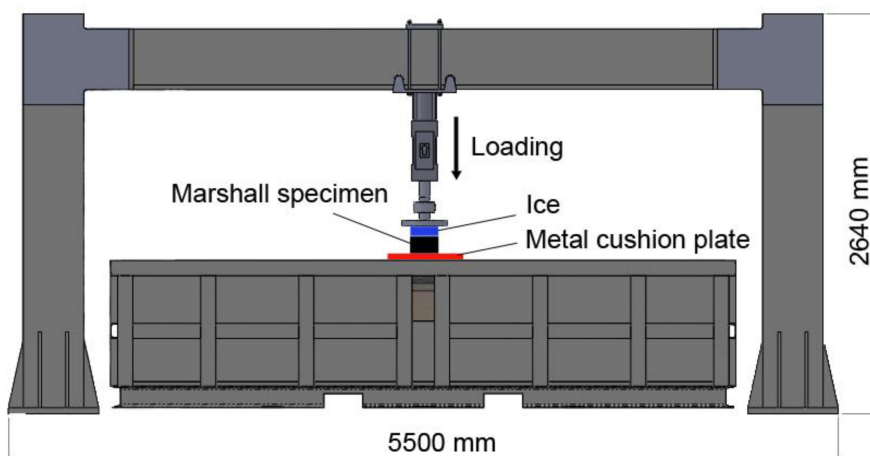
## Experimental Process

### Test Preparation

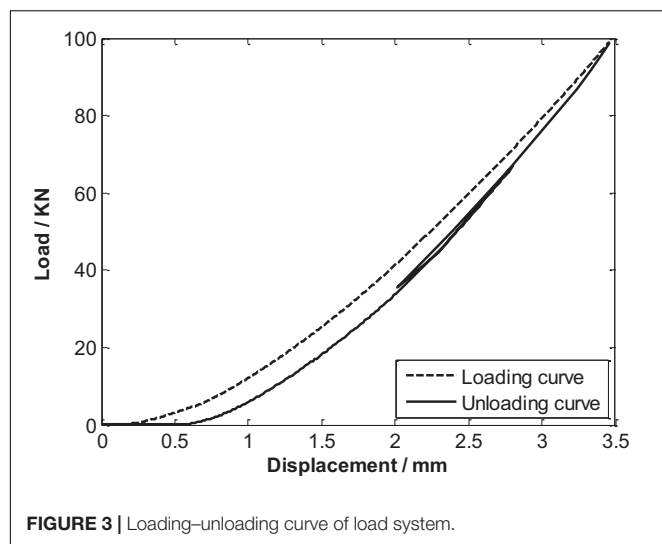
Before conducting the ice compressive test, the loading–unloading performance is tested. The loading–unloading curve is plotted in **Figure 3**. It can be seen from the diagram that the maximum load value is about 100 kN, and the system will unload if load is beyond 100 kN. In addition, the compressive strength under the unconfined condition is also tested for the purpose of estimating the failure load of the Marshall specimen. For instance, the failure load test curve of the Marshall specimen for  $-4^{\circ}\text{C}$  is illustrated in **Figure 4**. It can be seen that the peak load (failure load) value is about 90 kN and the compressive strength is about 11 MPa (the ratio of the peak



**FIGURE 1** | Schematic diagram of specimen with ice and ice surface after polishing.



**FIGURE 2** | Schematic diagram of uniaxial unconfined compressive system.



load to the contact area). Therefore, the effective test needs the precondition that the failure load and failure strength of ice should be lower than 90 kN and 11 MPa, respectively. Moreover, several compressive tests are conducted for testing

the deformation of the Marshall specimens under various temperature conditions.

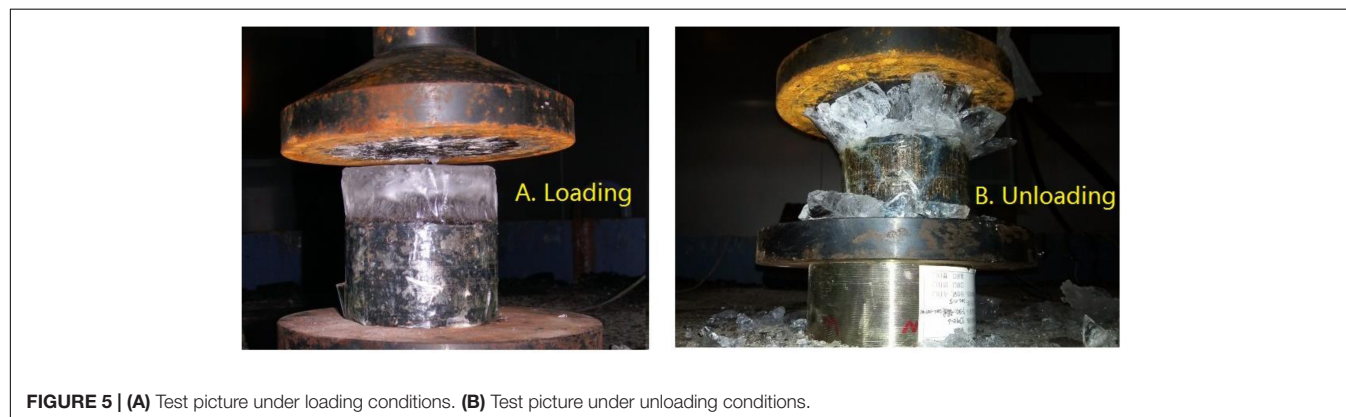
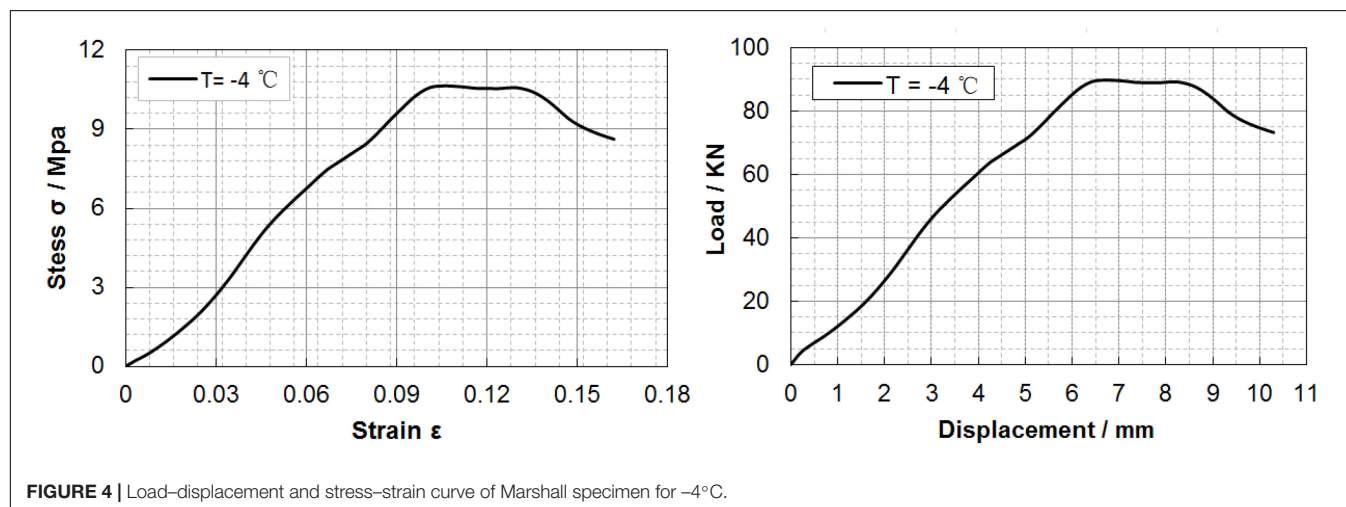
### Test Procedures

The test specimen with ice is placed on the test platform (**Figure 5A**), and it should be ensured that the test temperature is close to the ice temperature (the temperature change of ice can be neglected). Then, the movement of loading platen is controlled by the computer system and the speed is specified as 2 mm/min (the strain ratio is  $8.33 \times 10^{-4} \text{ s}^{-1}$ ) (Zhang L. M. et al., 2009; Zhang et al., 2011). During the test, the computer controlling system can automatically record load and displacement simultaneously. After stop loading, the loading platen is uplifted and separated from the ice surface (**Figure 5B**). Accordingly, the loading-unloading process is accomplished. The test cases depend on the ice temperatures from Zhang et al.  $-10$  to  $0^\circ\text{C}$ , which is accurately measured by the temperature sensor.

## RESULTS AND DISCUSSION

### Test Results of Ice Strength

According to the experimental scheme, uniaxial unconfined compressive strength failure tests of ice are carried out under



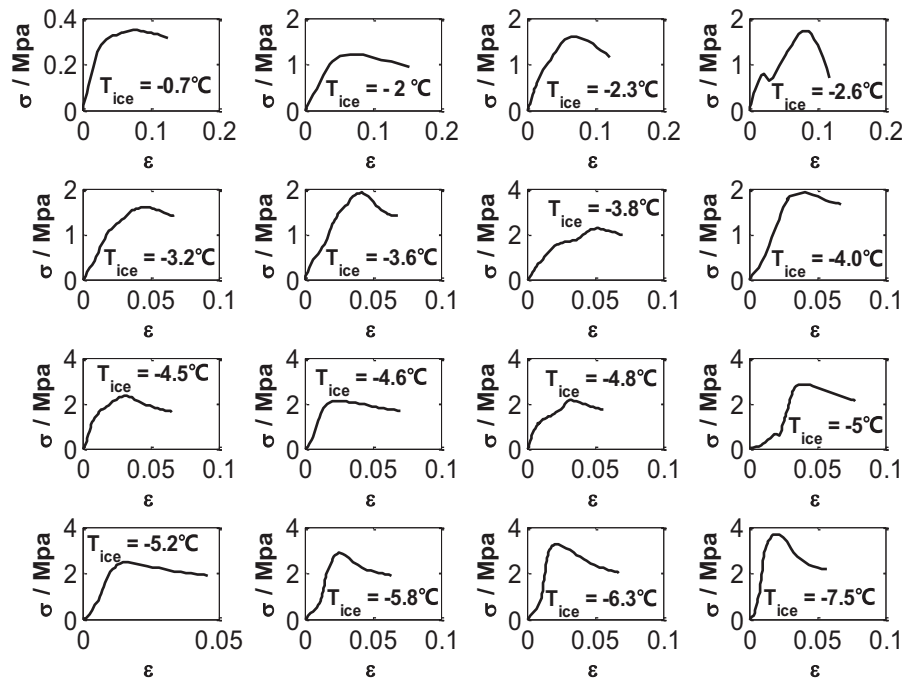


FIGURE 6 | Stress-strain curve of ice during compression process for different temperatures.

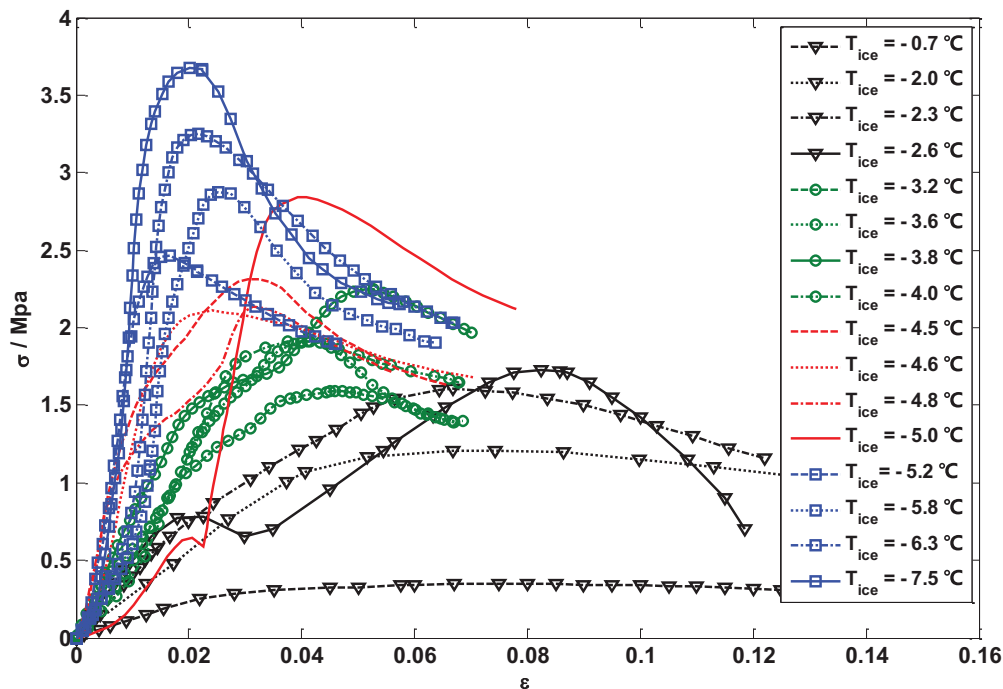


FIGURE 7 | Stress-strain curve of ice with various temperatures during compression process.

different ice temperatures, and the stress-strain curves are also obtained, which are shown in Figures 6, 7. The peak value of stress is the compressive strength and the gradient of the linear segment in the stress-strain curve is compressive modulus.

The test results are aggregated in Table 1. It can be seen from Figure 6 that the obvious peak value of stress can be observed in the sub-figures. Typically, the stress grows up with the strain increase and then falls down after the stress reaches its peak.



Furthermore, it can be seen from **Table 1** that all the peak load values do not exceed the critical load (the load when the Marshall specimen is failure).

**Figure 7** shows various positions that peak stress occurs in the stress-strain curves when ice temperatures are different. It indicates that the deformation properties of ice for various temperatures are not the same. The relationship between ice temperature and strain corresponding to the peak stress occurrence (i.e., failure strain of ice) is shown in **Figure 8**. Overall, the strain is smaller for lower ice temperature. That is to say, ice is less ductile for lower temperature.

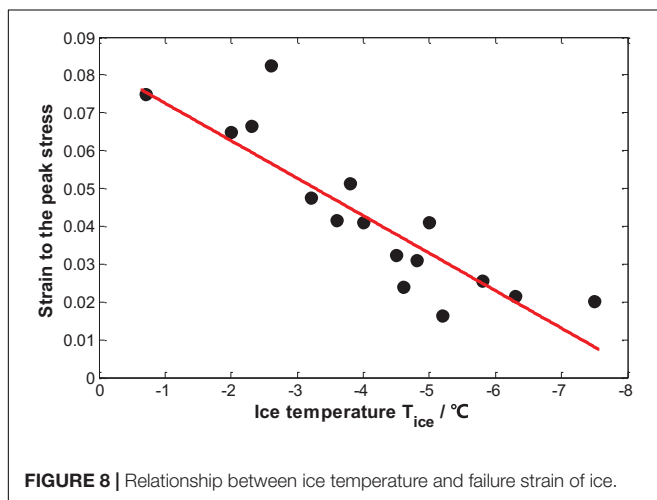
## Effect of Ice Temperature on the Compressive Strength and Modulus

It can be seen from **Table 1** that the compressive strength of ice distributes from 0.36 to 3.67 MPa when ice temperature varies

**TABLE 1** | Test results of uniaxial unconfined compressive strength of ice.

Test number	$T_{ice}$ (°C)	$L$ (mm)	$L/D$	Peak load (Kn)	$P_{ice}$ (MPa)	$E_C$ (MPa)
1	-0.7	38.6	0.38	2.94	0.36	11.7
2	-2.0	41.3	0.40	9.93	1.22	27.5
3	-2.3	42.8	0.42	13.08	1.60	41.7
4	-2.6	39.5	0.39	13.89	1.70	50.1
5	-3.2	40.6	0.40	12.91	1.58	65.3
6	-3.6	42.3	0.41	15.69	1.92	70.2
7	-3.8	41.1	0.40	18.35	2.25	75.7
8	-4.0	40.2	0.39	15.85	1.94	82.7
9	-4.5	40.5	0.40	18.80	2.30	126.7
10	-4.6	41.3	0.40	17.20	2.11	168.1
11	-4.8	38.4	0.38	17.45	2.14	157.9
12	-5.0	41.4	0.41	23.21	2.84	181.8
13	-5.2	42.0	0.41	20.18	2.47	260.1
14	-5.8	39.5	0.39	24.07	2.95	305.9
15	-6.3	40.7	0.40	26.56	3.25	337.4
16	-7.5	39.6	0.39	29.99	3.67	359.1

$L$  is the ice thickness, mm;  $D$  is the diameter of ice specimen, mm.



from  $-0.7$  to  $-7.5^{\circ}\text{C}$ . The scatter diagram is plotted to illustrate the relationship between ice failure strength and ice temperature (**Figure 9**). The expression to approximate the relationship of the ice failure strength and ice temperature is also obtained through regression and fitting method as shown in Eq. (1).

$$\begin{cases} P_{ice} = -0.4524T_{ice} + 0.279 \\ R^2 = 0.94 \end{cases} \quad T_{ice} \in [-0.7, 7.5] \quad (1)$$

where  $P_{ice}$  is the uniaxial unconfined compressive strength of ice (MPa) and  $T_{ice}$  is the ice temperature ( $^{\circ}\text{C}$ ). Eq. (1) shows the good linear relationship between compressive strength and ice temperature, and the correlation coefficient is 0.94. It agrees well with the test results obtained by Wang et al. (2007) and Zhang L. M. et al. (2009). Therefore, the results obtained in the laboratory test will help the mechanical deicing equipment to apply appropriate force on the pavement with ice. That is to say, the force can crush the ice on the one hand and not damage the pavement on the other hand.

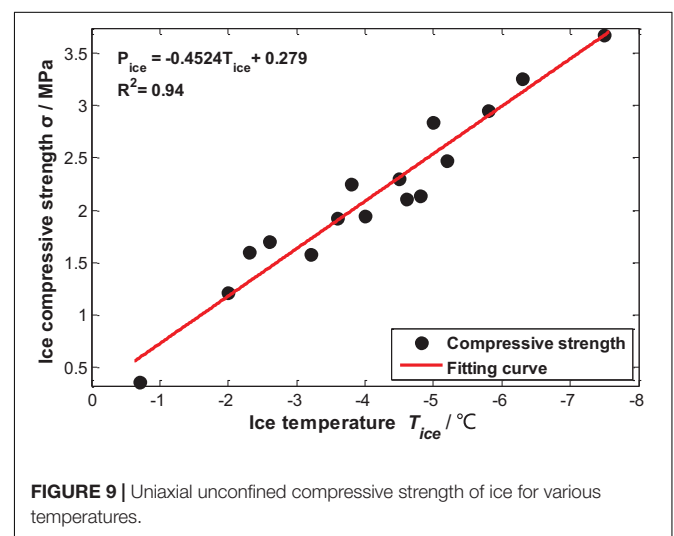
In addition, the compressive modulus of ice distributes from 11.7 to 395.1 MPa when ice temperature varies from  $-0.7$  to  $-7.5^{\circ}\text{C}$ . The scatter diagram is plotted to illustrate the relationship between ice compressive modulus and ice temperature (**Figure 10**). The approximate expression of the relationship between ice compression modulus and ice temperature is obtained through a regression and fitting method as shown in Eq. (2).

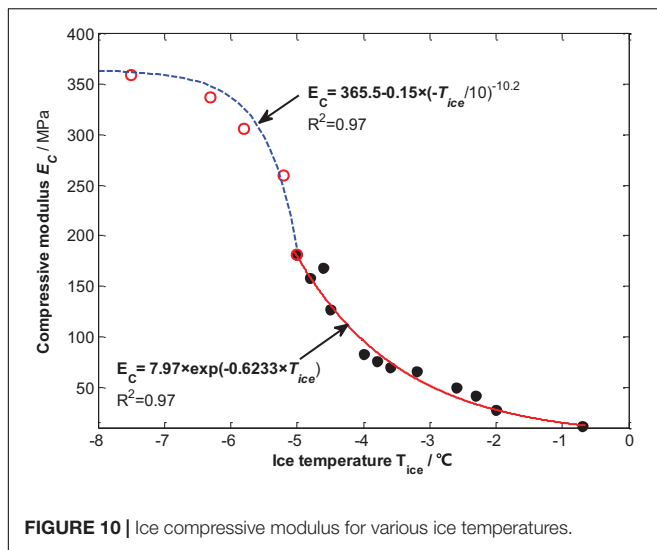
$$\begin{cases} E_C = 7.97 \exp(-0.6233T_{ice}) \\ R^2 = 0.97 \end{cases} \quad T_{ice} \in [-5, 0] \quad (2)$$

$$\begin{cases} E_C = 365.5 - 0.15 \left( -\frac{T_{ice}}{10} \right)^{-10.2} \\ R^2 = 0.97 \end{cases} \quad T_{ice} \in [-8, -5]$$

where  $E_C$  is the uniaxial unconfined compressive modulus of ice (MPa).

As can be seen from Eq. (2), when the ice temperature is higher than  $-5^{\circ}\text{C}$ , the relationship between ice compression modulus





and ice temperature is approximately exponential, and the correlation coefficient is 0.97. When the ice temperature ranges from  $-8$  to  $-5^{\circ}\text{C}$ , this kind of relationship can be approximated by power function, and the correlation coefficient is 0.97.

It can be seen apparently from **Figure 10** that the compression modulus improves with ice temperature decrease. The improvement tends to be gentle when ice temperature approaches  $-10^{\circ}\text{C}$ . According to other researchers (Wang et al., 2007; Yu et al., 2009), the improvement of compressive modulus with ice temperature is slight when ice temperature is below  $-10^{\circ}\text{C}$ , and it is affected by ice strain rate. Since the laboratory condition is limited, the compressive test is not conducted for lower ice temperature (below  $-10^{\circ}\text{C}$ ). Nevertheless, the test

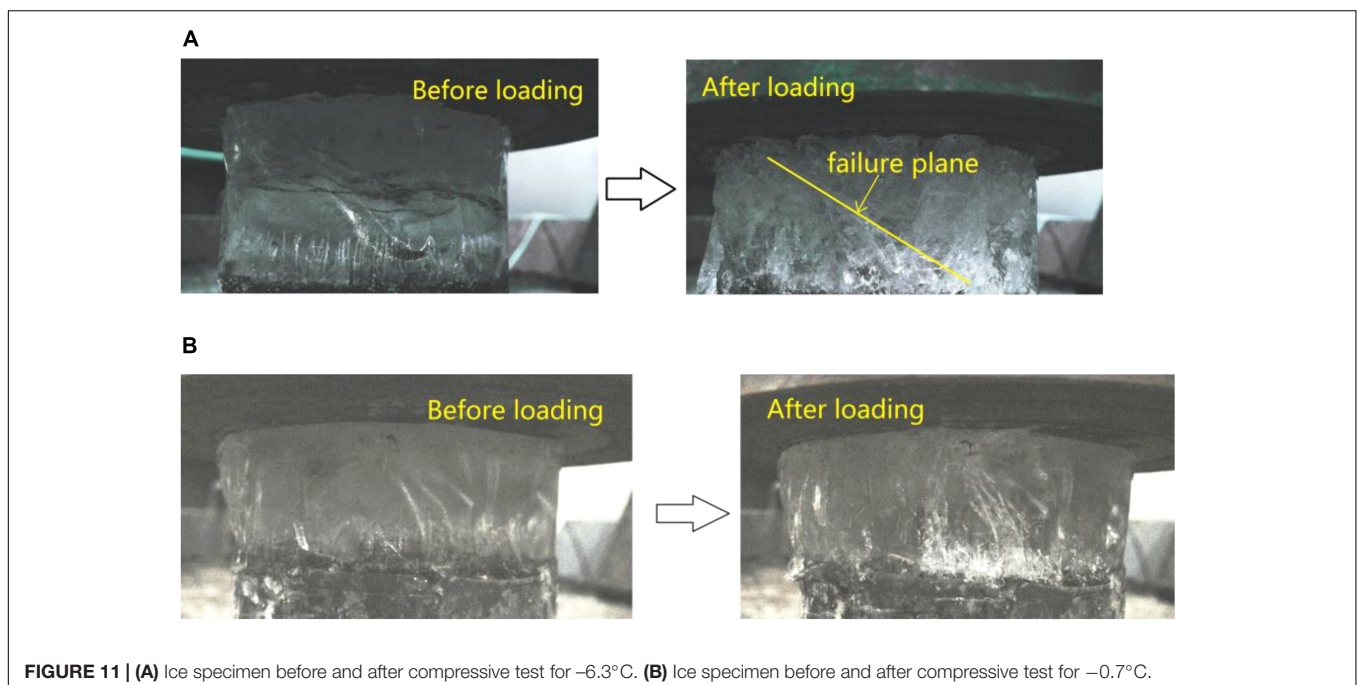
results can provide the value of compressive modulus of ice to facilitate the calculation in simulating the mechanical behavior of material and structure including ice layer.

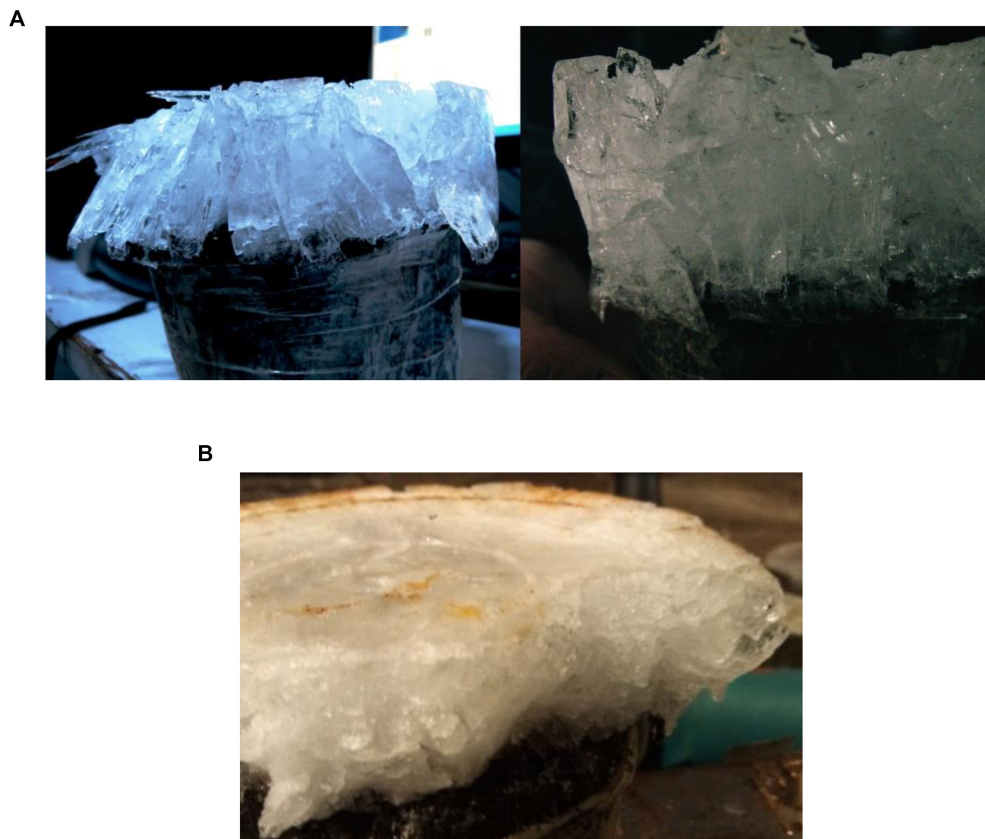
## Ice Failure Mode Under Different Temperature Conditions

According to some researches (Sinha, 1981; Timco and Frederking, 1982; Petrovic, 2003; Zhang X. Z. et al., 2009), ice failure mode depends on strain rate (i.e., load speed) and is affected by ice temperature as well. It can be found that the failure behaviors during the test process are obvious different for various ice temperatures.

**Figures 11A,B** show the schematic diagrams of ice failure subjected to load at  $-6.3$  and  $-0.7^{\circ}\text{C}$  respectively. When ice temperature is  $-6.3^{\circ}\text{C}$ , the visible cracks from top to bottom in the ice specimen develop quickly and connect gradually, accompanied by a crisp crush sound during the loading process. Significantly, it can be found from **Figure 11A** that an approximately incline failure plane (not accurate failure plane) appears and the ice particle partially moves along the plane, which can be observed. This phenomenon is regarded as ice shear failure. Because no lateral confinement is applied to the ice cylinder, the ice cylinder expands laterally and is compressed vertically. The obvious peak stress value can be obtained from the stress–strain curve (**Figure 7**) and the failure ice is mainly composed of large ice strips and bulks (**Figure 12A**).

While the failure phenomenon of ice at  $-0.7^{\circ}\text{C}$  is inconsistent with that of ice at  $-6.3^{\circ}\text{C}$ . Under this condition, ice cylinder is compressed vertically and expands laterally in the process of loading and does not have obvious failure plane like that at  $-6.3^{\circ}\text{C}$  (**Figure 11B**). It can be seen from the **Figure 12B**





**FIGURE 12 | (A)** Ice configuration after compression for lower ice temperature. **(B)** Ice configuration after compression for higher ice temperature.

that the failure ice is mainly composed of granular ice crystals, which is different from that of ice under the lower-temperature condition.

General conclusions can be drawn from the above experiment phenomenon, namely, that the failure mechanism of ice on the asphalt pavement under relatively lower temperature is due to the development of cut-through cracks inside the ice. The ice crack development results in the decline of ice-bearing capacity until it reaches whole failure state. The apparent failure plane inside the ice appears and no melting phenomenon can be observed. In contrast, for ice with relatively higher temperature especially the ice near melting point temperature, the visible cracks are less developed.

## CONCLUSION

The uniaxial unconfined compressive tests of ice under different cold temperature conditions are carried out. With the aid of a data acquisition system, the load–displacement curves and stress–strain curves of each test are obtained and the test results are analyzed. Accordingly, the experimental conclusions can be drawn as follows:

- (1) The different positions that peak stress occurs in the stress–strain curves illustrate that the deformation properties of

ice under various temperatures are not the same. Overall, the strain is smaller for the lower ice temperature. It indicates that the ice is less ductile for lower temperature.

- (2) The uniaxial unconfined compressive strength of ice is evaluated, and it distributes from 0.36 to 3.67 MPa when the ice temperature varies from  $-0.7$  to  $-7.5^{\circ}\text{C}$ . The relation of ice failure strength and ice temperature can be approximately evaluated in a linear manner. The strength can help the mechanical deicing equipment to apply appropriate force on the pavement with ice. That is to say, the force can crush the ice on the one hand and not damage the pavement on the other hand.
- (3) The compressive modulus of ice distributes from 11.7 to 359.1 MPa when the ice temperature ranges from  $-7.5$  to  $-0.7^{\circ}\text{C}$ . The expression to approximate the relation of ice compressive modulus and ice temperature is obtained through a regression and fitting method. It shows good power function and exponential relationships, respectively, when ice temperature ranges from  $-8$  to  $-5^{\circ}\text{C}$  and from  $-5$  to  $0^{\circ}\text{C}$ . The test results can provide the value of compressive modulus of ice to facilitate the calculation in simulating the mechanical behavior of material and structure including ice layer.
- (4) The failure mechanism of ice under relatively lower temperature is due to the crack development of

cut-through cracks inside the ice. The ice crack development results in the decline of ice-bearing capacity until it reaches a whole failure state. The relatively apparent failure plane inside the ice can be formed and no melting phenomenon can be observed. In view of the low strain rate, the ice failure mode for this kind of condition is shear failure and ductile, and the failure ice is mainly composed of large ice strips and bulks.

- (5) For ice with relatively higher temperature especially the ice near the melting point temperature, the visible cracks are less developed. In view of the low strain rate, the ice failure mode is compressive and ductile, and the failure ice is mainly composed of granular ice crystals.

## DATA AVAILABILITY STATEMENT

The raw data supporting the conclusions of this article will be made available by the authors, without undue reservation, to any qualified researcher.

## REFERENCES

- Chen, W., Du, X. H., and Wang, D. L. (2008). Analysis of the low temperature, ice- snow and freezing disasters in early 2008. *Sci. Meteorol. Sin.* 28(Suppl.), 84–87.
- Croutch, V. K., and Hartley, R. A. (1992). Adhesion of ice to coatings and the performance of ice release coatings. *J. Coat. Technol.* 64, 41–52.
- Dan, H. C., He, L. H., Zou, J. F., Zhao, L. H., and Bai, S. Y. (2014). Laboratory study on the adhesive properties of ice to the asphalt pavement of highway. *Cold Reg. Sci. Technol.* 104, 7–13. doi: 10.1016/j.coldregions.2014.04.002
- Dan, H. C., Tan, J. W., and Chen, J. Q. (2019a). Temperature distribution of asphalt bridge deck pavement with groundwater circulation temperature control system under high- and low temperature conditions. *Road Mater. Pavem. Des.* 20, 528–553.
- Dan, H. C., Zhang, Z., Liu, X., and Chen, J. Q. (2019b). Transient unsaturated flow in the drainage layer of a highway: solution and drainage performance. *Road Mater. Pavem. Eng.* 20, 528–553. doi: 10.1080/14680629.2017.1397049
- Dan, H. C., Tan, J. W., Du, Y. F., and Cai, J. M. (2020a). Simulation and optimization of road deicing salt usage based on Water-Ice-Salt model. *Cold Reg. Sci. Technol.* 169:102917. doi: 10.1016/j.coldregions.2019.102917
- Dan, H. C., Yang, D., Liu, X., Peng, A. P., and Zhang, Z. (2020b). Experimental investigation on dynamic response of asphalt pavement using SmartRock sensor under vibrating compaction loading. *Constr. Build. Mater.* 247:118592. doi: 10.1016/j.conbuildmat.2020.118592
- Dan, H. C., Zou, Z. M., Zhang, Z., and Tan, J. W. (2020c). Effects of aggregate type and SBS copolymer on the interfacial heat transport ability of asphalt mixture using molecular dynamics simulation. *Constr. Build. Mater.* 250:118922. doi: 10.1016/j.conbuildmat.2020.118922
- Gow, A. J., and Williamson, T. C. (1972). Linear compressibility of ice. *J. Geophys. Res.* 77, 6348–6352. doi: 10.1029/jb077i032p06348
- Gustafson, K. (1982). Icing conditions on different pavement structures. *Transp. Res. Rec.* 860, 21–28.
- Hanbali, R. M. (1994). Economic impact of winter road maintenance on road users. *Transp. Res. Rec.* 1442, 151–161.
- Haynes, F. D., and Mellor, M. (1977). Measuring the uniaxial compressive strength of ice. *J. Glaciol.* 19, 213–223. doi: 10.3189/s0022143000029294
- Kärnä, T., and Jochmarm, P. (2003). “Field observations on ice failure modes”, in *Proceedings of the 17th POAC Symposium on Ice*. Trondheim Norway: POAC International Committee.
- Kärnä, T., Lubbad, R., Loset, S., Mroz, A., Dalane, O., Bi, X., et al. (2010). “Ice failure process on fixed and compliant cones”, in *Proceedings of the HYDRALAB III Joint User Meeting*, Hannover, 1–4.
- Marion, G. M., and Jakubowski, S. D. (2004). The compressibility of ice to 2.0 kbar. *Cold Reg. Sci. Technol.* 38, 211–218. doi: 10.1016/j.coldregions.2003.10.008
- Montagnat, M., Castelnau, O., Bons, P. D., Faria, S. H., Gagliardini, O., Gillet-Chaulet, F., et al. (2014). Multiscale modeling of ice deformation behavior. *J. Struc. Geol.* 61, 78–108. doi: 10.1016/j.jsg.2013.05.002
- Oksanen, P. (1983). *Friction and Adhesion of Ice*. Espoo: Technical Research Centre of Finland, Publication, 36.
- Petrenko, V. F. (1999). Reduction of ice adhesion to stainless steel by ice electrolysis. *J. Appl. Phys.* 86, 5450–5454. doi: 10.1063/1.371544
- Petrovic, J. J. (2003). Review mechanical properties of ice and snow. *J. Mater. Sci.* 38, 1–6. doi: 10.1023/A:1021134128038
- Sarkar, D. K., and Farzaneh, M. (2009). Superhydrophobic coatings with reduced ice adhesion. *J. Adhes. Sci. Technol.* 22, 1215–1237. doi: 10.1163/156856109x433964
- Schulson, E. M. (2001). Brittle failure of ice. *Eng. Fract. Mech.* 68, 1839–1887. doi: 10.1016/S0013-7944(01)00037-6
- SHRP (1994). *Development of Anti-Icing Technology*. Washington, D.C.: SHRP - National Research Council. SHRP-H-385.
- Sinha, N. K. (1981). Rate sensitivity of compressive strength of columnar-grained ice. *Exp. Mech.* 21, 209–218. doi: 10.1007/bf02326843
- Sodhi, D. S. (2001). Crushing failure during ice-structure interaction. *Eng. Fract. Mech.* 68, 1889–1921. doi: 10.1016/s0013-7944(01)00038-8
- Taggart, D. G., Osama, I., and Milton, H. (2002). Application of jetting technology to pavement deicing. *Transp. Res. Rec.* 1794, 77–83. doi: 10.3141/1794-10
- Tan, Y. Q. (2008). Deicing technologies for the pavement in the ice disaster. *Trans. Constr. Manag.* 49, 86–87.
- Timco, G. W., and Frederking, R. M. W. (1982). Comparative strengths of fresh water ice. *Cold Reg. Sci. Technol.* 6, 21–27. doi: 10.1016/0165-232x(82)90041-6
- Wang, J. F., Yu, T. L., and Huang, M. L. (2007). Experimental research on uniaxial and unconfined compressive strength of river ice. *Low Temp. Archit. Technol.* 1, 11–13.

## AUTHOR CONTRIBUTIONS

HD and YR designed the experiments. DX carried out the experiments. WL and RZ analyzed the experimental results. WL and HD wrote the manuscript. All authors contributed to the article and approved the submitted version.

## FUNDING

This research has been supported by the National Natural Science Foundation of China (Grant No. 51908558), the Jiangxi Provincial Department of Communications Key Technology Foundation (Grant Nos. 2016C0058 and 2016C0004), the Science and Technology Project of Jiangxi Provincial Department of Transportation (Grant No. 2020Z0001), and the Guizhou Transportation Science and Technology Foundation (Grant No. 201622). The research was also assisted by the Jiangxi Transportation Science and Technology Foundation of China (Grant No. 2020H0028) and the Hunan Natural Science Foundation (Grant No. 2020JJ4730).



- Weertman, J. (1983). Creep deformation of ice. *Annu. Rev. Earth Plane. Sci.* 11, 215–240. doi: 10.1146/annurev.ea.11.050183.001243
- Yu, T. L., Yuan, Z. G., and Huang, M. L. (2009). Experimental study on mechanical behavior of river ice. *J. Liaon. Techn. Univ.* 28, 937–940.
- Yurtseven, H., and Kilit, E. (2009). Calculation of the compressibility and heat capacity of ice I in the pre-melting region. *Phys. Chem. Liquids* 47, 495–504. doi: 10.1080/00319100802290449
- Zhang, D. C., Liu, M. Y., and Bao, T. (2011). Experimental study on mechanical properties of fresh water ice subjected to uniaxial compressive load. *Eng. Mech.* 28, 238–244.
- Zhang, L. M., Li, Z. J., and Jia, Q. (2009). Experimental study on uniaxial compressive strengths of artificial freshwater ice. *J. Hydraul. Eng.* 40, 1392–1396.
- Zhang, X. Z., Bai, R. Y., and Jiang, A. M. (2009). Constitutive relation and compressive strength of oceanic ice. *Mech. Eng.* 31, 50–53.
- Zhu, Y. S., Xiang, H. L., and Zhang, X. D. (2012). The skid resistance performance of the asphalt pavement under freezing condition. *J. Wuhan Univ. Technol.* 36, 6–10.
- Conflict of Interest:** The authors declare that the research was conducted in the absence of any commercial or financial relationships that could be construed as a potential conflict of interest.

Copyright © 2020 Luo, Dan, Zeng, Rong and Xie. This is an open-access article distributed under the terms of the Creative Commons Attribution License (CC BY). The use, distribution or reproduction in other forums is permitted, provided the original author(s) and the copyright owner(s) are credited and that the original publication in this journal is cited, in accordance with accepted academic practice. No use, distribution or reproduction is permitted which does not comply with these terms.



# Analysis of the Influence of Temperature Field on the Dynamic Modulus of Rubber Asphalt Pavement

Guoqing Wang<sup>1</sup>, Xinqiang Wang<sup>1\*</sup>, Zhanyou Yan<sup>2</sup>, Lusheng Qin<sup>3</sup> and Zhanhua Gao<sup>4</sup>

<sup>1</sup>School of Civil and Transportation Engineering, Hebei University of Technology, Tianjin, China, <sup>2</sup>School of Civil Engineering, Shijiazhuang Tiedao University, Shijiazhuang, China, <sup>3</sup>Hebei Transportation Investment Group Corporation, Shijiazhuang, China, <sup>4</sup>Hebei Province Road Structure and Material Technology Research Center, Shijiazhuang, China

## OPEN ACCESS

### Edited by:

Hui Yao,  
Beijing University of Technology,  
China

### Reviewed by:

Yang Zhou,  
Southeast University, China  
Yunchao Tang,  
Zhongkai University of Agriculture and  
Engineering, China

### \*Correspondence:

Xinqiang Wang  
807039883@qq.com

### Specialty section:

This article was submitted to  
Structural Materials,  
a section of the journal  
Frontiers in Materials

**Received:** 23 July 2020

**Accepted:** 07 October 2020

**Published:** 30 October 2020

### Citation:

Wang G, Wang X, Yan Z, Qin L and  
Gao Z (2020) Analysis of the Influence  
of Temperature Field on the Dynamic  
Modulus of Rubber Asphalt Pavement.  
Front. Mater. 7:586457.  
doi: 10.3389/fmats.2020.586457

In this paper, asphalt mixture performance test is used to study the dynamic modulus of different types of rubber asphalt mixtures in the laboratory, based on the viscoelastic theory, in order to determine the actual dynamic modulus of different structural layers under the action of temperature field in the asphalt pavement. Based on the time-temperature equivalence principle and Sigmund model, the dynamic modulus main curve is established, and establish the correlation equation between temperature and dynamic modulus. The actual dynamic modulus of asphalt concrete at each pavement layer is calculated by referring to the test data of pavement temperature field in Shijiazhuang and Tangshan, and compare and analyze the design value and actual value of dynamic modulus. The results show that the influence of external factors such as temperature and frequency on the dynamic modulus of asphalt mixture is far greater than that of internal factors such as cement and gradation type. Affected by the temperature field, the dynamic modulus of concrete at different structural levels is dynamically changing. Taking the dynamic modulus at 20°C and 10 Hz as the limiting index for design data selection is inconsistent with reality and needs to be improved. This study not only provides the basis for dynamic modulus selection in asphalt pavement design, but also has certain reference value for improving the life of asphalt pavement.

**Keywords:** pavement, rubber asphalt mixture, different layers, dynamic modulus, temperature field

## INTRODUCTION

Waste tire rubber powder modified asphalt not only solves the environmental pollution of solid waste, but also realizes the reuse of waste resources. Many experts and scholars have studied rubber asphalt and mixture (Li et al., 2019; Fang et al., 2020; Xia et al., 2021), and proved that rubber asphalt mixture has excellent pavement performance. With the implementation of Highway Asphalt Pavement Design Code (JTG D50-2017), dynamic compression modulus is one of the important parameters in asphalt pavement design. The test and model estimation of dynamic compression modulus of asphalt mixture are still the research hotspots.

In order to determine the influencing factors of the dynamic modulus of asphalt mixture, 8 AC mixtures were selected in reference (Ali et al., 2016). Uniaxial dynamic moduli at various temperatures and frequencies were tested using asphalt mixture performance testers. The nonlinear regression model is established. The dynamic modulus is expressed as the test temperature and is loaded as a function of the frequency and volume parameters of the mixture.

In reference (Wang et al., 2019), specimens with different asphalt content layers were prepared and Superpave Simple Performance Tester was used for dynamic modulus test. The results show that the dynamic modulus of asphalt mixture increases with the increase of loading frequency and decreases with the increase of test temperature. The study of the main dynamic modulus curve of asphalt mixture (Ruan et al., 2018; Su et al., 2018) facilitated the selection of dynamic modulus in a wide range. In the field of dynamic modulus prediction of asphalt mixtures, literature (Nemati and Dave, 2018) developed an asphalt mixture dynamic modulus and phase Angle prediction model based on the laboratory test results of more than 4,300 asphalt mixtures in New England, USA. Literature (Ghasemi et al., 2019) developed an accurate finite element (FE) model using a mixture of elastic modulus and asphalt binder performance prediction. This model has been verified in nine different pavement projects in five regions in the United States, which proves that ANN modeling can accurately predict dynamic modulus.

In literature (Rahman et al., 2019), the Witczak dynamic modulus prediction equation based on viscosity was modified, and the dynamic modulus of asphalt concrete under 21 different conditions was tested. The results showed that the Witczak model based on viscosity underestimates the dynamic modulus, and the modified Witczak model based on viscosity had a higher accuracy in determining the dynamic modulus. In terms of the impact of asphalt aging on dynamic modulus of asphalt mixture, three types of asphalt mixture with different aging states were used in literature (Wen and Wang, 2019) to study the change of the impact of aging on dynamic modulus of asphalt mixture. In the literature (Arefin et al., 2019), asphalt mixture was prepared with four bitumen binators and one aggregate. The prediction model 1-37A and NCHRP 1-40D and the Global Aging System integrated in MEPDG were used to predict the dynamic modulus of short-term and long-term Aging HMA and foaming WMA mixtures. The results showed that the NCHRP 1-37A model generally underestimates the dynamic modulus of HMA mixtures, but provides better adhesion quality for foaming WMA mixtures. The NCHRP 1-40D model usually results in higher dynamic modulus values. In terms of dynamic modulus prediction of pavement performance, literature (Hou et al., 2016) evaluated pavement performance by using the predicted dynamic modulus for model analysis. In literature (Robbins and Timm, 2011), binder and mixture were used to estimate various frequencies and dynamic moduli in combination with the application of dynamic moduli of asphalt mixtures in the southeastern United States.

In terms of the influence of temperature field on the performance of asphalt concrete, the literature (Qian et al., 2020) found that the rolling temperature and layer thickness affect the overall temperature field in the compaction process, and the wind speed and air temperature mainly affect the hot mixed asphalt. (HMA) The temperature field of the upper layer. The temperature change of the bottom layer mainly affects the temperature field at the bottom of the layer. Literature (Chen et al., 2017) uses the Green's function method, taking solar radiation, wind speed and temperature and other climate factors as input parameters to obtain an analytical solution for

the temperature field in the multilayer pavement structure. Literature (Huang et al., 2016) uses the discrete element method to analyze the feasibility of the asphalt mixture temperature field. The test results show that the numerical simulation results are basically consistent with the experimental results. DEM may become a promising new method to study the temperature field distribution and other properties of asphalt mixtures. Literature (Sun et al., 2020) uses a multi-scale finite element method based on microstructure to study the influence of temperature field on the internal damage of asphalt pavement under traffic load, and recognize the importance of considering temperature field in pavement structure analysis.

Based on the above-mentioned documents, people have realized the influencing factors of the dynamic modulus of asphalt mixture, and carried out the dynamic modulus prediction model; the temperature field is an important factor affecting the damage of the asphalt pavement, and numerical simulations have been carried out. However, there are still some gaps in the impact of the temperature field on the dynamic modulus of asphalt concrete, the difference between the design dynamic modulus of asphalt pavement and the actual dynamic modulus, and the impact on the pavement performance.

In this paper, based on viscoelastic theory and asphalt mixture performance test (AMPT) method, the relationship between dynamic modulus of rubber asphalt mixture and temperature and loading frequency was determined by indoor AMPT test, and the main dynamic modulus curve was established. Based on the research results of temperature field of asphalt pavement in Hebei Province, the dynamic modulus of asphalt concrete in different layers was calculated, the influence of temperature field on dynamic modulus was analyzed, and the suggested indexes for dynamic modulus selection were put forward. This study not only determines the change rule and value range of the actual dynamic modulus of asphalt pavement, but also improves the pertinence of the selection of asphalt pavement design parameters, which has important research value and practical significance.

## THEORETICAL BASIS AND METHODS

### Viscoelastic Theory

General mechanical analysis, model construction and failure mechanism research of asphalt mixture (Teixeira et al., 2014; Liu et al., 2018; Zhang et al., 2019) are mostly based on viscoelastic theory. When the stress is the input and the strain is the stress response, the mathematical description of the material input and response is called the constitutive relationship. When describing the constitutive equations of Hooke's elasticity, Newtonian viscosity and viscoelastic, the spring is used to represent Hooke's elasticity, the viscous flow is used to represent Newtonian viscous flow, and the combination of spring and viscoelastic element is used to represent viscoelastic element. According to the number and combination of spring and clay pot elements, the viscoelastic model can be divided into Kelvin element, Maxwell element, three-element model and four-element model.

The viscoelastic model of asphalt mixture can be constructed by means of integral equation, differential equation and complex equation. The viscoelastic model can be divided into static and dynamic load forms according to the loading time. The stress generated by vibration load is called periodic alternating stress. Cyclic alternating stress can better represent the effect of moving vehicle on asphalt pavement than static test stress. In recent years, it has become an important method to analyze the mechanical response of viscoelastic materials with alternating stress. The stress can be described by Eq. 1 (Zhang, 2006).

$$\sigma(t) = \sigma_0 e^{i\omega t} = \sigma_0 (\cos \omega t + i \sin \omega t) \quad (1)$$

where,  $\sigma_0$  is the strain amplitude and  $\omega$  is the angular frequency. The stress at a certain moment can be divided into real part  $\varepsilon_0 \cos \omega t$  and imaginary part  $\varepsilon_0 \sin \omega t$ .

The volume constitutive equation is:

$$\frac{\sigma}{\eta} + \frac{\dot{\sigma}}{E} = \dot{\varepsilon} \quad (2)$$

After substituting Eq. 1 into Eq. 2, it can be obtained:

$$\dot{\varepsilon} = \left( \frac{1}{\eta} + i \frac{\omega}{E} \right) \sigma_0 e^{i\omega t} \quad (3)$$

So,

$$\varepsilon = \frac{\sigma_0}{i\omega} \left( \frac{1}{\eta} + i \frac{\omega}{E} \right) e^{i\omega t} = \frac{1}{E} \sqrt{1 + \frac{1}{\omega^3 \tau_r^3}} \sigma_0 e^{(i\omega - \delta)} = \varepsilon_0 e^{(i\omega - \delta)} \omega \quad (4)$$

where,  $\delta = \tan^{-1} \frac{1}{\omega \tau_r}$ .

The above equation shows that when the alternating stress vibrates at angular frequency  $\omega$ , the strain response has the same vibration frequency. But there is  $\delta$  difference between the stress vector and the strain vector. The ratio of the stress vector to the strain vector is the complex modulus of elasticity, represented by  $E^*$ .

$$E^* = \frac{\sigma}{\varepsilon} = \frac{\sigma_0 e^{i\omega t}}{\frac{1}{E} \left( 1 - i \frac{1}{\omega \tau_r} \right) \sigma_0 e^{i\omega t}} = E \frac{\omega^2 \tau_r^2 + i \omega \tau_r}{1 + \omega^2 \tau_r^2} \quad (5)$$

Let the real part be  $E' = E \frac{\omega^2 \tau_r^2}{1 + \omega^2 \tau_r^2}$ , and the imaginary part be  $E'' = E \frac{\omega \tau_r}{1 + \omega^2 \tau_r^2}$ , then:

$$E^* = E' + iE'' = |E^*| (E' \cos \delta + iE'' \sin \delta) \quad (6)$$

The modulus  $|E^*|$  of the complex function is called the dynamic modulus, and  $\delta$  is the phase Angle of stress and strain.  $E'$  represents the energy stored and released by the material under the action of alternating stress, which is called the storage modulus.  $E''$  represents the lost energy, which is called the loss modulus.

Since the mechanical behavior of viscoelastic materials is affected by the viscous component and the viscous flow deformation is a function of time, the mechanical behavior of viscoelastic materials is a function of time. Meanwhile, the flow characteristics of viscoelastic materials are also affected by temperature changes, as shown in Eq. 7.

$$E(T_1, t) = E(T_2, t/a_T) \quad (7)$$

The above equation shows that there is a certain conversion relation between time factor and temperature factor. This conversion is called the time-temperature conversion rule.

## Time-Temperature Equivalence Principle

At present, the time-temperature conversion calculation theory of asphalt mixture mainly adopts three methods (Rowe and Sharrock, 2011), Williams-Landel-Ferry (WLF) equation, Arrhenius equation and polynomial equation. Where, the WLF equation is shown in Eq. 8.

$$\log_{10} a(T) = \frac{-C_1 (T - T_r)}{C_2 + (T - T_r)} \quad (8)$$

where,  $a(T)$  is the shift factor,  $T$  is the temperature corresponding to the translation curve,  $T_r$  is the reference temperature (the temperature field of the road at the site of the project), and  $C_1, C_2$  are the regression coefficients.

Arrhenius equation is shown in Eq. 9.

$$\log_{10} a(T) = \frac{\Delta E_a}{19.14714} \left[ \left( \frac{1}{T} \right) - \left( \frac{1}{T_r} \right) \right] \quad (9)$$

where,  $\Delta E_a$  is the activation energy, which is related to the asphalt material itself and can be obtained in the regression analysis.

Polynomial equation means to move a test curve towards a curve with known test results. The reference temperature is one of the curves in the cluster. The value of the shift factor was obtained by regression analysis, as shown in Eq. 10.

$$\log_{10} a(T) = aT^2 + bT + c \quad (10)$$

where,  $a, b$  and  $c$  are regression coefficients. From the equation form, the value of the shift factor is a quadratic function of temperature.

Since WLF Eq. 8 is not well applied to low temperature, the polynomial equation cannot obtain the main curve at unknown temperature. Therefore, the Arrhenius equation was used as the calculation method of dynamic modulus shift factor in this paper.

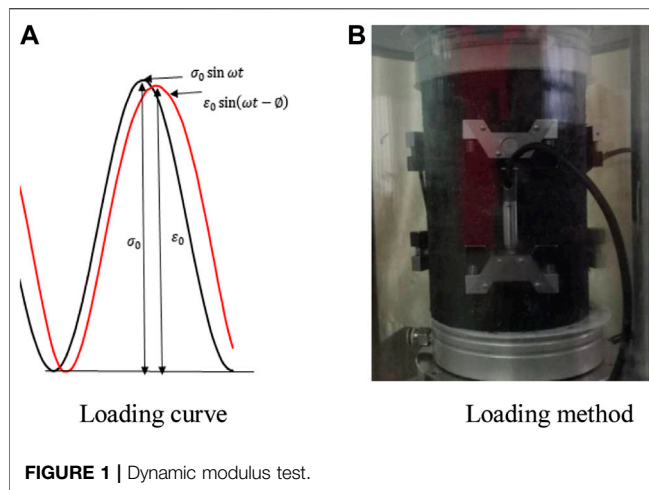
## Asphalt Mixture Samples

Based on the viscoelastic theory, the AMPT applied the load to the specimen in the form of input alternating stress. It can measure the mechanical behavior of concrete under different temperature and frequency and simulate the dynamic load response of asphalt pavement.

Figure 1A is the loading curve of the test dynamic modulus, and Figure 1B is the test equipment of the test dynamic modulus. The modulus loading curve is usually half sinusoidal. Dynamic modulus equipment can be applied at different temperatures, loads and frequencies.

Four frequency - modulus curves were obtained by four temperature dynamic modulus tests in the laboratory. Six frequencies are measured at each temperature. Select the pavement temperature of the project site as the reference temperature. Translate each curve to the reference temperature according to the Anius time-temperature conversion principle. The least square fitting of an S-shaped curve results in a modulus curve with a wide range of frequencies.





Major curve fitting was performed by Using Sigmoidal function (Su et al., 2018), as shown in Eq. 11.

$$\log|E^*| = \log(\min) + \frac{(\log(\max) - \log(\min))}{1 + e^{\beta + \gamma \left\{ \log \omega + \frac{\Delta E_a}{19.14714} \left[ \left( \frac{1}{T} \right) - \left( \frac{1}{T_r} \right) \right] \right\}}} \quad (11)$$

where,  $|E^*|$  is the dynamic modulus.  $\omega$  is the loading frequency (Hz) at the test temperature.  $\max$  represents the limited maximum modulus (MPa).  $\min$  is the limited minimum modulus (MPa).  $\beta$  and  $\gamma$  are the fitting parameters. The maximum modulus is obtained from Eqs 12 and 13.

$$|E^*|_{\max} = P_c \left[ 4\,200\,000 \left( 1 - \frac{VMA}{100} \right) + 435\,000 \left( \frac{VFA \times VMA}{10\,000} \right) \right] + \frac{1 - P_c}{\left[ \frac{(1 - \frac{VMA}{100})}{4\,200\,000} + \frac{VMA}{435\,000(VFA)} \right]} \quad (12)$$

$$P_c = \frac{\left( 20 + \frac{435\,000(VFA)}{VMA} \right)^{0.58}}{650 + \left( \frac{435\,000(VFA)}{VMA} \right)^{0.58}} \quad (13)$$

where, VFA is the saturation of asphalt mixture and VMA is the clearance rate of asphalt mixture ore.

## INDOOR DYNAMIC MODULUS TEST AND ANALYSIS OF ASPHALT MIXTURE

### Test Materials

The test material is modified asphalt with 30% and 40% rubber powder. The performance indexes of rubber powder modified asphalt are shown in Table 1.

The ore material is five-grade stone material, whose performance conforms to the specification requirements. They are mechanism sand, filler, 5~10, 10~15, 10~20 mm, respectively. According to the demand of the upper, middle and lower layers of pavement, the rubber asphalt mixture is of ARHM13, ARHM20 and ARHM30 respectively. The gradation of rubber asphalt mixture synthesis is shown in Table 2.

### Test Design

In order to determine the impact of asphalt binder on the dynamic modulus of rubber asphalt mixture, 30% and 40% rubber asphalt were used to prepare ARHM13 mixture for comparison test; ARHM20 and ARHM30 two mixtures used 40% rubber asphalt.

In the experiment, Marshall test method was used to determine the best whetstone ratio. The design void ratio was 4.0%, and the test process was not repeated. The optimum whetstone ratios of ARHM13, ARHM20 and ARHM30 were 6.4%, 4.5% and 4.0%, respectively. The dynamic modulus test piece was prepared on the rotating compacting instrument PCG, and the size test piece was  $\phi 50 \text{ mm} \times H170 \text{ mm}$ . Let cool at room temperature for 1 day. The specimen was processed into a size of  $100 \text{ mm} \times 150 \text{ mm}$  by means of drilling core and cutting, and its volume indexes were measured.

The test temperature is  $-10, 5, 20, 35^\circ\text{C}, 50^\circ\text{C}$ , respectively. The corresponding test frequency is 0.1, 0.5, 1, 5, 10, 25 Hz. An LVDT sensor was placed at  $120^\circ$  intervals along the circumference of the specimen. The dynamic modulus of asphalt mixture was measured after 5 h of heat preservation. The range of axial deformation of the specimen is  $85\text{--}135 \mu\text{e}$ .

### Test Results

#### Analysis of Influencing Factors of ARHM13 Dynamic Modulus

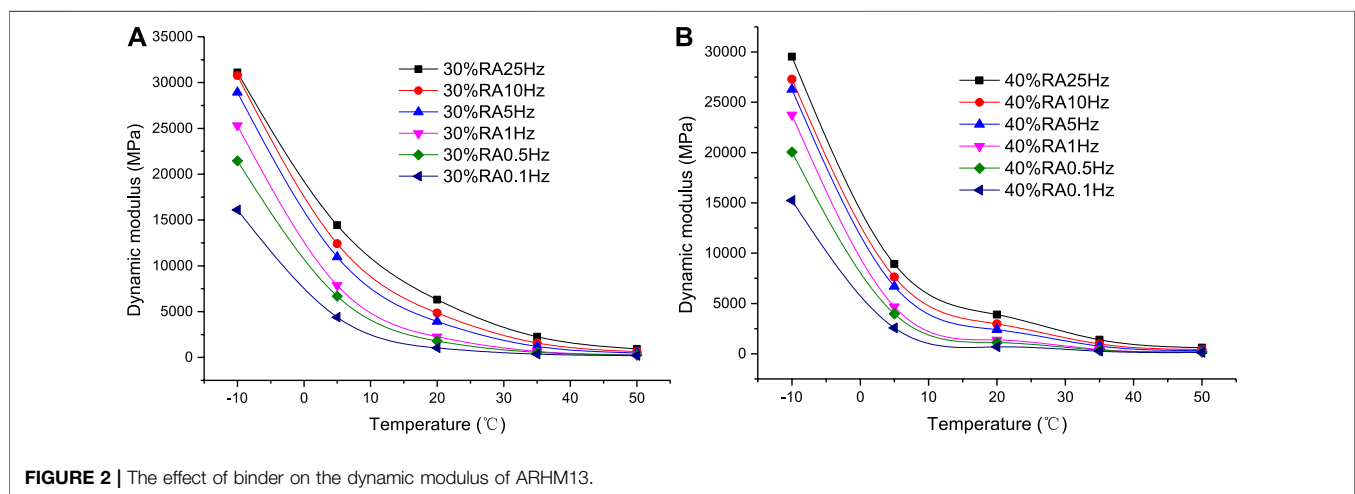
The dynamic modulus test results of ARHM13 mixtures with different binders are shown in Figure 2.

**TABLE 1 |** Performance index of rubber powder modified asphalt.

Test item	Modified asphalt with 30% rubber powder	Modified asphalt with 40% rubber powder
25°C penetration/0.1 mm	65	72
5°C ductility/cm	17	19
Softening point/°C	72.0	71.5
180°C viscosity (Pa·s)	2.8	3.5
After TFOT residue	Quality loss/% 25°C penetration rate/% 5°C degrees/cm	−0.30 76 12

**TABLE 2** | Types of rubber asphalt mixture.

Mesh size (mm)	Passing rate (%)			Mesh size (mm)	Passing rate (%)		
	ARHM13	ARHM20	ARHM30		ARHM13	ARHM20	ARHM30
37.5	—	—	100	4.75	25.3	24.4	25.0
31.5	—	—	95	2.36	21.5	19.2	19.7
26.5	—	100	84	1.18	17.8	15.1	15.5
19.0	—	90.5	66.5	0.6	14.2	9.0	12.3
16.0	100	79.2	58.9	0.3	12.7	7.1	9.7
13.2	97.3	68.5	51.4	0.15	10.4	6.5	7.6
9.5	66.1	52.2	40.8	0.075	10.0	5.4	6.0



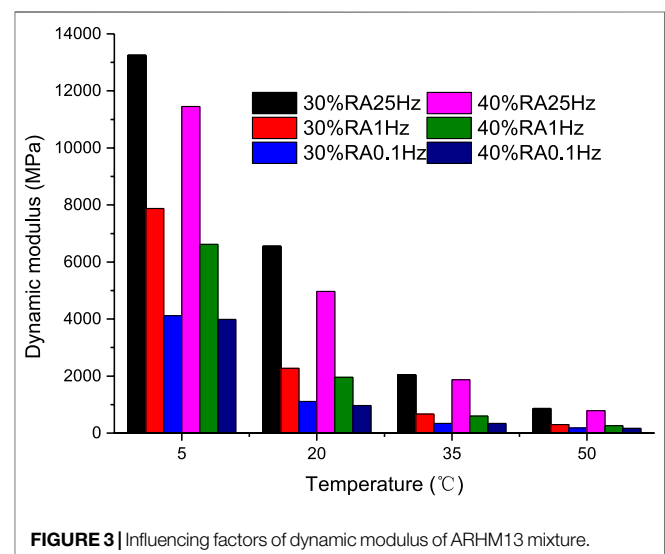
**Figure 2** shows that the dynamic modulus of different rubber asphalt mixtures has the same changing law, and is affected by temperature and loading frequency. With the increase of temperature, the dynamic modulus shows a decreasing trend; with the increase of loading frequency, the dynamic modulus is increasing trend.

Select three frequencies and four temperatures to analyze the factors affecting the dynamic modulus of the rubber asphalt mixture, as shown in **Figure 3**.

It can be seen from **Figure 3** that when the 30% RA mixture is at a frequency of 0.1 Hz, the dynamic modulus at 20, 35, and 50°C decreases by 73.0%, 91.7%, and 95.6%, compared to the dynamic modulus at 5°C; At 25 Hz, the dynamic modulus at 20, 35, and 50°C is relatively. The dynamic modulus decreased by 50.6%, 84.6% and 93.5% respectively at °C. The data shows that under the same loading frequency conditions, the dynamic modulus decreases with the increase of temperature; at the same temperature, the dynamic modulus increases with the increase of frequency. As the frequency increases, the dynamic modulus of asphalt mixture decreases gradually at 20°C relative to 5°C. Either increasing the temperature or reducing the frequency can achieve the purpose of reducing the dynamic modulus.

Comparing the dynamic modulus of the two rubber asphalt mixtures, it is found that under the conditions of

0.1 Hz and 5, 20, 35, 50°C, the dynamic modulus of 40%RA mixture relative to 30%RA mixture decreases by 3.1%, 12.79%, 0, 9.3%; under the conditions of 1 Hz and 5, 20, 35, 50°C, the dynamic modulus of 40%RA mixture relative to 30%



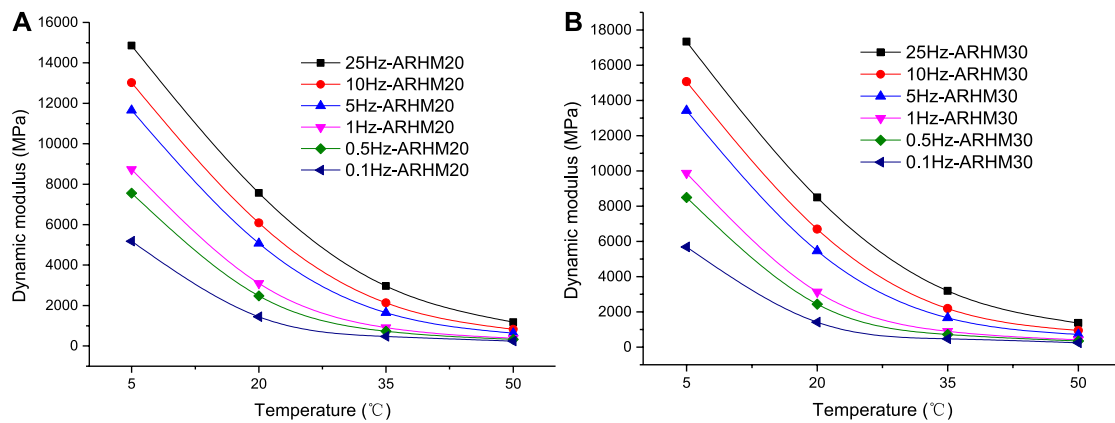


FIGURE 4 | Dynamic modulus of different types of rubber asphalt mixture.

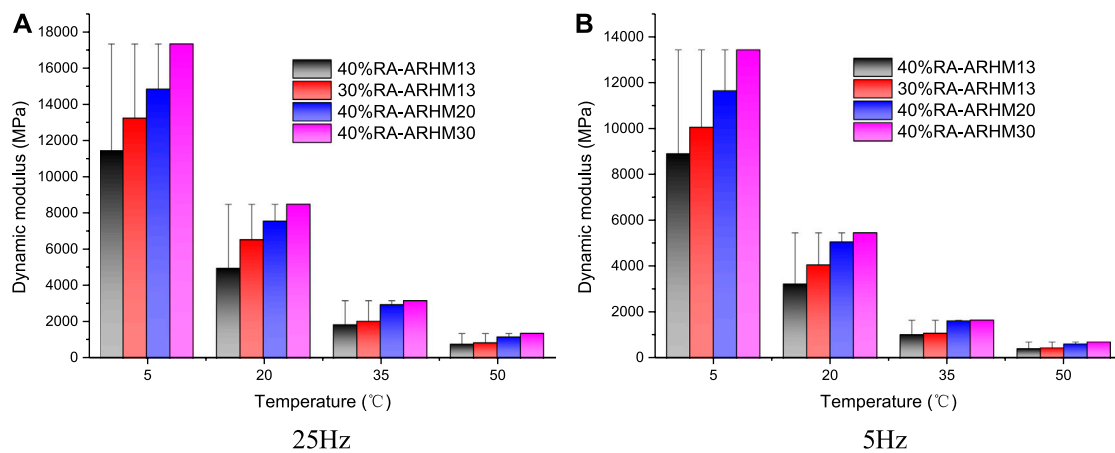


FIGURE 5 | Dynamic modulus of different types of mixtures.

TABLE 3 | Correlation equation model parameters.

Asphalt mixture type	a	b	R <sup>2</sup>
ARHM13 (40%RA)	13,868	-0.065	0.9987
ARHM13 (30%RA)	16,866	-0.067	0.993
ARHM20 (40%RA)	19,002	-0.062	0.9962
ARHM30 (40%RA)	21,441	-0.063	0.9963

RA mixture decreases by 8.8%, 16.9%, 2.3%, 6.5%; Under 25 Hz and 5, 20, 35, 50°C, the dynamic modulus of 40%RA mixture is reduced by 13.6%, 24.1%, 8.6%, 9.1, respectively %. It shows that the dynamic modulus of 30%RA mixture is higher than 40%RA under the same conditions.

Based on the above data, the influence of temperature and frequency on the dynamic modulus of the mixture is far greater than the influence of the cement on the dynamic modulus.

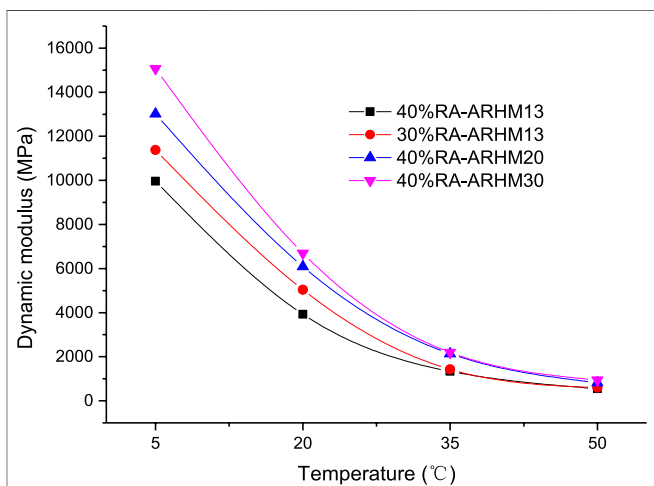
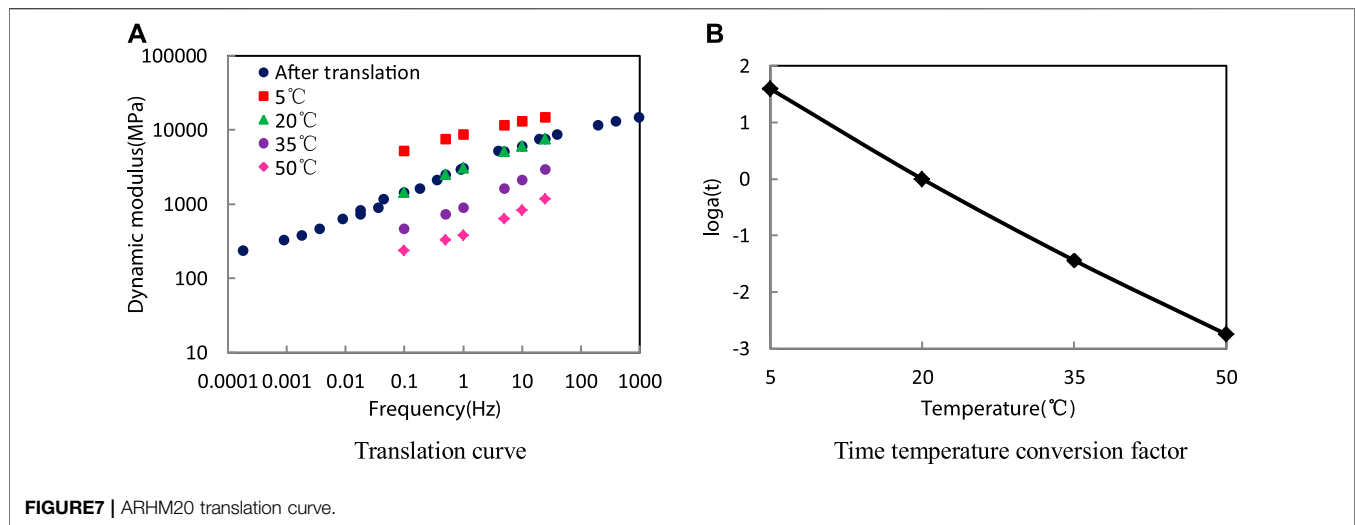


FIGURE 6 | Dynamic modulus and temperature correlation curve.



### Effect of Mixture Type on Dynamic Modulus

The test results of ARHM20 and ARHM30 asphalt mixtures are shown in **Figure 4**.

**Figure 4** shows that although the gradation type and oil-stone ratio of the two asphalt mixtures have changed, the dynamic modulus changes are consistent with the ARHM13 mixture. In order to determine the influence of gradation type on the dynamic modulus of asphalt mixture, the test data of **Figures 2 and 4** are combined. At 25 Hz and 5 Hz, the dynamic modulus of four asphalt mixtures is shown in **Figure 5**.

It can be seen from **Figure 5** that under the same conditions, the order of the dynamic modulus of the asphalt mixture from large to small is ARHM30, ARHM20, 30% RA-ARHM13, 40% RA-ARHM13, which can be achieved by changing the asphalt binder or gradation type. To achieve the purpose of adjusting the dynamic modulus of the asphalt mixture.

### Fitting the Relationship Between Dynamic Modulus and Temperature

Considering that the asphalt pavement is in a temperature-changing environment, the test data at 10 Hz is selected to fit the dynamic modulus and temperature. The fitting curve is shown in **Figure 6**.

According to the fitting curve in **Figure 6**, it is found that the dynamic modulus and temperature satisfy the exponential function model system, the dynamic modulus ( $y$ ) is set as the dependent variable and the temperature ( $x$ ) is the independent variable. The relationship between the two is  $y = ae^{bx}$ , The model parameters are shown in **Table 3**.

It can be seen from **Table 3** that the dynamic modulus of asphalt mixture has a high correlation with temperature, which is above 0.993. The dynamic modulus of asphalt mixture at any temperature can be solved by this model.

### Dynamic Modulus Master Curve

Taking ARHM20 mixture as an example, the dynamic modulus curve at different temperatures was translated to the reference

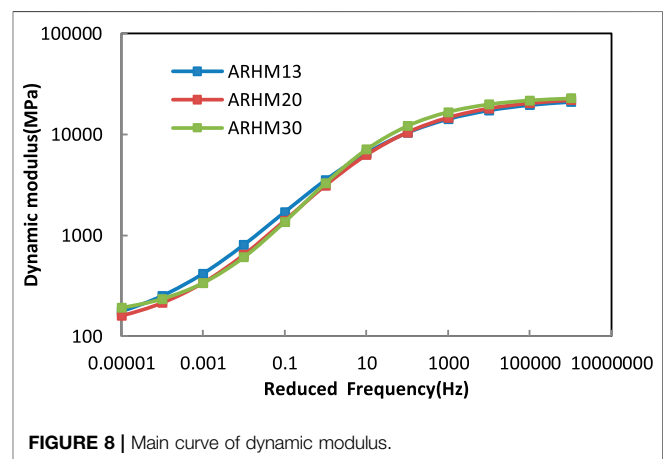
temperature (20°C) in combination with the time-temperature equivalence principle. The translation curve and displacement factor are shown in **Figure 7**.

After the dynamic modulus is translated, the three-dimensional space composed of temperature, dynamic modulus and loading frequency is transformed into a two-dimensional coordinate system of dynamic modulus and frequency.

Using the above method and using 20°C as the reference temperature, the master curve of the dynamic modulus of the three asphalt mixtures was fitted, as shown in **Figure 8**.

**Figure 8** shows that the dynamic modulus of the three types of mixtures varies slightly at different frequencies. The effect of gradation type on dynamic modulus is much less than that of temperature and frequency. The main curve model parameters of the three asphalt mixtures are shown in **Table 4**.

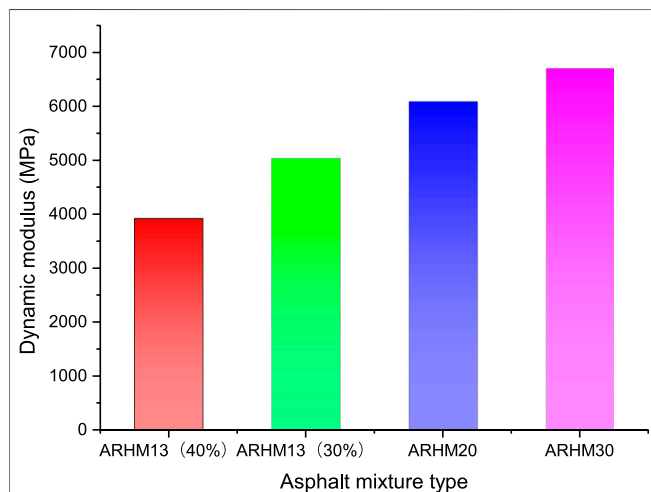
The main curve models of dynamic modulus of the three types of asphalt mixtures have a high correlation, which are 0.993, 0.991





**TABLE 4** | Main curve model parameters of different types of mixtures.

Parameter	Types of mixtures		
	ARHM13	ARHM20	ARHM30
Max	23089.89	23705.85	23705.85
Min	99.93596	106.1106	155.3557
$\beta$	-0.63811	-0.51116	-0.43372
$\gamma$	-0.55744	-0.60439	-0.71375
EA	162348.6	166142	156648.3
$R^2$	0.992923	0.991325	0.971128
Se/Sy	0.059487	0.065861	0.12015

**FIGURE 9** | Design value of dynamic modulus of asphalt mixture.

and 0.971, respectively. As the mixture type changes, the model parameters change accordingly. According to the main dynamic modulus curve, the dynamic modulus of asphalt mixture at any temperature or loading frequency can be solved. This curve is

helpful to study the dynamic modulus of the mixture in the wide band or temperature range.

## Dynamic modulus analysis of mixture in Different Asphalt Pavement

The thickness of the asphalt pavement above, in the middle and below shall be 4cm, 6cm and 8cm respectively. The pavement material is ARHM13, ARHM20 and ARHM30 mixture respectively. According to the main curve model of dynamic modulus and pavement temperature field data, the actual dynamic modulus of different pavement depths at 10 Hz can be solved and analyzed.

## Design Value of Dynamic Modulus of Asphalt Mixture

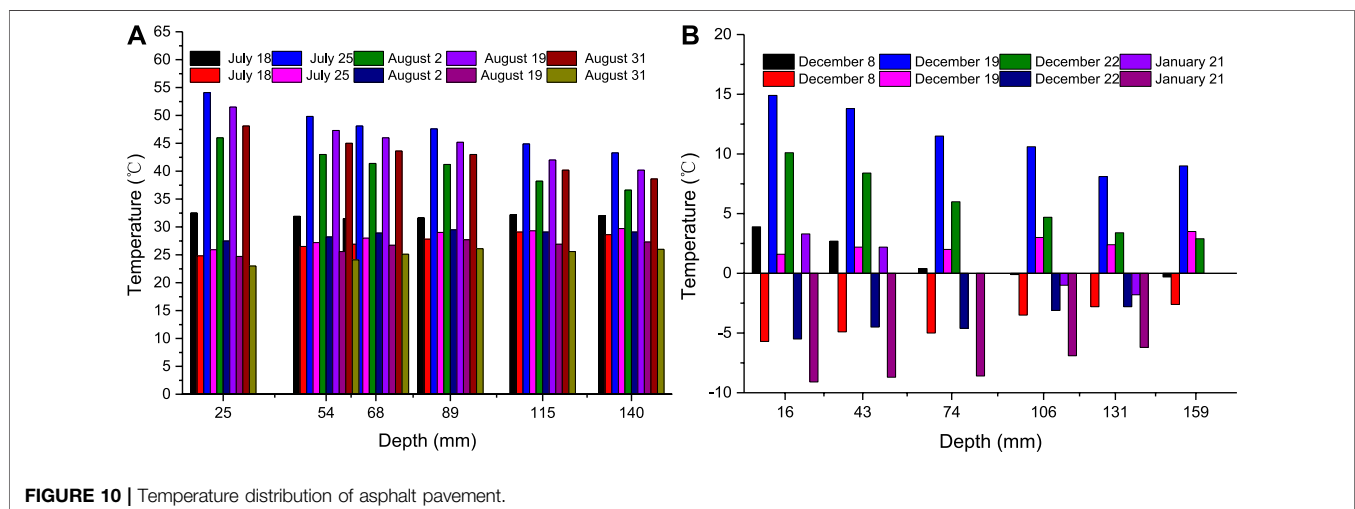
ARHM13, ARHM20 and ARHM30 mixtures are used for the surface layer, middle surface layer and lower layer, respectively. According to the test data of **Figures 3** and **5** and the "Code for Design of Highway Asphalt Pavement," the dynamic modulus of asphalt mixture at 20°C and 10 Hz is selected. It is the design value, as shown in **Figure 9**

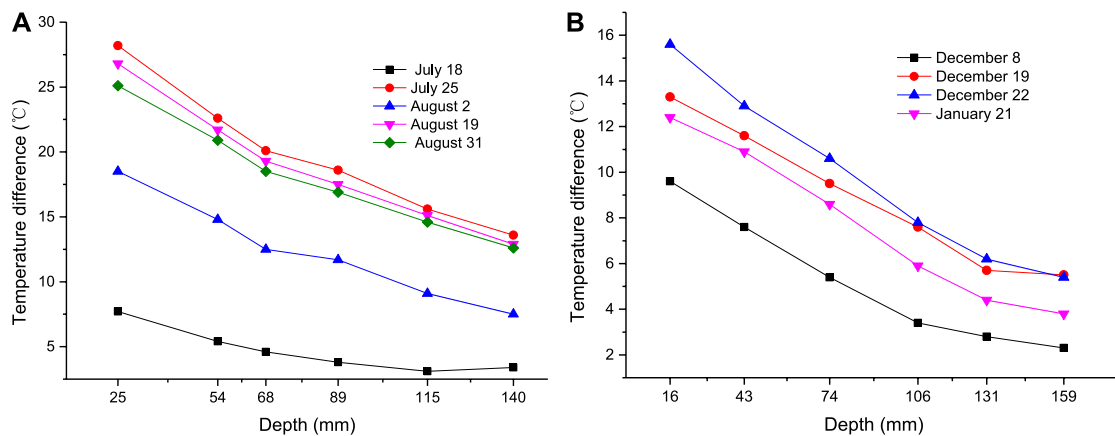
**Figure 9** illustrates that the dynamic modulus of the three-layer asphalt mixture changes to a fixed value. The change takes into account the change of the temperature field and causes the change of the dynamic modulus of the asphalt concrete.

## Distribution Law of Temperature Field of Asphalt Pavement

Combined with the results of previous research (Wang et al., 2014), the daily maximum and minimum temperatures at different depths of the road surface are shown in **Figure 10**.

It can be seen from **Figure 10** that the road temperature field varies with depth and seasons. Picture (a) the daily maximum temperature can reach 54.1°C and the lowest temperature is 23.1°C; figure (b) the daily maximum temperature can reach

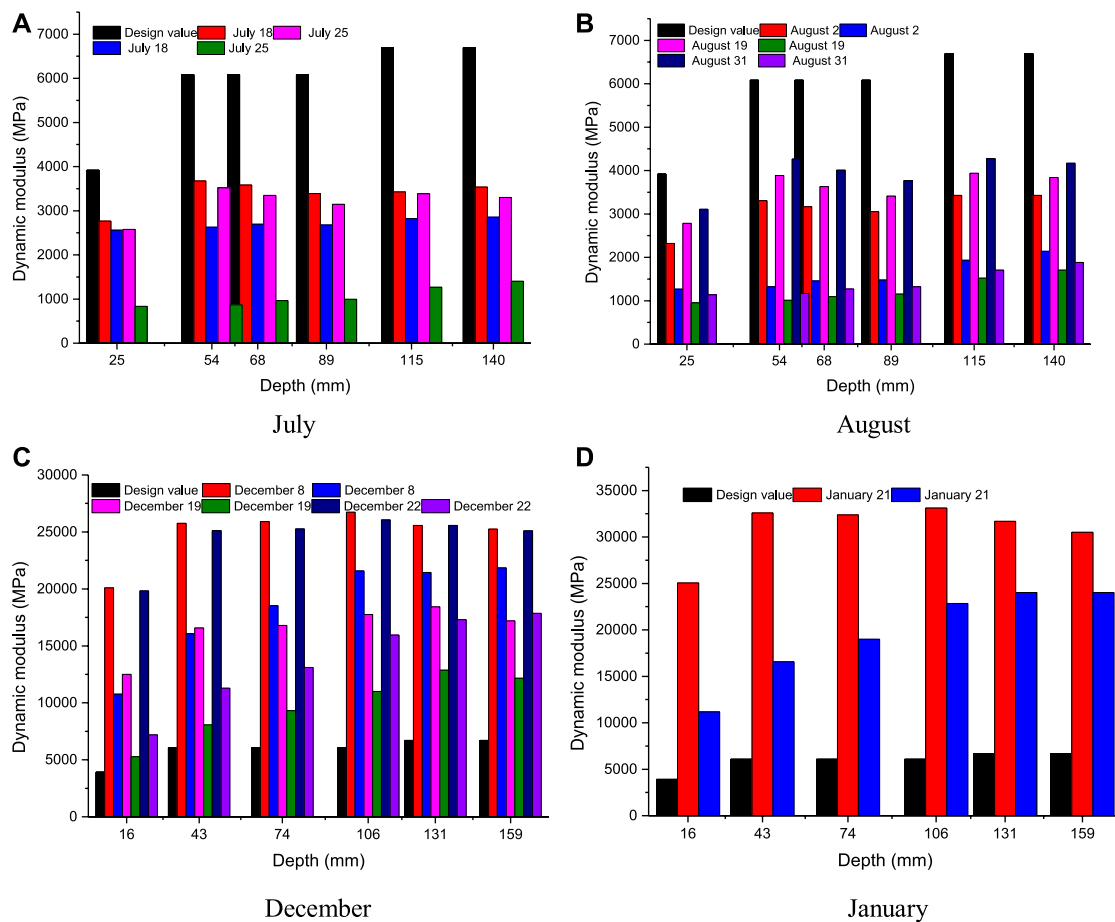
**FIGURE 10** | Temperature distribution of asphalt pavement.



**FIGURE 11 |** Temperature distribution of asphalt pavement.

14.9°C, the lowest temperature is  $-9.1^{\circ}\text{C}$ , and the extreme temperatures are concentrated around 20 mm deep on the road surface. Through calculation, the difference between the highest and lowest daily temperature is shown in **Figure 11**.

**Figure 11** shows that the daily temperature difference is a dynamically changing value, and the surface layer pavement temperature difference is the largest. As the road depth increases, it gradually decreases and tends to stabilize.



**FIGURE 12 |** Comparative analysis of dynamic modulus of asphalt pavement.

## Comparative Analysis of Dynamic Modulus of Pavement Structure Layers

Substitute the road temperature field data into the temperature and dynamic modulus correlation equation to solve the asphalt concrete dynamic modulus when the loading frequency is 10 Hz. In different months, the design and actual values of asphalt concrete are shown in **Figure 12**.

It is found from **Figure 12** that the actual dynamic modulus of pavement concrete is comprehensively affected by factors such as temperature, pavement depth, and asphalt mixture type. Among them, the change in dynamic modulus caused by the temperature difference between day and night is much greater than the impact of asphalt mixture type on dynamic modulus. In (A), the design values of the dynamic modulus of the surface layer, the middle layer and the lower layer are respectively 1.3 to 1.7 times, 1.4 to 2.0 times, and 1.6 to 2.0 times the actual dynamic modulus. In (B), the design values of the dynamic modulus of the surface layer, the middle layer and the lower layer are 1.5 to 4.7 times, 2.3 to 7 times, and 2.3 to 5.3 times of the actual dynamic modulus, respectively. The actual dynamic modulus is much smaller than the design value of the dynamic modulus, and there is a large gap between the actual stress state of the road surface and the design.

In (C), the design values of the dynamic modulus of the surface layer, middle layer and lower layer are respectively 15.6–31.4%, 18.7–36.7%, and 20.2–38.9% of the actual dynamic modulus; The design values of the dynamic modulus of the surface layer and the lower layer are respectively 25–74.5%, 32–75.4%, 27.9–60.9% of the actual dynamic modulus. The actual dynamic modulus is much larger than the design value of the dynamic modulus, and the asphalt pavement is in an elastic state.

## CONCLUSIONS

- (1) The dynamic modulus of rubber asphalt mixture is comprehensively affected by factors such as binder,

mixture type, temperature, and loading frequency. Among them, external factors such as temperature and loading frequency have a greater influence on the dynamic modulus of the mixture than the binder, mixture type, etc. Internal factors should pay attention to the influence of temperature on the dynamic modulus.

- (2) Through laboratory research on the dynamic modulus of different types of rubber asphalt mixtures, the correlation equation between dynamic modulus and temperature is established, which lays the foundation for the next step to study the dynamic modulus of asphalt concrete through the temperature field.
- (3) After analyzing the data of asphalt mixture design and actual dynamic modulus, it is found that the current asphalt pavement design specification uses 20°C and 10 Hz as the limiting conditions for the selection of dynamic modulus of all mixtures, which is far from the actual situation. The modulus data at the highest temperature of the structural layer is recommended as a design parameter.

## DATA AVAILABILITY STATEMENT

All datasets presented in this study are included in the article/supplementary material.

## AUTHOR CONTRIBUTIONS

GW: methodology, resources, supervision and writing-review. XW: conceptualization, experiments, methodology, writing-original draft, and editing. ZY: methodology and writing-review. LQ: investigation, visualization, formal analysis and writing-review. ZG: validation, experiments. All authors contributed to the article and approved the submitted version.

## REFERENCES

- Ali, Y., Irfan, M., Ahmed, S., Khanzada, S., Mahmood, T., et al. (2016). Investigation of factors affecting dynamic modulus and phase angle of various asphalt concrete mixtures. *Mater. Struct.* 49 (3), 857–868. doi:10.1617/s11527-015-0544-3
- Arefin, M. S., Quasem, T., Nazzal, M., and Dessouky, S. (2019). Accuracy of MEPDG dynamic modulus predictions for short-term and long-term aged asphalt mixtures. *J. Transp. Eng., Part B: Pavements* 145 (3). doi:10.1061/jpeodx.0000125
- Chen, J., Wang, H., and Zhu, H. (2017). Analytical approach for evaluating temperature field of thermal modified asphalt pavement and urban heat island effect. *Appl. Therm. Eng.* 113, 739–748.
- Fang, C., Guo, N., You, Z., and Tan, Y. (2020). Investigating fatigue life prediction of rubber asphalt mixture based on damage evolution using residual strain analysis approach. *Constr. Build. Mater.* 257, 119476. doi:10.1016/j.conbuildmat.2020.119476
- Ghasemi, P., Lin, S., Rollins, D., and Williams, R. (2019). Predicting dynamic modulus of asphalt mixture using data obtained from indirect tension mode of testing. *Chem. Biol. Eng. Pub.* 375. https://lib.dr.iastate.edu/cbe\_pubs/375
- Hou, H., Wang, T., Wu, S., Xue, Y., Tan, R., Chen, J., and Zhou, M. (2016). Investigation on the pavement performance of asphalt mixture based on predicted dynamic modulus. *Constr. Build. Mater.* 106, 11–17. doi:10.1016/j.conbuildmat.2015.10.178
- Huang, K., Xu, T., Li, G., and Jiang, R. (2016). The feasibility of DEM to analyze the temperature field of asphalt mixture. *Constr. Build. Mater.* 106, 592–599.
- Li, H., Dong, B., Zhao, D., Guo, P., and Zhang, J. (2019). Physical, rheological and stability properties of desulfurized rubber asphalt and crumb rubber asphalt. *Arabian J. Sci. Eng.* 44, 5043–5056. doi:10.1007/s13369-018-3684-2
- Liu, H., Luo, R., and Lv, H. (2018). Establishing continuous relaxation spectrum based on complex modulus tests to construct relaxation modulus master curves in compliance with linear viscoelastic theory. *Construct. Build. Mater.* 165, 372–384.
- Nemati, R., and Dave, E. (2018). Nominal property based predictive models for asphalt mixture complex modulus (dynamic modulus and phase angle). *Constr. Build. Mater.* 158, 308–319. doi:10.1016/j.conbuildmat.2017.09.144
- Qian, G., He, Z., Yu, H., Gong, X., and Sun, J. (2020). Research on the affecting factors and characteristic of asphalt mixture temperature field during compaction. *Constr. Build. Mater.* 257, 119509. doi:10.1016/j.conbuildmat.2020.119509
- Rahman, A. S. M. A., Islam, M. R., and Tarefder, R. A. (2019). Dynamic modulus and phase angle models for New Mexico's Superpave mixtures. *Road Mater. Pavement Des.* 20 (3), 740–753. doi:10.1080/14680629.2017.1422002

- Robbins, M., and Timm, D. H. (2011). Evaluation of dynamic modulus predictive equations for Southeastern United States asphalt mixtures. *Transp. Res. Rec.: J. Transp. Res. Board.* 2210, 122–129. doi:10.3141/2210-14
- Rowe, G. M., and Sharrock, M. J. (2011). Alternate shift factor relationship for describing temperature dependency of viscoelastic behavior of asphalt materials. *Transp. Res. Rec.* 2207 (1), 125–135. doi:10.3141/2207-16
- Ruan, L., Luo, R., Hu, X., and Pan, P. (2018). Effect of bell-shaped loading and haversine loading on the dynamic modulus and resilient modulus of asphalt mixtures. *Constr. Build. Mater.* 161, 124–131. doi:10.1016/j.conbuildmat.2017.11.038
- Su, N., Xiao, F., Wang, J., and Amirkhanian, S. (2018). Precision analysis of sigmoidal master curve model for dynamic modulus of asphalt mixtures. *J. Mater. Civ. Eng.* 30 (11), 04018290.1–04018290.11. doi:10.1061/(asce)mt.1943-5533.0002449
- Sun, Y., Du, C., Gong, H., Li, Y., and Chen, J. (2020). Effect of temperature field on damage initiation in asphalt pavement: A microstructure-based multiscale finite element method. *Mech. Mater.* 144, 103367.
- Teixeira, J. E. S. L., Kim, Y.-R., Souza, F. V., Allen, D. H., and Little, D. N. (2014). Multiscale model for asphalt mixtures subjected to cracking and viscoelastic deformation. *Transp. Res. Rec.* 2447 (1), 136–145. doi:10.3141/2447-15
- Wang, H., Zhan, S., and Liu, G. (2019). The effects of asphalt migration on the dynamic modulus of asphalt mixture. *Appl. Sci.* 9, 2747. doi:10.3390/app9132747
- Wang, G., Wang, Q., Liu, G., and Wang, L. (2014). Key technology of highway asphalt pavement [M]. Beijing, China: China Communications Press, 17–19 [in Chinese].
- Wen, Y., and Wang, Y. (2019). Effect of oxidative aging on dynamic modulus of hot-mix asphalt mixtures. *J. Mater. Civ. Eng.* 31 (1), 04018348. doi:10.1061/(asce)mt.1943-5533.0002547
- Xia, C., Lv, S., Cabrera, M. B., Wang, X., Zhang, C., and You, L. (2021). Unified characterizing fatigue performance of rubberized asphalt mixtures subjected to different loading modes. *J. Clean. Prod.* 279, 123740. doi:10.1016/j.jclepro.2020.123740
- Zhang, J., Li, Z., Chu, H., and Lu, J. (2019). A viscoelastic damage constitutive model for asphalt mixture under the cyclic loading. *Constr. Build. Mater.* 227, 116631.
- Zhang, X. (2006). *The principle and application of viscoelastic mechanics of asphalt and asphalt mixture [M]*. Beijing, China: China Communications Press, 51–53 [in Chinese].

**Conflict of Interest:** LQ was employed by the company Hebei Transportation Investment Group Corporation.

The remaining authors declare that the research was conducted in the absence of any commercial or financial relationships that could be construed as a potential conflict of interest.

Copyright © 2020 Wang, Wang, Yan, Qin and Gao. This is an open-access article distributed under the terms of the Creative Commons Attribution License (CC BY). The use, distribution or reproduction in other forums is permitted, provided the original author(s) and the copyright owner(s) are credited and that the original publication in this journal is cited, in accordance with accepted academic practice. No use, distribution or reproduction is permitted which does not comply with these terms.





# Aging Properties and Mechanism of Microwave-Activated Crumb Rubber Modified Asphalt Binder

Tao Zhou<sup>1</sup>, Jianing Zhou<sup>1,2</sup>, Qidong Li<sup>1,3</sup> and Bo Li<sup>1,2\*</sup>

<sup>1</sup>National and Provincial Joint Engineering Laboratory of Road & Bridge Disaster Prevention and Control, Lanzhou Jiaotong University, Lanzhou, China, <sup>2</sup>Research and Development Centre of Transport Industry of Technologies, Materials and Equipment of Highway Construction and Maintenance, Gansu Road and Bridge Group Co., Ltd., Lanzhou, China, <sup>3</sup>Key Laboratory of Highway Net Monitoring in Gansu Province, Gansu Hengda Road and Bridge Group Co., Ltd., Lanzhou, China

## OPEN ACCESS

### Edited by:

Zhanping You,  
Michigan Technological University,  
United States

### Reviewed by:

Ali Behnood,  
Purdue University, United States  
Peiwen Hao,  
Chang'an University, China

### \*Correspondence:

Bo Li  
libo@mail.lzjtu.cn

### Specialty section:

This article was submitted to  
Structural Materials,  
a section of the journal  
Frontiers in Materials

**Received:** 08 September 2020

**Accepted:** 16 November 2020

**Published:** 09 December 2020

### Citation:

Zhou T, Zhou J, Li Q and Li B (2020)  
Aging Properties and Mechanism of  
Microwave-Activated Crumb Rubber  
Modified Asphalt Binder.  
Front. Mater. 7:603938.  
doi: 10.3389/fmats.2020.603938

Although crumb rubber modified asphalt (CRMA) has a better performance than matrix asphalt (MA) in road engineering, the application bottlenecks of this material lies in its high viscosity, poor workability and bad storage stability. Microwave technology is one of the solutions to the above problems. The objective of this study was to investigate the physical and chemical changes before and after aging of CRMA which was prepared by microwave activated crumb rubber, and the aging mechanism of microwave-activated crumb rubber modified asphalt (MACRMA). Through penetration, softening point, ductility, viscosity and DSR test, the high and low temperature performance and temperature sensitivity of MA, CRMA and MACRMA before and after aging were studied. These tests results revealed that microwave treatment can improve the anti-rutting ability and the anti-aging performance of rubber asphalt. According to gel permeation chromatography (GPC) test, the distribution changes of the internal molecular content of the three asphalts were determined during the aging process. Its test results showed that aging effect accelerated the conversion of small molecules to large molecules in asphalt, and the value of large molecular size (LMS) increases more after long-term aging. The microwave activation made the swelling reaction more intense, thereby delayed the conversion of LMS in the rubber asphalt. In addition, LMS has a high correlation with test indicators. The fourier transform infrared spectroscopy (FTIR) test was used to measure the functional group changes of each asphalt. The FTIR spectra indicated that microwave activation is mainly a process of physical change. The carbonyl and sulfoxide functional group indices of MACRMA were lower than those of MA and CRMA, which also confirmed that MACRMA has a better anti-aging ability.

**Keywords:** rubber asphalt, microwave-activated, aging, physico-chemical properties, gel permeation chromatography, Fourier transform infrared spectroscopy

## INTRODUCTION

Currently, the process of global industrialization has become more and more complete, it is exploring towards environmental protection and sustainable development (Jeong et al., 2010; Presti, 2013; Sangiorgi et al., 2017). As a common problem in industrial development, the disposal and reuse of solid organic waste have been puzzling many researchers (Shu and Huang, 2014). Waste tires are one of the main sources of solid organic waste, its massive accumulation and combustion treatment have

caused serious resource waste and environmental pollution (Navarro et al., 2005; Moreno et al., 2012). There is an efficient recycling method, which is to prepare waste tires into crumb rubber (CR) modifier and apply it to pavement engineering. European countries and Asian and African countries have used CR modifier as pavement construction materials for many years (George et al., 2012). The performance of asphalt binder prepared with CR modifier can be improved remarkably (Paje and Bueno, 2010). Crumb rubber modified asphalt (CRMA) can improve rut resistance, reduce fatigue cracking and decrease water damage of pavement (Thodesen et al., 2009). Also, anti-aging ability of CRMA is stronger, which is because the crumb rubber increase the thickness of rubber asphalt film, and the crumb rubber contains carbon black and other antioxidant components. Compared with SBS modified asphalt which is more widely used in pavement (Xiang et al., 2015), CRMA has an obvious economic advantage due to its wide sources of raw materials and low processing cost (Karlsson and Isacson, 2003; Shen et al., 2009; Putman and Amirkhanian, 2010).

However, there are bottlenecks in the application of CRMA: poor workability due to high viscosity, bad storage stability on account of poor compatibility between CR modifier and matrix asphalt (MA) (Elvira, 2013). The most effective solution is to pre-activate CR. Treatment methods of activate CR includes: microwave method, ultrasonic method, active gas method, biological desulfurization method and so on (Nikolskii et al., 2014; Torretta et al., 2015; Kedarisetty et al., 2016). Study found that most of the pre-treatment is not controlled or activation process is complicated (Shatanawi et al., 2009), such as: ultrasonic method will destroy the C-C bond which is a useful chemical bond inside the asphalt during the activation process. Active gas method needs to feed the degraded CR with strong oxidizing gas under high temperature conditions, this process is complicated and expensive, which is not suitable for industrial production. This study use microwave technology to motivate CR.

Many studies revealed that microwave treatment is not only effective, but also easy to control, and is suitable for the application of pavement engineering. Xu found that microwave-activated crumb rubber asphalt (MACRMA) is superior to CRMA in terms of fatigue resistance and aging resistance (Xu et al., 2015). For the physical and chemical changes of CR, Aoudia found that microwave activation can break the C-S and S-S bonds, at the same time maintain the C-C bond (Aoudia et al., 2017). Ming used a microwave oven to irradiate 50 g of CR each time, the activation process lasts for 5 min and the power of the microwave oven is 500 W. He found that microwave has an effect of degradation and de-vulcanization on CR (Liang et al., 2017). When Zhang desulfurized the CR particles, he found that a shorter microwave action time can activate the CR more effectively (Poyraz et al., 2013). Long microwave exposure periods resulted in breaking of chemical bonds, decrease of insoluble phase content and increase the rubber fluidity (Garcia et al., 2015). Furthermore, microwave treatment can change the apparent morphology of the CR, which mainly increases the roughness of CR and sometimes makes CR appear holes (Yin et al., 2013). Although the microwave

treatment has higher activation efficiency, the activation mechanism is still unclear.

With regard to the aging research, all asphalt materials will age due to light, oxygen, water, high temperature and other factors, and MACRMA are no exception (Sun and Lu, 2003; Kang et al., 2007). Many studies have been reported about the aging simulation of rubber asphalt materials (Huang et al., 1996; Ghavibazoo and Abdelrahman, 2014). The international tests for short-term aging and long-term aging of asphalt are thin film oven test (TFOT) and pressure aging vessel (PAV) test. Rubber asphalt, due to the complex components, will undergo various polymerization, cracking and oxidation reactions after aging, and one or more reactions will occur simultaneously depending on the degree of aging. The CR will absorb the light components in asphalt and cause swelling. The swelling reaction will occur continuously during aging and lead to the difference of performance after aging (González et al., 2010). But Amir found that the aging of matrix asphalt is not affected by ordinary CR, and the anti-aging ability of CRMA cannot be increased by increasing the amount of CR (Ghavibazoo and Abdelrahman, 2014). He believed that aging made the temperature sensitivity of rubber asphalt worse, and the degree of aging depends on the interaction between crumb rubber and asphalt. Churchill and Mohamed found that with the aging continue, the penetration and ductility decreased, the softening point increased, the saturated and aromatic content in asphalt decreased, and the macromolecular substances such as gums increased (Dhalaan, 1982; Churchill and Amirkhanian, 1995).

As a kind of polymer, the physical and chemical properties of CRMA can be analyzed by many methods. For example, Mohamed used X-ray technology to analyses the changes of chemical substances in aged asphalt (Siddiqui et al., 2002). In this study, the technology of GPC and FTIR were used to test microstructure of asphalt materials. GPC is a simple and fast separation analysis technique developed in the 1960s, this method was used originally to study the molecular distribution characteristics of polymers in asphalt (Lee et al., 2009). Putman found that the asphaltenes which has the most molecular in asphalt have excellent correlation with the large molecular size fraction. At the same time, Doh showed that the content of LMS was correlated with the viscosity and temperature sensitivity of asphalt (Doh et al., 2008). FTIR can describe the changes of asphalt components intuitively, and it has been widely used in the research of asphalt blending mechanism and aging characteristics. Lu used FTIR-ATR to study the aging process of SBS modified asphalt, and he found that the number of hydroxyl in asphalt gradually increased, and pointed out that the addition of antioxidants could inhibit the increase of hydroxyl (Lu, 2010). Liu studied the functional groups of rubber asphalt during the aging process by FTIR, and found that the number of carbonyl group was significantly changed by aging effect (Liu et al., 2017). According to the current research, the explanation of aging mechanism is not uniform, and the influence of microwave activation on CRMA is not clear.

Pre-treating crumb rubber with microwave treatment to prepare MACRMA has already reported in our previous research. Thus, this work aims to further study the change

**TABLE 1 |** Technical properties of matrix asphalt.

Item	Specification	Result	Test method
Penetration (25°C, 100 g, 5 s) (0.1 mm)	80–100	82	T 0604-2011 (JTG E20-2011, 2011)
Softening point (°C)	>44	46	T 0606-2011 (JTG E20-2011, 2011)
Ductility (5 cm/min, 15°C) (cm)	>100	>100	T 0605-2011 (JTG E20-2011, 2011)
Wax content (%)	≤2.2	1.9	T 0615-2011 (JTG E20-2011, 2011)
Flash point (°C)	≥245	301	T 0611-2011 (JTG E20-2011, 2011)
Solubility (%)	≥99.5	99.5	T 0607-2011 (JTG E20-2011, 2011)
Dynamic viscosity (60°C) (Pa·s)	>140	145	T 0620-2011 (JTG E20-2011, 2011)

**TABLE 2 |** Technical properties of CR.

Item	Density	Water content	Metal content	Fiber content	Ash content	Acetone extract	Carbon black content	Rubber hydrocarbon
	(kg·m <sup>-3</sup> )	(%)	(%)	(%)	(%)	(%)	(%)	(%)
Specification	260–460	<1	<0.03	<1	≤8	≤22	28	≥42
Result	302.5	0	0.009	0.065	7.3	7.2	30	52

mechanism of the rubber asphalt performance after microwave treatment from the perspective of physical and chemical changes, as well as the effect of aging on MACRMA. Three kinds of asphalt (MA, CRMA, MACRMA) are analyzed by four common tests (penetration, softening point, ductility and viscosity test) and DSR test to study the physical indicators changes. GPC and FTIR techniques were used to quantitatively analyze the molecular composition and functional group changes of asphalt before and after aging. Finally, this work try to explain the mechanism of MACRMA changes by doing a statistical analysis of the correlation between the indicators.

## MATERIALS AND METHODS

### Matrix Asphalt

Matrix asphalt of penetration grade 80/100 was used to produce MACRMA, **Table 1** shows the basic properties of matrix asphalt.

### Crumb Rubber

The 40-mesh (the sieve size is 0.45 mm) CR which was made at room temperature was used in this study. **Table 2** shows the basic properties of CR.

### Preparation of MACRMA

In this study, the preparation of MACRMA mainly includes three steps (Li et al., 2019). **Figure 1** shows some detailed information of this process.

**Step 1:** Put the original CR in a constant temperature oven at 60°C for 30 min to dry and then weigh 100 g of dried CR for microwave treatment. The activation process lasts for 90 s and the power of the microwave oven is 800 W. Put treated CR in a desiccator to cool down for 24 h.

**Step 2:** Weigh 500 g of matrix asphalt binder into a beaker and heat it to a fully flowing state (approximately 135°C). Then put the beaker into a thermostatic magnetic stirrer for heat preservation.

**Step 3:** Raise the temperature of stirrer rapidly to 190°C and add the treated CR slowly to the matrix asphalt binder, at the same time start stirring. The stirring rate needs to be slowly increased to 1500 r/min. After 60 min of mixing and development, the MACRMA is ready.

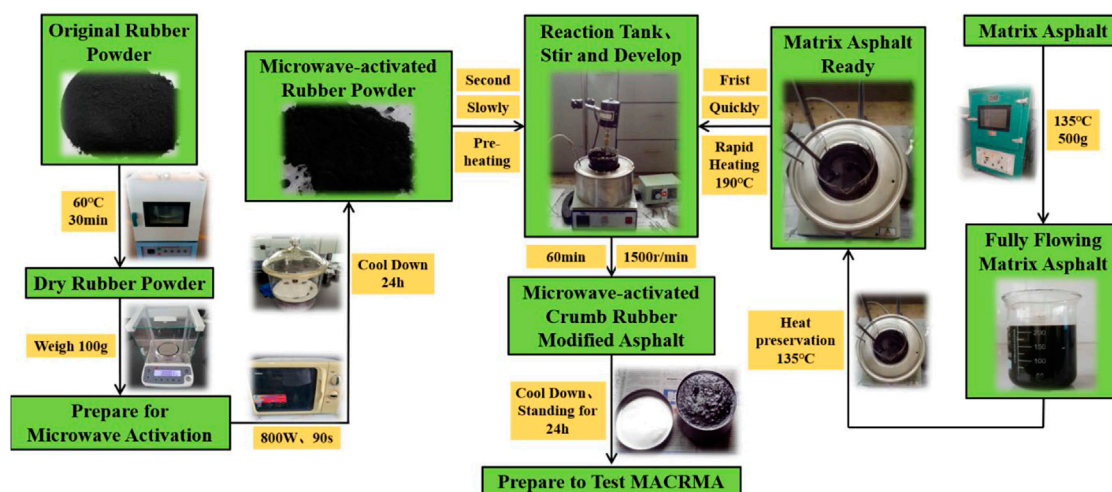
In addition, preparation of MACRMA should pay attention to maintaining the reaction temperature of each step. And **Figure 2** is SEM images of crumb rubber before and after microwave activation. In the image magnified 500 times, the microwave activation makes the CR fluffy. Many micropores appear on the surface of the CR and the aggregation of micro particles directly increases the specific surface area of CR, which makes the fusion between CR and asphalt more efficient.

### Experimental Design and Test Methods

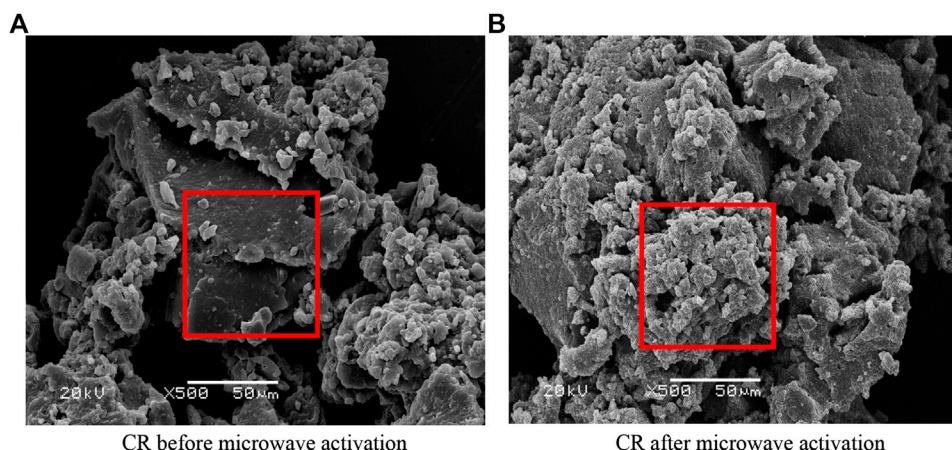
The experimental design and test method of this study are shown in **Figure 3**. Test method of matrix asphalt and CRMA (crumb rubber modified asphalt without microwave activation treatment) is the same as that of MACRMA. There are at least three groups for each test and sample.

This study uses TFOT and PAV test which are international standard test method to simulate the aging phenomenon of bitumen materials. TFOT is used to simulate short-term aging of asphalt during the production, transportation, mixing and construction process under high temperature and oxygen coupling. PAV test is used to simulate long-term aging of asphalt during actual road use.

In addition to the basic physical indicators of asphalt, the viscoelasticity of asphalt was also tested using a DSR. The test temperature of the temperature-sweep tests is 58–82°C, and the



**FIGURE 1** | Detailed preparation process of MACRMA.



**FIGURE 2** | SEM images of CR before and after microwave activation. (A) CR before microwave activation (B) CR after microwave activation.

change interval is 6°C. The parameters of this test are complex module ( $G^*$ ) and phase angle ( $\delta$ ).

GPC tested is generally used to determine the molecular distribution characteristics of polymers. When the polymer solution flows through the chromatographic column, the larger molecules are excluded from the pores of particles, which can only pass through the interparticle spaces between particles at a faster rate; while the smaller molecules can enter the holes in the particles at a much slower rate. Previous studies have shown that the content of asphaltene in asphalt has a good correlation with the macromolecules. In this study, the Waters 1,515 gel permeation chromatography produced by Waters Corporation of the United States was used. The mobile phase was tetrahydrofuran (THF), the flow rate was 1.0 ml/min, and the concentration of the sample solution was 1.0 mg/ml. The GPC tests were carried out on asphalt before and after aging to analyze the changes in molecular weight during asphalt aging.

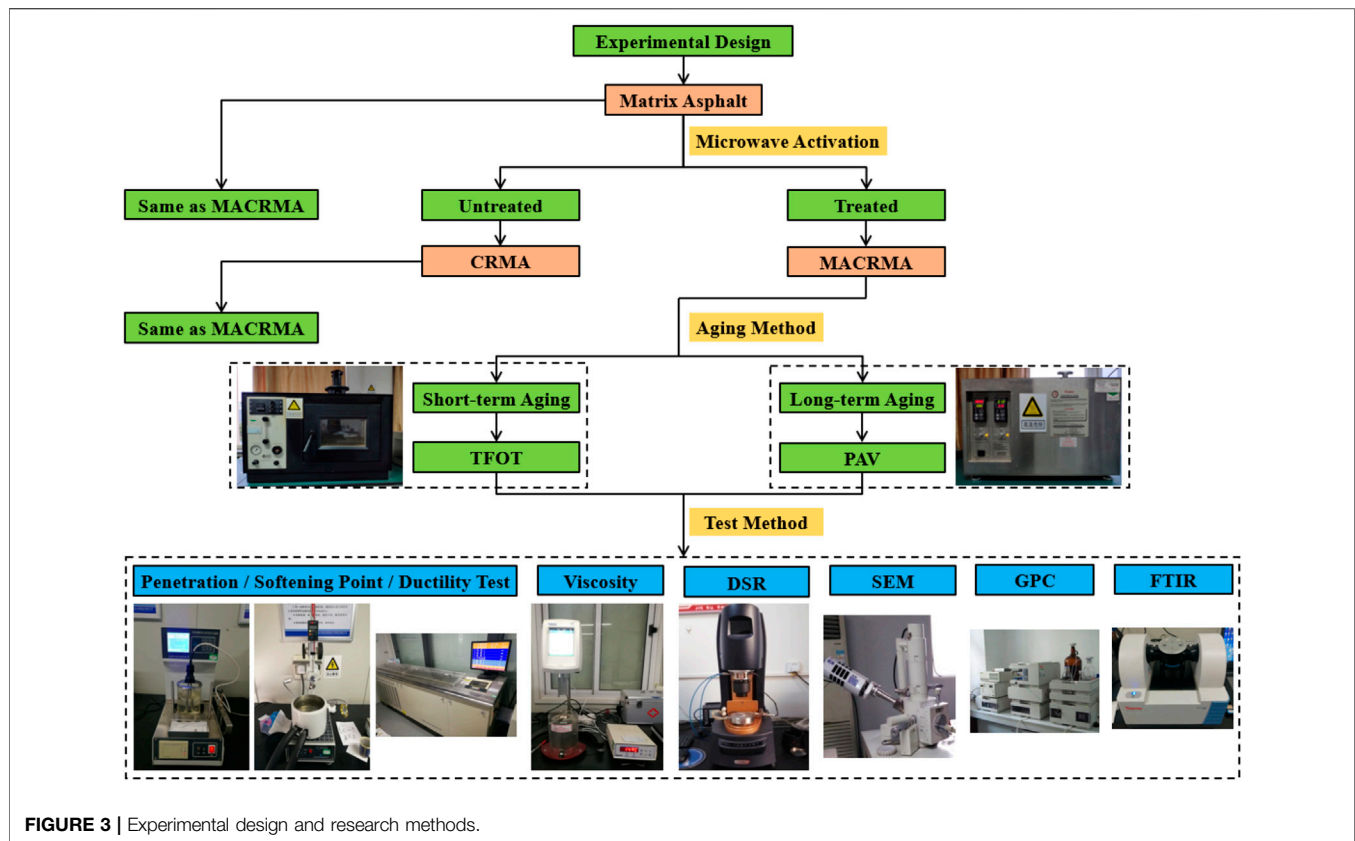
A Thermo Fisher Scientific Nicolet iS10 fourier transform infrared spectrometer matching the ATR accessory was used. Its infrared accessory is made of diamond crystal (refractive index 2.4), and the optical path is single reflection attenuated total reflection. The number of scans during the test is set to 32, the resolution is  $4\text{ cm}^{-1}$ , and the wavenumber range is  $4,000\text{--}650\text{ cm}^{-1}$ . This test method is simple, convenient and fast. Only need to smear or titrate asphalt on the diamond crystal plate to quickly collect its infrared spectrum test spectrum.

## RESULTS AND DISCUSSION

### Aging Index Analyses

The changes of matrix asphalt, CRMA and MACRMA before and after aging were calculated by using penetration, softening point, ductility and viscosity as evaluation indexes, and used as aging





factors to evaluate the aging resistance of rubber asphalt (as shown in **Figure 4**), so as to explore the effect of microwave activation of crumb rubber on the anti-aging properties of rubber asphalt.

### The Percentage of the Reduction of Penetration (PR)

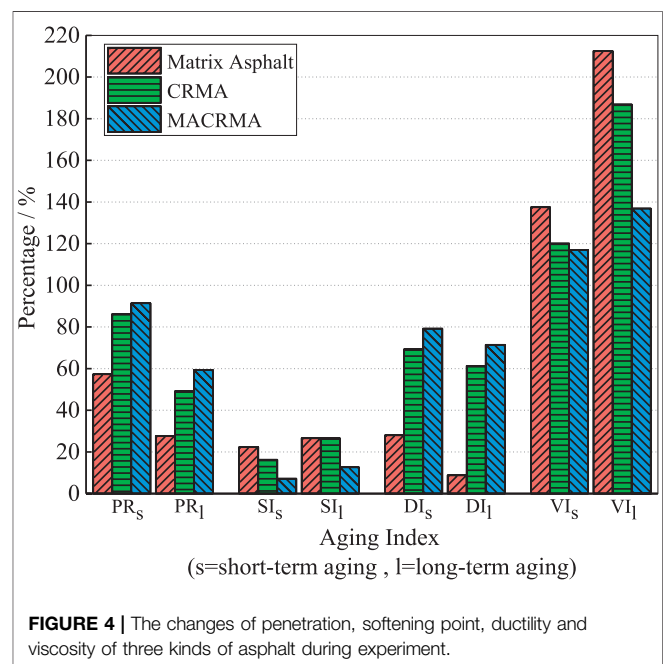
The asphalt will become brittle and hard after aging, and the penetration will be reduced to varying degrees. The reduction of penetration can reflect the degree of aging of asphalt. The larger the reduction value, the less likely the asphalt is to age. The value of *PR* is calculated as follows:

$$PR = \frac{P}{P_0} \times 100\% \quad (1)$$

where  $P_0$  is the value of penetration before aging,  $P$  is the value of penetration after aging.

**Table 3** shows the penetration test results of three kinds of asphalt before and after aging. Whether the short-term aging or long-term aging stage, the *PR* values of matrix asphalt is significantly lower than other two rubber asphalt, which indicates that the aging resistance of matrix asphalt is poor. The  $PR_s$  and  $PR_L$  of CRMA were 0.86 and 0.49 respectively. Compared with matrix asphalt, the aging resistance of CRMA is significantly improved. In addition, the *PR* value of MACRMA is 0.91 in the short-term aging and 0.58 in the long-term aging, indicating that the aging resistance of MACRMA is further improved compared with matrix asphalt and CRMA. There

are two main reasons for the improvement of the aging resistance of MACRMA. On the one hand, the specific surface area of activated crumb rubber is larger than that of ordinary





**TABLE 3 |** Penetration test results of three kinds of asphalts at different aging stages.

Types	Penetration (0.1 mm)			$PR_S$ (%)	$PR_L$ (%)
	Before aging	TFOT	PAV		
Matrix asphalt	90.7	52.0	25.1	57.33	27.67
CRMA	43.6	37.6	21.4	86.24	49.08
MACRMA	40.6	37.1	24.1	91.38	59.36

Note:  $PR_S$  = the value of PR after short-term aging,  $PR_L$  = the value of PR after long-term aging.

crumb rubber, it is easier to contact with asphalt binder. Therefore, there is still a severe swelling reaction in the aging process, which slows down the aging effect of asphalt. On the other hand, the activated crumb rubber contains internal content when it is dissolved into asphalt. Carbon black and other natural anti-aging components can be dissolved in asphalt, so as to better resist the thermal and oxygen aging effect to a certain extent. Therefore, the comprehensive action of the two can improve the anti-aging property of activated rubber asphalt.

### The Percentage of the Increase of Softening Point (SR)

Many studies have shown that it is highly reliable to use the softening point rise rate as the index to evaluate the anti-aging property of asphalt. The softening point of asphalt will increase after asphalt aging. By comparing the softening point difference before and after aging, the aging degree of asphalt can be evaluated. The softening point of different bituminous specimens is quite different. The higher the rate of softening point increase, the greater the increase in softening point after aging and the worse aging resistance. The value of SR is calculated as follows:

$$SR = \frac{SP - SP_0}{SP_0} \times 100\% \quad (2)$$

where  $SP_0$  is the value of softening point before aging,  $SP$  is the value of softening point after aging.

**Table 4** shows the softening point test results of three kinds of asphalt before and after aging. It can be seen from the table that the softening point of matrix asphalt before aging is 47.1°C. And the softening points of CRMA and MACRMA are 62.9 and 68.7°C, which are significantly higher than that of matrix asphalt. In addition, the increase rate of softening point of

matrix asphalt is significantly higher than that of other two rubber asphalt, either in the short-term or long-term aging stage, which indicates that the aging resistance of matrix asphalt is the worst. Compared with the increase rate of CRMA and MACRMA after aging, in the short-term aging stage the increase rate of CRMA is 0.16, and that of MACRMA is 0.07; in the long-term aging stage, the increase rate of CRMA is 0.23, and that of MACRMA is 0.13. The increase rate is small, and microwave can significantly improve the aging resistance of rubber asphalt and slow down the attenuation of asphalt performance.

### The Percentage of the Reduction of Ductility (DR)

Ductility is a test index to characterize the low-temperature performance of asphalt. The larger the ductility is, the better the low-temperature deformation ability of asphalt is, the stronger the low-temperature crack resistance is, and the less likely the asphalt pavement is to crack. In order to distinguish the low temperature ductility and flexibility between the matrix asphalt and rubber asphalt better, the test temperature of matrix asphalt is 10°C, and the test temperature of rubber asphalt is 5°C. Compared with the ductility value before and after aging, the greater the reduction is, the better the aging resistance of asphalt is. The value of  $DR$  is calculated as follows:

$$DR = \frac{D}{D_0} \times 100\% \quad (3)$$

where  $D_0$  is the value of ductility before aging,  $D$  is the value of ductility after aging.

**Table 5** shows the ductility test results of three kinds of asphalt in different aging stages. It can be seen from the table that the ductility value of three kinds of asphalt declines to different degrees after aging. The ductility value is related to the distribution of molecular content of asphalt. The more small molecular content is, the softer the asphalt is, and the greater the ductility value is. Aging changes the structure of components in asphalt, some small molecular substances such as aromatics are transformed into macromolecular substances such as asphaltic, which makes asphalt hard. Reduce the ductility. The ductility of matrix asphalt decreased significantly compared with rubber asphalt ductility.  $DR_S$  and  $DR_L$  were 0.28 and 0.09, which were lower than CRMA and MACRMA. The  $DR_S$  and  $DR_L$  values of MACRMA are 0.79 and 0.71, indicating that they have good aging resistance of short-term aging and long-term aging.

**TABLE 4 |** Softening point test results of three kinds of asphalts at different aging stages.

Types	Softening point (°C)			$SR_S$ (%)	$SR_L$ (%)
	Before aging	TFOT	PAV		
Matrix asphalt	47.1	57.6	59.6	22.29	26.54
CRMA	62.9	73.1	79.6	16.22	26.55
MACRMA	68.7	73.6	77.4	7.13	12.66

Note:  $SR_S$  = the value of SR after short-term aging,  $SR_L$  = the value of SR after long-term aging.

**TABLE 5 |** Ductility test results of three kinds of asphalts at different aging stages.

Types	Ductility (cm)			$DR_S$ (%)	$DR_L$ (%)
	Before aging	TFOT	PAV		
Matrix asphalt	100	28	8.8	28.00	8.80
CRMA	6.2	4.3	3.8	69.34	61.29
MACRMA	7.7	6.1	5.5	79.22	71.43

Note:  $DR_S$  = the value of DR after short-term aging,  $DR_L$  = the value of DR after long-term aging.

**TABLE 6 |** Viscosity test results of three kinds of asphalts at different aging stages.

Types	Viscosity (Pa·s) (135°C)			VR <sub>s</sub> (%)	VR <sub>L</sub> (%)
	Before aging	TFOT	PAV		
Matrix asphalt	0.32	0.44	0.68	137.50	212.50
CRMA	2.74	3.29	5.12	120.07	186.86
MACRMA	2.93	3.43	4.01	117.06	136.86

Note: VR<sub>s</sub> = the value of VR after short-term aging, VR<sub>L</sub> = the value of VR after long-term aging.

### The Changes of Viscosity (VR)

Another important index to evaluate the performance of rubber asphalt is viscosity values. The degree of change of viscosity of rubber asphalt with temperature reflects its temperature sensing performance, and the change of aging rubber asphalt with chemical structure must cause the change of viscosity. The value of VR is calculated as follows:

$$VR = \frac{V}{V_0} \times 100\% \quad (4)$$

where  $V_0$  is the value of viscosity before aging,  $V$  is the value of viscosity after aging.

**Table 6** shows the viscosity values of three kinds of asphalt in different aging stages. It can be seen from the table that the viscosity value of both matrix asphalt and rubber asphalt increases significantly after aging, which is due to the increase of macromolecular content in asphalt, the increase of friction resistance between asphalt molecules and the decrease of fluidity. According to the changes of VR value, the aging resistance of three kinds of asphalt is sorted: MACRMA > CRMA > MA, which is basically the same as those of above results.

### DSR Analyses

#### G\* & δ

Due to the chemical properties of asphalt is complexity, the routine physical index test can not characterize the asphalt performance completely. Therefore, this section uses DSR to test the viscoelasticity of asphalt and tries to establish a connection between the test indicators and pavement performance.

**Figure 5** present the temperature scanning curves of  $G^*$  and  $\delta$  of three kinds of asphalt. As seen from the data, the value of  $G^*$  (**Figures 5A–C**) decreases with the increase of test temperature, while the value of  $\delta$  (**Figures 5D–F**) shows the opposite trend, which is proportional to the increase of temperature. The increase of temperature changes the proportion of viscoelasticity of asphalt. The change trend of the temperature scanning curve of CRMA and MACRMA is the same as that of matrix asphalt, but the microwave action makes the height of the curve of  $G^*$  increase, and the curve from high to low is in order: MACRMA > CRMA > matrix asphalt. At the same time, the microwave action makes the curve height of  $\delta$  decrease, the height of the curve from high to low is: matrix asphalt > CRMA > MACRMA.

It should be noted that the effect of aging on the same rheological index is different. The gap between  $G^*$  of three

kinds of asphalt is gradually widened as the aging effect deepens. When the test temperature is 58°C, the  $G^*$  of matrix asphalt before aging is 2.421 KPa, and the  $G^*$  after short-term aging and long-term aging is 5.262 and 17.246 KPa, with an increase in 117.4 and 612.4% respectively. However, for CEMA and MACRMA, the effect of aging on the growth rate of  $G^*$  is significantly reduced. After short-term and long-term aging, the growth rates of  $G^*$  in CRMA are 30.6 and 111.1%, and that in MACRMA are 17.5 and 82.3%. Therefore, the effect of thermal oxygen aging on matrix asphalt is more significant than that of CRMA and MCMA. For MACRMA, compared with long-term aging, the temperature curve of  $G^*$  after short-term aging has little difference with that before aging, indicating that long-term aging has a greater influence of MACRMA.

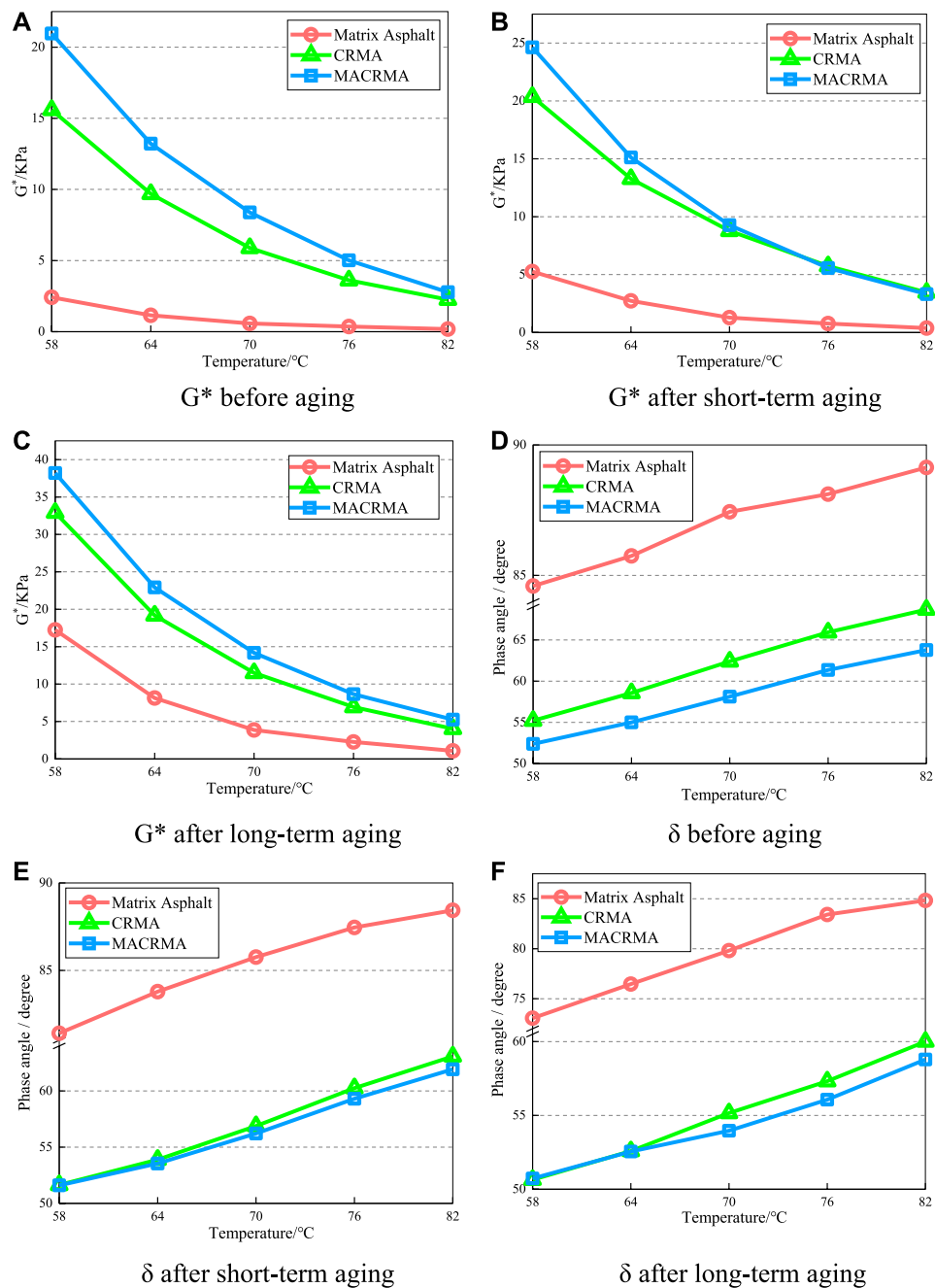
#### G\*/sinδ

The rutting factor ( $G^*/\sin\delta$ ) is used to describe the ability of asphalt materials to resist permanent deformation at high temperatures. The larger the  $G^*/\sin\delta$ , the better the high temperature stability.

The test results of  $G^*/\sin\delta$  was shown in **Figure 6**. From the data,  $G^*/\sin\delta$  of three kinds of asphalt decrease with the increase of scanning temperature, which shows that the viscosity of asphalt increases with the increase of temperature. The height of  $G^*/\sin\delta$  always meets the change of MACRMA > CRMA > matrix asphalt. Therefore, microwave activation enhances the high-temperature deformation resistance of rubber asphalt. With the aging process, the gap between  $G^*/\sin\delta$  of three kinds of asphalt increases gradually, but the increasing multiple of  $G^*/\sin\delta$  decreases gradually. When the test temperature is 58°C, the  $G^*/\sin\delta$  of the matrix asphalt before aging is 2.432 KPa, that of CRMA and MACRMA are 18.988 and 26.459 KPa, and the increase times are 6.81 and 9.88. After short-term aging and long-term aging, enhancement range of  $G^*/\sin\delta$  of three kinds of asphalt decreased. In short-term aging, that of CRMA and MACRMA were 25.977 and 31.426 KPa, with the increase times of 3.88 and 4.91. In long-term aging, that of CRMA and MACRMA were 42.573 and 49.361 KPa, with the increase times of 1.36 and 1.74. The results shown that aging can improve the high-temperature deformation resistance of rubber asphalt.

### GPC Analyses

Three kinds of asphalts were tested by GPC before and after aging, and the LMS value can be calculated from the chromatogram. In the chromatogram, the abscissa is transit time and the ordinate is signal value. The change in the curve area represents the changes in the content of different molecules in the asphalt. The GPC chromatogram can be divided into thirteen equal parts, which are divided into Large Molecular Size (LMS) (one to five equal parts), Medium Molecular Size (MMS) (six to nine equal parts) and Small Molecular Size (SMS) (10–13 equal parts) from left to right. Previous studies have shown that the value of LMS has a good correlation with asphalt properties (Kim and Lee, 2013), so this study only consider the changes of LMS.

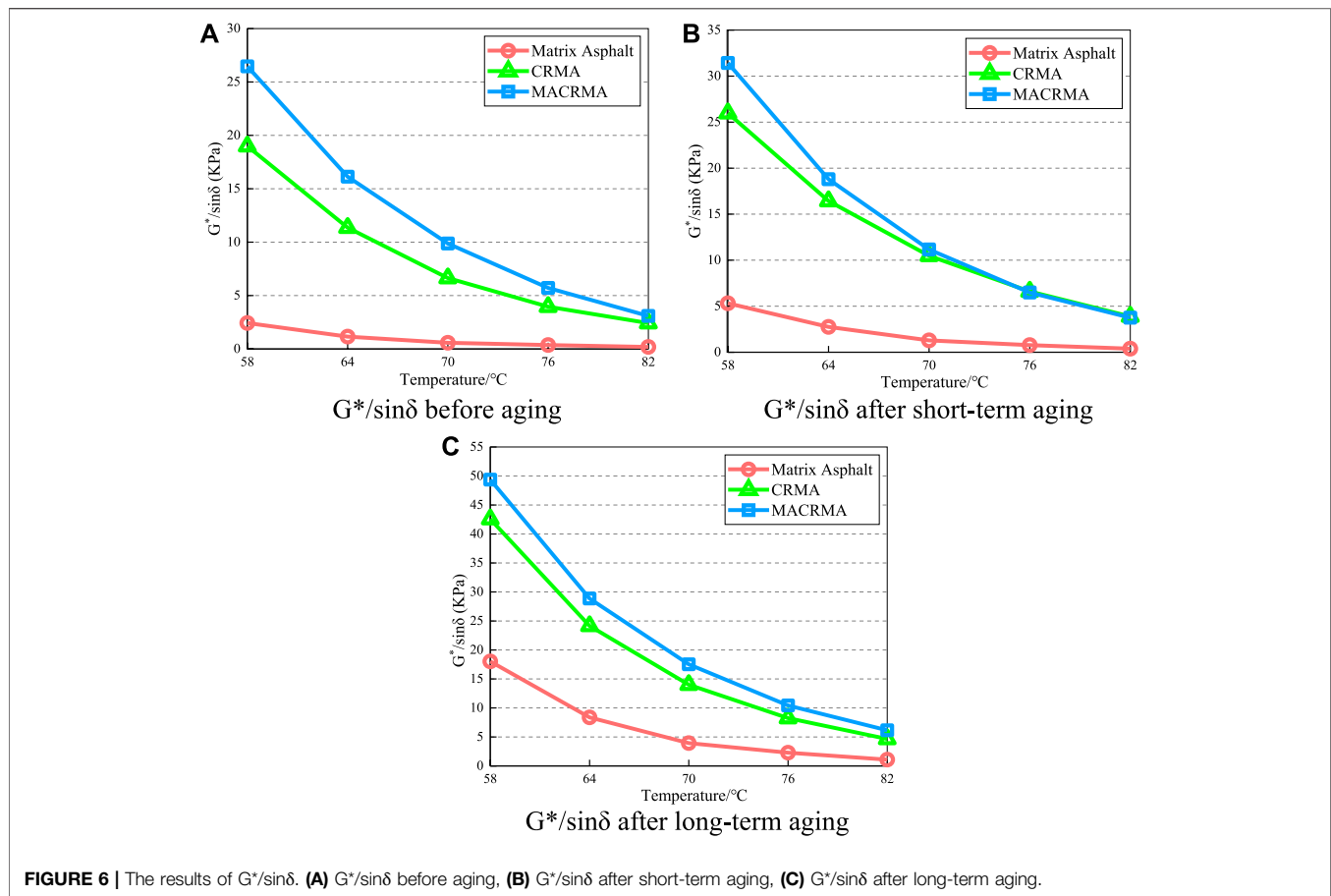


**FIGURE 5 |** The test results of  $G^*$  and  $\delta$ . (A)  $G^*$  before aging, (B)  $G^*$  after short-term aging, (C)  $G^*$  after long-term aging, (D)  $\delta$  before aging, (E)  $\delta$  after short-term aging (F)  $\delta$  after long-term aging.

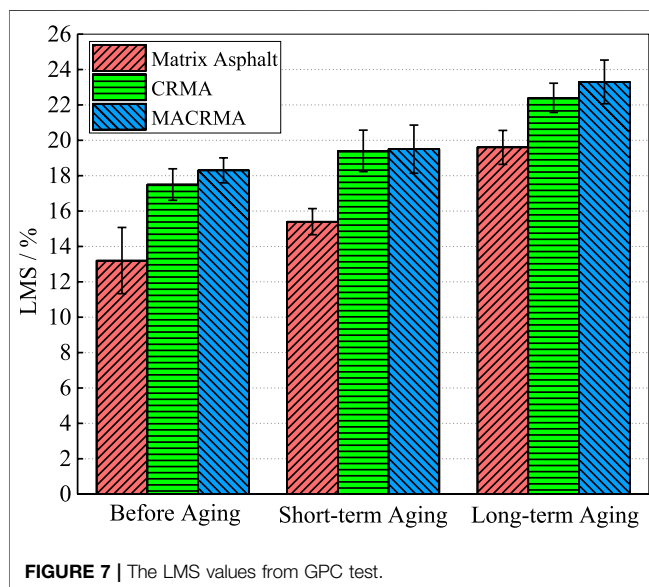
## LMS Content

The calculation result of LMS value is shown in **Figure 7**. From the data, the values of LMS of the matrix asphalt among three kinds of asphalts is the lowest, with an average of only 16.07%. Then it is CRMA, with an average of 19.77%, and the highest LMS content is MACRMA, with an average of 20.37%. Compared with the matrix asphalt, crumb rubber is added to the asphalt. After high-speed shearing, the light components

inside asphalt enter the rubber network structure, changing the colloidal structure of asphalt, increasing the asphaltene and saturated content, so the value of LMS increases. After microwave treatment, the surface activity of crumb rubber is enhanced, the mutual solubility between crumb rubber and asphalt is more intense, and the conversion of light components into asphaltene becomes easier, so the LMS content of MACRMA is further increased.



**FIGURE 6 |** The results of  $G^*/\sin\delta$ . (A)  $G^*/\sin\delta$  before aging, (B)  $G^*/\sin\delta$  after short-term aging, (C)  $G^*/\sin\delta$  after long-term aging.



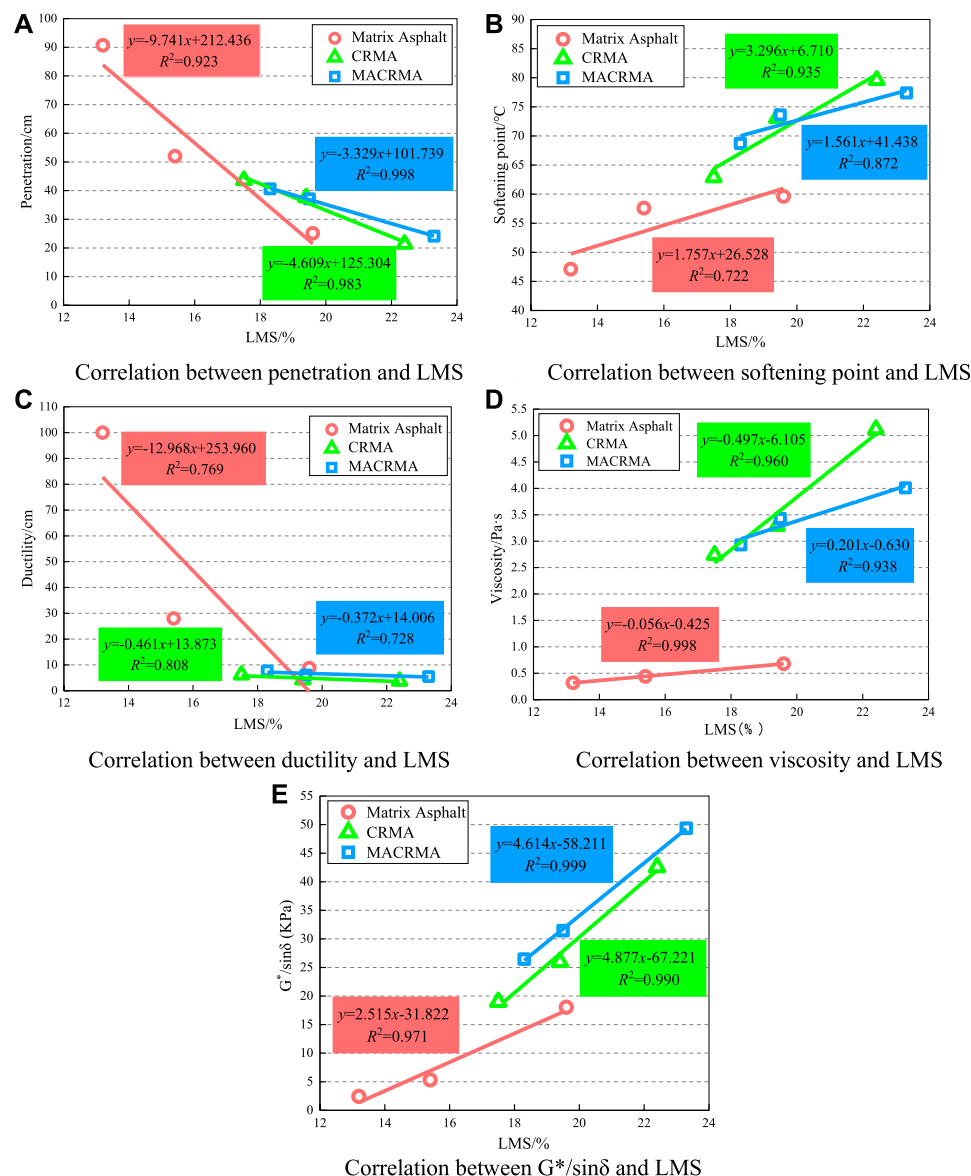
**FIGURE 7 |** The LMS values from GPC test.

Comparing the LMS values under different aging states, it can be found that after short-term aging and long-term aging, the LMS content of the three asphalts shows a significant increase trend. The LMS content of the matrix asphalt increased by 16.7

and 48.5% compared with that before aging. CRMA growth rates were 10.9 and 28.0%, and MACRMA growth rates were 6.6 and 27.3%. Obviously, the conversion rate of LMS content of MACRMA is the lowest. According to our previous research results (Yang, 2017), the specific surface area of the crumb rubber after microwave treatment for 90 s can reach 1.15 times that of untreated. Zhang's research shows that the crumb rubber surface is rough before aging, there are many angled small holes, after aging crumb rubber surface will become flat and smooth, the number of small holes reduced (Zhang, 2018). It can be reasonably inferred from this that because the microwave action increases the microscopic surface pores of the crumb rubber in advance, so that the crumb rubber can resist a longer aging effect, so the swelling reaction between the microwave activated crumb rubber and matrix asphalt can last longer. In the same aging time, the LMS value of MACRMA only reached a low level. Similarly, for the same LMS value, MACRMA can resist the aging effect for a longer time.

### Correlation Between Test Indicators and LMS Content

Correlation analyses of LMS content and test indicators can reveal the aging mechanism and explore the relationship between micro mechanism and macro law. The results are shown in Figure 8. The data presents that the correlation coefficients between the LMS content and the various indexes



**FIGURE 8 |** Correlation analyses between test indicators and LMS. **(A)** Correlation between penetration and LMS, **(B)** Correlation between softening point and LMS, **(C)** Correlation between ductility and LMS, **(D)** Correlation between viscosity and LMS, **(E)** Correlation between  $G^*/\sin\delta$  and LMS.

are high. For indicators of penetration, viscosity and rutting factor, their correlation coefficients are all greater than 0.9, especially between LMS and rutting factor, the correlation coefficient is 0.999. This proves that the LMS content has a significant effect on the penetration, viscosity and rutting factor of rubber asphalt. As for the ductility, the correlation is lower with the value of 0.808. The reason may be that, in ductility test, matrix asphalt will have a higher deformation, and the low fluidity caused by the friction between the rubber particles will hinder the deformation of asphalt, then the concentration of stress at the interface between the crumb rubber and the matrix asphalt makes the rubber asphalt fracture irregularly. The gradual increase of LMS value proves that during the aging process, the light

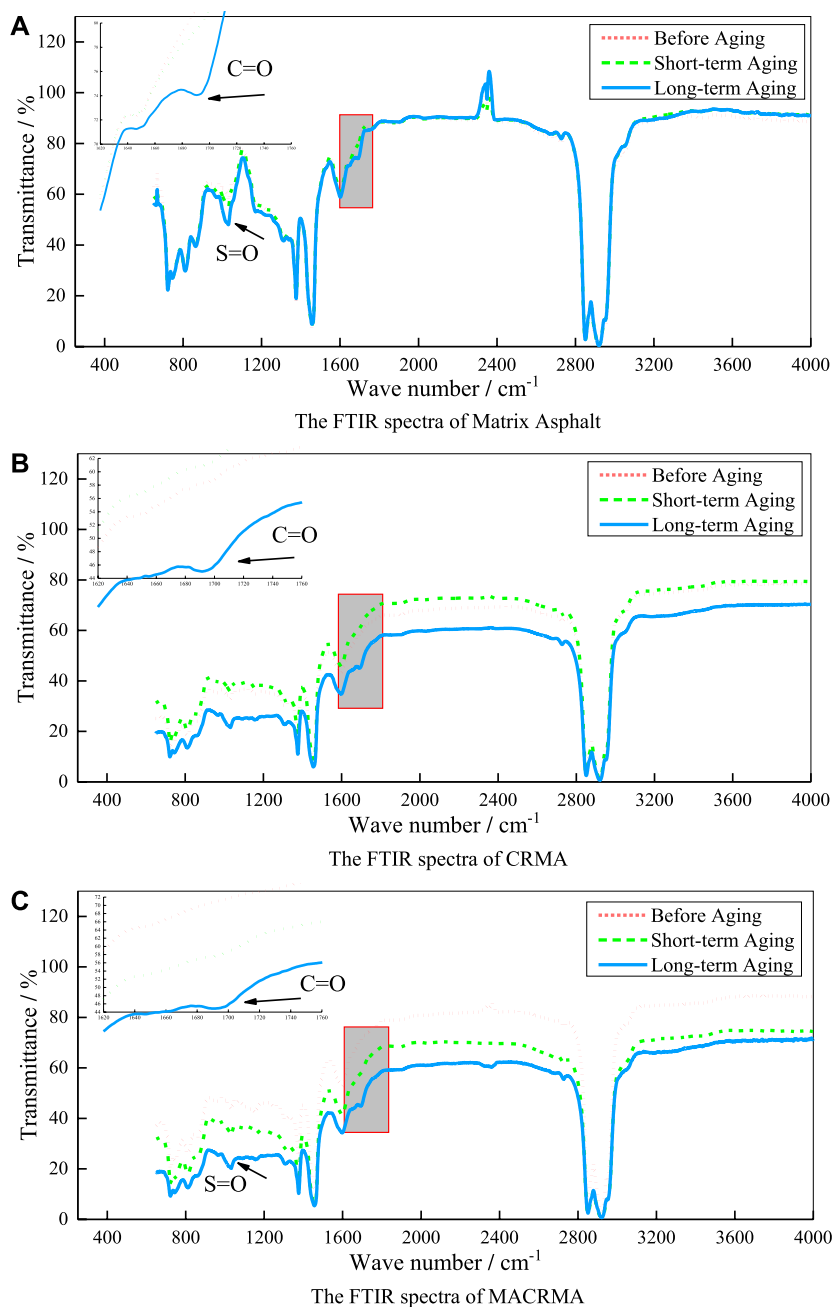
components in rubber asphalt are constantly volatilizing and are constantly being converted into asphaltenes. The change of LMS content has a significant impact on the test index. So, the performance change and aging state can be quantitatively characterized by LMS in rubber asphalt.

## FTIR Analyses

The microstructure changes of three kinds of asphalts before and after aging are quantitatively analyzed by FTIR. The test results are shown in **Figure 9**.

Firstly, by comparing different asphalt materials, we found that the functional groups in spectrum are basically the same. There are no new characteristic peaks and functional groups





**FIGURE 9 |** Changes in the FTIR spectra of three kinds of asphalt before and after aging. **(A)** The FTIR spectra of Matrix Asphalt, **(B)** The FTIR spectra of CRMA, **(C)** The FTIR spectra of MACRMA.

appeared in the MACRMA spectrum, only the peak intensity changed. It shows that the microwave effect is mainly physical, and it can only enhance or weaken certain properties of CRMA.

Then mainly discuss the effect of aging on rubber asphalt. Among the hydroxyl and carboxyl groups of asphalt aging products, only carboxyl groups are related to oxidation. All polymer materials will produce carboxyl groups after aging, so carboxyl groups have the effect of accelerating oxidation (Wang et al., 2015). Observing the spectrum of CRMA and MACRMA, it

can be found that the absorption peaks (caused by the C=C skeleton vibration of the conjugated double bond of the benzene ring) of the two rubber asphalts around 1,600 cm<sup>-1</sup> are slightly weakened. Compared with the unaged spectrum, the short-term aging of rubber asphalt did not appear new functional groups, and the long-term aging samples showed a weak carbonyl absorption peak near 1,700 cm<sup>-1</sup>, indicating the formation of carboxylic acid or ketone in the asphalt. The characteristic peak at 3,400 cm<sup>-1</sup> is the amines produced after the degradation of the

**TABLE 7 |** Functional groups index of three kinds of asphalt before and after aging.

Types	Condition	$A_{C=O}$	$A_{S=O}$	$A_{C-H}$	$CI$	$SI$
Matrix asphalt	Before aging	0	100.135	13,329.321	0	0.0075
	Short-term aging	18.192	118.573	10,846.120	0.0023	0.0109
	Long-term aging	75.311	181.943	9,393.762	0.0084	0.0193
CRMA	Before aging	0	101.234	15,931.91	0	0.0071
	Short-term aging	0	118.573	13,782.41	0	0.0086
	Long-term aging	78.586	181.504	13,393.83	0.0063	0.0146
MACRMA	Before aging	0	127.651	16,850.960	0	0.0075
	Short-term aging	0	119.027	14,115.700	0	0.0084
	Long-term aging	68.231	154.294	11,632.230	0.0058	0.0133

crumb rubber in the asphalt. So, an important conclusion can be drawn from this phenomenon, that is the aging of rubber asphalt materials includes two parts: one is the aging of matrix asphalt, and the other is the aging of crumb rubber.

During the short-term aging process, the characteristic peak of C=C is enhanced. During the long-term aging, the carbonyl and sulfoxide groups increase. This is because the light components in MACRMA react chemically with oxygen in the air to generate new chemical functional groups with macromolecular structures such as aldehydes, ketones, and sulfoxide groups. These functional groups have polarity, which makes the macromolecular substances in MACRMA aggregate with each other, promotes the conversion of light oils to asphaltenes on a microscopic level, increases the consistency of MACRMA on a macroscopic scale, and accelerates the hardening of MACRMA. These conclusions also explain the reason why the LMS value will continue to increase from a chemical point of view.

In long-term aging, the crumb rubber in asphalt will still undergo a strong swelling reaction. However, the swelling reaction of the crumb rubber in long-term aging is basically over, the asphalt materials mainly undergoes oxygen absorption reaction to generate carbonyl and sulfoxide groups. This is also consistent with the phenomenon of LMS content change in the previous section. The aging action causes the oxidation reaction of the functional groups in the rubber asphalt, which increases the interaction between the asphalt molecules, thereby hardening the asphalt and increasing the stiffness. In the range of 2000~4000  $\text{cm}^{-1}$ , the spectrum of MACRMA is basically similar to that of CRMA, indicating that the thermal oxygen reaction process of MACRMA and CRMA is basically the same, the main difference is only the intensity of the characteristic peak.

The greater the content of carbonyl and sulfoxide groups, the more severe the oxidation of asphalt. In order to further research the changes of chemical structure of three kinds of asphalt before and after aging, this work used carbonyl index and sulfoxide index to quantitatively characterize the evolution of functional groups during aging. The calculation methods and results are as follows:

$$CI = \frac{A_{C=O}}{A_{C-H}} \quad (5)$$

$$SI = \frac{A_{S=O}}{A_{C-H}} \quad (6)$$

where  $CI$  represents the carbonyl index,  $SI$  represents the sulfoxide index,  $A_{C=O}$  represents the carbonyl absorption peak area,  $A_{S=O}$  represents the sulfoxide absorption peak area,  $A_{C-H}$  represents the saturated C-H bond absorption peak area.

From the data in **Table 7**, we can see that the  $SI$  of asphalt materials shows an increasing trend with the increase of aging. There is no carbonyl functional group in the short-term aging stage, but only in the long-term aging stage, indicating that the presence or absence of carbonyl and sulfoxide groups in CRMA cannot be used as a sign of rubber asphalt aging, it can only be used to show whether a chemical reaction has occurred. It can be seen from the data that MACRMA does not show carbonyl groups in the short-term aging stage, but appears in the long-term aging, indicating that long-term aging can significantly accelerate the process of asphalt oxidation reaction. In addition, the sulfoxide index of MACRMA increases with the aging which is similar to the change law of CRMA. Comparing the functional group indexes of three kinds of asphalt, it was found that the carbonyl and sulfoxide functional group indexes of MACRMA are lower than those of CRMA and matrix asphalt, indicating that the aging resistance of MACRMA has been significantly improved, which is related to the physical modification of the crumb rubber by microwave treatment. It is also related to the fact that the activated crumb rubber contains many antioxidant components. The combined effect of the two makes MACRMA have a good anti-aging property.

## CONCLUSION

This work used DSR, GPC, FTIR and other test methods to comprehensively study the physical properties and chemical microstructure changes of MACRMA, and make a comparison with CRMA and matrix asphalt. The discussion results obtained from the test are mainly as follows:

- Compared with CRMA and matrix asphalt, MACRMA has the least performance degradation after aging. The order of anti-aging ability is as follows: MACRMA > CRMA > MA.
- The aging effect reduces the penetration and ductility of rubber asphalt, increases the softening point and viscosity.
- The LMS value of rubber asphalt gradually increased with the intensification of aging. The LMS has a high correlation with the test indicators, and the LMS can be used to quantitatively characterize the anti-aging degree of rubber asphalt materials.
- Microwave activation is mainly a physical process, it does not cause chemical changes of CR.
- The strong anti-aging ability of MACRMA caused by two parts: one is that the CR is physically modified by microwave activation, and the other is CR contains a lot of antioxidants.

## DATA AVAILABILITY STATEMENT

The raw data supporting the conclusions of this article will be made available by the authors, without undue reservation.

## AUTHOR CONTRIBUTIONS

TZ Conceptualization, Methodology. JZ Conceptualization, Writing—Original Draft and Editing, Visualization. QL Investigation. BL Conceptualization, Funding acquisition, Writing—Editing. All authors listed have made a substantial, direct, and intellectual contribution to the work and approved it for publication.

## REFERENCES

- Aoudia, K., Azem, S., Gratton, M., Pettarin, V., and Seghar, S. (2017). Recycling of waste tire rubber: microwave devulcanization and incorporation in a thermoset resin. *Waste Manag.* 60, 471–481. doi:10.1016/j.wasman.2016.10.051
- Churchill, E. V., and Amirkhanian, S. N. (1995). HP-GPC characterization of asphalt aging and selected properties. *J. Mater. Civ. Eng.* 7 (1), 41–49. doi:10.1061/(ASCE)0899-1561(1995)7:1(41)
- Dhalaan, M. A. (1982). *Characterization and design of recycled asphalt concrete mixture using indirect tensile test methods*. Austin, TX: The University of Texas at Austin
- Doh, Y. S., Amirkhanian, S. N., and Kim, K. W. (2008). Analysis of unbalanced binder oxidation level in recycled asphalt mixture using GPC. *Construct. Build. Mater.* 22 (6), 1253–1260. doi:10.1016/j.conbuildmat.2007.01.02
- Elvira (2013). *Micro-analysis of physicochemical interaction between the components of asphalt mixtures with rubber*. Ames, IA: Iowa State University
- Garcia, P. S., Sousa, F. D. B. D., Lima, J. A. D., and Cruz, S. A. (2015). Devulcanization of ground tire rubber: physical and chemical changes after different microwave exposure times. *Express Polym. Lett.* 9 (11), 1015–1026. doi:10.3144/expresspolymlett.2015.91
- González, V., Martínez-Boza, F. J., Navarro, F. J., Gallegos, C., Pérez-Lepe, A., and Páez, A. (2010). Thermomechanical properties of bitumen modified with crumb tire rubber and polymeric additives. *Fuel Process. Technol.* 91, 1033–1039. doi:10.1021/ef049699a
- George, B., Way, P. E., Kaloushand Kamil, E. (2012). *Asphalt rubber standard practice guide*. Available at: [http://www.rubberpavements.org/ARTIC/Guidelines/ARTIC\\_Guidelines\\_RPA\\_A1751.html](http://www.rubberpavements.org/ARTIC/Guidelines/ARTIC_Guidelines_RPA_A1751.html)
- Ghaviabazoo, A., and Abdelrahman, M. (2014). Effect of crumb rubber modification on short term aging susceptibility of asphalt binder. *Int. J. Pavem. Res. Technol.* 7 (4), 297–304. doi:10.6135/ijprt.org.tw/2014
- Huang, S. C., Tia, M., and Ruth, B. E. (1996). Laboratory aging methods for simulation of field aging of asphalts. *J. Mater. Civ. Eng.* 8 (3), 147–152. doi:10.1155/2018/3428961
- Jeong, K. D., Lee, S. J., and Amirkhanian, S. N. (2010). Interaction effects of crumb rubber modified asphalt binders. *Construct. Build. Mater.* 24 (5), 824–831. doi:10.1155/2013/415246
- JTG E20-2011 (2011). *Standard test methods of asphalt and asphalt mixtures for Highway engineering: JTG E20-2011*; Ministry of Communications of the People's Republic of China: Beijing, China,
- Kang, A. H., Xiao, P., and Ma, A. Q. (2007). Research on performance of microwave radiation CRM asphalt and its mixture *Highway* 2, 34. doi:10.3969/j.issn.0451-0712.2007.02.033
- Karlsson, R., and Isacson, U. (2003). Laboratory studies of diffusion in bitumen using markers. *J. Mater. Sci.* 38 (13), 2835–2844. doi:10.1023/A:1024476217060
- Kedarisetty, S., Biligiri, K. P., and Sousa, J. B. (2016). Advanced rheological characterization of Reacted and Activated Rubber (RAR) modified asphalt

## FUNDING

The research work reported in this paper was supported by the National Natural Science Foundation of China (51668038 and 51868042), Industry Support and Guidance Project by University and College in Gansu Province (2020C-13), the Distinguished Young Scholars Fund of Gansu Province (1606RJDA318).

## ACKNOWLEDGMENTS

The authors gratefully acknowledge many important contributions from the researchers of all reports cited in our paper. The authors thank the reviewers of this paper for their comments and suggestions.

- binders. *Construct. Build. Mater.* 122 (30), 12–22. doi:10.1016/j.conbuildmat.2016.06.043
- Kim, H., and Lee, S. J. (2013). Quantification of oxidative aging of polymer-modified asphalt mixes made with warm mix Technologies. *J. Mater. Civ. Eng.* 25 (1), 1–8. doi:10.1061/(ASCE)MT.1943-5533.0000479
- Lee, S. J., Amirkhanian, S. N., and Kim, K. W. (2009). Laboratory evaluation of the effects of short-term oven aging on asphalt binders in asphalt mixtures using HP-GPC. *Construct. Build. Mater.* 23 (9), 3087–3093. doi:10.1016/j.conbuildmat.2009.03.012
- Li, B., Zhou, J. N., and Zhang, Z. H. (2019). Effect of short-term aging on asphalt modified using microwave activation crumb rubber. *Materials* 12 (7), 1039. doi:10.3390/ma12071039
- Liang, M., Xin, X., and Fan, W. (2017). Thermo-stability and aging performance of modified asphalt with crumb rubber activated by microwave and TOR. *Mater. Des.* 127, 84–96. doi:10.1016/j.matdes.2017.04.060
- Liu, Y. J., Ye, Z. G., and Zhang, Y. Z. (2017). Study on the aging performance of crumb rubber modified asphalt. *Construct. Technol.* 46 (11), 53–56, 104. doi:10.7672/sjgs2017110053
- Lu, J. J. (2010). *Performance influence factors and mechanism of rubber asphalt*. Xi'an, China: Chang'an University.
- Moreno, F., Rubio, M. C., and Martínez-Echevarria, M. J. (2012). The mechanical performance of dry-process crumb rubber modified hot bituminous mixes: the influence of digestion time and crumb rubber percentage. *Construct. Build. Mater.* 26 (1), 466–474. doi:10.3390/su12198045
- Navarro, F. J., Partal, P., and Martínez-Boza, F. (2005). Influence of crumb rubber concentration on the rheological behavior of a crumb rubber modified bitumen. *Energy Fuels* 19 (5), 1984–1990. doi:10.1021/ef049699a
- Nikolskii, V. G., Dudareva, T. V., and Krasotkina, I. A. (2014). Development and properties of new nanomodifiers for road pavement. *Russ. J. Phys. Chem. B.* 577–583. doi:10.1134/S1990793114040071
- Paje, S. E., and Bueno, M. (2010). Acoustic field evaluation of asphalt mixtures with crumb rubber. *Appl. Acoust.* 71, 578–582. doi:10.1016/j.apacoust.2009.12
- Poyraz, S., Liu, Z., Liu, Y., and Zhang, X. (2013). Devulcanization of scrap ground tire rubber and successive carbon nanotube growth by microwave irradiation. *Curr. Org. Chem.* 17, 2243–2248. doi:10.2174/13852728113179990049
- Presti, D. L. (2013). Recycled tyre rubber modified bitumens for road asphalt mixtures: a literature review. *Construct. Build. Mater.* 49 (6), 863–881. doi:10.1016/j.conbuildmat.2013.09.007
- Putman, B. J., and Amirkhanian, S. N. (2010). Characterization of the interaction effect of crumb rubber modified binders using HP-GPC. *J. Mater. Civ. Eng.* 22 (2), 153–159. doi:10.1061/%28ASCE%290899-1561%282010%2922%3A2%28153%29
- Sangiorgi, C., Eskandarsefat, S., and Tataranni, P. (2017). A complete laboratory assessment of crumb rubber porous asphalt. *Construct. Build. Mater.* 132 (FEB.1), 500–507. doi:10.1016/j.conbuildmat.2016.12.016
- Shatanawi, K., Biro, S., and Thodesen, C. (2009). Effects of water activation of crumb rubber on the properties of crumb rubber-modified binders. *Int. J. Pavem. Eng.* 10 (4), 289–297. doi:10.1080/10298430802169424

- Shen, J., Amirkhanian, S., and Xiao, F. (2009). Surface area of crumb rubber modifier and its influence on high-temperature viscosity of CRM binders. *Int. J. Pavem. Eng.* 10 (5), 375–381. doi:10.1080/10298430802342757
- Shu, X., and Huang, B. (2014). Recycling of waste tire rubber in asphalt and portland cement concrete: an overview. *Construct. Build. Mater.* 67, 217–224. doi:10.1016/j.conbuildmat.2013.11.027
- Siddiqui, M. N., Ali, M. F., and Shirokoff, J. (2002). Use of X-ray diffraction in assessing the aging pattern of asphalt fractions. *Fuel* 81 (1), 51–58. doi:10.1016/S0016-2361(01)00116-8
- Sun, D. Q., and Lu, W. M. (2003). Investigation and improvement of storage stability of SBS modified asphalt. *Petrol. Sci. Technol.* 21, 901–910. doi:10.1081/LFT-120017456
- Thodesen, C., Xiao, F., and Amirkhanian, S. N. (2009). Modeling viscosity behavior of crumb rubber modified binders. *Construct. Build. Mater.* 23 (9), 3053–3062. doi:10.1016/j.conbuildmat.2009.04.005
- Torretta, V., Rada, E. C., and Ragazzi, M. (2015). Treatment and disposal of tyres: two EU approaches. A review. *Waste Manag.* 45, 152–160. doi:10.1016/j.wasman.2015.04.018
- Wang, Q., Yuan, Y., and Ouyang, C. F. (2015). Research on aging of waste rubber modified asphalt. *Polym. Bull.* 6, 19–28. doi:10.14028/j.cnki.1003-3726.2015.06.003
- Xiang, L., Cheng, J., and Kang, S. (2015). Thermal oxidative aging mechanism of crumb rubber/SBS composite modified asphalt. *Construct. Build. Mater.* 75, 169–175. doi:10.1016/j.conbuildmat.2014.08.035
- Xu, M., Liu, J., Li, W., and Duan, W. (2015). Novel method to prepare activated crumb rubber used for synthesis of activated crumb rubber modified asphalt. *J. Mater. Civ. Eng.* 27, 04014173. doi:10.1061/(ASCE)MT.1943-5533.0001115
- Yang, J. Y. (2017). *Research on modification mechanism of rubber asphalt prepared by microwave activated powder*. Lanzhou, China: Lanzhou Jiaotong University.
- Yin, J. M., Wang, S. Y., and Lv, F. R. (2013). Improving the short-term aging resistance of asphalt by addition of crumb rubber radiated by microwave and impregnated in epoxidized soybean oil. *Construct. Build. Mater.* 49, 712–719. doi:10.1016/j.conbuildmat.2013.08.067
- Zhang, L. H. (2018). Study on aging microstructure mechanism of rubber-modified asphalt. *Environ. Eng.*, 234–238.

**Conflict of Interest:** Authors JZ and BL were employed by the company Gansu Highway and Bridge Construction Group Co., Ltd. Author QL was employed by the company Gansu Hengda Road and Bridge Group Co., Ltd.

The remaining author declares that the research was conducted in the absence of any commercial or financial relationships that could be construed as a potential conflict of interest.

Copyright © 2020 Zhou, Zhou, Li and Li. This is an open-access article distributed under the terms of the Creative Commons Attribution License (CC BY). The use, distribution or reproduction in other forums is permitted, provided the original author(s) and the copyright owner(s) are credited and that the original publication in this journal is cited, in accordance with accepted academic practice. No use, distribution or reproduction is permitted which does not comply with these terms.



# Rutting Performance of Semi-Rigid Base Pavement in RIOHTrack and Laboratory Evaluation

Sheng Li<sup>1</sup>, Mengmeng Fan<sup>1</sup>, Lukai Xu<sup>1</sup>, Wendi Tian<sup>1\*</sup>, Huanan Yu<sup>1\*</sup> and Ke Xu<sup>2</sup>

<sup>1</sup>Engineering Research Center of Catastrophic Prophylaxis and Treatment of Road and Traffic Safety of Ministry of Education, School of Traffic and Transportation, Changsha University of Science and Technology, Changsha, China, <sup>2</sup>Yueyang City Highway Bridge Foundation Construction Corporation, Yueyang, China

## OPEN ACCESS

### Edited by:

Hui Yao,  
Beijing University of Technology,  
China

### Reviewed by:

Dongya Ren,  
Southwest Jiaotong University, China  
Ru Mu,  
Hebei University of Technology, China

### \*Correspondence:

Huanan Yu  
huanan.yu@csust.edu.cn  
Wendi Tian  
735017826@qq.com

### Specialty section:

This article was submitted to  
Structural Materials,  
a section of the journal  
Frontiers in Materials

**Received:** 02 August 2020

**Accepted:** 20 October 2020

**Published:** 05 January 2021

### Citation:

Li S, Fan M, Xu L, Tian W, Yu H and  
Xu K (2021) Rutting Performance of  
Semi-Rigid Base Pavement in  
RIOHTrack and Laboratory Evaluation.  
Front. Mater. 7:590604.  
doi: 10.3389/fmats.2020.590604

Through a simple performance dynamic modulus test (SPT), standard rutting test, Hamburg rutting test, French rutting test and asphalt pavement analyzer rutting test, the rutting resistance of asphalt mixtures in the middle and lower courses of three semi-rigid base asphalt pavement of Beijing full-scale test track road in China was evaluated. The test results show that the rutting resistance of asphalt mixtures of the middle and lower courses can be greatly improved by using low-grade asphalt, especially 30# asphalt. The rutting resistance of SBS modified asphalt mixtures is also better. The SPT dynamic modulus test can indirectly characterize the rutting performance of the asphalt mixture. The rutting test results of a laser road detection vehicle and 3 m ruler show that the asphalt grade has a significant impact on the rutting performance of semi-rigid base asphalt pavement. Compared with 70# asphalt used in the middle and lower courses, the rutting resistance of the pavement structure can be improved by more than 20%. The result also show that the APA rutting test results can closely characterize the full-scale test track results, which is an optimal test method for evaluating the rutting performance of semi-rigid base asphalt pavement. The research results can provide a theoretical basis and reference for the rational design and rutting evaluation of semi-rigid base asphalt pavement.

**Keywords:** road engineering, asphalt pavement, laboratory rutting test, full-scale test track (RIOHTrack), dynamic modulus

## INTRODUCTION

Currently, rutting is still one of the main forms of the damage of the asphalt pavement. Researchers in the field of road engineering have conducted extensive research on the rutting performance of asphalt pavement. In order to solve the problem of rutting of asphalt pavement, researchers have proposed methods from the aspects of structure and material, which include using high modulus asphalt and low-grade asphalt, optimizing the combination of the pavement structure, and the gradation of the mixture (Zhao et al., 2009; Dong et al., 2014; Li et al., 2018). But the rutting problem of asphalt pavement still exists, therefore, it is needed to combine laboratory tests or theoretical research with the field rutting performance to evaluate the rutting characteristics. In China, more than 90% of asphalt pavements use a semi-rigid base layer. How to effectively control or evaluate the rutting of semi-rigid base asphalt pavement is the focus of this research.

Guan et al. (2011), Ceng et al. (2013), and Tang et al. (2016), introduced the shear factor into the rutting prediction model for semi-rigid base asphalt pavement, and based on the basic idea of layered superposition, the rutting prediction model was verified by different mixture test results. Huang et al.



(2007), Li et al. (2011), Serigos et al. (2014), and Sireesh et al. (2019) studied the influencing factors and improvement measures of rutting tests for the asphalt mixture. Through field investigation and laboratory tests, the suitable thickness of rutting test specimens, rutting contribution of different layers and the relationship between rutting and temperature of the asphalt pavement's composite structure were put forward. Sireesh et al. (2019) proposed an optimized design method for asphalt pavement based on reliability by analyzing the influence of flexible layer thickness and elastic modulus on pavement fatigue and rutting damage. Sirin et al. (2006) obtained the anti-rutting performance of the asphalt pavement modified by SBS through the accelerated loading test of the road surface (Ziari et al., 2019). The rutting is mainly caused by the denseness of the asphalt mixture, while the unmodified asphalt mixture rutting is caused by the combination of compactness and push. Ziari et al. proposed asphalt mixture with waste rubber powder as a modifier and amorphous carbon powder as filler, which has shown good fatigue resistance and rutting resistance (Cai et al., 2017). Walubita et al. (2019) and Behnke et al. (2019) compared and evaluated the anti-rutting performance of asphalt mixture by dynamic modulus, flow value, repeated load permanent deformation, simple shearing and Hamburg rutting. Behnke et al. (2019) used the Finite Element simulation of tire-surface short-term and long-term interactions to estimate the long-term rutting performance of pavement structures (Rahman and Gassman, 2009). Rahman and Gassman (2009) developed a correlation between the laboratory measurement of subgrade soil resilience modulus and drop weight deflection tester, and studied the effect of the resilience modulus of subgrade soil on rutting by using the Mechanics-Experience Pavement Design Guide (MEPDG) (Hussan et al., 2019). Radhakrishnan et al. (2019) and Son et al. (2013) discussed the influence of different combinations of aggregate, binder, temperature and gradation on rut depth. In summary, the existing research mainly focuses on the indoor rutting test of asphalt mixture, the anti-rutting performance of the pavement structure and materials, and the rutting prediction. But there is still a lack of rutting performance inspection tools between the field and laboratory, and the relationship between laboratory testing and measured results is also not established.

At present, the rutting performance of asphalt pavement materials is mainly evaluated and determined by the laboratory test of small test pieces in the design phase. The physical engineering or test track can better reflect the actual anti-rutting performance of the pavement structure, but the test cost is large and the timeframe is long. Therefore, it is necessary to establish the relationship between laboratory tests and measured results, and to study the method for determining the rutting performance evaluation of asphalt pavement. This research combines the pavement material test, construction practice, and follow-up observation of Beijing full-scale pavement test track in the last 5 years. It also establishes the relationship between the test results of asphalt materials and asphalt mixture laboratory rutting tests and the observation results of field rutting, and determines the available laboratory test method for the scientific evaluation of rutting performance of semi-rigid base asphalt pavement. The research results can provide a theoretical basis and

reference for the rational design and rutting evaluation of semi-rigid base asphalt pavement.

## Pavement Structure Type and Raw Material Performance

### Full-Scale Test Track Overview and Research Objects

#### (1) Full-Scale Test Track Overview

In 2006, Academician Sha Qinglin of the Chinese Academy of Engineering advocated the construction of a full-scale accelerated loading test track to verify and improve the existing pavement design system. The RIOHTrack project in Beijing, which was the first full-scale pavement test track in China, started construction in December 2014 and was completed on November 14, 2015. The total length of the track is about 2,038 m, and the straight section is about 504 m, a circular curve with a radius of about 130.5 m is designed on both sides, and the width of the roadbed is 12 m. The design diagram is shown in **Figure 1**.

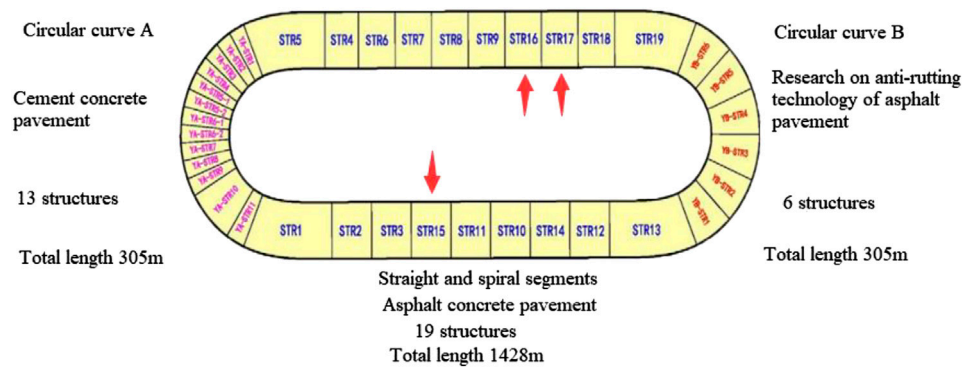
According to different design concepts, service condition and stiffness combinations, 25 typical asphalt pavement structures and 13 types of cement concrete pavement typical structures have been set in the full-scale test track, as shown in **Figure 2**. And 25 types of asphalt pavement structural combinations that cover the structural combination type and structural layer thickness of all highway asphalt pavements in China. Besides, it also includes the typically used structural types and thickness of flexible base asphalt pavement in Europe and America.

#### (2) Pavement Structure and Materials of the Research Object

About 90% of China's asphalt pavements use cement-stabilized semi-rigid bases, research has shown and confirmed that the rutting deformation of asphalt pavements mainly occurs in the middle and lower layers. The structure and materials of the middle and lower layers have a great impact on the anti-rutting ability of asphalt pavement (Dong and Peng, 2010; JTG F40-2004 Technical Specifications, 2004). So the focus of the study is to compare and analyze the rutting performance of the lower layer in the asphalt pavement, and to evaluate the impact of asphalt material on the anti-rutting performance, and then to evaluate the performance of semi-rigid base asphalt pavement through the comparison of field measured results and the indoor laboratory rutting test results. The test results are compared to determine the most suitable laboratory rutting test method for semi-rigid base asphalt pavement. Three semi-rigid base asphalt concrete pavement structures with the same straight-line segment in the full-scale test track were selected. The type and thickness of the asphalt surfacing mixture are shown in **Table 1**. The base layer type and thickness of Structure 2 and Structure 3 are identical, the two structures both use the 40 cm cement-stabilized semi-rigid base layer. The structure 1 adopts a 20 cm cement-stabilized semi-rigid base layer and a 44 cm graded gravel base layer, that is, the three pavement structures are in the same straight line segment and the base layer type and thickness are exactly the same. The gradation of the underlying asphalt mixture in the three pavement structures is the same. But there is a difference



**FIGURE 1** | Effect diagram of RIOHTrack.



**FIGURE 2** | Structural layout drawing of RIOHTrack.

**TABLE 1** | Structural combination and asphalt layer thickness of semi-rigid base asphalt pavement.

Pavement structural layer and thickness	Structure 1	Structure 2	Structure 3
Upper Layer (4 cm)	AC-13(SBS)	SMA-13(SBS)	SMA-13(SBS)
Middle Layer (8 cm)	AC-20(50#)	AC-20(SBS)	AC-20(30#)
Lower layer (24 cm)	AC-25(50#)	AC-25(70#)	AC-25(30#)

SBS indicates the modification of the matrix asphalt with Styrene-Butadiene-Styrene (SBS), and the number indicates the grading of the ordinary base asphalt.

in the asphalt. Especially the gradation, material, and thickness of the asphalt mixture of the structure 2 and the structure 3 are completely consistent. So it can be used well to analyze the degree of influence of asphalt materials on rutting, as well as to establish the relationship between the test results of asphalt mixture indoor rutting and the observation results of physical engineering rutting.

## Main Technical Properties of Raw Materials

### (1) Asphalt Material Properties

The asphalt used is 30#, 50#, and 70# ordinary road petroleum asphalt and Styrene-Butadiene-Styrene (SBS)

modified asphalt, the basic properties were tested following the “Technical Specifications for Highway Asphalt Pavement Construction” (Research Institute of Highway Ministry of Transport, 2004) of China. The results are given in **Table 2**, as shown in **Table 2** that all materials satisfied the standard requirement.

### (2) Aggregate Properties

Basalt and limestone are both used for the construction of the full-scale pavement test track and the aggregates used in the laboratory test. The aggregate above 4.75 mm is made of basalt, the aggregate used for the mixture of 4.75 mm and AC-20 and AC-25 is limestone. The aggregate gradation as shown in **Table 3**. The performance index of aggregates is tested following the method of China Highway Engineering Aggregation Test Regulations (JTG E20-2011 Standard Test, 2005), and the result shows that all the test indicators meet the requirements of the specification (JTG E42-2005 Test, 2005).

### (3) The Test of Mineral Powder Technical Performance

The mineral powder used for the asphalt mixture is made of ore powder produced in Nanning, Guangxi Province of China.

**TABLE 2 |** Test results of main technical properties of asphalt.

Asphalt type	Penetration at 25°C (mm)	Softening point (°C)	Ductility at 5°C (mm)	Viscosity at 135°C $\eta$ (Pa s)
Asphalt(30#)	2.22	61.1	—	1.3620
Asphalt(50#)	5.19	52.7	—	0.7100
Asphalt(70#)	7.5	48.4	—	0.4958
SBS Modified Asphalt	6.34	72.7	285	2.7180P

**TABLE 3 |** Main technical performance test of aggregate.

Particle size (mm)	Apparent density (g/cm <sup>3</sup> )	Dry density (g/cm <sup>3</sup> )	Bulk density (g/cm <sup>3</sup> )	Water absorption (%)
19	2.8420	—	—	—
13.2	2.8224	2.8069	2.7993	0.23
9.5	2.821	2.8003	2.7904	0.34
4.75	2.823	2.8007	2.7893	0.37
2.36	2.8191	2.7829	2.7636	0.66
1.18	2.8044	2.7499	2.7209	1.05
0.6	2.8058	2.7483	2.7171	1.12
0.3	2.8041	2.7558	2.7300	0.09
0.15	2.8300	—	—	—
0.075	2.8544	—	—	—
Technical requirement	≥2.60	—	—	≤2.0

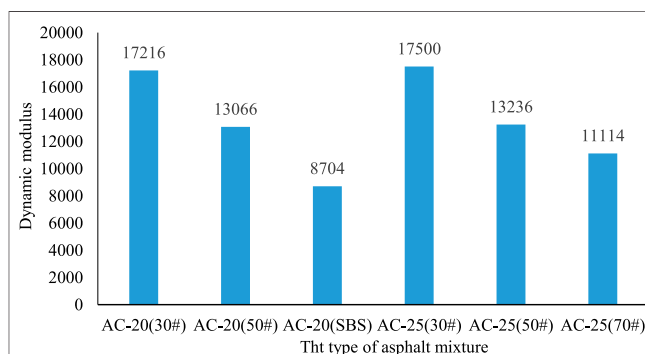
The apparent density of the ore powder is 2.7858 g/cm<sup>3</sup>, the percentage of the particles that are less than 0.6 mm is 100%, the percentage of those less than 0.15 less than mm is 98.6%, and the percentage of those less than 0.075 mm is 83.9%. The technical performance indexes of the mineral powder are satisfied with the requirements of the specification (JTG E42-2005 Test, 2005).

## ASPHALT MIXTURE LABORATORY RUTTING TEST

At present, the rutting performance of asphalt pavement materials is mainly evaluated by laboratory tests. The representative test methods including the standard rutting test, the Hamburg rutting test, the French rutting test, and the asphalt pavement analyzer (APA) rutting test, etc. The indirect characterization of the rutting by testing the dynamic modulus of the asphalt mixture by a simple performance tester (SPT) test method for performance. In this study, the rutting performance of the asphalt mixture of each structural layer of the full-scale test track asphalt pavement was tested by the above test methods.

### Rutting Characterization Based on Dynamic Modulus Test of SPT Asphalt Mixture

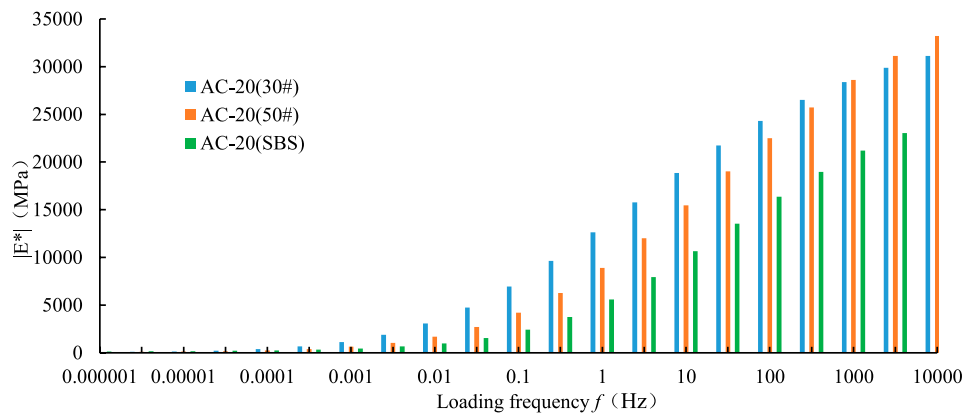
SPT can test the dynamic modulus  $|E^*|$  of the asphalt mixture, and obtain the phase angle  $\varphi$  and the dynamic modulus combination parameter  $|E^*|/\sin\varphi$ .  $|E^*|$  can be directly used as the design parameter for the design of asphalt pavement structure, as well as the evaluation for pavement performance. According to the design guide for Design of New and Rehabilitated Pavement Structures (AASHTO, 2002) and the statistical

**FIGURE 3 |** Dynamic modulus test results of the middle and lower course of asphalt mixture in each structure.

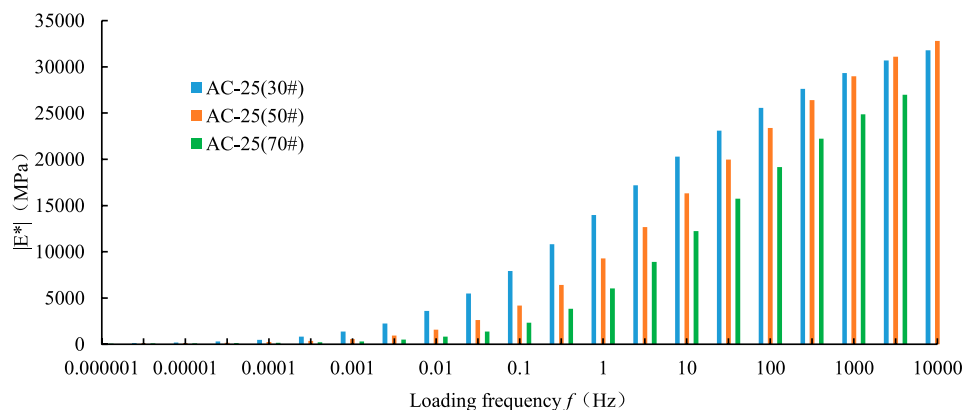
results of the NCHRP 9-19 project (NCHRP, 2002), an indicator of the  $|E^*|$  and  $|E^*|/\sin\varphi$  has a good correlation with the rutting test. Since the loading speed of the first 52 cycles of the full-scale circular road is about 30 km/h, which is equivalent to the loading frequency of 5 Hz, the reference frequency used for research and analysis is 5 Hz, the reference temperature is 20°C normal temperature.

#### (1) Dynamic Modulus Analysis of Asphalt Mixture

A cylindrical test piece with a height of  $170 \pm 2$  mm and a diameter of 150 mm is formed by a Shear Gyratory Compactor. A sample with a diameter of 100 mm is drilled by a core machine. A single-sided saw is used for cutting, all the test pieces that have passed the cutting are polished. A standard test piece having a smooth upper and lower surface and a height of 150 mm was



**FIGURE 4 |** Dynamic modulus of AC-20 asphalt mixture under different loading frequencies.



**FIGURE 5 |** Dynamic modulus of AC-25 asphalt mixture under different loading frequencies.

obtained. The SPT is applied to the cylindrical specimen by Haversine. The loading frequency is 10 frequencies from 0.01 to 25 Hz. The test temperature is 5, 15, 20, 30, 40, and 50°C. The entire test procedure was carried out in a closed environmental chamber. The results of the SPT dynamic modulus test of asphalt mixture at the reference temperature of 20°C and the reference frequency of 5 Hz are shown in **Figure 3**.

It is difficult to obtain the mechanical properties of the frequency and temperature range in laboratory tests with a short time. The experimental results are extended to obtain the dynamic modulus of the larger frequency range in the SPT-recommended strain range (70–110  $\mu\epsilon$ ) by using the Boltzman function (Guo and Prozzi, 2009). The results are given in **Figures 4 and 5**.

It can be seen from **Figures 4 and 5** that the dynamic modulus of asphalt mixture changes in almost the same way. As the loading frequency increases, the dynamic modulus generally increases. In the middle of the histogram, the dynamic modulus changes rapidly, indicating that the frequency has a great influence on the dynamic modulus at room temperature. The dynamic modulus of the asphalt mixture using 30# asphalt is

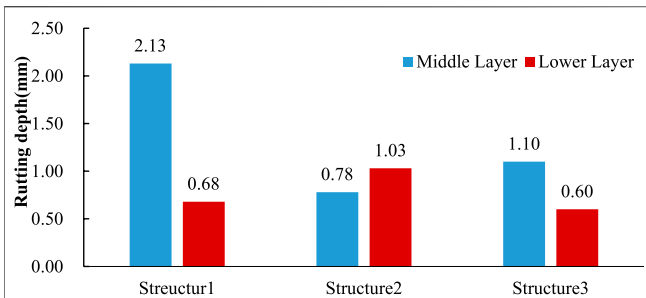
higher than that of the other two asphalt mixtures, indicating that the asphalt label has a great influence on the dynamic modulus of the asphalt mixture, which can indirectly characterize the low marked asphalt as having better anti-rutting performance.

### Analysis of Standard Rutting Test Results

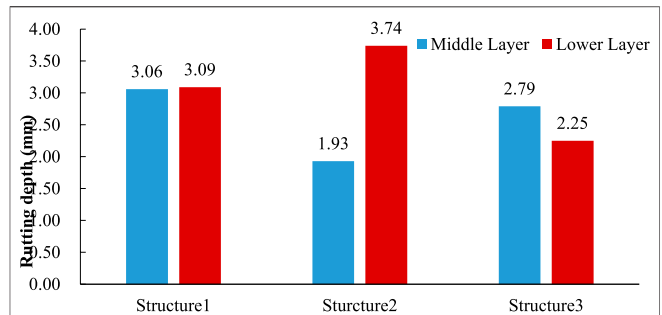
The standard rutting test is carried out according to T0719 in the industry regulations (Kanaan et al., 2014). The test wheel is made of rubber solid tire, the thickness of the rubber layer is 15 mm, the outer diameter of the tire is 200 mm, and the wheel width is 50 mm. The test piece is prepared by the wheel mill. The test piece size is 300 mm  $\times$  300 mm  $\times$  50 mm, loading speed is  $42 \pm 1$  time/min. The test results are shown in **Figure 6**.

### Analysis of Hamburg Rutting Test Results

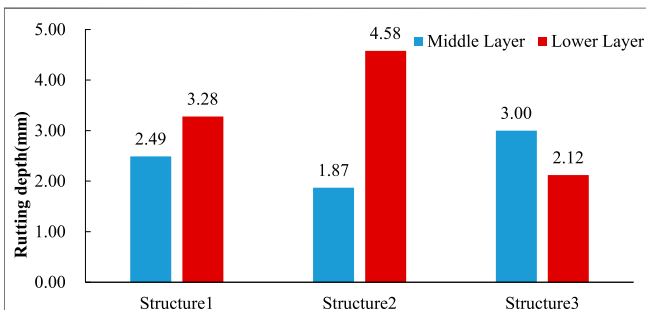
A test piece with a size of  $\Phi 150$  mm  $\times$  75 mm was formed by Shear Gyratory Compactor, and two test pieces were required for each test. The test sample is a rubber wheel with a diameter of 200 mm and a width of 47 mm, the wheel load is 700 N, the loading frequency is 20,000 times, the loading rate is  $52 \pm 1$  times/min. The sample holding time is more than 6 h, and the test



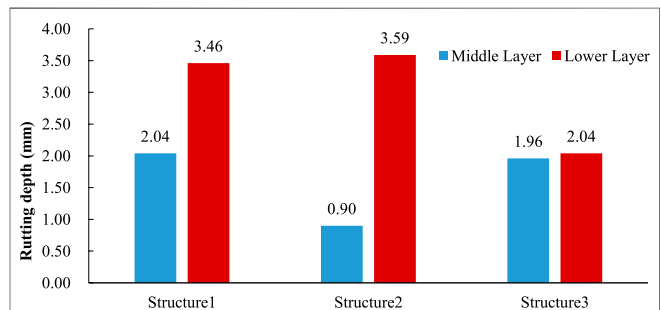
**FIGURE 6 |** Standard rutting test results of asphalt mixtures for each pavement structures.



**FIGURE 8 |** French rutting test results of asphalt mixtures for each pavement structure.



**FIGURE 7 |** Hamburg rutting test results of asphalt mixtures for each pavement structure.



**FIGURE 9 |** APA rutting test results of asphalt mixtures for each pavement structure (mm).

temperature is 60°C air bath. After pressing 20 times, 34 data points were collected and averaged as test results. The test results are shown in **Figure 7**.

## Analysis of French Rutting Test Results

The French Rutting Tester (FRT) was developed by the French LCPC. It can test two asphalt mixture pieces at the same time and load them with a vertical load of 5 kN. The width of the tires is 90 mm. The tire pressure was 600 kPa and the test loading frequency was 1 Hz. The test piece is produced according to the European standard EN12697-33:2013 (British Standard, 2013), and the test piece size of the middle layer and the lower layer asphalt mixture is 500 × 150 × 100 mm, the depth and relative deformation of the rutting loaded 3,000 times are small. The bulk density is used to calculate the quality of the test piece rather than the bulk density. Therefore, the density of the test piece is larger. The detailed test results are shown in **Figure 8**.

## Analysis of APA Rutting Test Results

APA is an asphalt mixture pavement analyzer developed by Georgia, USA. Its load wheel applies vertical load through a rigid rubber tube (with a diameter range of 12.7–29 mm) that is pressed against the top of the test piece (inflating pressure range is 0.827–1.38 MPa). The test piece of this test adopts a cylindrical test piece, which is formed by rotary compaction, the test piece size is Φ150 mm × 75 mm, and an 8,000 round-trip load test is carried out. The wheel

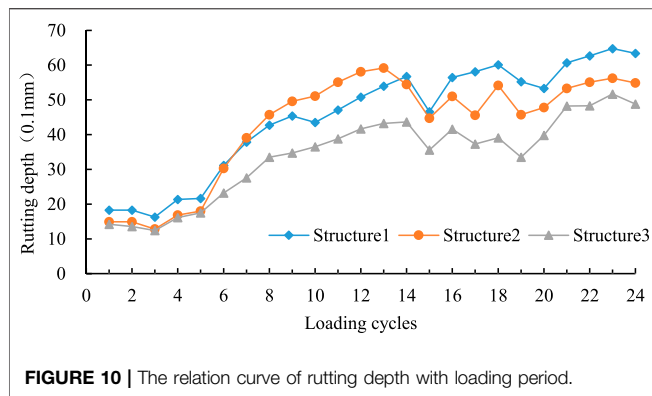
load speed is 0.6 m/s, and the test temperature is 60°C in the air bath. The test results are shown in **Figure 9**.

The test results in Figures 6–9 show that asphalt has a great influence on the rutting performance of asphalt mixture. Using low-grade asphalt, especially 30# asphalt can greatly improve the anti-rutting performance of the middle and lower asphalt mixture, the asphalt mixture with SBS modified asphalt has better rutting resistance.

## ON-SITE INSPECTION AND EVALUATION OF LABORATORY TEST METHODS

To study the evolution of the diversified service performance index of asphalt pavement under long-term and heavy load conditions, Beijing's full-scale pavement test track was loaded from November 2016, and the loading test used four 10-wheel Steyr heavy trucks. The axle weight of the loader is 16 t for a single axle and is loaded for 10,000 times. There are many causes of rutting on asphalt pavements, and differences in structural combinations or material properties can lead to differences in rutting changes and levels. The research mainly focuses on the above three semi-rigid base asphalt pavements with a certain representative of asphalt and asphalt mixture grading (Espinoza-Luque et al., 2019). The laser road detection vehicle and 3 m ruler are used for on-site inspection of the rutting, comparing and analyzing the results of laboratory rutting tests and on-site test results to determine the preferred





method for laboratory testing and evaluation of rutting performance of semi-rigid base asphalt pavement.

## Detection and Analysis of Full-Scale Pavement Test Track Rutting

### (1) Analysis of Detection Results of Laser Road Inspection Vehicles

During the research, the CICS laser road inspection vehicle carried out long-term tracking observation on the ruts of the above three semi-rigid base asphalt pavements in Beijing full-scale pavement test track. From 2016 to 2018, it is measured twice a month for a total of 48 cycles. The two measurements in the same month are averaged in the analysis, and the original 48 cycles are changed to 24 cycles, that is the monthly test result is one cycle. The relationship between the loading cycle and the measured depth of the rutting is shown in **Figure 10**. The measured result of the rutting depth is the rutting depth minus the zero-point calibration.

As can be seen from **Figure 10**, structure 3 uses 30# asphalt for the middle layer and the lower layer, and the asphalt mixture has a higher modulus and a lower rutting level. Compare structure 1 with 2, the middle and lower layer asphalt concrete of structure 1 is made of 50# asphalt, and the middle and lower layer of structure 2 is made of 70# asphalt, although the 70# asphalt used for the middle layer of structure 2 is modified by SBS. However, the results show that the rutting of structure 2 is still significantly smaller than structure 1. It can be seen from the rutting level of the three structures of the comprehensive structure 1, structure 2 and structure 3. The low-grade asphalt has a remarkable effect on improving the anti-rutting ability of the asphalt pavement, the 70# asphalt and the mid-layer asphalt with SBS are commonly used in the middle and lower layers. Compared with the modification, such as structure 2, the anti-rutting performance of the 30# asphalt pavement structure in the middle and lower layers can be increased by more than 20% (Schram et al., 2014).

### (2) Analysis of 3 m Ruler Test Results

The pavement rutting is mainly compacted rutting during the first 6 months of loading, that is the first 12 cycles. The rutting

deformation is small and the change trend is not obvious. At the later of cyclical loading, to better reveal the change trend of the rut, the manual detection method using the 3 m ruler is added besides the automatic detection of the rut by the laser road detection vehicle, and the 22nd to the 48th test results of the loading cycle is shown in **Figure 11**.

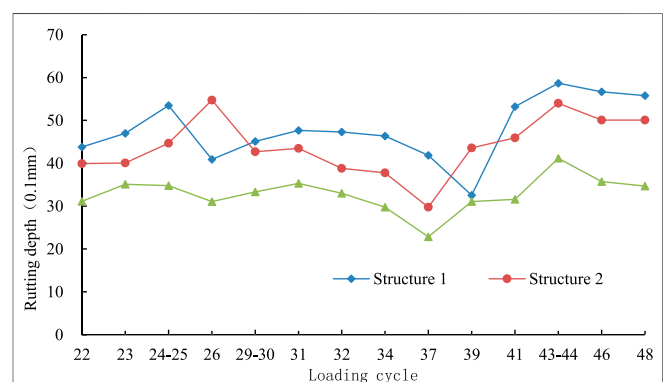
It can be seen from **Figure 11** that the rutting result conducted by 3 m ruler is consistent with the result detected by the laser road detection vehicle, the pavement structure with low-grade asphalt has better rutting resistance, the rutting depth of structure 3 is smallest, and the rutting depth of the structure of 70# asphalt is maximum.

## Comparison and Evaluation of Laboratory Rutting Test

Because the rutting of asphalt pavement mainly occurs in the middle and lower layers, the sum of the rutting deformation of the middle layer and lower layers can reflect the rutting condition of the asphalt pavement structure. So, the sum of the rutting deformation of the middle layer and lower layer of the asphalt mixture that was obtained from the laboratory rutting test can indirectly reflect the rutting size of each pavement structure. By comparing with the depth difference ratio of the rutting measured with the pavement structure, it can select the laboratory test method for evaluating the rutting performance of semi-rigid grass-roots asphalt road.

In order to compare with the actual measurement of the rutting in the full-scale test track, the deformations of the middle and lower layers obtained by the four laboratory rutting tests are added to characterize the rutting of each pavement structure obtained by the laboratory test indirectly. It can be seen from **Figure 10** that the depth of the road rutting in the last four cycles of loading is in a relatively stable stage, so the last cycle is the CICS vehicle actual measured data of the 24th cycle and the test results of the laboratory rutting are analyzed. The sum of the rutting in the four laboratory rutting tests and the bottom rutting and the actually measured rutting of the CICS vehicle are shown in **Table 4**.

It can be seen from **Table 4** that the actual measured rutting depth of the CICS vehicle, the standard rutting test, the French



**TABLE 4 |** Difference ratio between rutting test depth and inter-structural rutting.

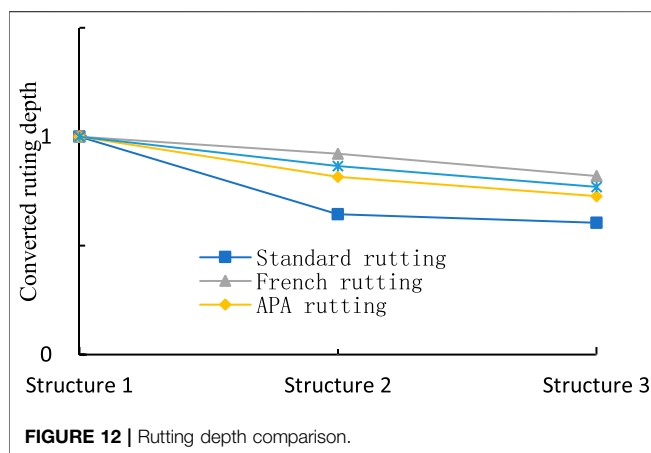
Testing method	Rutting depth (mm)			Difference ratio of the depth of inter-structural rutting (%)		
	Structure 1	Structure 2	Structure 3	Structure 1 and 2	Structure 1 and 7	Structure 2 and 3
Standard rutting	2.81	1.81	1.70	35.59	39.50	6.08
Hamburg rutting	5.77	6.45	5.12	11.79	11.27	20.62
French rutting	6.15	5.67	5.04	7.80	18.05	11.11
APA rutting	5.50	4.49	4.00	18.36	27.27	10.91
CICS rutting	6.34	5.49	4.88	13.41	23.03	11.11

**TABLE 5 |** Rutting depth after standardized conversion.

Testing method	Converted rutting depth		
	$S_{1-1}$	$S_{2-1}$	$S_{3-1}$
Standard rutting	1.00	0.64	0.60
French rutting	1.00	0.92	0.82
APA rutting	1.00	0.82	0.73
CICS vehicle	1.00	0.87	0.77

**TABLE 6 |** Rutting difference ratio between structures.

Testing method	Rutting depth difference ratio between structures (%)		
	$R_{1-2}$	$R_{1-3}$	$R_{2-3}$
Standard rutting	35.59	39.50	6.08
French rutting	7.80	18.05	11.11
APA rutting	18.36	27.27	10.91
CICS vehicle	13.41	23.03	11.11



rutting test, and the APA rutting test all show the trend of Structure 1 > Structure 2 > Structure 3. The rutting data obtained by the Hamburg rutting test is inconsistent with this trend, so there was no further comparative analysis with the measured results. Each laboratory rutting test method has different test specimens, loading methods, and standards. The paper uses direct and indirect comparative analysis methods to comprehensively evaluate the laboratory test method for the rutting performance of semi-rigid base asphalt pavements (Sel et al., 2014).

### (1) Direct Comparative Analysis

In order to facilitate the direct comparison and analysis of the rutting data of the four laboratory rutting tests and the actual rutting data of the CICS vehicle. The rutting depth measured by the four laboratory rutting tests and the CICS

vehicle is standardized by the study, in which the rutting depth corresponding to the structure 1 is defined as 1, and then converted to corresponding rutting depth for other structures. The specific conversion method is shown in Eq. (1). The converted rutting depth is shown in Table 5, and the rutting depth comparison chart is shown in Figure 12.

$$S_{i-1} = \frac{S_i}{S_1} \quad (1)$$

It can be seen from Table 6 and Figure 12 that when the rutting data is directly compared, the images of the APA rutting test and the French rutting test are closest to the actual measured data of the CICS vehicle, followed by the standard rutting test.

### (2) Indirect Analysis and Evaluation

By comparing the rutting difference ratio between the structures to evaluate the preferred laboratory test method can be evaluated indirectly. The rutting difference ratio is obtained as Eq. (2), and the results are shown in Table 6.

$$R_{i-j} = \frac{|d_i - d_j|}{d_i} \quad (2)$$

In the formula:  $R_{i-j}$  is the rutting difference ratio between structure-i and structure-j;  $d_i$  is the rutting depth of structure-i;  $d_j$  is the rut depth of structure-j.

The comparison between the laboratory rutting test and the actual measured results are determined by the ratio between the rutting difference ratio of the laboratory rutting test and the field measured rutting difference ratio of the corresponding structure. The closer the ratio to 1, the more this laboratory rutting test

**TABLE 7** | Closeness between laboratory rutting test results and field test results.

Testing method	$M_{1-2}$	$M_{1-3}$	$M_{2-3}$
Standard rutting	2.65	1.72	0.55
French rutting	0.58	0.78	1.00
APA rutting	1.37	1.18	0.98

method can better reflect the actual rutting level of the pavement structure. The closeness of the results of the laboratory rutting test to the actual results of the full-scale test track is determined by Eq. (3). The calculation results are shown in Table 7.

$$M = \frac{R_l}{R_m} \quad (3)$$

In the formula:  $M$  is the degree of closeness of the laboratory rutting test result to the measured full-scale test track result;  $R_l$  is the ratio of the laboratory rutting difference ratio;  $R_m$  is the measured rutting difference ratio.

It can be obtained by Table 7 that for structure-1 and structure-2, the order of closeness of the laboratory rutting test results to the actual rutting results of CICS vehicle is APA rutting > French rutting > standard rutting. For structures-1 and structures-3, the order of closeness of the laboratory rutting test results to the actual rutting results of CICS vehicle is: APA rutting > French rutting > standard rutting. For structure-2 and structure-3, the order of closeness of the laboratory rutting test results to the actual rutting results of CICS vehicle is French rutting > APA rutting > standard rutting. Therefore, the comprehensive order of closeness is APA rutting > French rutting > standard rutting.

The results of comprehensive direct and indirect analysis evaluation are as follows: the results of the APA rutting test are close to the actual results of the full-scale test track, the APA rutting test is the preferred testing method for evaluating the rutting performance of semi-rigid base asphalt pavements, followed by the French rutting test and the standard rutting test (Sel et al., 2014).

## CONCLUSION

By comparing and analyzing the results of four types of indoor rutting tests with the measured rutting data of the full-scale test track in Beijing, the relationship between the semi-rigid base asphalt material, indoor asphalt mixture rutting test, and the field pavement rutting results was established. The main conclusions are as follows:

Through SPT dynamic modulus test, standard rutting test, Hamburg rutting test, French rutting test, and APA rutting test, the high temperature performance of semi-rigid base asphalt pavement asphalt mixture was evaluated. The results show that the deformation resistance of the SBS modified asphalt mixture is

better than that of the base asphalt mixture, and the low-grade base asphalt mixture has better high temperature stability.

According to the principle of time-temperature superposition, the Boltzman function is used to expand the dynamic modulus of the larger frequency range. The results show that the asphalt grading has a great influence on the dynamic modulus of the asphalt mixture, and it shows that the low-grade asphalt has good rutting resistance, which is consistent with the laboratory rutting test and the on-site test results. The results indicate that the SPT dynamic modulus test can indirectly characterize the rutting performance of the asphalt mixture.

The results of the rutting test, of the laser road detection vehicle, and the 3 m ruler are consistent, the asphalt grading has a significant influence on the rutting performance of the semi-rigid base asphalt pavement. The rutting depth comparison for different asphalt grading is 70# asphalt mixture > 50# asphalt mixture > 30# asphalt mixture.

The APA rutting test method can closely represent the actual measurement results of the full-scale test track, followed by the French rutting test and Hamburg rutting, and finally the standard rutting test. It is suggested that the APA rutting test method should be used as the evaluation method of asphalt mixture high temperature stability.

## DATA AVAILABILITY STATEMENT

The original contributions presented in the study are included in the article/Supplementary Material, further inquiries can be directed to the corresponding authors.

## AUTHOR CONTRIBUTIONS

SL and MF conceptualization and writing/original draft preparation. MF and LX methodology. MF, LX, and KX investigation and numeral calculations; WT and HY writing-review and editing. SL funding acquisition. All authors contributed to the article and approved the submitted version.

## FUNDING

The research was supported by the National Natural Science Foundation of China (51878076) and the National Key Research and Development Plan (2018YFB1600200) and the Natural Science Foundation of Hunan Province (2018JJ2433) and the Open Fund of Engineering Research Center of Catastrophic Prophylaxis and Treatment of Road and Traffic Safety of Ministry of Education (kfj180402).

## REFERENCES

- Behnke, R., Wollny, I., Hartung, F., and Kaliske, M. (2019). Thermo-mechanical finite element prediction of the structural long-term response of asphalt pavements subjected to periodic traffic load: Tire-pavement interaction and rutting. *Comput. Struct.* 218, 9–31. doi:10.1016/j.compstruc.2019.04.003
- Cai, X., Wang, D. Y., Huang, W. K., Yu, J. M., and Wan, C. (2017). Evaluation of rutting performance of asphalt mixture with driving wheel pavement analyzer. *Adv. Mater. Sci. Eng.* 3, 1–10. doi:10.1155/2017/6301914
- Ceng, G. W., Liu, L. P., Su, K., Tang, W., and Chen, R. S. (2013). Rutting model considering shear behavior of asphalt pavement. *J. Southwest Jiaot. Univ.* 48 (4), 672–677. doi:10.3969/j.issn.0258-2724.2013.04.013
- Dong, Y., and Peng, M. J. (2010). Study on the influence of middle course on rutting resistance of asphalt concrete pavement. *J. China For. Highw.* 30 (4), 108–111. doi:10.14048/j.issn.1671-2579.2010.04.065
- Dong, Z. J., Xiao, G. Q., Gong, X. B., and Wang, Y. (2014). Rutting resistance analysis of structure combinations for asphalt pavement subjected to heavy loads. *J. Harbin Inst. Technol.* 46 (6), 72–78. doi:10.11918/j.issn.0367-6234.2014.06.014
- Espinoza-Luque, A. F., Al-Qadi, I. L., Ozer, H., and Pettinari, M. (2019). Laboratory characterization of low-rolling resistance Danish stone-matrix asphalt. *J. Transp. Eng. Part B-Pavements* 145, 1. doi:10.1061/JPEODX.0000094
- Guan, H. X., Zhang, Q. S., and Liu, J. (2011). Rutting test improving methods of asphalt mixture. *J. Traffic Transport. Eng.* 11 (3), 16–21. doi:10.19818/j.cnki.1671-1637.2011.03.004
- Guo, R. H., and Prozzi, J. A. (2009). A statistical analysis of Hamburg wheel tracking device testing results. *Road Mater. Pavement Des.* 10, 327–333. doi:10.1080/14680629.2009.9690249
- Huang, X. M., Fan, Y. W., Zhao, Y. L., and Yan, Q. L. (2007). Investigation and test of expressway asphalt pavement high-temperature performance. *J. Highw. Transp. Res. Dev.* 5, 16–20. doi:10.1007/978-3-319-42797-3\_30
- Hussan, S., Kamal, M. A., Hafeez, I., Farooq, D., Ahmad, N., and Khanzada, S. (2019). Statistical evaluation of factors affecting the laboratory rutting susceptibility of asphalt mixtures. *Int. J. Pavement Eng.* 20 (4), 402–416. doi:10.1080/10298436.2017.1299527
- JTG E20-2011 Standard Test. (2005). *JTG E20-2011 standard test methods of Bitumen and Bituminous mixtures for highway engineering*. Beijing: China Communication Press.
- JTG E42-2005 Test. (2005). *JTG E42-2005 test methods of aggregate for highway engineering*. Beijing: China Communication Press.
- JTG F40-2004 Technical Specifications. (2004). *JTG F40-2004 technical specifications JTG F40-2004 technical specifications for construction of highway asphalt pavement*. Beijing: China Communication Press.
- Kanaan, A. I., Ozer, H., and Al-Qadi, I. L. (2014). Testing of fine asphalt mixtures to quantify effectiveness of asphalt binder replacement using recycled shingles. *Transp. Res. Rec.* 2445, 103–112. doi:10.3141/2445-12(2014)
- Li, P. L., Zhang, Z. Q., Li, H. H., and Wang, B. G. (2011). Research on conditions of Hamburg wheel tracking test and evaluating indicator for asphalt mixture. *J. Wuhan Univ. Technol. (Transp. Sci. Eng.)* 35, 113–117. doi:10.4028/www.scientific.net/amm.178-181.1338
- Li, Y., Liu, L. P., and Sun, L. J. (2018). Prediction model on rutting equivalent temperature for asphalt pavement at different depth. *J. Jilin Univ. (Eng. Technol. Ed.)* 48 (6), 1703–1711. doi:10.13229/j.cnki.jdxbgxb.20170520
- Radhakrishnan, V., Chowdari, G. S., Reddy, K. S., and Chattaraj, R. (2019). Evaluation of wheel tracking and field rutting susceptibility of dense bituminous mixes. *Road Mater. Pavement Des.* 20 (1), 90–109. doi:10.1080/14680629.2017.1374998
- Rahman, M., and Gassman, S. (2009). Effect of resilient modulus of undisturbed subgrade soils on pavement rutting. *Int. J. Geotech. Eng.* 13 (2), 152–161. doi:10.1080/19386362.2017.1328773
- Schram, S., Williams, R. C., and Buss, A. (2014). Reporting results from the Hamburg wheel tracking device. *Transp. Res. Rec.* 2446 (1), 89–98. doi:10.3141/2446-10
- Sel, I., Yildirim, Y., and Ozhan, H. B. (2014). Effect of test temperature on Hamburg wheel-tracking device testing. *J. Mater. Civ. Eng.* 26 (8), 04014037. doi:10.1061/(asce)mt.1943-5533.0001036
- Serigos, P. A., Michael, M., Jorge, A., and Prozzi (2014). Evaluation of rut-depth accuracy and precision using different automated measurement systems. *J. Test. Eval.* 43, 201–211. doi:10.1520/jte20130121
- Sireesh, S., Pranav, R. T., and Munwar, B. (2019). Reliability perspective on optimum design of flexible pavements for fatigue and rutting performance. *J. Transp. Eng. B: Pavements* 7, 145–152. doi:10.1061/JPEODX.0000108
- Sirin, O., Kim, H. J., Tia, M., and Choubane, B. (2006). Comparison of rutting resistance of unmodified and SBS-modified Superpave mixtures by accelerated pavement testing. *Construct. Build. Mater.* 22 (3), 286–294. doi:10.1016/j.conbuildmat.2006.08.018
- Son, S., Al-Qadi, I. L., and Zehr, T. G. (2013). Rutting potential of thin and durable asphalt wearing courses: Laboratory prediction and field performance. *Airf. Highw. Pavement* 14 (2), 1240–1253. doi:10.1061/9780784413005.105
- Tang, W., Wu, X. J., and Sun, L. J. (2016). Study on multi-parameter prediction model of asphalt pavement rutting. *J. China For. Highw.* 36 (1), 45–49. doi:10.14048/j.issn.1671-2579.2016.01.011
- Walubita, L., Fuentes, L., Lee, S., Dawd, I., and Mahmoud, E. (2019). Comparative evaluation of five HMA rutting-related laboratory test methods relative to field performance data: DM, FN, RLPD, SPST, and HWTT. *Construct. Build. Mater.* 215, 737–753. doi:10.1016/j.conbuildmat.2019.04.250
- Zhao, L. D., Wan, J. J., Zheng, G. S., and Zhang, Y. J. (2009). Rheological study of paving performance of high modulus asphalt binders. *J. Build. Mater.* 22 (3), 127–134. doi:10.3969/j.issn.1007-9629.2019.01.019
- Ziari, H., Divandari, H., Hajiloo, M., and Amini, A. (2019). Investigating the effect of amorphous carbon powder on the moisture sensitivity, fatigue performance and rutting resistance of rubberized asphalt concrete mixtures. *Construct. Build. Mater.* 217, 62–72. doi:10.1016/j.conbuildmat.2019.05.039

**Conflict of Interest:** Author KX was employed by the company Yueyang City Highway Bridge Foundation Construction Corporation, Yueyang, China.

The remaining authors declare that the research was conducted in the absence of any commercial or financial relationships that could be construed as a potential conflict of interest.

Copyright © 2021 Li, Fan, Xu, Tian, Yu and Xu. This is an open-access article distributed under the terms of the Creative Commons Attribution License (CC BY). The use, distribution or reproduction in other forums is permitted, provided the original author(s) and the copyright owner(s) are credited and that the original publication in this journal is cited, in accordance with accepted academic practice. No use, distribution or reproduction is permitted which does not comply with these terms.



# An Experimental Investigation on the Repairing Performance and Fatigue Life of Asphalt Pavement Potholes With an Inclined Interface Joint

Linyu Li<sup>1,2</sup>, Yangquan Huang<sup>1,2</sup>, Zhutao Shao<sup>1,2</sup> and Dongya Ren<sup>1,2\*</sup>

<sup>1</sup>School of Civil Engineering, Southwest Jiaotong University, Chengdu, China, <sup>2</sup>Key Laboratory of Highway Engineering of Sichuan Province, Southwest Jiaotong University, Chengdu, China

## OPEN ACCESS

### Edited by:

Hui Yao,  
Beijing University of Technology,  
China

### Reviewed by:

Han-Cheng Dan,  
Central South University, China  
Liang He,  
Chongqing Jiaotong University, China

### \*Correspondence:

Dongya Ren  
dongyaren@swjtu.edu.cn

### Specialty section:

This article was submitted to  
Structural Materials,  
a section of the journal  
Frontiers in Materials

**Received:** 21 August 2020

**Accepted:** 24 November 2020

**Published:** 14 January 2021

### Citation:

Li L, Huang Y, Shao Z and Ren D  
(2021) An Experimental Investigation  
on the Repairing Performance and  
Fatigue Life of Asphalt Pavement  
Potholes With an Inclined  
Interface Joint.  
Front. Mater. 7:597523.  
doi: 10.3389/fmats.2020.597523

A pothole is a typical structural damage of asphalt pavements that significantly influence the life of asphalt pavements and driving safety. The durability of the existing pit repair methods is generally low. The existing studies in the context of pothole repair mainly focus on the selection and the amount of tack coat materials, nonetheless, very limited studies emphasize the effect of the joint interface shape. This study aims to investigate the influence of the interface joint shape on the service life of pothole repair by experimental testing. The strength and fatigue behavior of the joints were studied and the effectiveness of pothole repairs was evaluated under various conditions, including four temperature levels (5, 10, 15 and 25°C), four strain levels (750  $\mu\epsilon$ , 1,000  $\mu\epsilon$ , 1,250  $\mu\epsilon$ , and 1,500  $\mu\epsilon$ ) and three loading frequencies (2, 5, and 10 Hz). The optimal interface joint shape was obtained by orthogonal tests. The results indicated that the bond strength and fatigue life of the high viscoelastic emulsified asphalt with an area density of 0.6 kg/m<sup>2</sup> in the form of a 30° inclination joint was 473 and 80 times higher than those of traditional pothole repair (i.e., vertical joint form and no tack coat), respectively. Finally, a prediction model was proposed for the interface joint fatigue life considering external parameters through multiple regression analyses. This prediction model can provide a reference for the further study of asphalt pavement pothole repair.

**Keywords:** asphalt pavement, pothole patching, inclined interface joint, bond strength, fatigue life

## INTRODUCTION

Potholes are a kind of damage taking place on the surface of pavement in which the material fractures in a relatively short time period cause a steep depression (Nicholls et al., 2014). Potholes are a common form of distress on highway asphalt pavements, due to not repairing the pavement distresses at the initial stage of their development (Ghosh et al., 2018). Moisture and traffic load are considered as the two major causes of potholes (Kang and Sun, 2003; Little and Jones Iv, 2003; Lee et al., 2017). However, the causes are often complex and many factors may influence the performance of the repaired potholes, including the traffic load, the time interval for scheduled reconstruction, personnel, equipment, availability of materials and the tolerance of the traveling public (Wilson and Romine, 2001). Moreover, the formation of potholes can be dependent on the type of asphalt pavement surfacing and the materials used. When asphalt mixture is used on the road surface, potholes are developed because of cracking of asphalt surfacing, water penetration into the asphalt,



and traffic loading, while for the thin asphalt-surfacing seals, loss of surfacing, cracking, poor repairs, and poor adhesion between the base and seal coat may lead to pothole occurrence (Paige-Green et al., 2010).

The pavement reconstruction can eliminate the asphalt pavement pothole, but the cost is high. It is found that the service life of asphalt pavement with potholes can be extended to 5–10 years by conducting some low-cost treatment of potholes (Galehouse, 1998). Therefore, pothole repairing is one of the most common maintenance services carried out by highway agencies, especially in the regions with cold winters and hot and wet summers (Dong et al., 2014b). Pothole patching is usually employed either as an emergency repair under severe conditions, or as the regular maintenance scheduled service for the warmer and drier periods. Therefore, more attention is attracted to the patching materials and technology (Wang, 2011; Li, 2016). In the early 90s, the strategic highway research program (SHRP) provided a manual to describe the materials and procedures that can be used for the repair of potholes. Afterward, by conducting five years of further research on pothole repair, this manual was updated by the Federal Highway Administration's (FHWA) under Long Term Pavement Performance (LTPP) program (Wilson and Romine, 2001).

Several properties are usually considered when repairing potholes in the selection of patching material, such as workability and cohesion (Maher et al., 2001), traffic loading and environmental durability (Fragachan, 2008), bonding, freeze-thaw, and rutting potential (Dong et al., 2014b). For instance, Yang et al. (2015) proposed a pothole patching material for epoxy asphalt pavement on steel bridge decks. They evaluated the performance of their proposed material by conducting both experimental fatigue testing and numerical analyses. Kwon et al. (2018) carried out a study on the feasibility of using reclaimed asphalt pavement (RAP) as spray injection patching materials for pothole repair, which indicated that the mixtures containing RAP had better stability and adhesion properties compared to those which contained virgin aggregates. Li et al. (2019) introduced a high thermal conductivity asphalt pavement mastic and mixture for repairing potholes. They showed that the efficiency of the introduced mixture in terms of bond strength, rutting and cracking resistance met the standard requirements. The patching materials that are usually applied for repairing potholes include hot mixed asphalt mixture (HMA), cold mixed asphalt mixture using emulsified asphalt or cut-back asphalt, and other polymeric materials or resins. Ding et al. (2016) studied the performance of a cold mix asphalt mixture with a modified resin as a tack coat and its application in the pavement pothole repair. Moreover, they studied the strength of this cold mix mixture. However, although the cold-mix asphalt materials provide convenience in construction but they can provide limited scope of application (Yuan, 2017). Prowell and Franklin (Prowell and Franklin, 1996) evaluated different cold-mix patching materials for winter pothole repairs. HMA materials, on the other hand, can greatly improve pavement service life, but these have environmental drawbacks (Tong, 2014). It should be noted that several parameters considerably influence the testing

results of pothole patches such as the testing temperatures, compaction efforts and wheel loading (Dong et al., 2014b).

There are several patching techniques employed by highway agencies for repairing potholes, including the throw-and-roll, the semi-permanent, the spray-injection, and the edge seal methods (Wilson and Romine, 2001). Dong et al. (2014a) carried out a 14-month field survey to evaluate the cost-effectiveness of the two frequently used patching techniques throw-and-roll and semi-permanent with different combinations of materials and procedures. They found that the throw-and-roll patches were degraded very fast, mainly due to the severe freezing environment and insufficient compaction and curing. In addition, the semi-permanent patches demonstrated more cost-effectiveness in the long term. Their subsequent study investigated the service life of different throw-and-roll pothole patches under the influence of different factors including the length, width, and depth of patches, the traffic level, the speed limit and the freeze times using statistical analyses (Dong et al., 2015). Obaidi et al. (2017) proposed a new technology as a suitable method for repairing potholes and demonstrated that with continuous renewal of pothole repair materials, the service life of the repaired surface was similar to that of a newly surfaced road. Mao (2004) studied various maintenance technologies for potholes, and analyzed the appropriate potholes repair technology combined with various climate and construction conditions. Wang et al. (2013) reported the advantages of the spray method and compared it with different pothole repair techniques. They recommended emulsified asphalt as the bonding materials in the spray process. Li and Li (2016) pointed out the disadvantages of the traditional potholes repair methods. They reported the reasons for the low service life obtained from the traditional potholes repair methods as the shortcomings of the cold joint, the weak bonding between the new and old materials at the joint, the difficult compaction of new materials, the large porosity and easy water seepage. Moreover, they proposed a permanent pothole repair method for asphalt pavement based on microwave heating.

The above-mentioned studies mainly focus on the potholes repair material and patching process. However, few researchers focused on the treatment of the interface between the old and new pavement parts in repairing asphalt pavement potholes. Shi (2006) analyzed the pothole repair methods from three perspectives of technology, material, and mechanical equipment. It was found that to ensure the performance of pothole repair, the stability of the interface joint between the new and old pavement parts should be guaranteed. It was also proved that the dry maintenance of interface joints can significantly improve the service life of the repaired potholes (Jiang, 2017). It can be seen that the joint between the old and new pavement parts is the dominant factor affecting the service life of the repaired asphalt pavement potholes. Therefore, it can be mentioned that the joint between the old and new pavement parts has a considerable influence on joint performance (Li and Li, 2016; Shao et al., 2019). In previous studies, although the potholes and the interface problem have been studied, few

**TABLE 1 |** The aggregate gradation of mixture (SMA-13).

Sieve size (mm)	16	13.2	9.5	4.75	2.36	1.18	0.6	0.3	0.15	0.075
Passing rate (%)	100	95	62	27	20	19	16	13	12	10

studies comprehensively evaluated the performance of the joint between the new and old parts of asphalt pavement in potholes.

The purpose of this paper is to investigate the influence of the bond between the new and old pavement parts on the service performance and life of pothole repairs. The bond strength and fatigue behavior of the joints are used to evaluate the effectiveness of pothole repairs under various conditions. The orthogonal tests including the pull-out test and four-point bending fatigue test were conducted as laboratory tests and the effect of several parameters including the type and the amount of tack coat, the joint interface form, the test temperature, the load frequency and the strain level as test conditions are investigated. Moreover, the optimal interface joint form was obtained. Lastly, a prediction model of interface joint fatigue life taking into account several parameters is established through multiple regression analyses. This model can provide a reference for further study on asphalt pavement pothole repair.

## MATERIALS AND EXPERIMENTAL METHOD

### Materials

#### Asphalt Mixture

In this study, the composite beam with an interfacial joint was prepared by stone mastic asphalt (SMA-13) to simulate the pothole in asphalt layers. The gradation of SMA-13 mixture is in **Table 1**, and it was used as the median gradation according to the Chinese Standard of Test Methods of Bitumen and Bituminous Mixtures for Highway Engineering (Code of China, 2011). The asphalt-aggregate ratio of SMA-13 was 6.18%, the coarse aggregate was basalt gravel, the fine aggregate was machine-made sand, the mineral powder was limestone alkaline, and the fiber was lignin with the dosage of 0.3%. The properties of asphalt binder and asphalt mixture (SMA-13) met the requirement of the code (Code of China, 2011).

#### Tack Coat

Three kinds of emulsified asphalt including the ordinary emulsified asphalt (Type I), the highly viscous modified emulsified asphalt (Type II) and the resin emulsified asphalt (Type III) were considered as the tack coat. The properties of binders are listed in **Table 2**.

### Test Methods

#### Specimen Preparation

As mentioned in the previous section, the beam-shaped specimens prepared for testing were 400 mm long, 50 mm wide and 50 mm high. Each beam was made up of two parts

**TABLE 2 |** Properties of tack coat materials.

Property	Unit	Type I	Type II	Type III
Standard viscosity at 25°C	s	12	19	16
Evaporation residue content	%	59	61	52
Penetration degree (100 g, 25°C, 5 s)	0.1 mm	90	55	70
Ductility (5°C)	cm	41	86	75
Softening point	°C	62	98	78

and an interface joint in the middle. It should be noted that the preparation of the asphalt mixture followed the code (Code of China, 2011).

A customized steel mold with the dimension of 300 × 400 × 50 mm<sup>3</sup> was used to prepare the asphalt mixture. Firstly, a loose mixture (160°C) was laid in one-half of the mold and then uniformly distributed. Subsequently, a roller compactor was employed to compact the mixture in 2 min with vibrations so that the mixture reached its maximum density with a target air void content of 3.5%. Then, the compacted mixture was left to cool down to the room temperature for 1 day.

The asphalt materials used as a tack coat were the ordinary emulsified asphalt, the highly viscous modified emulsified asphalt and the resin emulsified asphalt. Moreover, the tack coats were heated up to the specified application temperature. Then, every tack coat was uniformly applied on the cleaned surface with 0.3, 0.6 and 0.9 kg/m<sup>2</sup>, respectively. Subsequently, the coated surface was left at room temperature for 2 h to allow the curing procedure to complete. Following the tack coat application and its curing, the second half of the mold was filled with the loose mixture and compacted using a similar method applied in the first half. The slab was allowed to cool down at room temperature before conducting the cutting operation. In the final step, each slab was then cut into six beams with the dimension of 50 × 50 × 400 mm<sup>3</sup> to prepare for the laboratory tests. **Figure 1** illustrates the procedures of fabrication of the specimens in the laboratory.

In this study, various interface joint patterns were considered by changing the auxiliary movable steel plate used in the middle of the steel mold, as shown in **Table 3**. The composite beam sections with different interface patterns are shown in **Figure 2**.

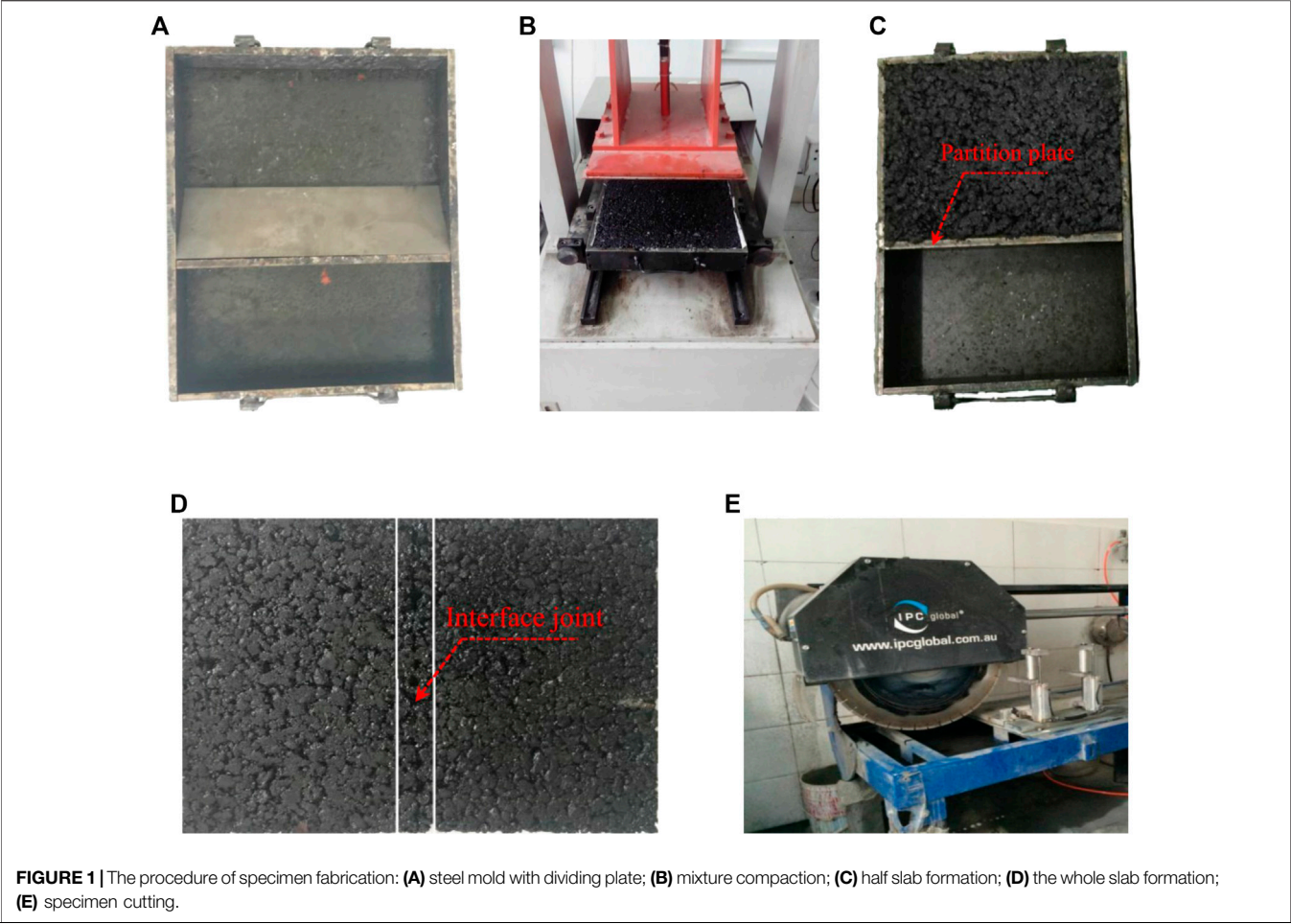
#### Pull-Out Test

The pull-out test device (shown in **Figure 3A**) is used to evaluate the bonding strength of the interface joint of the beam-shaped specimens and to study the ability of the interface joint of the repaired potholed to withstand direct tension. During the pull-out test, the two ends of the specimen were bonded to the mold by an epoxy resin, as shown in **Figure 3B**, and then the tensile force was applied to the specimen by top tension, as shown in **Figure 3C**.

The measured data from fatigue and the pull-out test results were automatically acquired and calculated by a data acquisition system.

#### Fatigue Test

A four-point bending test was implemented in the evaluation of the flexural fatigue performance of interface joint








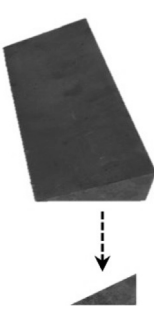
in beam-shaped specimens to determine the service lives of the repaired interface joints in pothole patches under repeated loading conditions. The apparatus, the fatigue loading mechanism, and the schematic diagram of loading and stress distribution are shown in **Figure 4A,B,C**, respectively.

## EFFECT OF INTERNAL FACTORS ON INTERFACE JOINT PERFORMANCE

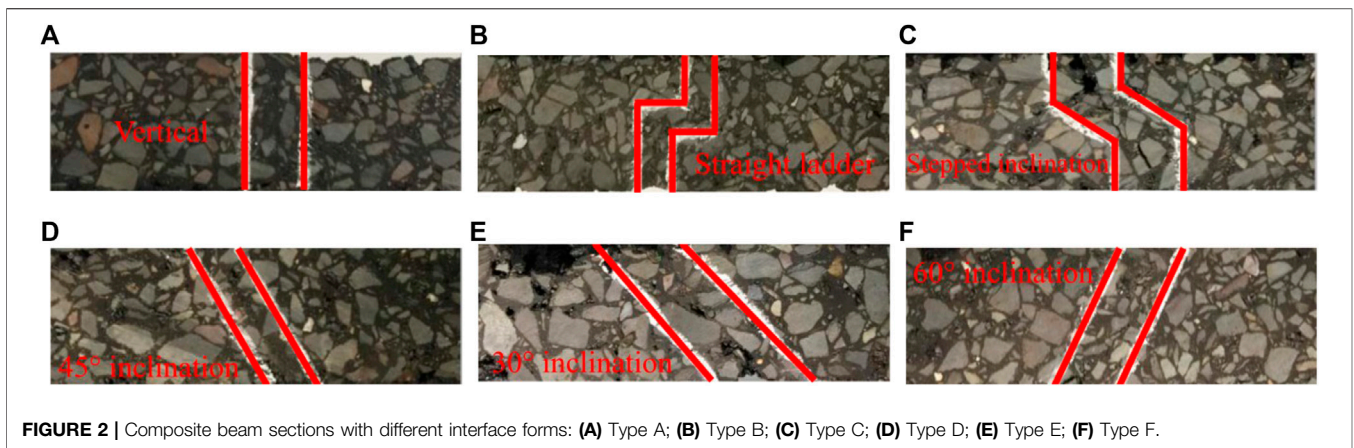
### Test Plan (Phase I)

It is important to guarantee the construction quality in the repaired potholes. The main factors affecting the pothole

**TABLE 3** | Auxiliary movable steel plate with different bonding surface forms.

Interface form	Vertical	Straight ladder	60° inclination	Stepped inclination	45° inclination	30° inclination
Auxiliary movable steel plate						
Steel plate section						





patching are the type and dosage of tack coat, and the form of the interface joint. The above factors can also interact and influence each other. Moreover, the effects of the three main factors on the properties of the new and old bond interfaces in pothole patches were studied. Three options were considered for the types of adhesive material and its application rate and six options were considered for the form of bonding surface (Table 4).

To facilitate the orthogonal analyses based on Table 4 and to improve test accuracy, the factors and corresponding levels were converted into three factors and three levels. The test scheme was designed based on the orthogonal tests and 18 test cases were obtained as shown in Table 5, respectively.

A previous study (Wang et al., 2002) showed that the most unfavorable temperature for fatigue failure of asphalt mixtures was within the range of 13–15°C. In this study, 15°C was selected as the test temperature and 750  $\mu\epsilon$  was considered as the strain level in the four-point bending test. Besides, the pull-out test was also conducted at 15°C.

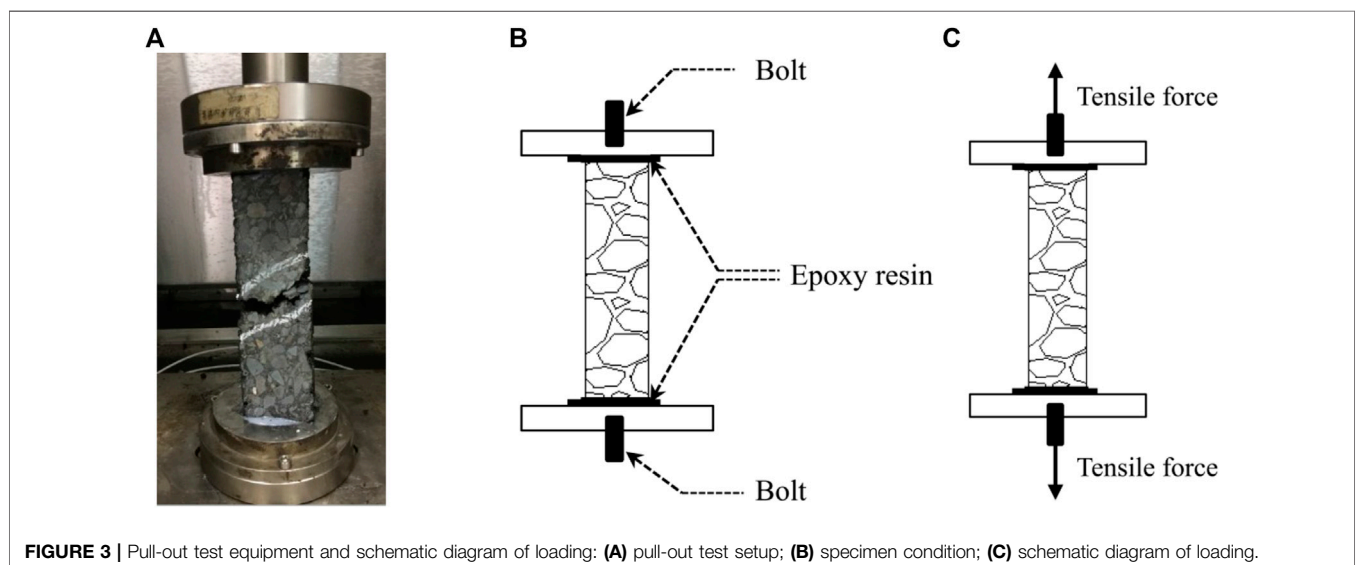
### Determination of Optimal Bonding Condition of Interface Joint

For each test case, three replications were considered, and the average values were calculated and presented. The test results are listed in Table 6.

The influence of factors A, B and C on the fatigue life and bond strength of the composite beam was analyzed by orthogonal tests. The results of the horizontal value analysis of each factor are shown in Figure 5.

The following findings were observed:

- (1) The most influencing factor on the fatigue life of the composite beam was the form of bonded surface. The fatigue life of the composite beam with 30° inclination interface joint was 5.54 times higher than that with a vertical interface joint. In addition to the bonding interface form, the type and dosage of bonding materials imposed an insignificant effect on the fatigue life of



**TABLE 4** | Experimental variables and the levels for internal conditions.

Variable	Factor level (FL)					
	1	2	3	4	5	6
Binder type (A)	Type I	Type II	Type III	—	—	—
Binder dosage (B)/(kg/m <sup>2</sup> )	0.3	0.6	0.9	—	—	—
Interface form (C)	Type A	Type B	Type C	Type D	Type E	Type F

composite beams. Consequently, in order to obtain the maximum fatigue life of the new and old interface bonding joints of the asphalt pavement, it is particularly important to consider the appropriate pavement cutting surface method.

- (2) The most important factor affecting the bond strength of the composite beam is the type of tack coat material. In this regard, the highly viscous modified emulsified asphalt outperforms other types while the ordinary emulsified bitumen showed considerably lower performance. The bond strength of the composite beam with high viscoelastic modified emulsified asphalt as binder was 1.64 times higher than that with ordinary emulsified asphalt.
- (3) In order to improve the fatigue life and bond strength of the composite beam, the highly viscous modified emulsified asphalt can be used as the best tack coat type. Moreover, the optimum binder dosage was 0.6 kg/m<sup>2</sup> and the appropriate cutting surface method among different surface types was 30° inclination for obtaining the optimum fatigue life and bond strength of composite beams.

Therefore, it can be concluded that in order to improve the overall performance of pothole patches with interface joint, the best combination is using 30° inclination as the cutting surface form, and executing bonding treatment with the high-viscous modified emulsified asphalt with an application rate of 0.6 kg/m<sup>2</sup>.

## Effect of Interface Bond Joint on Pavement Performance

Although the results of the above-mentioned orthogonal tests can be used for obtaining the optimal bonding condition for the new and old interface bonding joints of the pothole patches, to clarify the difference between the performances of the pavement before and after repair of pothole needs further research. In order to do this, various testing cases were conducted, as presented in **Table 7**, and their corresponding results are presented.

According to **Table 7**, it is obvious that the fatigue life of the composite beam is very low without treatment of the bonding surface (i.e., case 1). Considering the optimum condition for the bonding surface of the composite beam (i.e., case 2), the fatigue life of the composite beam was increased by 473 times. However, the specimen with the optimum bonding surface condition had only 11.3% of the fatigue life of the joint-less beam (i.e., case 3).

It can be concluded that although using the optimum bonding surface condition in pothole patches can considerably improve the fatigue life of the repaired pavement, the existence of the joints reduced the overall fatigue life of the pavement compared with

**TABLE 5** | Orthogonal test scheme.

Test number	Variable		
	Binder type (A)	Binder dosage (B)/(kg/m <sup>2</sup> )	Interface form (C)
1	Type I	0.3	Type A
2	Type I	0.6	Type B
3	Type I	0.9	Type D
4	Type II	0.3	Type B
5	Type II	0.6	Type D
6	Type II	0.9	Type A
7	Type III	0.3	Type D
8	Type III	0.6	Type A
9	Type III	0.9	Type B
10	Type I	0.3	Type C
11	Type I	0.6	Type E
12	Type I	0.9	Type F
13	Type II	0.3	Type E
14	Type II	0.6	Type F
15	Type II	0.9	Type C
16	Type III	0.3	Type F
17	Type III	0.6	Type C
18	Type III	0.9	Type E

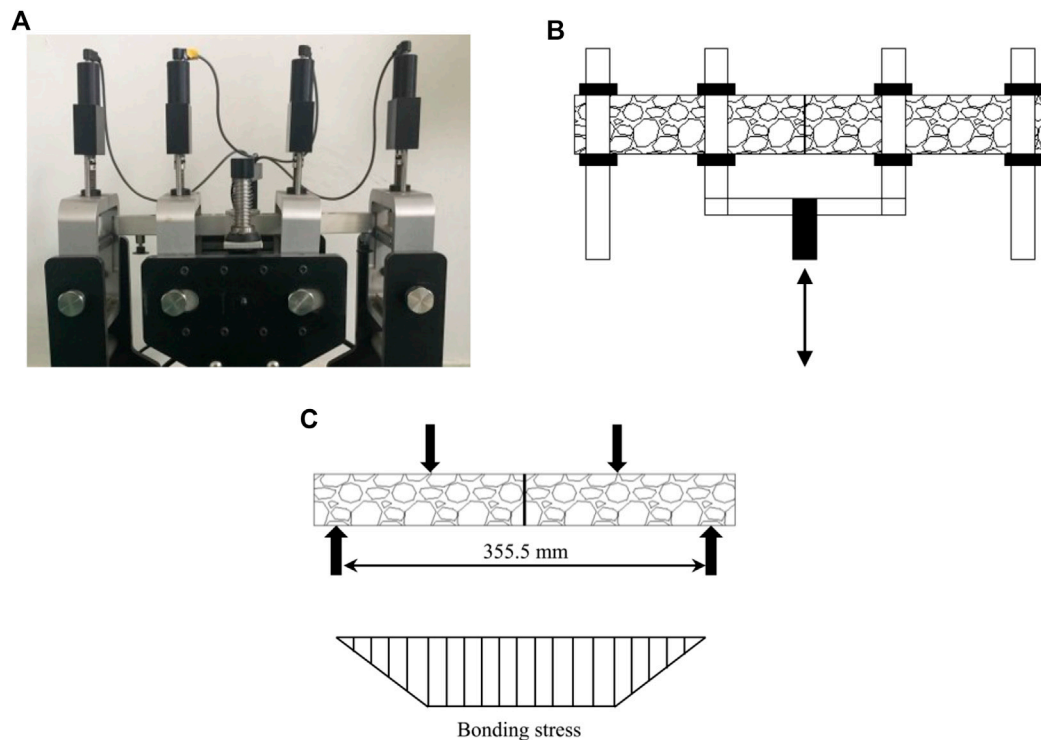
the undamaged one. Therefore, for the repaired pothole, the interface bonding joint can easily reduce the fatigue life and performance of the damaged asphalt pavement.

## FATIGUE PERFORMANCE OF INTERFACE JOINTS UNDER EXTERNAL FACTORS

### Test Plan (Phase II)

Using the determined optimum bonding condition, the four-point bending fatigue tests were carried out on the composite beams under different test temperatures, load frequencies and strain levels. In the fatigue test of four-point bending beam, the change in test frequency represents the change in load acting time on the beam specimen. The loading time reflects the driving speed in asphalt pavement. Thus, different test frequencies represent vehicles with different driving speeds. The load frequencies were selected as 2, 10 and 15 Hz according to **Eq. 1** (Mollenhauer et al., 2009), simulating the low speed of 8 km/h, the medium speed of 45 km/h, and the high speed of 70 km/h, respectively. In the fatigue test of four-point bending beam, the strain level reflects the deformation degree of the beam specimen, representing the load on the asphalt pavement. The strain levels used in the experimental tests were considered in a reasonable range. The strain levels of 750 µε, 1,000 µε, 1,250 µε, and 1,500 µε were





**FIGURE 4 |** Four-point bending test equipment and loading diagram: **(A)** four-point bending test setup; **(B)** fatigue loading mechanism; **(C)** schematic diagram of loading.

chosen to simulate four vehicle loads of small, relatively small, relatively large and large, respectively, acting on the pavement surface. Because the emulsified asphalt is usually used at normal temperature, the test temperature levels used in the experimental tests were 5, 10, 15 and 25°C, respectively.

$$f = 0.277v^{0.944}, \quad (1)$$

where  $f$  is the load frequencies, Hz; the  $v$  is the speed, km/h.

### Effect of Strain Level

**Figure 6** shows the fatigue life against the strain level for different loading frequencies of 2, 10, and 15 Hz, and different temperatures. It can be seen from **Figure 6** that the fatigue life decreases by increasing the strain level. Moreover, different decreasing trends and shapes of logarithmic regression curves seen in **Figure 6** at each frequency or temperature indicate that

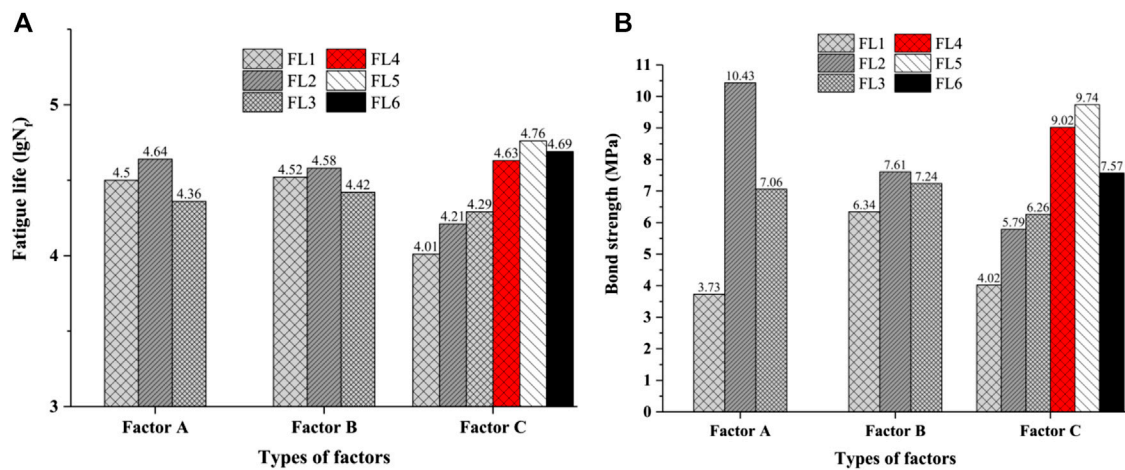
the fatigue life of the interface joint in the repaired potholes is significantly dependent on vehicle speed and temperature. At the same frequency, the higher the temperature and the greater the strain level, the lower the fatigue life of the pothole. This indicates that at the same speed, the truck can be considered as a more severe threat to the pothole patching on the asphalt pavement due to its heavyweight. Furthermore, as the temperature increased, the pothole repair life of the asphalt pavement was sharply reduced.

### Effect of Temperature

In order to assess the influence of temperature on the fatigue life of interface joints, changing trend of fatigue life as a regression curve under different strain levels and load frequencies is illustrated in **Figure 7**. It can be observed that the higher the temperature is, the lower the fatigue life of the interface joint is

**TABLE 6 |** Fatigue life and bond strength of composite beams.

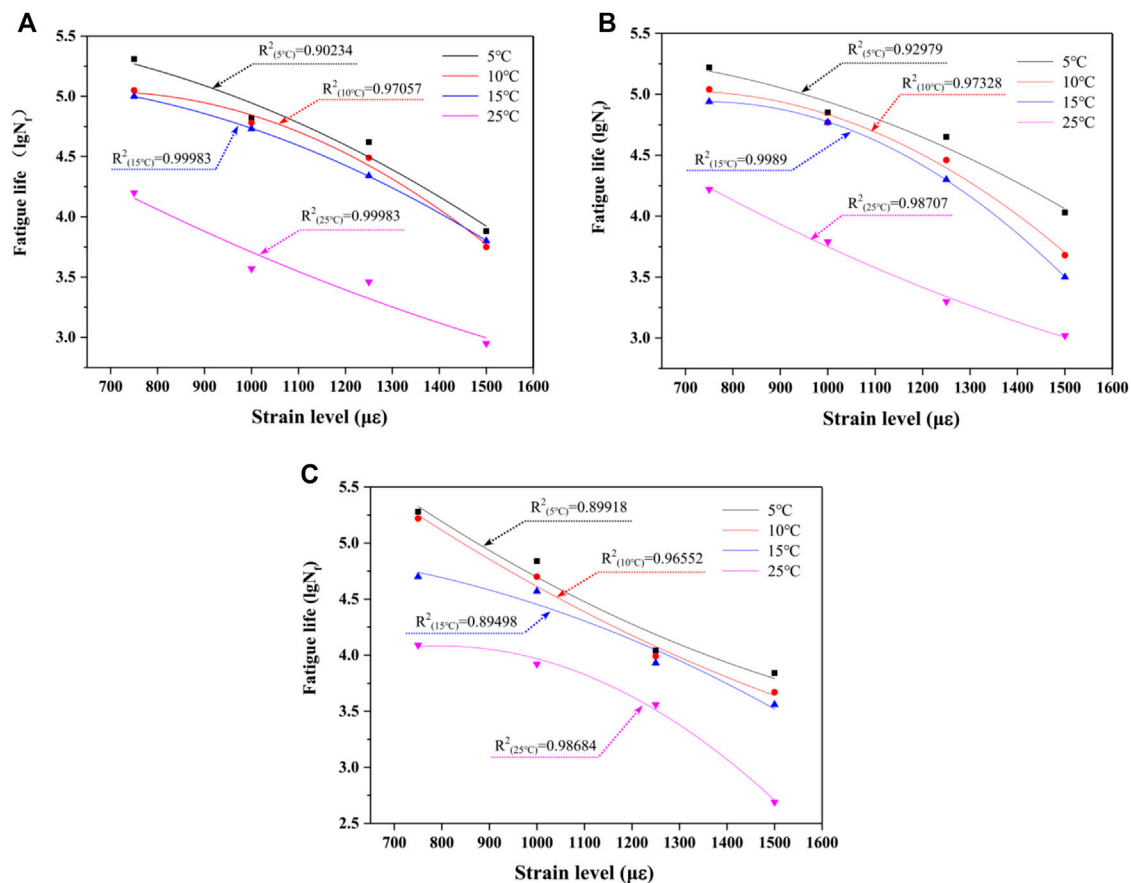
Test number	1	2	3	4	5	6	7	8	9
Fatigue life, $N_f$ (cycles)	775	3,522	7,112	23,062	38,369	11,213	13,854	18,696	21,658
Bond strength (MPa)	0.217	0.440	0.749	1.233	1.037	0.685	0.902	1.322	0.918
Test number	10	11	12	13	14	15	16	17	18
Fatigue life, $N_f$ (cycles)	58,698	62,577	55,365	79,849	69,598	34,671	21,495	35,694	27,584
Bond strength (MPa)	1.020	1.008	0.892	1.330	1.356	1.463	0.714	0.775	1.076



**FIGURE 5 |** Analysis test results for different factor levels: average value of (A) fatigue life for different factors and levels; (B) bond strength for different factors and levels.

for different loading frequencies. Once the temperature reached a certain value, the adhesion of the interface joint was considerably declined, leading to the failure of the interface joint. When the repaired pavement was located in a high-

temperature area, a tack coat with high-temperature resistance should be employed during the construction process, otherwise it may easily result in secondary damage of the repaired pothole.



**FIGURE 6 |** Effect of strain on the fatigue life: (A) 2 Hz; (B) 10 Hz; (C) 15 Hz.

**TABLE 7** | The different performances of the pavement before and after repair of pothole.

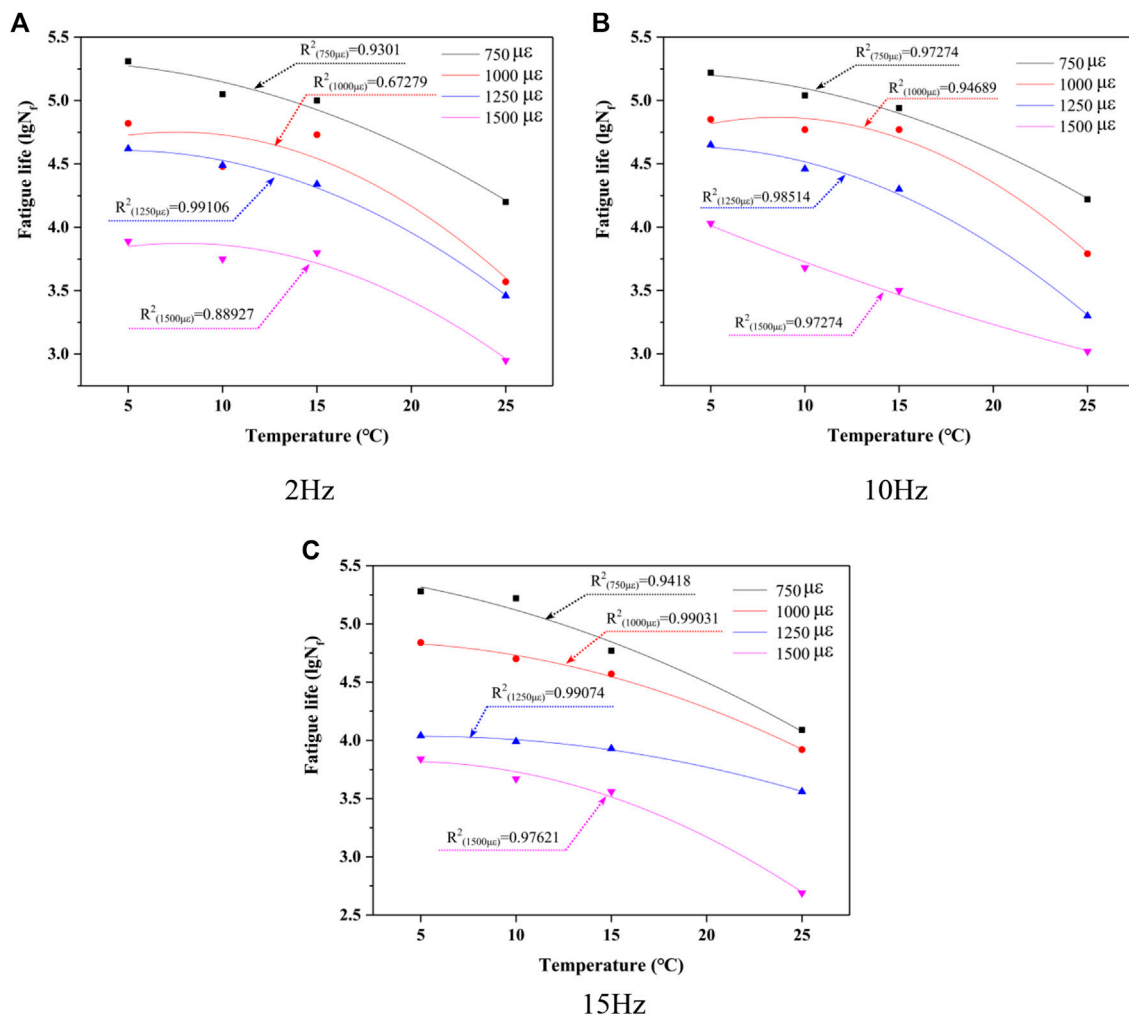
Study case	Test design		Test results	
	Bonding joint condition	Simulation case in the field	Fatigue life, $N_f$ (cycles)	Bond strength (MPa)
Case 1	Vertical joint without tack coat	Routine repair of pavement	205	0.0224
Case 2	Bonding joint with optimal condition	Improved repaired pavement	96,896	1.79
Case 3	Joint-less	Ordinary joint-less pavement	856,936	3.85

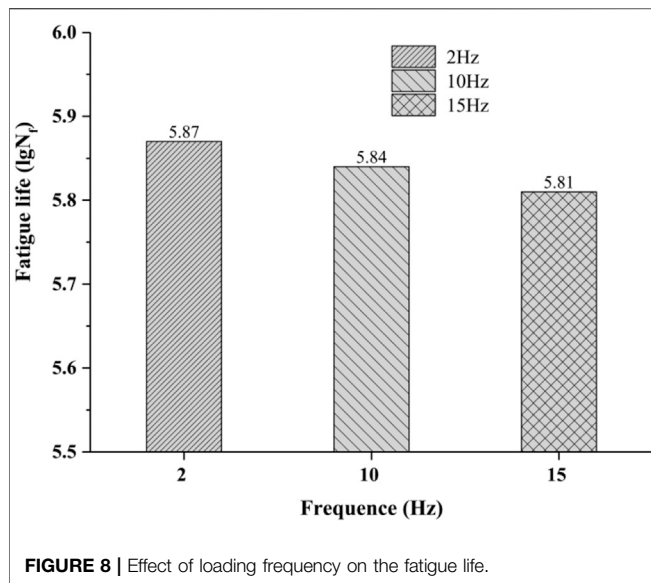
The results of studying the influence of temperature and strain level on fatigue life indicated that the average fatigue life of the optimal potholes repair condition can reach 780 cycles at a relatively high temperature of 25°C and a relatively large strain level of 1,500  $\mu\epsilon$  that was 3.8 times of the traditional potholes repair (i.e., vertical joint form and no tack coat) at 15°C and 750  $\mu\epsilon$ . The fatigue life of the best patching condition with an average value of 77,625 cycles in the temperature of 15°C and the strain level of 750  $\mu\epsilon$  was 379 times that of the traditional potholes repair (i.e., vertical joint form and no tack coat) under the same

condition. Therefore, obtaining the best pothole repair scheme of asphalt pavement is feasible with excellent performance.

## Effect of Loading Frequency

The effect of loading frequency on the fatigue life of the interface joint is presented in **Figure 8**. It can be seen that the maximum fatigue life was obtained at the frequency of 2 Hz followed by 10 and 15 Hz. It can be concluded that the interface joint under the same treatment condition has a longer service life if it is located in the low-speed driving area. On the contrary, if the interface joint

**FIGURE 7** | Effect of temperature on the fatigue life: (A) 2 Hz; (B) 10 Hz; (C) 15 Hz.



is located in the high-speed driving area, it is more likely to be damaged and the corresponding service life is shorter.

### Prediction Model of Fatigue Life

In order to predict the fatigue life of the repaired interface joints under the combined effect of various external factors, a multiple nonlinear regression model was established to predict the fatigue life ( $\lg N_f$ ) as a function of temperature ( $T$ ), frequency ( $Z$ ) and strain level ( $H$ ). The model is expressed in Eq. 2.

$$\lg N_f = 17.68 + 0.0183T - 0.0017T^2 + 0.0173Z - 0.0023Z^2 - 1.87 \ln H. \quad (2)$$

The correlation coefficient ( $R^2$ ) of the model is 0.931, indicating that the accuracy of the developed model is high. To further verify the accuracy of Eq. 2, some measured data were randomly chosen, and the resulting percentage errors were calculated, as presented in Table 8.

Table 8 shows that the percentage error between the measured and the predicted fatigue life is small, and that can further prove that the proposed model has high reliability in predicting the fatigue life of interface joints.

## CONCLUSION

In this study, the bond strength and fatigue life of different forms of interface joints for asphalt pavement pothole repair were studied under different experimental conditions, and the following conclusions are drawn:

This study investigate the influences of the joint surfaces of the pothole repairs and the types and dosage of tack coat materials on the bond strength and fatigue performance of the asphalt pavement potholes repair process through pull-out and four-point bending tests. The results showed that the repaired pothole with an inclined surface has a much higher bond strength between the existing pavement and the repaired pothole compared to the conventional vertical pothole repair surface. The pothole repaired with a 30° inclined surface and employing a high viscoelastic emulsified asphalt with a dosage of 0.6 kg/m<sup>2</sup> asphalt showed the highest bond strength amongst the investigated test conditions. The bond strength of this repaired pothole was 1.64 and 473 times of those with vertical joint potholes repair (vertical joint form and ordinary emulsified asphalt) and the traditional potholes repair (vertical joint form and without tack coat), respectively. Moreover, the fatigue life of the pothole repaired with a 30° inclined surface and a high viscoelastic emulsified asphalt with a dosage of 0.6 kg/m<sup>2</sup> asphalt was 5.54 and 80 times of those with vertical joint pothole repair (vertical joint form and ordinary emulsified asphalt) and the traditional potholes repair (vertical joint form without tack coat), respectively. Therefore, the optimum pothole repair was found for 30° inclination joint surface and high viscous modified emulsified asphalt with a dosage of 0.6 kg/m<sup>2</sup>.

Moreover, the performance of the recommended optimum condition of pothole repair was further investigated at various temperature levels of 5, 10, 15, and 25°C, the strain levels of 750 με, 1,000 με, 1,250 με, and 1,500 με and the loading frequencies of 2, 5, and 10 Hz. The experimental investigation on the influence of temperature and strain levels revealed that the fatigue life of the optimum pothole repair was an average of 780 cycles at a relatively high temperature of 25°C and a relatively large strain level of 1,500 με. Moreover, the fatigue life of the recommended optimum patching solution at the temperature of 15°C and the strain level of 750 με was averagely obtained as 77,625 cycles

**TABLE 8 |** Comparison between the measured and predicted values of fatigue life.

Number	Case	Measured fatigue life ( $\lg N_f$ )	Calculated fatigue life ( $\lg N_f$ )	Error (%)
1	2 Hz, 5°C, 750 με	5.31	5.37	1.13
2	2 Hz, 10°C, 1,000 με	4.78	4.80	0.42
3	2 Hz, 15°C, 1,250 με	4.34	4.26	-1.84
4	10 Hz, 10°C, 1,000 με	4.77	4.72	-1.05
5	10 Hz, 15°C, 1,250 με	4.3	4.12	-4.19
6	10 Hz, 25°C, 1,500 με	3.02	3.34	10.60
7	15 Hz, 15°C, 1,250 με	3.93	3.97	1.02
8	15 Hz, 25°C, 750 με	4.09	4.43	8.31
9	15 Hz, 5°C, 1,000 με	4.84	4.99	3.10

that was 379 times higher than the traditional pothole repair (vertical joint form without tack coat) under the same condition. Therefore, the recommended pothole repair condition of asphalt pavement showed excellent performance and was suitable for being employed at various temperature and loading conditions.

Based on the measured bond strength and fatigue life of the pothole repairs, a multivariate nonlinear regression model of fatigue life was developed for predicting the fatigue life of pothole repairs of asphalt pavements. The correlation coefficient of the regression model was  $R^2 = 0.931$ . By comparing the predicted values of the fatigue life regression model with the measured values, it was found that the error percentage was low. So, the model can be used to predict the fatigue life of the recommended pothole repair of asphalt pavement under different conditions.

## REFERENCES

- Code of China (2011). *Standard test methods of bitumen and bituminous mixtures for highway engineering*. Adyar, Chennai: People Transportation Press.
- Ding, Z., Li, Y., Hou, J., Song, J., and Geng, J. (2016). Application of modified resin cold mixing mixture in pavement pothole repair. *J. China Foreign Highway*. 36 (6), 212–214. doi:10.14048/j.issn.1671-2579.2016.06.048
- Dong, Q., Dong, C., and Huang, B. (2015). Statistical analyses of field serviceability of throw-and-roll pothole patches. *J. Transport. Eng.* 141 (9), 04015017. doi:10.1061/(ASCE)TE.1943-5436.0000786
- Dong, Q., Huang, B., and Jia, X. (2014a). Long-term cost-effectiveness of asphalt pavement pothole patching methods. *Transport. Res. Rec.* 2431 (2431), 49–56. doi:10.3141/2431-07
- Dong, Q., Huang, B., and Zhao, S. (2014b). Field and laboratory evaluation of winter season pavement pothole patching materials. *Int. J. Pavement Eng.* 15 (4), 279–289. doi:10.1080/10298436.2013.814772
- Fragachan, J. M. (2008). Accelerated testing methodology for evaluating pavement patching materials. Master degree. Worcester, MA: Worcester Polytechnic Institute.
- Galehouse, L. (1998). Innovative concepts for preventive maintenance. *Transport. Res. Rec.* 1627, 1–6. doi:10.3141/1627-01
- Ghosh, D., Turos, M., Hartman, M., Milavitz, R., Le, J.-L., and Marasteanu, M. (2018). *Pothole prevention and innovative repair*. St. Paul, MN: Minnesota Department of Transportation.
- Jiang, Z. (2017). Analysis on the application of circular grooves in pothole repairing of asphalt pavement. *J. Highway Transport. Res. Develop. Appl. Technol.* 13 (12), 131–132.
- Kang, J., and Sun, Z. (2003). *Mechanism analyses of pothole repair in asphalt concrete pavement*. Highway, 112–115.
- Kwon, J. B., Kim, D., Rhee, S. K., and Kim, Y. R. (2018). Spray injection patching for pothole repair using 100 percent reclaimed asphalt pavement. *Construct. Build. Mater.* 166, 445–451. doi:10.1016/j.conbuildmat.2018.01.145
- Lee, J., Moon, S. J., Im, J., and Yang, S. (2017). Evaluation of moisture susceptibility of asphalt mixtures using dynamic modulus. *J. Test. Eval.* 45 (4), 20150136. doi:10.1520/JTE20150136
- Li, J., Liu, J., Zhang, W., Liu, G., and Dai, L. (2019). Investigation of thermal asphalt mastic and mixture to repair potholes. *Construct. Build. Mater.* 201, 286–294. doi:10.1016/j.conbuildmat.2018.12.153
- Li, S., and Li, H. (2016). Repair technology for permanent asphalt pavement pothole based on microwave heating. *Guangdong Highway Commun.* 146 (5), 21–25. doi:10.3969/j.issn.1671-7619.2016.05.004

## DATA AVAILABILITY STATEMENT

The raw data supporting the conclusions of this article will be made available by the authors, without undue reservation.

## AUTHOR CONTRIBUTIONS

LL: original draft preparation, formal analysis; YH: investigation, data curation; ZS: investigation,

## FUNDING

This work was supported by the National Natural Science Foundation of China (Grant Nos. 51608457, 51878574).

- Li, Z. (2016). Research on fast durable bonding materials and repair technology of asphalt pavement potholes. Master degree. China: Xi'an University of Architecture and Technology.
- Little, D. N., and Jones IV, D. R. (2003). "Moisture Sensitivity of asphalt pavements—a national seminar," in *Chemical and mechanical processes of moisture damage IN hot-mix asphalt pavements*. College Station, Texas: Texas A&M University.
- Maier, A., Gucunski, N., Yanko, W., and Petsi, F. (2001). Report No.: 2001-02 Final Report. Evaluation of pothole patching materials. Available at: <https://cait.rutgers.edu/wp-content/uploads/2018/05/fhwa-nj-2001-002.pdf>
- Mao, Q. (2004). *Research on technology for pothole patching of asphalt concrete pavements*. McLean, IL: U.S. Department of Transportation.
- Mollenhauer, K., Wistuba, M., and Rabe, R. (2009). *Loading Frequency and fatigue: in situ conditions & impact on test results Braga of Portugal*. Braga, Portugal: University of Minho.
- Nicholls, C., Kubanek, C., Karcher, C., Hartmann, A., Adesiyun, A., Ipavec, A., et al. (2014). "Transport research arena conference: transport Solutions from Research to deployment," in Transport Research Arena (TRA) 5th conference: transport solutions from research to deployment. 14 April 2014, Paris, France.
- Obaidi, H., Gomez-Mejide, B., and Garcia, A. (2017). A fast pothole repair method using asphalt tiles and induction heating. *Construct. Build. Mater.* 131, 592–599. doi:10.1016/j.conbuildmat.2016.11.099
- Paige-Green, D. P., Maharai, A., Komba, J., and Stellenbosch (2010). *Potholes: technical guide to their causes, identification and repair*. South Africa: CSIR Built Environment.
- Prowell, B., and Franklin, A. (1996). Evaluation of cold mixes for winter pothole repair. *Transport. Res. Rec. J. Transport. Res. Board.* 1529, 76–85. doi:10.1177/0361198196152900110
- Shao, Z., Tao, J., Huang, Y., Ai, C., and Jiang, Y. (2019). Experiment on the influence of new and old asphalt pavement bonding interface treatment on pavement performance. *J. China Foreign Highway*. 39 (2), 33–37. doi:10.1177/0361198196152900110
- Shi, N. (2006). Analysis on saw cut repair of rehabilitaingt worn asphalt pavement. *J. Chongqing Jiaotong Univ* 25 (S1), 62–63–143. doi:10.3969/j.issn.1674-0696.2006.z1.020
- Tong, L. (2014). Research on the rapid repairing Material of asphalt pavement pothole. Master degree. Xi'an, China: Chang'an University.
- Wang, P., Liu, C., and Zhao, F. (2013). A brief discussion on bituminous concrete pavement pit repair spray technology. *Highways*. 58 (12), 210–213.
- Wang, X., Sha, A., and Xu, Z. (2002). *Dynamic characteristics and dynamic parameters of asphalt pavement materials*. Beijing: China Communications Press.



- Wang, Y. (2011). New emulsified asphalt mixture and repair technology. Master Degree. Xi'an, China: Chang'an University.
- Wilson, T. P., and Romine, A. R. (2001). *Materials and procedures for repair of potholes in asphalt-surfaced pavements—manual of practice*. McLean, IL: U.S. Department of Transportation.
- Yang, Y., Qian, Z., and Song, X. (2015). A pothole patching material for epoxy asphalt pavement on steel bridges: fatigue test and numerical analysis. *Construct. Build. Mater.* 94, 299–305. doi:10.1016/j.conbuildmat.2015.07.017
- Yuan, Z. (2017). Problems that should be paid attention to in repairing asphalt pavement pothole with cold filling asphalt mixture. *J. Highway Transport. Res. Develop. Appl. Technol.* 13 (6), 117–118.

**Conflict of Interest:** The authors declare that the research was conducted in the absence of any commercial or financial relationships that could be construed as a potential conflict of interest.

Copyright © 2021 Li, Huang, Shao and Ren. This is an open-access article distributed under the terms of the Creative Commons Attribution License (CC BY). The use, distribution or reproduction in other forums is permitted, provided the original author(s) and the copyright owner(s) are credited and that the original publication in this journal is cited, in accordance with accepted academic practice. No use, distribution or reproduction is permitted which does not comply with these terms.



# Effect of Gradation Variability on Volume Parameter and Key Performances of HMA

Shutang Liu<sup>1</sup>, Lin Zhu<sup>1</sup>, Huiqin Zhang<sup>2\*</sup>, Tao Liu<sup>2</sup>, Ping Ji<sup>2</sup> and Weidong Cao<sup>1\*</sup>

<sup>1</sup>School of Qilu Transportation, Shandong University, Jinan, China, <sup>2</sup>Shandong Hi-Speed Technology Development Group Co., Ltd., Jinan, China

## OPEN ACCESS

### Edited by:

Hui Yao,  
Beijing University of Technology,  
China

### Reviewed by:

Jiaying Hu,  
Southeast University, China  
Bin Yu,  
Southeast University, China

### \*Correspondence:

Huiqin Zhang  
478640619@qq.com  
Weidong Cao  
cwd2001@sdu.edu.cn

### Specialty section:

This article was submitted to  
Structural Materials,  
a section of the journal  
Frontiers in Materials

**Received:** 29 September 2020

**Accepted:** 24 November 2020

**Published:** 18 January 2021

### Citation:

Liu S, Zhu L, Zhang H, Liu T, Ji P and  
Cao W (2021) Effect of Gradation  
Variability on Volume Parameter and  
Key Performances of HMA.  
Front. Mater. 7:611409.  
doi: 10.3389/fmats.2020.611409

The graded mineral aggregate composed of coarse aggregate, fine aggregate, and mineral powder is the main component of hot asphalt mixture (HMA), and it occupies a mass ratio of more than 95% in HMA. The gradation variability of mineral aggregate is frequently an unavoidable problem in the construction of asphalt pavement engineering. In order to investigate the effect of gradation variability on the volume parameters and key performances of HMA, the asphalt concrete with a nominal maximum particle size of 20 mm (AC20) was selected as the research carrier. Firstly, a benchmark mineral aggregate gradation (BMAG) was designed based on the theory of dense skeleton gradation presented in the paper. Secondly, six types of HMA (that is, AC20) with variable gradations were also determined and all the specimens were prepared by rotary compaction process with the same optimum asphalt content (gradation varies but asphalt content remains the same), and finally based on asphalt pavement analyzer, the performances of all the specimens of each gradation were tested. The results show that, compared with the BMAG-HMA, the volume parameters such as air voids, voids in mineral aggregate, and voids filled with asphalt of the variable-graded HMA change in different directions, but the water stability and high-temperature performance both degrade greatly. The experimental results also show the feasibility and effectiveness of the dense skeleton gradation design theory adopted in this study.

**Keywords:** water stability, high-temperature performance, volume parameter, gradation variability, hot mix asphalt mixture

## INTRODUCTION

Hot mix asphalt mixture (HMA) has become the main material of flexible pavement because of its good performance. However, due to the aggregate particles with different sizes and the inevitable variability of aggregate sources in actual engineering, HMA often has a certain degree of gradation variability in the construction process. Gradation variability can take many forms. For example, compared with the design gradation at the beginning, the overall gradation curve deviates upward causing the mixture to become finer or deviates downward causing the mixture to become coarser, or coarse aggregate and fine aggregate separate producing segregation and so on. The varying of mineral aggregate gradation must have some influence on the volume parameter and performance of HMA. Cominsky et al. (1994) have shown that the air voids (AV) and voids in mineral aggregate (VMA) are the two most important volume parameters of HMA. Therefore, people often use AV and VMA as the volume parameter for evaluation in research on HMA. By the rank-sum test method, Tan et al.

(2012), Xu (2007) analyzed the law between the AV and the trend of the gradation curve through the study of 11 gradation curves, and the results show that the change of fine aggregate has the greatest influence on the AV under the condition that the content of asphalt and the amount of mineral powder remain unchanged. Liu et al. (2005) studied the influence of gradation curve on AV based on the principle of gray correlation analysis and believed that the greater the correlation between the gradation curve and the theoretical maximum density line, the smaller the AV. Wang et al. (2002) found a good correlation between VMA and the pass rate of 2.36 mm sieve size through statistical analysis for 150 groups of HMA. Lin (2005) studied the influence of gradation change on VMA and gave an equation to estimate its value. Praticò and Vaiana (2013) also showed that gradation is the internal factor that affects the VMA of HMA. By Bailey method Vavrik et al. (2002a), Vavrik et al. (2002b) indirectly showed the effect of gradation changes on the volume parameters, and gradation variability also affects the high-temperature performance, water stability, low-temperature performance, and fatigue performance of HMA. Yan (2007) showed that the effect of gradation on HMA accounts for 60–70%. Li (2016) conducted rutting tests on six gradations at 60°C under the condition of the optimum asphalt content and concluded that the dynamic stability is larger when the percentage passing the sieve of 2.36, 4.75, and 9.5 mm approaches the median gradation. Vavrik et al. (2004) analyzed the influence of the coarse aggregate ratio above the 4.75 mm sieve size on the high-temperature performance of the stone matrix asphalt (SMA), and the results show that the increase of larger particle size in the coarse aggregate can improve the high-temperature performance to a certain extent. Chen (2003) showed that increasing the amount of aggregate of 4.75–9.5 mm is conducive to improving high-temperature performance. Gholipour et al. (2012) divided the gradation range into upper, middle, and lower regions, analyzed the effects of gradation changes on rutting through Marshall Tests and dynamic creep tests, and found that the permanent deformation decreases when the gradation curve is close to the upper limit of the gradation. Matthews and Monismith (1992) studied, respectively, the effects of four kinds of temperature, two kinds of gradation and two kinds of asphalt on rutting, and found that when the gradation curve is close to the median gradation, the high-temperature performance is better than that of the coarse gradation. Using asphalt pavement analyzer (APA) as a test method, Kim et al. (2009) studied the high-temperature performance of four gradations, located, respectively, in the upper areas and lower areas beyond the control zone and the control zone. And the results show that the coarser gradation is more likely to produce ruts and the factor that affects the gradation performance is the degree of roughness and fineness of the gradation rather than the restricted area. Cheng et al. (2006) carried out the immersion Marshall test and freeze-thaw splitting test on four graded HMA with their respective optimal asphalt content (OAC), and the results show that the closer the gradation curve is to the theoretical maximum density line, the better the water stability is. Peng et al. (2013) selected five different gradations for the immersion Marshall test and

found that the water stability of HMA near the middle gradation is the best and the water stability of HMA with fine gradation is better than that of the coarse gradation. Xie (2011) showed that the best water stability of rubber HMA belongs to gap gradation. Huang et al. (2011) studied the effect of gradation on the water stability of AC13 (asphalt concrete with a nominal maximum diameter of 13 mm) using fractal theory and found that, in order to meet the freeze-thaw splitting strength ratio (>75%) of HMA, the fractal dimension value should not be < 2.432.

Zheng et al. (2012) showed that low-temperature damage is closely related to the gradation of HMA. Zhang et al. (2016) selected five kinds of rubber HMA for low-temperature bending test through the comprehensive parameters of bending strength, failure strain, and bending stiffness modulus, and the results show that the intermediate gradation has the best low-temperature performance. Ma et al. (2017) showed that increasing the fine aggregate content of HMA will reduce the resistance to low-temperature cracking. Garcia-Gil et al. (2019) discussed the effect of gradation of HMA overlay on the crack resistance at low temperature and concluded that the smaller the content of fine aggregate is, the smaller the nominal maximum particle size is and the stronger the crack resistance tends to be and concluded that the influence of fine aggregate content on the ductility of the mixture is greater than that of the nominal maximum particle size.

Kasu et al. (2019) evaluated the impact of nominal maximum particle size on the fatigue performance of the mixture at three stress levels and three loading frequencies, and the results show that a smaller nominal maximum particle size is beneficial to the fatigue performance. Valdes-Vidal et al. (2019) showed that fine aggregates could affect the energy dissipating in the process of HMA fatigue damage. Lv et al. (2020) showed that open-graded HMA has a better fatigue life than dense-graded HMA. Liu et al. (2019) used a uniaxial penetration test to study the fatigue performance of five kinds of HMA, and the results show that the fatigue performance of HMA with more fine aggregates and less coarse aggregates is better.

In summary, the above researches show that the aggregate gradation is directly related to the volume parameter, high-temperature performance, water stability, low-temperature performance, and fatigue performance of HMA, or it can be inferred that the change in gradation will bring changes to the volume parameters and performance parameters of HMA. However, firstly, these studies often focus on the direct comparison of HMA with different gradation, rather than specifically designing an aggregate gradation as the benchmark mineral aggregate gradation (BMAG) for comparison; therefore, in the strict sense, they are not studies on the influence of gradation variability on the performance of HMA. Secondly, these studies about the HMA were carried out with OAC of each aggregate gradation. However, in practical engineering, when the gradation variability occurs, the OAC designed for BMAG is often unchanged. Third, some of the conclusions of the above studies, such as the high-temperature performance, are inconsistent with each other. Therefore, it is still worth studying how the aggregate gradation variability

**TABLE 1** | Specific gravity and water absorption test results of aggregates with different particle sizes and mineral powder.

Technical parameter	10–20 (mm)	5–10 (mm)	0–5 (mm)	Mineral powder	Technical requirements
Bulk specific gravity	2.642	2.627	—	—	—
Apparent specific gravity	2.716	2.720	2.719	2.771	≥2.5
Water absorption (%)	1.05	1.30	1.14	—	≤2.0

**TABLE 2** | Particle composition of each grade of aggregate.

Size (mm)	Pass rate (%) of each sieve size (mm)											
	26.5	19	16	13.2	9.5	4.75	2.36	1.18	0.6	0.3	0.15	0.075
10–20	100	86.9	77.7	60.1	27.8	3.8	0	0	0	0	0	0
5–10	100	100	100	99.9	97.2	34.7	1.8	0.5	0.3	0.2	0.1	0
0–5	100	100	100	100	100	99.9	74	53.3	38	22.7	15.6	12.8
Mineral powder	100	100	100	100	100	100	100	100	100	99	90	75

**TABLE 3** | Pass rate of 4.75 mm sieve size for each gradation and VMA of HMA (%).

Parameter	Gradation number		
	Gradation 3 ( $\lambda = 1.20$ )	Gradation 4 ( $\lambda = 1.27$ )	Gradation 5 ( $\lambda = 1.46$ )
Pass rate of 4.75 mm sieve size (%)	36.6	39.2	46.5
VMA (%)	13.2	12.7	13.4

quantitatively affects the volume parameters and performance parameters of HMA.

Taking into consideration the fact that the OAC in practical engineering is always strictly controlled and will not change, the gradation inevitably changes due to the instability of the particle composition of aggregates. Hence, the objective of this paper is to study the change of volume parameters, water stability, and high-temperature performance of HMA (the other performances are not discussed in the limited space) when the OAC of BMAG remains unchanged and the gradation of aggregate varies and to provide an important reference for controlling construction quality of asphalt pavement. It should be pointed out that the BMAG, which is used to compare the gradation variability, is designed by using the optimal design theory of mineral aggregate gradation established by the first author.

## MATERIALS AND EXPERIMENTAL PROGRAM

### Experimental Material

#### Mineral Aggregate and Its Technical Parameters

The HMA used in the study was determined as AC20, and the maximum size of aggregate was selected accordingly. Limestone aggregate with the size of 0–5, 5–10, and 10–20 mm was used, and the filler was limestone powder.

The specific gravity and water absorption of the aggregate and mineral powder were tested in accordance with the Chinese test method, and the test results were shown in **Table 1**.

The results of the sieving tests for aggregates of various particle sizes were shown in **Table 2**.

### Asphalt and Its Properties

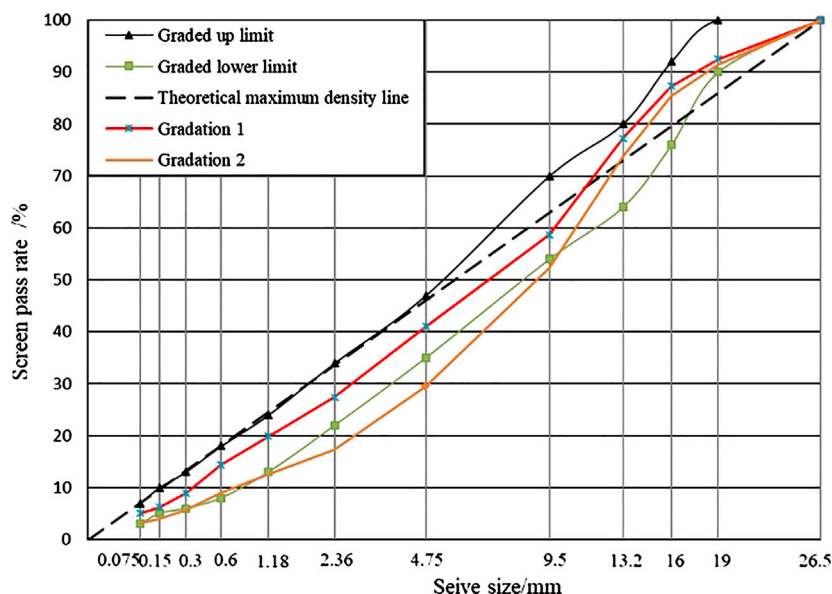
SBS-modified asphalt was used. The penetration (25°C, 100 g, 5 s) is 58 (0.1 mm), the ductility at 15°C is greater than 100 cm, and the softening point is 74.5°C, which were all measured according to the stand test method (JTG E20-2011, 2011).

## Mineral Gradation Design and Asphalt Content Determination

### Design of BMAG

To study the gradation variability problem, there needs a BMAG as the basis for judging the gradation variability. According to the optimal design theory of mineral aggregate gradation (Liu et al., 2015), the research intends to design a dense skeleton gradation (it should be pointed out that the skeleton density gradation here has a relative meaning and is different from SMA) as the basic gradation.

The design idea of the dense skeleton gradation of the literature is three steps (Zhang et al., 2016): firstly, a gradation curve (gradation no. 1) is drawn within the gradation range given in the specification, as shown in **Figure 1**. Secondly, according to the proportion of the determined mineral aggregate, the bulk specific gravity of composite coarse aggregate and apparent specific gravity of composite fine material (which is made up of fine aggregate and mineral powder) are calculated, and the voids of coarse aggregate as well as fine aggregates (4.75 mm is used as the boundary sieve size of coarse and fine aggregate in the



**FIGURE 1** | Preliminary proposed gradation curve and theoretical dense skeleton gradation.

**TABLE 4** | Average volume parameters of HMA for each gradation.

Gradation type	Volume parameter (%)		
	AV	VMA	VFA
BMAG	4.2	12.7	66.9
BMAG-F1	3.2	11.7	72.6
BMAG-F2	1.3	10.0	87.0
BMAG-C1	6.8	15.0	54.7
BMAG-C2	5.8	14.2	59.2
BMAG-D	5.5	13.7	59.9
BMAG-U	5.0	13.4	62.7

research for AC20; that is, aggregate with particle size greater than 4.75 mm is called coarse aggregate) are measured, respectively. Then, according to Eq. (1), the pass rate of 4.75 mm sieve size of the skeleton density gradation can be calculated.

$$x_0 = \frac{1}{1 + \frac{\gamma_{ca}}{\gamma_{fa}} \frac{1-V_{CA}}{1-v_{fa}} \frac{1}{V_{CA}}} \quad (1)$$

where  $x_0$  is the pass rate of 4.75 mm sieve size of the skeleton density gradation;  $\gamma_{ca}$  is the bulk specific gravity of composite coarse aggregates, which is calculated by the bulk specific gravities of coarse aggregates with different particle size;  $\gamma_{fa}$  is the apparent specific gravity of composite fine material, and it is calculated by the apparent specific gravity of fine aggregate and mineral powder;  $V_{CA}$  is the void of coarse aggregate, which is obtained through the vibration test;  $v_{fa}$  is the void of composite fine material, and it is recommended that the void value should be for the natural stacking state without any external force being applied. In this research,  $V_{CA}$  and  $v_{fa}$  tested are 39.2 and 36.9%,

respectively;  $\gamma_{ca}$  and  $\gamma_{fa}$  calculated are 2.640 and 2.720, respectively.

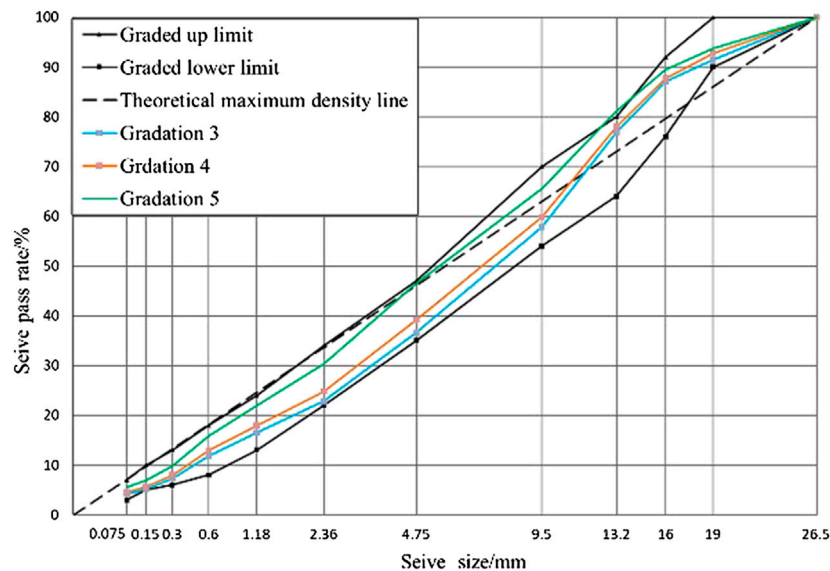
Substituting the above four parameters into Eq. (1), the pass rate of 4.75 mm sieve size can be calculated as 29.5%, and further calculation can give the dense skeleton gradation (gradation no. 2), as shown in Figure 1.

Note that gradation 2 has broken the lower limit of the gradation range. At the same time, it should be pointed out that Eq. (1) is established for graded mineral aggregate without asphalt and based on certain assumptions (such as ignoring the interference of fine aggregates on the arrangement of coarse aggregates). Therefore, the calculated gradation 2 is theoretically a dense skeleton gradation without any asphalt and formed by the vibration test (because the void of coarse aggregate is obtained by the vibration test). Actually, when the coarse aggregates and fine materials are mixed and gradually become dense under a certain compaction process, the fine aggregates inevitably have a certain interference effect on the coarse aggregate arrangement. Therefore,  $V_{CA}$  in the actual dense skeleton gradation will certainly be larger than that of the simple coarse aggregate vibration test. The practical dense skeleton gradation curve is necessarily located above the gradation curve 2, and its specific location could be obtained tentatively based on gradation 2.

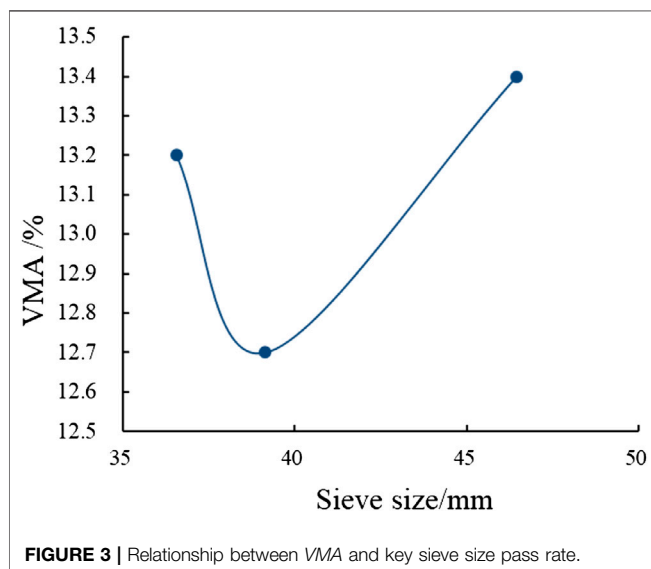
Assume that the interference of fine aggregate increases the void of coarse aggregate in dense skeleton gradation to  $\lambda V_{CA}$ . Here,  $\lambda$  is the coefficient, let  $\lambda$  be 1.20, 1.27, and 1.46, respectively, the corresponding  $x_0$  is recalculated according to Eq. (1), and three gradation curves are further calculated (the numbers are gradation 3, gradation 4, and gradation 5, respectively), which are shown in Table 3 and Figure 2.

The rotary compactor was employed to make the specimens of HMA; and the bulk specific gravities of the





**FIGURE 2** | Possible actual curves of dense skeleton gradation.



**FIGURE 3** | Relationship between VMA and key sieve size pass rate.

specimens were measured and VMA were calculated, as shown in **Figure 3**.

It can be seen from **Figure 3** that the VMA curve presents an asymmetric concave curve shape and gets the valley value when  $\lambda$  is 1.3. The smaller VMA is a typical feature of dense skeleton gradation and a criterion for determining whether a gradation is a dense skeleton gradation. Therefore, it can be determined that gradation 4 is the skeleton dense type gradation, and it should be taken as the BMAG.

### Design of Variability Gradation

There are many possible situations of gradation variability. As an experimental study, this research designs the following three types of gradation variability based on BMAG: 1) Keep the shape of the

gradation curve of the coarse aggregate section of the BMAG unchanged and change the gradation curve of the fine material section, and two variable gradations BMAG-F1 and BMAG-F2 are obtained (the two variability gradation curves are both above the BMAG curve. Because of the gradation characteristics of fine material employed in the research, it was not possible to design a variable gradation below the BMAG curve). 2) Keep the shape of the gradation curve of the fine material section of the BMAG unchanged and change the gradation curve of the coarse aggregate section, and two variable gradations BMAG-C1 and BMAG-C2 are obtained. 3) By deviating the whole gradation curve from the BMAG, two variability gradation curves BMAG-U and BMAG-D located, respectively, above and below the BMAG curve are obtained. The above six variability gradation curves are shown in **Figures 4–6**, respectively.

### Determination of Asphalt Content

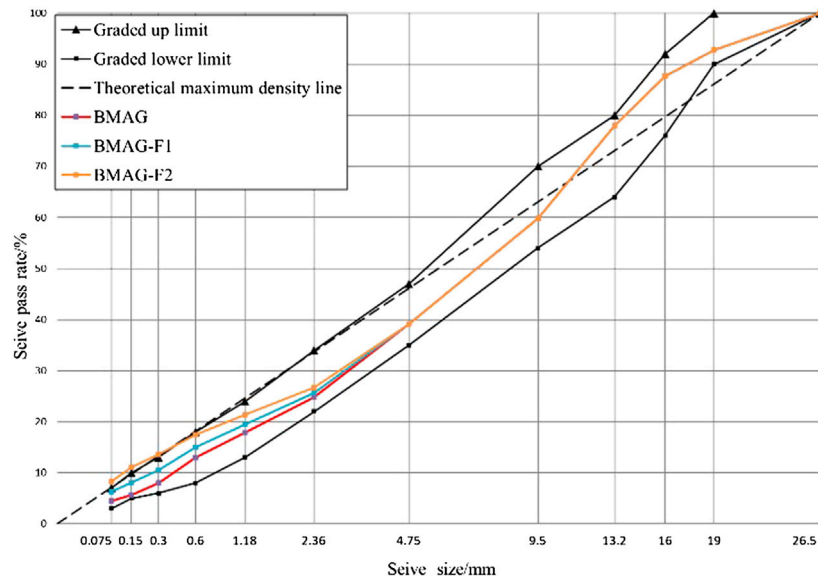
The asphalt-aggregate ratio ( $P_a$ ) for the BMAG should be designed firstly. In order to reduce the test workload and improve the efficiency of the study,  $P_a$  was estimated according to **Eq. (2)** and then verified by tests.

$$P_a = \left( \frac{100 - AV}{100 - VMA} \cdot \frac{1}{\gamma_{sb}} - \frac{1}{\gamma_{se}} \right) \cdot \gamma_a \quad (2)$$

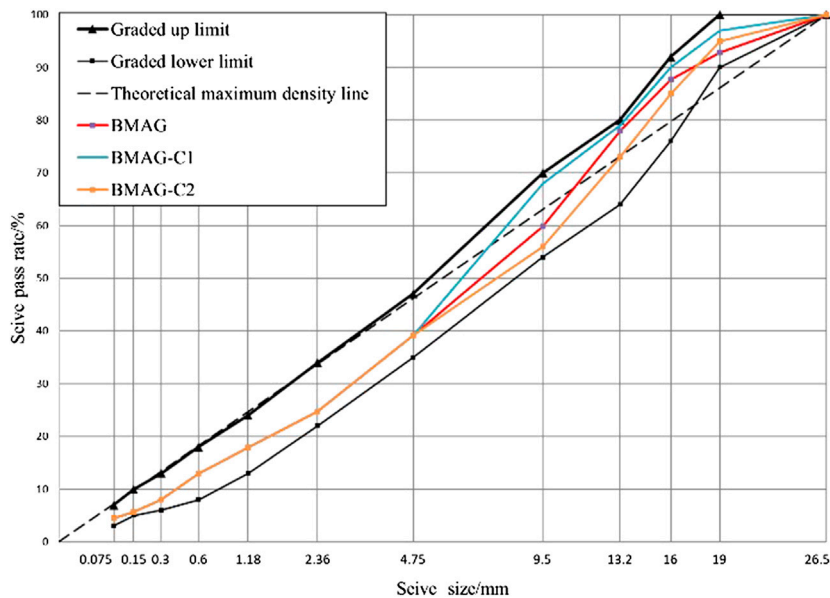
where  $P_a$  is the asphalt-aggregate ratio, %; AV and VMA are the air voids and voids in mineral aggregate of compacted HMA specimens, respectively, %;  $\gamma_{sb}$  and  $\gamma_{se}$  are bulk specific gravity and effective specific gravity of the composite mineral aggregates, respectively.

According to **Eq. (2)**, the estimated asphalt-aggregate ratio is 4.3%, and the OAC is 4.1%.

Two specimens were prepared for each gradation through the rotary compaction process, and the bulk specific gravities of



**FIGURE 4 |** Gradation curves of fine material variability.



**FIGURE 5 |** Gradation curves of coarse aggregate variability.

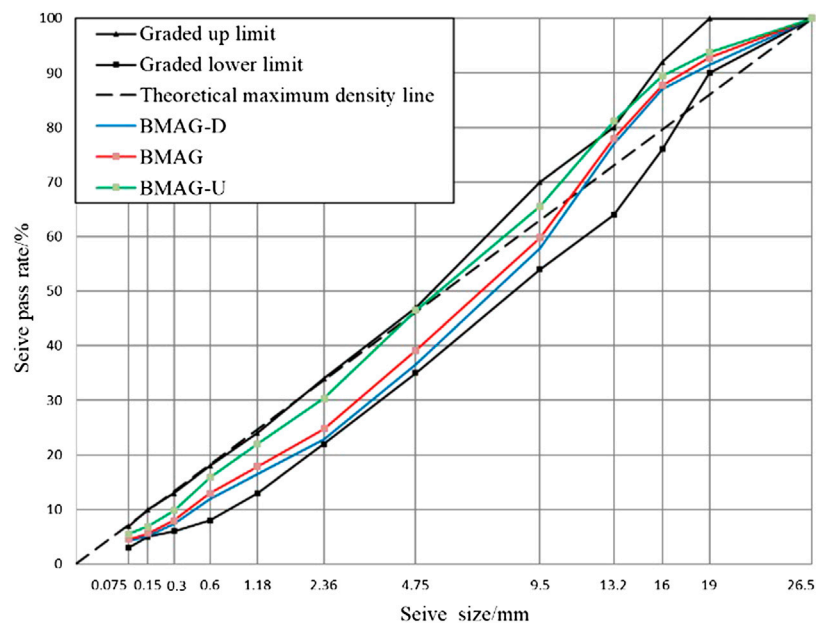
specimens were measured according to the test procedures. The *AV*, *VMA*, and *VFA* (void filled with asphalt) were further calculated, which were shown in **Table 4**.

Since this paper studies the situation of gradation variability and the *OAC* remains unchanged, therefore, the asphalt content used in each variability gradation is still 4.1%.

By transforming **Eq. (2)**, **Eq. (3)** is obtained.

$$AV = 100 - (100 - VMA) \times \left( \frac{P_a}{\gamma_a} + \frac{1}{\gamma_{se}} \right) \times \gamma_{sb} \quad (3)$$

It can be seen from **Eq. (3)** that when the asphalt-aggregate ratio remains unchanged, if the *VMA* changes due to the



**FIGURE 6 |** Gradation curves of coarse aggregate and fine material variability.

**TABLE 5 |** Coefficient values of regression equations for load cycle times and rut depth of BMAG and variability gradation HMA.

Coefficient	HMA of different gradations						
	BMAG	BMAG-F1	BMAG-F2	BMAG-C1	BMAG-C2	BMAG-D	BMAG-U
A	2,704.972	13.458	12.476	4.589	8.899	5.629	18.538
B	2,003,032.707	41,977.638	80,354.096	23,359.513	30,509.256	30,929.143	52,791.121
C	0.26047	0.72223	0.78893	1.39741	1.49947	0.80762	0.46848
$x_{SN}$	15,851	3,867	8,322	4,201	5,761	3,299	2,297
$\Delta x_{SN}$ (%)	0	-75.6	-47.5	-73.5	-63.7	-79.2	-85.5

$\Delta x_{SN}$  (%) stands for relative deviation.

gradation variability, the  $AV$  will change in the same direction.

## RESULTS AND ANALYSIS

### Influence of Gradation Variability on Volume Parameters

$AV$ ,  $VMA$ , and  $VFA$  were selected as the assessment indicators. The volume parameter results of each HMA can be seen in Table 4.

### Influence of Fine Material Variability on Volume Parameters

According to Table 4, compared with the volume parameters of BMAG-HMA, the  $AV$  and  $VMA$  of the BMAG-F1 and BMAG-F2 mixtures became smaller. This is because the composition and dosage of the coarse aggregate remain unchanged, the  $V_{CA}$  remains unchanged. When the amount of fine material increases, the extent to which the fine material fills the gap between the coarse aggregate particles increases, so the  $VMA$

decreases. Moreover, the variability of density parameter of mineral aggregate gradation is very small and can be ignored; therefore, according to Eq. (3), when the asphalt-aggregate ratio is constant, the decrease in  $VMA$  will inevitably lead to a decrease in  $AV$ . Compared with BMAG-F1, BMAG-F2 has finer materials, so its ability to fill the gaps of coarse aggregate is stronger, and  $AV$  and  $VMA$  of it are both smaller. The  $VFA$  values of the BMAG-F1 and BMAG-F2 mixtures are larger than those of BMAG. It can be inferred that when the fine material becomes finer than BMAG, the general rule is that the  $AV$  and  $VMA$  of HMA decrease and  $VFA$  increases.

### Influence of Variability of Coarse Aggregate on Volume Parameter

As can be seen from Table 4, compared with the BMAG,  $AV$  and  $VMA$  of BMAG-C1 and BMAG-C2 mixtures are increased. When analyzing the reasons for the increase of  $AV$  and  $VMA$ , it should be noted that BMAG mixture is a dense skeleton gradation and its  $VMA$  and  $AV$  are smaller. With the variability of coarse aggregate, its  $V_{CA}$  must change greatly or little. Because the amount of fine material is not changed, the

HMA with variable gradation becomes a skeleton void structure or suspension dense structure. According to the law of asymmetric concave shape change of the VMA revealed in the literature (Zhang et al., 2016), it can be inferred that the VMA with variable gradation will inevitably increase. As mentioned above, the density parameters of mineral aggregate gradation after variability can be considered to be approximately constant, so according to Eq. (3), when the asphalt-aggregate ratio is constant, the increase of VMA will lead to AV increasing. As for VFA, the values of BMAG-C1 and BMAG-C2 mixtures are smaller than that of BMAG. It can be speculated that, compared to BMAG gradation, after variability of coarse aggregate, the general rule is that both VMA and AV of the HMA increase, while VFA decreases.

### Influences of Variability of Coarse Aggregate and Fine Material on Volume Parameter

It can be seen from Table 4 that when coarse and fine aggregates have simultaneously variabilities, the VMA and AV of the two gradations of BMAG-D and BMAG-U compacted HMA both increase. The reason is the same as the situation that fine material gradation is basically unchanged but the coarse aggregate is changed visibly.

## Effects of Gradation Variability on Water Stability and High-Temperature Performance

### Test Instruments and Conditions

APA was employed to test the water stability and high-temperature performance of HMA. Because of the modified asphalt, the Hamburger wheel tracking test (HWTT) was conducted with cylindrical specimens under the condition of 60°C water in a bath (Izzo, 1999; Li et al., 2011; Zhang et al. 2018).

### Evaluation Parameter and Analysis Method

Wheel load times and rutting depth are the basic test data of HWTT, regarding the processing of experimental data, the traditional method provided by AASHTOT324 is curve fitting based on data. Then, the postcompaction stage, creep stage, and spalling stage were artificially distinguished to obtain spalling inflection point (SIP) and creep slope, which were used as the evaluation methodology of water stability and high-temperature performance, respectively. Obviously, the traditional method has many subjective factors and lacks a mathematical basis. In order to avoid this defect, Tsai and Harvey (2003) put forward the three-stage Weibull approach to fit rut curve. Based on this, Yin et al. (2014) proposed a new method to evaluate the performance of water stability and high-temperature performance by fitting the whole rutting process and proved the reliability of evaluation parameters. In this paper, the Yin fitting method is used to analyze the test results. The basic steps of the analysis are as follows:

- (1) The function of Eq. (4) is used for curve fitting.

$$RD(x) = A \times \left[ \ln\left(\frac{B}{x}\right) \right]^{-1/C} \quad (4)$$

where  $x$  is the load cycle times;  $RD(x)$  is the rutting depth corresponding to  $x$ ;  $A$ ,  $B$ , and  $C$  are model parameters.

The fitting curve includes two parts of negative curvature and positive curvature, and the connection point between the two parts is defined as the critical point.

- (1) Calculate the load cycle times  $x_{SN}$  corresponding to the critical point.

Take the second derivative of both sides of Eq. (4) with respect to  $x$  and set the derivative equal to zero to obtain  $x_{SN}$ , as shown in Eq. (5). The water stability of HMA is evaluated by  $x_{SN}$ , and the larger  $x_{SN}$  indicates that the water stability of HMA is better.

$$x_{SN} = B \times \exp\left(-\frac{1+C}{C}\right) \quad (5)$$

- (1) Obtain the viscoplastic strain function before the critical point and taking the derivative.

Rutting before the critical point is mainly the viscoplastic deformation of the HMA specimen under load, and Eq. (6) can be used to fit the viscoplastic strain of the deformation stage.

$$\varepsilon^{vp} = \varepsilon_{\infty}^{vp} \exp\left[-\left(\frac{a}{x}\right)^b\right] \quad (6)$$

where  $\varepsilon^{vp}$  is viscoplastic strain;  $\varepsilon_{\infty}^{vp}$  is saturated viscoplastic strain;  $a$  and  $b$  are model coefficients;  $\varepsilon_{\infty}^{vp}$ ,  $a$ , and  $b$  are obtained by nonlinear regression analysis.

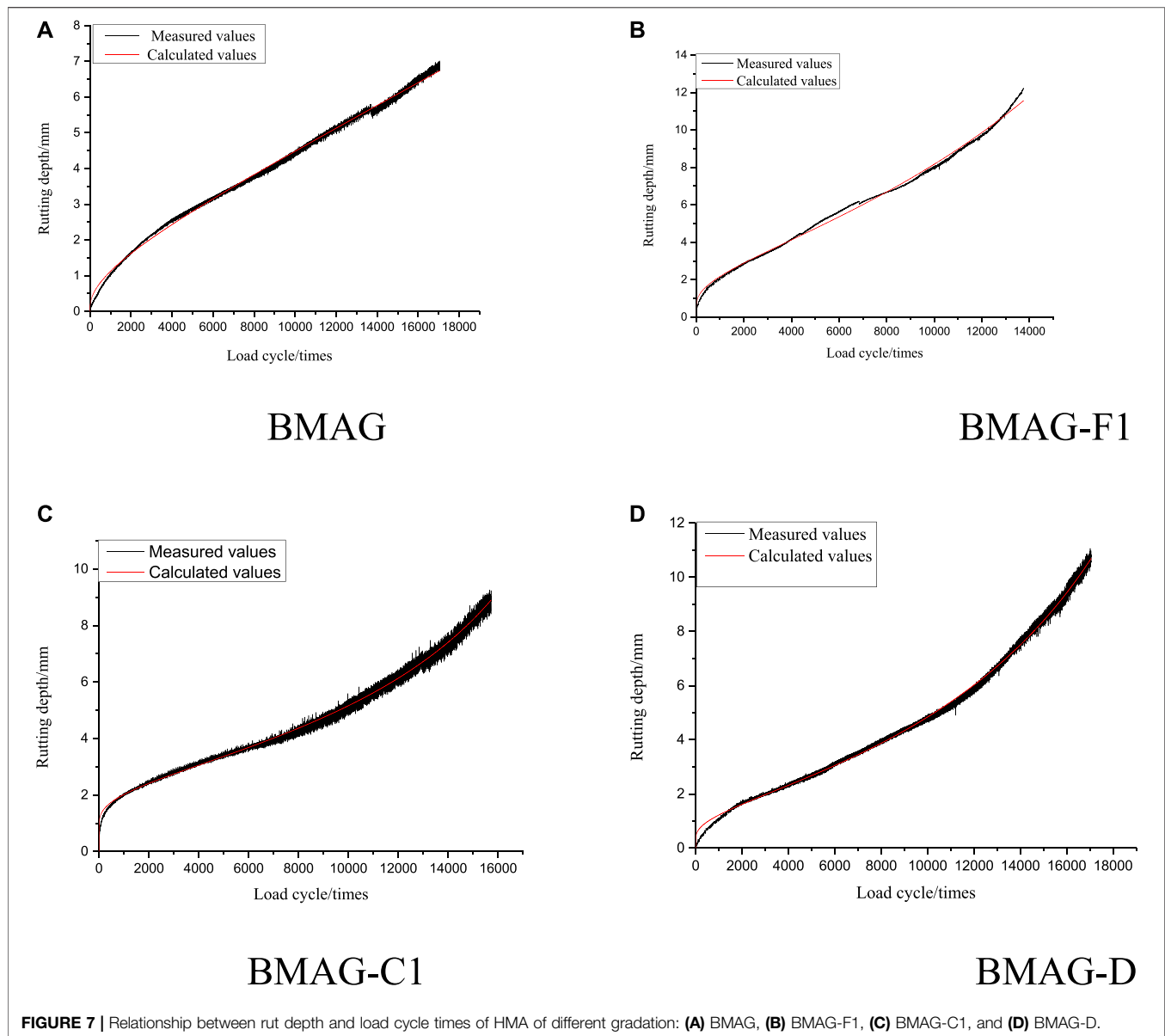
Take the derivative of both sides of Eq. (6) with respect to  $x$  and set  $x = 10,000$  obtaining Eq. (7). The viscoplastic strain rate  $\dot{\varepsilon}_{10000}^{vp}$  can be used to evaluate the high-temperature performance of HMA. A smaller  $\dot{\varepsilon}_{10000}^{vp}$  indicates that the HMA has a better high-temperature performance.

$$\dot{\varepsilon}_{10000}^{vp} = a^b b \varepsilon_{\infty}^{vp} \exp\left[-\left(\frac{a}{10,000}\right)^b\right] \times 10,000^{-(b+1)} \quad (7)$$

### Influence of Gradation Variability on Water Stability

The load cycle times of each graded HMA and the corresponding rut depth data were fitted with curves as shown in Eq. (4). To save space, for example, only the fitting curves of BMAG, BMAG-F1, BMAG-C1, and BMAG-D are given, as shown in Figure 7. The fitting parameters of all graded HMA are shown in Table 5;  $x_{SN}$  is calculated according to Eq. (5); and the analysis of the  $x_{SN}$  deviation percentage of each graded HMA from the BMAG-HMA is also listed in Table 5.

The parameters that affect water stability include the AV, VFA, and asphalt film thickness of HMA. It can be seen from Table 5 that, compared with the HMA of BMAG, the load cycle times of all variable-graded HMA decrease greatly, indicating that the water stabilities all decrease significantly, but the degree of decrease is quite different. As can be seen from Table 4, AVs of HMA of BMAG-F1 and BMAG-F2 are both smaller, but BMAG-F1 has more fine materials and smaller asphalt film thickness, so the reduction of  $x_{SN}$  of its HMA is larger. The



**FIGURE 7 |** Relationship between rut depth and load cycle times of HMA of different gradation: (A) BMAG, (B) BMAG-F1, (C) BMAG-C1, and (D) BMAG-D.

**TABLE 6 |** Viscoplastic strain parameters and high-temperature performance parameters of each gradated HMA.

Parameters	BMAG	BMAG-F1	BMAG-F2	BMAG-C1	BMAG-C2	BMAG-D	BMAG-U
$\epsilon_{\infty}^{VP}$	13.650	54.860	61.820	434.459	0.827	0.591	90.436
a	3.359E+18	1.250E+18	1.726E+17	1.077E+17	4.196E+06	1.735E+06	6.783E+14
b	0.050	0.058	0.062	0.075	0.115	0.169	0.079
$\dot{\epsilon}_{10000}^{VP}$ (10–6)	1.77	2.93	3.39	2.33	2.57	2.19	3.93
Relative deviation of $\dot{\epsilon}_{10000}^{VP}$ (%)	0.0	65.5	91.5	31.6	45.2	23.7	122.0

asphalt film thicknesses of BMAG-C1 and BMAG-C2 HMA are close to each other, but it can be seen from **Table 4** that *AV* of the former is larger, so the water stability of the HMA decreases more. The volume parameters of BMAG-U and BMAG-D HMA, such as *AV*, differ little, but the former's asphalt film thickness is small, so the decrease of water stability is more obvious.

### Effect of Gradation Variability on High-Temperature Performance

The rutting before the critical point is mainly the viscoplastic deformation of HMA under load, and **Eq. (6)** can be used to fit the viscoplastic strain of the deformation stage. For water damage of HMA, the strain before the critical point is fitted by the



Tseng-Lytton model (6). After obtaining the model parameters, the viscoplastic strain rate  $\dot{\epsilon}_{10,000}^{vp}$  is calculated according to Eq. (7), as shown in **Table 6**. The calculated and analyzed increase of  $\dot{\epsilon}_{10,000}^{vp}$  value of variability gradation compared with the reference gradation is also listed in **Table 6**.

It has been pointed out earlier that a smaller  $\dot{\epsilon}_{10,000}^{vp}$  indicates that the HMA is getting a better high-temperature performance. It can be seen from **Table 6** that the viscoplastic strain rate increased by 24–122% when the number of cyclic loadings was 10,000. Therefore, the high-temperature performance of the mixture of BMAG is the best, and the high-temperature performances of the variably graded mixtures have been significantly reduced in varying degrees.

Compared with BMAG-F1, the fine material of BMAG-F2 is finer, resulting in a more obvious viscoplastic strain rate and indicating that even though the HMA is a dense skeleton gradation, its high-temperature performance is very sensitive to the change of fine material. In comparison, the high-temperature performance of BMAG-C1 and BMAG-C2 mixture decreases relatively little, indicating that the high-temperature performance of HMA is less sensitive to the change of coarse aggregate. Compared with BMAG-C2, the high-temperature performance of BMAG-C1 mixture is slightly higher, which should be caused by more stone-stone contact points of the aggregates. Compared with BMAG-U, the overall BMAG-D gradation curve deviates a little bit from BMAG, while the former deviates farther from BMAG. The HMA of BMAG-U is a typical suspended dense structure, being with coarse aggregate particles far away from each other and no stone-stone contact, so its high-temperature performance degradation is more serious.

## CONCLUSION

In practical asphalt pavement engineering, it is inevitable that the gradation of HMA varies (Zhang et al. 2020). From the perspective of qualitative analysis, it is easy to infer that the gradation variability (asphalt content remains unchanged) will inevitably bring about changing of volume parameters and performances of HMA, but the changing direction and influence degree caused by the change may be known only through quantitative research. Based on the design of reasonable BMAG, this paper made an in-depth study on the change of HMA parameters caused by gradation variability and obtained the following main conclusions:

- (1) Once the skeleton density gradation designed according to the method in this paper changes, whether the gradation becomes coarser or finer, *AV*, *VMA*, and *VFA* of the compacted HMAs will change in different degrees. Compared with the HMA of BMAG, *AV* and *VMA* of the HMA decrease and *VFA* increases when the fine material becomes finer. *AV* and *VMA* of HMA increase while the *VFA* decreases after the coarse aggregate becomes coarser or finer.
- (2) Compared with the HMA of BMAG, the water stability of the designed variable gradation HMAs decreases by more than 50% on the whole. The thickness of asphalt film

decreases significantly when the amount of fine material increases, and the more the fine material is, the more the water stability decreases. After the variability of coarse aggregate, the change of asphalt film thickness is relatively small, but the change of *AV* is large, resulting in a decrease in water stability.

- (3) Compared with the HMA of BMAG, the high-temperature performances of all the HMAs of variable gradations decrease significantly. The more the fine material is, the lower the high-temperature performance gets. The higher the degree of suspension is, the greater the degradation of high-temperature performance will be.
- (4) The performance degradation of the variable gradation HMA shows that the performance of HMA of BMAG determined by the design theory for dense skeleton gradation is optimal, which indirectly reflects that the design theory for dense skeleton gradation adopted in this study is feasible and effective.
- (5) It is very important to determine the BMAG when studying the character change of HMA brought by gradation variation. If the unreasonable gradation is used as the BMAG, the properties of HMA may change in a good direction after gradation variation, so the problems caused by gradation variation cannot be found. As a theoretical basis for the study of gradation variation, the design theory for dense skeleton gradation established by the first author is a key technology, which has its originality and own characteristic.

## DATA AVAILABILITY STATEMENT

The original contributions presented in the study are included in the article/Supplementary Material; further inquiries can be directed to the corresponding authors.

## AUTHOR CONTRIBUTIONS

LS was responsible for the analysis of experimental data and the writing of the manuscript. ZL was mainly responsible for organizing test operation and data proofreading. ZH (the first corresponding author) was primarily responsible for the determination of the overall study program. LT assisted in the conduct of trials and the recording of trial data. JP was responsible for the preparation of test materials. And CW (the second corresponding author) proofread the test plan and supervised the test progress and plan execution.

## ACKNOWLEDGMENTS

This research was supported by the open fund from the Shandong provincial key laboratory of highway technology and safety assessment, China, and the authors would like to acknowledge the financial support.

## REFERENCES

- Chen, X. Q. (2003). *Effect of gradation type on performance of asphalt mixture*. Nanjing: Southeast University.
- Cheng, Y., He, X., and Dong, D. (2006). Effect of grading on water stability of AC-13C bituminous Mixture. *J. Wuhan Univ. Technol. (Transp. Sci. Eng.)*. 30 (3), 477–480. doi:10.4028/www.scientific.net/amm.178-181.1171
- Cominsky, R., Leahy, R. B., and Harrigan, E. T. (1994). Level one mix design: materials selection, compaction, and conditioning. 408.No. SHRP-A-1994.
- Garcia-Gil, L., Miró, R., and Félix, E. (2019). Evaluating the role of aggregate gradation on cracking performance of asphalt concrete for thin overlays. *Appl. Sci.* 9 (4), 628. doi:10.3390/app9040628
- Golalipour, A., Jamshidi, E., Niazi, Y., Afsharikia, Z., and Khadem, M. (2012). Effect of aggregate gradation on rutting of asphalt pavements. *Proc. Soc. Behav. Sci.* 53, 440–449. doi:10.1016/j.sbspro.2012.09.895
- Huang, W., Tao, L., and Yang, D. (2011). “Research of grading’s influence on asphalt mixture’s water stability,” in IEEE international conference on automation and logistics (ICAL), 456–460.
- Izzo, R. P. (1999). Evaluation of the use of the hamburg wheel-tracking device for moisture susceptibility of hot mix asphalt. *Transp. Res. Rec.* 1681 (1), 1999–2085.
- JTG E20-2011 (2011). *Highway engineering asphalt and asphalt mixture test procedures*. Beijing: China Communications Publishing.
- Kasu, S. R., Deb, S., Mitra, N., Muppireddy, A. R., and Reddy, K. S. (2019). Influence of aggregate size on flexural fatigue response of concrete. *Construct. Build. Mater.* 229, 116922. doi:10.1016/j.conbuildmat.2019.116922
- Kim, Y. R., Park, H. M., and Lutfi, J. E. S. (2009). Effects of aggregate structure on hot-mix asphalt rutting performance in low traffic volume local pavements. *Construct. Build. Mater.* 23 (6) 2177–2182. doi:10.1016/j.conbuildmat.2008.12.007
- Li, E. B. (2016). Effect of gradation variation on high temperature performance of asphalt mixture. *Arch. Eng. Technol. Des.* 2016 (9), 121–139. doi:10.1109/cecnet.2011.5769181
- Li, P., Zhang, Z., Li, H., and Wang, B. (2011). Research on cnditions of Hamburg Wheel Tracking tst and evaluating idicator for aphalt mxture. *J. Wuhan Univ. Technol. Transp. Sci. Eng.* 35 (1), 113–117. doi:10.3141/2446-10
- Lin, X. X. (2005). Revisiting HMA’s voids in mineral aggregate VMA. *Shang. Highw.* 4, 4–9. doi:10.31274/rtd-180813-13953
- Liu, G., Zhong chuan, M. A. O., Guo, Ze., and Peng, Yong. (2019). Experimental study on aggregate gradation influence on the performance-related properties of structural-layer asphalt mixtures. *Highway.* 5, 49. doi:10.31274/rtd-180813-13953
- Liu, S., Cao, W., Li, Y., Xue, Z., Zhang, H., and Guan, Y. (2015). Building and application research of physical model of VMA of mineral aggregate without adding asphalt. *China J. Highw. Transp.* 2, 8–13. doi:10.3403/00131804u
- Liu, S. T., Mao, H. L., and Yao, Z. Y. (2005). Research on relationships between volume of air voids and gradation curve of mineral aggregate. *J. Shandong Univ. (Eng. Sci.)*. 14, 98–101. doi:10.31274/rtd-180813-13953
- Lv, S., Peng, X., Liu, C., Ge, D., Tang, M., and Zheng, J. (2020). Laboratory investigation of fatigue parameters characteristics of aging asphalt mixtures: a dissipated energy approach. *Construct. Build. Mater.* 230, 116972. doi:10.1201/9781315281896-72
- Ma, H., Zhou, C., Feng, D., and Sun, L. (2017). Influence of fine aggregate content on low-temperature cracking of asphalt pavements. *J. Test. Eval.* 45 (3), 835–842. doi:10.1520/jte20150240
- Matthews, J. M., and Monismith, C. L. (1992). *The effect of aggregate gradation on the creep response of asphalt mixtures and pavement rutting estimates*. London: ASTM STP.
- Peng, H., Wang, F., Yang, T., and Ai, C. (2013). Experimental analysis on effect of aggregate gradation on pavement performance of asphalt mixture. *Highw. Eng.* 38 (2), 36–39.
- Praticò, F. G., and Vaiana, R. (2013). A study on volumetric versus surface properties of wearing courses. *Construct. Build. Mater.* 38, 766–775. doi:10.1520/stp24226s
- Tan, Y. Q., Li, Y., Rui, Z., Ji, L., and Xu, H. N. (2012). Effect of gradation on volume parameter of dense graded asphalt mixture. *J. China Foreign Highw.* 32 (1), 213–217. doi:10.12652/ksce.2015.35.6.1367
- Tsai, B. W., and Harvey, J. (2003). Application of Weibull theory in prediction of asphalt concrete fatigue performance. *Transp. Res. Rec.* 1832 (1), 121–130. doi:10.3141/1832-15
- Valdes-Vidal, G., Calabi-Floody, A., Sanchez-Alonso, E., and Miró, R. (2019). Effect of aggregate type on the fatigue durability of asphalt mixtures. *Construct. Build. Mater.* 224, 124–131. doi:10.1520/d8237-18
- Vavrik, W., Pine, W., and Carpenter, S. (2002b). Aggregate blending for asphalt mix design: bailey method. *Transport. Res. Rec.* 1789 (1), 146–153. doi:10.3141/1789-16
- Vavrik, W., Pine, W., and Carpenter, S. (2004). The factors that affect SMA mixture resulted from gradation of coarse aggregate. *J. Heilongjiang Inst. Technol.* 18 (3), 8–10. doi:10.4028/www.scientific.net/amr.700.179
- Vavrik, W. R., Huber, G., Pine, W. J., Carpenter, S. H., and Bailey, R. (2002a). Bailey method for gradation selection in HMA mixture design. *Transp. Res. Rec.* 14, 63–87. doi:10.1063/5.0000102
- Wang, D. Y., Zhang, X. N., and Wang, S. H. (2002). Influence of aggregate gradation on volumetric properties of asphalt mixture. *J. S. China Univ. Technol.* 3, 53–56. doi:10.1063/5.0000102
- Xie, S. B. (2011). Application of waste rubber powder modified asphalt in Jiujiang expressway pavement project. *Journal of Guizhou University of Finance and Economics* 12, 47–51. doi:10.22215/etd/1994-09818
- Xu, H. N. (2007). *The influnce of volume parameter on asphalt mixture's pavement performance*. Harbin: Harbin Institute of Technology.
- Yan, Y. Z. (2007). Research on the influence of temperature on the high temperature stability of asphalt mixtures. *J. Guizhou Univ. Fin. Econ.* 7, 33–47. doi:10.4028/www.scientific.net/amm.405-408.1871
- Yin, F., Arambula, E., Lytton, R., Martin, A. E., and Cicalon, L. G. (2014). Novel method for moisture susceptibility and rutting evaluation using Hamburg wheel tracking test. *Transport. Res. Rec.* 2446 (1), 1–7. doi:10.3390/ma13153269
- Zhang, H., Mao, X., Li, W., and Gou, J. (2016). “Effect of gradation and fineness on performance of rubber asphalt mixture at low temperature,” in 6th International conference on machinery, materials, environment, biotechnology and computer. Paris: Atlantis Press.
- Zhang, H., Yu, T., and Huang, Y. (2020). Comparative analysis of HMA aggregate variability based on impacting and gyratory compaction. *Construct. Build. Mater.* 242, 118055–118066. doi:10.1016/j.conbuildmat.2020.118055
- Zhang, Z., Luo, Y., and Zhang, K. (2018). Review on Hamburg Wheel-track device evaluation of asphalt mixture. *Mater. Rev.* 31 (3), 96–105. doi:10.1016/j.conbuildmat.2016.03.171
- Zheng, C., Zhao, D., Xiang, N., and Song, Z. (2012). Mechanism of low-temperature adhesion failure in asphalt mixtures with dense-suspension and void-skeleton structures. *Construct. Build. Mater.* 36, 711–718. doi:10.1016/j.conbuildmat.2012.06.058

**Conflict of Interest:** Authors ZH, LT, JP were employed by Shandong Hi-Speed Technology Development Group Co., Ltd.

The remaining authors declare that the research was conducted in the absence of any commercial or financial relationships that could be construed as a potential conflict of interest.

Copyright © 2021 Liu, Zhu, Zhang, Liu, Ji and Cao. This is an open-access article distributed under the terms of the Creative Commons Attribution License (CC BY). The use, distribution or reproduction in other forums is permitted, provided the original author(s) and the copyright owner(s) are credited and that the original publication in this journal is cited, in accordance with accepted academic practice. No use, distribution or reproduction is permitted which does not comply with these terms.



# Shear Fatigue Performance of Epoxy Resin Waterproof Adhesive Layer on Steel Bridge Deck Pavement

Ying Xu<sup>1,2</sup>, Xinpeng Lv<sup>1</sup>, Chunfeng Ma<sup>3</sup>, Fengming Liang<sup>3</sup>, Jiafei Qi<sup>3</sup>, Zhijing Chou<sup>1</sup> and Shifa Xu<sup>1,2\*</sup>

<sup>1</sup>School of Civil Engineering and Transportation, Beijing University of Civil Engineering and Architecture, Beijing, China, <sup>2</sup>Beijing Urban Transportation Infrastructure Engineering Technology Research Center, Beijing, China, <sup>3</sup>Henan Taihui Expressway Construction Co., Ltd., Henan, China

## OPEN ACCESS

### Edited by:

Dawei Wang,  
RWTH Aachen University, Germany

### Reviewed by:

Yanjuan Qiu,  
Southwest Jiaotong University, China

Leilei Chen,  
Southeast University, China

Yue Xiao,  
Wuhan University of Technology,  
China

Bin Hong,  
Harbin Institute of Technology, China

### \*Correspondence:

Shifa Xu  
xu-sf@126.com

### Specialty section:

This article was submitted to  
Structural Materials,  
a section of the journal  
Frontiers in Materials

**Received:** 16 October 2020

**Accepted:** 15 December 2020

**Published:** 21 January 2021

### Citation:

Xu Y, Lv X, Ma C, Liang F, Qi J, Chou Z  
and Xu S (2021) Shear Fatigue  
Performance of Epoxy Resin  
Waterproof Adhesive Layer on Steel  
Bridge Deck Pavement.  
Front. Mater. 7:618073.  
doi: 10.3389/fmats.2020.618073

In this study, the effects of temperature, shear stress, and coating quantity of waterproof adhesive layer on the shear fatigue performance of a steel bridge deck pavement were investigated. Direct shear fatigue tests of a pavement comprising an epoxy resin waterproof adhesive layer with stone matrix asphalt were conducted at different temperatures, stress levels, and coating quantities. The results show that temperature and stress have significant effects on the shear fatigue life. With increasing temperature and stress, the shear fatigue life of the waterproof adhesive layer decreased gradually. Therefore, for steel bridge deck pavements under high temperatures and heavy loads, the use of asphalt waterproof adhesive layers or pavement layers should be evaluated carefully while limiting the traffic of heavily loaded vehicles. Shear failure occurs at the waterproof adhesive layer–pavement interface and not at the steel–waterproof adhesive layer interface. The shear strength of the epoxy resin waterproof adhesive layer is mainly provided by the bond strength between the waterproof adhesive and pavement mixture as well as the interlocking force between the cured epoxy resin and the bottom interface of uneven pavement mixture. The shear strength increases with the coating quantity of the waterproof adhesive layer; however, after reaching the maximum value, the shear strength becomes stable. In contrast, the interlaminar shear fatigue life increases continuously with the coating quantity of the waterproof adhesive layer. Appropriately increasing the coating quantity is beneficial for improving the resistance of the waterproof adhesive layer to interlaminar shear fatigue failure.

**Keywords:** waterproof adhesive layer interface, epoxy resin adhesive, shear fatigue performance, interface failure, steel bridge deck

## 1 INTRODUCTION

In the construction of transportation infrastructure, steel bridges are used extensively because of their light weight, low cost, and ease of construction (Liu et al., 2016). The quality of the steel bridge deck pavement not only affects driving safety and comfort, it also affects the service life and investment benefit of a bridge system. However, owing to the complex stresses and poor thermal insulation of steel bridges, the waterproof adhesive layer interface between the steel plate and the asphalt mixture is usually the weakest part of a steel bridge deck pavement structure (Yao et al., 2016), which can easily cause interlayer displacement problems resulting from higher interlayer shear effects during service (Song et al., 2016; Wang et al., 2018).

The shear failure modes of the waterproof adhesive layer interface in steel deck pavement structures can be classified into shear strength failure (Medani 2001; Bocci and Canestrari 2012; Bocci and Canestrari 2013; Ge et al., 2014; Medani et al., 2008; Qiu et al., 2019) and shear fatigue failure under repeated loads (Boudabbous et al., 2013; Liu et al., 2016; Song et al., 2016). The failure of the waterproof adhesive layer is usually attributed to insufficient shear strength. Recent research has revealed that the interlayer bonding state of the bridge deck pavement is affected by the environment during service and is subjected to recurring wheel loads and vibration loads (Li and Yu 2014). Thus, it is in the state of overlapping stress changes for long periods, and experiences shear fatigue failure (Li and Yu 2014). Therefore, the traditional experimental method of shear strength failure cannot reflect the behavior of interlaminar shear fatigue.

Researchers have developed various test methods and devices to study the shear fatigue behavior of steel deck pavement structures. Currently, four methods are commonly used to evaluate the shear fatigue performance between the layers of a pavement structure: direct shear fatigue, four-point shear fatigue, slant shear fatigue, and double shear fatigue (Diakhate et al., 2006; Boudabbous et al., 2013; Li et al., 2014; Li and Yu 2014; Tozzo et al., 2014; Rahman et al., 2019). The double shear fatigue test method is often used for determining the shear fatigue damage and viscoelastic parameters of asphalt mixtures; it is less frequently used to study the interlayer shear fatigue performance between different material interfaces (Boudabbous et al., 2013). The slant shear fatigue test method can simulate the effect of vertical and horizontal forces simultaneously, but the loading angles of the forces cannot be adjusted, and the loading mode will intensify the stress concentration effect, resulting in inaccurate test results (Diakhate et al., 2006; Li et al., 2014; Li and Yu 2014). The four-point shear fatigue test method can produce a pure shear action at the interface of the specimen without superposition of the bending moment action and can apply normal stress to the interface at the same time. However, the procedure of this test method is more complex; hence, it is less commonly used at present (Rahman et al., 2019). The direct shear fatigue test method is easy to perform and can apply normal and shear stresses simultaneously. The accuracy of its test results is high; consequently, it has become the preferred test method for studying the shear fatigue performance of waterproof adhesive layers on steel bridge deck pavements (Tozzo et al., 2014).

At present, the research on the shear fatigue performance between the layers of a pavement structure is mainly focused on the asphalt concrete pavement structure and concrete bridge deck pavement structure (Li and Yu 2014; Tozzo et al., 2014; Song et al., 2016; Wang et al., 2017; Rahman et al., 2019). Research on steel deck pavement structures is relatively sparse. Wang et al. suggested that the interlaminar shear fatigue stress should be considered as an important design index in asphalt pavement structure design. Li et al. conducted shear fatigue tests on waterproof adhesive layers with different materials in a concrete bridge deck pavement, and found that the epoxy resin waterproof adhesive layer has better anti-fatigue performance. Qiu et al. (2019) conducted a shear fatigue test

on a steel bridge deck with modified asphalt concrete as the pavement layer and five types of waterproof adhesive layers. Their results showed that the setting of waterproof adhesive layers could significantly improve the shear fatigue life of the steel bridge deck pavement. Liu et al. (2016) performed shear fatigue tests on a steel deck pavement system with an SMA-13 pavement and a resin asphalt adhesive layer at three stress levels. It was revealed that the shear fatigue life decreased with increasing stress.

Regarding the influencing factors of the interlaminar shear fatigue life of pavement structures, Boudabbous et al. (2013) studied the shear fatigue performance of asphalt mixtures from the perspective of energy dissipation. They defined the plateau value as an index to evaluate the shear fatigue performance of the materials at different temperatures and stresses. Rahman et al. (2019) investigated composite beam specimens composed of SMA and asphalt concrete. They found that temperature and stress are significant factors affecting the shear fatigue life. The shear fatigue performance of the waterproof adhesive layer interface decreases with increasing temperature or stress. Wang et al. (2017) studied the shear fatigue performance of a thermoplastic waterproof adhesive layer material in an asphalt pavement, and obtained the shear fatigue life equation through temperature correction. Diakhate et al. (2011) investigated the influence of a waterproof adhesive layer on the interfacial shear fatigue performance of an asphalt mixture subjected to temperature and stress. They concluded that the waterproof adhesive layer has a considerable effect on the interlayer shear fatigue. Therefore, temperature and stress are the leading factors affecting the interlaminar shear fatigue life.

In summary, most of the existing studies are focused on pavements or concrete deck pavement structures. The number of studies on the interlaminar shear fatigue performance of steel deck pavements is fewer than that on the shear performance of waterproof adhesive layer materials. However, the shear fatigue life of bridge deck pavement is more sensitive than that of asphalt pavement (Chang et al., 2016). Moreover, the shear fatigue performance of steel deck pavement structures with epoxy resin as a waterproof adhesive layer is rarely studied. Compared with the traditional asphalt mixture, SMA has excellent high-temperature stability, low-temperature crack resistance, and deformation compatibility. The epoxy resin has high bond strength and is little affected by temperature, which is beneficial to enhance the bond between the pavement structure layer and steel plate and reduce defects such as interlayer void (Chen et al., 2020). Therefore, there are many steel deck pavement structures in China with SMA as the pavement layer and epoxy resin as the waterproof adhesive layer (Chen and Zhang 2004).

This study investigated the interlaminar shear fatigue performance of a typical steel deck pavement structure. Specifically, direct shear fatigue tests were performed to determine the shear resistance of a steel deck pavement considering the influence of temperature, stress, and coating quantity of the waterproof adhesive layer. The variation of shear fatigue life under different conditions was analyzed and the shear fatigue life equation of the waterproof adhesive layer



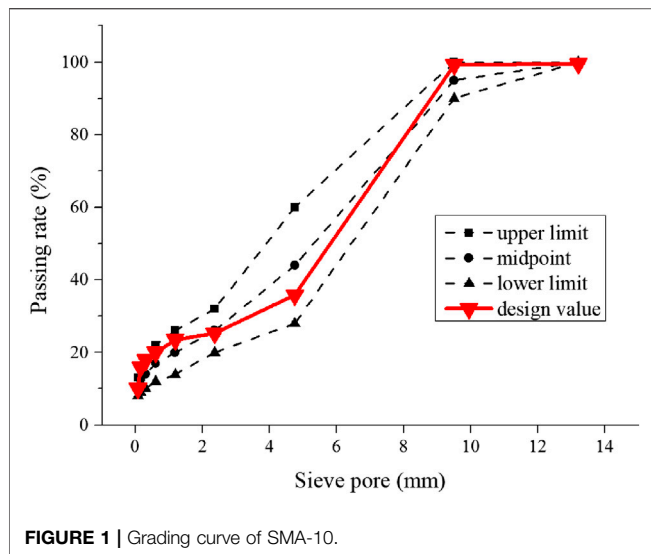


FIGURE 1 | Grading curve of SMA-10.

and bituminous mixtures for highway engineering (JTG E20-2011, 2011), are presented in **Table 1**. The optimal asphalt content of SMA-10 was determined as 6.2% using the Marshall design method.

### 2.1.2 Waterproof Adhesive Layer Material

The waterproof adhesive layer material used in this study was thermosetting epoxy resin adhesive type I (ER). The ER was composed of components A and B, with the mass ratio of component A to component B at 2:1. After the two components were mixed evenly, the mixture was applied in two layers. The first layer was coated with 1/3 of the total ER coating quantity, and breakstone with a particle size of 0.3–0.6 mm was sprayed at 300–400 g/m<sup>2</sup>. When the first layer of the waterproof adhesive was in the tack-free state, the second layer was applied, and breakstone with a particle size of 1.18–2.36 mm was sprayed at 500–800 g/m<sup>2</sup>. Subsequently, when the second layer was in the tack-free state, the SMA-10

TABLE 1 | Performance indices and test results of SBS modified asphalt.

Parameter	Unit	Test result	Technical specifications	Test method
Penetration degree at 25 °C	0.1 mm	65	60–80	T 0604
Softening point	°C	71	≥55	T 0606
Ductility at 5 °C	cm	38	≥30	T 0605
Elastic recovery at 25 °C	%	95.6	≥65	T 0662
RTFOT <sup>a</sup>				
Quality change	%	−0.21	≤ ±1.0	T 0609
Residual penetration ratio	%	68	≥60	T 0604
Residual ductility at 5 °C	cm	26	≥20	T 0605

<sup>a</sup> Rolling thin film oven test.

was established. Furthermore, the failure mechanism of the waterproof adhesive layer under different combinations of factors was examined. The objective of the study is to recommend measures for enhancing the design of steel deck pavement structures.

## 2 MATERIALS AND METHODS

### 2.1 Materials

#### 2.1.1 Pavement Materials

The research subject was the interlaminar shear performance between the pavement and steel plate. Modified asphalt SMA-10 and epoxy resin adhesive were used as the pavement layer and waterproof adhesive layer, respectively. SBS modified asphalt was composed of asphalt 70# and SBS modifier. The epoxy resin was type I epoxy resin binder, which is a kind of commercial adhesive that is used for steel bridge deck pavement. The specification of the steel plate was Q235.

The gradation of the SMA-10 is illustrated in **Figure 1**. Basalt was used as the coarse aggregate, limestone as fine aggregate and mineral powder, lignin fiber as fiber, and SBS modified asphalt as asphalt binder. The performance indices of the asphalt, which was evaluated in accordance with *Standard test methods of bitumen*

asphalt mixture was overlaid. The ER performance was tested according to *Specifications for design and construction of pavement on highway steel deck bridge* (JTG T3364-02-2019, 2019); the technical indices are listed in **Table 2**.

### 2.2 Test Methods

The relationship between the coating quantity of the ER waterproof adhesive and shear strength was established through shear strength tests. The optimum coating quantity of the waterproof adhesive layer was preliminarily determined. At this coating quantity, the effects of temperature and shear stress on the interlaminar shear fatigue properties were tested and analyzed through direct shear fatigue tests. Then, under the same shear stress, the influence of temperature and the waterproof adhesive layer quantity on the shear fatigue life was tested and analyzed.

#### 2.2.1 Shear Strength Test Method

The shear strength test was carried out in accordance with the test method described in Appendix C of *Specifications for design and construction of pavement on highway steel deck bridge* (JTG T3364-02-2019, 2019). The test used nine different quantities of the ER waterproof adhesive layer (0.7–1.5 kg/m<sup>2</sup>, increments of 0.1 kg/m<sup>2</sup>). The test temperature and shear failure displacement were set as 25°C and 5 mm, respectively.



**TABLE 2 |** Performance indices and test results of epoxy resin.

Parameter	Technical specifications	Test result	Test method
Bond strength with steel plate (MPa)	≥5.0	36.3	Appendix B of JTG T3364-02-2019 (2019)
Tensile strength at 23°C (MPa)	≥10.0	12	Appendix B of JTG T3364-02-2019 (2019)

**TABLE 3 |** Direct shear fatigue test parameters.

	Test group 1	Test group 2
Loading mode	Stress control	Stress control
Loading waveform and frequency	Sine wave, 10 Hz	Sine wave, 10 Hz
Shear stress (MPa)	0.28, 0.42, 0.56, 0.70	0.42
Coating quantity of waterproof adhesive layer (kg/m <sup>2</sup> )	Optimal quantity	0.5, 0.9, 1.3, 1.7
Temperature (°C)	−10, 15, 25, 50, 70	15, 30, 50
Failure criterion	Shear displacement reaches 5 mm	Shear displacement reaches 5 mm

The specimen fabrication simulated the actual construction process, i.e., coating two layers of the ER waterproof adhesive layer on a 100 × 100 × 16 mm steel plate, and then placing the plate in a rutting testing mold at 175°C. SMA-10 asphalt mixture at 175°C was poured into the rutting testing mold and compacted. Finally, after the rutting testing mold was cooled, a specimen with dimensions of 100 × 100 × 50 mm was cut. The average values of five parallel tests were taken as the experimental results. The shear strength was calculated using Eq. 1:

$$\tau = \frac{F}{S} \times \sin \alpha \quad (1)$$

where  $\tau$  is the shear strength (MPa),  $\alpha$  is the shear angle (°),  $F$  is the maximum load at failure (N), and  $S$  is the bottom surface area of the steel plate (mm<sup>2</sup>).

### 2.2.2 Direct Shear Fatigue Test Method

To investigate the effects of temperature, stress, and coating quantity of the waterproof adhesive layer on the shear failure performance of the steel deck pavement, two groups of tests were designed and conducted in this study. In the first group, the coating quantity of the waterproof adhesive layer was maintained at the optimal quantity. Different temperatures and stresses were selected for the tests. Considering the actual temperature range of steel bridge decks, the test temperatures were set as −10°C, 15°C, 25°C, 50°C, and 70°C. In a previous finite element analysis conducted by the team members, the maximum shear stress of the waterproof adhesive layer under a standard axle load of 100 kN was found to be approximately 1.4 MPa (Chou 2020). The values of the stress ratio in this test ranged from 0.2 to 0.5 (increasing by 0.1); therefore, the stresses were 0.28, 0.42, 0.56, and 0.70 MPa, respectively.

In the second group of tests, the stress was set as 0.42 MPa, and different temperatures and coating quantities of the waterproof adhesive layer were selected. The test temperatures were 15°C, 30°C, and 50°C, and the quantities of the waterproof adhesive layer were 0.5 kg/m<sup>2</sup>, 0.9 kg/m<sup>2</sup>, 1.3 kg/m<sup>2</sup>, and 1.7 kg/m<sup>2</sup>. The specific parameters are listed in Table 3.

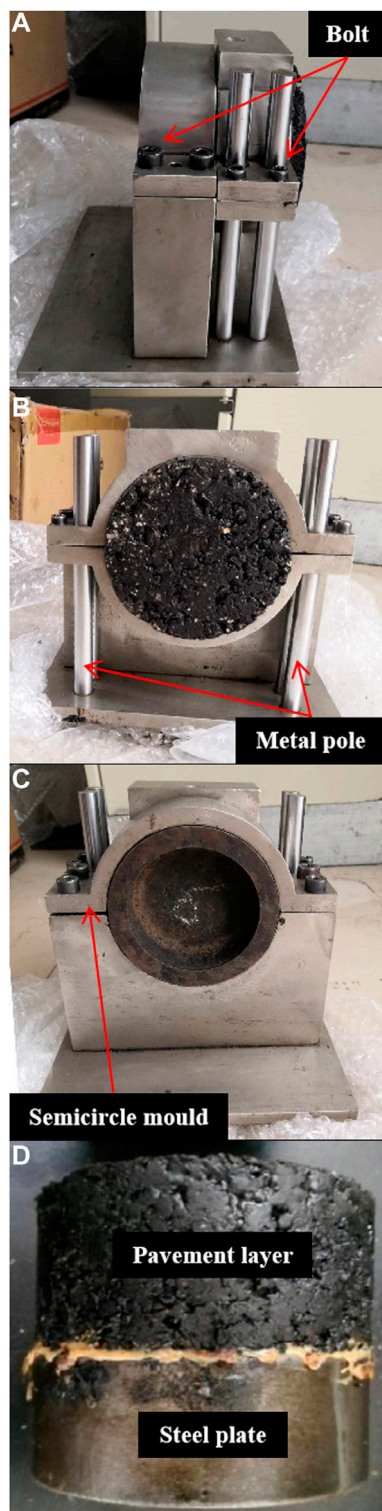
A test device based on a universal testing machine (UTM) was used for the direct shear fatigue test, as shown in Figure 2A. The device was divided into left and right parts. The left half could be moved up or down to fix the pavement layer (Figure 2B), whereas the right half could not be moved and was used to fix the steel plate (Figure 2C). Both parts were circular to ensure that the specimen could be evenly stressed. In this test, a cylindrical steel base with a diameter of 100 mm and a height of 50 mm was used. The height of the pavement mixture specimen was 40 mm, and the total height of the formed composite specimen was 90 mm (Figure 2D). The average values of five parallel tests were taken as the experimental results.

## 3 RESULTS AND DISCUSSION

### 3.1 Effect of Adhesive Quantity on Shear Strength

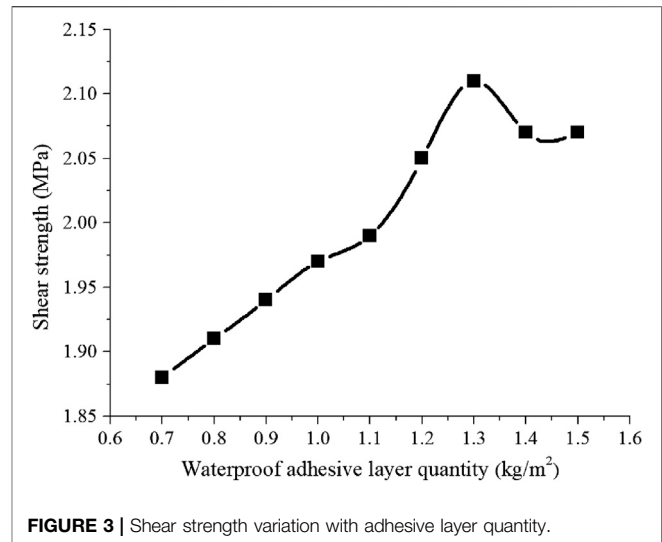
The relationship between the coating quantity of the waterproof adhesive layer and shear strength in the shear strength test is depicted in Figure 3. In the range of 0.7–1.5 kg/m<sup>2</sup>, the shear strength first increases with the coating quantity; then, it decreases and finally stabilizes. At the coating quantity of 1.3 kg/m<sup>2</sup>, the maximum shear strength is 2.11 MPa. Subsequently, any increase in the coating quantity causes the shear strength to decrease slightly, but it stabilizes at approximately 2.07 MPa.

For an asphalt waterproof adhesive layer, Liu et al. found that the shear strength of the interface between the steel plate and pavement increases with the coating quantity of the adhesive layer (Liu et al., 2017). However, after reaching the optimal value, a further increase in the coating quantity leads to a continuous decrease in shear strength. As a thermoplastic material, any excessive quantity of the asphalt waterproof adhesive will form a sliding layer at the interface. This sliding layer decreases the friction resistance between the layers, thus significantly reducing the interlaminar shear strength. However, after the shear strength of a thermosetting waterproof adhesive has reached the optimal quantity, it is no longer affected and remains unchanged.



**FIGURE 2 |** Direct shear fatigue test device.

The epoxy resin waterproof adhesive used in this study is a thermosetting material, and its shear strength variation is consistent with the result of the study by Liu et al. This is



**FIGURE 3 |** Shear strength variation with adhesive layer quantity.

because after paving and compacting, the interface between the pavement mixture and the steel plate becomes uneven (**Figure 4**). With any increase in the coating quantity of the waterproof adhesive layer, a larger amount of adhesive fills the uneven surface of the asphalt mixture. This increases the bonding area between the waterproof adhesive and asphalt mixture, which correspondingly increases the bond strength. After the asphalt mixture surface is completely filled with the waterproof adhesive, the optimal adhesive quantity is achieved. Subsequently, increasing further the epoxy resin waterproof adhesive quantity no longer increases the bonding area between the waterproof adhesive and pavement mixture. Moreover, owing to the high strength of the cured epoxy resin, the extra epoxy resin will not form a sliding layer between the layers similar to that of the asphalt waterproof adhesive layer. In addition, at the uneven interface between the waterproof adhesive layer and pavement layer, the interlocking force produced by the two materials will also contribute to the shear stress damage resistance. Therefore, the shear strength will not continue to decline after reaching the optimum adhesive quantity, but will be maintained at a high level.

## 3.2 Effect of Temperature and Stress on Shear Fatigue Life

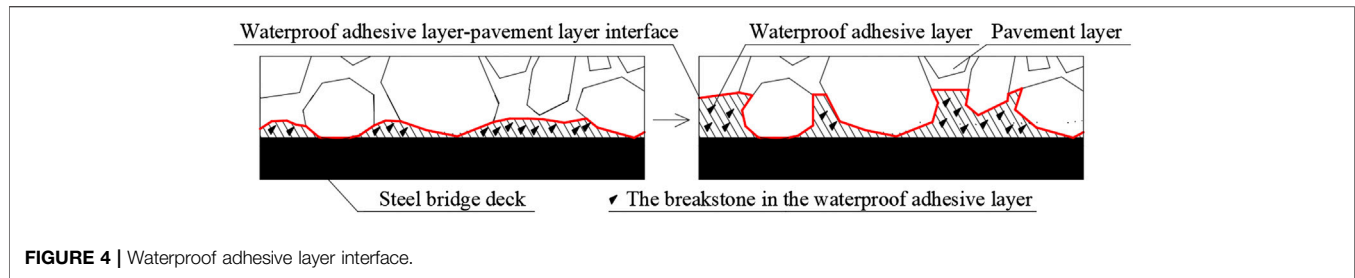
### 3.2.1 Significance Analysis

Under the optimum quantity of waterproof adhesive layer, the values of shear fatigue life at different temperatures and stresses are presented in **Table 4**.

The temperature and stress were analyzed by a two-way analysis of variance at 95% significance level. The  $F$  values of temperature and stress are 6.04 and 18.41, respectively, which are greater than the  $F_{\alpha}$  (0.05) values. It means that both factors have significant effects on the shear fatigue life.

### 3.2.2 Impact Trend Analysis

The shear fatigue life curves at different temperatures and stresses are displayed in **Figure 5**. It can be observed from **Figure 5A** that



**TABLE 4 |** Shear fatigue life ( $\times 10^4$ ) at different temperatures and stresses.

Temperature (°C)	Stress (MPa)			
	0.28	0.42	0.56	0.70
-10	69.34	31.25	16.87	9.57
15	67.30	28.85	15.47	8.74
25	65.73	25.89	13.83	7.28
50	43.30	11.07	3.36	0.94
70	5.00	0.86	0.53	0.15

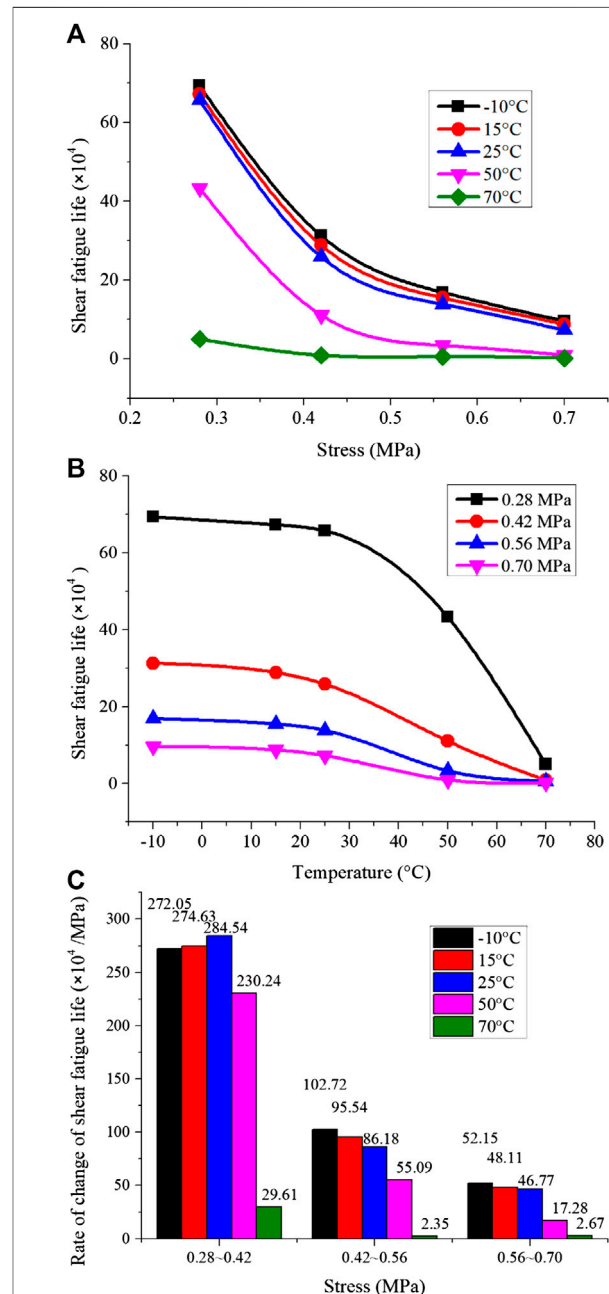
the shear fatigue life at the same temperature decreases with any increase in stress, and the rate of decrease gradually reduces. The influence of temperature on the rate of change of shear fatigue life at three different stress ranges of 0.28–0.42 MPa, 0.42–0.56 MPa, and 0.56–0.70 MPa is explained as follows:

$$R_i = (N_{i-1} - N_i) / (\tau_i - \tau_{i-1}) \quad (i = 1, 2, 3) \quad (2)$$

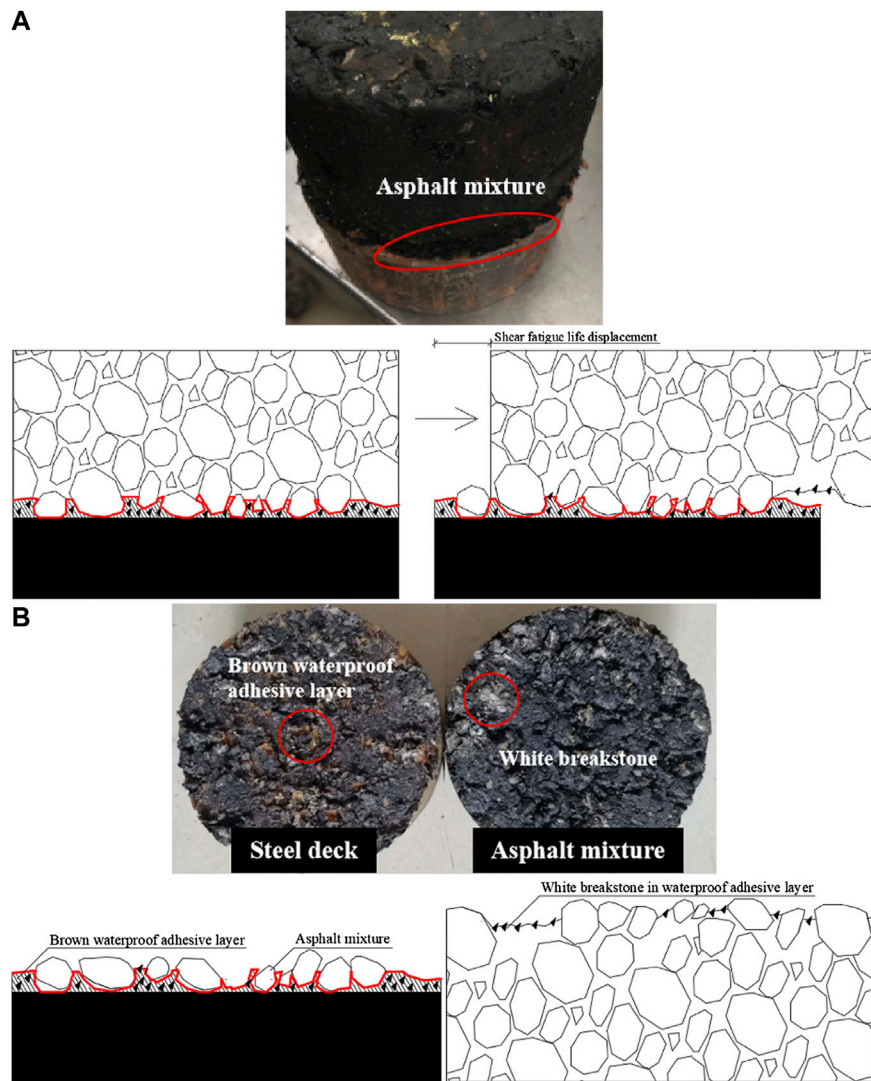
where  $R_1$ ,  $R_2$ , and  $R_3$  represent the change rates of shear fatigue life in the stress ranges of 0.28–0.42 MPa, 0.42–0.56 MPa, and 0.56–0.70 MPa, respectively;  $N_0$ ,  $N_1$ ,  $N_2$ , and  $N_3$  are the shear fatigue lives at 0.28, 0.42, 0.56, and 0.70 MPa, respectively; and  $\tau_0$ ,  $\tau_1$ ,  $\tau_2$ , and  $\tau_3$  represent the shear stresses at 0.28, 0.42, 0.56, and 0.70 MPa, respectively.

The change rates of shear fatigue life at the different stress ranges and temperatures were calculated using Eq. 2. As illustrated in Figure 5C, regardless of the temperature value, the change rate of shear fatigue life in the low stress range (0.28–0.42 MPa) is higher than that in the medium stress range (0.42–0.56 MPa) and high stress range (0.56–0.70 MPa). This indicates that the sensitivity of shear fatigue life decreases with increasing stress. In the same stress range, increasing temperature causes a gradual decrease in the change rate of the shear fatigue life. The change rate of the shear fatigue life changes slightly in the range of  $-10^\circ\text{C}$  to  $50^\circ\text{C}$ . However, when the temperature increases from  $50^\circ\text{C}$  to  $70^\circ\text{C}$ , the change rate of the shear fatigue life decreases sharply.

As shown in Figure 5B, under the same stress, the shear fatigue life decreases with increasing temperature, and the rate of decrease gradually increases. For similar interface conditions, an increase in temperature leads to a decrease in shear strength, which means that a high temperature is more likely to cause interface failure. It can also be seen from the figure that there are two stages of shear fatigue life variation with temperature. In the first stage ( $-10^\circ\text{C}$  to  $25^\circ\text{C}$ ), the shear fatigue lives at different



**FIGURE 5 |** Stress and temperature effect on shear fatigue life.



**FIGURE 6 |** Two kinds of shear fatigue failure states of specimens.

temperatures have negligible differences. Conversely, in the second stage (25°C–70°C), the shear fatigue lives decrease sharply. At 70 °C, regardless of the stress value, the shear fatigue life remains small. Chang et al. (2016) also found that the shear fatigue life of the thermosetting waterproof adhesive layer decreased sharply with the increase of the stress level at 60°C. When the stress level increased from 0.2 to 0.7, the shear fatigue life decreased by 99.3%.

The above observations can be explained by the following analysis. The pavement material selected in this study is SMA, and the softening point of modified asphalt is 71°C. When the temperature is in the range of 50°C–70°C, it is very close to the softening point of modified asphalt. At this point, the bond strength between the pavement layer and the epoxy resin waterproof adhesive layer is very weak. This leads to a sharp decrease in the interlayer shear fatigue life. In many parts of China, the temperature in summer may be above 35°C for a long

period. The maximum temperature of the pavement can reach 68.5°C, and the temperature can exceed 50°C per day for more than 9 h (Shen et al., 2018). If the steel deck pavement is subjected to large traffic volume or heavy traffic load, the pavement layer sustains a large shear stress, which is likely to result in interlayer slip or delamination failure. Therefore, for steel bridge deck pavements at high temperatures and under heavy loads, it is necessary to limit the traffic of heavily loaded vehicles; at the same time, the use of an asphalt waterproof adhesive layer or asphalt pavement layer should be evaluated carefully.

In summary, the shear fatigue life of the waterproof adhesive layer decreases with increasing stress and temperature, and the change rate of the shear fatigue life decreases with increasing stress. In the same stress range, an increase in temperature causes a decrease in the change rate of the shear fatigue life, and it varies only slightly in the range of –10°C to 50°C. However, when the temperature increases from 50°C to 70°C, the change rate of the



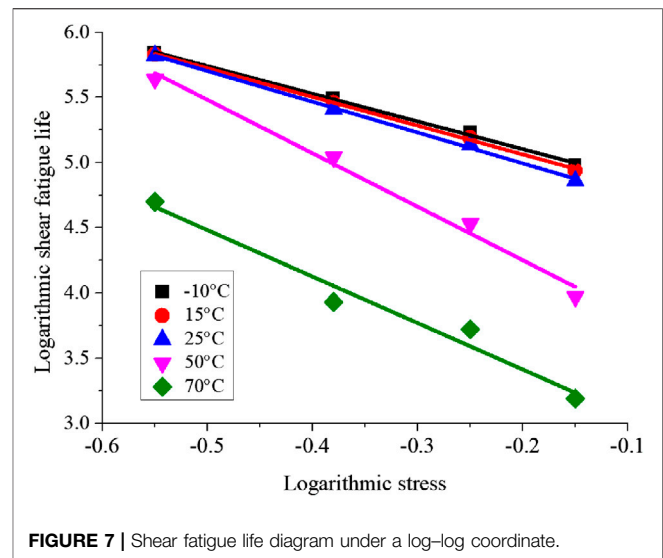
shear fatigue life decreases sharply. Taking 25°C as the boundary, the change rate of the shear fatigue life with temperature can be divided into two stages. At −10°C to 25°C, the shear fatigue lives at different temperatures have little differences. In contrast, when the temperature is higher than 25°C, the shear fatigue life decreases sharply. At 70°C, regardless of the stress value, the shear fatigue life remains small.

### 3.2.3 Failure Interface

The failure states of specimens at different temperatures are shown in **Figure 6**. At −10°C to 25°C (**Figure 6A**), when the shear displacement of the specimen reaches the failure standard and stops loading, the steel base and pavement mixture do not separate. In contrast, at 50°C–70°C (**Figure 6B**), most of the steel base and pavement mixture have completely separated. Based on the failure interface at different temperatures, the interface of the waterproof adhesive layer can be divided into two parts: steel–waterproof adhesive layer (S–W) and waterproof adhesive layer–pavement (W–P). It can be observed from **Figure 6** that the failure interface is not exposed to the surface of the steel base, and a layer of asphalt mixture is attached. This indicates that the failure interface is on the W–P part, and the bonding between the epoxy resin waterproof adhesive layer and steel base is very firm.

According to the analysis in **Section 3.1**, the shear resistance between the waterproof adhesive layer and the pavement layer originates from two factors. The first factor is the bond strength between the waterproof adhesive layer and the pavement mixture. The second factor is the interlocking force between the cured epoxy resin and the bottom interface of the uneven pavement mixture. When the temperature rises to a certain value, the asphalt on the stone surface at the bottom of the steel deck pavement will soften.

Subsequently, the bond strength between the asphalt and cured epoxy resin decreases significantly. This leads to a decrease in the shear resistance of the interface, which correspondingly reduces the shear fatigue life significantly. It can be seen from **Figure 6B** that some brown waterproof adhesive and part of the asphalt mixture are distributed on the surface of the steel base. This proves that the separated interface is the W–P portion. In addition, some white breakstone in the waterproof adhesive layer can be found at the bottom of the damaged pavement mixture. Therefore, during the loading process, the uneven interface between the asphalt mixture and waterproof adhesive is damaged when it resists the shear stress. This confirms that the interlocking force between the two materials makes an important contribution to the interfacial shear resistance. Chang et al. (2016) found that in the specimens damaged at high temperature, the pavement softened and the fracture surface was uneven, and a large amount of asphalt mixture adhered to the interface of the waterproof adhesive layer, which is consistent with the findings of this paper. Zhang and Ye (2014) reported that the fatigue resistance of the interface depends on the adhesive force of the waterproof adhesive layer and the frictional resistance between the layers, which is similar to the results obtained in this paper.



**FIGURE 7 |** Shear fatigue life diagram under a log-log coordinate.

Currently, most researchers generally refer to the waterproof adhesive layer interface as the steel–asphalt interface (Yao et al., 2016; Liu et al., 2018). Considering the experimental results of this study, this nomenclature is inaccurate. If the waterproof adhesive layer is asphalt material and the pavement material is an asphalt mixture, the high mixture temperature during the construction of the pavement mixture will integrate the asphalt waterproof adhesive layer and the asphalt mixture at the bottom of the pavement. Therefore, the shear resistance of the interface mainly originates from the bond strength between the steel plate and the asphalt waterproof adhesive layer, which can be called the steel–asphalt interface. However, this nomenclature is not accurate in the case of the epoxy resin thermosetting waterproof adhesive layer used in this study, because there are two interfaces between the steel and asphalt, specifically the S–W and W–P interfaces. The shear resistance of the W–P interface includes the bond force between the waterproof adhesive layer and pavement layer as well as the interlocking force between the cured waterproof adhesive layer and the asphalt mixture.

### 3.2.4 Fatigue Equation

The relationship between the stress and shear fatigue life is linear in a double logarithmic coordinate (Wang et al., 2018), as shown in **Eq. 3** and **Figure 7**.

$$\lg N_{SF} = a - b \lg \tau \quad (3)$$

where  $\lg N_{SF}$  is the logarithmic shear fatigue life,  $\lg \tau$  is the logarithmic stress,  $\tau$  is the stress (MPa), and  $a$  and  $b$  are parameters.

The prediction models for temperature and shear fatigue life are presented in **Table 5**. It can be observed that the slopes of the three fitting lines under low and normal temperatures (−10°C, 15°C, and 25°C) are almost the same. In addition, the slopes of the two fitting lines in the high-temperature region (50°C and 70°C) are similar. However, the slope at 25°C is significantly different from that at 50°C. The results of covariance analysis with 95%



**TABLE 5 |** Shear fatigue life prediction models for different temperatures.

Temperature (°C)	Fitting equation	Predictive models	R <sup>2</sup>
–10	$\lg N_{SF} = 4.670 - 2.143 \lg \tau$	$N_{SF} = 46,773.514(\tau)^{-2.143}$	0.995
15	$\lg N_{SF} = 4.617 - 2.210 \lg \tau$	$N_{SF} = 41,399.967(\tau)^{-2.210}$	0.997
25	$\lg N_{SF} = 4.517 - 2.367 \lg \tau$	$N_{SF} = 32,885.163(\tau)^{-2.367}$	0.996
50	$\lg N_{SF} = 3.420 - 4.115 \lg \tau$	$N_{SF} = 2,630.270(\tau)^{-4.115}$	0.979
70	$\lg N_{SF} = 2.682 - 3.600 \lg \tau$	$N_{SF} = 480.839(\tau)^{-3.600}$	0.959

confidence interval (Table 6) confirmed this significant difference.

To establish a unified shear fatigue life equation that considers the effects of temperature and stress, the temperature range was divided into –10°C to 25°C and 25°C–70°C to modify the shear fatigue equation (Wang et al., 2017; Fang et al., 2019). Setting –10°C and 25°C as the standard temperatures,  $N_{SFT0}$  was defined as the shear fatigue life at –10°C or 25°C.  $N_{SFT}$  was defined as the shear fatigue life at any temperature  $T$ . Based on  $N_{SF} = 46,773.514(\tau)^{-2.143}$  at –10°C and  $N_{SF} = 32,885.163(\tau)^{-2.367}$  at 25°C, it was found that there is a good linear relationship between  $N_{SFT}/N_{SFT0}$  and  $T/T_0$  in the two temperature ranges based on data fitting using the Origin software, as indicated in Eq. 4, where  $a$  and  $b$  are temperature correction factors for shear fatigue life.

$$\frac{N_{SFT}}{N_{SFT0}} = a - b \left( \frac{T}{T_0} \right) \quad (4)$$

After calculating the  $N_{SFT}/N_{SFT0}$  and  $T/T_0$  in the two temperature ranges and fitting using the Origin software, the shear fatigue lives at –10°C to 25°C and 25°C–70°C were obtained (Eq. 5):

$$\begin{cases} N_{SFT} = (0.966 - 0.0042T) \times 44773.15\tau^{-2.143} & -10 \leq T < 25 \\ N_{SFT} = (1.506 - 0.021T) \times 32885.16\tau^{-2.367} & 25 \leq T \leq 70 \end{cases} \quad (5)$$

### 3.3 Effect of Adhesive Quantity on Shear Fatigue Life

The shear fatigue life curves at different temperatures and coating quantity of the waterproof adhesive layer are presented in Figure 8.

As shown in Figure 8A, the shear fatigue life at the same temperature increases with the coating quantity of the ER

waterproof adhesive layer. From Figure 8B, the shear fatigue life decreases with any increase in temperature under different coating quantities of the adhesive. The change rate of the shear fatigue life depends on the shear fatigue life per unit of the coating quantity, as presented in Table 7. The results show that the fatigue life increases rapidly when the coating quantity is small. With increasing coating quantity, the increasing trend of the shear fatigue life tends to become stable and is generally linear. The fatigue life increases faster at low temperatures than at high temperatures. Moreover, within the range of 0.9–1.7 kg/m<sup>2</sup>, a linear relationship between the quantity of the waterproof adhesive layer and shear fatigue life is observed. The equations are shown in Figure 8A. Here,  $N_{SF}$  is the shear fatigue life and  $D_{wbl}$  is the quantity of the waterproof adhesive layer.

It should be noted that when the coating quantity of the waterproof adhesive layer increases, the change trends of the shear fatigue life and shear strength differ. As mentioned in Section 3.1, the shear strength reaches the maximum value at 1.3 kg/m<sup>2</sup> and remains essentially unchanged with increase in the coating quantity. In contrast, as described in this section, the shear fatigue life increases continuously with increasing coating quantity.

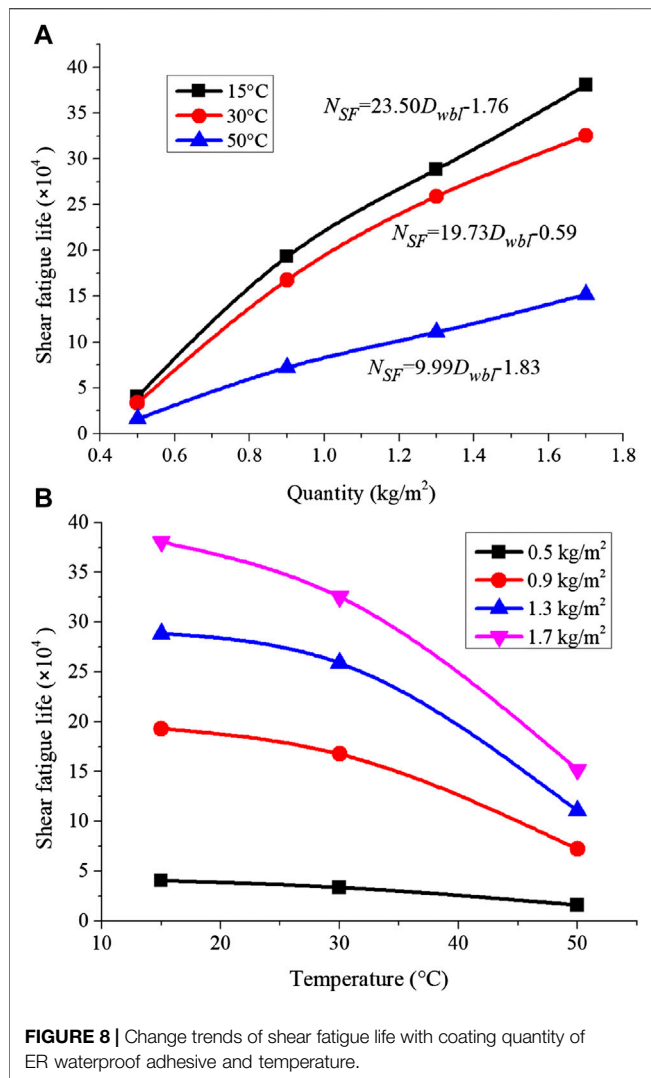
One possible reason is the use of the Superpave gyratory compactor in the shear fatigue test. In the process of compaction, the waterproof adhesive was fully bonded with the loose asphalt mixture and compacted. With the continuous increase in coating quantity of the waterproof adhesive, part of the excess waterproof adhesive penetrated into the air voids of the asphalt mixture forming a “hybrid layer” composed of epoxy resin and asphalt mixture. Yao et al. also observed the infiltration of waterproof adhesive into the pavement mixture (Yao et al., 2016). The cured epoxy resin could have increased the strength of the “hybrid layer,” which in turn might have reduced the shear fatigue damage in each stress cycle, i.e., the shear fatigue dissipated energy would have been reduced. Hence, the shear fatigue resistance increased gradually. However, the above hypothesis requires further experimental verification.

## 4 CONCLUSION

In this study, shear strength tests and direct shear fatigue tests were performed to analyze the influence of temperature, stress, and coating quantity of the waterproof adhesive layer on the shear fatigue performance of a steel bridge deck pavement with SMA as the pavement layer and epoxy resin as the waterproof adhesive layer. The conclusions are as follows:

**TABLE 6 |** Differential analysis of the slope of fitted equation.

Significant difference	Temperature (°C)				
	–10 and 15	15 and 25	25 and 50	50 and 70	25 and 70
$P$	0.571 insignificant	0.222 insignificant	0.008 significant	0.375 insignificant	0.039 significant



- (1) Temperature and stress have significant effects on the shear fatigue life. When the temperature reaches 50°C, the interlaminar shear fatigue life of the pavement structure decreases sharply. Taking 25°C as the boundary, the change rate of the shear fatigue life with temperature can be divided into two stages. At -10°C to 25°C, the shear fatigue lives at different temperatures have little differences. In contrast, when the temperature is higher than 25°C, the shear fatigue life decreases sharply. At 70°C, regardless of the stress value, the shear fatigue life remains small. Therefore, for steel bridge deck pavements subjected to high temperatures and heavy loads, it is necessary to limit the traffic of heavily loaded vehicles. In addition, the use of an asphalt waterproof adhesive layer or asphalt pavement layer should be evaluated intensively.
- (2) Temperature and stress have a linear relationship with shear fatigue life on a double logarithmic coordinate. The final

**TABLE 7 |** Change rate of shear fatigue life with coating quantity ( $\times 10^4$  m<sup>2</sup>/kg).

Temperature (°C)	Coating quantity (kg/m <sup>2</sup> )		
	0.5–0.9	0.9–1.3	1.3–1.7
15	38.15	23.88	23.04
30	33.51	22.85	16.62
50	14.08	9.64	10.34

predictive model of shear fatigue life is obtained by temperature correction and data fitting.

- (3) The interface of the epoxy resin waterproof adhesive layer can be divided into two parts: steel plate–waterproof adhesive layer (S–W) and waterproof adhesive layer–pavement (W–P). The damage interface of shear fatigue at different temperatures always occurs at the W–P interface. The shear strength of the epoxy resin waterproof adhesive layer is mainly provided by the bond strength between the waterproof adhesive and pavement mixture as well as the interlocking force between the cured epoxy resin and the bottom interface of the uneven pavement mixture.
- (4) With an increase in the quantity of the epoxy resin waterproof adhesive layer, the shear strength first increases to the optimal value (2.11 MPa) and then stabilizes, whereas the shear fatigue life increases continuously. Therefore, increasing the thickness of the waterproof adhesive layer is beneficial for resisting the interlayer shear fatigue failure.

## DATA AVAILABILITY STATEMENT

The raw data supporting the conclusions of this article will be made available by the authors, without undue reservation.

## AUTHOR CONTRIBUTIONS

YX and XL: Writing-original draft preparation, methodology, writing-review and editing. XL, CM, FL, JQ, and ZC: The data curation. YX and SX: Supervision, project administration and funding acquisition. All authors contributed to the article and approved the submitted version.

## FUNDING

This work was funded by the Science and Technology Project of the Beijing Municipal Education Commission (Grant No. SQKM201810016003), the Beijing Advanced Innovation Center for Future Urban Design (Grant No. UDC2019032624), and the research project of the Nation Natural Science Foundation of China (Grant No. 51978035).

## REFERENCES

- Bocci, E., and Canestrari, F. (2012). Analysis of structural compatibility at interface between asphalt concrete pavements and orthotropic steel deck surfaces. *J. Transport. Res. Rec. Board.* 2293 (1), 1–7. doi:10.3141/2293-01
- Bocci, E., and Canestrari, F. (2013). Experimental evaluation of shear resistance of improved steel-asphalt interfaces. *J. Transport. Res. Rec. Board.* 2370 (2370), 145–150. doi:10.3141/2370-18
- Boudabbous, M., Millien, A., Petit, C., and Neji, J. (2013). Energy approach for the fatigue of thermoviscoelastic materials: application to asphalt materials in pavement surface layers. *Int. J. Fatig.* 47 (FEB), 308–318. doi:10.1016/j.ijfatigue.2012.09.013
- Chang, Y., Chen, Z., and Zhang, Z. (2016). Shear fatigue performance of epoxy emulsified asphalt adhesive layer. *J. Jiangsu Univ. (Nat. Sci. Ed.)*. 2016 (3), 342–346 [in Chinese]. doi:10.3969/j.issn.1671-7775.2016.03.016
- Chen, L., Qian, Z., Chen, D., and Wei, Y. (2020). Feasibility evaluation of a long-life asphalt pavement for steel bridge deck. *Adv. Civ. Eng.* 2020, 1–8. doi:10.1155/2020/5890945
- Chen, S., and Zhang, H. (2004). Research and development of SMA Pavement Technology for steel bridge deck. *Highway Transp. Technol.* 21 (10), 5–8 [in Chinese]. doi:10.3969/j.issn.1002-0268.2004.10.002
- Chou, Z. (2020). *Analysis and optimization of steel deck pavement structure under various fatigue damage behaviors[D]*. Beijing University of Civil Engineering and Architecture, Beijing, China, (in Chinese)
- Diakhate, M., Phelipot, A., Millien, A., and Petit, C. (2006). Shear fatigue behaviour of tack coats in pavements. *Road Mater. Pavement Des.* 7, 201–222. doi:10.1080/14680629.2006.9690033
- Diakhate, M., Millien, A., Petit, C., Phelipot-Mardele, A., and Pouteau, B. (2011). Experimental investigation of tack coat fatigue performance: towards an improved lifetime assessment of pavement structure interfaces. *Construct. Build. Mater.* 25 (2), 1123–1133. doi:10.1016/j.conbuildmat.2010.06.064
- Fang, N., Wang, X., Ye, H., Sun, Y., and Yuan, L. (2019). Study on fatigue characteristics and interlayer design method of waterproof cohesive bridge deck layer. *Appl. Sci.* 9 (10), 2090. doi:10.3390/app9102090
- Ge, Z., Wang, Y., and Hang, M. (2014). New device and methodology for evaluating the shear behavior of steel bridge deck pavement pasted by gfrp sheets. *J. Test. Eval.* 42 (1), 20120343. doi:10.1520/JTE20120343
- JTG T3364-02-2019. (2019). *Specifications for design and construction of pavement on highway steel deck bridge*. Beijing: Ministry of Transport of the People's Republic of China.
- JTG E20-2011. (2011). *Standard test methods of bitumen and bituminous mixtures for highway engineering*. Beijing: Ministry of Transport of the People's Republic of China.
- Li, H., and Yu, B. (2014). Fatigue performance and prediction model of multilayer deck pavement with different tack coat materials. *J. Mater. Civ. Eng.* 26 (5), 872–877. doi:10.1061/(ASCE)MT.1943-5533.0000895
- Li, S., Liu, X., and Liu, Z. (2014). Interlaminar shear fatigue and damage characteristics of asphalt layer for asphalt overlay on rigid pavement. *Construct. Build. Mater.* 68 (oct.15), 341–347. doi:10.1016/j.conbuildmat.2014.06.053
- Liu, X., Feng, D., Tang, H., Zhou, C., and Li, J. (2016). Investigation on the bending fatigue and shear failure in steel bridge deck pavement systems. *J. Test. Eval.* 44 (2), 20150236. doi:10.1520/JTE20150236
- Liu, X., Zhou, C., Feng, D., Fan, X., and Xie, S. (2017). Experimental study on interlayer shear properties of ERS pavement system for long-span steel bridges. *Construct. Build. Mater.* 143, 198–209. doi:10.1016/j.conbuildmat.2017.03.144
- Liu, Y., Yao, B., Yu, C., Wu, J., Chen, J., and Zhang, L. (2018). Experimental evaluation of the shear performance of steel-asphalt interface considering temperature and humidity coupling. *Int. J. Adhesion Adhes.* 84, 360–367. doi:10.1016/j.ijadhadh.2018.04.011
- Medani, T. O. (2001). *Asphalt surfacing applied to orthotropic steel bridge decks (Report 7-01-127-1)*. Delft, The Netherlands: TU Delft.
- Medani, T. O., Liu, X., Huurman, M., Scarpas, A., and Molenaar, A. A. A. (2008). Experimental and numerical characterization of a membrane material for orthotropic steel deck bridges: part 1: experimental work and data interpretation. *Finite Elem. Anal. Des.* 44 (9-10), 552–563. doi:10.1016/j.finel.2008.01.013
- Qiu, Y., An, S., Rahman, A., and Ai, C. (2019). Evaluation and optimization of bridge deck waterproof bonding system using multi-objective grey target decision method. *Road Mater. Pavement Des.*, 1–15. doi:10.1080/14680629.2019.1568288
- Rahman, A. A., Huang, H., Ding, H., Xin, C., and Lu, Y. (2019). Fatigue performance of interface bonding between asphalt pavement layers using four-point shear test set-up. *Int. J. Fatig.* 121, 181–190. doi:10.1016/j.ijfatigue.2018.12.018
- Shen, C., Gao, P., and Zhang, H. (2018). Research on temperature field of steel deck pavement by finite element. *Highw. Eng.* 43 (3), 21–25 [in Chinese].
- Song, W., Shu, X., Huang, B., and Woods, M. (2016). Laboratory investigation of interlayer shear fatigue performance between open-graded friction course and underlying layer. *Construct. Build. Mater.* 115 (jul.15), 381–389. doi:10.1016/j.conbuildmat.2016.04.060
- Tozzo, C., Fiore, N., and D'Andrea, A. (2014). Dynamic shear tests for the evaluation of the effect of the normal load on the interface fatigue resistance. *Construct. Build. Mater.* 61 (jun.30), 200–205. doi:10.1016/j.conbuildmat.2014.03.010
- Wang, X., Fang, N., Ye, H., and Zhao, J. (2018). Fatigue damage analysis of cement-stabilized base under construction loading. *Applied Ence.* 8 (11), 2263. doi:10.3390/app8112263
- Wang, X., Su, Z., Xu, A., Zhou, A., and Zhang, H. (2017). Shear fatigue between asphalt pavement layers and its application in design. *Construct. Build. Mater.* 135 (MAR.15), 297–305. doi:10.1016/j.conbuildmat.2016.12.151
- Yao, B., Li, F., Wang, X., and Cheng, G. (2016). Evaluation of the shear characteristics of steel-asphalt interface by a direct shear test method. *Int. J. Adhesion Adhes.* 68, 70–79. doi:10.1016/j.ijadhadh.2016.02.005
- Zhang, H., and Ye, J. (2014). Research on the effect of interface contact conditions on the interlayer fatigue performance of concrete bridge deck pavement structure highway and transportation science and technology. *Appl. Technol. Ed.* 6 [in Chinese], 347–348. doi:10.3969/j.issn.1674-0610.2018.03.005

**Conflict of Interest:** Authors CM, FL, and JQ were employed by company Henan Taihui Expressway Construction Co., Ltd.

The remaining authors declare that the research was conducted in the absence of any commercial or financial relationships that could be construed as a potential conflict of interest.

Copyright © 2021 Xu, Lv, Ma, Liang, Qi, Chou and Xu. This is an open-access article distributed under the terms of the Creative Commons Attribution License (CC BY). The use, distribution or reproduction in other forums is permitted, provided the original author(s) and the copyright owner(s) are credited and that the original publication in this journal is cited, in accordance with accepted academic practice. No use, distribution or reproduction is permitted which does not comply with these terms.



# Study on Quantitative Characterization of Morphological Characteristics and High Temperature Performance Evaluation of Coarse Aggregate Based on Computer Vision

Zhanliang Liu<sup>1,2</sup>, Chen Zhang<sup>1,3\*</sup>, Linlong Shao<sup>1</sup> and Jiangfeng Wang<sup>1</sup>

<sup>1</sup>Key Laboratory for Special Area Highway Engineering of Ministry of Education, Chang'an University, Xi'an, China, <sup>2</sup>Department of Railway Engineering, Shijiazhuang Institute of Railway Technology, Shijiazhuang, China, <sup>3</sup>School of Energy and Architecture, Xi'an Aeronautical University, Xi'an, China

## OPEN ACCESS

### Edited by:

Hui Yao,  
Beijing University of Technology,  
China

### Reviewed by:

Jianning Hu,  
Southeast University, China  
Yunchao Tang,  
Zhongkai University of Agriculture and  
Engineering, China

### \*Correspondence:

Chen Zhang  
865916600@qq.com

### Specialty section:

This article was submitted to  
Structural Materials,  
a section of the journal  
Frontiers in Materials

**Received:** 16 September 2020

**Accepted:** 30 November 2020

**Published:** 02 February 2021

### Citation:

Liu Z, Zhang C, Shao L and Wang J  
(2021) Study on Quantitative  
Characterization of Morphological  
Characteristics and High Temperature  
Performance Evaluation of Coarse  
Aggregate Based on Computer Vision.  
Front. Mater. 7:607105.  
doi: 10.3389/fmats.2020.607105

The morphological characteristics of aggregate include outline shape, angularity, and surface texture, which determine the mutual extrusion and friction between aggregates, and significantly affect the performance of asphalt pavement. At present, the research on the morphological characteristics of coarse aggregate is mainly focused on indoor visual identification technology (AIMS, XCT, etc.), in which the applicability of the proposed aggregate shape characterization index is weak, and these instruments could not serve the practical engineering well. In this article, the Coarse Aggregate Morphological Identification System (CAMIS) is developed based on computer vision technology, and the system can recognize the shape features of aggregates above 2.36 mm particle size and carry out uninterrupted feeding and removal based on the mechanical arm system, which can realize large sample detection. Based on CAMIS aggregate identification system and laboratory tests (rutting test, dynamic modulus test, and penetration shear test), the shape identification and performance test of aggregate samples from construction site are carried out, and an aggregate performance evaluation index, CEI, suitable for high-temperature areas is proposed in combination with the improved response surface method. The processing parameters of vertical shaft impact aggregate crusher are optimized based on the CEI index, and the recommended processing parameters are verified by laboratory tests. The results show that the morphological characteristics of coarse aggregate affect the high temperature performance in order angularity, needle flake, axial coefficient, and convexity. The combination of processing parameters of vertical axis impact crusher is recommended to be of 45 m/s rotational speed, 3 t/h feed quantity, and 30% air intake. Verified by laboratory tests, the aggregate identification system CAMIS developed in this article and the proposed aggregate performance evaluation index, CEI, are highly reliable.

**Keywords:** asphalt pavement, coarse aggregate, computer vision, technology, mesomorphology, quantitative characterization, performance evaluation

## INTRODUCTION

The morphological characteristics of aggregate include outline shape, angularity, and surface texture, which are closely related to the formation of asphalt mixture spatial skeleton and the interaction between asphalt and aggregate, significantly affecting the road performance of asphalt mixture (Li et al., 2019). The shape, angularity, and surface texture of coarse aggregate determine the intercalation and friction between aggregates and make a certain contribution to the formation of good mechanical properties and structural strength of asphalt mixture. It is a key factor for asphalt pavement to overcome permanent deformation (Zhang et al., 2012). Many scholars have done in-depth research on the acquisition and characterization of morphological characteristics of coarse aggregate. Al-Rousan et al. (2007) revealed that the influence of coarse aggregates angularity and shape on the performance of asphalt mixture is significant, but the existing research techniques cannot distinguish the effect of angularity and shapes. Arasan et al. (2011) used the DIP technique to study the morphological characteristics of the aggregate and proposed some new evaluation indexes such as elongation and roundness. Rezaei and Masad (2013) quantitatively characterize the relationship between aggregate morphology and pavement skid resistance using the data of laboratory test and field investigation. In recent years, some scholars have used X-ray tomography (XCT) to obtain internal continuous tomographic images to reflect the three-dimensional spatial structure information of materials. The digital image obtained based on XCT technology can show the three-dimensional structural and geometric features of coarse aggregate more accurately and truly. Wang et al. (2016) used a modified Los Angeles Abrasion Test (LAAT) to change the shape of the aggregate and studied the correlation between aggregate shape parameters and high temperature performance of asphalt mixture. Ding et al. (2017) obtained the realistic shape of granular aggregates and made the statistical analysis to quantify the morphological differences. Ghuzlan et al. (2019) proposed the flatness index and roundness index as morphological evaluating indexes of coarse aggregate based on the image identification and image processing techniques. Kuang et al. (2019) proved that the average angular coefficient of coarse aggregate is also correlated with the high temperature stability, water stability, and low temperature performance of asphalt mixture. Singh et al. (2013) compared the morphological characteristic parameters (angularity, texture, and flatness) of aggregates with different lithologies (granite, rhyolite, and limestone) and found that the morphological characteristic parameters of coarse aggregate of different lithologies are different. Liu et al. (2016) optimized the Fourier transform interferometry (FTI) system and used the sphericity, flatness, elongation, angularity, and surface texture to identify the morphological characteristics of coarse aggregate. Kwon et al. (2017) studied the relationship between the aggregate morphology and the permanent deformation capacity of asphalt mixture and analyzed the key factors affecting the permanent deformation of the asphalt mixture. Wang et al. (2019a) proposed the sphericity, flatness, elongation, angularity, and surface texture

index to describe the morphological characteristics of coarse aggregate based on the AIMS experiment instruments. Thus, the research on the morphological characteristics of coarse aggregate is mainly focused on indoor visual identification technology (AIMS, XCT, etc.). The proposed aggregate shape characterization index lacks pertinence, and the testing equipment cannot effectively provide services for asphalt mixture site construction control because of economy and portability (Plati et al., 2016).

Through the limited experimental design of the set of sample points in the specified design space, the response surface method fits the global approximation of the output variable (system response) to replace the real response surface (Mohamed et al., 2016). However, for the morphological characteristics of coarse aggregate, the optimal solution corresponding to different evaluation indexes is different. Therefore, the traditional response surface design method needs to be improved. The improved method is to use gray correlation analysis according to different high temperature evaluation indexes. The comprehensive evaluation method of gray correlation degree can give an evaluation value to each evaluation index of the evaluation object according to the given conditions, so as to comprehensively judge the evaluation object under the interaction of multiple factors (Luo et al., 2016).

Machine vision is a modern comprehensive measurement technology that has been active in recent years, covering a wide range of fields, including computer vision, digital image processing, digital signal analysis, pattern recognition, artificial intelligence, and other technologies. In simple terms, it is to use a camera instead of the human eye to identify and judge the target object to be detected. First, the target image is acquired through the visual sensor, and then the image is transmitted to the host computer for a series of analyses such as digital image processing, and finally according to the pixel point distribution or image color, brightness and other information are used to complete the detection of target size, shape, and color. Chen et al. (2019) discussed the causes of global calibration errors in detail and built a four-camera vision system to obtain the visual information of targets including static objects and a dynamic concrete-filled steel tubular (CFST) specimen. Tang et al. (2019) presented a dynamic real-time detection method for surface deformation and full field strain in recycled aggregate concrete-filled steel tubular columns (RACSTCs). Majidifard et al. (2020) developed a U-net based model to quantify the severity of the pavement distresses and a hybrid model by integrating the YOLO and U-net models to classify the pavement distresses and quantify their severity simultaneously. Liu et al. (2019) adopted U-Net to detect the concrete cracks, and U-Net is found to be more elegant than DCNN with more robustness, more effectiveness, and more accurate detection. Wang et al. (2019b) used neural network technology to assist the robot patrol in an unknown work environment and to use faster R-CNN methods to find scattered nails and screws in real time, so that the robot can automatically recycle nails and screws.

Based on this, an expressway in Guangdong province is selected as a practical case, and a self-developed fast recognition system for the morphological characteristics of



**TABLE 1** | Basic performance test of aggregate.

Technical index	Test value	Specification requirements	Testing method
Crushing value (%)	12.3	≤26	T0316
Los Angeles wear loss (%)	15.4	≤28	T0317
Polishing value (%)	45	≥42	T0321
Water absorption rate (%)	0.60	≤2.0	T0304
Apparent density (g/cm <sup>3</sup> )	2.95	≥2.6	T0304

**TABLE 2** | The technical performance indexes of SBS modified asphalt.

Index	Units	Technical standards	Test results	Test methods
Penetration (25°C, 5 s, 100 g)	0.1 mm	60 ~ 80	69.5	T 0604
Softening point	°C	≥70	70.4	T 0606
Ductility (5°C)	cm	≥35	35.8	T 0605
Difference value of softening point in 48 h	°C	≤2.5	0.25	T 0606

coarse aggregate is used to quickly identify the needle flake, axial coefficient, angularity, and convexity of the aggregate used in the field engineering. Based on the Gray Correlation Response Surface Design method (GCRSD), the coarse aggregate monomer index is associated with dynamic stability, dynamic modulus, maximum shear stress, and internal friction angle. The evaluation index of aggregate performance suitable for the study area is put forward, and the reasonable operation parameters of aggregate processing equipment are recommended to reveal the road performance of asphalt mixture from the point of view of aggregate shape characteristics, so as to realize the effective control of asphalt pavement construction quality.

## OBJECTIVE

In order to enhance the applicability of mesomorphological characterization index of road aggregate, this research puts forward an aggregate performance evaluation index, CEI, which is suitable for high-temperature areas based on CAMIS aggregate identification system and laboratory test combined with improved response surface method. Finally, the processing parameters of vertical shaft impact aggregate crusher are optimized based on CEI index.

## RAW MATERIALS

### Aggregate

The basalt aggregate used in this study comes from the construction site, and the technical index of the aggregate is tested, as shown in **Table 1** (JTG E42-2005, 2005).

### Asphalt

SBS modified asphalt was employed in this study, and the content of SBS modifier is 3%. The technical performance indexes of SBS modified asphalt are shown in **Table 2**.

According to the situation of pavement construction on site, SMA-16 is selected as the gradation in this article, the best dosage of asphalt is 5.2%, and the amount of fiber is 0.3%.

## RESEARCH METHOD

### Aggregate Identification System

Based on the previous research results, the morphological characteristics of coarse aggregate are characterized by edge and angularity parameters, needle-like content, axial coefficient, and convexity (Gao et al., 2018). The specific algorithm of each index is as follows.

#### (1) Angular Value

Angular value is the square of the ratio of the circumferential polygon perimeter  $P_c$  to the equivalent elliptical perimeter  $P_E$ , which can characterize the angular properties of the particles. The larger the value, the better the angular property of the particles, such as

$$A_p = \left( \frac{P_c}{P_E} \right)^2 \quad (1)$$

#### (2) Needle Flake Content

Through the image recognition technology, the maximum length  $L$ , the maximum width  $w$ , and the maximum thickness  $t$  of the maximum length surface are determined ( $t < w < L$ ). The particles with  $L/t \geq 3$  are screened out as needle-like particles. Because the density of the same aggregate is the same, the needle-like content is calculated directly by volume. The equivalent ellipsoid method is used to calculate the needle-like particle volume  $V_i$  and the total aggregate volume  $V$ , as shown in (2). Finally, the needle-like content is calculated, as shown in (3).

$$V_i = \frac{4}{3} \pi L \times w \times t \quad (2)$$

$$Q_e = \frac{m_i}{M} \times 100 = \frac{V_i}{V} \times 100 \quad (3)$$

### (3) Axial Coefficient

The axial coefficient characterizes the needle-like size of the particles, and the larger the axial coefficient is, the greater the needle-like property of the particles is. It reflects the macroscopic state and characteristics of aggregate particles, and the calculation formula is shown in

$$A = L/W \quad (4)$$

In the formula,  $L$  is the maximum length of the particle equivalent ellipse and  $W$  is the secondary axis width of the particle equivalent ellipse.

### (4) Convexity

The original intention of the design of the convexity index is to consider that the coarse aggregate rapid identification system can directly measure the actual area of a particle  $S_A$  and calculate its circumscribed polygon area  $S_C$ . The convexity is the square root of the ratio of these two quantities, as shown in

$$C_R = \sqrt{\frac{S_A}{S_C}} \quad (5)$$

Based on the Python Programming Language and the above algorithms, a Coarse Aggregate Morphological Identification System (CAMIS) is developed independently, as shown in **Figure 1**.

The principle of the system is to first binarize the original aggregate image, then reduce the noise of the aggregate image, then calculate the geometric parameters of each aggregate based on the OPENCV computer vision module, and finally calculate the needle-like content, axial coefficient, angular value, and convexity of the coarse aggregate. The system can identify the shape characteristics of aggregates above 2.36 mm particle size and carry out uninterrupted feeding and removal based on the mechanical arm system, which can achieve large sample detection and improve the accuracy of calculation results. The response time of single aggregate result is less than 1 s.

## Improved Response Surface Method

First of all, the response surface design uses the sequential method to observe and analyze the factors that affect the response variables one by one and then uses the Box-Behnken central combination design method to design the experiment with four factors and three levels, so as to establish the quadratic equation of the response surface and use the mathematical method to find the optimal solution. The weight distribution of several evaluation indexes is carried out to determine the evaluation index value of the morphological index of coarse aggregate to the high temperature performance of asphalt mixture (Shen et al.,

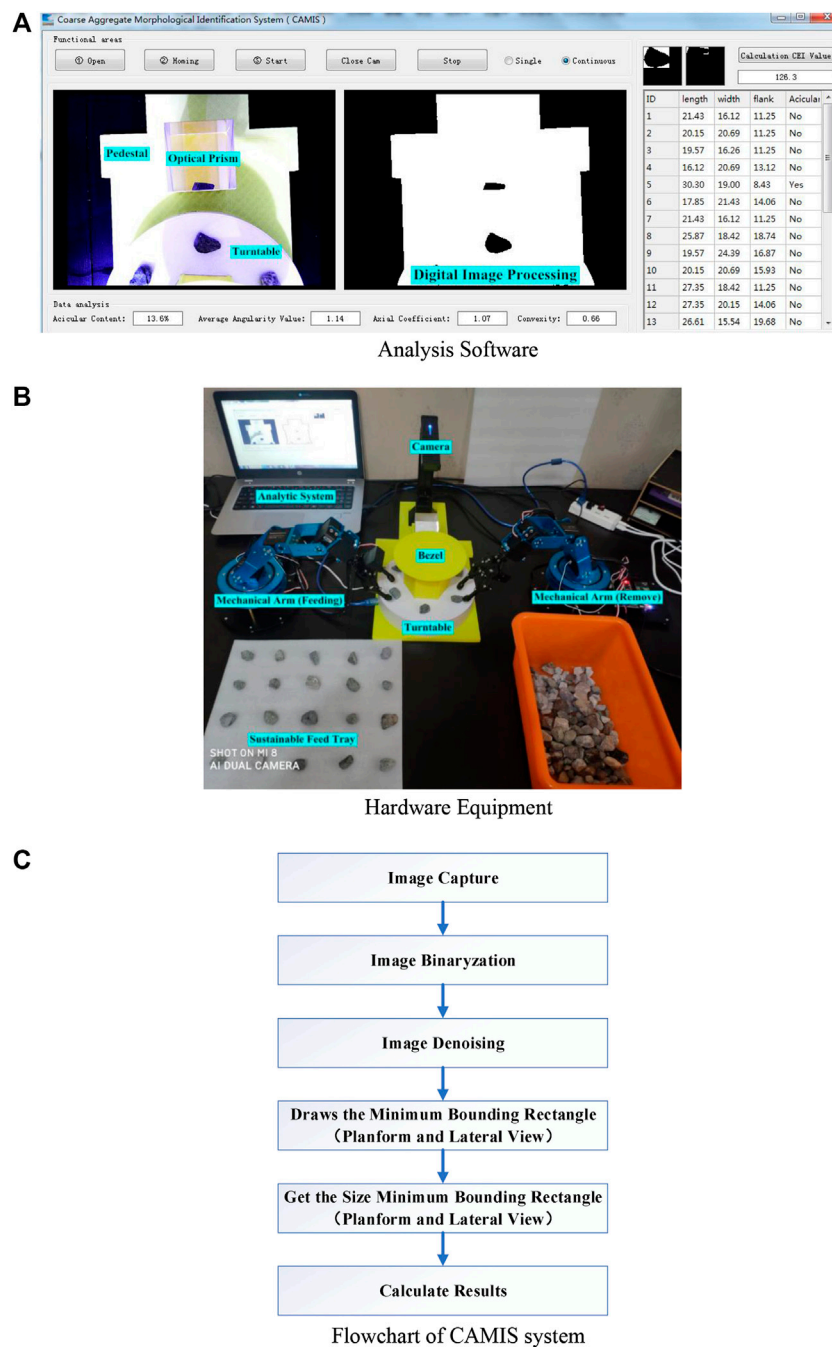
2014). In this study, the calculation processes of improved response surface method are as follows.

- (1) The angular value  $X_1$ , needle flake content  $X_2$ , axial coefficient  $X_3$ , and convexity  $X_4$  are selected as the four factors affecting the high temperature performance of asphalt mixture, and the evaluation indexes of high temperature performance of asphalt mixture are determined. The evaluation indexes of high temperature performance of asphalt mixture are dynamic stability, dynamic modulus, maximum shear stress, and internal friction angle. And the corresponding evaluation index value of high temperature performance of asphalt mixture is determined.
- (2) The aggregate of a stone factory in Guangdong Province is selected, and the local aggregate is scanned and tested by using the rapid recognition system of coarse aggregate morphological characteristics, and the ranges of angular value  $X_1$ , needle-like content  $X_2$ , axial coefficient  $X_3$ , and convexity  $X_4$  are determined.
- (3) Box-Behnken design (BBD) with four factors and three levels is used to carry on the response surface test design.
- (4) The gray correlation analysis is used to analyze the impact factor of four coarse aggregate morphological indexes on each response value, and the correlation degree between morphological index and each high temperature performance evaluation index is calculated. As a result, the proportion of each high temperature performance evaluation index in evaluating the high temperature performance of asphalt mixture can be calculated.
- (5) According to the proportion, the evaluation index values of each group of tests are calculated by comprehensively considering the dynamic stability, dynamic modulus, maximum shear stress, and internal friction angle, and the evaluation index value is taken as the response value for the establishment of the model.
- (6) The response surface test data were analyzed by quadratic multinomial regression fitting, analysis of variance, significance test, and response surface analysis with Design-Expert 8.0 software.
- (7) Finally, the model is constructed; that is, the functional relationship between each coarse aggregate shape index and evaluation index value is established.

## RESULTS AND DISCUSSION

### High Temperature Performance Test Sampling and Morphological Testing of Aggregates

The basalt aggregates used in the field were sampled and equally divided into 29 parts, which were used in rutting test, dynamic modulus test, and penetration shear test, respectively. The self-developed aggregate shape recognition system (CAMIS) is used to test the aggregate shape, and the average value of the 29 groups of aggregate shape data is shown in **Table 3**.



**FIGURE 1 |** Coarse aggregate morphological identification system. **(A)** Analysis software. **(B)** Hardware equipment. **(C)** Flowchart of CAMIS system.

## Rutting Test

The above 29 groups of aggregates with different morphological characteristics were used to form rutting specimens, and the automatic rut instrument was used to determine the dynamic stability of asphalt mixture. The size of the specimen is  $300 \times 300 \times 50$  mm, the total load applied is 780 N, the test wheel pressure is  $0.7 \pm 0.05$  MPa, the loading rate is 42 times/min, and the test temperature is  $60^\circ\text{C}$ .

According to the “Standard Test Methods of Bitumen and Bituminous Mixtures for Highway Engineering (JTGE20-2011),” the test results of dynamic stability of asphalt mixture are shown in **Figure 2**.

## Dynamic Modulus Test

In all the asphalt pavement designs based on mechanical methods, the modulus of asphalt mixture is one of the most

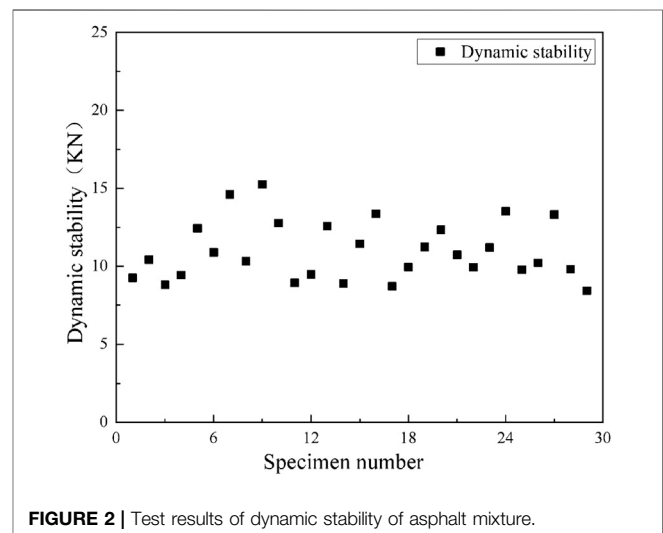
**TABLE 3** | Average value of sample aggregate shape data.

Group ID	Acicular content $X_1$	Average angularity value $X_2$	Axial coefficient $X_3$	Convexity $X_4$
	(Dimensionless)	(%)	(Dimensionless)	(Dimensionless)
1	1.15	16.20%	1.18	0.96
2	1.15	12.50%	1.18	0.46
3	1.15	14.35%	1.45	0.46
4	1.15	16.20%	1.18	0.46
5	1.10	14.35%	0.90	0.71
6	1.15	16.20%	1.45	0.71
7	1.15	14.35%	1.18	0.71
8	1.10	12.50%	1.18	0.71
9	1.15	14.35%	0.90	0.46
10	1.15	14.35%	1.18	0.71
11	1.15	14.35%	0.90	0.96
12	1.19	14.35%	1.18	0.96
13	1.15	12.50%	0.90	0.71
14	1.15	12.50%	1.18	0.96
15	1.15	14.35%	1.18	0.71
16	1.19	12.50%	1.18	0.71
17	1.15	16.20%	0.90	0.71
18	1.19	14.35%	1.45	0.71
19	1.19	14.35%	0.90	0.71
20	1.15	14.35%	1.18	0.71
21	1.15	12.50%	1.45	0.71
22	1.10	14.35%	1.18	0.46
23	1.10	16.20%	1.18	0.71
24	1.15	14.35%	1.45	0.96
25	1.15	14.35%	1.18	0.71
26	1.19	16.20%	1.18	0.71
27	1.19	14.35%	1.18	0.46
28	1.10	14.35%	1.45	0.71
29	1.10	14.35%	1.18	0.96

important parameters, and it is also the bridge between material performance and pavement structure. Therefore, the high temperature performance of asphalt mixture can be considered from the point of view of modulus (Lei et al., 2015). In this research, the dynamic modulus of asphalt mixture is measured by UTM-30, the cylindrical specimens with diameter of  $100 \pm 0.2$  mm and high  $150 \pm 0.2$  mm are formed by rotary compactor (SGC), and the asphalt mixture is molded with coarse aggregates with different morphological characteristics. There are 29 groups of specimens and there are three parallel specimens in each group, and the test results are taken as the average. Combined with the local climate and traffic conditions, the loading frequency is 0.5 hz and the experimental temperature is  $60^\circ\text{C}$ . The test results are shown in **Figure 3**.

### Penetration Shear Test

There is a good corresponding relationship between the penetration shear test index and the high temperature performance of asphalt mixture; the test parameters are easy to determine and have a good engineering application prospect (Tasdemir, 2009). Same as above, 29 groups of aggregate forming mixtures with different morphological characteristics are used, and the size of the specimen is  $100 \times 63.5$  mm pieces. There are 29 groups of specimens, each group has three parallel specimens,

**FIGURE 2** | Test results of dynamic stability of asphalt mixture.

and the test results are taken as the average. The loading rate is 1 mm hammer min, the size of the indenter is 28.5 mm, the test is carried out at  $60^\circ\text{C}$ , and finally the maximum shear stress and internal friction angle are obtained. The results are shown in **Figure 4**.

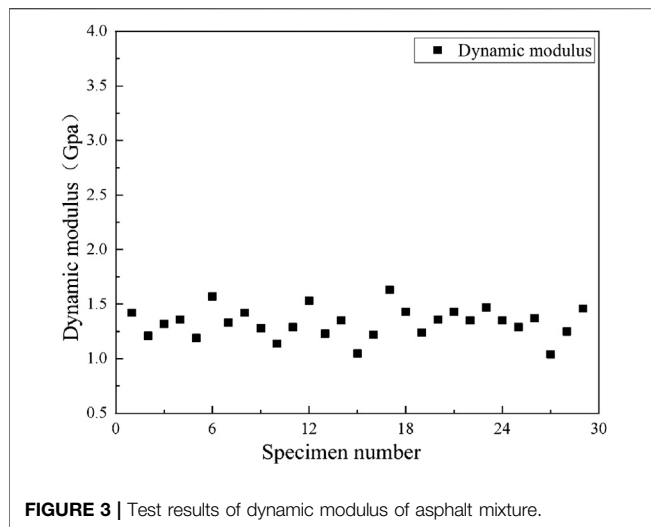


FIGURE 3 | Test results of dynamic modulus of asphalt mixture.

## Effect of Morphological Characteristics of Aggregate on High Temperature Performance of Mixture

Based on the aggregate shape data in Table 2, the response surface test factor level is established, as shown in Table 4.

The dynamic stability, dynamic modulus, maximum shear stress, and internal friction angle of asphalt mixture are used as control indexes to evaluate the high temperature stability of asphalt mixture. Four factors and three levels of test design are carried out by using Box-Behnken central combination design method, with a total of 29 groups of tests (Mourabet et al., 2012).

Combined with the test results in *High Temperature Performance Test*, the average value of each index is obtained by the method of gray correlation degree, in order to evaluate the influence of coarse aggregate shape index on the high temperature performance of mixture. The correlation degree analysis is shown in Table 5.

From the data in the Table 5, it can be seen that the influence degree of various morphological characteristics of coarse aggregate on high temperature evaluation index from high to low is angularity parameter > needle flake content > axial coefficient > convexity. Among them, the impact factor of angularity on the high temperature performance of asphalt mixture is the highest, while the influence of convexity is the least, which is consistent with the previous research results and the actual test results. Generally speaking, the coarse aggregate is rich in edges and corners, and when the surface texture is rougher, the mixture can form a good squeezing effect after compaction, which can increase the internal friction angle of the asphalt mixture and improve the strength of the asphalt mixture, and then improve the high temperature deformation resistance of asphalt mixture. The void age of asphalt mixture and the void age of mineral aggregate gradually increase with the increase of needle-like particle content of aggregate, while the asphalt saturation of gross bulk density decreases. The increase of

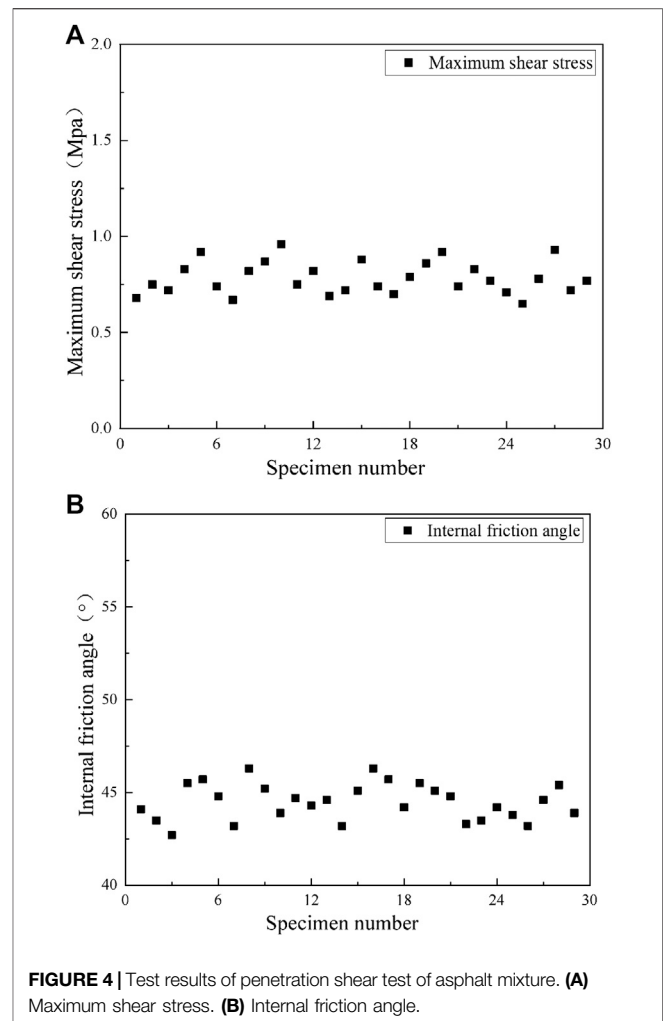


FIGURE 4 | Test results of penetration shear test of asphalt mixture. (A) Maximum shear stress. (B) Internal friction angle.

TABLE 4 | Response surface test factor level.

Factors	Level		
	-1	0	1
X <sub>1</sub> (angular value)	1.10	1.15	1.19
X <sub>2</sub> (needle flake content)	12.50	14.35	16.20
X <sub>3</sub> (axial coefficient)	0.90	1.18	1.45
X <sub>4</sub> (convexity)	0.46	0.71	0.96

Note: -1, 0, 1 represents the different value levels of the index.

needle-like content will reduce the high temperature stability of asphalt mixture to some extent.

## Construction of High Temperature Performance Evaluation Model of Aggregate Model Establishment

Based on the gray correlation analysis between the morphological eigenvalues of coarse aggregate and the high temperature



**TABLE 5 |** Correlation between morphological characteristics and high temperature performance index.

Morphological index	Performance index			
	Dynamic stability	Dynamic modulus	Maximum shear stress	Internal friction angle
$X_1$ (angular value)	0.75	0.77	0.78	0.89
$X_2$ (needle flake content)	0.71	0.76	0.74	0.79
$X_3$ (axial coefficient)	0.70	0.68	0.67	0.71
$X_4$ (convexity)	0.68	0.62	0.62	0.68

**TABLE 6 |** Response surface test design.

ID	$X_1$	$X_2$	$X_3$	$X_4$	Dynamic stability		Dynamic modulus		Maximum shear stress		Internal friction angle		CEI
					MV	CC	MV	CC	MV	CC	MV	CC	
1	1.15	16.20	1.18	0.96	0.60	0.60	0.70	0.70	0.61	0.56	44.1	0.52	123.16
2	1.15	12.50	1.18	0.46	0.79	0.79	0.79	0.69	0.75	0.75	43.5	0.70	123.87
3	1.15	14.35	1.45	0.46	0.62	0.62	0.71	0.71	0.63	0.63	42.7	0.61	118.86
4	1.15	16.20	1.18	0.46	0.67	0.67	0.73	0.73	0.72	0.72	45.5	0.62	126.69
5	1.10	14.35	0.90	0.71	0.67	0.67	0.70	0.70	0.55	0.55	45.7	0.43	133.37
6	1.15	16.20	1.45	0.71	0.83	0.83	0.69	0.69	0.69	0.69	44.8	0.55	128.87
7	1.15	14.35	1.18	0.71	0.53	0.53	0.95	1.00	0.66	0.66	43.2	0.65	132.67
8	1.10	12.50	1.18	0.71	0.89	0.89	0.88	0.69	0.52	0.78	46.3	0.72	130.61
9	1.15	14.35	0.90	0.46	0.42	0.42	0.85	0.67	0.57	0.57	45.2	0.66	138.65
10	1.15	14.35	1.18	0.71	0.70	0.70	0.86	0.62	0.41	0.56	43.9	0.53	130.03
11	1.15	14.35	0.90	0.96	0.66	0.66	0.77	0.67	0.43	0.69	44.7	0.69	123.49
12	1.19	14.35	1.18	0.96	0.65	0.65	0.89	0.61	0.41	0.80	44.3	0.78	124.71
13	1.15	12.50	0.90	0.71	0.63	0.63	0.83	0.73	0.48	0.78	44.6	0.76	130.97
14	1.15	12.50	1.18	0.96	0.55	0.65	0.83	0.73	0.46	0.70	43.2	0.65	120.21
15	1.15	14.35	1.18	0.71	0.78	0.90	0.86	0.52	0.42	0.70	45.1	0.70	129.35
16	1.19	12.50	1.18	0.71	0.62	0.62	0.80	0.74	0.31	0.81	46.3	0.59	136.51
17	1.15	16.20	0.90	0.71	0.69	0.69	0.88	0.51	0.42	0.67	45.7	0.71	126.20
18	1.19	14.35	1.45	0.71	0.72	0.72	0.84	0.74	0.46	0.86	44.2	0.60	125.11
19	1.19	14.35	0.90	0.71	0.66	0.86	0.89	0.70	0.32	0.70	45.5	0.79	130.37
20	1.15	14.35	1.18	0.71	0.66	0.76	0.92	0.92	0.42	0.62	45.1	0.82	132.35
21	1.15	12.50	1.45	0.71	0.71	0.82	0.87	0.66	0.45	0.74	44.8	0.65	128.10
22	1.10	14.35	1.18	0.46	0.67	0.77	0.85	0.77	0.32	0.70	43.3	0.76	122.92
23	1.10	16.20	1.18	0.71	0.69	0.89	0.82	0.72	0.43	0.87	43.5	0.56	126.45
24	1.15	14.35	1.45	0.96	0.75	0.75	0.88	0.70	0.42	0.59	44.2	0.68	132.63
25	1.15	14.35	1.18	0.71	0.78	0.78	0.88	0.88	0.41	0.62	43.8	0.78	123.15
26	1.19	16.20	1.18	0.71	0.59	0.79	0.86	0.86	0.41	0.89	43.2	0.76	123.33
27	1.19	14.35	1.18	0.46	0.59	0.59	0.88	0.53	0.55	0.55	44.6	0.68	132.43
28	1.10	14.35	1.45	0.71	0.54	0.74	0.84	0.74	0.31	0.73	45.4	0.76	126.76
29	1.10	14.35	1.18	0.96	0.57	0.57	0.87	0.63	0.42	0.82	43.9	0.52	121.18
Correlation degree					0.66		0.83		0.48		0.66		—
Proportion (%)					0.25		0.32		0.18		0.25		—

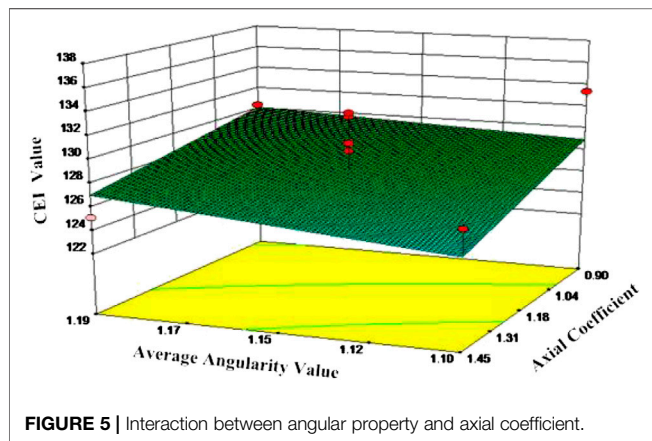
Note: *Mv* = measured value, *Cc* = correlation coefficient.

performance index, the evaluation index (Comprehensive Evaluation Index, CEI) for evaluating the high temperature performance of asphalt mixture is put forward, and the evaluation model of high temperature performance of aggregate is established based on the four morphological indexes of aggregate angularity  $X_1$ , needle flake content  $X_2$ , axial coefficient  $X_3$ , and convexity  $X_4$ . By embedding the evaluation model into the self-developed fast scanning and recognition system of coarse aggregate, it is more convenient to optimize or evaluate the aggregate at the construction site. The response surface test data are

shown in **Table 5**. Based on the Minitab platform, the step-by-step selection method is used to test the significance of the test data in **Table 6**, and the insignificant items are excluded (Yusoff et al., 2015).

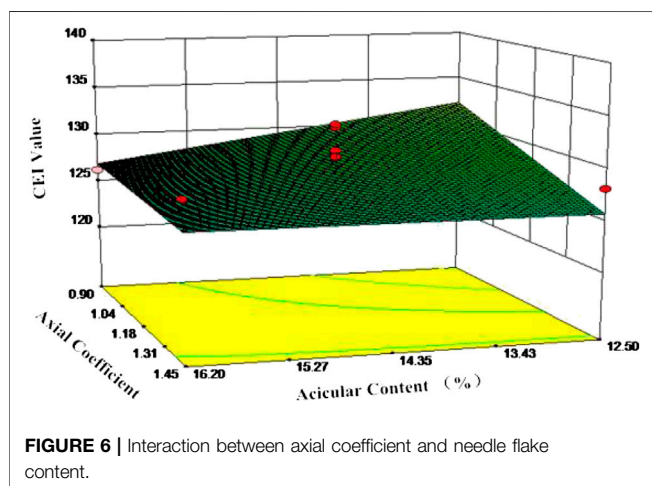
The quadratic function of aggregate performance evaluation index, CEI, on  $X_1$ ,  $X_2$ ,  $X_3$ , and  $X_4$  is established by using Design Expert 8.0 software. The standard deviation of the fitting equation is summarized in **Table 7**.

Finally, the high temperature performance evaluation model of aggregate is shown in (6). The higher the CEI value, the better the high temperature performance of the aggregate.



**TABLE 7 |** Summary of standard deviation of fitting equation.

S	R <sup>2</sup> (%)	R <sup>2</sup> (correction) (%)	R <sup>2</sup> (forecast) (%)
3.288	96.4	92.5	94.5

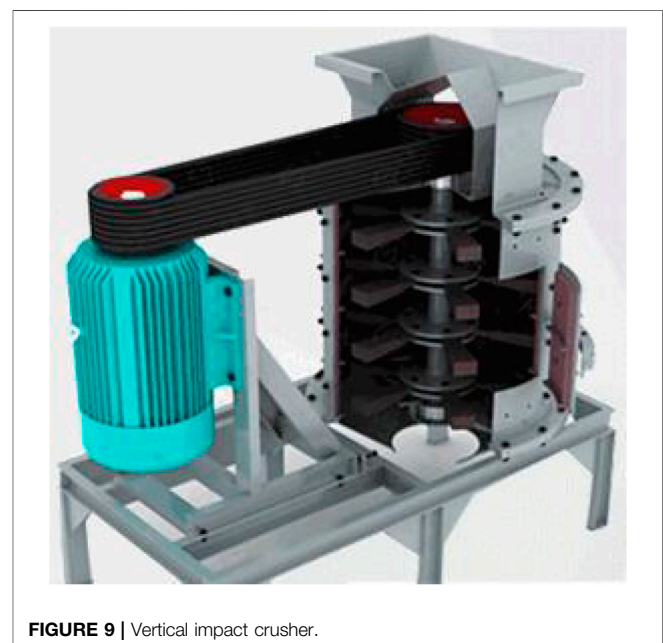
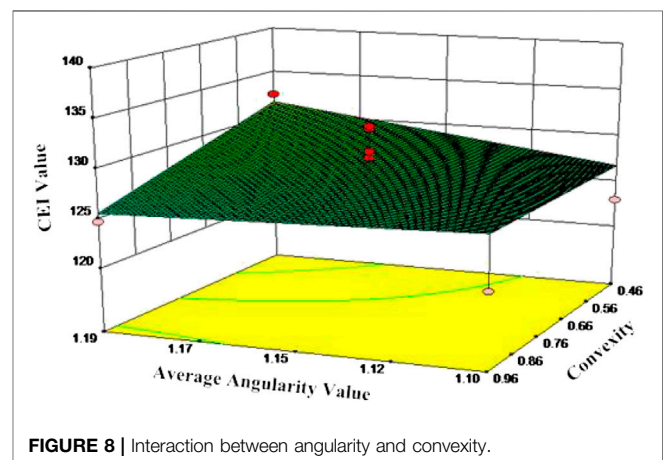
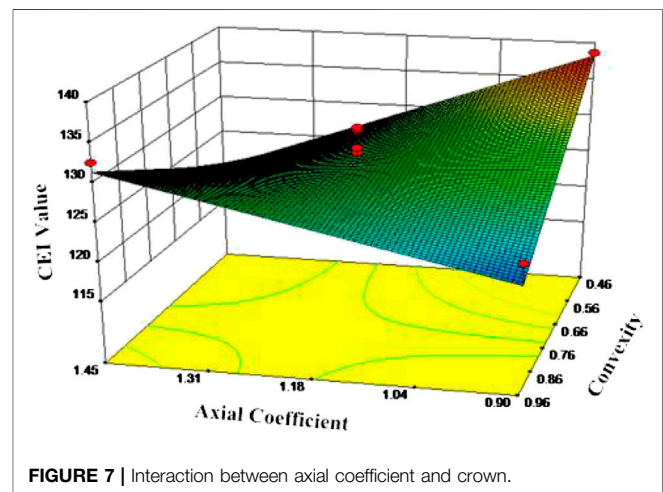


$$CEI = -255.59 + 471.69X_1 + 27.06X_2 - 151.87X_3 + 21.53X_4 - 27.09X_1X_2 + 27.27X_1X_3 - 132.89X_1X_4 + 2.72X_2X_3 + 0.07X_2X_4 + 105.20X_3X_4 \quad (6)$$

### Interaction Analysis of Morphological Indexes of Coarse Aggregate

In order to directly investigate the influence of the interaction of various factors on the high temperature performance of asphalt mixture, based on the above experimental data, the three-dimensional response surfaces of  $X_1$ ,  $X_2$ ,  $X_3$ , and  $X_4$  are established, as shown in **Figures 5–8**.

It can be seen from **Figure 5** that the larger the axial coefficient is, the smaller the CEI index is. This is because the larger the axial coefficient is, the flatter the aggregate is, which is more disadvantageous to the high temperature performance of



**TABLE 8** | Parameter combination of aggregate processing equipment.

ID	Factors			CEI
	Rotational speed (m/s)	Feed quantity (t/h)	Air volume (%)	
1	35	2	10	125.53
2	35	3	20	131.47
3	35	4	30	128.63
4	45	3	30	141.75
5	45	4	10	130.24
6	45	2	20	122.46
7	55	4	20	125.37
8	55	2	30	130.49
9	55	3	10	134.71

asphalt mixture. With the increase of the angular value, the CEI index value becomes larger, indicating that the angular value is positively correlated with the high temperature performance (Hülsheger et al., 2011). As can be seen from **Figure 6**, there is a negative correlation between axial coefficient, needle-like content, and CEI evaluation index, which is consistent with the actual situation. As can be seen from **Figure 7**, the smaller the convexity is, the smaller the actual area of the aggregate and the area of the circumscribed polygon are and the rougher the aggregate surface is, which is beneficial to the high temperature performance. On the other hand, the smaller the axial coefficient is, the closer the aggregate particles are to spherical or square, which will improve the high temperature performance of asphalt mixture. When the convexity and axial coefficient are taken to the minimum, the CEI evaluation index reaches the maximum value. It can be seen from **Figure 8** that the smaller the convexity is, the smaller the actual area of aggregate and the area of circumscribed polygon are and the better the angularity is. Therefore, when the convexity takes the minimum value and the angularity takes the maximum value, the evaluation index CEI of high temperature performance of asphalt mixture reaches the maximum value.

## Optimization and Verification of Processing Parameters of Coarse Aggregate

The proposed aggregate performance evaluation index CEI is embedded into the aggregate shape recognition system CAMIS, and the parameters of the vertical shaft impact aggregate crusher are optimized based on the improved CAMIS system, as shown in **Figure 9**.

Select the combination of three factors and three levels of parameters, including rotational speed (35, 45, 55 m/s), feed quantity (2, 3, 4 t/h), and air intake (10, 20, 30%). The experiment was designed based on the L9 (3<sup>4</sup>) orthogonal table, as shown in **Table 8**.

As can be seen from **Table 7**, the CEI value of the fourth group of processing parameters is the largest, so the processing parameters of S3 jaw crusher are recommended as rotational speed: 45 m/s feed: 3 t/h air intake: 30%. The recommended processing parameters are verified by laboratory tests, and the dynamic stability, dynamic modulus, maximum shear stress, and internal friction angle are selected as verification indexes, respectively. The aggregates needed for the test are prepared by using the processing parameters in **Table 7**, and the preparation parameters and test methods of the asphalt mixture used are the same as the previous ones, and the test results are shown in **Table 9**.

It can be seen from **Table 8** that the high temperature performance index corresponding to the fourth group of aggregate processing parameters is the best, and the results are consistent with the above, so the aggregate evaluation index CEI proposed in this article can be used to evaluate the high temperature performance of regional aggregates.

## CONCLUSIONS

- (1) A simple and economical coarse aggregate morphological feature recognition system (CAMIS) is developed based on computer vision technology. The system can identify needle-like content, axial coefficient, angular value, and convexity of aggregates above 2.36 mm particle size, can supply materials uninterruptedly, and realize mass inspection. The response time of single aggregate is less than 1 s.
- (2) Based on the CAMIS system, combined with the laboratory test, it is concluded that the impact factor of the morphological characteristics of coarse aggregate on the high temperature performance is angular > needle flake > axial coefficient > crown.
- (3) The evaluation model of high temperature performance of aggregate is established by using the improved response surface design method, the aggregate evaluation index CEI is put forward, and the effect of pairwise interaction of each morphological index on CEI index is analyzed. The results

**TABLE 9** | Verification of the test results.

Processing parameters	Dynamic stability (KN)	Dynamic modulus (Gpa)	Maximum shear stress (Mpa)	Internal friction angle (°)
1 (35, 2, 10)	12.6	1.48	0.82	45.3
2 (35, 3, 20)	12.9	1.43	0.85	44.2
3 (35, 4, 30)	11.7	1.52	0.78	45.2
4 (45, 3, 30)	14.9	1.57	0.94	46.9
5 (45, 4, 10)	13.9	1.39	0.88	44.7
6 (45, 2, 20)	14.3	1.45	0.82	45.7
7 (55, 4, 20)	13.7	1.51	0.76	43.8
8 (55, 2, 30)	13.2	1.37	0.84	46.3
9 (55, 3, 10)	12.5	1.47	0.91	45.7

show that CEI index can be used to evaluate the high temperature performance of aggregate.

- (4) The proposed aggregate performance evaluation index CEI is integrated into the aggregate shape recognition system CAMIS, and the parameters of S3 jaw aggregate crusher are optimized. The combination of processing parameters is recommended as rotational speed: 45 m/s feed: 3 t/h air intake: 30%. Laboratory tests show that the aggregate identification system CAMIS and the aggregate performance evaluation index CEI developed in this study are of high reliability.

## DATA AVAILABILITY STATEMENT

The original contributions presented in the study are included in the article/Supplementary Material; further inquiries can be directed to the corresponding author.

## REFERENCES

- Al-Rousan, T., Masad, E., Tutumluer, E., and Pan, T. (2007). Evaluation of image analysis techniques for quantifying aggregate shape characteristics. *Construct. Build. Mater.* 21 (5), 978–990. doi:10.1016/j.conbuildmat.2006.03.005
- Arasan, S., Yenera, E., Hattatoglu, F., Hınıslıoglu, S., and Akbulut, S. (2011). Correlation between shape of aggregate and mechanical properties of asphalt concrete: digital image processing approach. *Road Mater. Pavement Des.* 12 (2), 239–262. doi:10.3166/rmpd.12.239-262
- Chen, M., Tang, Y., Zou, X., Huang, K., Li, L., and He, Y. (2019). High-accuracy multi-camera reconstruction enhanced by adaptive point cloud correction algorithm. *Optic Laser. Eng.* 122, 170–183. doi:10.1016/j.optlaseng.2019.06.011
- Ding, X., Ma, T., and Gao, W. (2017). Morphological characterization and mechanical analysis for coarse aggregate skeleton of asphalt mixture based on discrete-element modeling. *Construct. Build. Mater.* 154, 1048–1061. doi:10.1016/j.conbuildmat.2017.08.008
- Gao, J., Wang, H., Bu, Y., You, Z., Hasan, M. R. M., and Irfan, M. (2018). Effects of coarse aggregate angularity on the microstructure of asphalt mixture. *Construct. Build. Mater.* 183, 472–484. doi:10.1016/j.conbuildmat.2018.06.170
- Ghuzlan, K. A., Obaidat, M. T., and Alawneh, M. M. (2019). Cellular-phone-based computer vision system to extract shape properties of coarse aggregate for asphalt mixtures. *JESTECH.* 22 (3), 767–776. doi:10.1016/j.jestech.2019.02.003
- Hülsheger, T., Brandt, C., Caon, A., Fiebrich, H. K., and Andreev, T. (2011). “The angular performance behavior of triple junction solar cells with different antireflection coatings for high temperature space missions,” in Proc. 9th European Space Power Conference, October, 2011, Saint Rafael, France: ESA Special Publication.
- JTG E42-2005 (2005). *Test methods of aggregate for highway engineering*. Beijing, China: China Ministry of Transport.
- JTG E20-2011, (2011). *Standard Test methods of Bitumen and Bituminous Mixture for Highway Engineering*. Beijing, China: China Ministry of Transport.
- Kuang, D., Wang, X., Jiao, Y., Zhang, B., Liu, Y., and Chen, H. (2019). Influence of angularity and roughness of coarse aggregates on asphalt mixture performance. *Construct. Build. Mater.* 200, 681–686. doi:10.1016/j.conbuildmat.2018.12.176
- Kwon, J., Kim, S. H., Tutumluer, E., and Wayne, M. H. (2017). Characterization of unbound aggregate materials considering physical and morphological properties. *Int. J. Pavement Eng.* 18 (4), 303–308. doi:10.1080/10298436.2015.1065997
- Lei, Z., Bahia, H., and Yi-qiu, T. (2015). Effect of bio-based and refined waste oil modifiers on low temperature performance of asphalt binders. *Construct. Build. Mater.* 86, 95–100. doi:10.1016/j.conbuildmat.2015.03.106
- Li, B., Zhang, C., Xiao, P., and Wu, Z. (2019). Evaluation of coarse aggregate morphological characteristics affecting performance of heavy-duty asphalt pavements. *Construct. Build. Mater.* 225, 170–181. doi:10.1016/j.conbuildmat.2019.07.092
- Liu, Y., Sun, W., Nair, H., Stephen Lane, D., and Wang, L. (2016). Quantification of aggregate morphologic characteristics as related to mechanical properties of asphalt concrete with improved FTI system. *J. Mater. Civ. Eng.* 28 (8), 04016046. doi:10.1061/(asce)mt.1943-5533.0001535
- Liu, Z., Cao, Y., Wang, Y., and Wang, W. (2019). Computer vision-based concrete crack detection using U-net fully convolutional networks. *Autom. Construct.* 104, 129–139. doi:10.1016/j.autcon.2019.04.005
- Luo, X., Wang, Y., Zhao, J., Chen, Y., Mo, S., and Gong, Y. (2016). Grey relational analysis of an integrated cascade utilization system of geothermal water. *Int. J. Green Energy* 13 (1), 14–27. doi:10.1080/15435075.2014.896259
- Majidifard, H., Adu-Gyamfi, Y., and Buttlar, W. G. (2020). Deep machine learning approach to develop a new asphalt pavement condition index. *Construct. Build. Mater.* 247, 118513. doi:10.1016/j.conbuildmat.2020.118513
- Mohamed, O. A., Masood, S. H., and Bhowmik, J. L. (2016). Mathematical modeling and FDM process parameters optimization using response surface methodology based on Q-optimal design. *Appl. Math. Model.* 40 (23–24), 10052–10073. doi:10.1016/j.apm.2016.06.055
- Mourabet, M., El Rhilassi, A., El Boujaady, H., Bennani-Ziatni, M., El Hamri, R., and Taitai, A. (2012). Removal of fluoride from aqueous solution by adsorption on Apatitic tricalcium phosphate using Box–Behnken design and desirability function. *Appl. Surf. Sci.* 258 (10), 4402–4410. doi:10.1016/j.apsusc.2011.12.125
- Plati, C., Georgiou, P., and Loizos, A. (2016). Influence of different roller compaction modes on asphalt mix performance. *Int. J. Pavement Eng.* 17 (1), 64–70. doi:10.1080/10298436.2014.925552
- Rezaei, A., and Masad, E. (2013). Experimental-based model for predicting the skid resistance of asphalt pavements. *Int. J. Pavement Eng.* 14 (1), 24–35. doi:10.1080/10298436.2011.643793
- Shen, C., Shen, B., Xu, H., Bai, J., Dai, L., Lv, Q., et al. (2014). Formulation and optimization of a novel oral fast dissolving film containing drug nanoparticles by Box–Behnken design–response surface methodology. *Drug Dev. Ind. Pharm.* 40 (5), 649–656. doi:10.3109/03639045.2014.884116
- Singh, D., Zaman, M., and Commuri, S. (2013). “Comparison of morphological properties of different types of coarse aggregates,” in *Airfield and Highway pavement 2013: sustainable and efficient pavements*, 1254–1263.
- Tang, Y., Li, L., Wang, C., Chen, M., Feng, W., Zou, X., et al. (2019). Real-time detection of surface deformation and strain in recycled aggregate concrete-filled steel tubular columns via four-ocular vision. *Robot. Comput. Integrated Manuf.* 59, 36–46. doi:10.1016/j.rcim.2019.03.001
- Tasdemir, Y. (2009). High temperature properties of wax modified binders and asphalt mixtures. *Construct. Build. Mater.* 23 (10), 3220–3224. doi:10.1016/j.conbuildmat.2009.06.010
- Wang, H., Bu, Y., Wang, Y., Yang, X., and You, Z. (2016). The effect of morphological characteristic of coarse aggregates measured with fractal

## AUTHOR CONTRIBUTIONS

ZL designed the experiments and wrote the paper; LS performed the experiments; JW analyzed the data; CZ contributed materials and funding. We confirm that the order of authors listed in the manuscript has been approved by all named authors. All authors have read and agreed to the published version of the manuscript.

## FUNDING

This research was funded by the China Postdoctoral Science Foundation (2020M683402), Open Fund of Key Laboratory for Special Area Highway Engineering of Ministry of Education (Chang'an University) (Program no. 300102210504), and the Science and Technology Planning Project of Xi'an (Program no. 2020KJRC0046).

- dimension on asphalt mixture's high-temperature performance. *Adv. Mater. Sci.* 2016, 1–9. doi:10.1155/2016/6264317
- Wang, A., Zhang, Z., Liu, K., Xu, H., Shi, L., and Sun, D. (2019a). Coral aggregate concrete: numerical description of physical, chemical and morphological properties of coral aggregate. *Cement Concr. Compos.* 100, 25–34. doi:10.1016/j.cemconcomp.2019.03.016
- Wang, Z., Li, H., and Zhang, X. (2019b). Construction waste recycling robot for nails and screws: computer vision technology and neural network approach. *Autom. ConStruct.* 97, 220–228. doi:10.1016/j.autcon.2018.11.009
- Yusoff, N., Saad, N. H., Nabipoor, M., Sulaiman, S., Ghawi, N. M. M. A., Jaffar, A., et al. (2015). Design of experiment using Minitab for screening breath sensor workability performance. *Jurnal Teknologi.* 76 (9), 1–5. doi:10.11113/jt.v76.5635
- Zhang, D., Huang, X., and Zhao, Y. (2012). Investigation of the shape, size, angularity and surface texture properties of coarse aggregates. *Construct. Build. Mater.* 34, 330–336. doi:10.1016/j.conbuildmat.2012.02.096
- Conflict of Interest:** The authors declare that the research was conducted in the absence of any commercial or financial relationships that could be construed as a potential conflict of interest.
- Copyright © 2021 Liu, Zhang, Shao and Wang. This is an open-access article distributed under the terms of the Creative Commons Attribution License (CC BY). The use, distribution or reproduction in other forums is permitted, provided the original author(s) and the copyright owner(s) are credited and that the original publication in this journal is cited, in accordance with accepted academic practice. No use, distribution or reproduction is permitted which does not comply with these terms.





# The Self-Healing Performance of Carbon-Based Nanomaterials Modified Asphalt Binders Based on Molecular Dynamics Simulations

Yan Gong<sup>1\*</sup>, Jian Xu<sup>1</sup>, Er-hu Yan<sup>1</sup> and Jun-hua Cai<sup>2</sup>

<sup>1</sup>Research Institute of Highway, Ministry of Transport, Beijing, China, <sup>2</sup>Sanming Puyan Expressway Group Corporation, Fujian, China

## OPEN ACCESS

### Edited by:

Feng Li,  
Beihang University, China

### Reviewed by:

Xiaoming Huang,  
Southeast University, China  
Chao Wang,  
Beijing University of Technology,  
China  
Quan Lv,  
Tongji University, China

### \*Correspondence:

Yan Gong  
gy.1991@163.com

### Specialty section:

This article was submitted to  
Computational Materials Science,  
a section of the journal  
Frontiers in Materials

**Received:** 27 August 2020

**Accepted:** 12 October 2020

**Published:** 22 February 2021

### Citation:

Gong Y, Xu J, Yan E, Cai J (2021) The Self-Healing Performance of Carbon-Based Nanomaterials Modified Asphalt Binders Based on Molecular Dynamics Simulations. *Front. Mater.* 7:599551. doi: 10.3389/fmats.2020.599551

In this study, the molecular dynamics simulation was used to explore the effects of carbon-based nanomaterials as binder modifiers on self-healing capability of asphalt binder and to investigate the microscopic self-healing process of modified asphalt binders under different temperature. An asphalt average molecular structure model of PEN70 asphalt binder was constructed firstly. Further, three kinds of carbon-based nanomaterials were added at three different percentages ranging from 0.5 to 1.5% to the base binder to study their effects on the self-healing capability, including two carbon nanotubes (CNT1 and CNT2) and graphene nanoflakes. Combining with the three-dimensional (3D) microcrack model to simulate the asphalt self-healing process, the density analysis, relative concentration analysis along OZ direction, and mean square displacement analysis were performed to investigate the temperature sensitive self-healing characters. Results showed that the additions of CNTs were effective in enhancing the self-healing efficiency of the plain asphalt binder. By adding 0.5% CNT1 and 0.5% CNT2, about 652% and 230% of the mean square displacement of plain asphalt binder were enhanced at the optimal temperatures. However, the use of graphene nanoflakes as an asphalt modifier did not provide any noticeable changes on the self-healing efficiency. It can be found that the self-healing capability of the asphalt was closely related to the temperature. For base asphalt, the self-healing effect became especially high at the phase transition temperature range, while, for the modified asphalt, the enhancement of the self-healing capability at the low phase transition temperature (15°C) became negligible. In general, the optimal healing temperature range of the CNTs modified asphalt binders is determined as 45–55°C and the optimal dosage of the CNTs is about 0.5% over the total weight of the asphalt binder. Considering the effect of carbon-based nanomaterials on the self-healing properties, the recommended carbon-based nanomaterials modifier is CNT1 with the aspect ratio of 1.81.

**Keywords:** molecular dynamics, self-healing, carbon-based nanomaterials, asphalt binder, optimal healing temperature

## INTRODUCTION

In recent decades, the traffic load supported by asphalt road pavements has significantly increased. At the same time, the climate change has caused a wide range of temperature variations throughout the year, and the weather has become more extreme. These conditions lead to the need for the modification of base asphalt to improve the performance of the material and enhance the mechanical response of road pavements under the severe service conditions (for example, adhesion, temperature sensitivity, oxidation resistance, aging and oxidation resistance, self-healing, and durability). Many kinds of additives have been used as asphalt modifier, including resins, rubbers, polymers, sulfur, metal complexes, fibers, and chemical reagents, especially the most widely applied polymer modifiers with the excellent elastic and thermoplastic properties (Yildirim, 2007; Shen, 2011; Guo et al., 2020). However, most polymer modifiers are thermodynamically incompatible with asphalt binders. This may cause the composite to delaminate during thermal storage and reduce the performance of the modified asphalt. Therefore, the development of new asphalt materials has attracted a lot of attention to avoid the premature performance degradation and ensure a longer service life of the asphalt road pavements. And nanotechnology has gradually been introduced into the field of modified asphalt. Since the microstructure determines macroscopic performance, nanomodified asphalt provides a significant improvement in the intrinsic properties, which is different from other common asphalt modification methods. In order to enhance the mechanical properties and functional applications of asphalt materials, various nanomaterials are used in the laboratory to enhance the performance characteristics of asphalt mixtures (Steyn, 2009; Zare-Shahabadi et al., 2010; Fang et al., 2013; Yao et al., 2013).

Nanomaterials have the morphological characteristics on the nanoscale, especially the special properties related to the nanoscale dimensions. In this respect, carbon-based nanomaterials, which are represented by graphene (Novoselov et al., 2004) and carbon nanotubes, have opened up many new research fields in construction engineering. On the one hand, the addition of carbon-based nanomaterials can enhance the mechanical properties of mixtures, such as the stiffness and strength of mixtures (Young et al., 2012; Du and Pang, 2015b). On the other hand, since the graphene nanoflakes (GNF) and the carbon nanotubes (CNT) have the large specific surface area, strong antioxidant characteristics, high stability, high electric and thermal conductivity, and good mechanical properties, they can be used to improve the functional and smart road pavements (Du and Pang, 2015a; Lee et al., 2017). Besides, it has been proved that the carbon-based nanomaterials can react with the hydrophobic nonpolar groups in asphalt binder and then form more stable nanocomponents, which could act as the buffers for connecting the asphalt binder and the nanoparticle and offer a continuous transition of stress (Cheng et al., 2011; Liu et al., 2014). Thus, the carbon-based nanomaterials provide the possibility to realize more durable and smarter asphalt

pavements. However, it must be noted that there are great differences in the chemical composition and mechanical properties of the nanomaterials and the pavement materials, such as the asphalt binders and the aggregates. Therefore, many efforts have been made to adapt the nanomaterials to the construction of more efficient and functional road infrastructures.

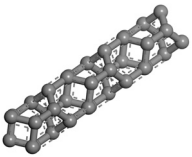
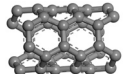
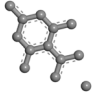
The carbon-based nanomaterials used as modifiers can improve the mechanical properties of pavement materials. Latifi and Hayati (Latifi and Hayati, 2018) reported that the addition of CNTs resulted in an enhancement in the stiffness, rutting resistance, and fatigue performance of hot mix asphalt, with the CNTs' optimum weight percentage of 1%. Faramarzi et al., (2011) found that the asphalt concrete adding CNTs showed improved Marshall stability compared to plain asphalt concrete. Wang et al., (2016) investigated the microwave healing performance of electrically conductive carbon fiber modified asphalt mixture beams and verified a partial recovery and healing process of cracked asphalt concrete with carbon fibers. In terms of self-healing performance, some studies have demonstrated that the application of induction heating was effective for healing cracks in asphalt mixture. Taking advantage of the large heat conductivity, the presence of CNT and GNF could modify the thermal conductivity of asphalt and its mixture, which will benefit to obtain the good self-healing and microwave healing effects. In Liu's study, the optimum heating temperature of 85°C was suggested to achieve the best healing effect (Liu et al., 2012). In addition, completely failed asphalt concrete was partially self-healed based on carbon materials added and induction heating method (Yoo et al., 2019). And the best healing capability was obtained for the specimens with 0.5% GNFs and CFs. Su et al., (2019) developed an improved mechanical properties set-up named the beam on elastic foundation to evaluate the self-healing efficiency of asphalt binder. The asphalt samples with graphene microcapsules containing oily rejuvenator were proved to keep a higher self-healing efficiency after five healing cycles under low temperature (Su et al., 2019) because of the high thermal conductivity of graphene. Based on this review, the positive effect of GNFs and CFs on asphalt binders has been demonstrated. However, there were varying trends in the obtained results because of affecting parameters such as the test temperature, the processing method, and the dosage of GNF and CF.

Nanotechnology testing methods are important for understanding asphalt modification. Molecular dynamics (MD) simulation is a modeling technique to simulate the atomic movements and dynamic behavior at nanoscale, which is widely applied to study the chemical interaction mechanism in road materials. The atoms and molecules move obeying the basic physical principles, Newton's law of mechanics, which are decided by the force field in the simulations (Maginn and Elliott, 2010). Actually, MD simulation is a powerful tool for understanding the macroscopic and intrinsic character of asphalt binders from the molecular scale, such as the physicochemical properties, the aging, and the bond energy of the asphalt-aggregate interface (Yao et al., 2016; Wang et al., 2017; Xu and Wang, 2017). In 2010, the healing analysis of asphalt

**TABLE 1** | Properties of PEN70 asphalt binder.

Asphalt binders	Penetration (25°C), 0.1 mm	Softening point, °C	Ductility (15°C), cm	Viscosity (60°C), Pa·s
PEN70	68	47.0	>100	272.5

**TABLE 2** | Lattice structure and physical properties of the carbon-based nanomaterials.

Nanomaterials	(m, n, k)	Chemical formula	Diameter, Å	Length, Å	L/D	Lattice structure
CNT1	(3, 0, 1)	C <sub>12</sub>	2.35	4.26	1.81	
CNT2	(3, 3, 1)	C <sub>12</sub>	4.07	2.46	0.60	
GNF	(-, -, 1)	C <sub>13</sub>	500–2,000	—	—	

binders was firstly investigated using MD simulation by Bhasin et al., (2010). Recently, Sun et al., (2018) constructed a three-dimensional (3D) microcrack model with 20 Å crack and used MD simulations to explain the microscopic process of asphalt self-healing and investigate the self-healing capability of neat asphalt binders at different temperatures [26].

Although a lot of effort has been made to improve the durability of pavement materials and to enhance the self-healing capability in recent years as mentioned above, limited works have been conducted to understand the self-healing character of asphalt binders by using MD simulation. Investigating the interaction between asphalt binder and carbon-based nanomaterials, which could help in understanding the effect of carbon-based nanomaterials on the self-healing properties of asphalt binders, is still lacking. Furthermore, the determination of the suitable type and dosage of carbon material and the selection of the optimal induction heating temperature are not clear. Thus, in this study, the effectiveness of using three different types of carbon-based nanomaterials (CNT1, CNT2, and GNF) on improving the self-healing performance of asphalt binder was investigated. The average molecular structure models of the PEN70 asphalt binder were firstly constructed based on the measured structure parameters through a series of physical chemical experiments. Then, based mainly on MD simulations, the temperature sensitive self-healing character of damaged asphalt binders with and without carbon-based nanomaterials was quantitatively estimated under different temperature conditions. Lastly, the self-healing character of asphalt binders was analyzed to determine the suitable type and dosage of carbon material and the optimal heating temperature for self-healing.

## MATERIALS

### Asphalt Binders

In this study, the asphalt binder with the penetration grade of 70 (named PEN70) was selected to construct the corresponding average molecular model and investigate the temperature sensitive self-healing performances. The basic physical properties of the asphalt binder are shown in **Table 1**.

### Carbon-Based Nanomaterials

Two types of carbon-based nanomaterials (CNT and GNF) were used as the modifiers in the PEN70 asphalt binder to enhance the mechanical properties and achieve the self-healing capacity. According to the diameter and length, two kinds of CNTs were adopted to investigate the effect of aspect ratio (L/D) on the self-healing performance of the asphalt binder. Herein, L and D are the length and the diameter, respectively. Meanwhile, the nanomaterials were added at three different weight percentages ranging from 0.5% to 1.5% to the base asphalt. The lattice structure and physical properties of the carbon-based nanomaterials are listed in **Table 2**. Their scanning electron microscope images had been shown in the previous study (Yoo et al., 2018; Yoo et al., 2019).

The CNT1 and CNT2 have the same chemical formula but different aspect ratio depending on how the carbon atomic layer sheet is rolled up. The GNF is a kind of two-dimensional nanomaterial composed of carbon atoms, which form hexagonal honeycomb lattice. Mostly, the GNF fibers used in industry were the multiple graphene films with a larger diameter than CNTs rather than the single ones because of the high prices

**TABLE 3 |** Average molecular structure parameters of PEN70 asphalt binder.

Structure parameters	PEN70
Molecular weight	1,406
Atomicity	241
Chemical formula	$C_{99}H_{138}N_1O_2S_1$
$C_T$	99
$C_A$	35
$C_N$	13
$C_P$	51
$C_\alpha$	8.5
$C_{AP}$	18
$C_I$	17
$H_T$	138
$H_A$	9
$H_\alpha$	17
$H_\beta$	83.5
$H_\gamma$	28
$R_T$	13.5
$R_A$	9.5
$R_N$	4

*C, H, and R stand for the number of carbon atoms, hydrogen atoms, and rings, respectively. T, A, and N stand for the total, the aromatic, and cycloalkyl ones, respectively.  $C_\alpha$  stands for the number of  $\alpha$  carbon atoms of aromatic rings.  $C_{AP}$  and  $C_I$  stand for the number of carbon atoms around and inside aromatic rings.  $C_F$  stands for the number of carbon atoms of pericondensed aromatic rings.  $H_\alpha$ ,  $H_\beta$ , and  $H_\gamma$  stand for the number of hydrogen atoms attached to  $\alpha$  carbon,  $\beta$  carbon, and  $\gamma$  carbon of aromatic rings, respectively.*

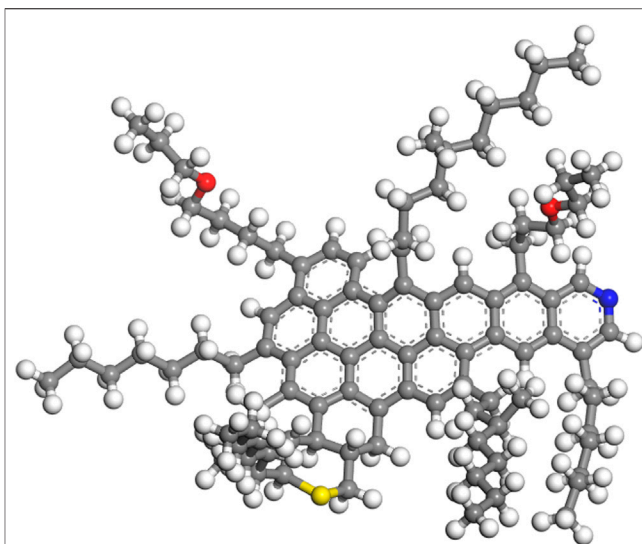
and low industrial production of the single layer GNF. But in this paper, a single atomic layer graphene was constructed based on MD simulation method to analyze the enhancement effect on the self-healing capacity, as shown in **Table 2**. Note that the superlayer graphene also suffered the geometry optimization process due to the selected superlattice period.

## SIMULATION MODELS

### Average Molecular Structure Model of Asphalt

To achieve the average molecular structure model of PEN70 asphalt binder, a series of investigations were conducted, including the elemental analyzer, gel permeation chromatography, and proton nuclear magnetic resonance ( $^1H$ -NMR). The elements C, H, N, and S contents were calculated by a Vario EL-III elemental analyzer. And the structure parameters, including molecular weights, atomicity, and chemical formula, were obtained by gel permeation chromatography and element compositions. AVANCE-III HD500 (Bruker) was adopted to get the proton nuclear magnetic resonance ( $^1H$ -NMR) spectra, which identified the chemical shifts and distribution of hydrogens atoms. Based on these experiment results, the number of aromatic carbon atoms, naphthenic carbon atoms, and alkane branched chain carbon atoms was calculated according to the improved B-L methods (Katayama et al., 1975). The main structure parameters of PEN70 asphalt binder are listed in **Table 3**.

As shown in **Figure 1**, the average molecular structure model of PEN70 asphalt binder was constructed in the software

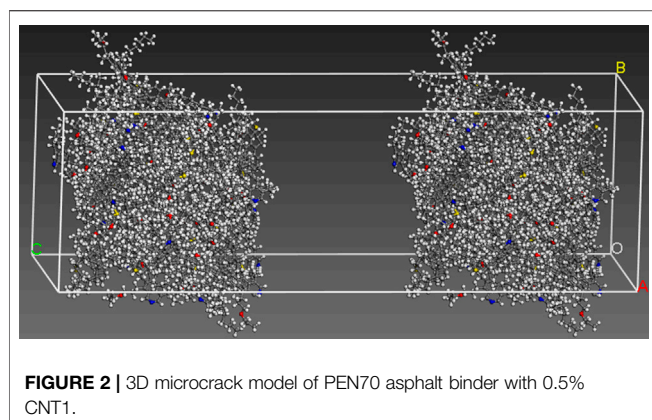
**FIGURE 1 |** Average molecular structure model of PEN70 asphalt binder.

Materials Studio 8.0, the specific construction process of which was not repeated in this article. More detailed information could be found in the author's other paper (Gong et al.). The dark gray and white atom, respectively, stand for carbon and hydrogen. The colored atoms represent different heteroatoms (the yellow one stands for sulfur, the red one stands for oxygen, and the blue one stands for nitrogen).

Using amorphous cell module, a bulk asphalt binder model was subsequently constructed, including the base PEN70 asphalt and the carbon-based nanomaterials modified asphalt. For the base PEN70 asphalt binder, the bulk system consisted of 20 average asphalt molecules, while, for the carbon-based nanomaterials modified asphalts, the modifiers were added in the bulk base asphalt system, and the amount depended on the molecular weight and the weight percentage of the modifiers. Taking the 1.5% CNT1 bulk modified asphalt for example, it consisted of 20 average PEN70 asphalt molecules and three CNT1 molecules. The initial densities of the cubic lattice of the bulk asphalt binder models were both set as  $0.1 \text{ g/cm}^3$  for each binder. Then, the bulk asphalts were stabilized by processing the geometry optimization, canonical (NVT) ensemble simulation, and isothermal-isobaric (NPT) ensemble simulation in Forcite module to gradually reduce the total energy. In the geometry optimization simulation, the molecules in the bulk systems were subjected to 5,000 iterations of energy minimization by smart algorithm. The cutoff distance of the van der Waals terms was  $12.5 \text{ \AA}$ . The NPT and NVT ensemble simulations were both performed with a time step of  $1 \text{ fs}$  ( $10^{-15} \text{ s}$ ) and a total time of  $150 \text{ ps}$  ( $10^{-12} \text{ s}$ ). The temperature was  $298.15 \text{ K}$  ( $25^\circ\text{C}$ ) and the pressure was  $1.01 \times 10^{-4} \text{ GPa}$ .

When obtaining the final densities from the NPT ensemble simulation, the confined asphalt layers were reconstructed. Similarly, all the confined asphalt layers suffered the geometry optimization, NVT ensemble, and NPT ensemble





simulation to achieve the flat surface for the self-healing molecular models.

### Self-Healing Molecular Model

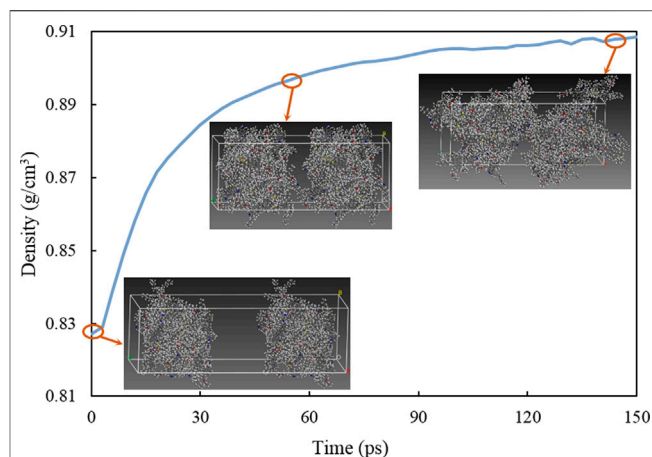
The 3D microcrack model was constructed by positioning the confined asphalt layer-3 on the confined asphalt layer-1 through Build Layer module. A vacuum layer-2 with a thickness of 20 Å was added between two asphalt layers. The 3D microcrack model is showed in **Figure 2**, taking 0.5% CNT1 modified asphalt as an example. The volume parameter of the amorphous cell (0.5% CNT1) was  $35.9 \text{ Å}^3 \times 35.9 \text{ Å}^3 \times 89.7 \text{ Å}^3$ . To investigate the self-healing characters, the MD simulation was selected to in this section simulate the interactions and molecular movements at the 3D microcrack interface models. In simulation systems, the Universal forcefield and NPT ensemble were applied for the analysis of self-healing capability. The simulated temperature was set within 15–55°C, including 288.15 K (15°C), 298.15 K (25°C), 308.15 K (35°C), 318.15 K (45°C), and 328.15 K (55°C).

## RESULTS AND DISCUSSION

### Density Analysis

The dynamics simulation of the 3D microcrack model was conducted, and the volume parameter of the amorphous cell changed to  $34.58 \text{ Å}^3 \times 34.58 \text{ Å}^3 \times 86.36 \text{ Å}^3$  after 150 ps (PEN70 asphalt binder with 0.5% CNT1). The density analysis simulation was further carried out. The density curve varying with time was shown in **Figure 3**, taking PEN70 asphalt binder with 0.5% CNT1 as an example. The initial density was  $0.81 \text{ g/cm}^3$ . With the increase of time, the density increased. After 100 ps, the density value tended to be stabilized at  $0.91 \text{ g/cm}^3$ , which was very close to that of the undamaged PEN70 asphalt binder with 0.5% CNT1, as shown in **Table 4**. The 3D microcrack model results showed that the healing behavior of the carbon-based nanomaterials modified PEN 70 asphalt could occur spontaneously over time.

In fact, based on the polymer self-healing theory, the discontinuity in materials can be automatically eliminated through the molecular wetting and diffusion process between the discontinuous interfaces, which is called self-healing (Kim



**FIGURE 3** | Density curve during self-healing (PEN70 asphalt binder with 1.5% CNT1, 55°C).

**TABLE 4** | Simulated density of different asphalt binders at 25°C (Unit:  $\text{g/cm}^3$ ).

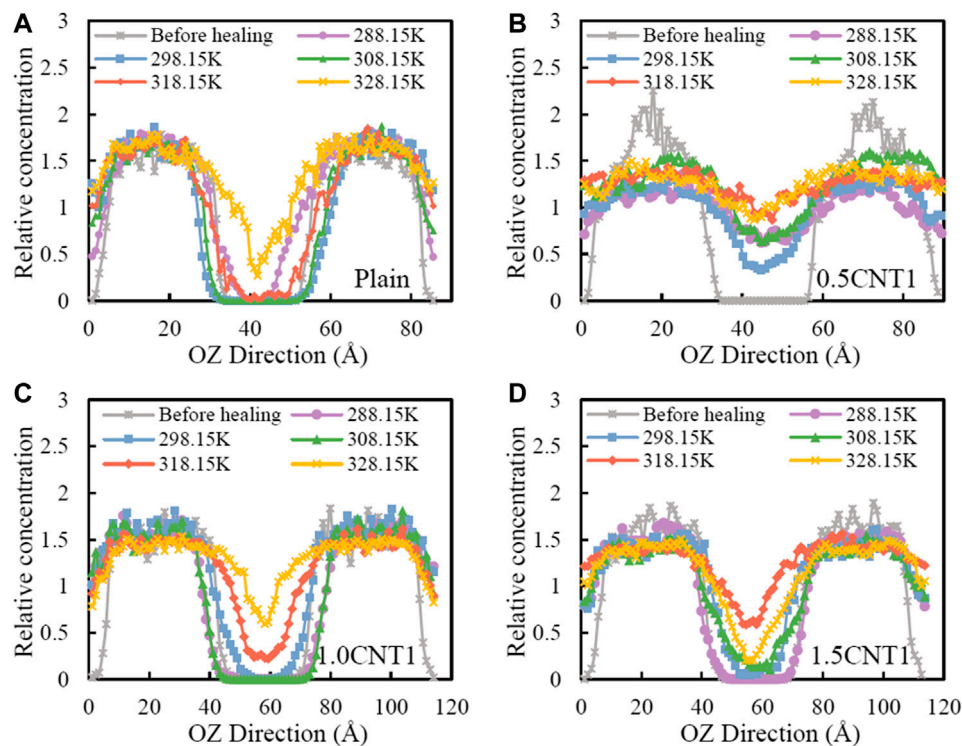
Dosage (%)	CNT1	CNT2	GNF
0.5	1.014	1.015	1.011
1.0	1.016	1.018	1.012
1.5	1.011	1.020	1.004

et al., 2001a; Agzenai et al., 2015). Due to the similarity of the components, many studies on the healing phenomenon of asphalt have referred to the theories and research results in long-chain polymers, especially the asphalt self-healing processes (Ayar et al., 2015; Sun et al., 2017). At the same time, the complexities of the asphalt compositions, microstructure, and possible interactions determine the difference from long-chain polymers, which requires further research. It can be concluded from the density analysis that the diffusion process of molecules on the crack surface can be completed in a relatively short time. However, it is worth noting that the disappearance of the crack does not mean that the damage in asphalt has been repaired. The crack healing is completed in two stages: the morphological healing and the mechanical healing. Once the crack is eliminated outwardly, there are still some imperceptible voids in the crack. These voids disappear after reaching the equilibrium of molecular diffusion, thereby achieving morphological healing (Kim et al., 2001b; Qiu, 2012). In the initial stage of the asphalt molecules getting together, the entanglement of the molecules has not fully formed at the fractured interface. Therefore, a longer time is needed to the establish the molecular interaction (that is, the recovery of strength) after the morphological healing (Qiu et al., 2012).

### Relative Concentration Analysis

In order to study the self-healing process of the crack in the 3D microcrack model, we mainly analyzed the relative concentration distribution along OZ direction, which was perpendicular to the





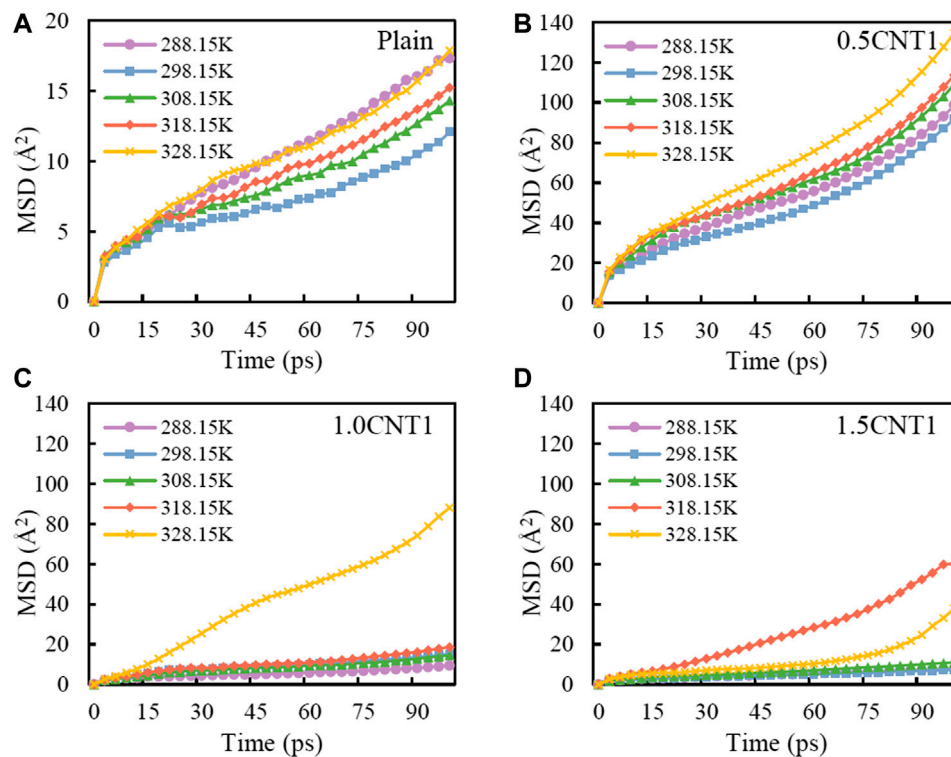
**FIGURE 4** | Relative concentrations along OZ direction of the CNT1 modified PEN70 asphalt binders with different weight percentage: **(A)** plain; **(B)** 0.5% CNT1; **(C)** 1.0% CNT1; **(D)** 1.5% CNT1.

direction of the crack surface. The relative concentration distribution along OZ direction is defined as the percentage of the molecules number in the unit volume perpendicular to the direction of the crack surface. The relative concentration was obtained by calculating the density distribution of the 3D microcrack model. The relative concentration analysis simulation in Forcite module was carried out on the 3D microcrack model after the NPT ensemble simulation with 150 ps. The relative concentrations along OZ direction of the CNT1 modified PEN70 asphalt binders with different weight percentage are shown in **Figure 4**. In order to further study the effect of nanomaterials on the test results, the PEN70 asphalt binder was used as the controlled group for comparison, which was denoted as “Plain.” The extremely low relative concentration in the range of about 34–54 Å (for PEN70 asphalt binder) indicated the scarce molecules in the crack area before healing. It increased particularly after healing at high temperature, meaning that the molecules got cross the crack surface and blended to each other spontaneously.

As shown in **Figure 4A**, the relative concentration values of plain PEN70 asphalt binder were near 0 in the crack area before healing. When the temperature increased, the relative concentration was gradually higher. When the temperature was 55°C, the relative concentration was less than 1.0 in the length range of 38–51 Å. In our opinion, the molecular structure was continuous without gaps when the relative concentration was

greater than 1.0, which was the average value of the relative concentrations of the CNT1 modified binder at 55°C. So, the length of the crack was reduced from 20 to 13 Å at 55°C. Generally, as the temperature decreased, the healing effect would be weakened because the molecular movement was not active according to Newton’s law and the diffusion rate and range were small at low temperature. However, it was found that the concentration in the crack area at 15°C was higher than that at 25°C, which led to the higher self-healing capacity. This result was caused by the low phase transition temperature ranges of the PEN70 asphalt binder (6–18°C) (Sun et al., 2018). The asphalt suffered the phase transition process at 15°C and the molecules diffused frequently and strenuously, resulting in the self-healing of the microcracks. In the temperature range without phase transition, due to the rapid movement of molecules after absorbing heat, high temperature was the main factor that led to more effective self-healing behavior. Besides, the volume of the 3D crack model varied with the rising temperature during the NPT ensemble simulation, accompanied by the change of the length along OZ direction.

With regard to 0.5% CNT1 modified PEN70 asphalt binder, as shown in **Figure 4B**, the self-healing behavior occurred at different temperature, which was more distinct than the plain PEN70 asphalt binder. Meanwhile, the self-healing capacity varied at different temperatures and was the highest at 55°C. After adding 0.5% CNT1, the molecules could diffuse more



**FIGURE 5 |** Mean square displacement of the healing process of CNT1 modified PEN70 asphalt: **(A)** plain; **(B)** 0.5% CNT1; **(C)** 1.0% CNT1; **(D)** 1.5% CNT1.

effectively to the crack surface so that the concentration value in the crack area was close to 1.0 along the entire length at higher temperatures (above 45°C). It indicated that the microcrack was morphologically healed, while, for the 1.5% CNT1 modified PEN 70 asphalt, the most appropriate temperature for self-healing was 45°C rather than 55°C, indicating that too high temperature may be not beneficial to the healing after adding 1.5% CNT1 into the asphalt. As shown in **Figure 4D**, the length of the crack was reduced from 20 to 14 Å at 45°C, which was similar to the plain one at 55°C. Thus, it is worth noting that, when adding too much CNT1, the self-healing effect was undesirable on the contrary. In general, the self-healing of 0.5% CNT1 modified PEN 70 asphalt at different temperature was relatively obvious, and there existed an optimal weight percentage range of CNT1 for asphalt healing.

### Mean Square Displacement Analysis

To study the self-healing capability of the three carbon-based nanomaterials modified PEN70 asphalt binders, the MSD analysis was conducted and the results were shown in **Figures 5–7**. In the MSD analysis, the average distances of the asphalt and nanomaterial molecules over time are measured. The value of MSD stands for the mean squared magnitude of the vector distance traveled by particle, as shown in **Eq. 1**.

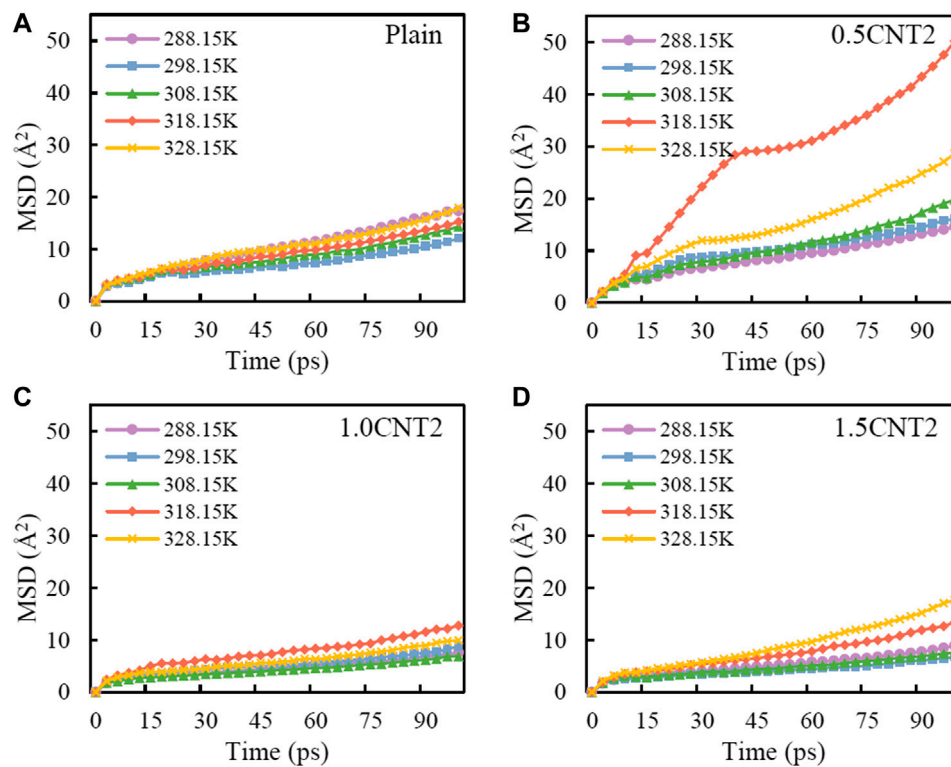
$$MSD(t) = \sum_i \langle (r_i(t) - r_{i0})^2 \rangle \quad [1]$$

where  $i$  stands for the different molecule,  $r_{i0}$  is the initial position, and  $r_i(t)$  is the position vector at time  $t$ . It can be seen from **Figures 5–7** that the MSD gradually increased in the crack area at each temperature after healing and the molecules of layer-1 and layer-3 got through the vacuum layer. The self-healing of asphalt binders should be quicker when the value of MSD was larger.

### CNT1 Modified PEN70 Asphalt

The MSD analysis results of the PEN70 asphalt binder are shown in **Figure 5A**. The MSD values of four binders were different at different temperatures, indicating that the healing efficiency was related to the temperature, which accorded with the practical experiment results and the analysis in *Relative Concentration Analysis*. The MSD values of the PEN70 asphalt at 15 and 55°C (near two phase transition temperatures of the PEN70 asphalt binder (Sun et al., 2018)) were stronger, while, at other temperatures, the MSD values of the PEN70 asphalt were lower. It reconfirmed that the healing ability of the asphalt was related with the phase transition temperatures. When at the temperatures range of 25–55°C, the MSD values became larger as the temperature increased. It was because the energy absorbed by the molecules was larger at the higher temperature, indicating the diffusion rate and range were high.

The CNT1 was added to the PEN70 asphalt binder at three different percentages (i.e., 0.5, 1.0, and 1.5%) of the weight of the base binder, of which the MSD analysis results are shown in **Figures 5A–D**. It showed that adding CNT1 had a noticeable increase in MSD value of modified samples especially at higher



**FIGURE 6 |** Mean square displacement of the healing process of CNT2 modified PEN70 asphalt: **(A)** plain; **(B)** 0.5% CNT2; **(C)** 1.0% CNT2; **(D)** 1.5% CNT2.

temperatures. When the percentage of CNT1 was 0.5%, the MSD values were about five times larger than the results of the control group at the same temperatures. The above phenomena indicated that the diffusion rate and range of 0.5% CNT1 modified asphalt could be the largest, thus resulting in the best self-healing efficiency of the microcrack. It was obvious that the MSD at 45–55°C reached the larger value for the four binders; however the low phase transition temperature (15°C) was negligible when the percentage of CTN1 was more than 1.0%. It might be because the low temperature transition became unstable due to the addition of the nanomaterials. Based on this MSD analysis, considering high temperature may lead to energy dissipation and permanent deformation, the proper temperature for healing damage to asphalt binder was around 45°C and the proper dosage of CNT1 was about 0.5%, which effectively healed the cracks simultaneously.

### CNT2 Modified PEN70 Asphalt

As shown in **Figure 6**, the MSD analysis of CNT2 modified PEN70 asphalt at different temperatures was conducted. Similarly, when the percentage of CNT2 was 0.5%, the MSD values were remarkable at 45°C, which meant the healing of the cracks was most efficient especially around 45°C. Since the CNT1 and CNT2 had the same chemical formula but different aspect ratio, the optimal dosage for both was 0.5%, indicating that the aspect ratio has little influence on the optimal dosage of the CNT1 and CNT2. However, it was found that the more CNT2 could not

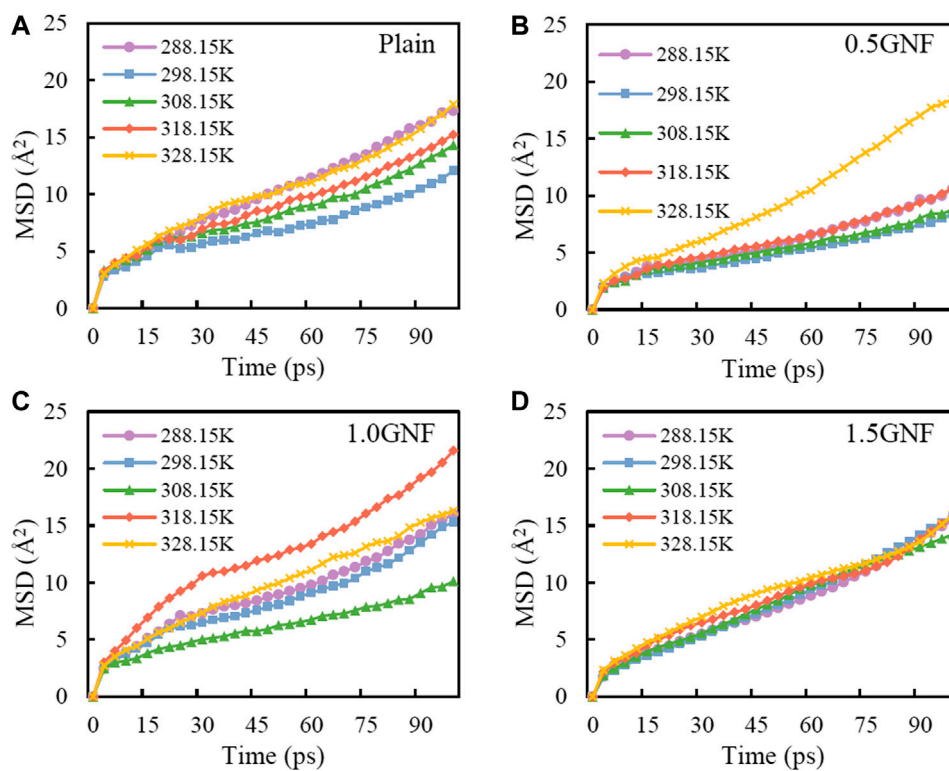
enhance the MSD value of the modified PEN70 asphalt. For instance, when at the same temperature 45°C, the MSD values of the plain group and 1.5% CNT2 modified asphalt were 17.87 and 17.66, respectively. It was deductive that adding too many CNT2 nanomaterials into the asphalt binders would result in the mixing difficulties of the composites.

### GNF Modified PEN70 Asphalt

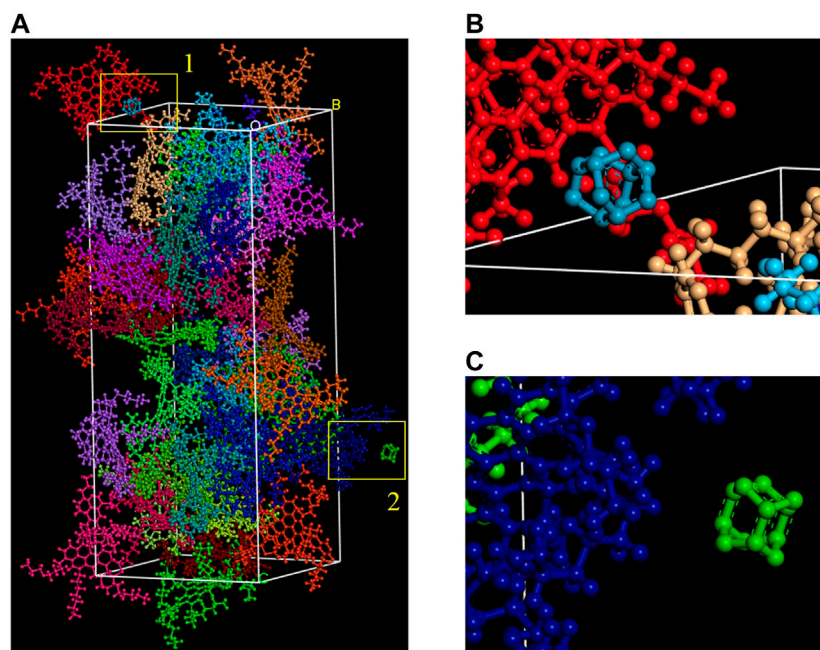
The MSD analysis results of GNF modified PEN70 asphalt at different temperature are shown in **Figure 7**. As for 0.5% GNF and 1.0% GNF modified asphalt, the difference in the MSD value was very small, and the maximum value was 18.5 and 21.6, respectively. And for 1.5% GNF modified asphalt, the distribution trend of the MSD values was basically the same at different temperatures. It can be seen that the improvement of MSD by adding GNF into the asphalt binder was limited relative to CNT. This phenomenon might be caused by the structural differentiation and the difficulties in the mixture process of the PEN70 asphalt and GNF molecules. Besides, it was reconfirmed that the phase transition at 15°C was suppressed so that the peculiar efficient diffusion and self-healing effect of the molecules disappeared.

### Effect of Carbon Nanomaterials on Self-Healing Efficiency

With regard to the different dosage of nanomaterials, it was found that the CNTs modified asphalt binders respectively shown in

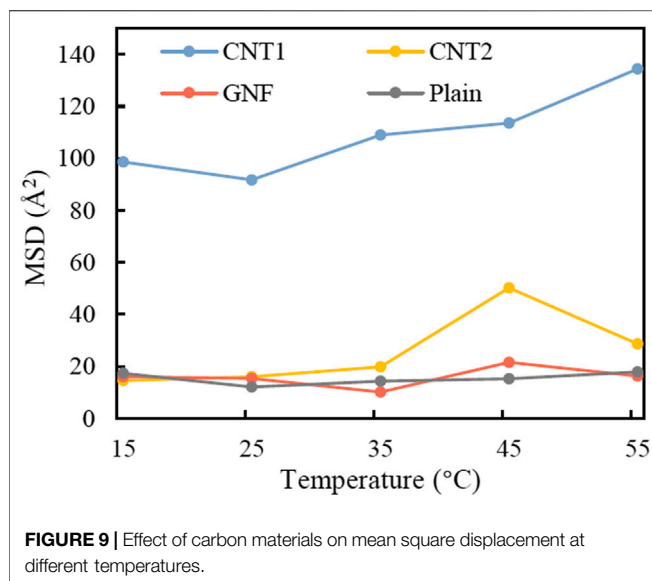


**FIGURE 7 |** Mean square displacement of the healing process of GNF modified PEN70 asphalt: **(A)** plain; **(B)** 0.5% GNF; **(C)** 1.0% GNF; **(D)** 1.5% GNF.



**FIGURE 8 |** Molecular structures of 1.0% CNT1 modified PEN70 asphalt after self-healing at 55°C: **(A)** original; **(B)** enlarged Area 1; **(C)** enlarged Area 2.





Figures 5–7 exhibited similar healing potential tendency. When the dosage was less than 5%, the self-healing capability of all the modified asphalt binders was improved rapidly due to the addition of carbon nanomaterials. When the dosage exceeded 10%, the self-healing ability was weakened, which showed that the slope of the MSD-time curve and the final MSD value were both close to the plain group. According to the MSD simulation results, the additions of 0.5% CNT1 and CNT2 were effective in enhancing the MSD values, as well as the self-healing efficiency of plain asphalt binders. By adding 0.5% CNT1 and 0.5% CNT2, about 652% and 230% of the MSD of plain asphalt binder were enhanced at the optimal temperatures, which were 55°C and 45°C, respectively. However, the addition of GNF did not provide any noticeable changes on the MSD. In order to observe the interactions in modified asphalt binders more clearly and intuitively, the enlarged molecular structures are shown in Figure 8, taking 1.0% CNT1 modified PEN70 asphalt after self-healing at 55°C for example. Based on the simulation results of the MD method, the interaction strength between molecules can be judged from their distance. It can be seen from Figure 8B that the CNT1 molecule was very close to the long-chain branch structure of the asphalt average molecule in Area 1, indicating that strong interactions (such as entanglement) have occurred between the CNT1 and asphalt molecules. This phenomenon reposed carbon-based nanomaterials could react with the hydrophobic long-chain branches in asphalt binder and then might form more stable nanocomponents (Cheng et al., 2011; Liu et al., 2014). Moreover, the CNT1 molecule in Area 2 has been far away from the 3D molecular self-healing model, which was more frequently observed in the higher dosage of CNTs. As the dosage increased, the CNTs could not mix well with the asphalt molecules. After a period of molecular movement, the interaction between CNTs and asphalt became very weak. Thus, when too much nanomaterial was added, the effect on improving self-healing capability could be ignored. This explanation was also consistent with the simulation result that GNF and asphalt molecules were farther apart in GNF

modified asphalt binders. This was due to the inharmonious two-dimensional structure of GNF, which resulted in the difficult mixing process of asphalt binders and incorporated GNFs. Besides, the discordant GNFs might act as obstacles to reduce the diffusion of asphalt molecules at the interface, rather than promoting diffusion.

To verify the effect of carbon nanomaterials on self-healing efficiency at different temperatures, the MSD analysis of three kinds of nanomaterials at their optimal dosages are shown in Figure 9. For three kinds of carbon materials, the MSD reached the highest values when the temperature was in the high phase transition temperature range (45–55°C), while the low temperature transition (15°C) became negligible. It is worth noting that the phase change occurred in a temperature range, rather than a certain temperature value. So, especially with the change of adding percentage of carbon-based materials, the temperature of the maximum MSD value might change in small range. At 45–55°C, the asphalt suffered the transition from the high elastic state to the viscous flow state and released energy. Since the phase transition generated a large amount of heat, the increase of temperature was not the main factor for the improvement of self-healing efficiency in this temperature range. At this time, the molecular movement and the diffusion rate were determined by two factors in the modified asphalt system. One was the heat obtained by the molecules, and the other was the uniformity of the heat distribution. Notably, the excellent thermal conductivity of CNTs enabled the modified asphalt to rapidly reach thermal equilibrium, and all the molecules move more intensely resulting in the enhancement of the self-healing efficiency. However, the molecular diffusion rate and range did not show this especial increase at the low phase transition temperature. Meanwhile, it was also found that the self-healing capability was more obviously suppressed after adding an excessive content of nanomaterials. It is reasonable to infer that the insignificant improvement of the diffusion rate and range was due to the changes in molecular structures caused by the introduction of nanomaterials. In addition, although graphene has excellent properties, it did not significantly improve the self-healing ability of the modified asphalt binders since its molecular structure is not in harmony with the asphalt.

## CONCLUSION

Aiming to evaluate the effectiveness of carbon-based nanomaterials on improving the self-healing performance of asphalt binder and to investigate the determination of the suitable type and dosage of carbon material and the selection of the optimal induction heating temperature, three different types of carbon-based nanomaterials (CNT1, CNT2 and GNF) were employed in this study. The average molecular structure models of the PEN70 asphalt binder were firstly constructed based on the measured structure parameters. Then, based mainly on MD simulations, the temperature sensitive self-healing character of damaged asphalt binders with and without carbon-based nanomaterials were quantitatively estimated under different temperature condition. Lastly, the self-healing character of asphalt binders was analyzed to determine the



suitable type and dosage of carbon material and the optimal heating temperature for self-healing.

Conclusions are listed as follows:

- (1) The asphalt molecules diffused and got across the microcrack spontaneously, so that the density of the 3D cracked asphalt reached about 1.0 g/cm<sup>3</sup> after a period of simulation time.
- (2) The additions of CNTs were effective in enhancing the MSD values, as well as the self-healing efficiency of the plain asphalt binder. By adding 0.5% CNT1 and 0.5% CNT2, about 652% and 230% of the MSD of plain asphalt binder were enhanced at the optimal temperatures. Adding too much CNTs led to the undesirable self-healing effect on the contrary. However, the use of GNF as an asphalt modifier did not provide any noticeable changes on the self-healing efficiency.
- (3) The self-healing capability of the asphalt was closely related to the temperature. The higher temperature resulted in the more effective self-healing. For base asphalt, the self-healing effect became especially high at the phase transition temperature range, while, for the modified asphalt, the enhancement of the self-healing capability at the low phase transition temperature (15°C) became negligible.
- (4) In general, the optimal healing temperature range of the CNTs modified asphalt binders is determined as 45–55°C and the optimal dosage of the CNTs is about 0.5% over the total weight of the asphalt binder. Considering the effect of carbon-based nanomaterials on the self-healing properties, the recommended carbon-based nanomaterials modifier is CNT1 with the aspect ratio of 1.81.

## REFERENCES

- Agzenai, Y., Pozuelo, J., Sanz, J., Perez, I., and Baselga, J. (2015). Advanced self-healing asphalt composites in the pavement performance field: mechanisms at the nano level and new repairing methodologies. *Recent Pat. Nanotechnol.* 9 (1), 43–50. doi:10.2174/1872208309666141205125017
- Ayar, P., Moreno-Navarro, F., and Gámez, M. C. R. (2015). The healing capability of asphalt pavements: a state of the art review. *J. Clean. Prod.* 113, 28–40. doi:10.1016/j.jclepro.2015.12.034
- Bhasin, A., Bommavaram, R., Greenfield, M. L., and Little, D. (2010). Use of molecular dynamics to investigate self-healing mechanisms in asphalt binders. *J. Mater. Civ. Eng.* 23 (4), 485–492. doi:10.1061/(ASCE)MT.1943-5533.0000200
- Cheng, I. F., Xie, Y., Allen Gonzales, R., Brejna, P. R., Sundararajan, J. P., Fouetio Kengne, B. A., et al. (2011). Synthesis of graphene paper from pyrolyzed asphalt. *Carbon* 49, 2852–2861. doi:10.1016/j.carbon.2011.03.020
- Du, H., and Pang, S. D. (2015a). Enhancement of barrier properties of cement mortar with graphene nanoplatelet. *Concr. Res.* 76, 10–19. doi:10.1016/j.cemconres.2015.05.007
- Du, H., and Pang, S. D. (2015b). “Mechanical response and strain sensing of cement composites added with graphene nanoplatelet under tension,” in *Nanotechnology in construction*. Cham, Switzerland: Springer, Cham, 377–382. doi:10.1007/978-3-319-17088-6\_49
- Fang, C., Yu, R., Liu, S., and Li, Y. (2013). Nanomaterials applied in asphalt modification: a review. *J. Mater. Sci. Technol.* 29, 589–594. doi:10.1016/j.jmst.2013.04.008

## DATA AVAILABILITY STATEMENT

The original contributions presented in the study are included in the article/Supplementary Material; further inquiries can be directed to the corresponding authors.

## AUTHOR CONTRIBUTIONS

Conceptualization was done by YG and JX; methodology, software, formal analysis, investigation, data curation, writing, original draft preparation, review, editing, and funding acquisition were done by YG; validation was done by EY; resources were collected by EY; visualization was done by YG and JX; supervision was done by JX; project administration was done by JC; All authors have read and agreed to the published version of the manuscript.

## FUNDING

This research was funded by the Basic Scientific Research Foundation of Research Institute of Highway, grant number 2020-9050; the China Postdoctoral Science Foundation, grant number 2020M670252; and the National Natural Science Foundation of China (NSFC), grant number 51908261.

## ACKNOWLEDGMENTS

The authors would like to appreciate the support given by group members in Research Institute of Highway.

- Faramarzi, M., Arabani, M., Haghi, A. K., and Mottaghitalab, V. (2011). “A study on the effects of CNT’s on hot mix asphalt marshal-parameters,” in International symposium on advances in science and technology, Iran, Bandar-Abbas, March 7–8, 2013, 1–19.
- Gong, Y., Xu, J., Yan, E., Chang, R. (2020). *Intrinsic temperature and moisture sensitive adhesion characters of asphalt-aggregate interface based on molecular dynamics simulations*. *Constr. Build. Mater. CONBUILDMAT-D-20-03624*. (revised)
- Guo, M., Liu, H., Jiao, Y., Mo, L., Tan, Y., Wang, D., et al. (2020). Effect of WMA-RAP technology on pavement performance of asphalt mixture: a state-of-the-art review. *J. Clean. Prod.* 266, 121704. doi:10.1016/j.jclepro.2020.121704
- Katayama, Y., Hosoi, T., and Takeya, G. (1975). Structural analysis of coal tar pitches and petroleum heavy oil distillation residues using a computer. *Nippon Kagaku Kaishi* 1, 127–134. doi:10.1246/nikkashi.1975.127
- Kim, Y. R., Lee, H., and Little, D. N. (2001a). “Microdamage healing in asphalt and asphalt concrete,” in *Volume IV: A viscoelastic continuum damage fatigue model of asphalt concrete with microdamage healing*. College Station, TX: Texas Transportation Institute.
- Kim, Y. R., Little, D. N., and Lytton, R. L. (2001b). Evaluation of microdamage, healing, and heat dissipation of asphalt mixtures, using a dynamic mechanical analyzer. *J. Trans. Res. Rec.* 1767 (1), 60–66. doi:10.3141/1767-08
- Latifi, H., and Hayati, P. (2018). Evaluating the effects of the wet and simple processes for including carbon nanotube modifier in hot mix asphalt. *Constr. Build. Mater.* 164, 326–336. doi:10.1016/j.conbuildmat.2017.12.237
- Lee, S.-J., You, I., Zi, G., and Yoo, D.-Y. (2017). Experimental investigation of the piezoresistive properties of cement composites with hybrid carbon fibers and nanotubes. *Sensors* 17 (11), 2516–2531. doi:10.3390/s17112516

- Liu, Q., Schlangen, E., van de Ven, M., van Bochove, G., and van Montfort, J. (2012). Evaluation of the induction healing effect of porous asphalt concrete through four point bending fatigue test. *Constr. Build. Mater.* 29: 403–409. doi:10.1016/j.conbuildmat.2011.10.058
- Liu, Z., Tu, Z., Li, Y., Yang, F., Han, S., Yang, W., et al. (2014). Synthesis of three-dimensional graphene from petroleum asphalt by chemical vapor deposition. *Mater. Lett.* 122, 285–288. doi:10.1016/j.matlet.2014.02.077
- Maginn, E. J., and Elliott, J. R. (2010). Historical perspective and current outlook for molecular dynamics as a chemical engineering tool. *Ind. Eng. Chem. Res.* 49 (7), 3059–3078. doi:10.1021/ie901898k
- Novoselov, K. S., Geim, A. K., Morozov, S. V., Jiang, D., Zhang, Y., Dubonos, S. V., et al. (2004). Electric field effect in atomically thin carbon films. *Science* 306, 666–669. doi:10.1126/science.1102896
- Qiu, J. (2012). *Self healing of asphalt mixtures: towards a better understanding of the mechanism*. Delft, Netherlands: TU Delft, Delft University of Technology.
- Qiu, J., Van de Ven, M., Wu, S., Yu, J., and Molenaar, A. (2012). Evaluating self healing capability of bituminous mastics. *Exper. Mech.* 52 (8), 1163–1171. doi:10.1007/s11340-011-9573-1
- Shen, J. A. (2011). *Pavement performance of asphalt and asphalt concrete*. Beijing, China: China Communication Press. [in Chinese, with English summary].
- Steyn, W. J. (2009). Potential applications of nanotechnology in pavement engineering. *J. Transp. Eng.* 135, 764–772. doi:10.1061/(asce)0733-947x(2009)135:10(764)
- Su, J.-F., Guo, Y.-D., Xie, X.-M., Zhang, X.-L., Mu, R., Wang, Y.-Y., et al. (2019). Smart bituminous material combining anti-icing and self-healing functions using electrothermal graphene microcapsules containing oily rejuvenator. *Constr. Build. Mater.* 224, 671–681. doi:10.1016/j.conbuildmat.2019.07.098
- Sun, D., Sun, G., Zhu, X., Pang, Q., Yu, F., and Lin, T. (2017). Identification of wetting and molecular diffusion stages during self-healing process of asphalt binder via fluorescence microscope. *Constr. Build. Mater.* 132, 230–239. doi:10.1016/j.conbuildmat.2016.11.137
- Sun, D., Sun, G., Zhu, X., Ye, F., and Xu, J. (2018). Intrinsic temperature sensitive self-healing character of asphalt binders based on molecular dynamics simulations. *Fuel* 211, 609–620. doi:10.1016/j.fuel.2017.09.089
- Wang, H., Lin, E., and Xu, G. (2017). Molecular dynamics simulation of asphalt-aggregate interface adhesion strength with moisture effect. *Inter. J. Pav. Eng.* 18 (5), 414–423. doi:10.1080/10298436.2015.1095297
- Wang, Z., Dai, Q., Porter, D., and You, Z. (2016). Investigation of microwave healing performance of electrically conductive carbon fiber modified asphalt mixture beams. *Constr. Build. Mater.* 126, 1012–1019. doi:10.1016/j.conbuildmat.2016.09.039
- Xu, G., and Wang, H. (2017). Molecular dynamics study of oxidative aging effect on asphalt binder properties. *Fuel* 188, 1–10. doi:10.1016/j.fuel.2016.10.021
- Yao, H., Dai, Q., and You, Z. (2016). Molecular dynamics simulation of physicochemical properties of the asphalt model. *Fuel* 164, 83–93. doi:10.1016/j.fuel.2015.09.045
- Yao, H., You, Z., Li, L., Lee, C. H., Wingard, D., Yap, Y. K., et al. (2013). Rheological properties and chemical bonding of asphalt modified with nanosilica. *J. Mater. Civil Eng.* 25 (11), 1619–1630. doi:10.1061/(asce)mt.1943-5533.0000690
- Yildirim, Y. (2007). Polymer modified asphalt binders. *Construct. Build. Mater.* 21, 66–72. doi:10.1016/j.conbuildmat.2005.07.007
- Yoo, D. Y., Kim, S., Kim, M.-J., Kim, D., and Shin, H.-O. (2019). Self-healing capability of asphalt concrete with carbon-based materials. *J. Mater. Res. Technol.* 8 (1), 827–839. doi:10.1016/j.jmrt.2018.07.001
- Yoo, D. Y., You, I., and Lee, S.-J. (2018). Electrical and piezoresistive sensing capacities of cement paste with multi-walled carbon nanotubes. *Arch. Civil Mech. Eng.* 18 (2), 371–384. doi:10.1016/j.acme.2017.09.007
- Young, R. J., Kinloch, I. A., Gong, L., and Novoselov, K. S. (2012). The mechanics of graphene nanocomposites: a review. *Compos. Sci. Technol.* 72, 1459–1476. doi:10.1016/j.compscitech.2012.05.005
- Zare-Shahabadi, A., Shokuhfar, A., and Ebrahimi-Nejad, S. (2010). Preparation and rheological characterization of asphalt binders reinforced with layered silicate nanoparticles. *Constr. Build. Mater.* 24 (7), 1239–1244. doi:10.1016/j.conbuildmat.2009.12.013

**Conflict of Interest:** Author JC was employed by company Sanming Puyan Expressway Group Corporation.

The remaining authors declare that the research was conducted in the absence of any commercial or financial relationships that could be construed as a potential conflict of interest.

Copyright © 2021 Gong, Xu, Yan and Cai. This is an open-access article distributed under the terms of the Creative Commons Attribution License (CC BY). The use, distribution or reproduction in other forums is permitted, provided the original author(s) and the copyright owner(s) are credited and that the original publication in this journal is cited, in accordance with accepted academic practice. No use, distribution or reproduction is permitted which does not comply with these terms.



# BIC-Based Data-Driven Rail Track Deterioration Adaptive Piecewise Modeling Framework

Yaqin Yang<sup>1</sup>, Peng Xu<sup>1\*</sup>, Guotao Yang<sup>2</sup>, Long Chen<sup>1</sup> and Junbo Li<sup>3</sup>

<sup>1</sup>School of Traffic and Transportation, Beijing Jiaotong University, Beijing, China, <sup>2</sup>China State Railway Group Co., Ltd., Beijing, China, <sup>3</sup>China Academy of Railway Sciences, Beijing, China

The records of maintenance activities are required for modeling the track irregularity deterioration process. However, it is hard to guarantee the completeness and accuracy of the maintenance records. To tackle this problem, an adaptive piecewise modeling framework for the rail track deterioration process driven by historical measurement data from the comprehensive inspection train (referred to as CIT) is proposed. The identification of when maintenance activities occurred is reformulated as a model selection optimization problem based on Bayesian Information Criterion. An efficient solution algorithm utilizing adaptive thresholding and dynamic programming is proposed for solving this optimization problem. This framework's validity and practicability are illustrated by the measurement data from the CIT inspection of the mileage section of K21 + 184 to K220 + 308 on the Nanchang-Fuzhou railway track from 2014 to 2019. The results indicate that this framework can overcome the disturbance of contaminated measurement data and accurately estimate when maintenance activities were undertaken without any historical maintenance records. What is more, the adaptive piecewise fitting model provided by this framework can describe the irregular deterioration process of corresponding rail track sections.

**Keywords:** maintenance activities identification, Bayesian information criterion, track irregularity, adaptive thresholding, dynamic programming

## INTRODUCTION

Track irregularity directly impacts the running stability and safety of trains. Maintaining tracks in an acceptable condition is essential, but it consumes many physical and staff resources. In order to develop cost-effective and rational maintenance plans under limited resources, prior information about track irregularity is required. Thus, this study on predicting the deterioration of track irregularity is critical to railway operation. Many kinds of research have been carried out to forecast track irregularity. Meier-Hirmer et al., (2006) modeled the changes in standard deviation of longitudinal level within a maintenance cycle using the Gamma process. Veit and Marsching, 2010 developed an exponential function to model the behavior of track quality deterioration between two adjacent maintenance events and discussed the interrelations between deterioration rate and the initial quality. Zhu et al., (2013) applied a Gaussian random process to model track irregularities of profile and alignment and studied their power spectral densities. Considering that the evolution of track irregularity is periodic, exponential, and has multiple stages, Xu et al., (2012) employed a multi-stage linear fitting model to describe the track irregularity deterioration process between two adjacent maintenance actions. Lee et al., (2018) combined an

## OPEN ACCESS

### Edited by:

Hui Yao,  
Beijing University of Technology,  
China

### Reviewed by:

Teng Wang,  
University of Kentucky, United States  
Hualiang Tang,  
University of Nevada, United States

### \*Correspondence:

Peng Xu  
peng.xu@bjtu.edu.cn

### Specialty section:

This article was submitted to  
Computational Materials Science,  
a section of the journal  
Frontiers in Materials

**Received:** 23 October 2020

**Accepted:** 05 January 2021

**Published:** 26 February 2021

### Citation:

Yang Y, Xu P, Yang G, Chen L and Li J  
(2021) BIC-Based Data-Driven Rail  
Track Deterioration Adaptive  
Piecewise Modeling Framework.  
Front. Mater. 8:620484.  
doi: 10.3389/fmats.2021.620484

artificial neural network (ANN) and support vector regression (SVR) to better represent the deterioration phenomena of track segments for optimizing the maintenance plans in terms of time and cost. In their experiments, at least two years of maintenance records were required to obtain a stable prediction of track deterioration. Mercier et al., (2012) conjointly utilized longitudinal and transversal leveling indicators using a bivariate Gamma process to predict track quality. Vale and Lurdes (2013) developed a stochastic model based on the Dagum distribution for longitudinal level.

Considering that maintenance activities, including tamping, grinding, and others obviously recover track irregularity and have an effect on the deterioration modes (Quiroga and Schnieder, 2010), the aforementioned studies mainly focus on the deterioration process between adjacent maintenance activities. Some studies for multiple maintenance periods have been developed under the following two main assumptions. One is that maintenance records are accessible for modeling; the other is that deterministic mathematical models can express the relationship between deterioration rates and initial qualities right after maintenance actions. Accordingly, segmenting the deterioration process of track irregularity according to maintenance activities is fundamental for exploring the deterioration rules based on historical measurement data. However, the complete and accurate records of maintenance activities are unobtainable because most of the previous records have been lost. Thus, it has become an urgent task to establish an algorithm to automatically identify when maintenance activities were carried out in the process of deterioration (referred to as maintenance-points). Each maintenance-point is tagged by the detection date, which is right after the maintenance activities.

Identification of maintenance-points in the process of track irregularity deterioration is equivalent to making inferences about unknown multiple change-points in the field of applied statistics. There are vast amounts of studies on multiple change-points analysis in different applied contexts, for example, in econometrics (Dias, 2004), in biology (Xi et al., 2011), in climatology (Reeves et al., 2007; Lu et al., 2010), and in hydrology (Perreault et al., 2000). It has also been introduced to traffic flow data for freeway incident detection. Yang et al., (2014) proposed the coupled Bayesian RPCA by extending the Bayesian robust principal component analysis (RPCA) approach for detecting unusual traffic events. The traffic events were localized based on coupling the multiple traffic data streams. Liu et al., (2008) developed an automated traffic incidents detection algorithm on the basis of the cumulative sum (CUSUM). Moreover, in order to achieve real-time defect detection of high-speed train wheels, Wang et al., (2020) utilized the Bayesian dynamic linear model (DLM) to detect change-points in strain monitoring data from high-speed train bogies. Many effective methods have been developed and verified, such as maximum likelihood, Bayes-type, cumulative sum, and others (Jandhyala et al., 2013). Among them, information criteria provides a method for multiple change-points estimation without any priori information on their locations and number (Hall et al., 2013). Bayesian Information Criterion (referred to as BIC) is

popularly applied (Watanabe, 2012; Hall et al., 2015). BIC was proposed by Schwarz (1978) and is widely applied as a model selection criterion. Regarding the number of change-points as the dimension of the model, Yao (1988) applied BIC for making inferences about the change-points when the means of observations on different time periods were distinct. However, Zhang and Siegmund (2007) found that the classic BIC had poor performance when applied to irregular statistical models. Thus, Zhang proposed a modified BIC that differently penalized the model dimension components of BIC's objective function. Hannart and Naveau (2012) improved BIC for multiple change-points analysis by introducing priori information on the relative positions and amplitude of change-points and deriving a closed-form mathematical expression of the criterion based on Laplace approximation. Successes in applying BIC to other practical problems such as detecting change in acoustics have been widely reported in the literature (Chen and Gopalakrishnan, 1998; Kotti et al., 2006).

The major contribution of this paper is to propose an adaptive piecewise modeling framework that is driven by historical measurement data from CIT and enables us to describe the rail track deterioration process. This framework is capable of tolerating contaminated measurement data and automatically identifying maintenance-points in the process of deterioration. This problem is reformulated as a model selection optimization problem by taking advantage of BIC. Linear regression (referred to as LR) is applied to model each subsequence individually divided by maintenance-points. Then the objective function is derived according to the framework of BIC and is modified by incorporating an optimized weight for the model complexity component. Based on the effect of maintenance activities on deterioration rate, an efficient solution algorithm for minimizing the objective function is developed by comprehensively utilizing the adaptive thresholding and dynamic programming. The proposed framework is validated by the measurement data for the Nanchang-Fuzhou railway track through CIT collection from 2014 to 2019.

The rest of the article is organized as follows. In *Modeling framework based on Bayesian Information Criterion Section*, we derive an objective function based on BIC and modify it by incorporating a weight coefficient. In *Solution algorithm Section*, we develop a solution algorithm based on adaptive thresholding and dynamic programming. Then, we discuss the optimal value of weight coefficient. In *Empirical analysis Section*, the performance of the proposed framework is evaluated by practical measurement data. Finally, we summarize the research and discuss our ongoing work related to this article.

## MODELING FRAMEWORK BASED ON BAYESIAN INFORMATION CRITERION

For Chinese railways, the track quality index (TQI) is employed to quantify track irregularity. It is the sum of standard deviations of seven geometrical parameters for a 200 m-long track section (Xu et al., 2011). The standard deviation for each geometrical parameter is calculated from measurement data collected by CIT.

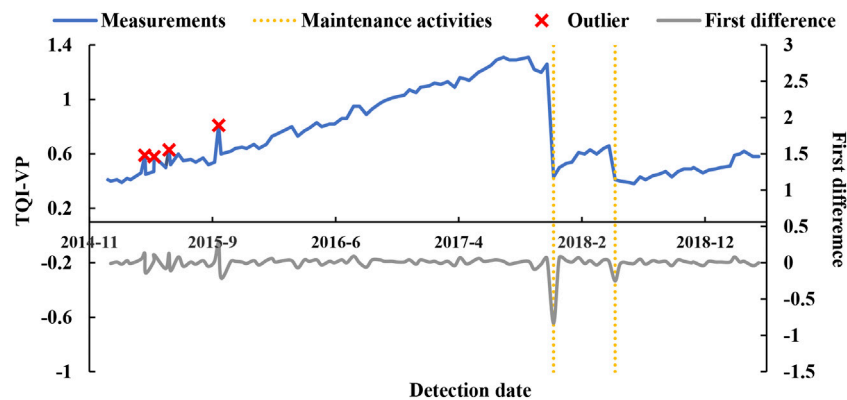


FIGURE 1 | The different characteristics of maintenance activities and contaminated measurement data.

Among the seven geometrical parameters, track profile irregularity is particularly related to mechanized maintenance activities. Thus, the inference about maintenance-points is studied on the basis of track profile irregularity (referred to as  $TQI_p$ ).

The inference of change-points based on BIC is a model selection procedure that minimizes a constrained function based on the maximum likelihood method defined by BIC (Gang and Ghosh, 2011). Accordingly, we reformulate the inference on the number and locations of maintenance-points in the deterioration process of  $TQI_p$  into a model selection problem based on BIC. Denoting the set of all piecewise LR models as  $\Omega$  and each model in it as  $M \in \Omega$ . BIC defines the optimal fitting model from  $\Omega$  as the one that minimizes Eq. 1.

$$BIC = -2 \ln(L) + K \ln(N) \quad (1)$$

wherein  $N$  is the sample size,  $L$  is the maximized likelihood of fitting model  $M$ , and  $K$  is the number of parameters to be estimated.

In a certain time period, suppose that  $n$  inspections have been accomplished for a 200 m-long track section, the set of difference in days between the  $i^{th}$  detection date and the first detection date are denoted by  $t = (t_1, t_2, \dots, t_n)$  while the set of corresponding detection values of  $TQI_p$  by  $y = (y_1, y_2, \dots, y_n)$ . And there are  $m$  maintenance-points in  $y = (y_1, y_2, \dots, y_n)$ . The maintenance-points split  $y = (y_1, y_2, \dots, y_n)$  into  $m + 1$  independent subsequences. Denoting  $\tau_k$  ( $0 \leq k \leq m + 1$ ) as the maintenance-point that splits the  $k^{th}$  and the  $(k + 1)^{st}$  subsequences and  $\tau_0 = 0$ ,  $\tau_{m+1} = t_n$ . Each subsequence is modeled by LR. Thus, the LR model  $\hat{M}_k$  for the  $k^{th}$  subsequence is denoted as

$$y_i = \beta_{k0} + \beta_{k1} t_i + \varepsilon_k (\tau_{k-1} \leq t_i < \tau_k) \quad (2)$$

where  $\beta_k = (\beta_{k0}, \beta_{k1})$  is the corresponding parameter vector for  $\hat{M}_k$  and the random error term  $\varepsilon_k$  is iid. Denoting the variance of  $\varepsilon_k$  as  $\sigma_k^2$ , we obtain that  $\varepsilon_k \sim N(0, \sigma_k^2)$ . Based on the assumption on the distribution of  $\varepsilon_k$ , for  $\tau_{k-1} \leq t_i < \tau_k$ , we obtain that  $y_i \sim N(\beta_{k0} + \beta_{k1} t_i, \sigma_k^2)$ . Denoting the value of  $TQI_p$  in the

$i^{th}$  ( $0 < i \leq n$ ) detection as  $y_i$  and the probability density function of  $y_i$  is expressed as

$$P(y_i) = \frac{1}{\sigma_k \sqrt{2\pi}} e^{-\frac{1}{2\sigma_k^2} (y_i - \beta_{k0} - \beta_{k1} t_i)^2} \quad (3)$$

the maximum likelihood estimation of  $\hat{M}_k$  is

$$L(\hat{M}_k | \beta_k, \sigma_k^2) = \frac{1}{(2\pi\sigma_k^2)^{\frac{\tau_k - \tau_{k-1}}{2}}} e^{-\frac{1}{2\sigma_k^2} \sum_{t_i=\tau_{k-1}}^{\tau_k} (y_i - \beta_{k0} - \beta_{k1} t_i)^2} \quad (4)$$

$$\sigma_k^2 = \frac{1}{\tau_k - \tau_{k-1}} \sum_{t_i=\tau_{k-1}}^{\tau_k} (y_i - \beta_{k0} - \beta_{k1} t_i)^2 \quad (5)$$

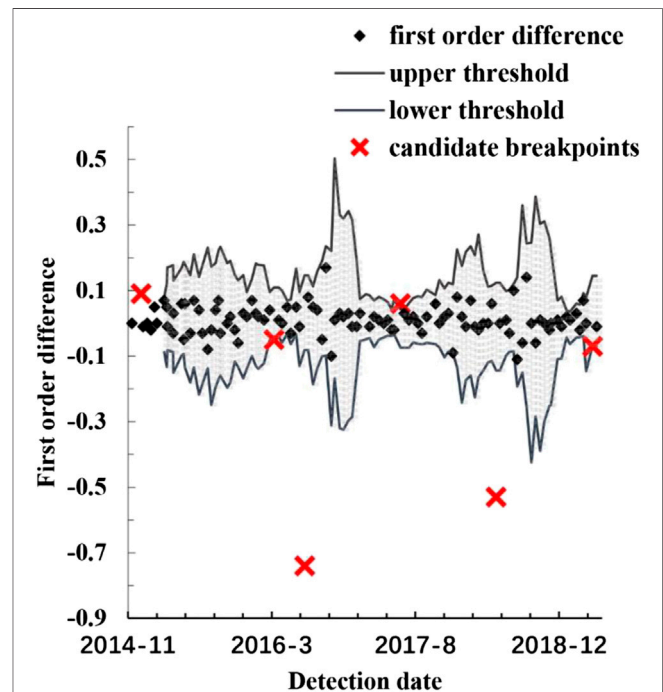


FIGURE 2 | A typical realization of the adaptive thresholding method.



---

**Algorithm 1:** Candidate Breakpoints Identifying(Adaptive thresholding)
 

---

**Input:**  $y$ : a series of TQI-VP;  $S_{win}$ : the sliding window;  $L_{win}$ : size of the sliding window;  $n$ ;  $Q_{90}$

**Output:**  $I_{outlier}$ : the set of index of candidate breakpoints

```

1  $l_{win} \leftarrow 0; index \leftarrow 1; d_1 \leftarrow 0;$ 
2 for  $j \leftarrow 2; j \leq n; j \leftarrow j + 1$  do
3    $d_j = y_{j+1} - y_j$ ;
4  $Q_{90}$  is 90%-quantile of  $(|d_1|, \dots, |d_n|)$ ;
5 while  $l_{win} < L_{win}$  do
6   while  $index \leq n$  do
7     if  $|d_{index}| < Q_{90}$  then
8        $index$  is added into  $I_{outlier}$ ;
9     else
10       $d_{index}$  is added into  $S_{win}$ ;
11       $l_{win} \leftarrow l_{win} + 1$ ;
12     $index \leftarrow index + 1$ ;
13 while  $index \leq n$  do
14    $\sigma \leftarrow \sqrt{\frac{1}{L_{win}} \sum_{i=1}^{L_{win}} (w_i - \bar{w})^2}$ ;
15    $f \leftarrow AR(p)$ ; (the parameters of  $AR(p)$  are estimated by Yule-Walker based on the elements of  $S_{win}$ );
16    $\tilde{d} \leftarrow f(index)$ ;
17    $T_{upper} \leftarrow \tilde{d} + 3 \times \sigma$ ;
18    $T_{lower} \leftarrow \tilde{d} - 3 \times \sigma$ ;
19   if  $d_{index} \leq T_{upper}$  and  $d_{index} \geq T_{lower}$  then
20     the earliest element in  $S_{win}$  is removed;
21      $d_{index}$  is added into  $S_{win}$ ;
22   else
23      $index$  is added into  $I_{outlier}$ ;
24    $index \leftarrow index + 1$ ;
  
```

---

**FIGURE 3** | Pseudo code for the adaptive thresholding method.

Suppose that  $\hat{M} = \{\hat{M}_1, \hat{M}_2, \dots, \hat{M}_{m+1}\}$ ,  $\beta = \{\beta_1, \beta_2, \dots, \beta_{m+1}\}$ , the maximum likelihood estimation of  $\hat{M}$  is

$$L(\hat{M}|\beta, \sigma^2) = \frac{1}{(2\pi)^{\frac{n}{2}} \sigma^2} e^{-\frac{\sum_{k=1}^{m+1} (\tau_k - \tau_{k-1})}{2}} \quad (6)$$

$$\sigma^2 = \prod_{k=1}^{m+1} (\sigma_k^2)^{\frac{\tau_k - \tau_{k-1}}{2}} \quad (7)$$

The number of parameters to be estimated, including  $[(\beta_{10}, \beta_{11}), \dots, (\beta_{(m+1)0}, \beta_{(m+1)1})]$ ,  $(\tau_1, \dots, \tau_m)$ , and  $\sigma^2$  is  $3m$ . Based on Eq. 1, we obtain

$$BIC(\hat{M}) = n(\ln 2\pi + 1) + \ln \sigma^2 + 3m \ln(n) \quad (8)$$

$n(\ln 2\pi + 1)$  in Eq. 8 is fixed when the series is given. Accordingly, the objective function of  $BIC(\hat{M})$  is redefined as

$$BIC(\hat{M}) = \ln \sigma^2 + 3m \ln(n) \quad (9)$$

where  $\ln \sigma^2$  is the sum of squared residuals that reflects the precision of the model and  $3m \ln(n)$  is the penalty term of

model complexity. We denote  $\zeta$  ( $0 < \zeta \leq 1$ ) as a weight coefficient for the complexity of the fitting model. The weight coefficient is determined according to a guideline which will be introduced in *The optimal value of the weight coefficient Section*. Thus, the object function is

$$BIC(\hat{M}) = \ln \sigma^2 + \zeta \times 3m \ln(n) \quad (10)$$

The optimal fitting model  $\hat{M}$  for the deterioration process is defined as the one that minimizes Eq. 10. And we consider that the change-points of  $\hat{M}$  are the maintenance-points which will be identified in the deterioration process.

## SOLUTION ALGORITHM

Since the number of maintenance-points is unknown, a large amount of computation is needed for attaining the optimal fitting model based on Eq. 10. In order to reduce computation load and



**FIGURE 4 |** Location of the Nanchang-Fuzhou rail line.

to make the algorithm practical, we propose an efficient solution algorithm based on the characteristics of maintenance-points.

## The Different Characteristics of Maintenance-Points and Contaminated Measurement Data

This paper is targeted to automatically identify the maintenance-points in the deterioration process of  $TQI_p$  for exploring the deterioration rules of track irregularity. However, outliers in the

deterioration process caused by contaminated measurement data might interfere with the identification of maintenance-points. Each outlier is tagged by the corresponding detection date. Maintenance-points and outliers are characterized as follows.

The deterioration process of  $TQI_p$  of a 200 m-long track section on the Nanchang-Fuzhou railway from 2014 to 2019 is shown in **Figure 1**. As shown in **Figure 1**, the value of  $TQI_p$  drops obviously after maintenance activities. Denoting the first order difference of  $y = (y_1, y_2, \dots, y_n)$  as  $d = (d_1, d_2, \dots, d_n)$  where  $d_1 = 0$  and  $d_i = y_i - y_{i-1}$ .  $d_i$  is much greater/smaller than the neighboring values if maintenance activities were carried out at  $t_i$ . The outliers caused by contaminated measurement data display the same characteristics. The difference between the maintenance-points and outliers is their different impact on the current deterioration process. The maintenance-points terminate the current deterioration cycle, reduce the value of  $TQI_p$  to a specified scope, and start a new deterioration cycle. Outliers show significant deviations from the current deterioration process but have no impact on the current deterioration rate.

**TABLE 1 |** The statistic results for different values of weight coefficient.

$\zeta$	PRC = 100 (%)	RCL = 100 (%)	$F_1$
0.05	6.06	75.76	0.112
0.1	9.09	75.76	0.162
0.15	9.09	72.73	0.162
0.2	18.18	72.73	0.291
0.25	24.24	72.73	0.364
0.3	33.33	66.67	0.444
0.35	51.52	63.64	0.569
0.4	60.61	63.64	0.621
0.45	69.70	60.61	0.648
0.5	81.82	57.58	0.676
0.55	81.82	57.58	0.676
0.6	87.88	63.64	0.738
0.65	87.88	66.67	0.758
0.7	90.91	48.48	0.632
0.75	93.94	48.48	0.640
0.8	93.94	42.42	0.584
0.85	93.94	42.42	0.584
0.9	93.94	42.42	0.584
0.95	93.94	39.39	0.555
1	93.94	39.39	0.555

## Candidate Breakpoints Identified by Adaptive Thresholding Method

The maintenance-points and outliers in the deterioration process are collectively referred to as “candidate breakpoints”. Distinguishing the maintenance-points from outliers within candidate breakpoints will greatly reduce computation load. Accordingly, we develop a method for identifying candidate breakpoints in the deterioration process based on the aforementioned characteristics of maintenance-points and outliers. Constant thresholding is not feasible since track

**TABLE 2 |** The evaluation for the identification results of different rail track sections.

No	Starting mileage of a 200 m-long section	M <sub>man</sub>	T <sub>est</sub>	F <sub>est</sub>	RCL (%)	PRC (%)	N <sub>outlier</sub>
1	K49.849	5	5	0	100.00	100.00	3
2	K50.555	4	4	0	100.00	100.00	5
3	K50.815	3	3	0	100.00	100.00	5
4	K50.976	4	2	0	50.00	100.00	1
5	K51.367	3	3	2	100.00	60.00	4
6	K53.996	1	1	0	100.00	100.00	5
7	K57.509	2	1	0	50.00	100.00	6
8	K59.081	2	2	0	100.00	100.00	1
9	K59.357	3	2	0	66.67	100.00	1
10	K71.482	3	1	1	33.33	50.00	3
11	K72.609	2	2	0	100.00	100.00	1
12	K73.598	4	2	0	50.00	100.00	2
13	K79.195	3	2	1	66.67	66.67	1
14	K79.747	2	2	0	100.00	100.00	0
15	K82.812	3	3	0	100.00	100.00	0
16	K84.601	2	2	0	100.00	100.00	2
17	K85.881	3	2	0	66.67	100.00	0
18	K89.275	2	1	0	50.00	100.00	4
19	K89.696	3	2	0	66.67	100.00	2
20	K90.194	3	1	0	33.33	100.00	5
21	K100.927	3	3	0	100.00	100.00	1
22	K102.077	3	3	0	100.00	100.00	2
23	K103.334	3	2	0	66.67	100.00	0
24	K106.551	3	3	0	100.00	100.00	1
25	K111.410	2	2	0	100.00	100.00	2
26	K111.778	2	2	0	100.00	100.00	2
27	K112.791	3	3	1	100.00	75.00	1
28	K116.079	2	2	0	100.00	100.00	3
29	K117.137	2	2	0	100.00	100.00	6
30	K139.513	2	2	0	100.00	100.00	0
31	K156.778	1	1	0	100.00	100.00	1
32	K157.582	1	1	0	100.00	100.00	2
33	K162.900	3	3	0	100.00	100.00	5

irregularity recovers at different degrees after maintenance among track sections. What is more, outliers cannot be within a predetermined range. Adaptive thresholding provides a solution to this problem (Breier and Branišová, 2015; Wang, 2015). On the basis of adaptive thresholding, we develop a method combining the autoregressive model (referred to as AR) to identify candidate breakpoints in the deterioration process.

Candidate breakpoints are localized by applying this method to the first order difference  $d = (d_1, d_2, \dots, d_n)$  of  $TQI_p$ . The values of  $(d_1, d_2, \dots, d_n)$  are dynamically stable within a small range if there is no candidate breakpoint, while the similarity in the distribution of  $(d_1, d_2, \dots, d_n)$  is destroyed if there is a candidate breakpoint. Thus, we define a sliding window, and

the value at the current moment is predicated based on the historical values which are selected into the sliding window. AR is applied to predicate the value at the current moment based on the historical values. The values of the upper threshold and lower threshold are adjusted via the predicated value and variance of historical values in the sliding window. The difference between predicated value and actual value at the current moment decides whether there is a candidate breakpoint or not. We consider  $t_i$  as a candidate breakpoint if  $d_i$  exceeds the preset thresholds. The method is divided into five steps as follows.

Step one: calculate the first order difference  $d = (d_1, d_2, \dots, d_n)$  of  $TQI_p$ .

Step two: denote the sliding window as  $w = (w_1, w_2, \dots, w_l)$  where  $l$  is the window size and the absolute value of every element in  $d$  as  $d_{abs} = (|d_1|, |d_2|, \dots, |d_n|)$ .  $q_{90}$  is defined as the 90%-quantile of  $d_{abs}$ . Starting with the first element in  $d_{abs}$ ,  $d_i$  is added into  $w$  if  $|d_i| \leq q_{90}$  while  $t_i$  is tagged as a candidate breakpoint if  $|d_i| > q_{90}$ , then the remaining elements are recursively checked in sequence until the sliding window is full.

Step three: fit  $w$  with  $AR(p)$  through the Yule-Walker method (Brockwell et al., 1987), where  $p$  is the order of the AR model. Denote the predicated value at the current moment by  $AR(p)$  as  $\tilde{d}_i$ .

Step four: according to the Pauta criterion ( $3\sigma$  criterion), the proportion of outliers in a series is less than 0.3% under the constraint of  $3\sigma$  (Li et al., 2016). We denote the upper threshold as  $T_{upper}$  and the lower threshold as  $T_{lower}$ , then

$$T_{upper} = \tilde{d}_i + 3 \times Sd \quad (11)$$

$$T_{lower} = \tilde{d}_i - 3 \times Sd \quad (12)$$

where  $Sd$  is the standard deviation of historical values in  $w$ .

Step five: if  $d_i \notin [T_{lower}, T_{upper}]$ ,  $t_i$  is tagged as a candidate breakpoint, and  $w$  is not changed. Otherwise,  $d_i$  is added into  $w$  while the earliest element in  $w$  is removed. Return to Step three until all of the elements in  $d$  have been detected.

The candidate breakpoints identified by the aforementioned method are denoted by  $\tau_c = (\tau_1, \tau_2, \dots, \tau_{\tilde{m}})$  where  $\tilde{m}$  is the number of candidate breakpoints. The composite diagram of a typical realization is shown in **Figure 2**, in which dots represent the first order difference of  $TQI_p$ , the shaded part represents the limitation range of thresholds, and red crosses represent the identified candidate breakpoints. Moreover, the pseudocode of the adaptive thresholding method is provided in **Figure 3**.

## Dynamic Programming for Finding Optimal Fitting Model

Dynamic programming is a multi-stage optimization method and is applicable to various practical problems (Bellman and Dreyfus, 1962). We now consider a method based on the principle of dynamic programming to find an optimal fitting model that achieves the minimum of **Eq. 10**. Suppose that  $r(1 \leq r \leq \tilde{m})$  breakpoints are selected from all the candidate breakpoints  $\tau_c = (\tau_1, \tau_2, \dots, \tau_{\tilde{m}})$  and then the series  $y = (y_1, y_2, \dots, y_n)$  is divided

**TABLE 3 |** The distributions of PRC and RCL.

RCL	RCL = 100%	50% ≤ RCL < 100%	RCL < 50%
Count	22	9	2
PRC	PRC = 100%	50% ≤ PRC < 100%	PRC < 50%
Count	29	4	0

**TABLE 4 |** The comparison results among different values of  $F_{Sd}$ .

Starting mileage of a 200 m-long section	$F_{Sd}$	Time(s)	Number of candidate breakpoints	Estimation results of maintenance-points				
K49.849	2.5	3	20	2015/06/12	2015/10/18	2017/08/12	2018/06/26	2018/09/11
	3	1	15	2015/06/12	2015/10/18	2017/08/12	2018/06/26	2018/09/11
	4	1	10	2015/06/12	2015/10/18	2017/08/12	2018/06/26	2018/09/11
K50.555	2.5	4	25	2015/06/24	2015/10/18	2017/07/26	2018/12/11	
	3	2	21	2015/06/24	2015/10/18	2017/07/26	2018/12/11	
	4	1	13	2015/06/24	2015/10/18	2017/07/26	2018/12/11	
K50.815	2.5	3	26	2015/09/08	2015/10/18	2017/08/26		
	3	1	13	2015/09/08	2015/10/18	2017/08/26		
	4	1	8	2015/09/08	2015/10/18	2017/08/26		
K51.367	2.5	5	30	2015/10/18	2017/09/12	2018/12/11		
	3	2	13	2015/10/18	2017/09/12	2018/12/11		
	4	0	11	2015/10/18	2017/09/12			
K84.601	2.5	5	27	2015/07/24	2017/12/12			
	3	2	21	2015/07/24	2017/12/12			
	4	1	7	2017/12/12				
K100.927	2.5	1	13	2016/06/14	2017/08/12	2018/01/12		
	3	1	7	2016/06/14	2017/08/12	2018/01/12		
	4	1	3	2016/06/14	2017/08/12	2018/01/12		
K106.551	2.5	3	24	2016/07/14	2017/09/12	2018/01/26		
	3	1	15	2016/07/14	2017/09/12	2018/01/26		
	4	1	13	2016/07/14	2017/09/12	2018/01/26		
K112.791	2.5	52	52	2016/06/26	2017/09/12	2018/01/26		
	3	20	39	2016/06/26	2017/09/12	2018/01/26		
	4	1	16	2016/06/26	2016/05/26			

into  $r + 1$  subsequences. To find the optimal fitting model, LR is employed to fit each subsequence by the least-square method, independently. Then,  $BIC(\hat{M})$  is calculated according to Eq. 10. Finally, the optimal fitting model is acquired by iterating to the minimum. Let  $\text{Min}(z)$  be the minimum of object  $z$ . When the number of the selected breakpoints is  $r$ ,  $\text{Min}[BIC(\hat{M}|r)]$  is equal to  $\text{Min}[S(\tau_1, \tau_2, \dots, \tau_r)]$  where

$$S(\tau_1, \tau_2, \dots, \tau_r) = \ln(\sigma^2) = \sum_{k=1}^{r+1} \left[ \frac{\tau_k - \tau_{k-1}}{2} \ln(\sigma_k^2) \right] \quad (13)$$

$c(\tau_{k-1}, \tau_k)$  is defined as the sum of squared residuals for the subsequence, which is constrained in  $(\tau_{k-1}, \tau_k)$ . We obtain

$$c(\tau_{k-1}, \tau_k) = \frac{\tau_k - \tau_{k-1}}{2} \ln(\sigma_k^2) \quad (14)$$

$$S(\tau_1, \tau_2, \dots, \tau_r) = \sum_{k=1}^{r+1} c(\tau_{k-1}, \tau_k) \quad (15)$$

For  $0 \leq j \leq r$ , defining  $b_{r-j}(\tau_j)$  as the minimum of  $S(\tau_1, \tau_2, \dots, \tau_r)$  on the basis that the first  $j$  breakpoints are confirmed, we obtain

$$b_{r-j}(\tau_j) = \text{Min}_{\tau_{j+1}, \dots, \tau_r} \left[ \sum_{k=j+1}^{r+1} c(\tau_{k-1}, \tau_k) \right] \quad (16)$$

Considering the tamping will not be operated for a rail track section twice in a month, we set the constraint that  $\tau_{j+1} - \tau_j > 30$  and suppose that  $\tau_0 = t_0, \tau_{r+1} = t_n$ . Searching the optimal combination of candidate breakpoints is equivalent to solving the following recursive problem:

$$\begin{aligned} b_{r-j}(\tau_j) &= \text{Min}_{\tau_j+30 < \tau_{j+1} < \tau_{j+1}-30 \times (r-j-1)} \left\{ c(\tau_j, \tau_{j+1}) + \text{Min}_{\tau_{j+2}, \dots, \tau_r} \left[ \sum_{k=j+2}^{r+1} c(\tau_{k-1}, \tau_k) \right] \right\} \\ &= \text{Min}_{\tau_j+30 < \tau_{j+1} < \tau_{j+1}-30 \times (r-j-1)} \left\{ c(\tau_j, \tau_{j+1}) + b_{r-j-1}(\tau_{j+1}) \right\} \end{aligned} \quad (17)$$

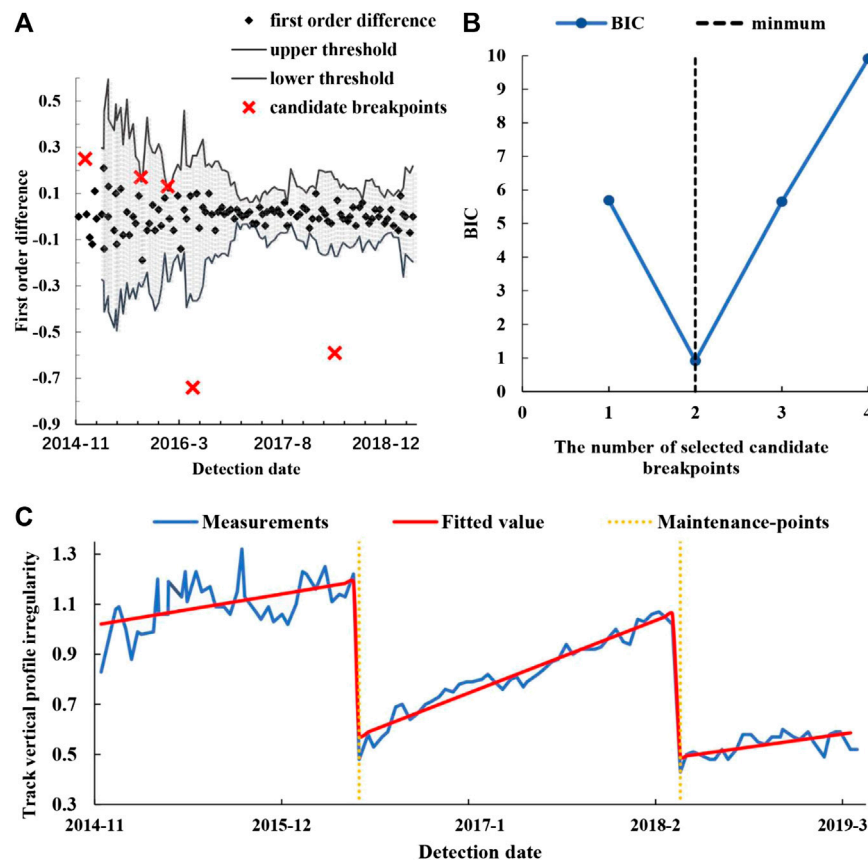
To sum up, the recurrence formulas are

$$\begin{cases} b_0(\tau_r) = c(\tau_r, \tau_{r+1}) \\ b_{r-j}(\tau_j) = \text{Min}_{\tau_j+30 < \tau_{j+1} < \tau_{j+1}-30 \times (r-j-1)} \{ c(\tau_j, \tau_{j+1}) + b_{r-j-1}(\tau_{j+1}) \} \quad (0 \leq j < r) \end{cases} \quad (18)$$

From the previous, it is concluded that  $\text{Min}[BIC(\hat{M}|r)] = b_r(\tau_0)$ . What is more,  $\text{Min}[BIC(\hat{M}|r+1)]$  can be calculated based on the intermediate results for computing  $b_r(\tau_0)$ . Denoting  $f_r(\tau_z)$  as the optimal results for the subsequence which begins at  $\tau_z$  under the circumstance that the number of selected candidate breakpoints is  $r$ , then the recurrence formulas of  $f_r(\tau_z)$  are

$$\begin{cases} f_r(\tau_z) = c(\tau_z, \tau_{r+1}) \\ f_r(\tau_z) = \text{Min}_{\tau_z+30 < \tau_1 < \tau_{r+1}-30 \times (r-1)} \{ c(\tau_z, \tau_1) + f_{r-1}(\tau_1) \} \quad (1 \leq r \leq \tilde{m}) \end{cases} \quad (19)$$

Searching the optimal results under the assumption that there are  $r$  maintenance-points in the deterioration process of  $TQI_p$  is equivalent to calculating  $f_r(\tau_0)$ . The iteration is terminated if the aforementioned constraint cannot be satisfied. For  $1 \leq r \leq \tilde{m}$ , the set of optimal results with a different number of selected candidate breakpoints is denoted by  $f(\tau_0) = [f_1(\tau_0), f_2(\tau_0), \dots, f_{\tilde{m}}(\tau_0)]$  and



**FIGURE 5 |** The identified maintenance-points and piecewise fitting model of section one: **(A)** the candidate breakpoints identified by the adaptive thresholding method; **(B)** the value of BIC for a different number of selected candidate breakpoints; **(C)** the piecewise fitting model.

the optimal piecewise fitting model is the one that achieves  $\text{Min}[f(\tau_0)]$ . The change-points of this model which are selected from the set of candidate breakpoints, are the maintenance-points, while others are outliers.

## The Optimal Value of the Weight Coefficient

The value of the weight coefficient  $\zeta$  in Eq. 10 has a significant impact on the accuracy and reliability of the results identified by the aforementioned framework. Relying on the historical measurement data from 2014 to 2019 for the nearly 200 km-long track sections of the Nanchang-Fuzhou rail line (as shown in Figure 4), we obtain the optimal value of  $\zeta$  which enables the identified maintenance-points to almost correspond with the actual ones. The measurement data are acquired from CIT, which inspects the railways twice a month on average in China. In particular, the preprocessing and transforming of measurement data, which include mileage correction, historical waveform data alignment, and the TQI calculation of each geometric parameter, have been completed relying on the system developed by our team (Xu et al., 2015). Thus, we consider that the data are complete and reliable. Meanwhile, we obtain a set of actual maintenance-points of each track section via manual analysis. They were considered as correctly identified maintenance-points if they were also included in the set of the actual ones.

To assess the performance of the proposed framework with different values of  $\zeta$ , we employ the precision (referred to as PRC) and recall rates (referred to as RCL) given by:

$$\text{PRC} = \frac{T_{\text{est}}}{T_{\text{est}} + F_{\text{est}}} \times 100\% \quad (20)$$

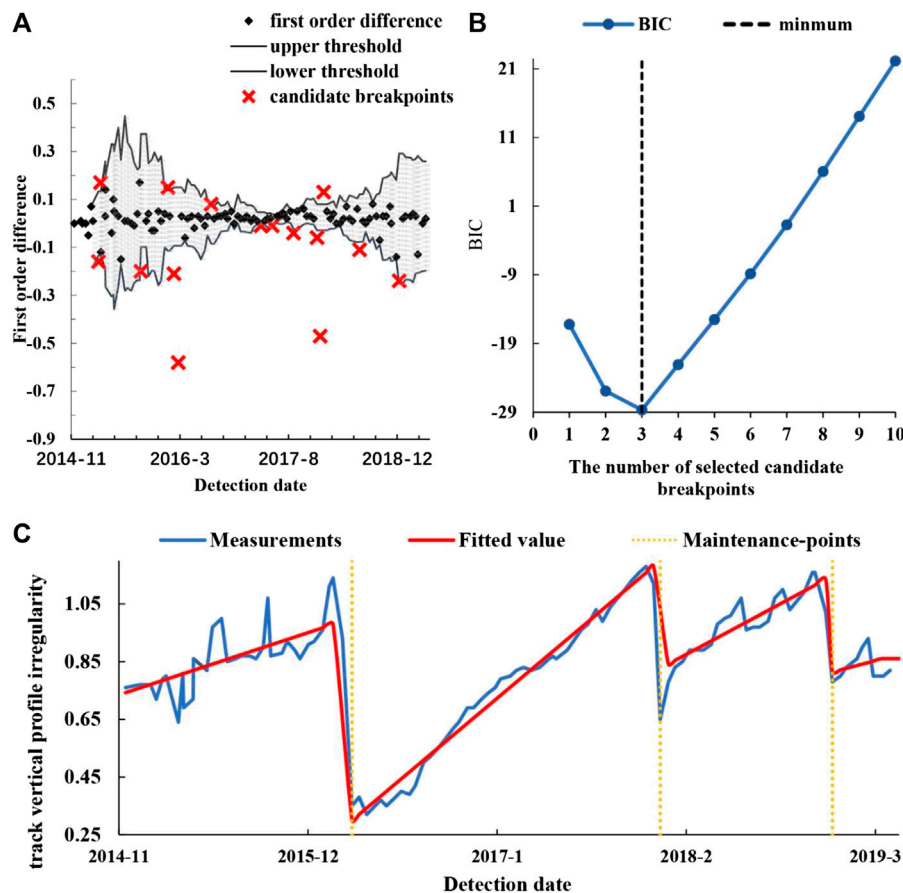
$$\text{RCL} = \frac{T_{\text{est}}}{M_{\text{man}}} \times 100\% \quad (21)$$

where  $T_{\text{est}}$  denotes the number of correctly identified maintenance-points from candidate breakpoints,  $F_{\text{est}}$  is the number of erroneous ones, and  $M_{\text{man}}$  is the number of actual maintenance-points from manual analysis.  $F_1$  defined by Eq. 22 is also considered. The higher the value of  $F_1$ , better performance is obtained.

$$F_1 = \frac{2 \times \text{PRC} \times \text{RCL}}{\text{PRC} + \text{RCL}} \quad (22)$$

To find the optimal value of  $\zeta$ , the maintenance-points of each rail track section are estimated by the proposed framework, whose  $\zeta$  gradually increases by 0.05. By contrast, using the estimated maintenance-points to the actual ones, we obtain the PRC and RCL of each section. For each  $\zeta$ , the proportion of sections whose  $\text{PRC} = 100\%$  and sections whose  $\text{RCL} = 100\%$  are counted separately, while the results are tabulated in Table 1.





**FIGURE 6 |** The identified maintenance-points and piecewise fitting model of section two: **(A)** the candidate breakpoints identified by adaptive thresholding method; **(B)** the value of BIC for a different number of selected candidate breakpoints; **(C)** the piecewise fitting model.

From **Table 1**, it is concluded that RCL is getting smaller while PRC is getting larger with the increase of  $\zeta$ . Based on  $F_1$ , the optimal value of  $\zeta$  is determined as 0.65.

## EMPIRICAL ANALYSIS

In this section, 33 track sections of 200 m in length are further analyzed to demonstrate the performance of the presented framework with  $\zeta = 0.65$ . Then, the calculation procedure of this framework is displayed through two track sections in detail.

### Performance Analysis

PRC and RCL for each track section are calculated based on the comparison between the estimated maintenance-points and the actual ones. To evaluate the accuracy of the presented framework with the interference of contaminated measurement data, we have investigated the outliers due to the contaminated measurement data of each track section.  $N_{outlier}$  is denoted as the number of outliers. The results of the metrics are tabulated in **Table 2**. Based on that, we obtain the distributions of PRC and RCL, which are tabulated in **Table 3**.

From **Table 3**, we obtain that the proposed framework owns a high PRC and RCL for most rail track sections. It indicates that this framework is capable of overcoming the disturbance of contaminated measurement data and accurately distinguishing the maintenance-points from outliers within candidate breakpoints. Meanwhile, the RCL of a few sections are not satisfactory. Through analyzing further, we find that it has resulted from the fact that not all maintenance-points are included in the set of candidate breakpoints.

### Sensitivity Analysis

A large range of thresholds in *Candidate Breakpoints Identified by the Adaptive Thresholding Method Section* leads to an excessive number of candidate breakpoints, requiring more time to obtain the minimum of **Eq. 10**. However, the actual maintenance-points might be left out if the range of thresholds is too small. Accordingly, the sensitivity of this framework to the range of thresholds is discussed in this section. According to **Eqs 11, 12**, we find that the range of thresholds is significantly affected by the times of  $S_d$  (the standard deviation of historical values selected into the sliding window), which is denoted by  $F_{S_d}$ . To access the sensitivity, we apply this framework to some of the sections in **Table 2** for each  $F_{S_d} \in \{2.5, 3, 4\}$ . The other values of parameters

in the implementation of this framework are kept consistent with those in *Performance Analysis Section*. The comparison results among different values of  $F_{sd}$  are tabulated in **Table 4**. The computation time in seconds and the number of candidate breakpoints are given in column 3, 4, while the estimated maintenance-points of each section with different values of  $F_{sd}$  are given in column 5.

From **Table 4**, we obtain that compared with  $F_{sd} = 3$ , the computation time is increased by 145% on average for  $F_{sd} = 2.5$ . What is more, the estimated maintenance-points are the same between  $F_{sd} = 3$  and  $F_{sd} = 2.5$ . Although it requires less computation time when  $F_{sd} = 4$ , some of the actual maintenance-points are left out as the estimation results of the sections starting at K51.367, K84.601, and K112.791 indicate. Thus, it is reasonable that  $F_{sd} = 3$  in *Candidate Breakpoints Identified by the Adaptive Thresholding Method Section*.

### Section One: K117 + 137–K117 + 337

This section is on a tangent track. The candidate breakpoints identified by the adaptive thresholding method are shown in **Figure 5A**. The value of  $\text{Min}[BIC(\hat{M}|r)]$  for a different number of selected candidate breakpoints are shown in **Figure 5B** and  $BIC(\hat{M})$  obtains the minimum when the number is 2. The identified maintenance-points are 2016-05-26 and 2018-04-13. The estimated maintenance-points and piecewise fitting model are shown in **Figure 5C**. The maintenance-points estimated by the proposed framework are exactly as the actual ones. The deterioration process is divided into three subprocesses. Although there are lots of outliers caused by contaminated measurement data in the first subprocess, the maintenance-points are accurately identified.

### Section Two: K162 + 900–K163 + 100

This section is on a curved track. The candidate breakpoints identified by the adaptive thresholding method are shown in **Figure 6A**, and the value of  $\text{Min}[BIC(\hat{M}|r)]$  for this section are shown in **Figure 6B**. The number of selected candidate breakpoints corresponding to the optimal result is 3. The estimated maintenance-points and piecewise fitting model are shown in **Figure 6C**. The identified maintenance-points are 2016-3-14, 2018-01-12, and 2018-06-26. The outliers caused by contaminated measurement data are mainly located in the first subprocess. The slope of the fitting model for each subprocess reflects its deterioration rate. It is obvious that the deterioration rates are different before and after maintenance activities. Thus, we believe that the deterioration rates might be affected by maintenance activities.

## CONCLUSION

In this paper, a rail track deterioration modeling framework driven by historical measurement data from CIT is proposed.

## REFERENCES

- Bellman, R. E., and Dreyfus, S. E. (1962). Applied dynamic programming. *J. Am. Stat. Assoc.* 59, 366. doi:10.2307/2282884

The modeling framework requires no historical maintenance records and does not assume the quality of track measurement data. The proposed framework formulates the identification of maintenance activities with a model selection optimization problem, based on a modified Bayesian Information Criterion by incorporating an optimized weight for the model complexity component into the objective function. An efficient solution algorithm utilizing adaptive thresholding and dynamic programming is proposed for the model selection problem, taking the characteristics of the effect of maintenance on track deterioration trend.

The proposed track deterioration modeling framework is applied to the historical measurement data from 2014 to 2019 for the nearly 200 km-long track sections of the Nanchang-Fuzhou rail line. Based on that application, the optimal value of the weight coefficient which is incorporated for the model complexity is discussed in *The Optimal Value of the Weight Coefficient Section*. Moreover, the assessment indicators are calculated based on 33 200 m-long track sections. As the assessment indicators indicate, the proposed framework is capable of accurately identifying the maintenance-points and creating an adaptive piecewise model of the deterioration process.

However, for a few track sections, the estimated maintenance-points are less than the actual ones, which resulted from the fact that not all maintenance-points were included in the set of candidate breakpoints. Therefore, one of the emphases for the next step will be on improving the algorithm to ensure that the set of candidate breakpoints contains all of the maintenance-points.

## DATA AVAILABILITY STATEMENT

The raw data supporting the conclusions of this article will be made available by the authors, without undue reservation

## AUTHOR CONTRIBUTIONS

YY: model-establishment and paper-writing. PX, GY, and JL: theoretical-guidance, paper-review and editing. LC: data preprocessing. All authors contributed to the article and approved the submitted version

## FUNDING

This research is supported by the Science and Technology Research and Development Program of China Railway's "Intelligent Operation and Maintenance Technology for Beijing-Zhangjiakou HSR (Grand No. P2018G051)" project.

- Breier, J., and Branišová, J. (2015). A dynamic rule creation based anomaly detection method for identifying security breaches in log records. *Wireless Pers. Commun.* 94, 1–15. doi:10.1007/s11277-015-3128-1
- Brockwell, P. J., Davis, R. A., Berger, J. O., Fienberg, S. E., and Singer, B. (1987). *Time series: theory and methods*. Berlin, Germany: Springer-Verlag.

- Chen, S. S., and Gopalakrishnan, P. S. (1998). "Clustering via the Bayesian information criterion with applications in speech recognition," in IEEE international Conference on acoustics, speech and signal processing, Seattle, WA, May 15–15, 1998 (IEEE).
- Dias, A. (2004). *Change-point Analysis for dependence structures in finance and insurance*. Risk Measures for the 21st Century. 321–335. Available at SSRN: <https://ssrn.com/abstract=2464242>
- Gang, S., and Ghosh, J. K. (2011). Developing a new BIC for detecting change-points. *J. Stat. Plann. Inference* 141, 1436–1447. doi:10.1016/j.jspi.2010.10.017
- Hall, A. R., Osborn, D. R., and Sakkas, N. (2013). Inference on structural breaks using information criteria. *The Manchester School* 81, 54–81. doi:10.1111/manc.12017
- Hall, A. R., Osborn, D. R., and Sakkas, N. (2015). Structural break inference using information criteria in models estimated by two-stage least squares. *J. Time Ser. Anal.* 36, 741–762. doi:10.1111/jtsa.12107
- Hannart, A., and Naveau, P. (2012). An improved bayesian information criterion for multiple change-point models. *Technometrics* 54, 256–268. doi:10.1080/00401706.2012.694780
- Jandhyala, V., Fotopoulos, S., Macneill, I., and Liu, P. (2013). Inference for single and multiple change-points in time series. *J. Time Ser. Anal.* 34 (4), 423–446. doi:10.1111/jtsa.12035
- Kotti, M., Benetos, E., Kotropoulos, C., Gustavo, L., and Martins, P. M. (2006). Speaker Change Detection using BIC: a comparison on two datasets. *Int. Symp. Commun.* Available at: <http://hdl.handle.net/10044/1/12249>
- Lee, J. S., Hwang, S. H., Choi, Y., and Kim, I. K. (2018). Prediction of track deterioration using maintenance data and machine learning schemes. *J. Transport. Eng.* 144, 04018045. doi:10.1061/jtepbs.0000173
- Li, L., Wen, Z., and Wang, Z. (2016). Outlier detection and correction during the process of groundwater level monitoring base on Pauta criterion with self-learning and smooth processing," in Asian simulation conference SCS autumn simulation multi-conference. October 8–11, 2016.
- Liu, Y. U., Lei, Y. U., Yi, Q. I., Wang, J., and Wen, H. (2008). Traffic incident detection algorithm for urban expressways based on probe vehicle data. *J. Transp. Syst. Eng. Inf. Technol.* 8, 36–41. doi:10.1016/s1570-6672(09)60001-5
- Lu, Q., Lund, R., and Lee, T. C. M. (2010). AN MDL approach to the climate segmentation problem. *Ann. Appl. Stat.* 4, 299–319. doi:10.1214/09-aos289
- Meier-Hirmer, C., Senee, A., Riboulet, G., Sourget, F., and Roussignol, M. (2006). "A decision support system for track maintenance," in *Computers in railways X: computer system design and operation in the railway and other transit systems*. Editors J. Allan, C. A. Brebbia, A. F. Rumsey, G. Sciotto, S. Sone, and C. J. Goodman (Southampton: Computational Mechanics Publication Ltd), 217.
- Mercier, S., Meier-Hirmer, C., and Roussignol, M. (2012). Bivariate Gamma wear processes for track geometry modelling, with application to intervention scheduling. *Struct. Infrastruct. Eng.* 8, 357–366. doi:10.1080/15732479.2011.563090
- Perreault, L., Parent, É., Bernier, J., Bobée, B., and Slivitzky, M. (2000). Retrospective multivariate Bayesian change-point analysis: a simultaneous single change in the mean of several hydrological sequences. *Stoch. Environ. Res. Risk Assess.* 14, 0243–0261. doi:10.1007/s004770000051
- Quiroga, L. M., and Schnieder, E. (2010). A heuristic approach to railway track maintenance scheduling. *COMPRAIL 2010* 114. doi:10.2495/cr100631
- Reeves, J., Chen, J., Wang, X. L., Lund, R., and Lu, Q. Q. (2007). A review and comparison of changepoint detection techniques for climate data. *J. Appl. Meteorol. Climatol.* 46, 900. doi:10.1175/jam2493.1
- Schwarz, G. (1978). Estimating the dimension of a model. *Ann. Stat.* 6, 461–464. doi:10.1214/aos/1176344136
- Vale, C., and Lurdes, S. M. (2013). Stochastic model for the geometrical rail track degradation process in the Portuguese railway Northern Line. *Reliab. Eng. Syst. Saf.* 116, 91–98. doi:10.1016/j.res.2013.02.010
- Veit, P., and Marschnig, S. (2010). "Sustainability IN track - a precondition for high speed traffic," in ASEM 2010 joint rail conference AMER SOC MECHANICAL ENGINEERS, Urbana, Illinois, April 27–29, 2010, 349–355.
- Wang, H. (2015). Anomaly detection of network traffic based on prediction and self-adaptive threshold. *Int. J. Future Gener. Commun. Networking* 8, 205–214. doi:10.14257/ijfgcn.2015.8.6.20
- Wang, Y. W., Ni, Y. Q., and Wang, X. (2020). Real-time defect detection of high-speed train wheels by using Bayesian forecasting and dynamic model. *Mech. Syst. Signal Process.* 139. doi:10.1016/j.ymssp.2020.106654
- Watanabe, S. (2012). A widely applicable bayesian information criterion. *J. Mach. Learn. Res.* 14, 867–897. doi:10.1002/cem.2494
- Xi, R., Hadjipanayis, A. G., Luquette, L. J., Kim, T. M., Lee, E., Zhang, J., et al. (2011). Copy number variation detection in whole-genome sequencing data using the Bayesian information criterion. *Proc. Natl. Acad. Sci. U.S.A.* 108, E1128–E1136. doi:10.1073/pnas.1110574108
- Xu, P., Liu, R.-K., Wang, F.-T., and Sun, Q.-X. (2012). A novel description method for track irregularity evolution. *Int. J. Comput. Intell. Syst.* 4, 1358–1366. doi:10.1080/18756891.2011.9727886
- Xu, P., Sun, Q., Liu, R., Souleyrette, R. R., and Wang, F. (2015). Optimizing the alignment of inspection data from track geometry cars. *Comput. Aided Civ. Infrastruct. Eng.* 30, 19–35. doi:10.1111/mice.12067
- Xu, P., Sun, Q., Liu, R., and Wang, F. (2011). A short-range prediction model for track quality index. *Proc. Inst. Mech. Eng.—F J. Rail Rapid Transit* 225, 277–285. doi:10.1177/2041301710392477
- Yang, S., Kalpakis, K., and Biem, A. (2014). Detecting road traffic events by coupling multiple timeseries with a nonparametric bayesian method. *IEEE Trans. Intell. Transp. Syst.* 15, 1936–1946. doi:10.1109/tits.2014.2305334
- Yao, Y.-C. (1988). Estimating the number of change-points via Schwarz' criterion. *Stat. Probab. Lett.* 6, 181–189. doi:10.1016/0167-7152(88)90118-6
- Zhang, N. R., and Siegmund, D. O. (2007). A modified Bayes information criterion with applications to the analysis of comparative genomic hybridization data. *Biometrics* 63, 22–32. doi:10.1111/j.1541-0420.2006.00662.x
- Zhu, M., Cheng, X., Miao, L., Sun, X., and Wang, S. (2013). Advanced stochastic modeling of railway track irregularities. *Adv. Mech. Eng.* 5. doi:10.1155/2013/401637

**Conflict of Interest:** GY was employed by China State Railway Group Co., Ltd.

The remaining authors declare that the research was conducted in the absence of any commercial or financial relationships that could be construed as a potential conflict of interest.

Copyright © 2021 Yang, Xu, Yang, Chen and Li. This is an open-access article distributed under the terms of the Creative Commons Attribution License (CC BY). The use, distribution or reproduction in other forums is permitted, provided the original author(s) and the copyright owner(s) are credited and that the original publication in this journal is cited, in accordance with accepted academic practice. No use, distribution or reproduction is permitted which does not comply with these terms.



# Relation Between Adhesion Properties and Microscopic Characterization of Polyphosphoric Acid Composite SBS Modified Asphalt Binder

Liangying Li<sup>1</sup>, Zhiwei Li<sup>1</sup>, Yongning Wang<sup>1,2</sup>, Xiaolan Li<sup>1,3</sup> and Bo Li<sup>1\*</sup>

<sup>1</sup>National and Provincial Joint Engineering Laboratory of Road and Bridge Disaster Prevention and Control, Lanzhou Jiaotong University, Lanzhou, China, <sup>2</sup>Gansu Province Highway Traffic Construction Group Co., Ltd., Lanzhou, China, <sup>3</sup>Gansu Provincial Transportation Research Institute Group Co., Ltd., Lanzhou, China

## OPEN ACCESS

### Edited by:

Zhanping You,  
Michigan Technological University,  
United States

### Reviewed by:

Ali Behnood,  
Purdue University, United States  
Pouria Hajikarimi,  
Amirkabir University of  
Technology, Iran

### \*Correspondence:

Bo Li  
libo@mail.lzjtu.cn

### Specialty section:

This article was submitted to  
Structural Materials,  
a section of the journal  
Frontiers in Materials

**Received:** 25 November 2020

**Accepted:** 06 January 2021

**Published:** 02 March 2021

### Citation:

Li L, Li Z, Wang Y, Li X and Li B (2021)  
Relation Between Adhesion Properties  
and Microscopic Characterization of  
Polyphosphoric Acid Composite SBS  
Modified Asphalt Binder.  
Front. Mater. 8:633439.  
doi: 10.3389/fmats.2021.633439

The purpose of this study was to investigate the adhesive properties of polyphosphoric acid compounded SBS (PPA/SBS) modified asphalt. Three base asphalt binders, one SBS, one dibutyl phthalate (DBP), one furfural extraction oil, and two polyphosphoric acids (PPA), were used to produce the modified binders. The adhesive properties tested in this study included contact angle, cohesive work, adhesive work, and peak area ratio. Cohesive work and adhesive work indicators were calculated from the contact angle, the contact angle between PPA/SBS modified asphalt and three liquids (distilled water, glycerin, formamide) were tested by the contact angle tester, and the peak area ratio of the microscopic adhesion performance index by AFM. The relation between the microscopic adhesion performance characterization method (peak area ratio) and the macroscopic adhesion performance index (cohesive work, adhesion work) was established. The test results indicated that the PPA/SBS modified asphalt had the highest cohesive work and adhesion work under the conditions of 0.5% PPA, 1% DBP, 1.5% extracted oil, and 3.5% SBS, which was clearly greater than the original SBS modified asphalt, while the peak area ratio was consistent with the cohesive work and adhesive work, in which the correlation coefficient between the peak area ratio and cohesive work was 0.77788, and that between the peak area ratio and adhesion work was 0.87203. We recommend adopting the peak area ratio to characterize PPA/SBS modified asphalt's microscopic adhesion properties.

**Keywords:** polyphosphoric acid compounded SBS modified asphalt, surface free energy theory, atomic force microscopy, adhesion properties, peak area ratio

## INTRODUCTION

Asphalt pavement is the primary material used in high-grade pavement, most of which is distributed in regions with cold winters and hot summers. Asphalt materials require the properties of high and low temperature performance, requirements that ordinary base asphalt cannot meet (Zhang et al., 2016). As part of the implementation of the strategic highway research program (SHRP) binder specification, various properties of asphalt binder can be improved significantly by adding modifiers such as polymer and rubber powder (Wang et al., 2018a; Wang et al., 2018b). Among them, SBS

**TABLE 1** | properties of virgin asphalt.

Properties	Unit	SK90#	ZH90#	XT90#
Penetration (25°C, 100 g, 5 s)	0.1 mm	85.5	87.6	86.4
Softening point	°C	45.6	47	46.2
Ductility (15°C, 5 cm/min)	Cm	> 100	> 100	> 100
Residue after RTFOT (163°C, 85 min)				
Mass loss	%	0.07	0.12	0.1
Penetration ratio	%	70	61	65
Ductility (10°C, 5 cm/min)	Cm	9.0	8.0	8.3

ZH90#, Zhen Hai virgin asphalt with penetration grade 90; XT, Xi Tai virgin asphalt; SK, SK virgin asphalt.

modified asphalt is used widely because of its good high temperature stability and low temperature crack resistance (Liang et al., 2015). However, with the rise in oil and polymer prices, the price of polymer modified asphalt has increased (Cai et al., 2018). Thus, the application of a cheap polyphosphoric acid (PPA) modifier in road asphalt modification has attracted the attention of domestic and foreign scholars gradually, and many researchers have carried out the preparation process, and identified PPA modified asphalt's microstructure and modification mechanism, and have drawn many useful conclusions that has laid the foundation for PPA modified asphalt's further development (Bishara et al., 2003; Romagosa and Martin, 2009; Fee and Maldonado, 2010; Yan et al., 2013; Wang et al., 2017). Previous studies have shown that PPA reduces the modification cost to a certain extent and improves SBS modified asphalt's high-temperature performance significantly (Baumgardner, 2006; Kodrat et al., 2007; Jiang et al., 2019). However, it has been reported that PPA can react with asphalt only when it contains polymer with a high dielectric constant (Masson, 2008). Therefore, some scholars have proposed that a certain amount of SBS modifier can be added to improve the PPA's related properties (Aflaki and Hajikarimi, 2012; Zegeye et al., 2012).

Research on PPA/SBS modified asphalt's high and low temperature rheological properties and chemical composition changes has been conducted commonly (Jiang et al., 2012; Zegeye et al., 2012; Alam and Hossain, 2017), but there is little research on its water sensitivity. As an early road surface disease of asphalt pavement, water damage shortens the pavement's service life and affects road safety seriously. In

recent years, researchers at home and abroad have believed that the mechanism of water damage consists primarily of cohesive and adhesion failure (Kvasnak and West, 2009; Howson et al., 2010), largely by using the adhesion properties of asphalt and aggregate to appraise the asphalt mixture's water stability. The evaluation methods include the bitumen bond strength test, boiling water test, freeze-thaw splitting experiment, Hamburg Wheel Tracking Device (HWTDD) experiment, and so on (Reinke et al., 2010; Park et al., 2017; Gang et al., 2018). However, these experiments on the adhesion between the asphalt and aggregate are macro experiments, which are influenced greatly by subjective factors and result in inconsistent research results, while no explanation has been given of the mechanism from the micro level. To study the adhesion of asphalt and aggregate from the microscopic aspect quantitatively, the surface free energy (SFE) theory and atomic force microscopy (AFM) have been used constantly over the years, and proven to be a powerful way to study asphalt materials' adhesion properties quantitatively.

Ji et al. studied asphalt mixture system's adhesiveness in the presence and absence of water through the surface free energy theory, and found that this method is feasible (Ji et al., 2017). Moraes et al. compared the asphalt bonding strength (ABS) test with the surface energy test, and found that different asphalt samples' ABS has a good correlation with the surface energy index, indicating that the surface energy test's use can measure the water stability between asphalt and aggregate effectively (Moraes et al., 2017). In addition, AFM, as an auxiliary verification method, not only detects asphalt binders' nanoscopic adhesion characteristics, but also provides a new and better research method to understand asphalt's microstructure and mechanical properties accurately. Guo et al. investigated the interfacial interaction between asphalt and aggregate with the AFM test, and found that the influence thickness is approximately 1  $\mu\text{m}$  (Guo et al., 2017). Ma et al. used the AFM test to investigate the change in asphalt binder's bond performance after aging and regeneration, and found a very good correlation between the AFM and macro test results. In addition, AFM can be used to characterize the asphalt's bonding properties better after aging and regeneration (Ma et al., 2019). Li et al. used the force-distance curve of the AFM experiment to investigate the influence of the original material composition on SBS modified asphalt's nano adhesion properties, which showed that AFM can

**TABLE 2** | performance of SBS modifier.

Modifier	Structure	Block ratio(S/B)	Volatile content/%	Tensile strength/MPa	Elongation at break/%	Shore hardness/A	Melt flow rate/(g/10 min)
SBS (1,301)	Liner	30/70	0.7	15.0	70	≥68	0.10–5.00

**TABLE 3** | Physical indices of PPA.

P <sub>2</sub> O <sub>5</sub> content/%	Sulfate/%	Viscosity/centipoise	Chroma/black	Heavy metal/Pb	Iron content/%	Arsenic content/%
≥84	≤0.01	35,000	50	≤0.01	≤0.01	≤0.01



**TABLE 4 |** Performance of the extracted oil.

Color	40°C Viscosity/(Pa·s)	Content of Aromatic/%	Flash Point/°C
Brown black	2,500	55.0	200

SBS modifier consists of two molecular structures: Linear and star-shaped. In this paper, SBS modified asphalt was prepared with the 1,301 linear SBS modifier used commonly in Gansu. The primary physical indices are displayed in **Table 2**.

### (3) Polyphosphoric acid (PPA)

**TABLE 5 |** Physical indices of DBP.

Acetate content/%	Density/(g/cm <sup>3</sup> )	Flash point/°C	Burning residue (sulfate meter)/%	Volatile matter/%	Free acid/%	Heating alkali amount/%
≥99.5	1.0463–1.0475	160	0.003	≤0.3	≤0.05	0.3

**TABLE 6 |** Physical indices of stabilizer.

Color	Apparent density/ (g/cm <sup>3</sup> )	Water content/%	Melting point/°C
Gray- black	0.5–0.7	0.2	120

be used to study the water stability between asphalt and aggregate quantitatively (Li et al., 2019). A large number of studies has shown that both the surface energy and AFM tests can characterize the adhesion of asphalt and the adhesion between asphalt and aggregate quantitatively. However, few scholars have given attention to the change in PPA/SBS modified asphalt's adhesion and adhesion performance.

In this paper, different raw materials' influence on the adhesion performance of PPA/SBS modified asphalt was studied by the surface energy theory and AFM test. The PPA/SBS modified asphalt's water damage resistance was characterized by adhesion work and cohesion work, and its nano adhesion properties were characterized through the peak area ratio. At the same time, the correlation between the surface energy test results and AFM test results was analyzed to promote the application of AFM technology by characterizing the PPA/SBS modified asphalt's adhesion properties.

## MATERIALS AND EXPERIMENTAL METHODS

### Raw Materials

#### (1) base asphalt

The Gansu Luqiao Construction Group Co., Ltd. supplied the three base asphalts used, and **Table 1** shows the base asphalt binders' performance.

#### (2) SBS modifier

In this paper, the PPA Shanghai Zhanyun provided was used to improve the asphalt's high temperature properties. Its main technical performance indices are shown in **Table 3**.

#### (4) Furfural extraction oil

Extracted oil was used to improve the compatibility of SBS and asphalt, thereby enhancing SBS modified asphalt's low-temperature plasticity and ductility. The main technical indicators are shown in **Table 4**.

#### (5) Dibutyl phthalate (DBP)

To prevent the low temperature properties of PPA in the matrix asphalt deteriorating in the modification process, DBP provided by Wuxi was used to improve its low temperature performance. The principal technical indicators are shown in **Table 5**.

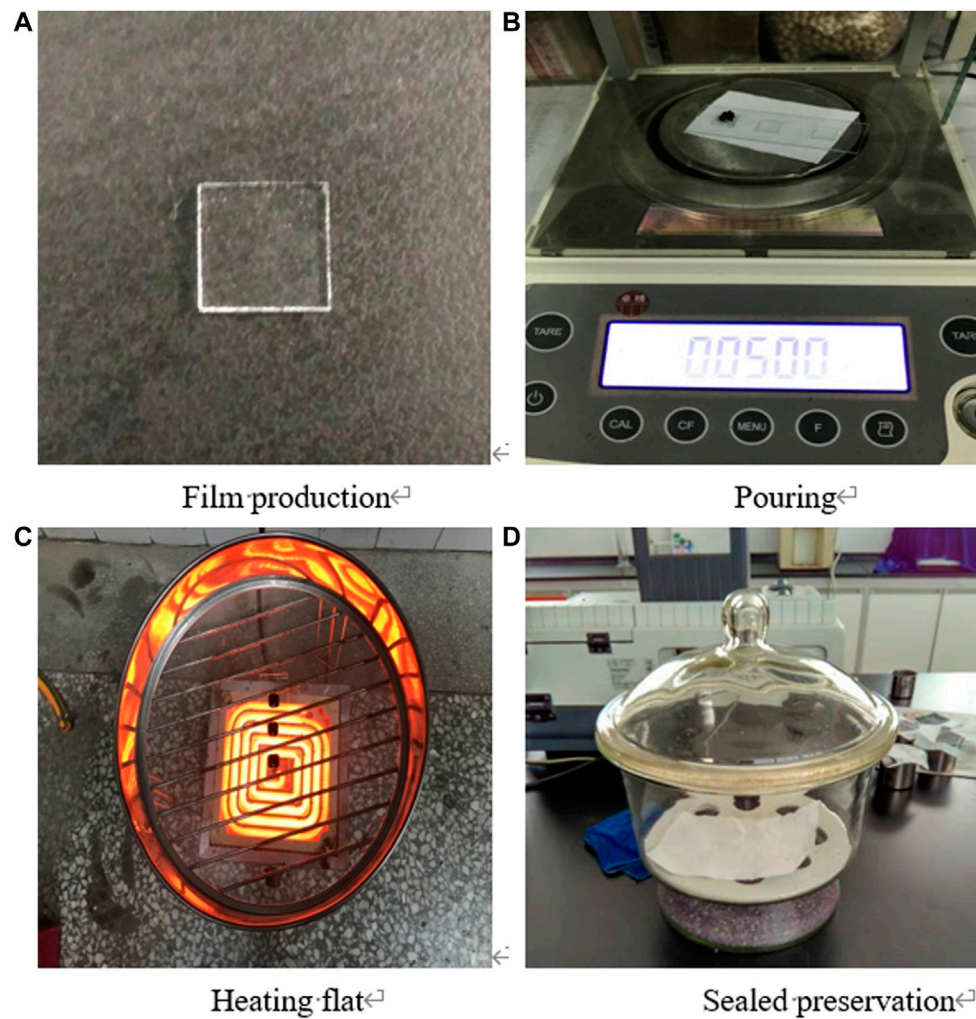
#### (6) Stabilizer

In addition, to avoid phase separation in SBS modified asphalt and increase its storage stability, a certain amount of high-quality stabilizer Gansu Provincial Road Surface Engineering Technology Research Center provided was added when preparing the SBS modified asphalt. The major physical indicators are shown in **Table 6**.

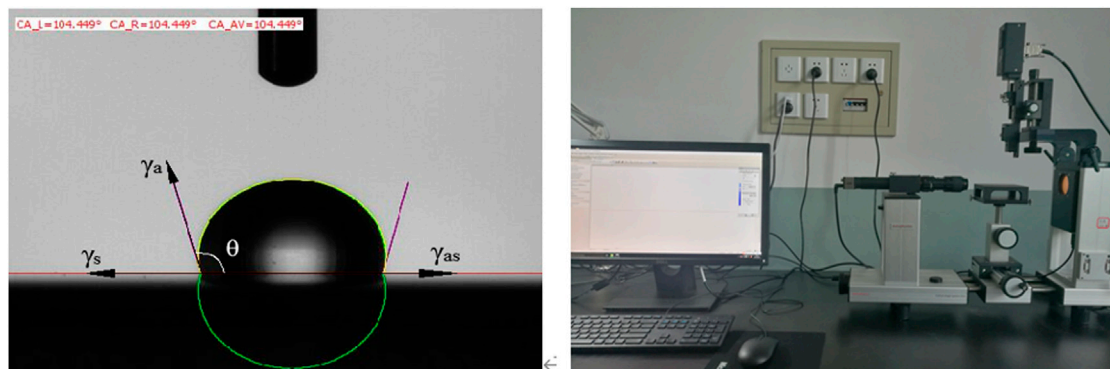
## Sample Preparation

#### (1) Preparation of PPA/SBS modified asphalt

PPA/SBS modified asphalt is made with a high-speed shearing machine. The specific test procedure was as follows (Li et al., 2021): 1) The matrix asphalt was heated to 140°C, and a certain amount of extracted oil was added and stirred evenly; 2) The evenly mixed asphalt was placed in the heating device and heated to 160°C, and the required amount of DBP was added and stirred uniformly; 3) the temperature was raised rapidly to approximately 175°C, SBS modifier was



**FIGURE 1 |** AFM sample preparation process. (A) Film production. (B) Pouring. (C) Heating flat. (D) Sealed preservation.



**FIGURE 2 |** Schematic representation of the contact angle formed between a probe liquid and an asphalt surface and drop shape analyser (OCA25).

added, and the mixture was stirred thoroughly and allowed to swell for approximately 10 min; 4) the set content of PPA in the swollen modified asphalt was heated, and placed under a

high-speed shearing machine to control and stabilize the temperature at approximately 175°C at 5000 r/min, and was sheared for 30 min; 5) the stabilizer was set and stirring



FIGURE 3 | AFM test system.

continued for 10 min; 6) the modified asphalt was developed continuously for 2.5 h to obtain the compound asphalt required for the test.

## (2) Preparation of contact angle sample preparation

The asphalt samples were prepared by the drop method. First, the asphalt binder was heated and weighed and  $1.5 \pm 0.1$  g was placed on the slide. Thereafter, it was placed on a horizontal heating frame and heated for 5 min to form a uniform asphalt film. Finally, the asphalt sample was placed in a drying dish for 12 h (Li et al., 2021).

## (3) AFM sample preparation

The preparation process of the AFM sample was as follows: First, 0.05g of the fluid state asphalt mixture was weighed onto a 1 cm × 1 cm glass slide, and then placed on a

leveled and high-rise heating frame, at a temperature of approximately 163°C and heated continuously until a smooth horizontal asphalt test surface was obtained. It was moved to room temperature to cool, and then placed in a sealed dry container horizontally for approximately 24h to obtain an AFM sample. The preparation process is shown in Figure 1.

## Sample Test

### (1) Contact angle test

A contact angle test is required to calculate PPA/SBS modified asphalt's adhesion performance index (cohesive work and adhesion work) (Li et al., 2021). Figure 2 shows the contact angle formed between the liquid and the asphalt sample. In addition, it shows the test instrument for the contact angle.

PPA/SBS modified asphalt's adhesion performance indices can be calculated from the contact angle test results; for the detailed calculation process, refer to Li et al. (Li et al., 2021). The calculation equation is shown in Eqs 1, 2:

$$W_{as} = \gamma_a (1 + \cos \theta) = 2\sqrt{\gamma_a^d \gamma_s^d} + 2\sqrt{\gamma_a^+ \gamma_s^-} + 2\sqrt{\gamma_a^- \gamma_s^+} \quad (1)$$

$$W_{cohesion} = 2\gamma_a \quad (2)$$

in which  $\gamma^p$  is the polar component,  $\gamma^d$  is the dispersion component,  $\gamma^+$  is the Lewis acid component,  $\gamma^-$  is the Lewis base component,  $\gamma^a$  is the bitumen surface energy,  $\gamma^s$  is the aggregate surface energy, and  $\gamma^{as}$  is the interface energy between the bitumen and the aggregate contact surface.

$W_{as}$  is the adhesion work, and  $W_{cohesion}$  is the cohesion work.

### (2) AFM test

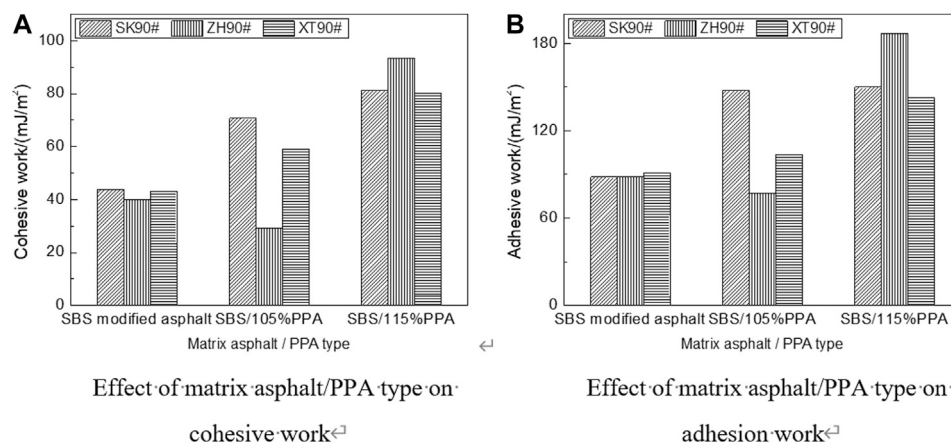
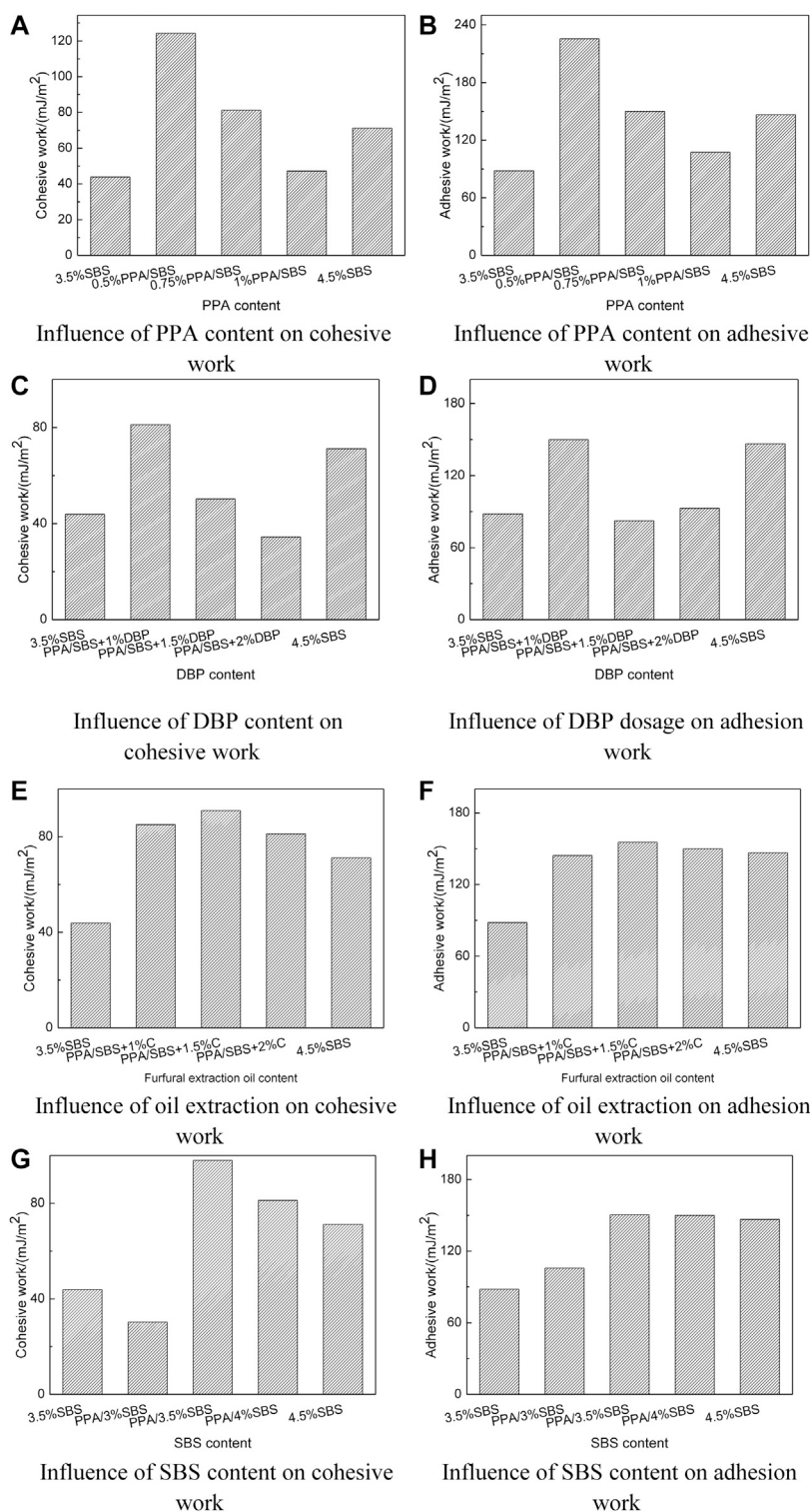
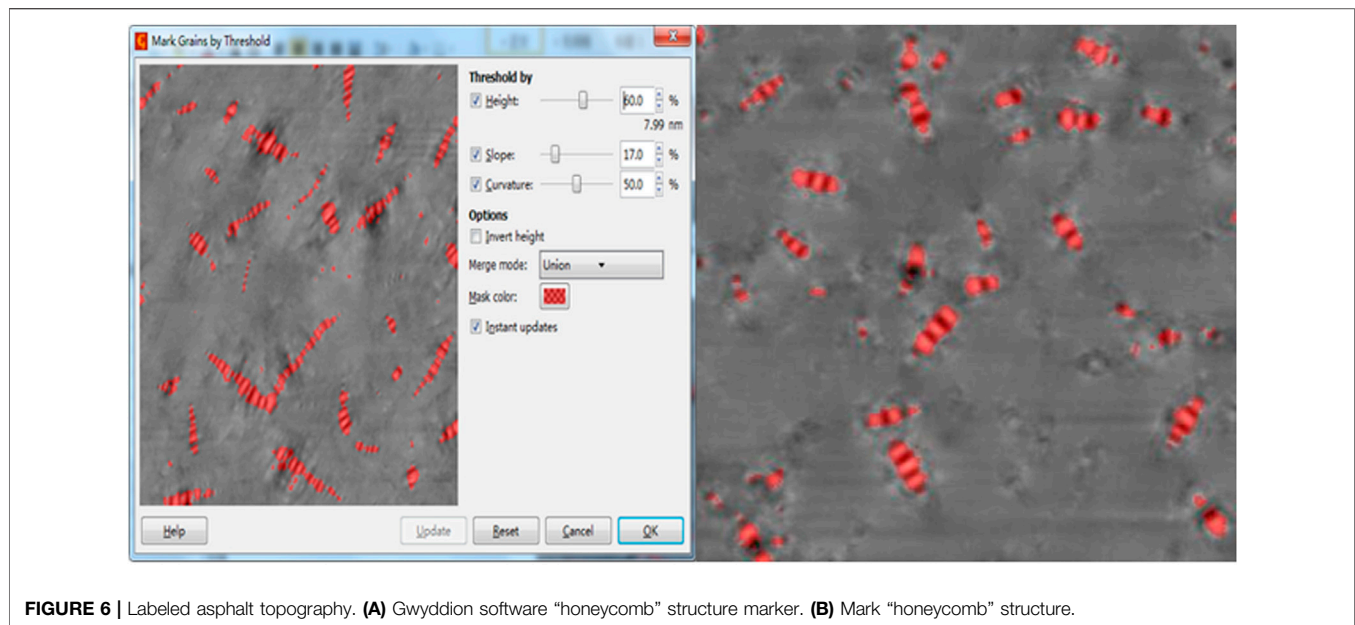


FIGURE 4 | Effect of matrix asphalt/PPA type on PPA/SBS modified asphalt's adhesion characteristics, (A) Effect of matrix asphalt/PPA type on cohesive work, (B) Effect of matrix asphalt/PPA type on adhesion work.





**FIGURE 5 |** Effect of the raw materials' content on PPA/SBS modified asphalt's adhesion characteristics. **(A)** Influence of PPA content on cohesive work. **(B)** Influence of PPA content on adhesive work. **(C)** Influence of DBP content on cohesive work. **(D)** Influence of DBP dosage on adhesion work. **(E)** Influence of oil extraction on cohesive work. **(F)** Influence of oil extraction on adhesion work. **(G)** Influence of SBS content on cohesive work. **(H)** Influence of SBS content on adhesion work.



**FIGURE 6 |** Labeled asphalt topography. **(A)** Gwyddion software "honeycomb" structure marker. **(B)** Mark "honeycomb" structure.

In this paper, Bruce's Icon-type atomic force microscope and Budget Sensors Tap300Al-G probe were used to test the asphalt samples' morphology and mechanical indices in the peak force light mode (PFT QNM). The probe elastic constant was 1 Hz, scanning frequency was 1.0 Hz, scanning range was  $20\text{ }\mu\text{m} \times 20\text{ }\mu\text{m}$ , resolution was  $512 \times 512$ , and test temperature was  $25^\circ\text{C}$ , as shown in **Figure 3**.

## RESULTS AND DISCUSSION

### Raw Materials' Influence on PPA/SBS Modified Asphalt's Adhesion Characteristics

#### (1) Matrix asphalt/PPA type

The adhesion performance indices (cohesive work and adhesion work) of PPA/SBS modified asphalt prepared from three kinds of base asphalt (SK90# and ZH90# and XT90#) and PPA type (105% PPA and 115% PPA) are shown in **Figure 4**.

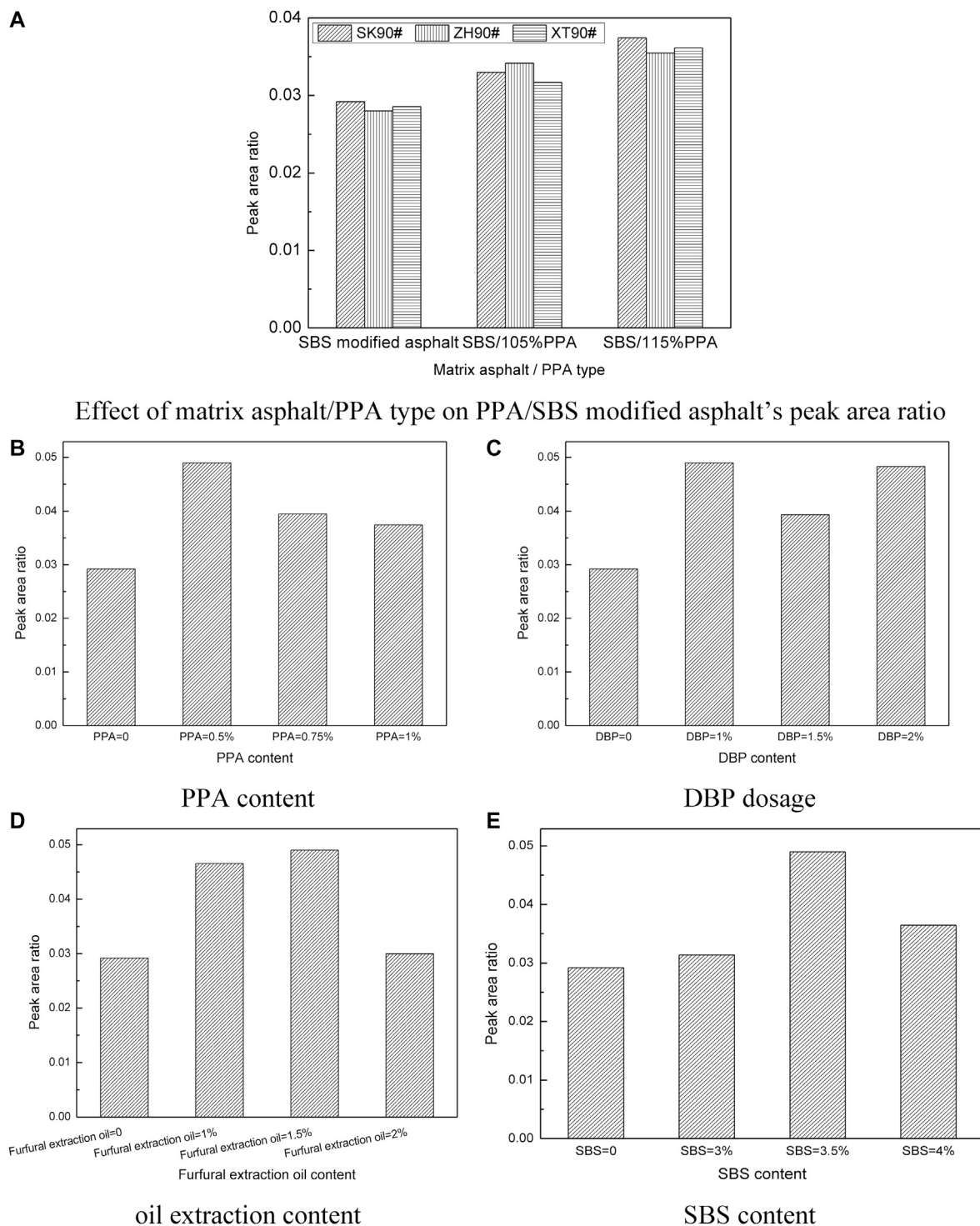
As illustrated in **Figure 4**, both the base asphalt and the type of PPA influence PPA/SBS modified asphalt's adhesion work and cohesive work. Among them, when the base asphalt is SK asphalt, and the PPA is 105%, the PPA/SBS modified asphalt's adhesion and cohesion effects improved. The results indicated that different types of raw materials have different effects on PPA/SBS modified asphalt's adhesion properties, and types of asphalt and PPA with good performance should be chosen when selecting raw materials.

#### (2) Different dosages

The adhesion performance index (adhesive work and adhesion work) of PPA/SBS modified asphalt prepared with various PPA dosages (0.5, 0.75, and 1.0%), DBP content (1, 1.5, and 2.0%), oil extraction amounts (1, 1.5, and 2.0%), and SBS content (3, 3.5, and 4.0%) is shown in **Figure 5**.

**Figure 5** shows that compared to 3.5% SBS modified asphalt, the cohesion work and adhesive work PPA/SBS modified asphalt provided increased, which indicates that after adding PPA, PPA, and SBS modified asphalt reacted and consumed energy, resulting in a change in the SBS modified asphalt's molecular network structure, which improved its bonding performance (Liang et al., 2017). However, as the PPA and DBP dosage increased, the cohesive work and adhesive work decreased, and as the furfural extract oil and SBS dosage increased, the cohesion work and adhesion work increased first and then decreased, indicating that when PPA, DBP, furfural extract oil, and SBS are within a certain range, the PPA/SBS modified asphalt's adhesiveness and cohesiveness will increase, but beyond this range, they will decrease. Moreover, with 0.5% PPA content, 1% DBP content, 1.5% furfural extract oil content, and 3.5% SBS modifier content, the cohesion work and adhesion work were the largest, even more than the actual production of high content SBS modified asphalt, and the adhesion properties also improved significantly. These results indicated that under this condition, the PPA/SBS modified asphalt has good cohesiveness and adhesiveness with the aggregate and its water damage resistance is the greatest.



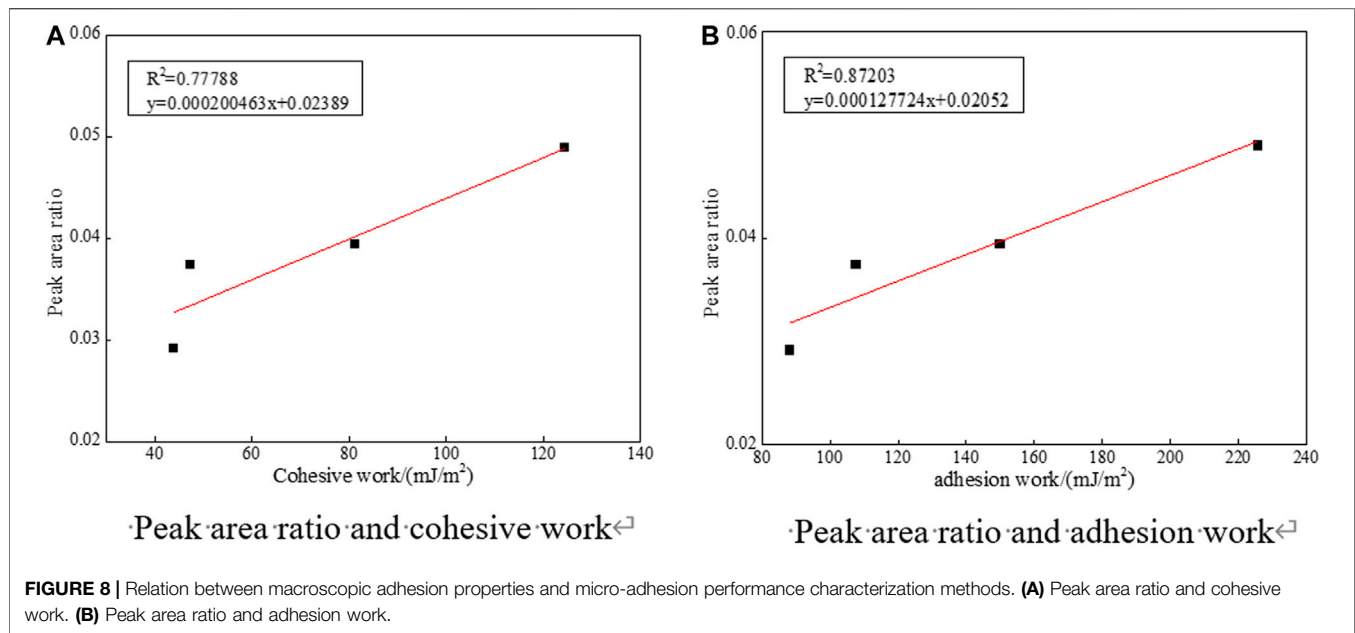


**FIGURE 7 |** Effect of raw material content on PPA/SBS modified asphalt's peak area ratio. **(A)** Effect of matrix asphalt/PPA type on PPA/SBS modified asphalt's peak area ratio. **(B)** PPA content. **(C)** DBP dosage. **(D)** oil extraction content. **(E)** SBS content.

## Raw Materials' Effect on PPA/SBS Modified Asphalt's Peak Area Ratio

Gwyddion is a professional scanning microscope image processing software, in which the Grains Mark function can distinguish the

microstructure according to the height. In this paper, Gwyddion was used to mark the matrix phase and the "honeycomb" structure according to the height of different phases, as shown in **Figure 6**. The area of the marked protrusion was calculated, and the ratio of



the area of the entire scanning area (900  $\mu\text{m}^2$ ) was obtained, which is the peak area ratio.

The atomic force microscope was used to explore the original materials' effect on the PPA/SBS modified asphalt's microstructure, and their effect on the PPA/SBS modified asphalt's peak area ratio was studied further. The results are shown in Figure 7.

Figure 7A shows different matrix asphalt types and different PPA types' effect on the PPA/SBS modified asphalt's peak area ratio. The analysis chart shows that the peak area ratio was SK base asphalt > XT base asphalt > ZH base asphalt, which is the same as the matrix asphalt without SBS modifier, indicating that the addition of SBS modifier has no effect on the "honeycomb" structure. After PPA was added to the SBS modified asphalt, the three matrix asphalts' peak area ratio increased, and the peak area ratio of 115% PPA to 105% PPA was larger, indicating that the appropriate amount of PPA increased the SBS modified asphalt's peak. The area ratio was the same as the change trend in the adhesion properties index of the SBS modified asphalt with the matrix asphalt and PPA type.

Figure 7B shows that as the PPA content increased, the peak area ratio increased first and then decreased, and the peak occurred when the dosage was 0.5%, indicating that PPA/SBS is 0.5% PPA/SBS. Further, the modified asphalt had a greater effect. Figure 7C illustrates that the peak area ratio was highest when the DBP dosage was 1%. As the amount of doping continued to increase, the peak area ratio decreased sharply. When the amount was too high, the peak area ratio was as well. The increase indicated that the change in the amount of DBP causes a "honeycomb" structure change. It can also be seen in Figure 7D that the effect of the amount of extracted oil on the peak area ratio increased first and then decreased, indicating that the "honeycomb" structure changed. This may be attributable to the formation of the asphalt component after the oil was extracted, and when the

number of light components was too great, the "honeycomb" area decreased gradually. Figure 7E shows that the effect of the increase in SBS dosage on the peak area ratio also increased first and then decreased, indicating that a moderate amount of SBS content and asphalt molecules form a relatively stable spatial network structure, making asphaltene more dispersed, and resulting in an increase in the honeycomb area ratio.

## Relation Between Adhesion Performance Index and Peak Area Ratio

Based on the previous discussion of the raw material types and dosages' influence on the PPA/SBS modified asphalt's adhesive performance, taking the influence of PPA content on the PPA/SBS modified asphalt's bond properties as an example, the relation between the microscopic bond performance characterization method and the macro bond performance was established; the results are shown in Figure 8.

Figure 8 shows that the PPA/SBS modified asphalt micro adhesive property characterization method (peak area ratio) and macroscopic adhesion performance index (viscoaggregation work and adhesion work) were correlated positively, but for the microscopic adhesion properties, the correlation coefficient between the characterization method and the macroscopic adhesion performance index was small. The correlation coefficient between the peak area ratio and macroscopic adhesion performance index was better, and the coefficients of cohesion work and adhesion work were 0.77788 and 0.87203, respectively. Further, the correlation coefficient of modified asphalt with more polyphosphoric acid improved significantly. It was proven fully that PPA can disperse the "honeycomb" structure between SBS modified asphalt and form a relatively stable spatial reticular structure with SBS, making the peak area ratio change trend of PPA/SBS modified asphalt closer to the

results of the macro bond performance index. The peak area ratio is considered the evaluation index of the PPA/SBS modified asphalt's micro-adhesion properties.

## CONCLUSION

In this paper, PPA/SBS modified asphalt's adhesion work and cohesion work were studied by the surface energy theory, and its peak area ratio was studied with the AFM test; the correlation between the two indices was analyzed, and the specific conclusions are as follows:

- (1) As the PPA and DBP content increased, the PPA/SBS modified asphalt's cohesive work, adhesive work, and peak area ratio showed a decreasing trend.
- (2) As the amount of oil extracted and SBS increased, the PPA/SBS modified asphalt's cohesive work, adhesive work, and peak area ratio increased first and then decreased.
- (3) PPA/SBS modified asphalt's cohesive work, adhesion work, and peak area comparison showed that 3.5% SBS modified asphalt demonstrated an increasing trend. The PPA/SBS modified asphalt had the largest cohesive work, adhesion work, and peak area compared with SBS modified asphalt with a 0.5% PPA dosage, 1% DBP dosage, 1.5% furfural extract oil dosage, and 3.5% SBS modifier dosage.
- (4) The correlation coefficient between PPA/SBS modified asphalt's peak area ratio and macroscopic adhesion performance index was the highest. The peak area ratio is considered to characterize PPA/SBS modified asphalt's micro-adhesive properties.

## REFERENCES

- Aflaki, S., and Hajikarimi, P. (2012). Implementing viscoelastic rheological methods to evaluate low temperature performance of modified asphalt binders. *Constr. Build. Mater.* 36, 110–118. doi:10.1016/j.conbuildmat.2012.04.076
- Alam, S., and Hossain, Z. (2017). Changes in fractional compositions of PPA and SBS modified asphalt binders. *Constr. Build. Mater.* 152, 386–393. doi:10.1016/j.conbuildmat.2017.07.021
- Baumgardner, G. (2006). "Appropriate application of chemical Modification." in Presented at the meeting of the association of modified asphalt producers annual meeting, Wisconsin Rapids, WI, November 4–November 6, 2006. America.
- Bishara, S. W., King, G. N., Mahoney, D., and Reynolds, R. L. (2003). Modification of binder with acid. advantages and disadvantages. *J. Transp. Res. Rec.* 2, 37–45.
- Cai, L., Shi, X., and Xue, J. (2018). Laboratory evaluation of composed modified asphalt binder and mixture containing nano-silica/rock asphalt/SBS. *Constr. Build. Mater.* 172, 204–211. doi:10.1016/j.conbuildmat.2018.03.187
- Fee, D., Maldonado, R., Reinke, G., and Romagosa, H. (2010). Polyphosphoric acid modification of asphalt. *Transp. Res. Rec.* 2179, 49–57. doi:10.3141/2179-06
- Gang, H., Wang, P., and Liu, B. S. (2018). Study on the performance of polyphosphoric acid modified asphalt. *West. Transp. Sci. Technol.* (06), 5–10. doi:10.16339/j.cnki.hdxzbk.2017.05.013
- Guo, M., Tan, Y., Yu, J., Hou, Y., and Wang, L. (2017). A direct characterization of interfacial interaction between asphalt binder and mineral fillers by atomic force microscopy. *Mater. Struct.* 50 (2), 141. doi:10.1617/s11527-017-1015-9

## DATA AVAILABILITY STATEMENT

The original contributions presented in the study are included in the article/Supplementary Material, further inquiries can be directed to the corresponding author.

## AUTHOR CONTRIBUTIONS

LL: Conceptualization, Methodology, Data curation, Writing-original draft. ZL: Validation, Data curation, Writing-review and editing. YW: Writing-review and editing. XL: Validation, Writing-review and editing. BL: Investigation, Writing-review and editing.

## FUNDING

The research work reported in this paper was supported by the National Natural Science Foundation of China (Grant Nos. 51668038 and 51868042), Industry Support and Guidance Project by University and College in Gansu Province (No. 2020C-13), the Distinguished Young Scholars Fund of Gansu Province (No. 1606RJDA318).

## ACKNOWLEDGMENTS

The authors gratefully acknowledge many important contributions from the researchers of all reports cited in our paper.

- Howson, J., Masad, E., Amit, B., Little, D., and Lytton, R. (2010). Comprehensive analysis of surface free energy of asphalts and aggregates and the effects of changes in pH. *Constr. Build. Mater.* 25 (5). doi:10.1016/j.conbuildmat.2010.11.098
- Ji, J., Yao, H., Liu, L., Suo, Z., Peng, Z., Yang, X., et al. (2017). Adhesion evaluation of asphalt-aggregate interface using surface free energy method. *Appl. Sci.* 7 (2), 156. doi:10.3390/app7020156
- Jiang, X., Li, P., Ding, Z., Yang, L., and Zhao, J. (2019). Investigations on viscosity and flow behavior of polyphosphoric acid (PPA) modified asphalt at high temperatures. *Constr. Build. Mater.* 228, 116610. doi:10.1016/j.conbuildmat.2019.07.336
- Kodrat, I., Sohn, D., and Simon, A. M. (2007). Hesp. comparison of polyphosphoric acid-modified asphalt binders with straight and polymer-modified materials. *Transport. Res. Rec.* (1), 1998. 10.3141/1998-06
- Kvasnak, A. N., and West, R. C. (2009). "Case study of warm-mix asphalt moisture susceptibility in birmingham, Alabama," in Transportation Research Board 88th Annual Meeting, Washington, DC, January 11–January 15, 2009.
- Li, B., Cui, Y., Liu, X., Li, H., and Li, X. (2019). Effect of material composition on nano-adhesive characteristics of styrene-butadiene-styrene copolymer-modified bitumen using atomic force microscope technology. *Int. J. Adhes. Adhes.* 89, 168–173. doi:10.1016/j.ijadhadh.2019.01.002
- Li, B., Li, X., Kundwa, M. J., Li, Z., and Wei, D. (2021). Evaluation of the adhesion characteristics of material composition for polyphosphoric acid and SBS modified bitumen based on surface free energy theory. *Constr. Build. Mater.* 266 (PB), 121022. doi:10.1016/j.conbuildmat.2020.121022
- Liang, M., Liang, P., Fan, W., Qian, C., Xin, X., Shi, J., et al. (2015). Thermo-rheological behavior and compatibility of modified asphalt with various styrene-butadiene structures in SBS copolymers. *Mater. Des.* 88, 177–185. doi:10.1016/j.matdes.2015.09.002

- Liang, P., Liang, M., Fan, W., Zhang, Y., Qian, C., and Ren, S. (2017). Improving thermo-rheological behavior and compatibility of SBR modified asphalt by addition of polyphosphoric acid (PPA). *Constr. Build. Mater.* 139, 183–192. doi:10.1016/j.conbuildmat.2017.02.065
- Ma, W., Huang, T., Guo, S., Yang, C., Ding, Y., and Hu, C. (2019). Atomic force microscope study of the aging/rejuvenating effect on asphalt morphology and adhesion performance. *Constr. Build. Mater.* 205, 642–655. doi:10.1016/j.conbuildmat.2019.01.151
- Masson, J.-F. (2008). Brief review of the chemistry of polyphosphoric acid (PPA) and bitumen. *Energy Fuels* 22 (4), 2637–2640. doi:10.1021/ef800120x
- Moraes, R., Velasquez, R., and Hussain, B. (2017). Using bond strength and surface energy to estimate moisture resistance of asphalt-aggregate systems. *Constr. Build. Mater.* 130, 156–170. doi:10.1016/j.conbuildmat.2016.10.043
- Park, D. W., Seo, W. J., Kim, J., and Vo, H. V. (2017). Evaluation of moisture susceptibility of asphalt mixture using liquid anti-stripping agents. *Constr. Build. Mater.* 144, 399–405. doi:10.1016/j.conbuildmat.2017.03.214
- Reinke, G., Glidden, S., Herlitzka, D., and Veglahn, S. (2010). “PPA modified binders and mixtures: Aggregate and binder interactions, rutting and moisture sensitivity of mixtures,” in *Asphalt Paving Technologists-Proceedings of the Technical Sessions*, Sacramento, CA, March 7–March 10, 2010, 719
- Romagosa, H., and Martin, J. V. (2009). “Best practices for PPA modification of asphalt,” in *Presented at the 2009 PPA Workshop*, Minneapolis, MN, April 7–April 8, 2009.
- Wang, J., Yuan, J., Xiao, F., Li, Z., Wang, J., and Xu, Z. (2018a). Performance investigation and sustainability evaluation of multiple-polymer asphalt mixtures in airfield pavement. *J. Clean. Prod.* 189. doi:10.1016/j.jclepro.2018.03.208
- Wang, L., Wang, Z., and Li, C. (2017). High temperature rheological properties of polyphosphoric acid modified asphalt. *Acta Mater. Compos. Sin.* 34 (7), 1610–1616. doi:10.13801/j.cnki.fhclxb.20160921.001
- Wang, T., Xiao, F., Zhu, X., Huang, B., Wang, J., and Amirkhanian, S. (2018b). Energy consumption and environmental impact of rubberized asphalt pavement. *J. Clean. Prod.* 180, 139–158. doi:10.1016/j.jclepro.2018.01.086
- Yan, K., Zhang, H., and Xu, H. (2013). Effect of polyphosphoric acid on physical properties, chemical composition and morphology of bitumen. *Constr. Build. Mater.* 47, 92–98. doi:10.1016/j.conbuildmat.2013.05.004
- Zegeye, E. T., Moon, K. H., Turos, M., Clyne, T. R., and Marasteanu, M. O. (2012). Low temperature fracture properties of polyphosphoric acid modified asphalt mixtures. *J. Mater. Civ. Eng.* 24 (8).doi:10.1061/(asce)mt.1943-5533.0000488
- Zhang, H. L., Su, M. M., Zhao, S. F., Zhang, Y. P., and Zhang, Z. P. (2016). High and low temperature properties of nano-particles/polymer modified asphalt. *Constr. Build. Mater.* 114, 323–332. doi:10.1016/j.conbuildmat.2016.03.118

**Conflict of Interest:** Author YW was employed by the company Gansu Province Highway Traffic Construction Group Co., Ltd. Author XL was employed by the company Gansu Provincial Transportation Research Institute Group Co., Ltd.

The remaining authors declare that the research was conducted in the absence of any commercial or financial relationships that could be construed as a potential conflict of interest.

Copyright © 2021 Li, Li, Wang, Li and Li. This is an open-access article distributed under the terms of the Creative Commons Attribution License (CC BY). The use, distribution or reproduction in other forums is permitted, provided the original author(s) and the copyright owner(s) are credited and that the original publication in this journal is cited, in accordance with accepted academic practice. No use, distribution or reproduction is permitted which does not comply with these terms.



# Compaction Characteristics of Cold Recycled Mixtures with Asphalt Emulsion and Their Influencing Factors

Decai Wang<sup>1,2</sup>, Hui Yao<sup>3\*</sup>, Jinchao Yue<sup>2</sup>, Shengneng Hu<sup>1</sup>, Junfu Liu<sup>3</sup>, Mei Xu<sup>3</sup> and Siyu Chen<sup>4</sup>

<sup>1</sup>Department of Transportation, School of Civil Engineering and Communication, North China University of Water Resources and Electric Power, Zhengzhou, China, <sup>2</sup>Department of Transportation, School of Water Conservancy and Environment, Zhengzhou University, Zhengzhou, China, <sup>3</sup>Beijing Key Laboratory of Traffic Engineering, College of Metropolitan Transportation, Beijing University of Technology, Beijing, China, <sup>4</sup>Department of Civil and Environmental Engineering, Michigan Technological University, Houghton, MI, United States

## OPEN ACCESS

### Edited by:

Yu-Fei Wu,  
RMIT University, Australia

### Reviewed by:

Xiaoming Huang,  
Southeast University, China  
Syed Minhaj Saleem Kazmi,  
RMIT University, Australia

### \*Correspondence:

Hui Yao  
huiyao@mtu.edu

### Specialty section:

This article was submitted to  
Structural Materials,  
a section of the journal  
Frontiers in Materials

**Received:** 24 June 2020

**Accepted:** 19 January 2021

**Published:** 05 April 2021

### Citation:

Wang D, Yao H, Yue J, Hu S, Liu J,  
Xu M and Chen S (2021) Compaction  
Characteristics of Cold Recycled  
Mixtures with Asphalt Emulsion and  
Their Influencing Factors.  
Front. Mater. 8:575802.  
doi: 10.3389/fmats.2021.575802

The objective of this study is to investigate the compaction characteristics of cold recycled mixtures with asphalt emulsion (CRME) using the Superpave gyratory compactor (SGC) method. Five characteristic parameters were proposed and calculated including the compaction energy index, the compaction energy index, three compaction energy indicators at different compaction stages. The influence of these parameters and material compositions were analyzed for the pavement performance. The difference between SGC and Marshall double-sided compaction/heavy compaction method was compared. The results show that the proposed parameters can better reflect the compaction characteristics of CRME, and the mixture effect with SGC of 50 gyrations was close to that with 75 blows using the Marshall compaction. The asphalt emulsion contents and compaction temperatures had a significant effect on compaction characteristics, but the effect of aggregate gradations was not significant. The appropriate asphalt emulsion and the new aggregate content can increase the capability of the CRME to resist the permanent deformation. The optimum mixing water content of CRME obtained by the SGC method was reduced by 18%, but the density increased by 3.5%, compared with the heavy compaction method. Finally, a new idea to determine the optimum emulsified asphalt content of CRME was provided through analyzing the compaction characteristic parameters.

**Keywords:** pavement engineering, cold recycled mixture with asphalt emulsion, gyratory compaction, compaction characteristic parameters, compaction temperatures

## INTRODUCTION

The requirements for asphalt pavements become stricter with the increase of heavy traffics and overloading of vehicles. Severe distress is observed for the surface layer after years of serving. Therefore, thousands of semi-rigid asphalt pavements that were constructed decades ago need to be reconstructed and maintained, which will generate a large amount of reclaimed asphalt pavement (RAP). Cold recycling technology with asphalt emulsion can use almost 100% of RAP without heating, reducing pollution and waste emissions, as well as the aged asphalt mixtures deposited at landfills (Lin et al., 2017; Xiao et al., 2018; Rodríguez-Fernández et al., 2019). The environmental and



economic benefits of cold recycling make it an attractive alternative for pavement conservation and rehabilitation (Turk et al., 2016).

Recently, cold recycling technology has been used in more and more road maintenance and reconstruction projects. However, there is no widely accepted design method for Cold Recycled Mixes with Asphalt Emulsion (CRME). Besides, the inconsistent compaction between lab and field discourages the wide use of such technology (Martinez-Echevarria et al., 2012). The current mixture design method (JTG/T5521-2019) for the CRME is based on the modified Marshall method without considering the horizontal shearing behavior caused by traffic loads. Moreover, the specimen density is expected to be increased as the blow number increases, and there are also some problems, including second compaction and poor test reproducibility. Numerous studies have been conducted to study the compaction characteristics of asphalt mixtures (MOC of PRC, 2019). It was claimed that the mixture that using the Superpave Gyratory Compactor (SGC) method obtained a material that has more similar properties to the materials on the field in terms of particle alignment and density (Tarefder and Ahmad, 2016). Therefore, it is necessary and meaningful to study the compaction characteristics of CRME to improve project quality and guide the construction practice.

Currently, researchers have different opinions on the mixture design and parameters of CRME using the SGC method. Hillgren et al. proposed to determine the design gradation number at 96% of the target density. The target density was the specimen density after 200 gyrations times (Hillgren et al., 1989). Gao et al. (2014) analyzed the parameters sensibility for the CRME using the SGC method and obtained a regression equation based on design compaction number, compaction temperature, and emulsified asphalt content. They also provided a new method to determine the optimum moisture content of the cold mixture. In terms of the compaction method, Yan observed that the specimen density of the CRME that was compacted with 50–70 blows using the Marshall method was equivalent to the specimen density that was compacted with 30–50 gyrations using the SGC method (Yan, 2006). Flores et al. (2019) developed a new design methodology for cold recycled mixtures with emulsions and a Global Performance Index was proposed to compare the formula and optimize the mixture. The conditions were investigated for the compaction of cold recycled mixtures with emulsions and 100% RAP. It was recommended to apply a compaction energy level of 100 gyrations for specimens with 100 mm diameter and 60 mm height, and an energy level of 200 gyrations for specimens with 100-mm diameter and 100 mm height (Flores et al., 2020). A research project has been conducted to adapt to the current French experimental device. It is called “PCG3,” which was devoted strictly to hot mix asphalt (HMA) characterization to allow for the compaction of cold mixes by adding the functionality of collecting extruded water due to emulsion breaking (Wendling et al., 2015). A new volumetric mix-design procedure was developed for cold in-place recycling (CIR) asphalt mixtures by utilizing the SGC method. The procedure required that the density of specimens was close to that in the field. The performance of CIR mixtures from the new mix-design procedure was evaluated by the mechanistic-empirical pavement design guide (MEPDG) models, as well as in the field testing (Lee

et al., 2016). The SGC metrics were recommended to quantify workability and compactability. The curing temperature generally had a more significant influence on test results than cure time (Casillas and Braham, 2020).

The data from the SGC compaction curve was mainly used to analyze the compaction properties of the HMA. The compaction curve from SGC was divided into two stages in where the construction energy index (CEI) and traffic densification index (TDI) were defined respectively. The two indicators were used to characterize the HMA performance during the construction stage and the pavement serving stage. The test results showed that the nominal maximum aggregate size, aggregate gradation, and asphalt content of HMA had significant effects on CEI, and the TDI can accurately predict the high-temperature stability of the mixes (Dessouky et al., 2004). The compaction dissipation energy index can better evaluate the significance of each influencing factor of asphalt mixture (DelRio-Prat et al., 2011). It has been proved that the higher temperature of RAP results in better compaction of the cold mixture in the field (Kim and Lee, 2011). The CEI and the compacted curve slope of HMA have been defined based on the SGC compaction curve, and the workability and road stability of HMA were analyzed (Zhang et al., 2005). Based on the HMA compaction characteristics, the number of rollers required on-site is determined from the perspective of energy equivalence (Li et al., 2011). In summary, the researchers conducted lots of research for the HMA mixtures on the characteristics of the compaction curve based on the SGC method and defined different compaction stages and corresponding characteristic parameters, which played a good role in the construction control of the mixture. However, there are limited studies that evaluated CRME compaction properties. The analysis method used in the HMA can partly be used on the CRME. Also, there is no unified method to determine the design parameters, including the optimum emulsified asphalt content, the optimum moisture content, and the compaction temperature (Brovelli and Crispino, 2012; Kim, 2012). These problems in CRME motivated this research.

The objectives of this paper are to 1) investigate the compaction characteristics of CRME by analyzing the SGC densification curves, 2) and propose the compaction characteristic parameters that can be used to analyze the compaction characteristics of the mixture. Also, the article attempts to propose a reasonable method to determine the optimum content of emulsion and moisture for CRME and specific compaction temperature. Finally, this research may help to better understand the material properties of CRME and provide a reference idea for the design of CRME to improve the construction quality.

## MATERIALS AND METHODS

### Materials RAP

The RAP was obtained from an expressway maintenance project in Henan Province, China, in which the recycled asphalt content was 4.87%. In terms of the binder properties, the penetration at 25°C was 3.1 mm; the ductility at 15°C was 12.7 cm; the softening point

**TABLE 1** | Properties of CSS emulsion.

Property	Value	Requirements (JTG/T5521-2019)
Residue by distillation (%)	64.1	> 60
Emulsifier content (%)	2.8	—
Penetration of residue, 25°C	67.8	50–130
Ductility of residue, 15°C	> 100	≥40
Storage stability at 1 d (%)	0.4	≤1
Storage stability at 5 d (%)	2.5	≤5

was 61.8°C; the viscosity at 60°C was 2457 Pas, which indicated the asphalt binder was highly aged after 12 years in service.

### Asphalt Emulsion

A cationic slow-cracking fast-setting emulsifier for cold recycled asphalt mixture was used in this study, and asphalt emulsion was prepared with Zhenhai #70 petroleum asphalt using the colloidal mill in the laboratory. Tap water was utilized to prepare the asphalt emulsion and mix the cold recycled asphalt mixture. The basic properties of the asphalt emulsion are shown in **Table 1**.

### Aggregate Gradation

To reduce the RAP variability, the milled RAP was divided into sizes of 0–3, 3–5, 5–10, and 10–20 mm. Based on the specification requirements of JTG/T5521-2019, the gradation of CRME was designed. The design gradation of CRME included 90% RAP and 10% limestone gravel (size from 10 to 20 mm). There were also two sets of comparison gradations. One gradation included 80% RAP and 20% limestone gravel, and the other gradation was composed of 70% RAP, 20% limestone gravel, and 10% fine aggregate. Technical indicators, including crushing value, gross volume density, percentage of flat-elongated particles, and sand equivalent were measured in accordance with JTG F40 (MOC of PRC, 2004). The gradations of CRME were displayed in **Figure 1**.

Cement is an important component to improve the early-stage performance of CRME. 1% PC32.5 cement by weight of the aggregates was used in the CRME. The cement was obtained from Hebei province. Its initial setting time was 264 min, and the final setting time was 387 min. The water requirement for the normal consistency of cement paste was 26.8%.

## METHODS

### Compaction Characteristic Analysis

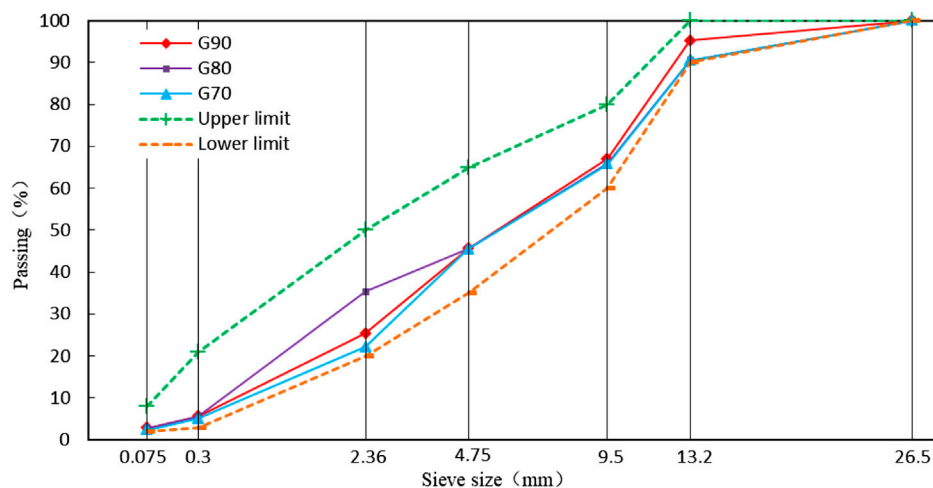
The SGC compaction curve provides the most important information to understand the CRME compaction characteristics. As shown in **Figure 2**, the typical gyratory compaction curve clearly describes that the mixture density increases as the gyration level increases.

The compaction curve is a power-law function, and the fitting equation is shown in **Eq. 1**:

$$\gamma_i = AN^b \quad (1)$$

where A and b are regression parameters, N is gyration number,  $\gamma_i$  is the percent of maximum theoretical density after the number of gyrations.

The compaction curve was divided into three different intervals to reflect the characteristics of CRME at different stages. The first stage was the initial compaction stage, in which the degree of compaction rapidly increased at first. The aggregates move and contact gradually due to emulsified asphalt and water, and the increase rate of the density decreases with the gyration number increasing. The curvature radius of the compaction curve changed from large to small. There is a minimum radius of curvature that is corresponding to the initial compaction number ( $N_{ini}$ ). The second stage was a design compaction stage when the air voids content achieved the design requirement, where the gyration number was set as the design compaction number ( $N_{des}$ ). The third stage was an ultimate compaction stage after the CRME reached the designed air

**FIGURE 1** | The aggregates gradation of CRME passing (%).

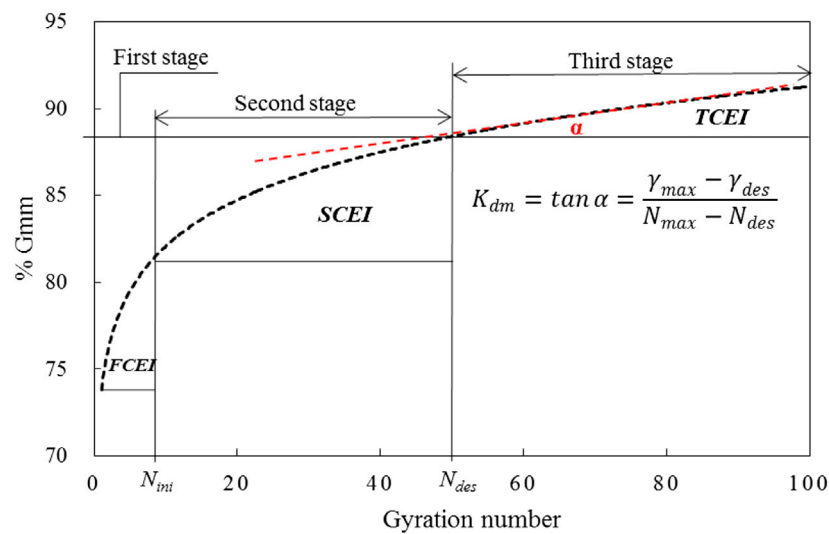


FIGURE 2 | Typical gyratory compaction curve of CRME.

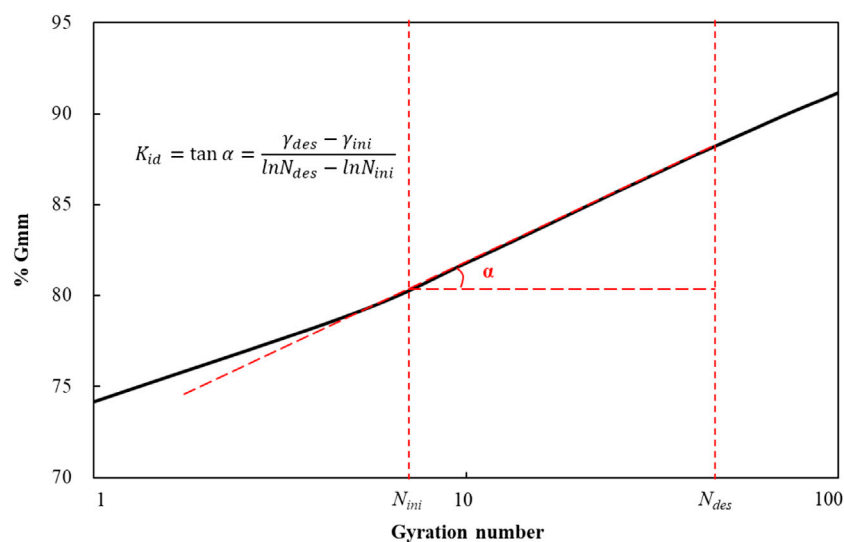


FIGURE 3 | Semilogarithmic compaction curve of CRME.

voids content. At this stage, the compaction degree was small as the gyration number increased, and the emulsions began to show instability. In this study, the maximum gyration number ( $N_{max}$ ) was set at 100.

### Compaction Characteristic Parameters

#### The Slope of the Densification Curve

The densification curve is usually used to reflect the compaction property of the mixes. As shown in Figure 3, the densification curve from  $N_{ini}$  to  $N_{des}$  is a straight line expressed with an average slope of  $K_{id}$  in semi-logarithmic coordinates. The calculation formula is shown in Eq. 2. A larger  $K_{id}$  indicates higher compaction of the mixes. The slope

of  $K_{dm}$  is used to reflect the compaction characteristics of CRME after opening traffic, which represents the compactability from  $N_{des}$  to  $N_{max}$ . The average slope of the densification curve is  $K_{dm}$ , which can be obtained with linear regression. As shown in Eq. 3, a larger  $K_{dm}$  indicates a higher compactability of the mixes after open traffic as well as worse the deformation resistance.

$$K_{id} = \frac{\gamma_{des} - \gamma_{ini}}{\ln N_{des} - \ln N_{ini}} \quad (2)$$

$$K_{dm} = \frac{\gamma_{max} - \gamma_{des}}{N_{max} - N_{des}} \quad (3)$$

Where

$\gamma_{ini}$  = percentage of maximum theoretical density after  $N_{ini}$  gyrations.

$\gamma_{des}$  = percentage of maximum theoretical density after  $N_{des}$  gyrations.

$\gamma_{max}$  = percentage of maximum theoretical density after  $N_{max}$  gyrations.

$N_{ini}$  = initial gyration number when the maximum curvature occurs.

$N_{des}$  = design gyration number when the design air voids content is obtained.

$N_{max}$  = maximum number of gyrations.

### Compaction Energy Index

Although the slopes of the densification curve partly reflected the compaction characteristics of the mixes, they cannot accurately show the total compaction energy. Therefore, an energy-related index was proposed. The compaction energy index (CEI) can be calculated by measuring the area under the compaction curve between any two points, which indicated the required energy under the gyration compactor. Based on the three-stage compaction characteristics of CRME, the first stage compaction energy index (FCEI), the second stage compaction energy index (SCEI), and the third stage compaction energy index (TCEI) were proposed.

As shown in **Figure 2**, The FCEI was calculated by measuring the area under the compaction curve from one to  $N_{ini}$  gyrations, which reflects the workability of the mixes. The SCEI was calculated by measuring the area under the compaction curve from  $N_{ini}$  to  $N_{des}$  gyrations, which reflects the compaction characteristics of the mixes during the paving and rolling stages. The TCEI was calculated by measuring the area under the compaction curve from  $N_{des}$  to  $N_{max}$  gyrations. A larger TCEI indicated a stronger deformation resistance of CRME. The approximate calculations of FCEI, SCEI, and TCEI can be seen in **Eqs. 4–6**.

$$FCEI = \int_1^{N_{ini}} AN^b dN - (N_{ini} - 1)\gamma_1 \quad (4)$$

$$SCEI = \int_{N_{ini}}^{N_{des}} AN^b dN - (N_{des} - N_{ini})\gamma_{ini} \quad (5)$$

$$TCEI = \int_{N_{des}}^{N_{max}} AN^b dN - (N_{max} - N_{des})\gamma_{des} \quad (6)$$

Where

$\gamma_i$  = percent of maximum theoretical density after some gyrations.

$N_{ini}$  = when the radius of curvature for the compaction curve is a minimum, which is an initial compaction number.

$N_{des}$  = when air void of mixes attains design requirements, which is design number.

$N_{max}$  = the maximum number of gyrations is set at 100 in this study, A and b are the regression parameters of the densification curve.

### Modified Marshall Method (JTG T5521-2019)

The modified Marshall method included three processes for the mix design of CRME. First, the optimum moisture content of the CRME was selected at an asphalt emulsion content of 3.5% by the maximum dry density of samples. Second, the optimum asphalt emulsion content was determined by the Indirect Tensile Strength (ITS) and dry-wet ITS ratio. The samples were prepared by the Marshall method using 75 blows on both sides at the optimum determining moisture content. The air voids content should be controlled at 8–13%. Third, the performance of CRME was evaluated by ITS and moisture damage resistance.

### Heavy Compaction Test (JTG T5521-2019)

The optimum moisture content of CRMEs was determined by the heavy compaction test in standard JTG E40 (MOC of PRC, 2007). The CRME was compacted in layers in the standard compaction apparatus. When the maximum particle size of CRME was 20 mm, a compaction cylinder with an inner diameter of 100 mm was used, and the compaction effort was 2687 kJ/m<sup>3</sup>. When the maximum particle size of CRME was 40 mm, a compaction cylinder with an inner diameter of 152 mm was used, and the compaction effort was 2677 kJ/m<sup>3</sup>. The wet density of compacted specimens is calculated by the compaction cylinder volume and CRME mass. The dry density was calculated as **Eq. 7**.

$$\rho_d = \frac{\rho}{1 + 0.01w} \quad (7)$$

where  $\rho_d$ ,  $\rho$ , w represent dry density (g/cm<sup>3</sup>), wet density (g/cm<sup>3</sup>), moisture content (%), respectively.

### Indirect Tensile Strength (ITS) Test

The ITS is a key indicator for the mix design of CRME. Two groups of specimens were prepared for the ITS tests (JTG/T5521-2019). Three replicate specimens in the first group were saturated in a water bath at 25°C for 23 h, then placed in a water bath at 15°C for 1 h before measuring wet ITS strength (ITS<sub>w</sub>). Three replicate specimens in the second group were soaked only in a water bath at 15°C for 1 h before measuring dry ITS (ITS<sub>d</sub>). The ITS test was conducted at 15°C at a loading rate of 50 mm/min. The percentage of the ITS ratio (ITSR) is calculated by **Eq. 8**.

$$ITSR = \frac{ITS_w}{ITS_d} \times 100\% \quad (8)$$

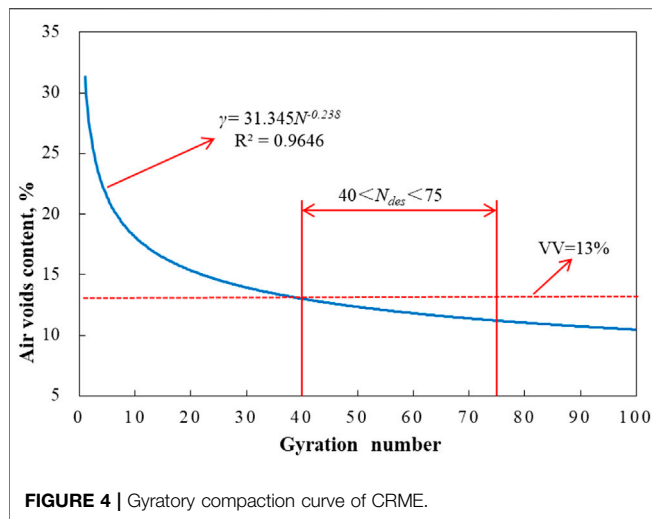
where ITSR is the dry-wet ITS ratio. ITS<sub>w</sub> is wet ITS (Unit: MPa). ITS<sub>d</sub> is dry ITS (Unit: MPa).

### Performance Evaluation Methods

#### Water Damage Resistance Performance

The water damage resistance was evaluated by an indirect tensile strength ratio (TSR) test, following the JTG E20 procedure (MOC of PRC, 2011). The TSR was determined as the ratio of the tensile strength of dry specimens to the tensile strength of the conditioned specimens. The saturated specimens were





conditioned at  $-18^{\circ}\text{C}$  for 24 h and then submerged in the water bath at  $60^{\circ}\text{C}$  for another 24 h.

### Rutting Resistance Performance

The rutting resistance was evaluated by a wheel tracking test, following a standard procedure in JTG E20-2011. The test specimen was a slab ( $300 \times 300 \times 80 \text{ mm}^3$ ) prepared by a roller compactor. During the wheel tracking test, the asphalt concrete slab was loaded by a repeated solid rubber tire with a contact pressure of 0.7 MPa at a speed of 42 cycles per minute. The test took 1 h and the rutting depth was recorded. The dynamic stability (DS) was defined as the average loading cycles that achieved a 1 mm rutting depth. A higher DS value was preferable for the rutting resistance.

### Low-Temperature Performance

The low-temperature performance was evaluated via a three-point beam bending test at  $10^{\circ}\text{C}$ , following a standard procedure in JTG/E20-2011. The specimen size was  $50 \text{ mm} \times 50 \text{ mm} \times 250 \text{ mm}$ . A vertical load was applied until the beam was fractured. The flexural strength, flexural stiffness, and fracture strain were obtained.

## RESULTS AND DISCUSSION

### Effect of Gyration Number

The compaction of CRME should not only simulate the compaction on the field but also ensure consistency between laboratory compaction and on-site construction. It was important to determine the gyration number, which affected the property of CRME. If the design gyration number was too low, the designed properties of CRME cannot be achieved. If the design gyration number was too high, the construction quality may not be able to meet the design requirements. It was observed that lots of asphalt emulsions were pressed out from the CRME at an extremely high gyration number, which cannot reflect the design performance of the mixture.

The CRME was prepared as cylinder specimens with a height of 63.5 mm and a diameter of 100 mm. The asphalt emulsion

content and mixed water content was 3.5 and 2.8% by weight of aggregates, respectively. The gradation of  $G_{90}$  was used. The prepared specimens were aged for about 24 h at  $25^{\circ}\text{C}$  and then were cured rapidly in an air-circulating oven at  $40^{\circ}\text{C}$  for 72 h. A compaction curve is shown in **Figure 4**.

As shown in **Figure 4**, the relationship between the air voids content of the specimen and the gyration number can be fitted as a power-law function. By calculating the derivative of the regression curve equation, the slope of any point on the compaction curve can be calculated, which reflected the compaction rate at certain gyration numbers. As the gyration number increased, the compactibility gradually decreased and finally tended to be 0.

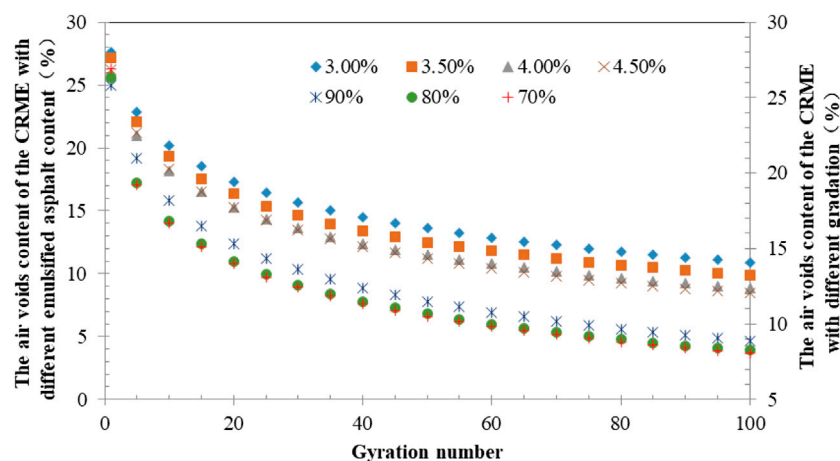
When the gyration number was between 0 and 10 gyrations, the air voids content of the specimen changed sharply and the difference is about 8%. From 10 to 30 gyrations, the air voids content of the specimen slowly decreased, with a decrease of 4.7%. From 30 to 50 gyrations, the air voids content decreased by 2.1%. From 50 to 75 gyrations, the air voids content slightly decreased by 1.6%. It was observed that some emulsions were squeezed out from the mixture after 50 gyrations, as is shown in **Figure 5**. When the gyration number was about or more than 75 gyrations, a large number of emulsions were squeezed out from the bottom of the mold, which affected the performance of the mixes. It was required in the specification JTG/T5521-2019 that the air voids content of CRME should in the range of 8–13%, and the ideal air voids content of the CRME is typically controlled at about  $11 \pm 1\%$ . Based on that, the preliminary design gyration number was set at 50.

To further understand the impact of gyration number on the CRME, the volume parameter changes of the CRME for four different emulsion contents (3.0, 3.5, 4.0, and 4.5%) with  $G_{90}$  gradation and three different RAP proportions (70, 80, and 90%) in the same asphalt emulsion content (4.0%) were studied. The optimum water content for the CRME, including the water in asphalt emulsion, in the virgin aggregate and the RAP, and



**FIGURE 5 |** Specimens of CRME molding process.





**FIGURE 6 |** The air voids content of the CRME for different emulsified asphalt contents and gradation changes with the gyration number.

mixing water, was determined at the maximum dry density. Therefore, when the asphalt emulsion content changes, the mixing of water content changes accordingly. In this article, since the aggregates are all dried, the influence of gradation changes on the mixing water is not considered. The specimens were compacted at 100 gyrations and the air voids contents at different gyrations were calculated. The results are summarized in **Figure 6**.

As seen in **Figure 6**, the air voids content of all specimens sharply decreased as the compaction number increased from 0 to 10 gyrations, and the maximum decrease was about 10%. From 10 to 30 gyrations, the change of air voids content began to slow down, with a reduction of 4.9%. From 30 to 50 gyrations, the compaction difficulty further increased, since the air voids content reduced by 2.3%. After 50 gyrations, there is a little effect on the volumetric parameters of the mixes, as compaction increased. Similarly, it was found that some emulsions began to be squeezed out with more than 50 gyrations. Considering the changing trend in air voids content and specification requirements, it was feasible to determine the design gyration number at 50.

As shown in **Figure 6**, it can be found when the emulsified asphalt content changed from 3.0 to 3.5% at 50 gyrations, the air voids content decreased by 8.1%, and the emulsified asphalt content changed from 3.5 to 4.0%. At the same time, the air voids content decreased by 7.9%. But when the emulsified asphalt content changed from 4.0% to 4.5, the air voids content decreased only by 2.6%. The results show that the emulsified asphalt of 4% by weight of aggregates is an obvious point for the change of volumetric parameters. When the emulsified asphalt content is less than 4.0%, the air voids content decreases significantly. When the emulsified asphalt content is greater than 4.0%, the change of air voids content is small, which indicates that emulsified asphalt content has an important effect on compaction, but the impact becomes smaller and smaller. As the gyration number increased, the compactness of the CRME for different proportions of RAP increase. However, the effect of aggregate gradation on the air voids content was very small. In summary, the content of asphalt emulsion had a higher effect on compactness than the gradation.

**TABLE 2 |** Regression results for different materials.

Regression parameters	Asphalt emulsion				RAP		
	3.0%	3.5%	4.0%	4.5%	90%	80%	70%
A	71.993	72.564	73.817	73.356	73.817	74.444	74.225
B	0.0464	0.0475	0.0461	0.0485	0.0461	0.0464	0.0476
R <sup>2</sup>	0.9985	0.9987	0.9985	0.9982	0.9985	0.9950	0.9908

**TABLE 3 |** Compaction characteristic parameters for different aggregate gradations.

Gradation	FCEI	SCEI	TCEI	K <sub>id</sub>	K <sub>dm</sub>
G <sub>90</sub>	41.6750	173.5808	79.6088	9.0228	0.0574
G <sub>80</sub>	42.3134	176.3450	80.9083	9.1671	0.0583
G <sub>70</sub>	43.3246	180.9912	83.1705	9.4111	0.0600

Note: FCEI is calculated by the **Eq. 4**, SCEI is calculated by the **Eq. 5**, TCEI is calculated by the **Eq. 6**, K<sub>id</sub> is calculated by the **Eq. 2**, and K<sub>dm</sub> is calculated by the **Eq. 3**.

## Effect of Material Composition Analysis of Compaction Characteristic Parameters for Different Aggregate Gradations

Based on the data in **Figure 6**, the regression parameters of the compaction curve for different materials are shown in **Table 2**. To analyze the effect of aggregate gradation, the compaction parameters for the three different aggregate gradations were calculated by the defined compaction parameters and the regression equation. The calculation results are shown in **Table 3**.

As seen in **Table 3**, in terms of compaction energy, the more new materials were added, the higher FCEI value was during the initial compaction stage. It indicated that a larger proportion of new materials resulted in worse workability of CRME. In the design compaction stage, the higher the proportion of new materials, the higher the SCEI value was, which indicated the compactibility difficulty of CRME as more new materials were added. In the third compaction stage, the larger the proportion of new materials is, the greater the compaction energy required, which

**TABLE 4** | Compaction characteristic parameters for different emulsion contents.

Emulsion (%)	FCEI	SCEI	TCEI	$K_{id}$	$K_{dm}$
3.0	40.9202	170.5390	78.2445	8.8653	0.0564
3.5	42.2625	176.5189	81.1047	9.1783	0.0585
4.0	41.6750	173.5808	79.6088	9.0228	0.0574
4.5	43.6607	182.7221	84.0648	9.5030	0.0606

indicates CRME needs a stronger ability to resist deformation. In terms of the average slope, the more the new materials are added, the larger  $K_{id}$  and  $K_{dm}$  are. It indicates the fewer new materials there is, the faster the compaction rate of the design compaction stage and the ultimate compaction stage. As the new material increased, the internal friction angle of CRME increases, which indicated the proper addition of the new materials to cold recycled mixes was helpful to resist deformation. Therefore,  $G_{90}$  is chosen as the optimal design gradation in this paper.

### Analysis of Compaction Characteristic Parameters for Different Asphalt Emulsion Contents

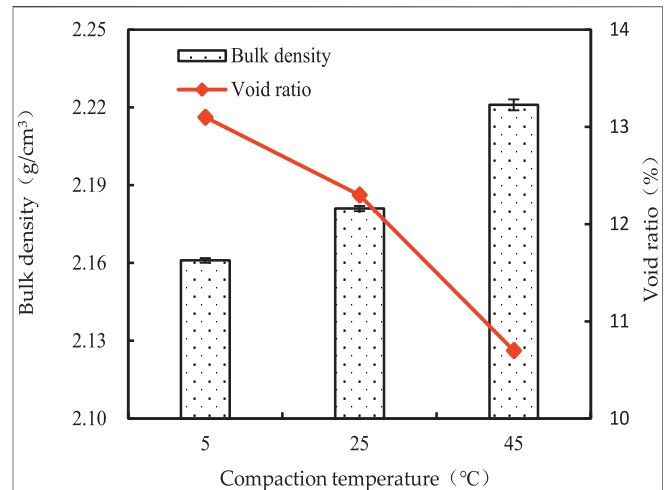
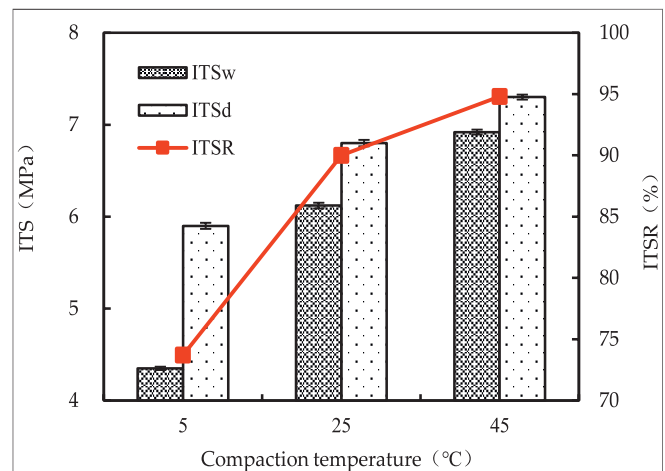
In order to analyze the effect of the asphalt emulsion content, the compaction parameters for different emulsions content were calculated. The calculation results are shown in **Table 4**.

As observed from **Table 4**, the  $FCEI$ ,  $SCEI$ ,  $TCEI$ ,  $K_{id}$ , and  $K_{dm}$  of CRME increased as the emulsified asphalt content increased from 3 to 3.5%. That is because the mixes are at the condition of optimum moisture content, the asphalt emulsion content increase, and the added water decreases accordingly, which may increase the viscosity of the mixes and the compaction energy. It was observed that there were minimum values of compaction energy index and curve slope at the emulsified asphalt content of 4.0%, which indicated better workability during the initial compaction stage and design compaction stage, and a lower compaction rate in the third stage. Besides, it should be noted that the  $K_{dm}$  of different materials was close to 0, which indicated that the compactness of the CRME hardly changed after 50 gyrations. Therefore, the optimum content of emulsified asphalt was determined to be about 4.0% by weight of aggregates ( $G_{90}$ ) using 50 gyrations.

### Effect of Compaction Temperature

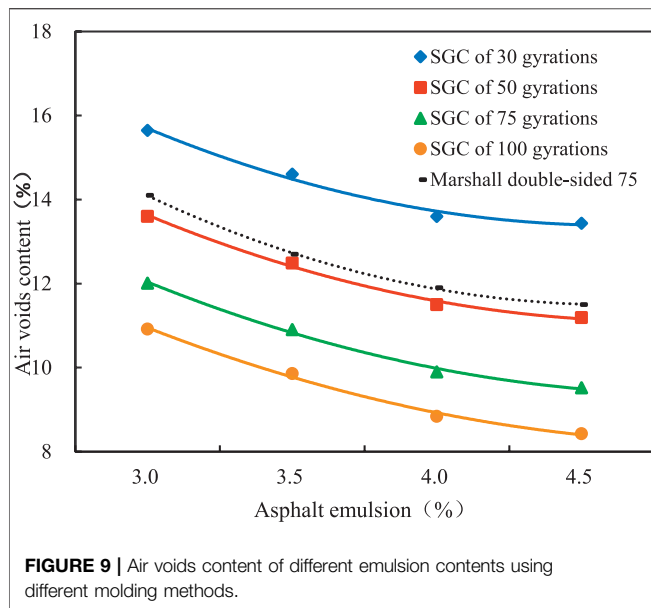
Compared with the HMA, the compactibility of the CRME is more susceptible to construction temperatures. Nevertheless, most institutions often ignore the effect of temperature when designing CRME. It is, therefore, necessary to study the effect of compaction temperature on the CRME. In the lab, raw materials were first prepared with RAP, new aggregates, emulsified asphalt, and mixing water, which were placed in incubators at 5, 25, and 45°C, respectively. The materials were evenly mixed after the temperature has been maintained for about 6 h. Then the mixes were also placed in the incubator at mixing temperature for 2 h before compaction. The specimens were compacted for 50 gyrations using SGC. **Figure 7** shows the effect of compaction temperature on the bulk density and the air voids content. The effect of compaction temperature on ITS value is displayed in **Figure 8**.

**Figure 7** shows that as the compaction temperature increased, the bulk density of the specimen increased. As a contrast, the air

**FIGURE 7** | Effect of compaction temperature on volumetric parameters.**FIGURE 8** | Effect of compaction temperature on ITS.

voids content of the specimen significantly decreased as the compaction temperature increased. As the compaction temperature increased from 5 to 25°C, the bulk density of the specimen increased by about 7%, while the air voids content of the specimen decreased by about 6.1%. As the compaction temperature increased from 25 to 45°C, the bulk density increased by about 7%, while the air voids content decreased by about 13%. It exhibited that a higher compaction temperature can significantly improve the compactness of CRME.

**Figure 8** shows that the  $ITS_d$ ,  $ITS_w$ , and  $ITS_r$  of the specimens increase significantly as the compaction temperature of CRME increases, especially when the compaction temperature of CRME increases from 5 to 25°C. At the compaction temperature of 5°C, the  $ITS_d$ ,  $ITS_w$ , and  $ITS_r$  were relatively low, which did not meet the requirements of JTG/T5521-2019. As the compaction temperature increased from 5 to 25°C,  $ITS_d$ ,  $ITS_w$ , and  $ITS_r$  increased by 15, 41, and 22%, respectively. As the compaction temperature increased



from 25 to 45°C, and the  $ITS_d$ ,  $ITS_w$ , and  $ITSR$  increased by 7, 13, and 5%, respectively. Based on the difference in  $ITS$  values at three compaction temperatures, the CRME specimens that were compacted at 25°C can obtain a good performance in terms of  $ITS$  and water stability. This can be attributed to the lower viscosity of asphalt at a higher compaction temperature. Since emulsion residue and recycled asphalt had lower viscosities when compacting at higher temperatures, the uniformity of wrapped aggregate increased, and more structural asphalt improved the tensile properties of cold recycled mixes. Besides, the viscosity of emulsified asphalt becomes smaller at higher temperatures, which was more likely for the internal movement of aggregates during the compaction process.

## Comparison of Compaction Methods

### The SGC and Modified Marshall Method

To further study the CRME compaction characteristics, the SGC method and modified Marshall methods were compared and analyzed at the compaction temperature of 25°C. Specimens were all in the same size, 63.5 mm in height and 100 mm in diameter. Five compaction modes and four emulsion contents were used. The specimens were compacted at four different gyrations (30, 50, 75, and 100) using the SGC method and at 75 blows using the Marshall method, separately. In addition, the four emulsion contents included 3.0, 3.5, 4.0, and 4.5% by weight of the aggregates. The air voids content and  $ITS_d$  are shown in **Figure 9** and **Figure 10**, respectively.

In **Figure 9**, the air voids content of the specimen decreases as the compact increases. When the gyratory number increased from 30 to 50 gyrations, the air voids content of the specimen decreased by more than 2.3%, while the  $ITS_d$  increased by more than 0.15 MPa (**Figure 10**). The decrease of air voids content and the increase of  $ITS_d$  slowed down after 50 gyrations. From 50 to 75 gyrations, the air voids content of the specimen decreased by 1.6%, and the  $ITS_d$  increased by 0.08 MPa, which indicated that the effect of compaction after 50 gyrations on air voids content

and  $ITS$  was insignificant. Based on that, it was also reasonable that CRME can be compacted for 50 gyrations using the SGC method.

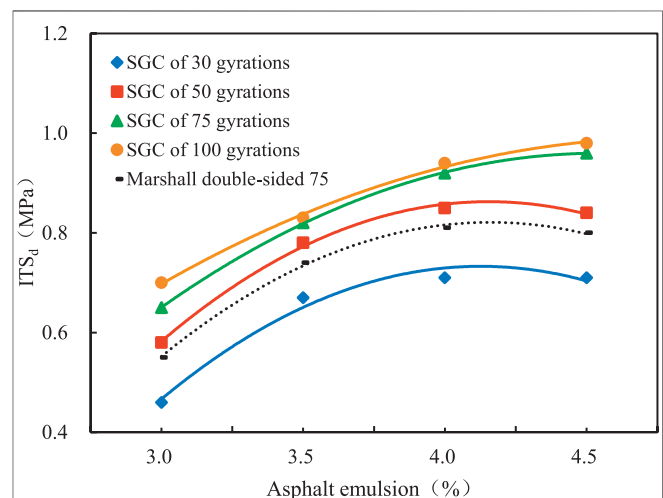
In terms of air voids content and the  $ITS_d$  value, the specimens with 75 blows using the modified Marshall method was equivalent to the specimens with around 45 gyrations using the SGC method. It was beneficial to establish the correspondence between the gyrations using the SGC method and the blows using the modified Marshall method in JTG/T5521-2019.

From the changing trend of  $ITS_d$  with the content of emulsified asphalt, there was a maximum value of  $ITS_d$  using SGC of 50 gyrations at the emulsified asphalt content of 4%, which the maximum  $ITS_d$  is determined to be 0.85 MPa, and the specimen air voids content can be controlled at about 11.5%. The results indicated that the air voids content and strength well meet the specification (JTG/T5521-2019) requirements of the air voids content of 8–13%, and the strength greater than 0.4 MPa. At the same time, it was proved that it was reasonable and feasible to determine the optimum emulsified asphalt content by analyzing the compaction characteristic parameters.

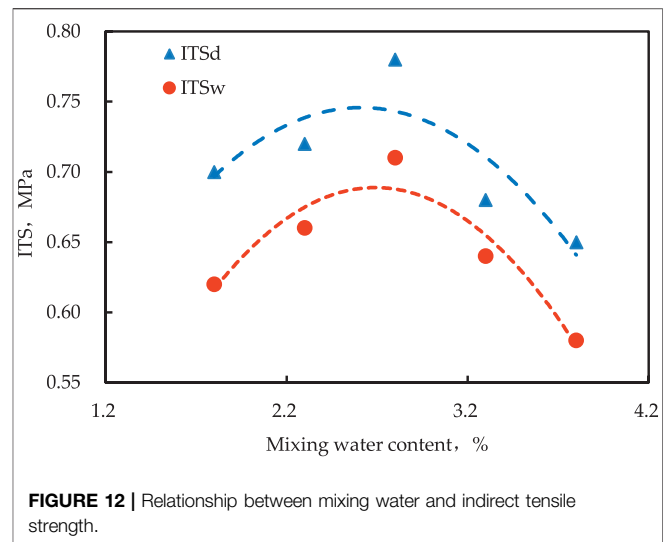
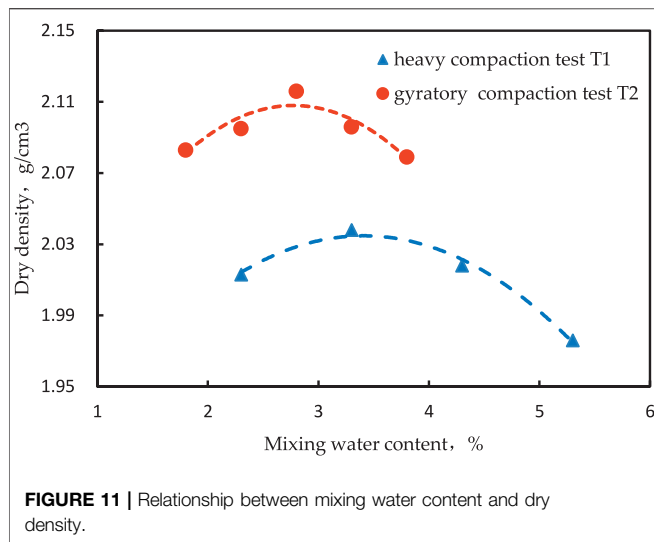
## The SGC and Heavy Compaction Method

To determine the optimum moisture content required for CRME, two sets of tests, including T1 (the optimum moisture content test using the heavy compaction method in JTG/E40-2007) and T2 (the optimum moisture content using the SGC) were analyzed and compared. The test results are shown in **Figure 11**.

In **Figure 11**, the maximum dry density of CRME is 2.035 g/cm<sup>3</sup> from the T1 test, and the corresponding optimum mixing water of CRME is determined to be about 3.4%. As a contrast, the maximum dry density of CRME is 2.108 g/cm<sup>3</sup> from the T2 test, and the corresponding optimum mixing water of CRME is determined to be about 2.8%, which the optimum moisture content is 4.053% by weight of aggregates. It was found that the optimum mixing water of CRME obtained by the SGC method was 0.6% smaller than that of the heavy compaction method, and the maximum dry density of



**FIGURE 10 |**  $ITS_d$  of different emulsion contents using different molding methods.



CRME obtained by the SGC method was 3.6% higher than that of the heavy compaction method.

The results showed that the SGC method obtained a greater dry density than the heavy compaction method at the same mixing water content, which indicates the SGC method may more helpful for the CRME compaction. In practice, the optimum mixing water of CRME determined by the heavy compaction method was larger than on-site construction, which will cause a higher air voids content and additional costs. Therefore, it was recommended that the optimum moisture content of CRME should be determined using the SGC method.

To understand the relationship between moisture content and ITS, five groups of test specimens were compacted at 50 gyrations using the SGC method. The test results are shown in Figure 12.

It was observed that the maximum  $ITS_d$  was about 0.75 MPa at 2.6% water content and the maximum  $ITS_w$  was about 0.69 MPa at 2.7% water content, which meets the requirements of JTG/T 5521-2019. When the specimen ITS was at the maximum value, The CRME achieved almost the same optimum water content. Therefore, the results indicated that the density and strength of CRME had a positive correlation.

Based on the above research results, the CRME specimens were compacted for 50 gyrations at 25°C using the SGC method. The specimens used 4% emulsified asphalt and 2.6% mixing water (by weight of the aggregates). Technical performance was tested in the lab. As shown in Table 5, the test results can meet all the technical requirements of JTG/T5521-2019. The results suggested that the SGC method provides better overall performance, and can better meet the requirements of field application.

## CONCLUSION

The compaction characteristics of CRME were studied in this paper. The main influencing factors, including aggregate gradation, the content of asphalt emulsion and moisture, the

**TABLE 5 |** Test results of the CRME performance.

Technical indexes	Results	Requirements	Test method
$ITS_d$ (MPa)	0.83	$\geq 0.4$	JTG/T5521-2019
$ITS_w$ (MPa)	0.71	$\geq 0.4$	JTG/T5521-2019
TSR (%)	87.7	$\geq 75$	JTG/E20-2011
Dynamic stability at 60°C (/mm <sup>-1</sup> )	4153	$\geq 2,000$	JTG/E20-2011
Failure strain ( $\mu\epsilon$ )	2160	—	JTG/E20-2011
Cohesion (g/cm <sup>2</sup> )	257.4	—	ASTM D1560
Wear loss (%)	0.77	—	ASTM D7196

compaction temperature, and the compaction method were discussed. Based on the analysis of the results, the obtained conclusions can be summarized as follows:

- (1) Five compaction characteristic parameters are proposed and derived. As a result, a new idea by analyzing the compaction characteristic parameters is used to determine the optimum emulsified asphalt content of the CRME. It is beneficial that appropriately increasing emulsion content and adding new aggregate in the mixture for deformation resistance under traffic loads.
- (2) The asphalt emulsion content and compaction temperature have a significant effect on the compaction characteristics of the CRME, and the aggregate gradation has an insignificant effect. It is suggested to pave the CRME at the atmosphere temperature, which is higher than 25°C, to improve the road performance of the CRME.
- (3) Compared with the heavy compaction method, the optimum mixing water content obtained by the SGC method is reduced by 18%, but the density is increased by 3.5%. This process avoids the problems of small compactness and high engineering cost caused by excess moisture.



- (4) The gyratory method can be effectively applied to the CRME mixture design and it is a more realistic compaction method, which is close to the situation at the worksite. The mixture with 50 gyrations is close to that with 75 blows using the modified Marshall method and the mixture can achieve a high density and strength.

## DATA AVAILABILITY STATEMENT

The raw data supporting the conclusions of this article will be made available by the authors, without undue reservation.

## REFERENCES

- Brovelli, C., and Crispino, M. (2012). Investigation into cold recycled materials: influence of rejuvenant, mix design procedure and effects of temperature on compaction. *Constr. Build. Mater.* 37 (12), 507–511. doi:10.1016/j.conbuildmat.2012.07.070
- Casillas, S., and Braham, A. (2020). Quantifying effects of laboratory curing conditions on workability, compactability, and cohesion gain of cold in-place recycling. *Road Mater. and Pavement Des.* (4), 1–23. doi:10.1080/14680629.2020.1753101
- DelRio-Prat, M., Vega-Zamanillo, A., Castro-Fresno, D., and Calzada-Perez, M. (2011). Energy consumption during compaction with a gyratory intensive compactor tester. Estimation models. *Constr. Build. Mater.* 25 (2), 979–986. doi:10.1016/j.conbuildmat.2010.06.083
- Dessouky, S., Masad, E., and Bayomy, F. (2004). Prediction of hot mix asphalt stability using the superpave gyratory compactor. *J. Mater. Civil Eng.* 16 (6), 578–587. doi:10.1061/(asce)0899-1561(2004)16:6(578)
- Flores, G., Gallego, J., Miranda, L., and Marcobal, J. (2020). Cold asphalt mix with emulsion and 100% rap: compaction energy and influence of emulsion and cement content. *Constr. Build. Mater.* 250 (7), 118804. doi:10.1016/j.conbuildmat.2020.118804
- Flores, G., Gallego, J., Miranda, L., and Marcobal, J. (2019). Design methodology for in situ cold recycled mixtures with emulsion and 100% rap. *Constr. Build. Mater.* 216 (5), 496–505. doi:10.1016/j.conbuildmat.2019.05.042
- Gao, L., Ni, F., Charmot, S., and Luo, H. (2014). Influence on compaction of cold recycled mixes with emulsions using the superpave gyratory compaction. *J. Mater. Civil Eng.* 26 (11), 1–8. doi:10.1061/(asce)mt.1943-5533.0000987
- Hillgren, G., Svenson, A., and Wallin, T. (1989). “Asphalt Institute Manual series No 14,” in *In-plant cold recycling and cold mix in Sweden-developments in laboratory testing*. 3rd Edition.
- Kim, Y. (2012). Performance evaluation of cold in place recycling mixtures using emulsified asphalt based on dynamic modulus, flow number, flow time, and raveling loss. *KSCSE J. Civil Eng.* 16 (4), 586–593. doi:10.1007/s12205-012-1376-0
- Kim, Y., and Lee, H. (2011). Influence of reclaimed asphalt pavement temperature on mix design process of cold in-place recycling using foamed asphalt. *J. Mater. Civil Eng.* 23 (7), 961–968. doi:10.1061/(asce)mt.1943-5533.0000274
- Lee, K., Brayton, T., Mueller, M., and Singh, A. (2016). Rational mix-design procedure for cold in-place recycling asphalt mixtures and performance prediction. *J. Mater. Civil Eng.* 28 (6), 04016008. doi:10.1061/(ASCE)MT.1943-5533.0001492
- Li, H., Gao, Y., and Yu, W. (2011). Compaction characteristics of hot mixed asphalt and number of roller passes. *J. Southeast Univ.* 41 (01), 186–189. doi:10.3969/j.issn.1001-0505.2011.01.036
- Lin, J., Hong, J., and Xiao, Y. (2017). Dynamic characteristics of 100% cold recycled asphalt mixture using asphalt emulsion and cement. *J. Clean. Prod.* 156, 337–344. doi:10.1016/j.jclepro.2017.04.065
- Martínez-Echevarría, M., Miro Recasens, R., Rubio Gamez, M., and Ondina, A. (2012). In-laboratory compaction procedure for cold recycled mixes with bituminous emulsions. *Constr. Build. Mater.* 36 (6), 918–924. doi:10.1016/j.conbuildmat.2012.06.040
- MOC of PRC (2011). “Standard test method of bitumen and bituminous mixtures for highway engineering (JTG E20-2011),” in *Ministry of Communications of the people's Republic of China* (Beijing: China Communications Press).
- MOC of PRC (2004). “Technical specification for construction of highway asphalt pavements (JTG F40-2004),” in *Ministry of Communications of the people's Republic of China* (Beijing: China Communications Press).
- MOC of PRC (2019). “Technical specifications for highway asphalt pavement recycling (JTG T5521-2019),” in *Ministry of Communications of the people's Republic of China* (Beijing: China Communications Press).
- MOC of PRC (2007). “Test methods of soils for highway engineering (JTG E40-2007),” in *Ministry of Communications of the people's Republic of China* (Beijing: China Communications Press).
- Rodríguez-Fernández, I., Lastra-González, P., Indacoechea-Vega, I., and Castro-Fresno, D. (2019). Recyclability potential of asphalt mixes containing reclaimed asphalt pavement and industrial by-products. *Constr. Build. Mater.* 195, 148–155. doi:10.1016/j.conbuildmat.2018.11.069
- Tarefder, R., and Ahmad, M. (2016). Effect of compaction procedure on air void structure of asphalt concrete. *Measurement* 90, 151–157. doi:10.1016/j.measurement.2016.04.054
- Turk, J., Pranjić, A., Mladenović, A., Cotić, Z., and Jurjavčič, P. (2016). Environmental comparison of two alternative road pavement rehabilitation techniques: cold-in-place-recycling versus traditional reconstruction. *J. Clean. Prod.* 121, 45–55. doi:10.1016/j.jclepro.2016.02.040
- Wendling, L., Gaudefroy, V., Gaschet, J., Ollier, S., and Gallier, S. (2015). Evaluation of the compactability of bituminous emulsion mixes: experimental device and methodology. *Constr. Build. Mater.* 17 (1), 71–80. doi:10.1080/10298436.2014.925553
- Xiao, F., Yao, S., Wang, J., and Amirkhanian, S. (2018). A literature review on cold recycling technology of asphalt pavement. *Constr. Build. Mater.* 180, 579–604. doi:10.1016/j.conbuildmat.2018.06.006
- Yan, J. (2006). Asphalt pavement cold recycling design method and performance evaluation. Master thesis. Chongqing (China): Southeast University.
- Zhang, Z., Yuan, Y., and Wang, B. (2005). Information of gyratory compaction densification curve of asphalt mixture and its application. *China J. Highway Transport* 18 (3), 1–6. doi:10.19721/j.cnki.1001-7372.2005.03.003

## AUTHOR CONTRIBUTIONS

DW and HY conceived of this project and revised this article. DW, JY, and SH drafted the article. JL, MX, and SC provided technical support for this project.

## FUNDING

This work is supported by the National Key Research and Development Program of China (2018YFE0120200) and the National Natural Science Foundation of China (51878623).

**Conflict of Interest:** The authors declare that the research was conducted in the absence of any commercial or financial relationships that could be construed as a potential conflict of interest.

Copyright © 2021 Wang, Yao, Yue, Hu, Liu, Xu and Chen. This is an open-access article distributed under the terms of the Creative Commons Attribution License (CC BY). The use, distribution or reproduction in other forums is permitted, provided the original author(s) and the copyright owner(s) are credited and that the original publication in this journal is cited, in accordance with accepted academic practice. No use, distribution or reproduction is permitted which does not comply with these terms.





# Study on the Properties and Mechanisms of a Cement-Stabilized Aggregate Mixture With Vibration Mixing

Ping Li<sup>1,2</sup>, Di Wei<sup>1</sup>, Dongmei Zhang<sup>1,3\*</sup>, Jianping Xiong<sup>4</sup> and Sheng Xu<sup>1</sup>

<sup>1</sup> School of Traffic and Transportation Engineering, Changsha University of Science and Technology, Changsha, China,

<sup>2</sup> National Engineering Laboratory of Highway Maintenance Technology, Changsha University of Science and Technology, Changsha, China, <sup>3</sup> Hunan International Scientific and Technological Innovation Cooperation Base of Advanced Construction and Maintenance Technology of Highway, Changsha University of Science and Technology, Changsha, China, <sup>4</sup> Guangxi Transportation Science and Technology Group Co., Ltd., Nanning, China

## OPEN ACCESS

### Edited by:

Hui Yao,  
Beijing University of Technology,  
China

### Reviewed by:

Yue Li,  
Beijing University of Technology,  
China  
Mulian Zheng,  
Chang'an University, China  
Yinghao Miao,  
University of Science and Technology  
Beijing, China

### \*Correspondence:

Dongmei Zhang  
dmzhang@csust.edu.cn

### Specialty section:

This article was submitted to  
Structural Materials,  
a section of the journal  
Frontiers in Materials

Received: 27 November 2020

Accepted: 16 March 2021

Published: 20 April 2021

### Citation:

Li P, Wei D, Zhang D, Xiong J and  
Xu S (2021) Study on the Properties  
and Mechanisms of a  
Cement-Stabilized Aggregate Mixture  
With Vibration Mixing.  
Front. Mater. 8:634336.  
doi: 10.3389/fmats.2021.634336

In order to understand the influence of the vibration mixing method on the performance of cement-stabilized aggregate mixture (CSAM), in this study, an unconfined compressive strength test, drying shrinkage test and the influence of gradation characteristics on compressive strength were used to systematically analyze the performance of CSAM based on vibration mixing. At the same time, the influence mechanism of vibration mixing on the interface transition zone of cement aggregate was analyzed by use of a scanning electron microscope (SEM), and the influence of the mixing method on cement dispersion uniformity was studied by the ethylene diamine tetraacetic acid (EDTA) titration method. The results show that 7 days of unconfined compressive strength and crack resistance of the CSAM with vibration mixing is better than those of the ordinary mixing, and the aggregate grade has a great influence on the compressive strength of the CSAM. Vibration mixing can improve the micro-water-cement ratio uniformity of CSAM and significantly improve the bonding condition of the interface transition zone between cement paste and aggregate, thus enhancing the structural compactness of CSAM. The dispersion uniformity of cement under the vibration mixing is better than that of ordinary mixing.

**Keywords:** cement-stabilized aggregate mixture, compressive strength, dry shrinkage, influence mechanism, vibration mixing

## INTRODUCTION

The semi-rigid base has the characteristics of high strength, excellent stability and high economical efficiency, and since the 1980s, it has therefore become the most widely used grass-roots road construction in China. However, the semi-rigid base has the disadvantage of easy cracking. At the same time, with the rapid increase in heavy load and overload vehicles, it also has poor durability and cracks. The main reason for these issues is that the semi-rigid base material is uneven and divided. Cement-stabilized aggregate mixture (CSAM) is a typical semi-rigid base material, which is a kind of heterogeneous material with low cement dosage. It easily causes segregation, crushing, loosening and other defects in the mixing, transportation, paving and rolling stages, but improving

the uniformity of the mixture can solve these defects to a certain extent. Researches on the impact of mixing methods on the mixture found that vibration mixing can make up for the defects of ordinary mixing, fully tap the potential of materials, reduce the amount of cement, enhance the strength of the mixture and reduce cracking.

For the research on the CSAM with vibration mixing (Dong et al., 2019), analyzed the influence of vibration on the mixing process of CSAM by testing the mixing power curve of different mixing methods and carried out a comparative test of vibration mixing and ordinary mixing. The results show that the vibration mixing improves the homogeneity of CSAM, and the microstructure is uniform and dense, which leads to high compressive strength and good dry shrinkage. Zhang et al. (2018) established the equivalent relationship between the modified laboratory vibration mixing and the site vibration mixing through a series of tests. It was found that the design result of laboratory CSAM vibration mixing was better than that of site CSAM vibration mixing, and the unconfined compressive strength of CSAM was greater than that of the mixture mixed by site vibration mixing. Zhao L. J. et al. (2018) carried out the comparative test of vibration mixing and ordinary mixing, and the results showed that under the condition of vibration mixing, the influence of mixing time on the compressive strength of mixture is the greatest, followed by vibration frequency and mixing speed, and the influence of wet mixing time is the least. With the increase in mixing parameters, the compressive strength increases as well, and the coefficient of variation decreases. On the basis of reasonable mixing parameters, the vibration mixing can significantly improve the strength index of the mixture, but with the increase of cement content, the strength improvement rate of CSAM with the vibration mixing decreases.

Chen et al. (2019) analyzed the influence of different design parameters of CSAM with vibration mixing on the mechanical properties of the mixture by using gray correlation theory. The test results show that the most significant design parameter affecting the mechanical properties of CSAM is the cement dosage, followed by dry density, aggregate gradation, compactness and water content. Liang (2018) carried out a freeze-thaw test and dry shrinkage test of CSAM under vibration and ordinary mixing methods, and they found that the frost resistance and crack resistance of the specimens under vibration mixing are better. Zhang and Zhang (2016) found that the appearance of vibration mixing can improve the mixing uniformity of the mixture and ensure the engineering quality at the mixing stage. Liu and Xiong (2018) compared the unconfined compressive strength, splitting strength and dry shrinkage coefficient of CSAM produced by vibration mixing and ordinary mixing with laboratory specimens with core samples of solid engineering. The results show that the unconfined compressive strength of CSAM made by vibration mixing is higher than that of ordinary mixing, and the unconfined compressive strength of laboratory vibration mixing specimens is better than that of site vibration mixing conditions. Duan et al. (2020) prepared skeleton-dense CSAM specimens by static pressure and vibration compaction and pre-cracked at the early stage of maintenance. The development laws of the pre-splitting degree, mechanics, dry shrinkage and crack

resistance of CSAM after early pre-cracking treatment under different molding methods were studied. The results indicate that the pre-splitting degree of the specimen increases first and then decreases under the action of vibration. Before reaching the maximum pre-splitting degree, the pre-splitting degree of the static pressure specimen is higher than that of the vibration specimen; however, under the same pre-splitting parameters, the self-healing performance of the vibration specimen is better than that of the static pressure specimen, and the tensile strength index of the static pressure specimen is the worst. After the pre-splitting treatment, the dry shrinkage of the vibration and static pressure specimens can be reduced by 35.8 and 35.3%, respectively. After pre cracking treatment, the crack resistance of the specimens increases by 2–3 times. Zheng et al. (2018) used a fiber tensile test, splitting tensile test and bending test to analyze the influence of the two mixing methods on the mechanical properties of reinforcement, comparing the vibration mixing and the ordinary mixing. The findings show that vibration mixing can effectively improve the fiber distribution in the concrete and increase the fiber density to effectively improve the mechanical properties of steel fiber reinforced concrete. Zhou and Li (2019) compared the difference in compaction standards, mechanical strength, shrinkage characteristics and mineral gradation decay determined by the cement stabilized recycled gravel mixture with the compaction and static pressure method. The compacted moisture content and dry shrinkage determined by the vibration test deformation and gradation decay of minerals were lower, while maximum dry density and mechanical strength were higher. Zhao K. Y. et al. (2018) used two mixing methods for preparing C60 high-strength concrete, using one-step mixing technology and three-step mixing technology to carry out comparative experiments. The study finds that under the two mixing conditions, the viscosity of concrete was significantly reduced, the fluidity and compressive strength improved, and the most suitable mixing methods and mixing processes for C60 high-strength concrete were vibration mixing and three-step mixing.

By searching the existing data, it is found that the existing research on vibration mixing mainly focuses on the impact of vibration mixing on the performance of CSAM, such as compressive strength, dry shrinkage performance, etc., which can provide a reference for the study of this paper. However, the influence of aggregate gradation on the compressive strength of mixture and the influence mechanism of vibration mixing on the interface transition zone of cement aggregate are less involved, so the influence of vibration mixing technology on the performance of CSAM is not fully evaluated. Based on the double horizontal shaft vibration mixer (DT60ZBW), as a test, this paper compared the strength and crack resistance of the mixture, the relationship between the bearing capacity of coarse aggregate and the compressive strength of the mixture under two different mixing methods of vibration mixing and ordinary mixing. Meanwhile, we analyzed the influence mechanism of CSAM with vibration mixing and its influence on cement dispersion uniformity to guide the construction of CSAM, and improving road durability has a guiding role.

## MATERIALS AND METHODS

### Materials

#### Raw Materials

In this paper, the Portland cement (P.O 42.5) produced by Hunan Pingtang Nanfang Cement Co., Ltd. was used. The limestone produced in Yueyang was used as the aggregates, and the domestic tap-water was used as the mixing water. All the raw materials met the requirements of the *Technical Guidelines for Construction of Highway Roadbases* (hereafter *Technical Guidelines*).

#### Aggregate Gradation

The gradation selected in this paper is shown in **Figure 1**.

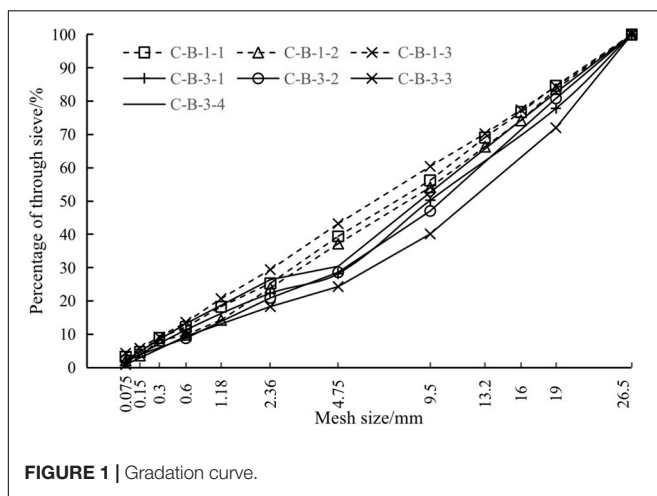
#### Mix Proportion of the CSAM

Combined with the actual project and related research results, the cement dosage is determined as 3, 3.5, 4, 4.5, and 5% by using the external mixing method. The optimal moisture content is obtained according to the compaction test, and the results are shown in **Figure 2**.

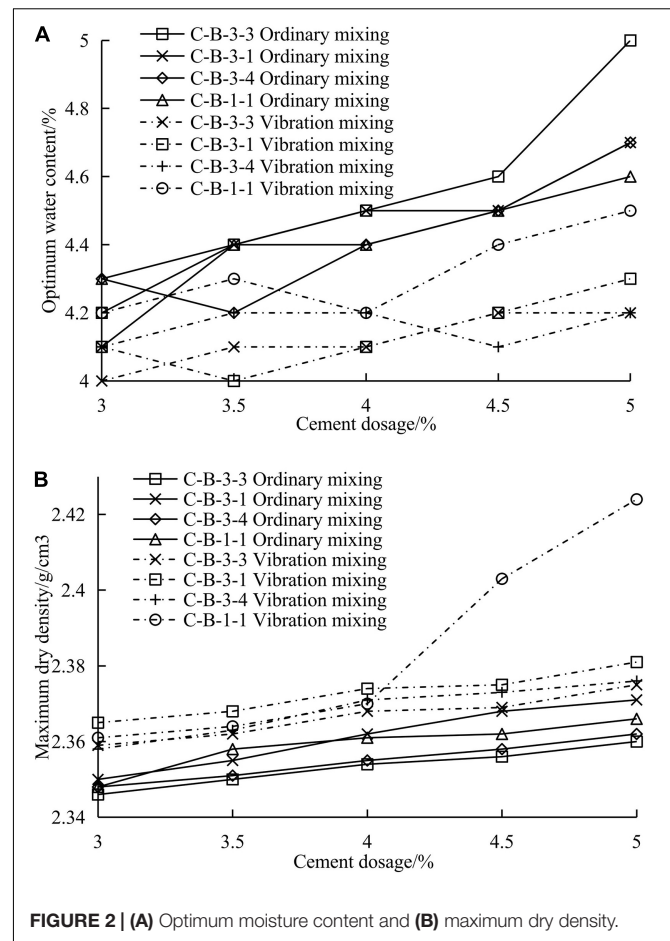
### Testing Methods

#### Mixing of Cement-Stabilized Aggregate

A double horizontal shaft vibrating mixer (DT60ZBW) with a nominal capacity of 60L developed by Detong vibration mixing company, Xuchang City, Henan Province, was adopted. DT60ZBW is mainly composed of a mixing driving mechanism, vibration driving mechanism, mixing cylinder, vibration exciter, synchronous device, transmission device, etc. The maximum stirring time was 55 s, the stirring speed was 55 r/min, the stirring blades were 14, and the vibration intensity was 3–5 g. Weigh the mass of aggregate, water and cement required by each test piece, add water to the weighed aggregate for 2 h, add the corresponding cement, and put it into the mixer to mix for 15 s until it is even. When the mixing motor and vibration motor are started at the same time, it is vibration mixing combined with conventional mixing; only starting the mixing motor is ordinary mixing. The equipment is shown in **Figure 3**.



**FIGURE 1** | Gradation curve.



**FIGURE 2** | (A) Optimum moisture content and (B) maximum dry density.

#### Unconfined Compressive Strength Test

The unconfined compressive strength test (T 0805-1994) of CSAM was carried out according to *Test Methods of Materials Stabilized with Inorganic Highway Engineering* JTG E51-2009 (hereinafter, *Test Methods*). The 7 days unconfined compressive strength was determined to evaluate its ultimate strength under the condition of no lateral pressure. Through the contrast test of different mixing methods, the influence of the mixing method on the compressive strength of CSAM is analyzed.

#### Coarse Aggregate Penetration Test

The maximum nominal particle size of aggregate used in this paper is 26.5 mm. According to the Bailey method, the boundary particle size of coarse and fine aggregate is calculated: 0.22 times the maximum nominal particle size of aggregate is taken as the boundary point of coarse and fine aggregate (5.83 mm). According to the principle of closest particle size of aggregate, 4.75 mm is taken as the boundary particle size of coarse and fine aggregate in which the aggregate above 4.75 mm is coarse aggregate.

The computer-controlled electronic universal testing machine was used to carry out penetration tests on coarse aggregate above 4.75 mm. A total of 12 mm was taken as the standard depth of penetration test, and the penetration load was recorded to study



**FIGURE 3 |** Double horizontal shaft vibrating mixer (DT60ZBW).

the skeleton bearing capacity of coarse aggregate with different aggregate gradation.

### Dry Shrinkage Test

According to the *Test Methods*, the dry shrinkage test (T 0854-2009) of CSAM was developed. The beam type specimen with the size of 100 mm × 100 mm × 400 mm is formed by the static pressure method, and the compactness was 98%. After 6 h, the specimen is taken out by dismantling the mold and placed in the standard curing room for 7 days. When the temperature and humidity in the drying shrinkage test chamber reach  $20 \pm 1^\circ\text{C}$  and  $60 \pm 5\%$ , put the beam specimen and shrinkage meter into the drying shrinkage test chamber for drying shrinkage test, read the dial indicator at the same time every day, and record the length change of the specimen. The moisture change of the same specimen is determined by measuring the mass of the specimen, and the drying shrinkage coefficient of the specimen is calculated according to the drying shrinkage strain and water loss rate. At the end of the 29 days test period, the test pieces are put into the oven, dried to constant weight, and the standard length of the test pieces is measured. Through the contrast test of different mixing methods, the influence of mixing methods on dry shrinkage performance of CSAM is analyzed.

### Dispersion Uniformity Test

On the basis of the ethylene diamine tetraacetic acid (EDTA) titration method (T 0809-2009) in the *Test Methods*, four groups of parallel tests are carried out for each mixture (different mixing methods and cement dosage). In each parallel test, four different areas of the mixture in the mixing bin are selected to carry out the tests, and the ratio is that between the standard deviation and the average of the measured cement dosage of different parts of the mixture in the mixing bin. The coefficient of variation is obtained, and the averages of the four groups of the parallel tests are taken to evaluate the dispersion uniformity of CSAM under different mixing methods.

### Scanning Electron Microscope

The S-3000N produced by Hitachi company of Japan was used to scan the specimens prepared by different mixing methods. The scanning area is divided into cement matrix, aggregate surface and aggregate cement interface to evaluate the effect

of different agitation methods on cement particle distribution and gel structure, pore saturation of aggregate surface and cracking of mixture.

### Experimental Scheme

The mechanism of the experimental scheme is seen in **Table 1**.

## RESULTS

### Unconfined Compressive Strength Test

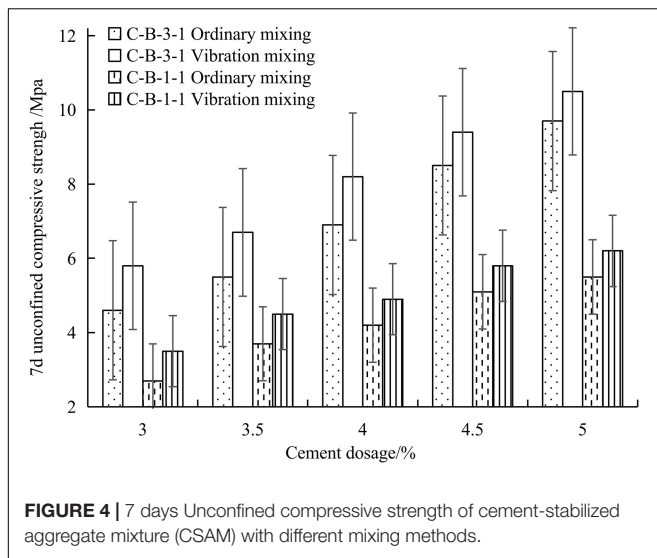
By changing the mixing method, cement dosage and aggregate gradation, the unconfined compressive strength of CSAM was tested. According to the test results of four parallel groups, the average value and the results are shown in **Figure 4**.

The 7-day unconfined compressive strength of CSAM with vibration mixing is better than that of CSAM with ordinary mixing. It is because vibration can break up the water film wrapped on the outer surface of the cement mass, and increase the dispersion and hydration of cement particles in the mixture. On the other hand, vibration mixing can improve the movement speed of aggregate and the collision frequency between aggregate particles, which is conducive to the coating of cement and aggregate particles, so as to enhance the bond between cement and aggregate, and enhance the strength of the interface

**TABLE 1 |** Design of experimental scheme.

Performance and mechanism	Research contents	Test
Service performance	Compressive strength	Unconfined compressive strength test
	Crack resistance	Dry shrinkage test
Construction performance	Mixing uniformity	Dispersion uniformity test
	Particle size distribution and gel structure of cement	Scanning electron microscope (SEM)
Mechanism	Surface porosity saturation of aggregate	
	cracking of concrete	





transition zone (Feng and Wang, 2009; Zhao et al., 2015; Wang et al., 2020).

The 7-day unconfined compressive strength of the C-B-3-1 mixture is higher than that of the C-B-1-1 mixture under the two mixing methods. The C-B-3-1 mixture belongs to the skeleton dense structure, and the degree of intercalation between aggregates is more obvious. While the C-B-1-1 mixture belongs to the suspension dense structure, the degree of intercalation of aggregates is insufficient, and the compressive strength is mainly provided by the bonding of cement hydration products (Wang, 2017), resulting in the above results at the same cement dosage.

The 7-day unconfined compressive strength of the C-B-3-1 and C-B-1-1 mixture increased linearly with the cement dosage under the two mixing methods, and the correlation coefficients were all over 0.97 (Table 2), indicating a good correlation. This is due to the increase of cement dosage, which shows that the effective cement particles participating in hydration reaction in the mixture increase, and the content of viscous hydrated calcium silicate increases, which further improves the strength of the interface transition zone; on the macro level, the compressive strength of the mixture increases (Han and Li, 2016).

Four kinds of aggregate gradation are selected: C-B-3-1, C-B-3-2, C-B-3-3, and C-B-3-4. In order to eliminate the influence of cement dosage difference on the compressive strength of the mixture, the cement dosage was set at 4%.

**TABLE 2 |** Linear regression coefficient between 7 days unconfined compressive strength and cement dosage with a different mixing method.

Mixing method	$R^2$	$k$
C-B-3-1 (Ordinary mixing)	0.9927	2.64
C-B-3-1 (Vibration mixing)	0.9954	2.42
C-B-1-1 (Ordinary mixing)	0.9816	1.4
C-B-1-1 (Vibration mixing)	0.9784	1.34

The 7-day unconfined compressive strength results of four kinds of coarse aggregate penetration are tested and their corresponding mixtures under different mixing methods are shown in Figure 5.

There is a good linear relationship between the penetration load of coarse aggregate and the 7-day unconfined compressive strength of CSAM. The correlation coefficient between the penetration load of coarse aggregate and the compressive strength of CSAM with ordinary mixing is 0.8417, and that of CSAM with vibrating mixing is 0.7835. Due to the increase of penetration load of coarse aggregate and the increase of aggregate resistance to deformation under external force, resulting in the increase of compressive strength of CSAM.

## Dry Shrinkage Test

The drying shrinkage test results of C-B-3-1 and C-B-1-1 mixtures with ordinary mixing and vibration mixing are shown in Figures 6, 7.

The cumulative water loss rate and the cumulative dry shrinkage both show the law of gentle in the initial stage and rapid increase in the later stage. When the cumulative water loss rate is the same, the common mixing mixture has a greater cumulative dry shrinkage.

Under the same cement dosage, the dry shrinkage performance of the CSAM with vibration mixing is better than that of the ordinary mixing. The vibration mixing ensures the water and cement in the CSAM are more evenly distributed, and the bonding part is denser and uniform; meanwhile, the strength is improved, the crack resistance is enhanced, and the corresponding dry shrinkage coefficient is reduced. After the mixture is evenly mixed, the large pores decrease, and the small pores increase; this enhances the water holding capacity, reduces the cracking caused by water evaporation and reduces the drying shrinkage coefficient accordingly. The hydration products are evenly distributed among the aggregate pores, making the mixture specimen more uniform and dense, improving its overall coordination deformation ability and thus reducing the overall dry shrinkage strain (Bai, 2013).

Under the same dosage and mixing mode, the dry shrinkage performance of the C-B-3-1 mixture is better than that of the C-B-1-1 mixture. This is because the C-B-3-1 mixture belongs to the skeleton dense structure, and the C-B-1-1 belongs to the suspended dense structure. In the dense skeleton mixture, the coarse aggregate forms a skeleton, which contains fine aggregate and cement. Therefore, the volume change can occur inside the coarse aggregate, which will weaken the overall volume change of the mixture (Xue, 2016).

Vibration mixing can improve the crack resistance of the mixture by reducing the cement dosage. The dry shrinkage coefficient of the CSAM of 3% of the cement in vibration mixing is smaller than that of the ordinary mixing. According to the strength test results, the unconfined compressive strength of the mixture with 3% cement and 3.5% of the cement for 7 days meets the specification requirements. This shows that the cracking problem of mixture can be



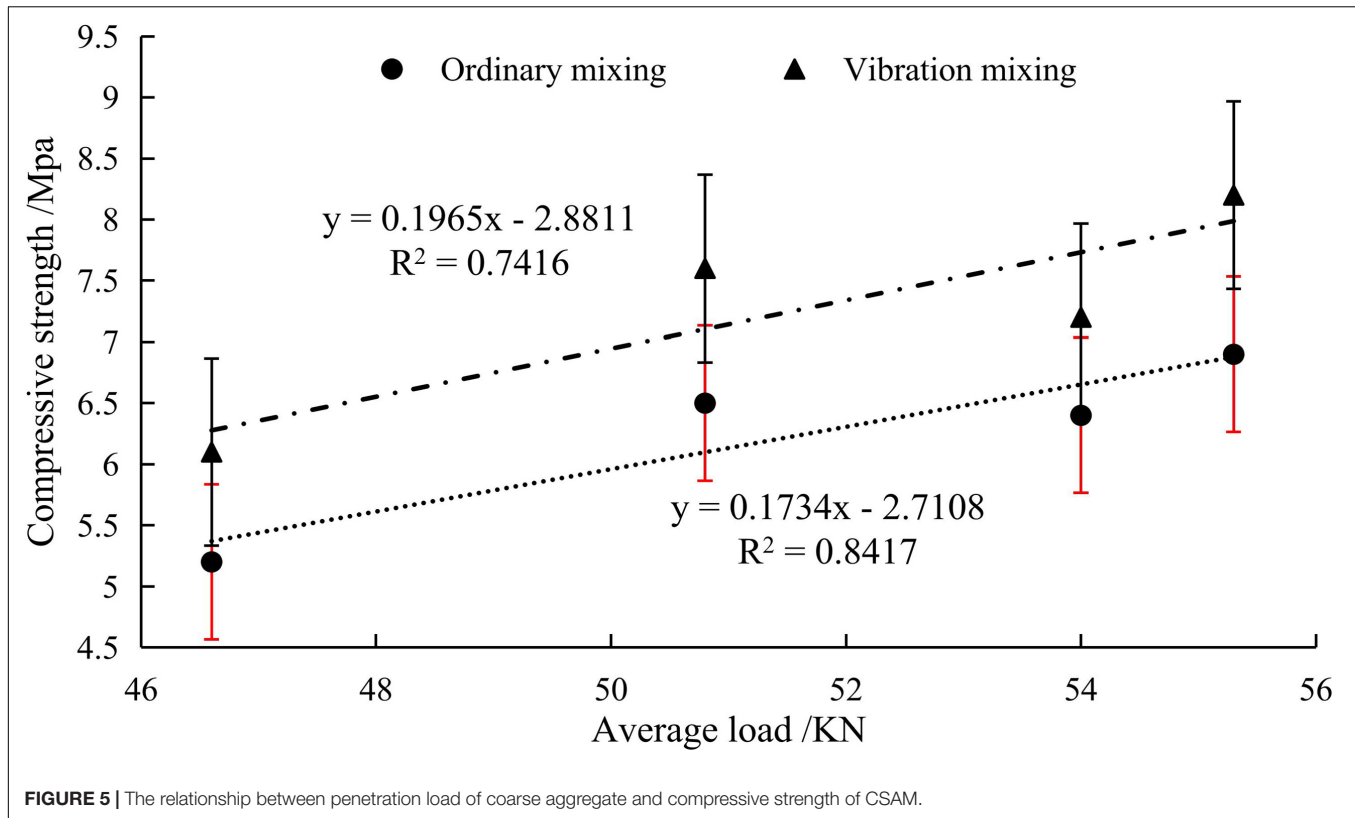


FIGURE 5 | The relationship between penetration load of coarse aggregate and compressive strength of CSAM.

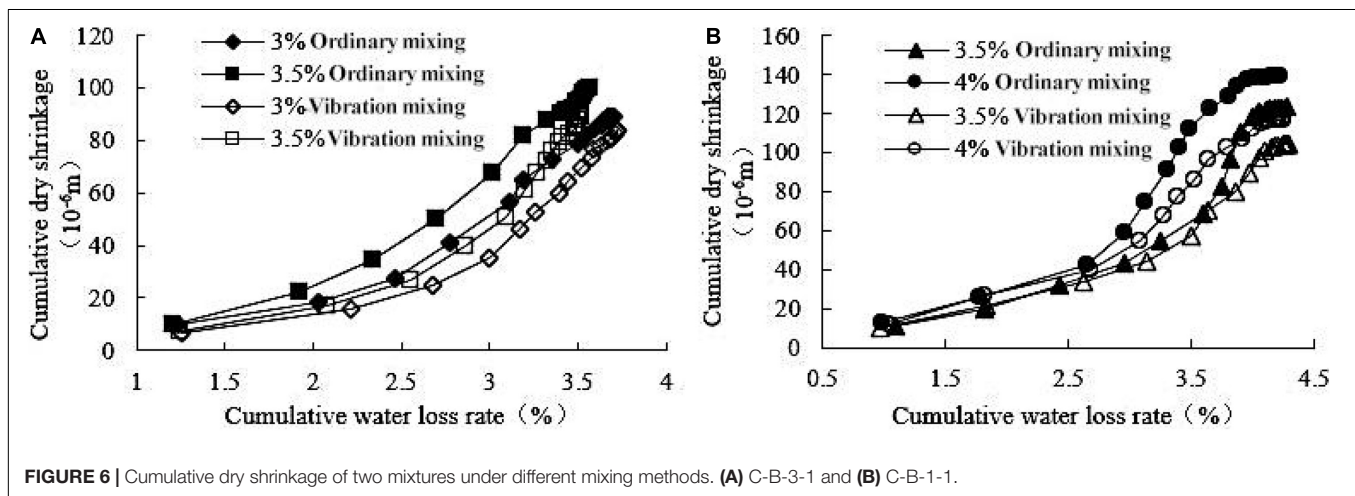


FIGURE 6 | Cumulative dry shrinkage of two mixtures under different mixing methods. (A) C-B-3-1 and (B) C-B-1-1.

reduced significantly when the cement content is reduced and when the base strength is guaranteed under the same grading condition.

### Dispersion Uniformity Test

According to the EDTA titration method in the test procedures, the cement dosage of fresh CSAM in the mixing bin under different mixing methods was tested. The cement dispersion uniformity of the C-B-3-1 and C-B-1-1 mixtures with vibration mixing is better than that of ordinary mixing. Figure 8 shows that the variation coefficient of cement dose of vibration mixing

is basically smaller than that of ordinary mixing. The average variation coefficient of cement dosage with the 3 and 3.5% C-B-3-1 mixtures under ordinary mixing is 1.4 and 1.7% higher than that of vibration mixing, respectively. The average coefficient of cement dosage with the 3.5 and 4% C-B-1-1 mixtures under vibration mixing decreased by 3.9 and 3.5%, respectively, compared with the ordinary mixing. It should be that the high-frequency vibration wave emitted by the vibration source at the mixing shaft will disperse the agglomerated cement particles evenly in the mixture to improve the overall uniformity of the mixture.

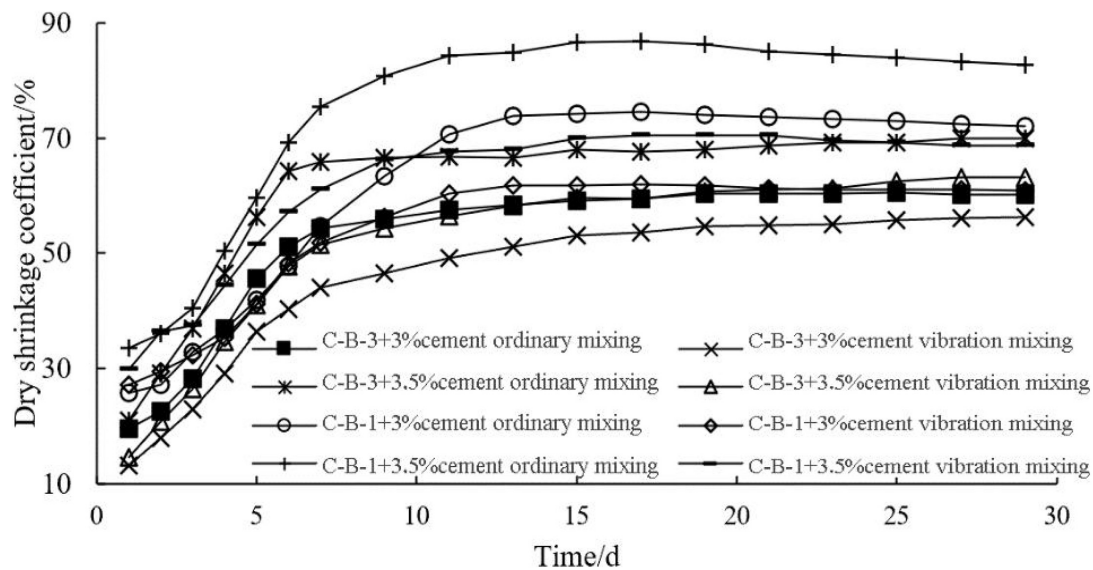


FIGURE 7 | The results of dry shrinkage test.

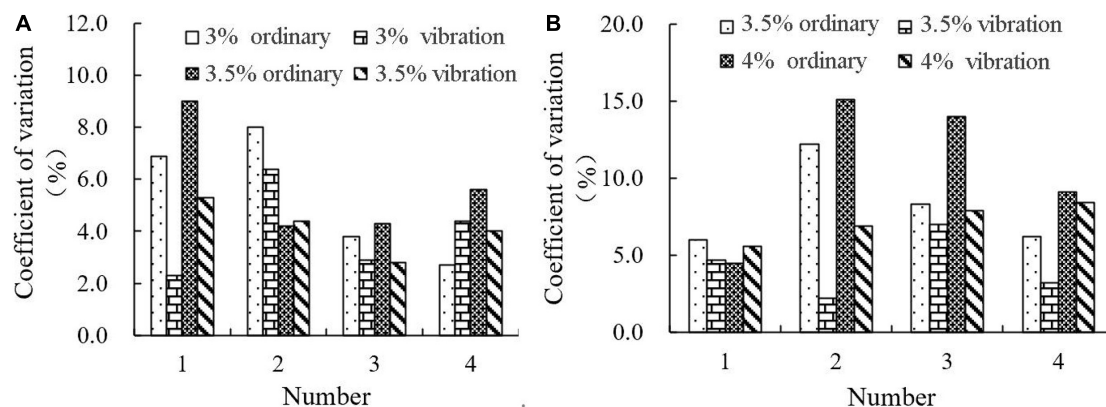


FIGURE 8 | Coefficient of variation of CSAM under different mixing methods. (A) C-B-3-1 and (B) C-B-1-1.

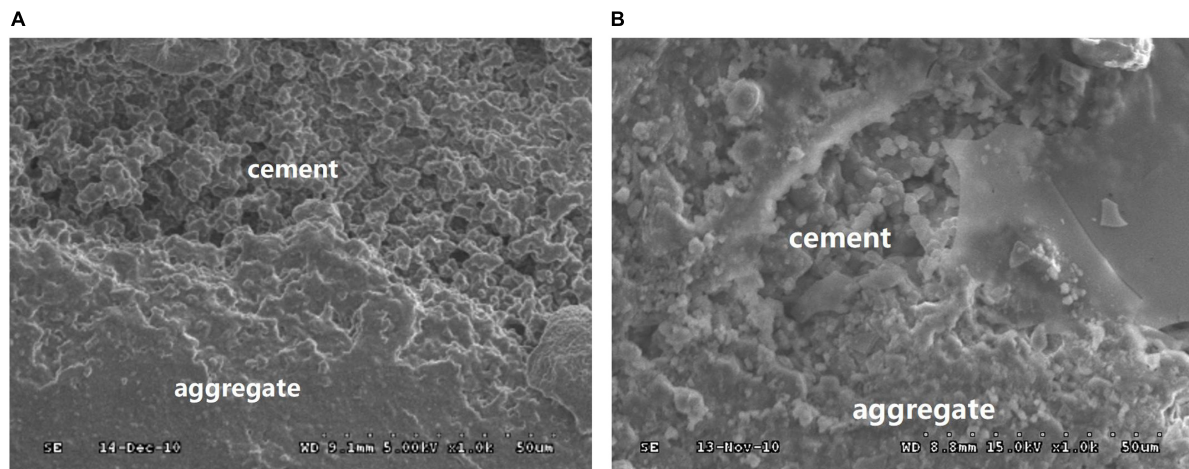
## Scanning Electron Microscope

The C-B-1-1, C-B-1-2, and C-B-1-3 mixtures with 4.0% cement dosages at a curing age of 28 days under different mixing methods were cut into samples of 5 mm by a precision cutting machine and polished by sandpaper from coarse to fine to obtain a smooth plane to be measured and sealed for preservation. The interface transition zone was found by an electron microscope at 100 times magnification, and then the cracks and cement hydration products were observed at 1,000 times magnification. The scanning area was divided into cement matrix, aggregate surface, aggregate and cement interface. During scanning, the more comprehensive and typical areas were taken as far as possible to make one picture include three expected contents. The scanning results are shown in Figures 9–11.

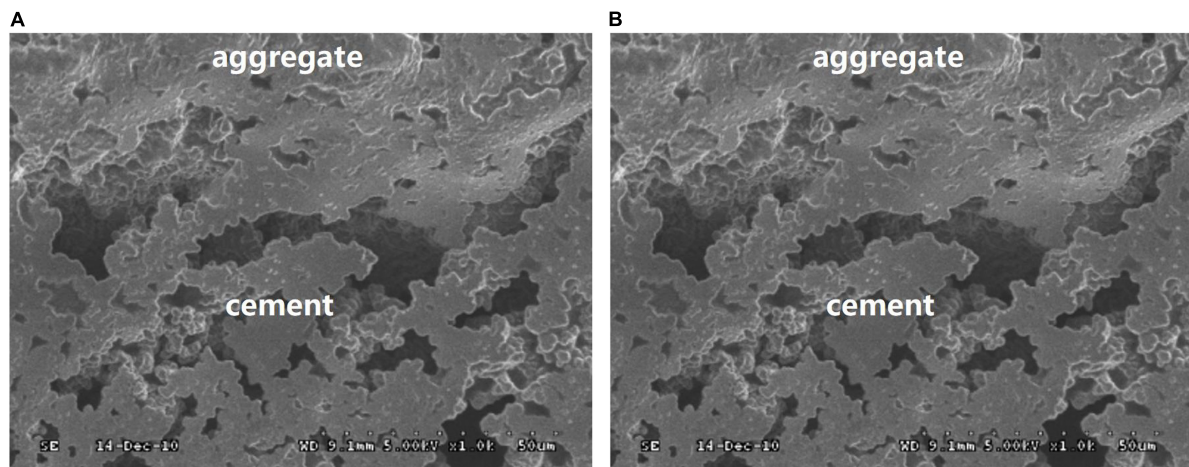
In Figure 9A, the cement matrix is similar to the cluster formed by spherical particles, and there are some small pores

and gullies between the cement particles. This indicates that although cement hydration has reached a certain degree, there may be hydrated particles inside the spherical particles. In Figure 9B, the particles of cement hydration products in the cement matrix are more delicate, and some are even flocculent and evenly distributed. The results show that the hydration of cement in CSAM is more sufficient under vibration mixing. Cement and free water become loose under high-frequency vibration with vibration mixing, which means the cement comes into contact with free water more fully, there is less cement agglomeration, and cement hydration products are distributed more evenly and widely.

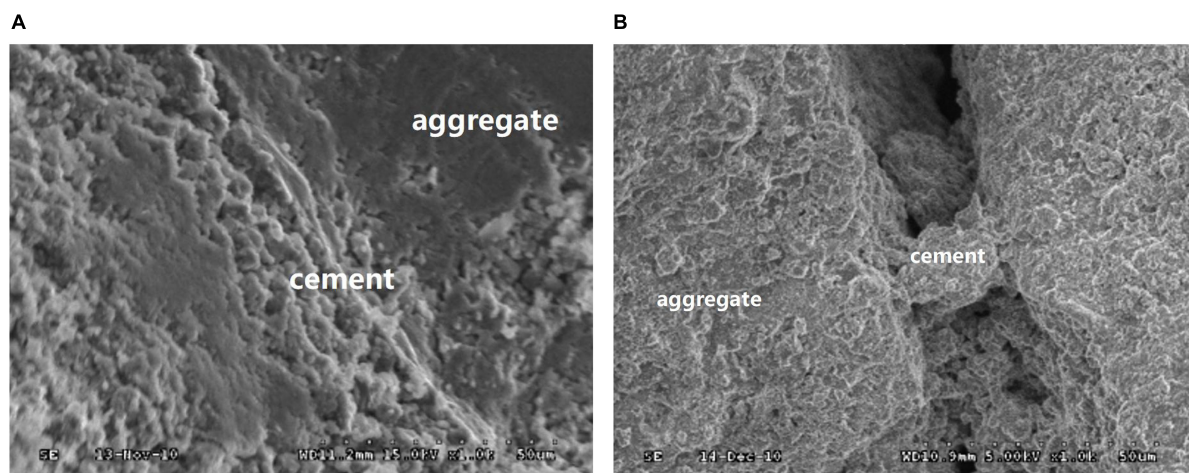
In Figure 10A, there are a large number of small pores in the joint of aggregate and cement and cement matrix under ordinary mixing. In Figure 10B, there is an obvious crack in



**FIGURE 9** | Scanning electron microscope (SEM) picture of C-B-1-3 (1000 $\times$ ). **(A)** C-B-1-3 with ordinary mixing and **(B)** C-B-1-3 with vibration mixing.



**FIGURE 10** | Scanning electron microscope picture of C-B-1-1 (1000 $\times$ ). **(A)** C-B-1-1 with ordinary mixing and **(B)** C-B-1-1 with vibration mixing.



**FIGURE 11** | Scanning electron microscope picture of C-B-1-2 (1000 $\times$ ). **(A)** C-B-1-2 with ordinary mixing and **(B)** C-B-1-2 with vibration mixing.



the interface transition zone of CSAM with vibration mixing, but the transition areas at other positions are in close contact, which shows that the probability and degree of internal defects in vibration mixing are lower than in ordinary mixing, and the effect of vibration mixing is better. This is due to the insufficient contact between the cement and free water in the mixture with ordinary mixing, and the free water wrapped in the dry cement cannot contact with the cement inside the matrix, resulting in insufficient hydration degree of cement, voids in the transition zone and agglomeration in the cement matrix. In **Figure 11A**, there is an obvious boundary between the interface transition zone of aggregate and cement, meanwhile, there are obvious gaps between the aggregates. In **Figure 11B**, the cement matrix and aggregate in the interface transition zone of CSAM with vibration mixing are closely combined with the aggregate, and there are small gullies on the surface, but no obvious cracks and pores are found. This illustrates that the internal structure of vibration is more compact than that of ordinary mixing.

This can be attributed to the fact that the aggregate and cement particles in the CSAM are close to each other under vibration, the gap between particles is reduced, and the contact between particles and free water is enhanced, which makes the cement hydration more sufficient and the overall structure more compact.

## DISCUSSION

In this paper, the compressive strength and dry shrinkage of cement are prepared by vibration mixing and ordinary mixing, the relationship between the bearing capacity of coarse aggregate and compressive strength of mixture is compared, and the influence of vibration mixing on the interface transition zone of cement aggregate is analyzed. The main conclusions are as follows:

- (1) The 7-day unconfined compressive strength of CSAM with vibration mixing is better than that of CSAM with ordinary mixing, and the enhancement rate of mixture strength by vibration mixing shows a decreasing trend with the increase of cement dosage. The 7-day unconfined compressive strength of the C-B-3-1 mixture is higher than that of the C-B-1-1 mixture with ordinary mixing, and the strength difference presents an upward trend with the increase of cement dosage.

- (2) Under the same cement dosage, the dry shrinkage performance of CSMA with vibration mixing is better than that of ordinary mixing. The cumulative water loss rate of two kinds of aggregate gradation changes little with the mixing method, while the cumulative dry shrinkage increases with the increase of water loss rate. Under the same cement dosage and mixing method, the dry shrinkage performance of the C-B-3-1 mixture is better than that of the C-B-1-1 mixture.
- (3) Vibration mixing can significantly improve the bonding condition of the interface transition zone between cement paste and aggregate. The cement matrix and aggregate in the interface transition zone are closely combined, and there are small gullies on the surface, but no obvious cracks and pores are found.

## DATA AVAILABILITY STATEMENT

The datasets presented in this study can be found in online repositories. The names of the repository/repositories and accession number(s) can be found in the article/supplementary material.

## AUTHOR CONTRIBUTIONS

All authors listed have made a substantial, direct, and intellectual contribution to the work and approved it for publication.

## FUNDING

This research was financially supported by the National Natural Science Foundation of China (Grant Nos. 51878075 and 52008045), Guangxi Natural Science Foundation (2018GXNSFAA294146), Open Fund of Hunan International Scientific and Technological Innovation Cooperation Base of Advanced Construction and Maintenance Technology of Highway (Changsha University of Science and Technology, kfj190801), The Natural Science Foundation of Hunan Province (2020JJ5595), Guangxi Major Science and Technology Project (Gui Ke AA18242032, AB19245019, and AB17292035), and Scientific Research Project of Hunan Education Department (19C0067).

## REFERENCES

- Bai, X. (2013). *Research on Anti-cracking Ability Evaluation of Cement Stabilized Crushed Stone Base*. dissertation/master's thesis, Chongqing Jiaotong University, Chongqing, CQ.
- Chen, K., Liang, S., Zhang, H. T., and Yang, H. S. (2019). Analyses on the influence of parameters vibration-stirred water-stabilized crushed stone on mechanical properties of based on grey correlation analysis method. *Sci. Technol. Eng.* 19, 321–324.
- Dong, W., Xie, S. Y., Zhao, L. J., and Feng, Z. X. (2019). Influence of vibration on mixing process of cement stabilized macadam and its performance. *China J. Highway Transp.* 32, 181–190.
- Duan, K. R., Gao, Y. L., Zhou, W. J., Pei, G. P., and He, B. (2020). Mechanical properties of pre-cracked cement-stabilized crushed stone molded by dynamic and static methods. *Mater. Rep.* 34, 10068–10075.
- Feng, Z. X., and Wang, W. Z. (2009). Reinforcement methods of concrete interfacial bond strength. *J. Chang' Univ.* 29, 91–94.
- Han, H. M., and Li, J. (2016). Experimental study on strength properties of cement stabilized aggregate base. *Road Mach. Constr. Mech.* 33, 41–45.
- Liang, S. (2018). *Application Research of Vibratory Mixing Technology in Cement-stabilized Graded Aggregate*. dissertation/master's thesis, Northeast Forestry University, Harbin, HLJ.
- Liu, Q., and Xiong, Y. (2018). Pavement performance of cement stabilized macadam through vibrating mixing. *Road Mach. Constr. Mech.* 35, 74–77.

- Wang, J. W. (2017). *Research on Expansion Cracking of Asphalt Pavement by Cement Stabilized Macadam Base*. dissertation/master's thesis, Chang' an University, Xi'an, SX.
- Wang, Y. L., Zhang, J. B., Wang, X. T., and Zhang, Z. (2020). Laboratory investigation on the performance of cement stabilized recycled aggregate with the vibration mixing process. *Math. Probl. Eng.* 2020, 1–11. doi: 10.1155/2020/6625370
- Xue, S. Q. (2016). *Vibratory Mixing Mechanism and Experimental Study on Improving the Cement Stabilized Macadam Performance*. dissertation/master's thesis, Chang' an University, Xi'an, SX.
- Zhang, H. T., Liang, S., Yang, H. S., and Yu, L. Z. (2018). Study on performance of cement-stabilized crushed stone based on indoor vibration mix. *China J. Highway Transp.* 31, 58–65.
- Zhang, Z. X., and Zhang, L. Q. (2016). Application of vibratory mixing technology in construction of cement-stabilized base course. *Road Mach. Constr. Mech.* 33, 31–36.
- Zhao, K. Y., Zhao, L. J., Liu, S. S., and Hou, J. R. (2018). Effect of three-step mixing technology based on vibratory mixing on properties of high-strength concrete. *IOP Conf. Ser. Mater. Sci. Eng.* 542:1. doi: 10.1088/1757-899X/542/1/012003
- Zhao, L. J., Jiang, W. Z., Hou, J. R., Feng, Z. X., and Xue, S. Q. (2018). Influence of mixing methods on performance of compressive strength for cement stabilized macadam mixture. *China J. Highway Transp.* 31, 151–158.
- Zhao, W., Wang, B., Zhao, L. J., and Feng, Z. X. (2015). Improving concrete strength based on the mixing process. *J. Chang' Univ.* 35, 148–153.
- Zheng, Y. X., Wu, X. L., He, G. X., Shang, Q., Xu, J., and Sun, Y. (2018). Mechanical properties of steel fiber-reinforced concrete by vibratory mixing technology. *Adv. Civil Eng.* 2018:9025715. doi: 10.1155/2018/9025715
- Zhou, J., and Li, J. Y. (2019). Experimental study on vibration test of recycled mixture with cement stabilized macadam. *J. China Foreign Highway* 39, 250–256.

**Conflict of Interest:** JX was employed by the company Guangxi Transportation Science and Technology Group Co., Ltd., Nanning, China.

The remaining authors declare that the research was conducted in the absence of any commercial or financial relationships that could be construed as a potential conflict of interest.

Copyright © 2021 Li, Wei, Zhang, Xiong and Xu. This is an open-access article distributed under the terms of the Creative Commons Attribution License (CC BY). The use, distribution or reproduction in other forums is permitted, provided the original author(s) and the copyright owner(s) are credited and that the original publication in this journal is cited, in accordance with accepted academic practice. No use, distribution or reproduction is permitted which does not comply with these terms.



# Advantages of publishing in Frontiers



## OPEN ACCESS

Articles are free to read  
for greatest visibility  
and readership



## FAST PUBLICATION

Around 90 days  
from submission  
to decision



## HIGH QUALITY PEER-REVIEW

Rigorous, collaborative,  
and constructive  
peer-review



## TRANSPARENT PEER-REVIEW

Editors and reviewers  
acknowledged by name  
on published articles

## Frontiers

Avenue du Tribunal-Fédéral 34  
1005 Lausanne | Switzerland

**Visit us:** [www.frontiersin.org](http://www.frontiersin.org)

**Contact us:** [frontiersin.org/about/contact](http://frontiersin.org/about/contact)



## REPRODUCIBILITY OF RESEARCH

Support open data  
and methods to enhance  
research reproducibility



## DIGITAL PUBLISHING

Articles designed  
for optimal readership  
across devices



## FOLLOW US

@frontiersin



## IMPACT METRICS

Advanced article metrics  
track visibility across  
digital media



## EXTENSIVE PROMOTION

Marketing  
and promotion  
of impactful research



## LOOP RESEARCH NETWORK

Our network  
increases your  
article's readership